InPAC 2023

11th Indian Particle Accelerator Conference

March 13-16, 2023

DAE Convention Centre
Anushaktinagar, Mumbai

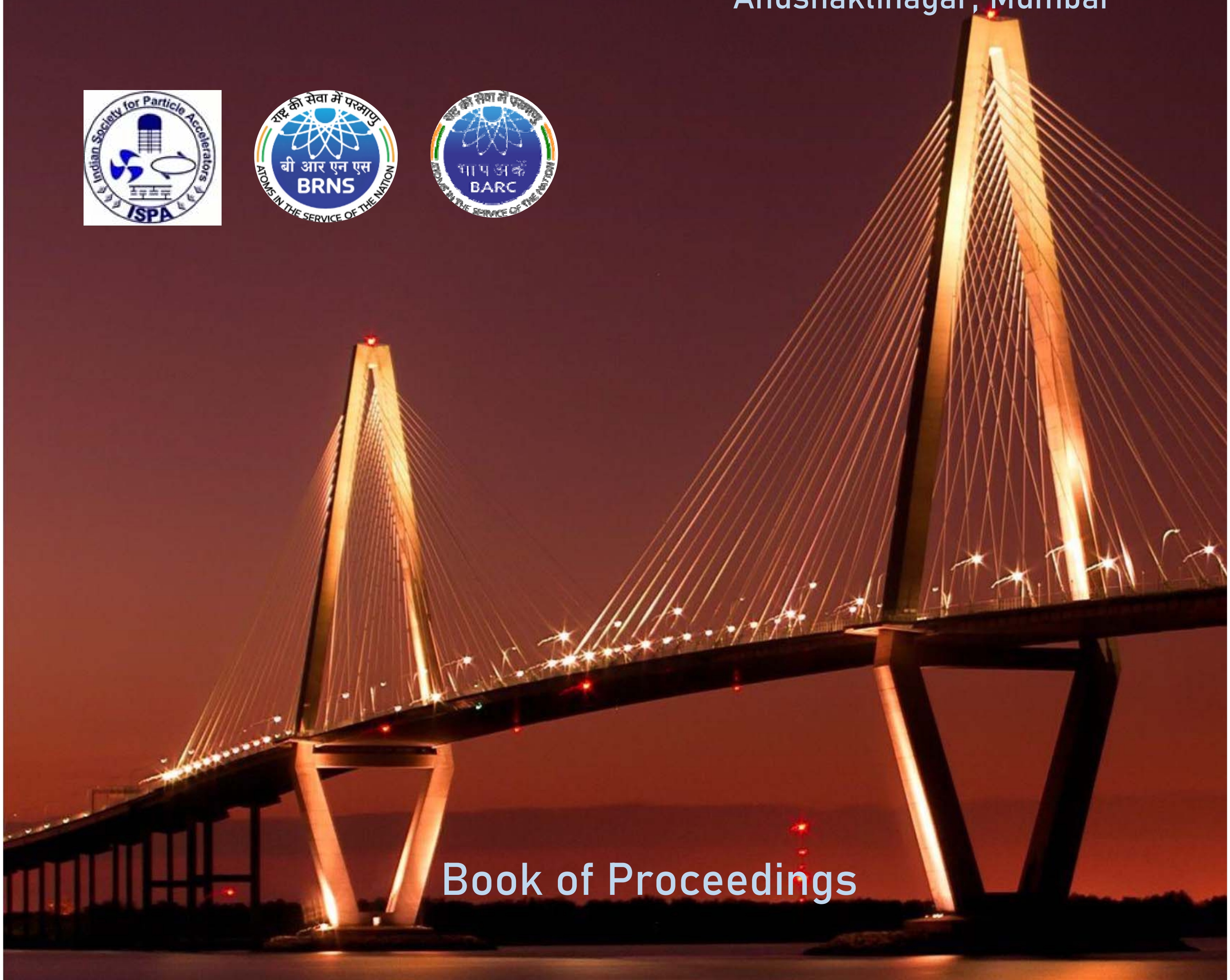

Book of Proceedings

Editors:
S Krishnagopal
Rajesh Kumar
Sista V L S Rao
Jose V Mathew

Contents

34	Ram Prakash	*Dark Current calculation in SRF Elliptic Cavities*
35	Kuldeep Kumar Singh	*Development of Transfer Function Measurement System for Elliptical High Beta Superconducting RF Dressed Cavity*
36	Nitin Nigam	*Design Methodology for Forming Tooling of SCRF cavities*
37	Alok Kumar Gupta	*Power Combining topology for CW 32kW-650 MHz Solid State RF Amplifier (SSPA) installed at Horizontal Test Stand (HTS) facility, RRCAT*
38	Syed Moulali	*Study and Development of Various Dissimilar Metal Joints of Superconducting Radio Frequency cavities*
39	Anurag C	*Thermal Characteristics and Frequency Tuning Methodology for 325 MHz RFQ structure*
40	Kriti Pathak	*RF characterization of 32 kW and 40 kW, 650 MHz Solid State RF Power Amplifiers*
41	Vikas Tiwari	*Design and development of unipotential Electrostatic focusing element for heavy metal ion beam isotopes*
42	Shampa Aich	*Effect of Dy Substitution at Nd Sites in Melt-spun Nd-Fe-B Permanent Magnet Ribbons*
43	Mahima	*Design, development and characterization of three electrode ion beam extraction system for magnetron sputter ion source*
44	Mukesh Kumar Pal	*Study of cumulative beam breakup instability in spoke resonator section of a 1 GeV pulsed H- linac*
45	Shantonu Sahoo	*FPGA based digital I/Q demodulator for LLRF control system at RIB Facility in VECC*
46	Mukesh Kumar Pal	*Development of a computer program for design of diode type electron gun*
47	Vinit Kumar	*A review of calculation of emittance growth for some common cases in accelerator physics*
48	Rinky Dhingra	*Three-dimensional Electromagnetic Simulations of a Constant Gradient Traveling Wave Accelerating Structure Integrated with RF Couplers*
49	Ambar Vohra	*Design and Construction of an ISO Class-4 Cleanroom Facility for SRF Cavity Processing and Assembly*
50	Manish Pathak	*Optimization of Operating Parameters of ECR Proton Source in Pulsed Mode*
51	Janvin Itteera	*Electromagnetic Design of Bending magnets for LBNF beamline*
52	Rohit Mishra	*Remote Control Applications for operation of Hydrogen Negative Ion Source*
53	Kumud	*Development, fringe field optimization & cryogenic qualification of pre-series 6T conduction cooled magnet assemblies for High Intensity Proton accelerators*
54	Tushar Dave	*Design studies for a pill box type accelerating structures with beam ports and coupling loop using analytical and perturbation techniques*
55	Ekansh Mishra	*Auto-configurable Clock Divider for Digital Low-Level Radio Frequency System of Infrared Free Electron Laser*
56	Deepak Kumar Mishra	*Electromagnetic Simulation of 107.5 MHz Co-axial RF Cavity and Its Higher Order Mode identification.*
57	Bhuban Kumar Sahu	*Final Commissioning of the high-power RF system for Conditioning of the RF photocathode gun at higher field gradient*
58	Rajesh Keshwani	*Unscented Kalman Filter as SC cavity detuning estimator*
59	Rajesh Keshwani	*Statistical Methods for assessment of RF amplifier linearization*
60	Shubham Tripathi	*Development of Prototype LLRF System for 18 MeV Cyclotron*
61	Sabyasachi Pathak	*Design, Development & Commissioning of Series Regulator based High Voltage Regulated RF Power Supply for K-130 Room Temperature Cyclotron*
62	T Reghu	*Development of Test stand for Performance Evaluation of High Voltage PFN Capacitors*
63	Balkrishna Arora	*DESIGN AND SIMULATION OF 8-WAY HIGH RF POWER COMBINER AT 75.6MHz*
64	Jitendra Kumar	*Horizontal Test Stand for the Testing of Single Spoke Resonator Superconducting RF Cavities at BARC*
65	Nitesh Mishra	*Design and Development of PLC Based RF Cavity Tuner System for 31.6MHz RF Cavities in Indus complex*
66	Dheeraj Sharma	*Digitally Controlled Precision RF Signal Synthesis for LLRF Applications*

67	Vikash Sahoo	*Multipacting Analysis of the Radio Frequency Cavity for Compact Superconducting Medical Cyclotron*
68	Janardhan Musuku	*Development of Multi-Channel Programmable Trigger Generator for Linac of Electron Beam Radiation Processing Facility*
69	Vikash Sahoo	*Upgradation of Low Level RF System for K500 Super Conducting Cyclotron*
70	Rinky Dhingra	*Development of a Computer Program for Longitudinal Beam Dynamics Studies in a Traveling Wave Constant Impedance Electron Linac*
71	Pallavi Priyadarshini	*Physics design of MEHIPA LEBT for 30 keV proton beam*
72	Pallavi Priyadarshini	*Analogy of particle-core model with a variable-length pendulum*
73	Pallavi Priyadarshini	*Tomographic reconstruction of the phase-space distribution*
74	Rajni Pande	*Coherent and Incoherent Space Charge Resonances in a Drift Tube Linac*
75	Deepak N Mathad	*Development of pulse and event synchronization system for LEHIPA*
76	Rahul Gaur	*Cold test and RF tuning of the first section of 3 MeV, 325 MHz RFQ at RRCAT*
77	Kapil Deo	*Initial Investigations on distribution of absorbed dose in waste water treatment using electron beam*
78	Dr. B V Ramarao	*Experience of Design and Commissioning of High Power Waveguide Systems for LEHIPA*
79	Yashwant Kumar	*Prototype development of four channel 2kV/5A power supply using pulse step modulation technique*
80	Ponagani Bhumeshwar	*Design of FPGA based RF Interlock system and Power Monitoring*
81	Vikas	*Study of the effect of location of laser tracker on alignment uncertainty of components in circular particle accelerators*
82	Dr. B V Ramarao	*Status of Design and Testing of 20 kW solid-state RF Power Amplifier for Buncher Cavity of LEHIPA*
83	B M BARAPATRE	*Integration and Commissioning of 150kV Solid State Pulse Modulator*
84	Ashok Kumar	*Development of Helmholtz Coil based Measurement System for Characterization of Permanent Magnet Blocks*
85	Ashwin Pandey	*Design and development of floating pulse power supply for triode electron gun*
86	Parul	*Numerical studies for evolving measurement methodology for characterization of single cell in constant gradient traveling wave linac*
87	Moonooku Prasad	*Design, Fabrication and Characterization of HOM Damped RF Cavity*
88	Moonooku Prasad	*Design, Development and RF Characterization of Tunable RF Cavity for LLRF Control Systems*
89	ASHISH MAHAWAR	*Design and Development of Pulse 2 kW Solid State amplifiers for Energizing S-Band Pre-Buncher Cavity of 10 MeV, 10 kW LINAC developed at RRCAT*
90	Sachin Rathi	*Installation and commissioning of high voltage DC power supply with electron gun for power testing of photon absorbers*
91	Gautam Sinha	*Design and characterisation of anodised aluminium strip solenoids*
92	Namrata Joshi	*Development of Protocol Converter for C based application and EPICS*
93	Shashikant Suhane	*Processing and Cleanroom Preparation of SCRF Cavities for Performance Testing in VTS Cryostat*
94	Vivek Kumar Srivastava	*Development of Titanium gr-2 Bellows for HB 650 MHz 5-cell SCRF cavities*
95	Abhishek Mitra	*Cryogenic Transfer Line for Cryomodule of e-LINAC at VECC*
96	VIJAYAKUMARV	*EB welding of Helium Vessel Assembly for 650 MHz SCRF Dressed Cavities*
97	Sweta Agarwal	*Prototyping of FPGA Based Timing and Interlock System for ECR Ion Source*
98	B. B. Shrivastava	*Development and Preliminary Evaluation Results of Prototype 100 nm Spatial Resolution Digital Beam Position Monitor Envisaged for High Brilliance Synchrotron Radiation Source*
99	Manitosh Kumar Singh	*Improvement in Indus-2 Coolant Temperature Stability During Beam Energy Ramp up with Flooded Evaporator Type Chiller System*

100	Rishi Pal Yadav	*A Digital Beam Position Indicator Design and Development on VME Platform for Orbit Control Applications in Indus-2*
101	Lakshmikanta Aditya	*Design and Development of NiAlCo Ferrites for High Power Circulator at S-Band*
102	Alok Kumar Ghosh	*Design of Three-electrode BeamEextraction System for ECR Ion source using IBSimu code*
103	Yashwant Kumar	*Design, development and testing of 200V, 1A power supply for grid electrode of RF amplifier tube of MC18 cyclotron*
104	Gaurang Agrawal	*Simulation of feedback control of beam position and an implementation of algorithm for beam focusing in BARC-TIFR Pelletron Accelerator*
105	Sonal Sharma	*High power (30 kW) testing of resonant ring in traveling-wave mode*
106	Elina Mishra	*RF Characterization and Tuning of 11-20 MeV DTL for LEHIPA*
107	Narendra Kumar	*Development and Commissioning of a Thermal Profile Data Logging and Protection Subsystem for Indus-2 RF Cavity*
108	Santhosh Chittimalla	*Study of thermal effects of proton beaminteraction with accelerating structures to derive the response time of fast protection system*
10ф	R T Keshwani	*Kalman Filter as detuning estimator for experimental RF cavity*
1мл	Sonal Sharma	*Thermo-mechanical analysis of MEHIPA couplers*
1м1	Sanjay Kumar Jain	*Control and Instrumentation system of Indigenous LHP100 Helium Liquefier Plant at BARC*
112	Chinnathambi S	*Development of a versatile low temperature irradiation system for radiation damage studies*
1м3	Nair Jayprakash Parameswaran	*Low Flux Heavy Ion irradiation Set up at BARC-TIFR Pelletron Accelerator*

DESIGN, FABRICATION AND TESTING OF FIN TUBE HEAT EXCHANGER FOR 1MV DC ELECTRON BEAM ACCELERATOR

R. Barnwal#, S. R. Ghodke, M. Kumar, S. Nayak, P. C. Saroj, R. I. Bakhtsingh, A. Sharma,
Accelerator and Pulse Power Division, BARC, Trombay, Mumbai, 400085, INDIA

Abstract

Compact fin tube heat exchangers are used in many industrial heat transfer processes where at least one of the fluids is gas, and a large heat transfer area is desired. 1MeV DC electron beam accelerator is being developed in BARC for industrial applications. The high voltage column, electron emitter, and accelerating tubes are assembled inside a pressure vessel at 6 bar nitrogen gas pressure. There is continuous heat generation inside the vessel from high-voltage columns and other electronics. A suitable compact plain fin tube heat exchanger is designed to remove the heat inside the vessel. Process water is used as a coolant in heat exchanger tubes. After formulating the fin tube configurations, the heat transfer capacity, and gas side pressure drop are calculated using suitable heat transfer and friction factor correlations. This design has been validated by CFD modelling of heat exchangers in ANSYS Fluent. The heat exchanger is fabricated with all quality control to make system as per specification. The preliminary testing of the heat exchanger assembly is done in an open atmosphere. Fan capacity, and water flow rate are adjusted to match the design. Water temperatures are kept on the lower side and the rise in air temperature is recorded when passed through the heat exchanger tubes, therefore verifying the heat transfer design. The capacity of the heat exchanger from the CFD model is 4.95 kW which is very close to 4.84 kW capacity calculated by suitable Nusselt number heat transfer correlations [1] and [2]. The pressure drop across the gas side from the model comes to 2.81 Pa, also near the 2.78 Pa calculate from the friction factor and pressure drop correlations [5] and [6].

INTRODUCTION

BARC plans to set up a demonstration plant for wastewater treatment based on a 1 MeV DC electron beam accelerator. Fig.1 shown is the schematic of the DC accelerator housed inside the pressure vessel. The total heat load from HV column, Electron gun and other electronic components is estimated to be about 5 kW. Nitrogen gas at 6 bar pressure is filled inside the vessel to dissipate the heat. The heat exchanger, fan and motor assembly are placed at the top of the assembly inside the vessel, as shown in schematic (Fig 1).

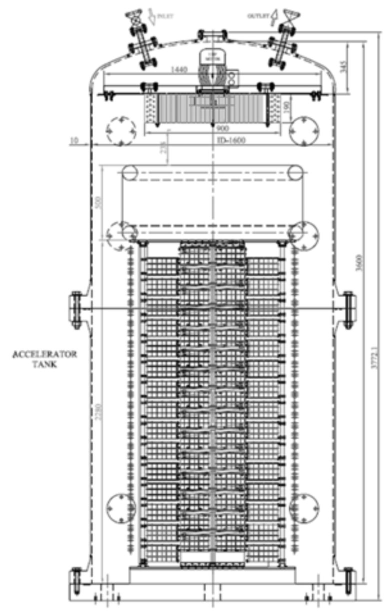

Figure 1: Schematic of DC electron beam accelerator

Selection of heat exchanger and design details

Compact heat exchangers are typically used when a large heat transfer surface area per unit volume is desired and at least one of the fluids is gas. Heat transfer and flow characteristics have been determined for specific configurations of fins tube arrangements. The high-density fins increase the heat transfer area associated with gas flow from the heat exchanger. The centrifugal fan is mounted at the centre, takes gas from the centre opening and discharges radially outward over the fin tubes. On the cold side cold water flows through the heat exchanger tubes.

Table 1: Specification of the heat exchanger

Size of HX assembly	900X900 mm
Depth	190 mm
Tube configuration	6X3 staggered tubes pitch 25mm
Tubes details	Φ12mm, 20SWG, SS304L
Fin details	Al fins size 75X190mm and spacing 2mm
Fan Flow rate	200cfm
Cooled water input	60 lpm at 24^{0}C

#rbarnwal@barc.gov.in

Thermal design and CFD model

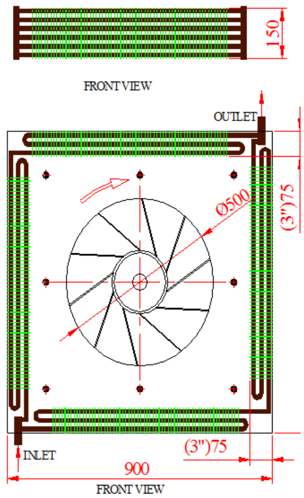

Figure 2: Heat exchanger tubes configuration.

Cold side heat transfer coefficients have been calculated by following Dittus-Boelter correlation for Nusselt number for fully developed pipe flow given in reference [1]:

$$Nu_D = 0.023(Re_D)^{\frac{4}{5}}(Pr)^{0.4} \tag{1}$$

The hot side heat transfer coefficients have been determined by Nusselt number and Colburn j-factor correlation for N≥ 2 plain fin tube heat exchanger given in reference [2] and [3] as

$$Nu = j.Re_{D_C}.Pr^{\frac{1}{3}} \tag{2}$$

$$j = 0.086Re_{D_c}^{P3}N^{P4}\left(\frac{F_p}{D_c}\right)^{P5}\left(\frac{F_p}{D_h}\right)^{P6}\left(\frac{F_p}{X_T}\right)^{-0.93} \tag{3}$$

From this calculation, the overall heat transfer coefficient is evaluated. Effectiveness NTU (ε method is used for calculating the heat transfer capacity of this type of heat exchanger as given in reference [4]

$$\varepsilon = \frac{1}{C}\left[1 - e^{-3KC}\left(1 + CK^2(3-K) + \frac{3(C)^2K^4}{2}\right)\right] \tag{4}$$

Pressure drops have been determined using the friction factor correlation for plain fin tube heat exchanger as per equations 5 and 6.

$$f = 0.0267Re_{D_c}^{F1}\left(\frac{X_T}{X_L}\right)^{F2}\left(\frac{F_p}{D_c}\right)^{F3} \tag{5}$$

$$\Delta P = \frac{G_c^2}{2\rho_i}\left[(1+\sigma^2)\left(\frac{\rho_i}{\rho_o} - 1\right) + \frac{fA_o}{A_c}\frac{\rho_i}{\rho_m}\right] \tag{6}$$

This design of a plain fin tube heat exchanger has been validated through the CFD model in ANSYS Fluent. Only a sector of fin tube geometry is modeled because of symmetric nature of the flow. Symmetry conditions are also considered on the mid plane between two fins. Boundary layer mesh is incorporated around the tube wall.

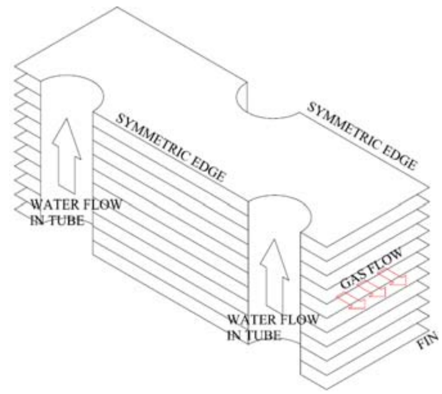

Figure 3: CFD heat exchanger gas flow model description.

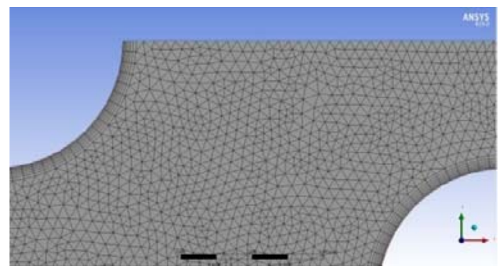

Figure 4: Boundary layer mesh around tube face.

Nitrogen gas at 6 bar pressure is used in the model. At the upstream boundary (inlet), uniform flow with constant velocity and constant temperature are taken based on the design flow rate from fan and gas temperature. At the downstream end of the computational domain (outlet), stream wise gradient (Neumann boundary conditions) for all the variables is set to zero. The no-slip boundary condition is used at the fins and the tube surfaces. Among various turbulent models available, k-ω model is used, which showed the best model convergence and closed matching with the numerical calculations. The cold side tube walls are imposed with heat transfer coefficients at the water inlet temperature based on the numerical calculation obtained in equation (1). The model is solved for continuity, momentum, and energy equations in ANSYS Fluent CFD solver.

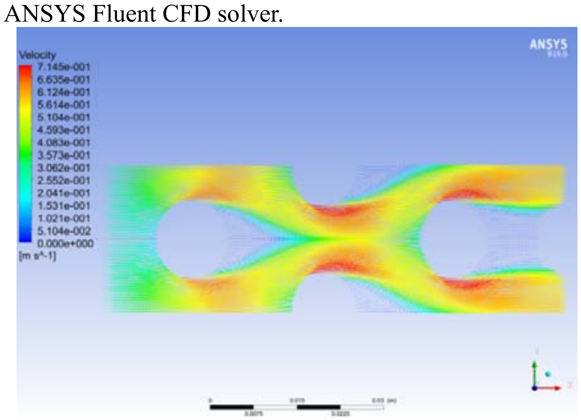

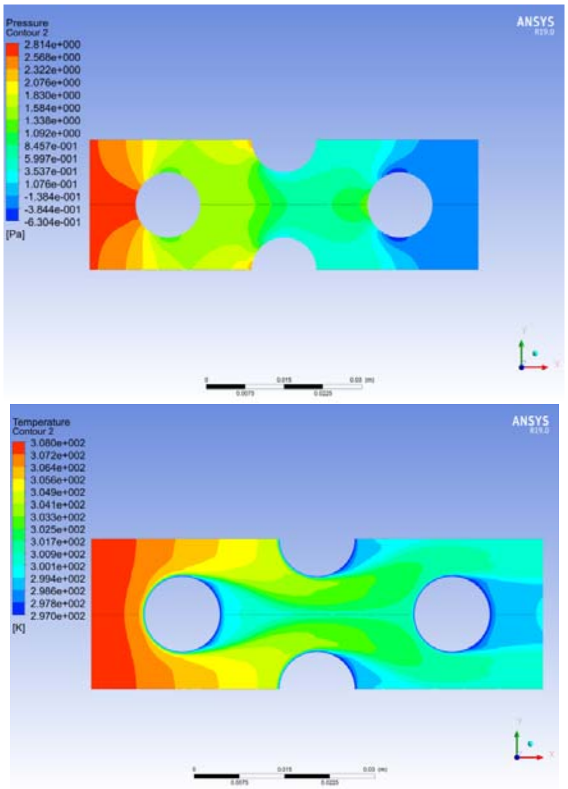

Figure 4: Velocity, pressure and temperature distribution in heat exchanger

Fabrication, quality control and preliminary testing

The heat exchanger was locally developed. Thw materials of the tubes are SS304L, and all tube joints are made by TIG welding with suitable electrodes and fillers. The final integrity of the heat exchanger tube assembly is tested by pneumatic test at 10 bar pressure. The helium leak test by mass spectrometer leak detection in sniffer mode ensures a leak rate of 7.2 $x10^{-6}$ mbar l/s. After the fabrication of the heat exchanger, it is assembled with a fan and motor. The trial run test of the fan is conducted and the fan, motor performance is checked.

Figure 5: Heat exchanger, fan and motor assembly.

Figure 6: Fan air flow velocity measurement

Results and discussion

Table 2: Results summary

	From correlation	**CFD model**
Capacity(Q)	4.84 kW	4.95 kW
Temperature drop gas side	7.63K	7.81K
Pressure drop across heat exchanger	2.785 Pascal	2.814 Pascal

Plain fin tube heat exchanger capacity calculation by effectiveness NTU method and correlation provided for Colburn j-factor and Nusselt number found to be in line with the CFD model. Pressure drop and friction factor correlation across heat exchangers is also validated with the CFD model, and results show a reasonable proximity. Fan capacity is also measured and related to half of its motor RPM using variable frequency drive to get the desired design flow. The Adequacy of motor power at desired flow in nitrogen at 6 bar pressure is also verified.

Acknowledgements

The authors are thankful to the entire DC accelerator team for their motivation and helps during this work.

REFERENCES

[1] Chi-Chuan Wang, Kuan-Yu Chi, Chun-Jung Chang, Heat transfer and friction characteristics of plain fin-and-tube heat exchangers, part II: Correlation, International Journal of Heat and Mass Transfer 43 (2000) 2693-2700.

[2] Chi-Chuan Wang, Kuan-Yu Chi, Heat transfer and friction characteristics of plain fin-and-tube heat exchangers, part I: new experimental data, International Journal of Heat and Mass Transfer 43 (2000) 2681-2691

RESIDUAL STRESS DISTRIBUTION IN TITANIUM ALUMINA BRAZING JOINT WITH EFFECTS OF THERMAL CYCLES IN ACCELERATING TUBE OF DC ACCELERATOR

Ajit Singh[1#], R. Barnwal[1], S. Nayak[1], M. Kumar[1], Kumar Sajal[1], S. R. Ghodke[1], P. C. Saroj[1], R. I. Bhaktsingh[1], and Archana Sharma[1]

[1]Accelerator & Pulse Power Division, BARC, Mumbai

ABSTRACT

A 1 MeV 100 kW electron beam DC accelerator has been designed and developed for waste water treatment at EBC, Kharghar. Accelerating tubes are an inevitable requirement items in beamline assembly for the high energy electron beam production. These tubes consist of ceramic rings which are bonded with titanium electrodes for generation of high potential difference electric field in beamline and to accelerate the electron beam. In fabrication of accelerating tubes brazing process is required for joining two base dissimilar materials, i.e. alumina and titanium. These materials express different response to thermo-mechanical conditions during heating and cooling phases of brazing process. Due to different coefficient of thermal expansion (CTE) of ceramic and titanium, induced residual stresses are developed during brazing process. Such residual stresses can lead failure in brazing joints of accelerating tubes before design limits if not addressed properly. The failure of brazing joint leads to vacuum breakdown in beamline which can cause to severe damage to high voltage components of accelerator. The purpose of study is to assess residual stresses with effect of thermal cycles by performing thermo-mechanical analysis of brazing process in ceramic titanium assembly through finite element analysis (FEA) technique.

INTRODUCTION

Modern ceramic materials are more and more widely used in the manufacturing industry with the rapid development of science and technology. Superior mechanical properties, corrosion resistance, thermal stability, electronic insulation, relatively low manufacturing cost and chemical inertness of Al_2O_3 ceramic has potential applications in electron beam accelerator, aerospace, nuclear, automotive, biomedical and tool industries for years [1-3]. In the electron beam DC accelerators cylindrical shaped accelerating tubes are used for high voltage development in beam line. These tubes have many metal-ceramic joints as shown in Fig.1 and brazing is applied to join dissimilar materials by heating up to melting point of the filler metal in order to ensure that the molten filler flows via capillary action between the two mating surfaces inside furnace. The difference in thermal and mechanical properties leads to generation of thermal stresses near ceramic-metal interface during fabrication and application of accelerating tubes [4-5]. This phenomenon can deteriorate the strength of brazed Al_2O_3-metal joint. In this particular brazing process, alloying would occur by the diffusion of the molten brazing filler with the mating materials to form a metallurgical bond [6]. A true understanding of deformation behaviour of metal-ceramic brazed joint in tubes and its dependence on brazing thermal cycles inside vacuum furnace are highly necessary. In this study, we have attempted to carry out the Finite Element Analysis of Alumina-Titanium brazed joint of accelerating tubes using CuSil filler (50 µm thick foil) to investigate residual stresses distribution in joint under brazing thermal conditions by ANSYS software.

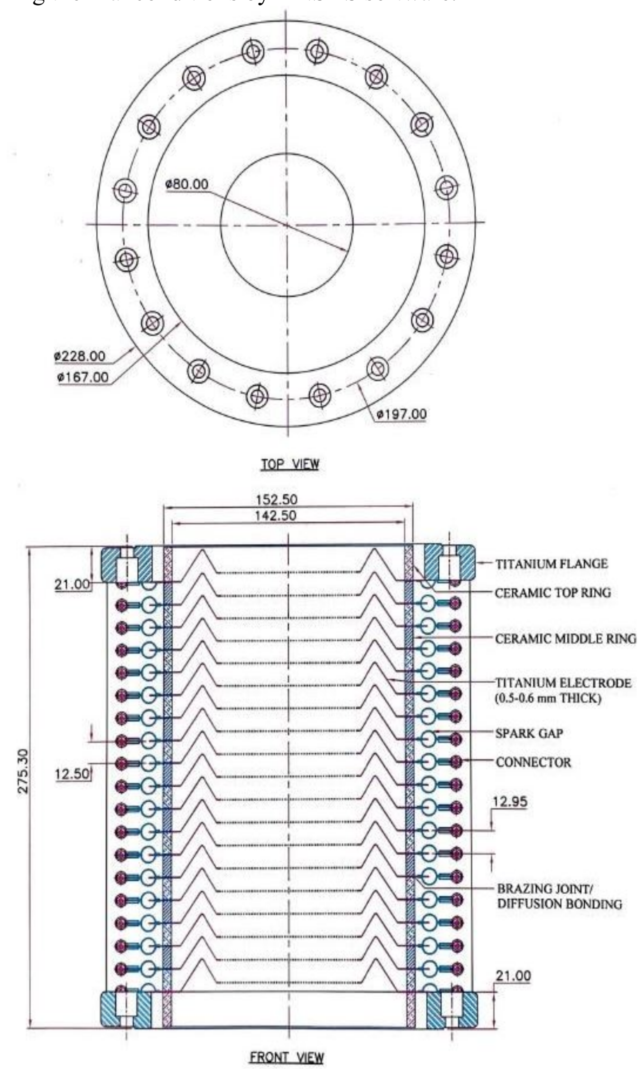

Figure 1: Accelerator tube assembly

#ajitsingh@barc.gov.in

MODEL DESCRIPTION

Brazing is a transient heat transfer process which mainly involves the coupling of stress and temperature field. Continuum models are considered for calculation of residual stress that is developed in Al_2O_3-titanium joint, when brazed and then cooled down to room temperature. In order to be closer to the FEM simulation of brazing process, perfectly elastic model is adopted in current simulations. A sandwich structure containing titanium ring in between two ceramics rings with CuSil fillers (50 µm thickness) at joints, is designed as per accelerating tube dimensions mentioned in Fig.1 for brazing joint simulation, which results in the non-linearity of geometry and material properties in our model. 3D model used in simulations with symmetric boundary conditions is shown in Fig. 2. A model with symmetric boundary conditions requires 1/4th part of complete assembly of aluminium-titanium rings and less time for transient simulation. Dissimilar materials are assumed to be perfectly bonded at the interfaces. Numerical solutions are obtained employing finite element method in Ansys Workbench 15.0 to solve partial differential equations [7]. In a coupled temperature – displacement finite element model, total strain increment at a material point from t → t + Δt can be expressed as

$$\Delta\varepsilon_{ij} = \Delta\varepsilon_{ij}^{e} + \Delta\varepsilon_{ij}^{th}$$

Ansys calculates thermal expansion as follows:

$$\varepsilon_{ij}^{th} = \alpha\Delta T$$

Where, ε_{ij}^{th} is thermal strain tensor

α is coefficient of thermal expansion

ΔT is temperature variation

The elastic part obeys Hooke's law and reads as follows:

$$\dot{\varepsilon}_{ij}^{e} = C_{ijkl}\dot{\sigma}_{kl}\,,\; C_{ijkl} = \frac{1+\upsilon}{E}\left(\delta_{ik}\delta_{jl} - \frac{\upsilon}{1+\upsilon}\delta_{ij}\delta_{kl}\right)$$

where C_{ijkl} is the elastic stiffness matrix, ε_{ij}^{e} is the elastic strain tensor, σ_{ij} is the stress tensor and a dot denotes the differentiation with respect to the time, E is Young's modulus, υ is Poisson's ratio, and δ_{ij} is Kronecker's delta.

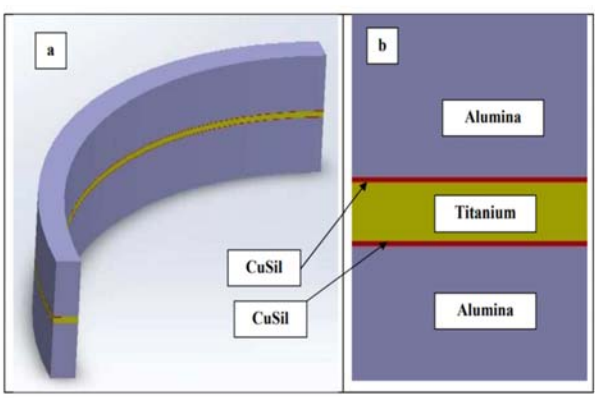

Figure 2: Geometry construction (a) Alumina titanium annulus ring (1/4th part) (b) Magnified portion showing CuSil fillers

Quadrilateral elements are considered in meshing for all the simulations. The size of the mesh determines the simulation time of the program. After fine meshing requisite boundary condition are applied for carrying out the analysis.

Material properties considered for the simulations are given in Table 1.

Table 1: Properties of Alumina, Titanium and CuSil Filler

S. No.	Properties of material	Alumina	Titanium	CuSil
1	Young's Modulus (GPa)	300	96	83
2	Poisson's Ratio	0.22	0.36	0.36
3	Density (g/cm^3)	3.65	4.6	10
4	CTE (1/^{o}C)	7e-6	9.4e-6	18e-6
5	Thermal conductivity (W/m^{o}C)	19	17	370
6	Specific heat (J/kg^{o}C)	880	523	280

THERMAL CONDITIONS USED IN SIMULATIONS

For carrying out thermal analysis a heating rate of 5 ^{O}C/min is applied to the outer surface of all the components of assembly in range of 30^{o}C-780^{o}C, with a holding time of 10 minutes at 780^{o}C subsequently cooling the whole assembly back to 30^{o}C. The optimized cooling and heating rates have been chosen on the basis of various literature reviews. To study the effects of thermal cycles on residual stresses in brazing process of alumina-titanium joint four sets of simulations are carried out as per different thermal cycle conditions.

Table 2: Brazing Parameters used in Finite Element Analysis.

Brazing temperature (in ^{o}C)	Holding time (in min.)	Heating/Cooling rate (in ^{o}C/min)
780	10	5

Simulation number 1: No thermal cycle, thermal condition is shown in Fig. 3.

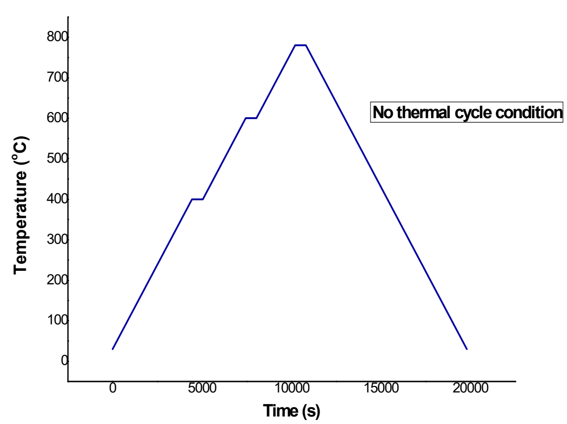

Figure 3: Thermal condition in simulation number 1 (No thermal cycle)

Simulation number 2: 3 thermal cycles, thermal condition is shown in Fig. 4.

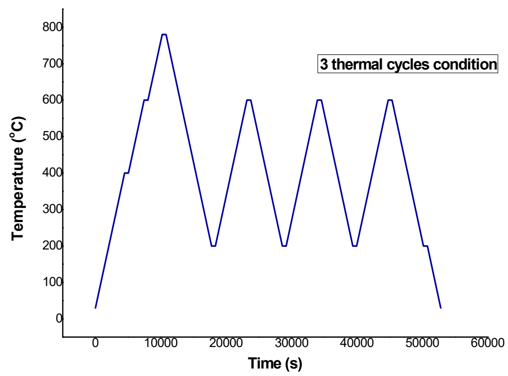

Figure 4: Thermal condition in simulation number 2 (3 thermal cycles)

Simulation number 3: 6 thermal cycles, thermal condition is shown in Fig. 5.

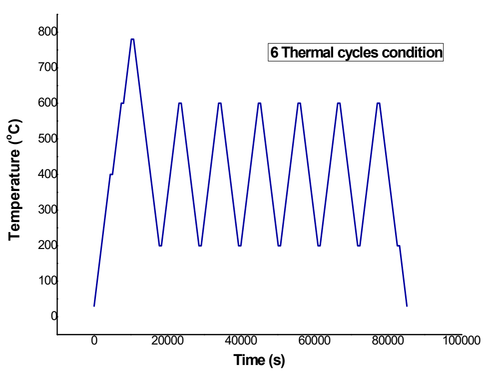

Figure 5: Thermal condition in simulation number 3 (6 thermal cycles)

Simulation number 4: 10 thermal cycles, thermal condition is shown in Fig. 6.

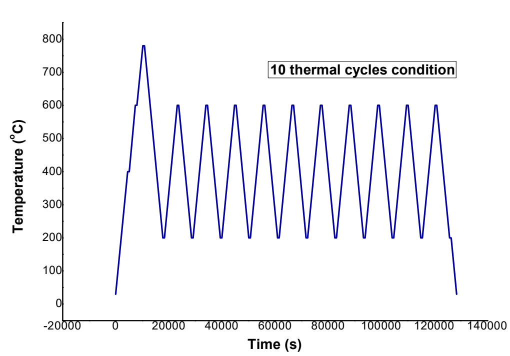

Figure 6: Thermal condition in simulation number 4 (10 thermal cycles)

SIMULATION DETAILS WITH RESULTS

Problem Setup in ANSYS

For the simulation, the cylindrical butt joint of Alumina, Titanium, and brazing alloy (CuSil) is used, as illustrated in Fig. 2. Due to symmetrical geometry, a 3D model with symmetrical boundary conditions is created in ANSYS. To capture the stresses, brazing alloy, 50 microns thickness, sandwiched between Alumina and Titanium disks is modeled. The conditions of symmetrical boundary conditions ensure a very less number of mesh elements, and so the calculation time, without compromising the accuracy or calculation efficiency by the software, as compared to the complete 3D model.

Meshing of Finite Element (FE) Model

Mesh is composed of quadrilateral elements. Biasing is given to the mesh to have high mesh density of elements at the interface location to capture the details of the thin braze alloy layer (which is merely 50 µm thick). As the analysis is performed for the cooling and heating cycles, the contacts between Titanium, the braze alloy, and Alumina are considered bonded with the elastic behavior of the brazing alloy.

Analysis Settings, Assumptions and Loads

The implemented simulation methodology consists of steady sate heating and cooling load step approach (e.g. ambient → 780°C, heating; 780°C → ambient, cooling), as per thermal conditions in simulations. The zero strain temperature for the FEA is assigned at ambient temperature. This assignment of boundary condition ensures no residual strain would be present in the brazed joint during the start of heating during brazing process. The assembly is then allowed to heat isothermally to 780°C then cool down to room temperature. The isothermal approximation can be discerned as the assembly is having high thermal diffusivity and small size. As the brazing material causes non-linearity in the analysis, therefore non-linearity attributes are used for the solution.

FEA Results

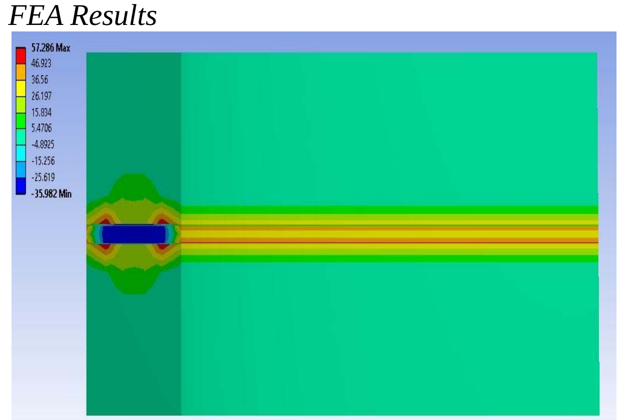

Figure 7: Residual stresses (MPa) distribution when no thermal cycle given during brazing process

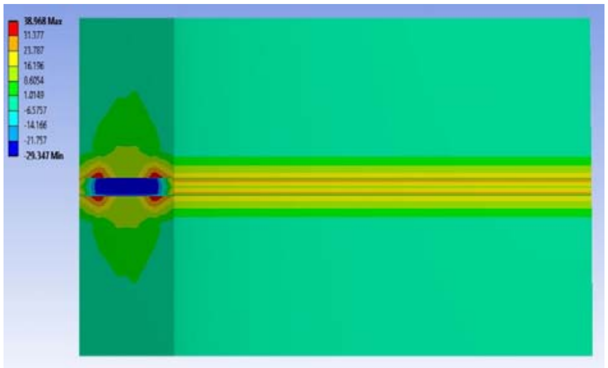

Figure 8: Residual stresses (MPa) distribution when 3 thermal cycles given during brazing process

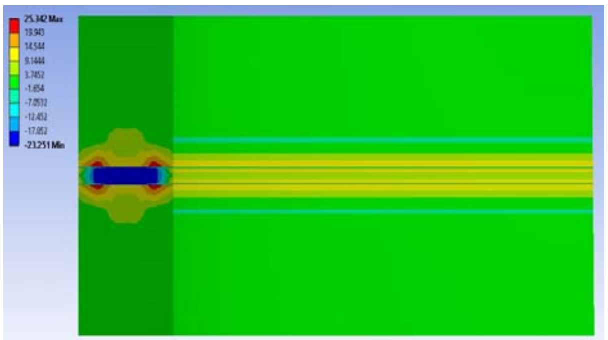

Figure 9: Residual stresses (MPa) distribution when 6 thermal cycles given during brazing process

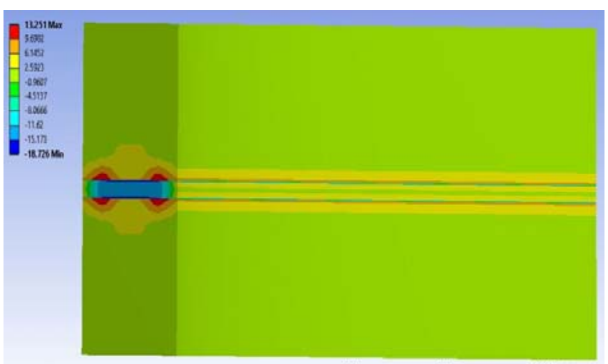

Figure 10: Residual stresses (MPa) distribution when 10 thermal cycles given during brazing process

CONCLUSION

The accelerating tube ceramic to titanium brazing joint was analyzed at different thermal conditions by finite element method. The maximum tensile and compressive stresses were observed in simulations at brazing joint by considering 5°C cooling and heating rates. The effects of number of thermal cycles on induced residual stresses have been shown in simulation results. As we increase number of thermal cycles on brazing joint it leads to decrease in stresses at joint due to redistribution of stresses during brazing process. Minimum 5 to 10 thermal cycles should be used in brazing process to reduce residual stresses. Lower the residual stresses in brazing joint enhance the reliability of accelerating tube during operation of accelerator.

Table 3: Results summary

Simulation number	Number of thermal cycles	Max. tensile stress at brazing joint (MPa)	Max. compressive stress at brazing joint (MPa)
1	0	57.28	35.98
2	3	38.96	29.34
3	6	25.34	23.25
4	10	13.25	18.72

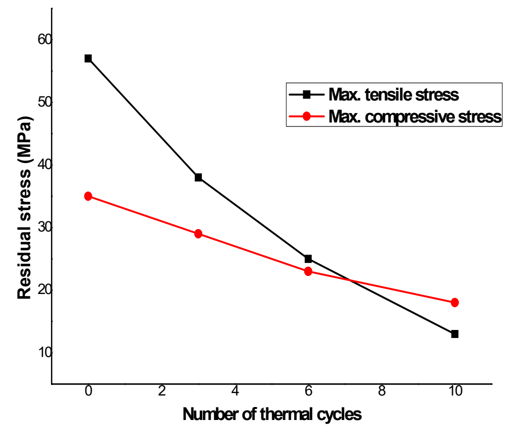

Figure 11: Effects of thermal cycles on residual stress induced at brazing joint

REFERENCES

1. Huang, Y.H.; Jiang, D.L.; Zhang, X.F. Enhancing toughness and strength of SiC ceramics with reduced graphene oxide by HP sintering. J. Eur. Ceram. Soc. **2018**, 38, 4329–4337.
2. Yu, Y.; Dong, H.Y.; Ma, B. Effect of different filler materials on the microstructure and mechanical properties of SiC/SiC joints joined by spark plasma sintering. J. Alloy. Compd. **2017**, 708, 373–379.
3. Katoh, Y.; Snead, L.L.; Henager, C.H. Current status and recent research achievements in SiC/SiC composites. J. Nucl. Mater. **2014**, 455, 387–397.
4. Zhao B, Jiang G, Qi H. Joining aluminum sheets with conductive ceramic films by ultrasonic nano welding. Ceram.Int (2016);42:8098-101.
5. Xin C, Liu W, Li N, Yan J, Shi S. Metallization of Al2O3 ceramic by magnetron sputtering Ti/Mo bilayer thin films for robust brazing to Kovar alloy. Ceram.Int92016);42:9599-604.
6. Humpston G, Jacobson DM (1993) Principles of soldering and brazing. ASM International, USA.
7. Ansys workbench/transient solver.

Thermal Analysis of Beam Locating Aperture for Beam Diagnostics in Electron Beam DC Accelerator

Ajit Singh[1], R. Barnwal[1], S. Nayak[1], M. Kumar[1], Kumar Sajal[1], S. R. Ghodke[1], P. C. Saroj[1], R. I. Bhaktsingh[1], and Archana Sharma[1]

[1]Accelerator & Pulse Power Division, BARC, Mumbai

ABSTRACT

A beam locating aperture (BLA) is an essential non-destructive diagnostics part of electron beam DC accelerator which provides information about the beam size and its misalignment in beamline. It is composed of SS and copper brazed parts with recommended aperture size for Gaussian profile beam. It also has 6 numbers of equally spaced thermocouples in 360^0 to sense position of beam by measuring temperature. There is a water convective cooling channel to control the temperature of BLA. The purpose of this study is to find out temperature distribution in BLA at different positions (offset values) of beam in beamline using finite element methods (FEM) simulations. The temperature distribution profile in BLA helps in determining the position, path deviation and misalignment of beam. In fabrication of BLA brazing joint is required for joining SS and copper. Due to hitting of beam during misalignment problem of beam, the higher temperature on BLA can lead failure in brazing joint of BLA. This problem can lead to vacuum breakdown in beamline and severe damage to high voltage components of accelerator. The purpose of study is to assess temperature distribution in BLA using FEM simulations at optimum water flow rate in cooling channel.

INTRODUCTION

Electron linear DC accelerators (1MeV, 100 kW) can be used for waste water treatment in commercial industries. Efficient irradiation of the waste water can be ensured only if the electron beam is guided precisely and the required dosage profile is thereby applied. As the beam passes through the accelerating vacuum tubes, it is accelerated by electromagnetic fields that depend on the beam position and geometry. The beam trajectory may be deflected from the beamline center due to a variety of reasons [1]. That is why having a beam position monitoring system is highly needed in accelerators. The size and alignment of the electron beam can be checked by BLA as full accelerated beam passes through it and then corrected by means of magnets [2]. It is a non-destructive diagnostics used most frequently in electron beam accelerators. The beam locations are detected by a number of resistance temperature detector (RTD) sensors around the BLA device. The beam should be ideally located at the beamline center. To assure proper positioning and alignment of the beam, the beam position should be monitored continuously in real time. A BLA normally provides information about the beam size and alignment position by using RTD sensors. In most DC accelerators, BLA assembly consists of 6 numbers of RTDs which are equally spaced *360^0*. The beam position is achieved by comparing the picked up temperatures of each RTD [3]. The beam position is determined from the relative measured values of temperatures by RTDs. If the beam is exactly located in the center of the beamline, the temperature distribution on the BLA is exactly uniform, so the pickup temperatures of the RTDs are the same. The misalignment in beam can cause hitting of beam to accelerator components in beamline which can be damaged due to local heat deposition. Degassing rate will be increased due to hitting of beam to any metal surface in beamline which can degrade vacuum condition and machine will be tripped in that case. The study of thermal analysis of BLA for beam diagnostics and its incorporation in beamline assembly is essential to quantify beam alignment and its size.

BLA DESIGN AND FABRICATION

BLA assembled in DC accelerator was designed and fabricated into a zero length conflate SS flange [4]. It consists of SS and copper brazed parts with 52 mm beam aperture size at center of copper part for electron beam. The BLA has 6 thermocouples which are equally spaced in 360^0. Six equi-spaced slots are also provided in copper part of BLA assembly to enhance the sensitivity of device and to define local area temperature for each RTD. There is a water cooling channel (6 mm × 6 mm) to control the temperature of BLA as shown in figure 1. The following configuration of BLA produces a compact beam diagnostics inside accelerator.

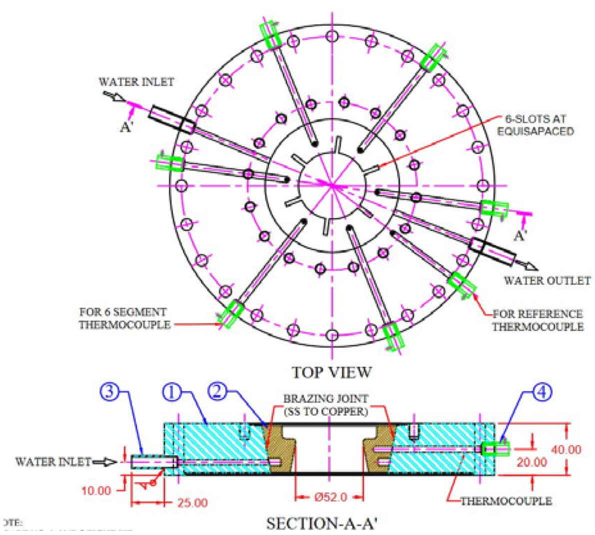

Fig.1. BLA drawing assembly

Fig.2. Fabricated BLA assembly

BEAM PROFILE AND HEAT LOAD

The electron beam has Gaussian beam profile which has high flux density at center and decrease exponentially in radial direction. The heat flux distribution in beam profile follows full width at half maximum (FWHM) as shown in figure 3. The beam size is considered as 30 mm for 1 MeV at 30 kW power and is represented as per equation 1.

$$q = Ke^{-cx^2} \quad \textbf{(1)}$$

q = heat flux (W/m^2)
K = constant (W/m^2)
c = constant (m^{-2})
x = radial distance in beam profile (m)

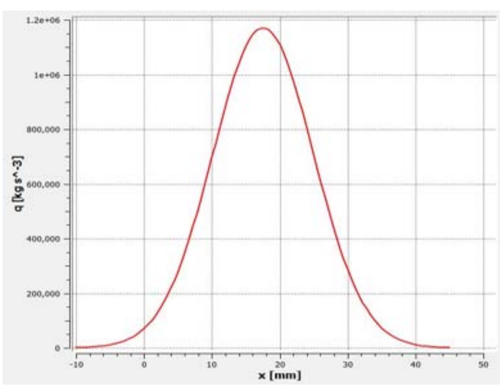

Fig.3. Heat flux distribution in radial direction of BLA

THERMAL MODELING AND FEM RESULTS

A 3-D model of BLA assembly was designed in computer aided design (CAD) software as per drawing in figure 1. For the heat transfer coefficient calculation, Dittus – Boelter correlation was used and given in equation 2 [6].

$$\mathbf{Nu = 0.023Re^{0.8}Pr^{0.4}} \quad \textbf{(2)}$$

Nu = Nusselt number, Re = Reynolds number, Pr = Prandtl number

From above equation heat transfer coefficient for SS part channel at 5 lpm measured flow rate in BLA for convective cooling, h_{SS} = 12452 W/m^2K and heat transfer coefficient in copper part channel, h_{Cu} = 7152 W/m^2K

A user defined heat flux function was used according to equation 1 for considering heat load input in BLA. FEM simulations were completed at different beam offset values (0 – 8 mm) from beamline center [5].

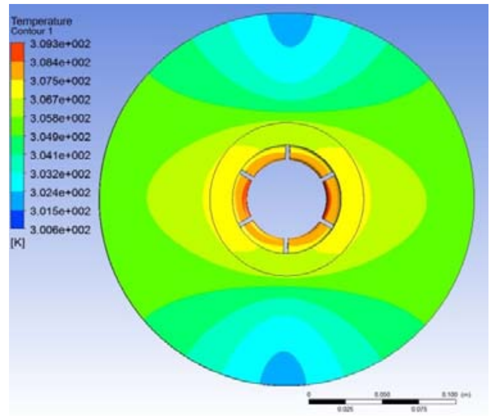

Fig.4. Temperature distribution in BLA (0 mm beam offset)

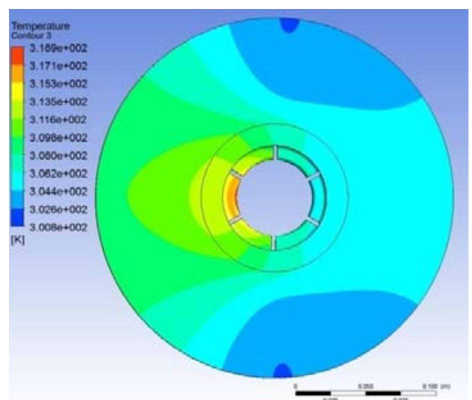

Fig.5. Temperature distribution in BLA (2 mm beam offset)

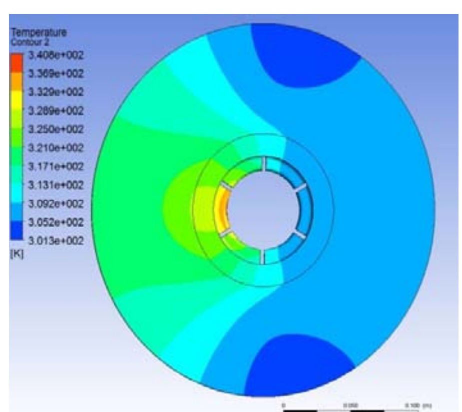

Fig.6. Temperature distribution in BLA (4 mm beam offset)

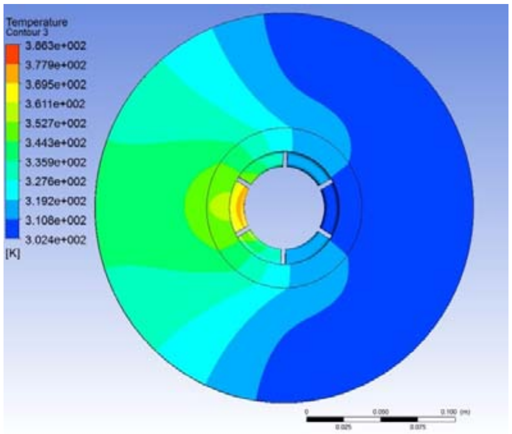

Fig.7. Temperature distribution in BLA (6 mm beam offset)

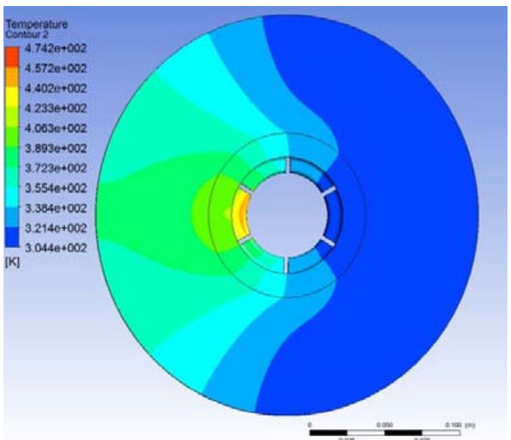

Fig.8. Temperature distribution in BLA (8 mm beam offset)

RESULTS AND DISCUSSION

A BLA assembly has been successfully fabricated with forced convective cooling as per drawing shown in figure 1. Maximum temperature in BLA was observed in simulations at beam offset in range of (0 – 8 mm) from its center as shown in table 1. As the beam offset or misalignment of beam occurs temperature on brazing joint also increases which can cause to joint failure. It is being used as a beam diagnostics device in DC accelerator at EBC Kharghar. The actual temperature measurement in BLA has been done during operation of accelerator and is shown in figure 9.

Table 1. Simulation results

Beam power	Beam offset (mm)	Flow rate (lpm)	BLA max. temperature (°C)
30 kW	0	5	36
	2		45
	4		67
	6		113
	8		201

Fig.9. Temperature measurement in BLA during misalignment of beam

REFERENCES

[1] V.N.Boriskin, "**Monitoring and Visualization of Electrons Beam Parameters in Industrial Linacs**", Proceedings of ICALEPCS2003, Gyeongju, Korea.

[2] Stefan Trummer, "**Beam position monitor for electron linear accelerator**", Germany.

[3] Artem Kuskov, "**Beam position monitoring system in accelerators**", Department of Electrical and Information Technology Lund University, Lund, Sweden",

[4] Artem Kuskov, "**Characterization of a Beam Position Monitor for Linear Accelerators**", B.S., University of New Mexico, 2014.

[5] Ansys workbench/transient solver.

[6] **Heat transfer** by JP Holman, McGraw Hill Publication.

E-mail: ajitsingh@barc.gov.in

DEVELOPMENT OF A PROTOTYPE INDUCTION HEATING SYSTEM FOR SOLID AND METAL ION BEAM GENERATION IN ECR ION SOURCES*

Mou Chatterjee[1#], Sumitra Majhi[2], Kishore Rana[3], Dipak Verma[4], P.Y. Nabhiraj[5], Arup Bandopadhayay[6]

[1,2,3,4,5,6] Variable Energy Cyclotron Centre. Department of Atomic Energy, Kolkata, India

Abstract

Recently in VECC, metal ion beam was generated and delivered from one of the two 14.45GHz ECR ion sources using MIVOC facility and has been successfully accelerated by K130, room temperature cyclotron. Although being a simple method, MIVOC has several disadvantages like contaminating the ECR chamber and poor transport efficiency. To overcome these problems, a prototype induction heating system along with temperature monitoring facility has been developed to explore the possibilities of solid and low melting point metal ion beam generation in ECR. This method is a cleaner, efficient and alternative technique to MIVOC. Here, a ZVS, parallel resonant type inverter generating 250 kHz frequency has been designed and developed for this purpose along with a thermocouple-based temperature monitoring system which monitors the workpiece temperature. The sample metal or solid is taken in a ceramic crucible which is placed inside a cylindrical shaped, hollow iron work piece. Successful in vacuum experiments have been carried out in prototype arrangement for different metal sample evaporation. Mg, Bi, Zn. Pb, Ag and Cu are the few metals which have been evaporated. The efficiency of the system is found out to be around 78%. This paper describes the development, vacuum evaporation and performance analysis of the system developed.

INTRODUCTION

In Variable Energy Cyclotron Centre (VECC), there are two 14.45GHz Electron Cyclotron Resonance (ECR) Ion Sources. Recently one of these sources has successfully generated metal ion beam using MIVOC (Metal Ions from Volatile Compound) technique. Although being a simple method, this technique has few drawbacks like it contaminates the plasma chamber and entire cleaning is required to restore the performance of the system. Moreover, other atoms, mostly carbon and hydrogen are present as the contamination in the metal beam generated if a metallocene compound is chosen. Other alternative to the MIVOC method is the resistive oven. Advantages of using inductive oven over a resistive one is, less current requirement in the coil, non-contact heating of the sample, and concentrated heating on the sample surface whereas resistive heating may cause oxidation of the coil hence making the oven unfit for reuse and leading to lesser efficiency of the system. As an efficient and cleaner alternative, development and exploration of a prototype induction oven system is taken up. Similar kind of work has been reported in [1][2][3][4].

A half bridge, ZVS resonant inverter has been developed to be used as the driver circuit for the induction heater. This is a self-resonant, push pull type oscillator. IRF540 MOSFETs are used as the switching elements. A cylindrical iron work piece is fabricated in house to accommodate a ceramic crucible inside it where the metal sample is kept for heating. A cold junction compensated thermocouple-based temperature monitoring system has also been developed and incorporated to measure the temperature of the work piece as reported in [5].

Evaporation experiment has been carried out inside a prototype vacuum chamber and evaporated metal vapour was allowed to deposit on a glass surface in front of the heater assembly inside the chamber. The result obtained was recorded for performance analysis of the system.

DRIVER CIRCUIT

Circuit Description

This is simple half bridge self-resonant circuit where two MOSFETs are used as switching devices. The switches are turned ON/OFF alternately to generate square wave output. The primary coil of a centre tapped (6+6) transformer (L=1.12uH) forms the resonance tank circuit along with a capacitor of 330nF/1000V. Illinois make polypropylene capacitor is used for better performance. The voltage across the transformer primary is a sine wave of frequency determined by the L and C of the tank circuit.

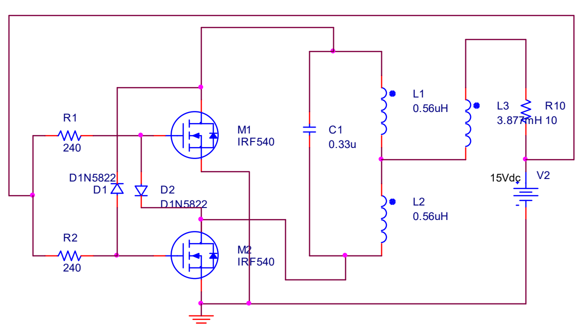

Figure 1: Driver circuit of the Induction heater.

Connecting a choke L1 of 3.8mH in series with the power supply prevents the oscillator circuit from drawing huge current and removes any current spike. The resistance

*Work supported by … VECC/DAE

#mou@vecc.gov.in

R1 and R2 limits the overdrive to the gates and Diodes D1 and D2 ensures that the voltage at the gates is at ground potential when the voltage on the opposite legs of the tank is at ground potential. The circuit diagram of the driver is shown in Fig 1.

Circuit Operation

When power is applied, oscillation starts and switches are turned on and off alternately generating a square wave. Heat sinks are used with the switches to avoid damage due to overheating. The voltage across the transformer primary as shown in Fig 1, which works as the work coil, is a sine wave. The values of L and C of the tank circuit and the number of turns of L are optimised to be accommodated inside the plasma chamber which resulted in a frequency of 250KHz. The tank is tuned to the resonant frequency for full power. Pspice simulation has been carried out to optimise the component values to estimate the power dissipation across the components. While simulated voltage across the work coil was 40V, actual in the circuit is 53.6V. The practical circuit resonated at a frequency of 214KHz.The variation of actual result from the simulated one can be justified due to the tolerances in the component values and the significant stray parameters in that high frequency.

Work Coil and Workpiece design

The work coil of the induction heater is fabricated with solid copper wire of 2mm diameter. The coil is of 12 turns, centre tapped, air core one with an inner diameter of 14mm and outer diameter of 18mm. The workpiece is fabricated from a cylindrical iron tube of 50mm length, 7mm inner diameter and 8.5mm outer diameter. One side of the tube is open and the other side has a small hole to insert the temperature sensor. Inside the iron cylinder, a cylindrical shaped ceramic crucible is kept to hold the metal sample to be heated. The complete assembly is kept inside the coil isolated by a ceramic holder. Finally, the coil is brazed to the vacuum feedthrough pins. For the experiments carried out in prototype set up, about 1100°C could be achieved without any cooling arrangement.

The iron piece works as the shorted secondary of a transformer. The magnetic flux generated by the primary is coupled to the workpiece. Closer the workpiece to the coil more is the heat transfer. Fig 2 shows the complete coil assembly. Instead of heating the metal directly, using iron workpiece gives an added advantage for the nonmetals as well as the metals having evaporation temperature lower than iron to utilise the hysteresis heating of iron due to induction till iron reaches the curie temperature.

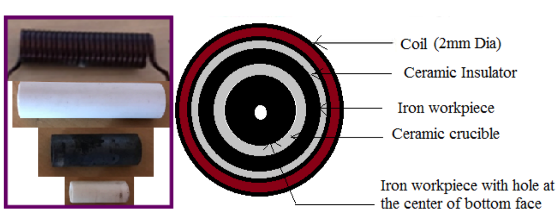

Figure 2: Cross sectional view of the coil assembly.

TEMPERATURE MEASUREMENT

To melt or heat the samples up to a certain temperature, measurement of the workpiece temperature is essential. Using Thermocouple is the simplest and inexpensive method to measure the temperature, [6][7][8][9]. In many occasions, IR based temperature measurement technique is used for this purpose. It needs a clean environment, sophisticated interface, and an IR transparent window through which temperature of the sample kept inside vacuum chamber can be measured. Thermocouple measurement in the induction heating environment is quite difficult due to the enormous EMI generated by the high frequency switching; still it is preferred in this case due to its simplicity and reliability.

A cold junction compensated microcontroller-based temperature measurement unit is developed using DSPIC microcontroller and MAX31855 IC. The temperature of the workpiece is displayed on the front panel of a LCD. Proper measures have been taken to minimise the error introduced in the temperature data due to the EMI generated in the switching circuit [10]. Fig 3 shows the schematic of the temperature measurement circuit.

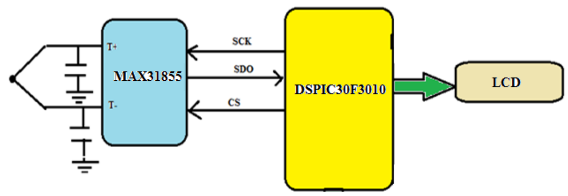

Figure 3: Schematic of temperature measurement circuit

VACUUM EVAPORATION OF METALS

Vacuum chamber Preparation

A CF100SS chamber of 8” length having suitable ports for vacuum pumps and feed through connections was selected as the prototype and prepared for vacuum evaporation. The induction coil was inserted through feed through and brazed with the feed through pins to avoid melting of solder joints at elevated temperature. The coil was cleaned thoroughly before inserting in the vacuum chamber. The thermocouple wires were inserted through ceramic twin hole sleeves to avoid any out gassing and only the tip was inserted into the sample holder through the small hole at the back of the iron piece. The whole thermocouple assembly was shielded by wrapping it with OFHC copper foil for vacuum compliance.

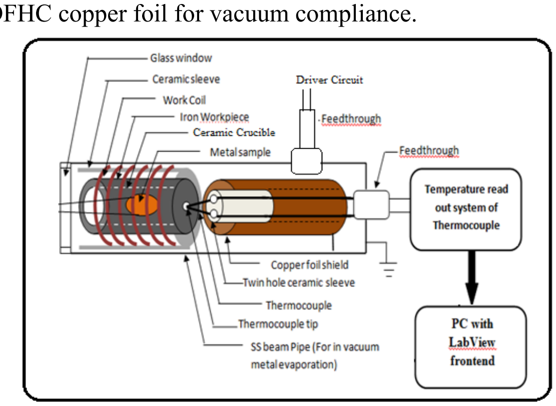

Figure 4: Block Schematic of the experimental set up

Before putting the sample inside the vacuum chamber, its weight was taken and starting time and temperature was recorded. After achieving vacuum of the order 10^{-6} mbar, power was given to the system. After carrying out the experiment for some time and getting noticeable amount of vapour deposited on the front glass surface, the power to the circuit is switched off and the time is recorded again. The residual sample is again weighed after experiment. This gives the idea of the amount of sample evaporated. The schematic of the arrangement is shown in Fig 4 and the complete set up of the experiment is shown in Fig 5.

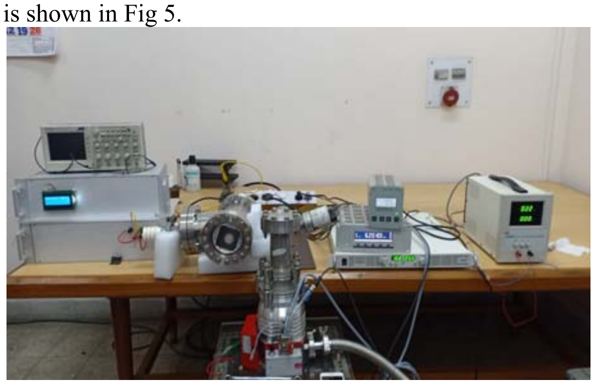

Figure 5: Complete setup of the experiment

Sample Evaporation

Several sample metals could be evaporated successfully using this set up. Fig 6 shows the Ag and Cu deposits on a glass window after evaporation.

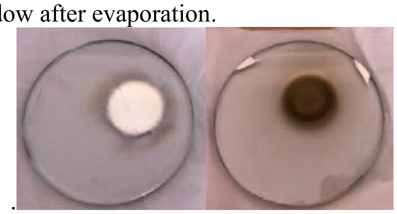

Figure 6: Successful evaporation of Silver and Copper

RESULT AND ANALYSIS

Equivalent Circuit of the induction Heater

For analysing the power delivered to the load by the induction oven, equivalent circuit of the heater system has been derived [11] as shown in Fig 7a. The heating coil and the secondary are modelled as a transformer with a shorted secondary and all the magnetic flux generated by the coil is penetrated in the iron workpiece. Simplified equivalent circuit of the oven results in a LC tank circuit of 0.79ohm impedance, across which a sinusoid is generated.

The amplitude of the sinusoid is determined by the bias voltage given and the frequency is determined by the L and C values of the tank circuit. More is the bias given, current flowing through LC is more hence generating more heat. Fig 7b shows the oven assembly while in operation.

Power, Efficiency and Evaporation rate

The system was operated at a bias of 15V dc and current drawn from the supply was 4A. The voltage measured across the tank capacitor was 27V and the current through the L as calculated is found to be 11.34A. Hence power output across the coil as calculated from Eqn. 1 is as follows

$$P_{out} = (I_L / \mathrm{sqrt}\ 2)^2 x Z_{eqv\ (oven)}$$
$$= (8.01)^2 \times 0.8 = 51.45W \qquad [1]$$

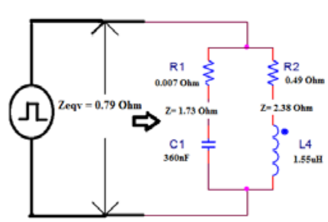

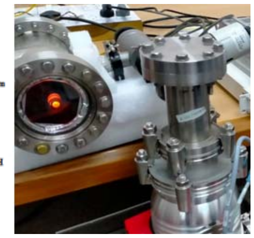

Fig 7a Fig 7b

Fig 7a: Equivalent circuit of the induction oven
Fig7b: Heated oven assembly in vacuum chamber

For Bi metal experiment, evaporation was carried out for 2 mins and 20.21mg of mass was evaporated during this period. Considering total heat required by the process to evaporate this mass, it was found that 5657J was consumed in 2 mins. Hence around 47W out of 60W was delivered to the load for heating, which gives an efficiency of around 78%.The evaporation rate was found to be *168µgm/s for Bi. From other similar experiments, evaporation rate of 2 µgm/s for Ag and 0.5 µgm/s for Cu were achieved.*

CONCLUSION

A prototype induction oven assembly has been developed as an alternative to the MIVOC and resistive oven for metal and solid beam generation in ECR ion sources. Successful evaporation of different metals has been carried out. Reasonable efficiency and evaporation rate were achieved with this system. With suitable and required modifications to the prototype, it will be integrated with the ECR system for generation of metal and solid beams.

REFERENCES

[1] R. Lang, J. Bossler et al. Review of Scientific Instruments **71**, 651 (2000); doi:10.1063/1.1150338.
[2] Yushi Kato, et al. Rev. Sci. Instrum. 77, 03A335 (2006); doi: 10.1063/1.2163290.
[3] M.Cavenago et al Proceedings of EPAC 2002, Paris, France.
[4] T. Takenaka et al. Rev.Sci. Instrum. 83, 02A327 (2012); doi: 10.1063/1.3669798.
[5] Mou Chatterjee et al. (2020, Oct). 4th International Conference on Electronics, Materials Engineering & Nano-Technology(IEMENTech).
[6] Feng Li, et al. Applied sciences. 2019
[7] Jiin-Yuh Jang et al. Applied Thermal Engineering, 2007.
[8] Mark William Kennedy, Licentiate Thesis, Sweden, Stockholm 2013.
[9] Abdil Kus et al. *Sensors* 2015, *15*, 1274-1291; doi:10.3390/s150101274.
[10] Mou Chatterjee et al. (2021, Sep). 5th International Conference on Electronics, Materials Engineering & Nano-Technology (IEMENTech).
[11] E. J. Davis and P. G. Simpson, Induction Heating Handbook. New York: MaGraw-Hill, 1979.

STUDY OF BEAM DYNAMICS IN A SUPERIMPOSED SOLENOID AND DIPOLE MAGNET

Swadhiti Maji, Animesh Goswami, Arup Bandyopadhyay
Variable Energy Cyclotron Centre, 1/AF, Bidhan Nagar, Kolkata-700 064, India

Abstract

In this work, we have studied the beam dynamics in a superimposed solenoid and dipole magnet using transfer matrix and sigma matrix method. We first obtained the paraxial ray equations of motion in the combined fields of solenoid and dipole magnet. From these equations, we have obtained the transfer matrix and calculated the beam envelope as a function of path length through the magnet. We have studied the emittance evolution for different input beam conditions and observed substantial emittance growth at the exit of the composite magnet.

INTRODUCTION

Solenoid magnets are used for focussing low energy beam in the beam transport line. Bent solenoid channel is a combination of solenoid and dipole magnet that can be used for longitudinal cooling in case of muon beam [1]. Here the strong magnetic field of solenoid provides transverse focussing and the transverse dipole field provides dispersions required for emittance exchange.

Solenoid lens with embedded dipole, as beam focussing device can be used as pre injector stage of an accelerator. In order to study the optical characteristics of beam in solenoid with embedded dipole we require transfer matrices. Starting from the Hamiltonian we have obtained the equations of motion of a particle in the superimposed solenoid and dipole magnet. Equations of motion are then solved analytically with hard edge solenoidal and dipole field and get the transfer matrix. Using the transfer matrix, we have calculated the beam envelopes and emittances through the superimposed magnets.

THEORETICAL ANALYSIS

We consider a beam propagating through a solenoid with embedded dipole having an axial momentum $P = \beta\gamma mc$, where β and γ are relativistic parameters, m is mass of the particle with charge q. A particle's motion can be described by (x, y, s) and canonical momenta (p_x, p_y, p_z) where s is along the axial direction. In this section, we first get the analytical transfer matrix of solenoid with embedded dipole which is then verified from solving equation of motions numerically. Finally, the beam envelopes and the projected emittances in two transverse planes are obtained by solving coupled differential equations, using well-known sigma matrix method.

Hamiltonian and equations of motion

The normalized Hamiltonian of particle in a solenoid with embedded dipole can be expressed as, [1]

$$H = \frac{1}{2}\left(p_x^2 + p_y^2\right) + \frac{1}{2}k^2\left(x^2 + y^2\right) - k\left(xp_y - yp_x\right) + \frac{x^2}{2\rho^2} \tag{1}$$

where $k^2 = (qB_s/2P)^2$ is the normalised strength of the solenoid, $1/\rho = qB_d/P$ is curvature of reference trajectory due to dipolar field. B_s and B_d are the magnetic fields of solenoid and dipole respectively. The equation of motions of a particle can be derived from the Hamiltonian as,

$$\begin{gathered} x' = p_x + ky, y' = p_y - kx, \\ p_{x'} = -k^2x - \frac{x}{\rho^2} + kp_y, p_{y'} = -k^2y - kp_x \end{gathered} \tag{2}$$

where dash denotes the derivative with respect to s. The Hamiltonian in Eq. 1 in the concise form as [2,3]

$$H = \frac{1}{2}\tilde{x}^{T}\tilde{H}\tilde{x}, \qquad \tilde{x}' = S\tilde{H}\tilde{x} = Q\tilde{x} \tag{3}$$

where $\tilde{x} = (x, p_x, y, p_y)^T$ and S is skew symmetric matrix with $S^2 = -1$, $Q = S\tilde{H}$ and $\tilde{H}$ is given by,

$$\tilde{H} = \begin{pmatrix} k^2 + \frac{1}{\rho^2} & 0 & 0 & -k \\ 0 & 1 & k & 0 \\ 0 & k & k^2 & 0 \\ -k & 0 & 0 & 1 \end{pmatrix} \tag{4}$$

Transfer matrix

The general solution of Eq. 3 can be written as

$$\tilde{x}(s) = \exp(Qs)\tilde{x}(0) = M(s)\tilde{x}(0) \tag{5}$$

where $M(s)$ is the transfer matrix at any location s. The matrix exponential $M(s)$ is given by,

$$M(s) = exp(Qs) = 1 + Qs + \ldots \tag{6}$$

The transfer matrix of this superimposed magnet calculated using this technique with the help of Mathematica and is given by,

$$M = \begin{pmatrix} M_{11} & M_{12} & M_{13} & M_{14} \\ M_{21} & M_{22} & M_{23} & M_{24} \\ M_{31} & M_{32} & M_{33} & M_{34} \\ M_{41} & M_{42} & M_{43} & M_{44} \end{pmatrix} \tag{7a}$$

From the symmetry of the system it is noted that $M_{11} = M_{22}$; $M_{33} = M_{44}$; $M_{31} = -M_{24}$; $M_{32} = -M_{14}$; $M_{42} = -M_{13}$; $M_{41} = -M_{23}$; Say, $\alpha^2 = 1 + 4k^2\rho^2$. The matrix elements are as follows

$$M_{11} = \frac{2k^2\rho^2 + (1 + 2k^2\rho^2)\cos\left(\frac{s\alpha}{\rho}\right)}{\alpha^2}, M_{13} = kM_{12},$$

$$M_{12} = \frac{\sin\left(\frac{s\alpha}{\rho}\right)}{\left(\frac{\alpha}{\rho}\right)}, M_{43} = kM_{42} = -kM_{13},$$

$$M_{14} = k\frac{\sin^2\left(\frac{s\alpha}{2\rho}\right)}{\left(\frac{\alpha}{2\rho}\right)^2}, M_{33} = \frac{1+2k^2\rho^2\left(1+\cos\left(\frac{s\alpha}{\rho}\right)\right)}{\alpha^2},$$

$$M_{21} = \frac{-k^2 s}{\alpha^2} - \frac{(1+2k^2\rho^2)^2}{\rho\alpha^3}\sin\left(\frac{s\alpha}{\rho}\right),$$

$$M_{23} = \frac{k(1+2k^2\rho^2)\left(-1+\cos\left(\frac{s\alpha}{\rho}\right)\right)}{\alpha^2},$$

$$M_{24} = \frac{-\mathrm{ks}}{\alpha^2} + \frac{2k\rho(1+2k^2\rho^2)}{\alpha^3}\sin\left(\frac{s\alpha}{\rho}\right), M_{34} = \frac{s}{\alpha^2} + \frac{4k^2\rho^3}{\alpha^3}\sin\left(\frac{s\alpha}{\rho}\right). \quad (7b)$$

It is verified that this transfer matrix satisfies the symplectic conditions for equation of motion i.e. ($M^T(s)SM(s) = S$) and Det($M(s)$) = 1. This transfer matrix in this form is very useful in the study of coupled motion in the superimposed solenoid and dipole magnet.

Emittance evolution

The beam matrix σ in the transverse planes is

$$\sigma = \begin{pmatrix} \sigma_x & t \\ t^T & \sigma_y \end{pmatrix}_{4\times 4} \quad (8)$$

where σ_x and σ_y matrices represent the x and y phase space projections of the beam and t describes the x–y coupling. The beam matrix $\sigma(s)$ at position s can be obtained from $\sigma(s) = M\sigma(0)M^T$. where M is the transfer matrix at s. Since superimposed solenoid and dipole field couples the two transverse phase spaces, an uncorrelated input beam becomes correlated when it passes through it. The off diagonal 2 × 2 matrices in the resultant sigma matrix of the beam are non-zero matrices. The beam sizes and the projected x and y emittances can be obtained from:

$$X(s) = \sqrt{\sigma_{11}(s)};\, Y(s) = \sqrt{\sigma_{33}(s)}$$
$$\varepsilon_x(s) = \sqrt{\det(\sigma_x(s))};\, \varepsilon_y(s) = \sqrt{\det\left(\sigma_y(s)\right)} \quad (9)$$

From our calculation, if we choose at initial position $\varepsilon_x = \varepsilon_y$ then we get at any position s, $\sigma_x = \sigma_x^T$, $\sigma_y = \sigma_y^T$.

RESULTS AND DISCUSSIONS

In the numerical calculation, we have considered 10 keV proton beam propagating through a solenoid with field 0.038T, length 30 cm and a dipole with same length and angle 10^0 embedded exactly inside of solenoid which produces field around 0.008T. To check the validity of the transfer matrix formulated in previous section, we performed paraxial ray calculations, first using the transfer matrix and then by direct numerical integration of the equations of motion. In both the cases we used the same input parameters x = 0.5 cm, p_x= -10 mrad and y = 0.2 cm, p_y= 10 mrad. Results are shown in Fig. 1. Solid lines represent the results obtained using infinitesimal transfer matrix of the combined magnet, whereas symbols represent the results obtained by direct numerical integration of the equations of motion. The identical results obtained by these two methods support that the transfer matrix developed by us is correct.

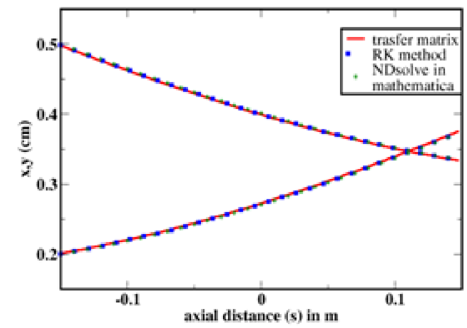

Figure 1: Comparison of the paraxial coordinates x and y through the superimposed solenoid and dipole magnet.

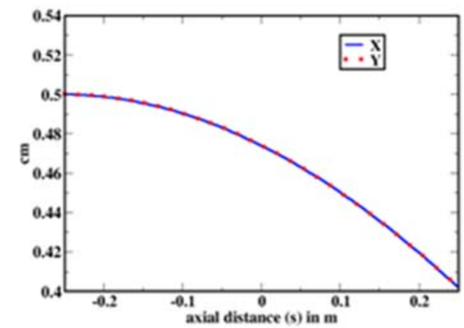

Figure 2(a): Beam envelopes through the solenoid magnet for axisymmetric input beam, $X(0)$=$Y(0)$=0.5 cm; The input emittances are $\varepsilon_x = \varepsilon_y$= 10π mmmrad.

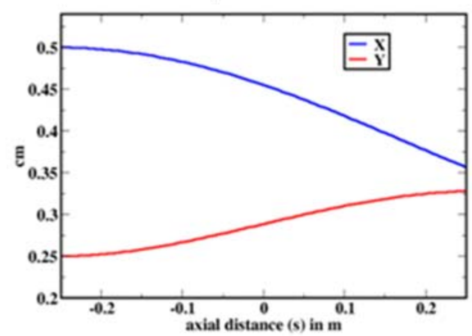

Figure 2(b): Beam envelopes through the solenoid magnet for nonaxisymmetric beam, $X(0)$=0.5 cm and $Y(0)$=0.25 cm. Here $\varepsilon_x = \varepsilon_y$= 10π mmmrad.

Assuming an initial uncoupled beam with $\varepsilon_x = \varepsilon_y$= 10π mmmrad at the entry point, now we have considered a solenoid length 50 cm and a dipole with length 10 cm and angle 10^0 embedded exactly inside of solenoid which produces field around 0.025T, we obtained the beam parameters as a function of s using Eq. 9. Fig. 2(a) and Fig. 3(a) shows the beam envelopes for equal beam sizes ($X(0) = Y(0)$= 0.5 cm) for solenoid and composite magnet respectively. The beam envelopes in both the planes are similar as expected for this circular symmetric input beam, because solenoid magnet exerts equal focusing forces in both the planes, but when dipole magnet is superimposed beam envelope changes. Beam envelopes for different values of beam sizes *X(0)* = 0.5 cm, *Y(0)*= 0.25 cm, but with equal emittances at the input are shown in Fig. 2(b) and Fig. 3(b) for solenoid and for composite magnet respectively. In this case the behaviour of the beam envelopes are different in the two transverse planes.

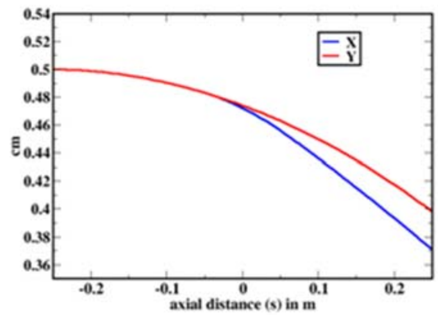

Figure 3(a): Beam envelopes through the superimposed solenoid and dipole magnet for axisymmetric input beam.

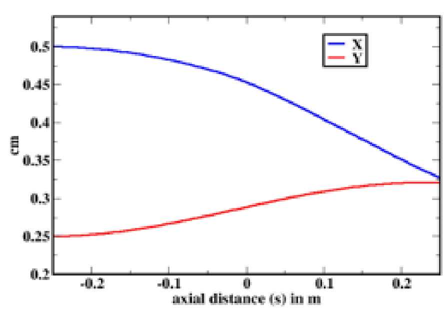

Figure 3(b): Envelopes through the superimposed solenoid and dipole magnet for non-axisymmetric input beam.

We now explore the evolution of magnitudes of projected emittances under various circumstances. Fig.4 shows the behaviour of the projected *x* and *y* emittances as a function *s*, as the beam passes through the combined magnet for axisymmetric and non-axisymmetric input beams with equal emittances of 10π mmmrad in both planes. In the case of the axisymmetric beam (*X*(0) = *Y*(0)= 0.5 cm), the growth in emittances in the *x* and *y* planes are small at all the points downstream. However, for non-axisymmetric beam (*X*(0)=0.5 cm and *Y*(0)=0.25 cm), there is a growth in the emittances. At any point downstream, their magnitudes are always equal to each other. The magnitude of the emittances at the exit is greater than the initial emittances showing a substantial emittance growth in both planes due to the coupling.

In Fig 5 we have plotted the transverse projected emittances through the superimposed magnet when the initial emittances are uncoupled and unequal in magnitude. We have considered two cases. In the first case we have chosen $\varepsilon_x = 10\pi$ mmmrad and $\varepsilon_y = 5\pi$ mmmrad, whereas in the second case $\varepsilon_x = 10\pi$ mmmrad and $\varepsilon_y = 25\pi$ mmmrad. The input beam sizes are same in both cases i.e. *X(0)*=*Y(0)*=0.5 cm. In these cases, the emittances behave differently as the beam passes through the combined magnet compared to earlier case where the emittances were equal in both planes. The emittance reduces in the plane where the initial emittance is high whereas it grows in the other plane where the initial emittance is low.

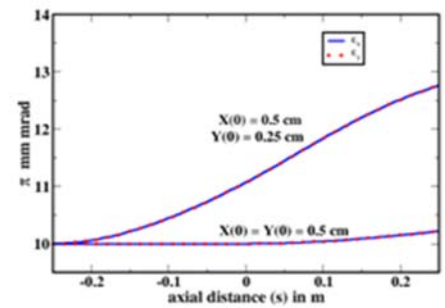

Figure 4: Transverse projected emittances through the superimposed solenoid and dipole magnet for axisymmetric and non-axisymmetric input beam.

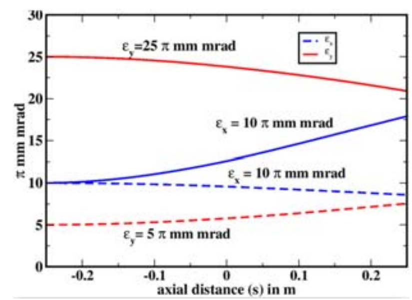

Figure 5: Transverse projected emittances through the superimposed solenoid and dipole magnet for unequal input emittances. The input beam sizes are same.

CONCLUSION

The transfer matrix of superimposed solenoid and dipole magnet has been obtained in this work. The transfer matrix developed can be used for the estimation of beam envelopes for more general case of initial beam conditions. To study of the evolution of beam envelope and emittance growth, we have used here the sigma matrix method. This is usually valid in the absence of the space charge effects. The transfer matrix developed for solenoid with embedded dipole can also be utilized as an infinitesimal matrix dividing the whole length of the magnet in small intervals. Such infinitesimal transfer matrix then can be used further to study the beam transport in the regime of linear space charge effect.

REFERENCES

[1] Wang, Nuclear Instruments and Methods in Physics Research A 503 (2003) 409–413

[2] A. Goswami et al., Nuclear Instruments and Methods in Physics Research A 678 (2012) 14–20

[3] Edwards & Teng, IEEE Transactions on Nuclear Science (Volume: 20, Issue: 3, June 1973).

STUDY OF 30 MV HIGH ENERGY ELECTRON LINEAR ACCELERATOR TECHNOLOGY FOR MEDICAL AND OTHER APPLICATIONS*

Sivaranjani R#, Deepak Yadav, Jyoti Mishra, Tanuja Dixit, Abhay Deshpande, SAMEER, IIT B Campus, Powai, Mumbai 400076

Abstract

Medical radio isotopes for imaging techniques are important part of medical practice. A clean and economical way of producing isotopes is by Electron Accelerator technology. Study shows that up to 30MeV energy photon is sufficient to produce ^{99}Mo that eventually decays to ^{99m}Tc [1]. SAMEER is successful in developing 15MeV high current LINAC and the necessity of generation of ^{99}Mo propelled developing even higher energy and high beam power LINAC [2,4]. In this paper studies are carried out for energy distributions in cavities, energy gain, input power requirements and beam loading characteristics.

Introduction

^{99m}Tc produced from parent ^{99}Mo having a half-life of 66 hrs. The half-life of ^{99m}Tc is only 6.6hrs. Presently the major source of ^{99}Mo is from nuclear reactors using enriched Uranium targets. However, studies have been carried out to obtain the GDR curve for (γ,n) reaction of ^{100}Mo. And calculations show that 30MeV beam energy when directly hits ^{100}Mo target, gives activity of about 55 GBq[3].

SAMEER has been developing 15 MeV S-Band side coupled standing wave LINAC which gives an average output current of ~70μA with resonant frequency 2998 MHz [4]. To achieve 30MeV energy, two independent 15 MeV LINACs connected in series is designed. A Klystron with a peak power of 7.5 MW and an average power of 38 kW is used as the RF source. The layout of the structure is as shown in the Figure 1. which has two LINACs, a 90º bending magnet with beam dump assembly and a retractable tungsten target within the movable shielding of HDPE along the beam line.

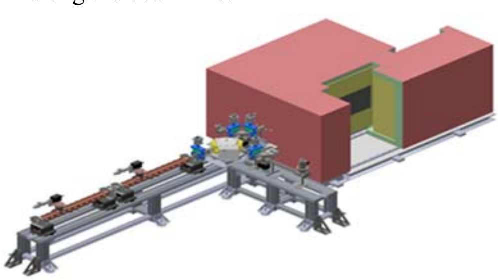

Figure 1. 30MeV System Layout

Energy Gain Simulations

The electron beam dynamics calculations are carried out for each resonant cavity that build up a LINAC. Using the cavity field details, the motion of electrons are calculated. The energy gained (ε) by electron upon entering the accelerating gap at a particular phase ϕ_o w.r.t to RF field by relativistic equations of motion as in equation [1] [2]. Initially the calculations were done for individual 15MeV LINAC using above formulae for initial parameters as in Table 1.

$$\varepsilon = 511[(1 + A^2)^{\frac{1}{2}} \quad \ldots [1]$$

$$A = \sqrt{(\frac{511+Vi}{511})^2 - 1} + \frac{\alpha}{2\pi}(\sin(\varphi + \varphi o) - \sin(\varphi)) \ldots [2]$$

Where, V_i is the injection voltage and α is the normalized energy gain.

Table 1: 15 MeV LINAC Input Parameters

Input Parameters	
Number of Cells	24
Center Frequency	2998 MHz
Injection Voltage	20 KV
Electric Field	30 MV/m

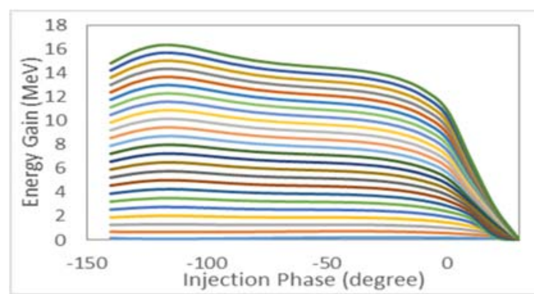

Figure 2. Energy Gain in LINAC I

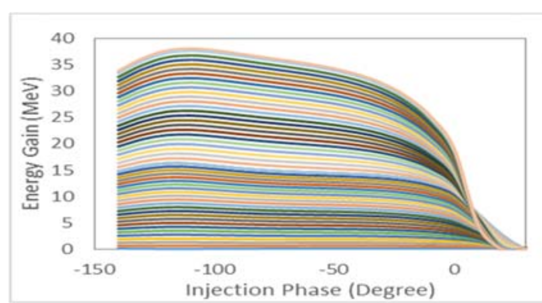

Figure 3. Energy Gain Simulation for 30MeV

The maximum energy gain obtained from 23-½ LINAC structure is 16.31 MeV by simulation (Figure 2). The capture efficiency is 44.44%. These results are close to that obtained experimentally. First LINAC where the electron gun is connected requires buncher section for bunching of

*Work supported by Ministry of Electronics and Information Technology, Government of India

electrons but in subsequent LINAC since electrons are already relativistic no buncher cavities are required. Proper synchronization is required for the beam to pass from one LINAC to other without loss. Calculations were carried out to check the synchronization of the beam in two LINACs ensuring the particle phase at the exit of first LINAC is same as the phase at the entrance of second LINAC. The energy gain distribution (Figure 3), gives a maximum energy of ~36MeV with similar capture efficiency.

Input Power Calculations

The input power is given to the two LINACs from two RF Klystron source, ensuring a constant electric field of ~30MV/m. For LINAC I (23-½), the maximum energy gain is obtained as 16.31 MeV. From the experimentally obtained shunt impedance and the quality factor for LINAC I, the loaded impedance are evaluated and tabulated as in Table 2.

Table 2 Power Requirement for Phase I

	LINAC I	LINAC II
Energy Gain	16.31 MeV	20.75 MeV
Beam Current	70 mA	70 mA
Beam Power	1.142 MW	1.45MW
Shunt Impedance	102.27 MΩ	103.8 MΩ
Input Power	**4.15 MW**	**6.22 MW**

In order to maintain similar electric field pattern in both LINACs, the input power requirement for LINAC II (23-½) will be higher as in the table.

For experimental purpose we have developed a smaller LINAC of 11-½ cavities (Figure 8) to check for beam characteristics of the structure without buncher section. Together with LINAC I will give a total energy of ~27MeV at the exit. So initial testing are carried out for this LINAC.

Transient Response of LINAC

In standing wave LINAC, the RF energy for acceleration of electrons is supplied in the form of pulses of few microseconds. The RF behavior of LINAC changes in presence of electron beam because of beam loading. Therefore, to know the transient response of cavity beam energy (E), reflected power (P_r), stored power (P_s), beam power (P_b), dissipated power (P_d) and reverse power (P_{rev}) are calculated using conservation of energy equations and unloaded quality factor (Q_u) obtained experimentally.

$$P_c = {dU}/{dt} + P_s + P_b \qquad (1)$$

$$P_s = {U\omega_0}/{Q_u} \qquad (2)$$

$$P_b = i\sqrt{{\omega_0 UR}/{Q_u}} \qquad (3)$$

It is crucial to find the total energy which gets reflected back into the source inside and outside the pulse and find the coupling factor that minimizes the reverse energy for a particular beam current. For no beam loading optimum coupling is the β=1 (critical coupling), however as beam current increases, cavity becomes more over-coupled in order to ensure minimum reverse power as in Figure 4.

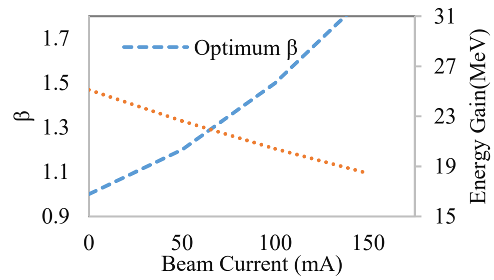

Figure 4. Optimum Coupling

It is observed that for beam current of ~70mA, optimum coupling is β=1.3. With mathematical calculations the effect of source coupling on total energy gain and reverse power is studied as shown in Figure 5.

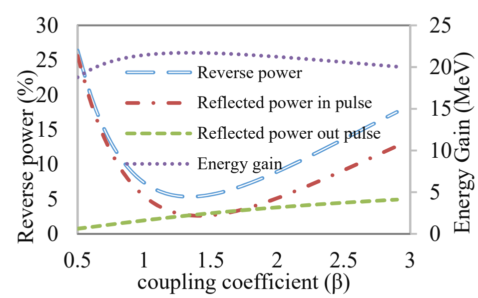

Figure 5. Effect of source coupling

Measured Parameters

The LINAC I is designed and tuned accurately to the desired frequency and obtained π/2 frequency as 2997.78 MHz. The shunt impedance of the structure is obtained as 102.27 MΩ using the Bead Pull Perturbation Technique. The dispenser type electron gun attached to the LINAC is activated and tested at high kV and obtained the peak current at different injection voltage (kV) (Figure 6).

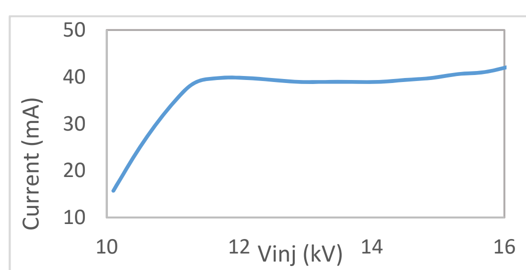

Figure 6. Beam current variation

Since the present test facility is limited to 2MW peak power from magnetron based RF source, and testing is done only at low PRF and maximum high voltage of 16kV. Upon extrapolation to ~4 MW input power we will get about 70mA beam current.

The optimum beta obtained in Figure 4 corresponds to the condition of full load. The VSWR measurement carried out of the LINAC I on VNA corresponds to unloaded condition. According to the calculations, β=1.3 corresponds to VSWR of 2.01 considering the loaded and unloaded impedances. And experimentally it is obtained as 1.966 as in Figure 7.

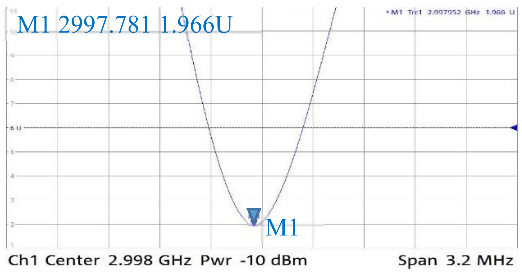

Figure 7. VSWR=1.96 on beam unloading

Also, it is critical to get the π/2 of LINAC II within the bandwidth of first. As mentioned earlier, for testing purpose second LINAC is a 11-½ structure whose resonant frequencies is tuned successfully to be within 100 kHz difference in π/2 value (Figure 8).

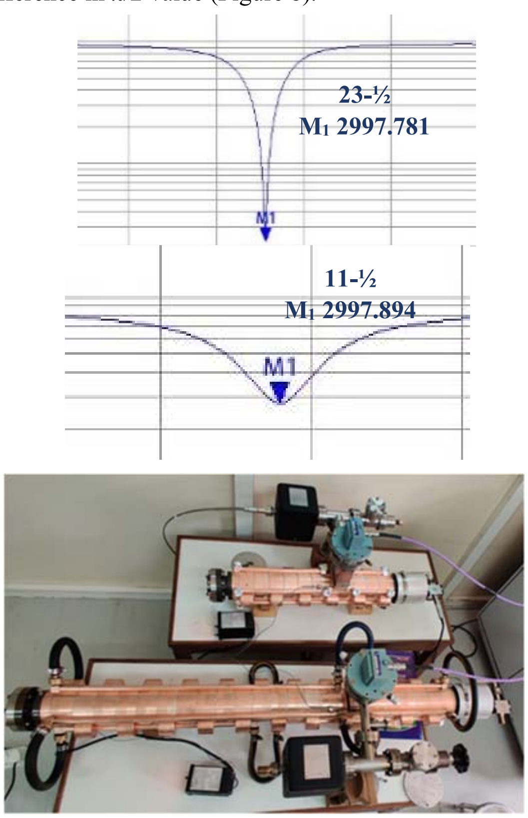

Figure 8. π/2 of 23-½ and 11-½ structure

Also temperature effects on π/2 frequency are studied experimentally on a LINAC whose π/2 was recorded with variation in temperature. It is found that about ±52kHz variation in centre frequency is observed for one degree fall/ rise in water cooling temperature from the slope of the plot (Figure 9). Therefore, any adjustments for synchronization can also be done by controlling the water cooling temperatures.

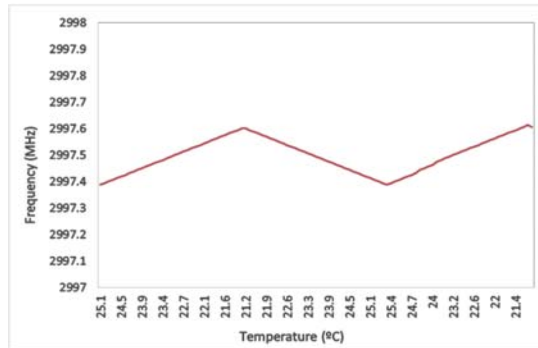

Figure 9.Temperature v/s π/2 frequency

Summary

LINAC for 30MeV are fabricated and resonant frequencies of LINAC are tuned to within 100 KHz and presently testing is being done on low power magnetron based RF source. Testing on full 7.5 MW RF power will commence soon. Synchronization experiment of LINAC under high power RF is planned. Preliminary experiments with natural Molybdenum target will be done soon[5].

References

1. Ralph Benett et al, "A System of 99mTc Production based on distributed Electron Accelerators and thermal separation" Nuclear Technology Vol 126, April 1999.
2. Deshpande Abhay, Dixit Tanuja, Krishnan R., Tiwari T, Vidwans Mandar, Pandit, V.S. (Ed.). (2013). Proposal for 30 MeV, 10 kW linear electron accelerator. India: Variable Energy Cyclotron Centre. Proceedings of the Indian particle accelerator conference.
3. Aqsa Shaikh, Tanuja Dixit, Abhay Deshpande, R. Krishnan, "GEANT4 based simulation study of converter and direct target design and optimization of target for 99Mo production using 30 MeV electron linear accelerator", Applied Radiation and Isotopes 185 (2022) 110239
4. R. Krishnan, Tanuja Dixit, Abhay Deshpande et al, "S-Band Linac Tube Developmental work in SAMEER" Proceedings of Particle Accelerator Conference 2009, Vancouver, pp. 1-3.
5. Tanuja Dixit, Abhay Deshpande, Mandar Vidwans, Paresh Jadhav, Sandesh Bhat, Sivaranjani R, Deepak Yadav, Jyoti Mishra, Shubhra Chaturvedi, Pooja Panwar ,Status of High Energy Electron LINAC Development for Medical Isotopes Production at,Paper ID 558,InPAC 2023

BEAM DYNAMICS SIMULATION OF 300 KEV RF MODULATED GRIDDED TRIODE ELECTRON GUN

Shreya G Sarkar#, J. Mondal, Kandaswamy E and R. I. Bakhtsingh, Accelerator & Pulse Power Division, Bhabha Atomic Research Centre, Mumbai, India

Abstract

Superconducting resonant cavity based high average current electron injector systems are required for the photo fission process to produce radioactive ion beams. The injector system requires a 300 kV, 10 mA electron gun to emit and accelerate beam up to β value necessary for the optimal capture and acceleration in the superconducting cavity section. A thermionic gridded cathode is an ideal candidate for such electron gun since beam bunching as well as current modulation can be achieved by feeding RF power at the grid of the cathode. In this work we present design and beam dynamics simulation of 300 kV electron gun with grid modulation at 650 MHz RF frequency. Analytical and numerical simulations were carried out to design a 300 keV electron gun. The gun geometry was optimized using “CST particle studio”. For beam dynamics simulation, PIC code “GPT” was used to determine the bunch length, beam emittance and other beam parameters at the gun exit.

INTRODUCTION

High average current electron injector systems are in demand for various applications such as radio isotope production [1], injector for free electron laser, radiation therapy etc [2]. A superconducting CW linear accelerator (linac) is usually employed for such a purpose. For the optimal performance of the linac, the electron beam source design is crucial. A 300 keV high average current (10 mA) electron gun is ideal since the beam from the gun output can be directly injected into a Superconducting RF cavity section with β=1. In this work, we present the design and beam dynamics aspect of a 300 keV electron gun system. Table 1, lists the typical design parameters of an electron gun.

Table 1: Electron gun design specification

Parameter	Design Value
Beam Energy	300 keV
Average Current	10 mA
Bunch charge	16 pC
Bunch length	200 ps
Modulation Frequency	650 MHz
Transverse emittance at gun exit	5 mm mrad normalised

#shreyag@barc.gov.in

GUN DESIGN

For, the electron gun design, a triode type of gridded thermionic cathode geometry has been considered [3]. A pierce type of gun geometry has been considered where the cathode, grid and focussing electrode are biased at −300 kV with respect to the anode at ground [4]. The grid has been kept slightly at a negative bias with respect to cathode. RF power is directly applied to the grid for grid current modulation. When the superimposed RF field and DC field values at the grid exceed a cut off voltage electrons are emitted from the cathode and accelerated towards anode. The grid is modulated at 650 MHz frequency. The electrons are emitted in bunches only in a phase window of a portion of RF cycle which is called the conduction angle. The conduction angle is controlled by changing the RF voltage amplitude and Grid negative DC bias. Adopting this methodology of grid modulation has two distinct advantages. Bunch length of the emitted electrons from the gun can be controlled to match the acceleration RF bucket in RF cavity section. An additional requirement of buncher or chopper is not required. Secondly, the amplitude of beam current can be controlled by grid bias.

Figure 1 depicts the typical geometry of the electron gun. The gun has a pierce type of geometry. A dispenser cathode of diameter 8 mm is chosen. The grid is 0.16 mm distance away from the cathode. Both cathode and grid are connected to a coaxial cavity output where the inner tube diameter holds the cathode and the grid is fitted to the outer tube. The cathode and grid are floated at a negative bias. The HV isolator is 30 cm in length. Hence an inverted anode-type geometry has been adopted for the gun where the anode is extended inside the HV isolator. The cathode anode distance is kept at 95 mm.

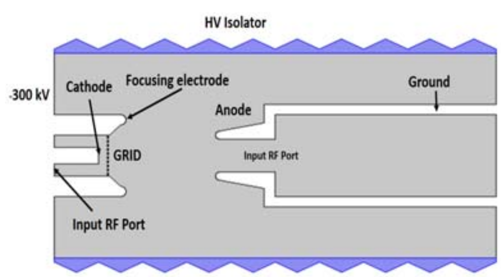

Figure 1: Layout of electron gun

RF MODULATION OF GRID

Analytical simulations were performed to simulate the RF modulation property of the grid corresponding to different grid bias voltage and RF voltage. If V_{RF} is the applied RF voltage to the grid at 650 MHz frequency (f) and grid bias voltage is $-V_b$, then total grid voltage as a function of time t is given by

$$V_{\mathrm{Grid}} = V_{RF} \cos(2\pi ft) - V_b \tag{1}$$

Assuming current is emitted in space charge-limited regime, the current density corresponding to V_{Grid} can be calculated using Child-Langmuir's law. Figure 2 shows the simulated emitted current as a function of V_{Grid} for a typical RF cycle of 650 MHz. When the bias voltage is -425 V and RF voltage is 440 V, the corresponding beam current is shown in Fig 2. The conduction angle is calculated to be +/- 16 ^{0} and the bunch charge 23.8 pC for the simulation value.

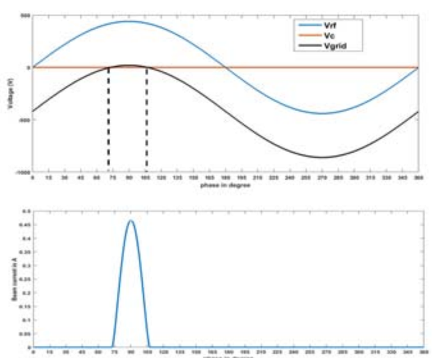

Figure 2: Simulated emitted current as a function of grid driving voltage

By modifying the grid DC bias and RF voltage, the bunch length and bunch charge can be controlled. Figure 3 depicts the correlation between bunch lengths as a function of Grid bias. From the figure, it is evident that bunch length decreases with the increase of grid DC bias almost linearly. Figure 3b shows the increase of total bunch charge as a function of bunch length.

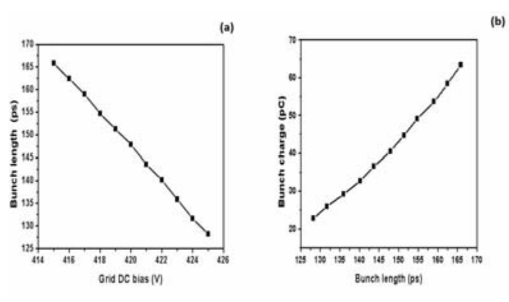

Figure 3 (a): Bunch length as a function of Grid DC bias. (b) : Bunch charge as a function of bunch length

GUN GEOMETRY OPTIMISATION

The electron gun is having Pierce type of geometry. The focusing electrode and anode geometry were optimized using "CST Particle Studio" where the simulation was performed assuming a CW beam of 10 mA of current from the cathode with spatial uniform distribution. The aim of the simulation was to focus the beam effectively to ensure full transport of the beam through the anode exit and to produce the required beam parameter at the anode exit. Figure 4 depicts the electron beam trajectory of the electron gun. From the figure it is evident full beam transport has been achieved up to HV isolator end flange. The beam is reaching the 300 keV energy level at the anode exit. CST simulation also indicates that the maximum electric field is below 7 MV/m.

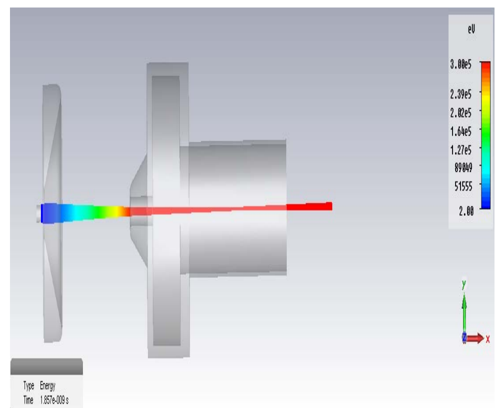

Figure 4: Simulated Trajectory of the electron gun

Beam size and the emittance are calculated at the gun exit and shown in Figure 5. The normalised transverse emittance is 4.98 π mm mrad which is matching the design goal of the gun of 5 π mm mrad value. The transverse beam size is 24 mm at anode exit without any application of the magnetic field assuming uniform beam distribution from the source. Since the anode has inverted geometry, the beam had to travel in field-free region of 200 mm distance post anode. Further focusing of the beam is required to be done post HV insulator flange by employing a solenoid magnet.

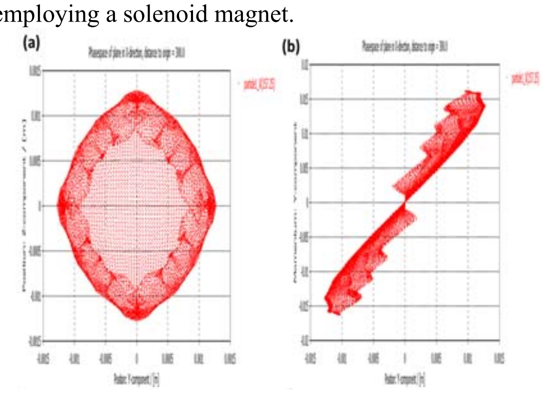

Figure 5: Beam size and emittance at gun exit (CST Simulation)

BEAM DYNAMICS SIMULATION

For Beam dynamics analysis of the gun, “General Particle tracer (GPT) ” a PIC based code has been used. The electrostatic field of the gun has been calculated using “POISSON Superfish” and the field values are imported into GPT software. The RF-modulated beam as calculated from analytical calculation has been used to define an appropriate charge distribution of the input beam in the time domain. The results of GPT simulations are depicted in Figure 6 and 7. The results correspond to +/- 16^0 conduction angle with a beam charge 24 pC which is kept higher than the design value since beam loss at grid was not considered in the simulation.

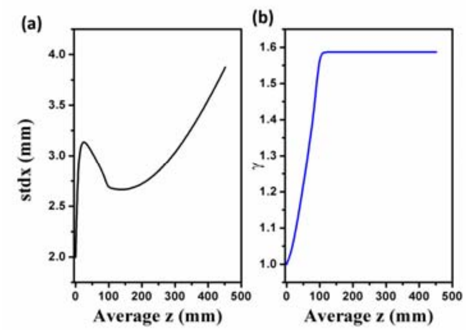

Figure 6: GPT Simulation result

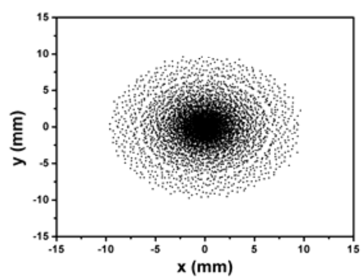

Figure 7: Transverse beam at 300 mm from the cathode

Fig 6a depicts the σ_x value as a function of the average z distance traversed by the beam. The σ_x value reaches 3 mm at 300 mm from the cathode which is the exit of HV isolator flange. The energy gain of the beam as a function of the distance is shown in Fig. 6b, where the average gamma reaches 1.578 value which corresponds to 300 keV energy. The transverse beam size at 300 mm from the cathode at the gun exit is shown in Fig. 7. Table 2 compares the simulation results with the design goal and the results shows good agreement.

Table 2: Comparison of Simulation results with design value

Parameter	Design Value	Simulation Result
Beam Energy	300 keV	300 keV
Average Current	2 mA	10 mA
Bunch charge	16 pC	23.8 pC
Bunch length	200 ps	170 ps
Emittance	5 mm mrad	4.98 mm mrad

CONCLUSIONS

A preliminary design simulation of a 300 keV RF modulated gridded gun has been done in this work. Analytical calculations were performed to find out the beam bunch length and current as a function of Grid bias voltage and RF voltage. The Pierce geometry of the gun was optimised using “CST PS” to meet the design goal and for full transport of the beam through Gun geometry. Finally a PIC-based software “GPT” was used for the trajectory tracking and beam parameter calculations at the anode exit. The simulation results indicate good agreement of the beam parameter values with design goal.

REFERENCES

[1] K. Fong, D. Storey, “Design of an RF modulated thermionic electron source at TRIUMF”, Proceedings of the 9th International Particle Accelerator Conference (IPAC), 2018.

[2] Zhang L, Adam G, Militsyn B, He W, Cross AW, “ Electron Injector Based on Thermionic RF-Modulated Electron Gun for Particle Accelerator Applications”, IEEE Transactions on Electron Devices. 2020;67(1):347-53.

[3] G. Adam, L. Zhang, A. W. Cross and B. Militsyn, “Beam dynamic analysis of RF modulated electron beam produced by gridded thermionic guns”, Proceedings of the 12th International Particle Accelerator Conference (IPAC), August 2021.

[4] F. Ames, K. Fong, B. Humphries, S. Koscielniak, A. Laxdal, Y. Ma, T. Planche, S. Saminathan, E. Thoeng, “Operation of an RF modulated electron source at TRIUMF”, Proceedings of the 9th International Particle Accelerator Conference (IPAC), 2018.

DESIGN AND DEVELOPMENT OF 100 KW, 325 MHZ TETRODE TUBE BASED HIGH POWER RF PULSE AMPLIFIER

G. Kanyal, M. K. Jain, R. K. Deo, A. Bohrey and M. Lad,
RF Systems Division, Raja Ramanna Centre for Advanced Technology, Indore

Abstract

Vacuum tubes were the earliest of switching devices and are still used at high power RF systems for their compact and cost effective design. [1] In this paper, we will discuss design of a tetrode tube based pulsed high power radio frequency power amplifier (RFPA) along with its control, monitor and interlocking system, suitable to energize radio frequency quadrupole (RFQ) structure. This RFPA is designed for 100 kW output power at 325 MHz for 10% duty cycle. Control, monitoring and interlocking (CMI) unit for RFPA is realized with programmable logic control (PLC) based system for its rugged performance and programmability.

INTRODUCTION

TH391 is a ceramic-metal tetrode tube with force air cooled coaxial structure, specially designed for high power pulse operation in very high frequency (VHF) band and lower ultra-high frequency (UHF) band. [2] Compact and light structure of tube eases the process of installation and maintenance. Class of operation decides trade off among efficiency and harmonics, thus it is proposed to operate the tetrode TH 391 in grounded grid configuration under class B mode, thus achieving lower harmonic distortion than class C but higher efficiency than in class A. A quiescent anode current of 10 mA at -230 V control grid voltage, 14 kV anode voltage and 1 kV screen grid voltage are selected for operating point. Table 1 lists various design parameters of RFPA. Discussion about power supplies, CMI unit and matching networks is carried out in subsequent sections.

Table 1: Design Parameters of RFPA

Parameters	Symbol	Value
Operating frequency	f	325 MHz
RF Power output	Po	100 kW
Anode loading impedance	Ro	720 Ω
Anode RF Voltage	Vo,rf	12 kV
Anode RF Current	Io,rf	16.7 A
Anode Peak Current	Io,pk	33.4 A
Anode DC current	Ip	10.6 A
Anode DC Voltage	Ep	14 kV
DC anode power	Pa	148.6 kW
Input RF drive	Pn	6.3 kW
Cathode RF Drive	Vg1,m	280 V
DC grid bias	Eg1	-230 V
Grid current	igm	~0.2 A
Loaded input impedance	Ri	15.8 Ω
Screen grid bias	Eg2	1.0 kV
Power gain	G	12 dB
Anode efficiency	η	67.3 %

POWER SUPPLIES

The most critical and complicated DC power source is anode power supply of tetrode RFPA, that will deliver almost all of the output power. The maximum-pulsed power to the anode is 148.6 kW and the average power is only 14.86 kW. Thus, an energy storage capacitor in shunt with 14 kV/ 2A DC power supply is selected. In addition, for the protection, an arrangement of complimentary driven series-shunt IGBT based switches are used. For normal operation series switch will be closed while shunt switch will be open. In case of malfunction, series will open, thus breaking electrical path to tetrode tube while shunt switch will provide discharge path for capacitor. Value of energy storage capacitor is calculated as 50 µF, for 446 V drupe of anode voltage, which is found tolerable from constant current characteristics of TH-391 tube. [2]

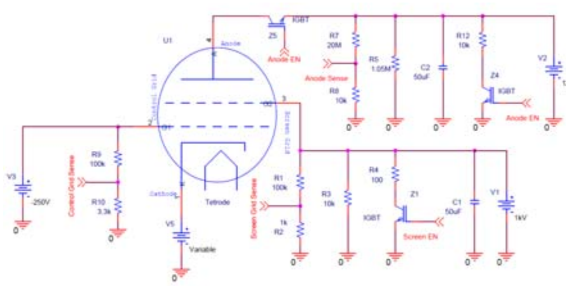

Figure 1: Biasing electrical circuit of RFPA.

Table 2: Power supply specifications

Power Supply	Maximum Rating	Remarks
Anode	14 kV/ 2A	Voltage regulated
Screen Grid	1 kV/ 1A	
Control Grid	-300 V/ 1 A	Two quadrant
Filament	10 V / 250 A	Voltage ramping

In similar manner, energy storage capacitor and shunt discharge IGBT switch are used at screen grid terminal. For the protection of screen grid power supply from discharges within tetrode tube specifically from anode, a bleeder resistor in parallel is used. The value of bleeder resistance is minimally selected such that, bleeder current is higher than the current drawn by screen grid under DC operation. The average screen grid current is 60 mA, thus let the resistor current be 100 mA for DC mode. In addition, the screen grid voltage is 1000 V, so a 10 kΩ bleeder resistor is used.

For sensing purpose, resistor divider circuits are used at anode, screen grid and control grid terminal, whereas cathode voltage is directly measured. Figure 1 shows biasing electrical circuit of RFPA. The performance specifications of all power supplies are listed in Table 2.

CONTROL, MONITORING AND INTERLOCK UNIT

CMI systems are integral part of a high power RFPA. These enable protection algorithms and circuits for safe and reliable operation of RFPA. Within a tetrode tube RFPA, biasing supplies and RF input are required to be switched ON/OFF in a predefined sequential manner for safety of tetrode tube and other subsystems. [1] The on/off cycle of TH-391 requires heater voltage to be gradually increased/decreased to/from the operating heater voltage, in not less than 8 minutes. Thales recommends one heater thermal cycling per day for tube life expectancy. [2]

A Siemens make S7-CPU-315-2DP (CPU) PLC based system is designed and developed for execution of pre-programmed operation sequence and interlocking of cooling system along with currents and voltages of all biasing supplies. Siemens make human machine interface (HMI) KPT1000 is being used for command input, status cum alarm display unit. The CMI system is designed for triple stage (black heat, standby and transmit) operation of RFA. Black heat stage is designed to prevent multiple on-off cycle of tube, while at standby stage, tube is just ready for high voltage operation and with active transmit stage RFPA is in ready state for amplification of RF input power. Figure 2 shows flow chart of CMI unit.

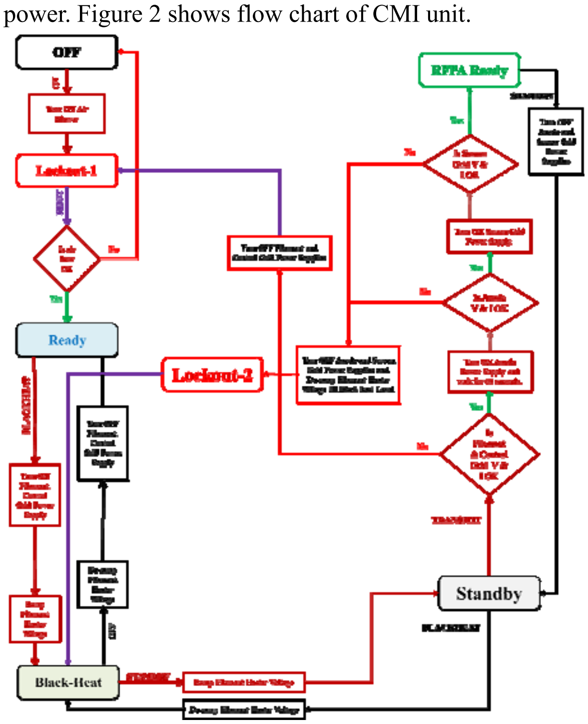

Figure 2: Flow chart of CMI unit of RFPA.

Since tetrode tube is old and was kept in storehouse at RRCAT, thus this CMI unit was deployed for testing of tetrode tube under DC pulse operation. Filament of tetrode tube is heated with 7.8 V DC voltage and 190 A DC current. In addition, tube is biased with 12.5 kV anode voltage and 1000 V screen grid potential. Figure 3 shows plot of anode currents obtained for different values of control grid potential for tetrode tube TH 391 under DC pulse operation.

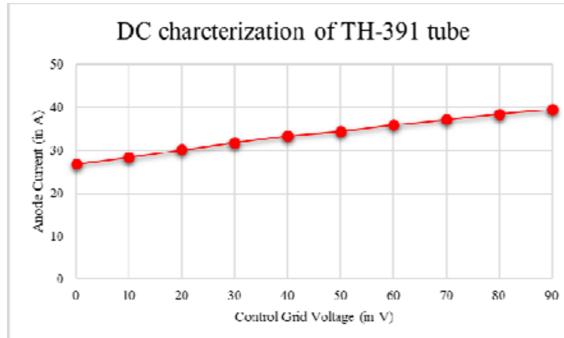

Figure 3: DC characterization plot of TH-391 tetrode for 250 Ω anode load.

MATCHING NETWORKS

Coaxial transmission line and resonant cavity based matching structures are used to realize matching of desired cathode and anode impedances with standard 50 Ω impedance of source and load. Mechanical plunger based tuning strategy is implemented for realization of ±5 MHz tuneable RF bandwidth. The integrated cavity-circuit assembly- consisting of input & output cavity and respective tuning & matching system, tube socket, various DC biasing assemblies are realized in form of distributed RF networks of coaxial transmission lines, designed using microwave network approach. Figure 4 shows exploded 3D CAD view of amplifier structure.

Output Matching Network

Output matching & tuning assembly are realised in form of a rectangular resonant cavity, which, at centre is electrically coupled with electron beam of tetrode tube TH-391, and at surface is magnetically loop coupled to 50 Ω, 3-1/8” EIA coaxial line output port. Rectangular cavity is designed for 325 MHz RF frequency and equipped with mechanical plungers for precise tuning of output resonant circuit. In 3D CAD model of figure 4, part A is rectangular output Cavity, part B is magnetic coupling loop, part C is 3-1/8” EIA output port and part H is mechanical plunger. Apart from this, part D is anode DC Blocking and socket assembly, part E is tetrode tube TH391, part F is anode-cooling chimney and part G is air inlet-outlet structure as shown in figure 4.

Input Matching Network

Input matching & tuning assembly was realised in form of a folded λ/4 coaxial line section which, at one end, is shorted by a movable plunger, and at other end is connected to control-grid and cathode loaded by capacitance contact which is taped into a 7/8" EIA coaxial line input port near shorted end. As central conductor of coaxial line is extended to input RF source, it is conductor coupled.

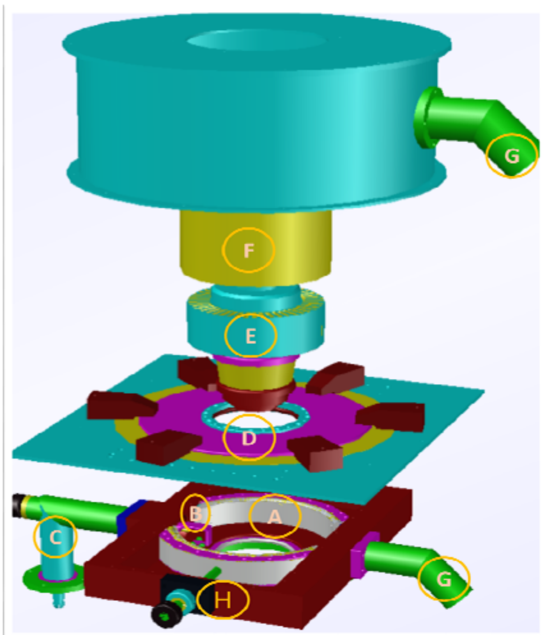

Figure 4: Exploded view of amplifier structure.

SIMULATION RESULTS

Various dimensional parameters of the RF cavity-circuit structure are simulated and optimized using CST MWS for getting required RF performance parameters. Figure 5 and 6 shows simulated electric field distribution of input and output matching circuits respectively. Field distributions are found within the permissible breakdown limit of material. Electric field, marked in red in figure 6 are inside the tetrode tube, which is in vacuum. Figure 7 shows simulated RF voltage at cathode terminal (Left side), return loss at input port (Right side). Figure 8 shows simulated RF voltage at anode terminal for 17.5 A anode current (Left side), return loss at output port and transmission between anode terminal and output port (Right side).

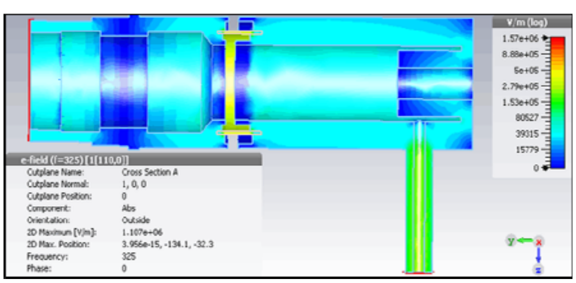

Figure 5: Electric field distribution of input matching circuit at 325 MHz.

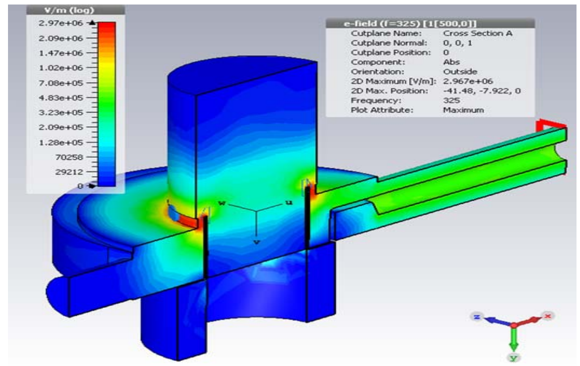

Figure 6: Electric field distribution of output cavity at 325 MHz.

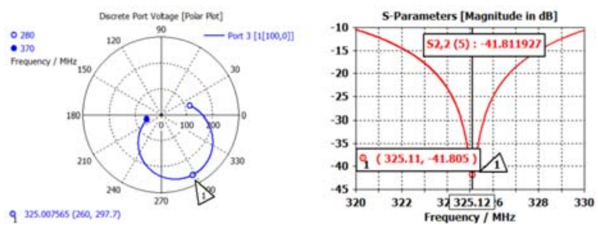

Figure 7: Simulation results of input matching circuit.

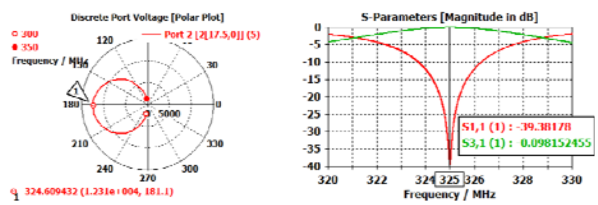

Figure 8: Simulation results of output cavity.

SUMMARY AND CONCLUSION

In this design, a tetrode tube based RFPA at 325 MHz having pulse output power, of 100 kW and 10 % duty cycle is designed. Input and output matching structures are simulated in CST MWS and is currently under fabrication process. A PLC based CMI unit for RFPA is designed. With this unit, tetrode tube TH-391 is characterized for up to 40 A DC pulse anode current.

REFERENCES

[1] Goryashko, V., Dancila, D., Ekelof, T., Gajewski, K., Hermansson, L., Johansson, N., Lofnes, T., Noor, M., Ruber, R., Rydberg, A., Santiago-Kern, R., Wedberg, R., Yogi, R., & Ziemann, V. (2012). Proposal for Design and Test of a 352 MHz Spoke RF Source. FREIA Report Series.

[2] THALES, `TH391: high-power tetrode,' technical specification56998694.

SIMULATION OF FREQUENCY CORRECTION OF QUARTER WAVE RESONATOR USING ELECTROPOLISHING

N. K. Mishra[1, 2], B. Srinivasan[1], R. G. Pillay** and A. K. Gupta[1, 2]
[1]*NPD, Bhabha Atomic Research Centre, Mumbai – 400085*
[2]*Homi Bhabha National Institute, Mumbai – 400094*

Abstract

To widen the mass acceptance of the Superconducting LINAC booster at TIFR[1], it is planned to retrofit the first cryo-module with four low velocity, β(=v/c)=0.07, 150 MHz superconducting niobium Quarter Wave Resonators (QWR). The basic electromagnetic design of the resonator was reported in an earlier conference [2,3]. A QWR is a transmission line terminated by a drift tube at one end and shorted at the other. Dimensional inaccuracies which are inevitable during fabrication will shift the electromagnetic resonant frequency away from the design value. Electropolishing of the QWR is one way to correct this frequency offset, once Δf/f falls within the range of 10^{-5}. Simulations were carried out to evaluate the resonant frequency correction of the QWR using the technique of electropolishing. In general, in a Quarter wave cavity, electropolishing of the bottom half (high electric field end), causes the effective capacitance to decrease and consequently the resonant frequency will increase. On the other hand, if electropolishing is done in the upper half (high magnetic field end) the effective inductance will increase leading to a decrease in resonant frequency. A systematic study of these effects has been performed and presented in this paper.

INTRODUCTION

Electropolishing of the surfaces of the QWR exposed to the RF field/current removes material from the surfaces which in turn changes the cavity volume and hence the resonant frequency. This procedure was previously used to adjust the resonant frequency of the OFHC copper resonators used in the Superconducting LINAC booster[1]. However, in the present case since the geometry of the resonators is different, studies have been undertaken to adapt the process for the niobium QWRs. If we uniformly etch a few micrometers of material from the inner and outer conductors, then to a first approximation the transmission line characteristic impedance changes, but the overall resonant frequency will be unaffected. However, due to the tapered geometry of the central conductor in the low beta cavity the resonant frequency keeps on increasing linearly with thickness of material removal, if the entire RF surface is electropolished. Electropolishing of only the bottom half (high electric field end), causes the capacitance to decrease and consequently the resonant frequency increases. In general, the capacitance between the beam drift tubes is much higher than the capacitance between the central drift tube and the end plate. In the simulations, the full volume from the bottom plate to above the drift tubes is included to simulate the variation of frequency. On the other hand, if electropolishing is done only in the upper half (high magnetic field end) the inductance increases leading to a decrease in resonant frequency. These opposite effects on the resonant frequency depending upon which end of the resonator is being polished implies the existence of an inversion length which defines the maximum useable height of the column of electropolishing solution in either case.

SIMULATION METHODOLOGY

Simulations have been performed using COMSOL Multiphysics software to study the rate of frequency change with material removal under the various scenarios as described above and also for the full length of the cavity. A parametric model has been made in order to facilitate the simulation geometry.

To capture the effect of change in dimensions of the order of microns, mesh independency test has been performed. The resonant frquency has been monitored while varing the mesh size i.e., increasing the number of mesh elements. As Fig.1 shows that the resonant frequency saturates and becomes independent of the number of mesh elements beyond $2x10^5$. For all the simulations more than $2x10^5$ mesh elements have been considered.

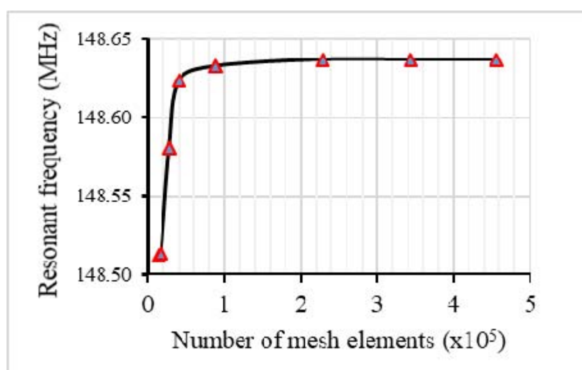

Figure 1: Variation of resonant frequency (MHz) w.r.t number of mesh elements

*nkmishra@barc.gov.in
** Retired Senior Prof., TIFR and ex-RRF & Visiting Prof., IIT Ropar

Electropolishing of the full resonator

The electropolishing removes material from all over the surface of the resonator. The x axis in Fig.2 below shows the thickness of material removed and y axis is the change in resonant frequency in kHz. The resonant frequency increases linearly as the EP thickness increases.

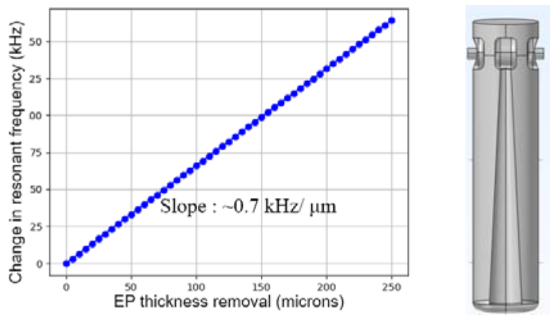

(a) (b)

Figure 2: (a) Variation of resonant frequency (kHz) w.r.t EP thickness removal (b) parametric model

For full length electropolish of the QWR we get slope of approximately 0.7 kHz/μm.

Determination of inversion point for electropolish

The electropolishing simulation for various EP (Electro-Polishing) lengths of the QWR is done from the open end for a fixed thickness removal of 15 microns by electropolishing. The effect of change in resonant frequency w.r.t. length of EP has been studied. The simulation shows no significant change in resonant frequency for increasing EP length starting from open end up to drift tubes which translates to 0 to 30 mm of height of EP as shown in Fig. 3. The change in frequency observed lies within few tens of Hz. To have a smooth surface on the drift tubes, the next simulation point is chosen so that it is past the drift-tubes i.e., 90 mm from the open end. As the length of EP is increased to 90mm the resonant frequency changes drastically due to the inclusion of the higher capacitance zone, as mentioned earlier, between the drift tubes. On further increase in length of EP towards the shorted end, the rate of increase in resonant frequency decreases and after a certain height the inductive effect dominates and the frequency change becomes negative. Consequently, an inversion length which defines the maximum height of the column of electropolishing solution to be used for decreasing the frequency was observed at a height of 212 mm from the open end, with inductive effects or frequency increase beginning to happen for greater heights.

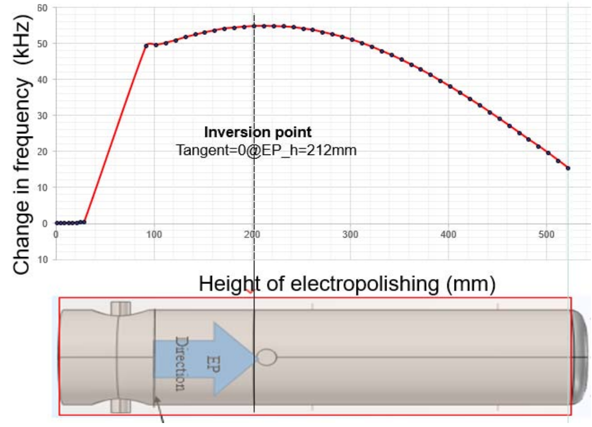

Figure 3: Change in frequency vs height of electropolishing column

Partial electropolishing near high capacitative end below the inversion point

The inversion length separates the two opposite effects on resonant frequency. The simulation was carried out for various electropolishing thickness removal (material etched) from 1 to 20 μm up to inversion length. The material from the RF surface is being removed in this process hence the distance between the drift tubes increases leading to an increase in the resonant frequency. It was observed that the resonant frequency increases linearly as the electropolishing thickness as shown in Fig. 4. In this case the capacitance effect is dominant and the rate of frequency change of 3.5 kHz/μm is obtained.

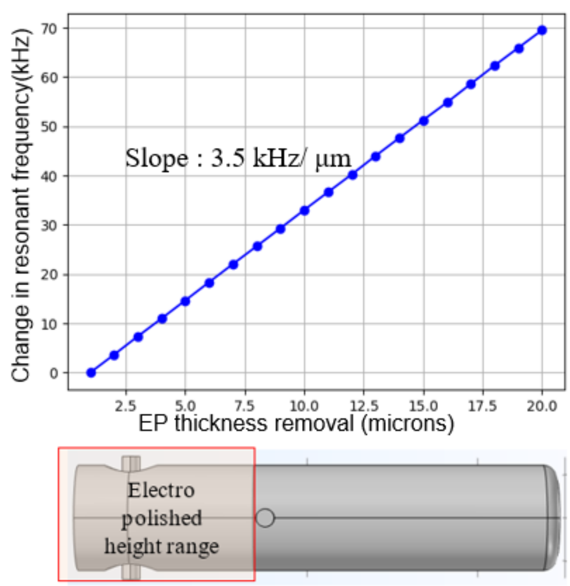

Figure 4: Change in resonant frequency for EP near capacitative end

Partial electropolishing near high inductive end above the inversion point

The simulation was carried out for electropolishing of QWR from the inversion length to the shorted end. The material removal leads to an increase in inductance. Thus, the resonant frequency decreases linearly w.r.t. the electropolishing thickness as shown in Fig. 5.

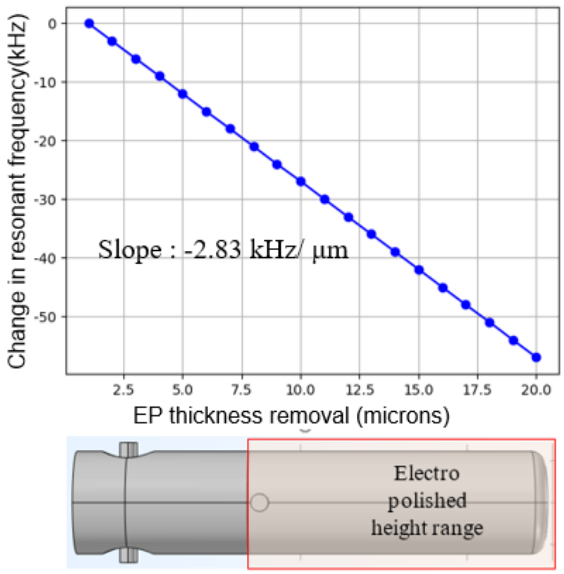

Figure 5: Change in resonant frequency for EP near inductive end

CONCLUSION

For electropolishing at the capacitative end a rate of frequency change of ~3.5 kHz/µm is obtained and for electropolishing at the inductive end the corresponding value is -2.8 kHz/µm. For the full length electropolish of the QWR, the two effects nearly cancel, as expected, and a value ~0.7 kHz/µm is obtained. An inversion length of 212 mm as measured from the open-end of the QWR was obtained which separates the dominant capacitative and inductive effects on the resonant frequency.

REFERENCES

[1] Pillay R G, InPAC (2015) Proceedings.
[2] N.K. Mishra, *et al*. InPAC (2022), VECC Kolkata.
[3] N.K. Mishra, *et al*. InPAC, 227-228 (2019) IUAC New Delhi.

PRELIMINARY PHYSICS DESIGN OF A 50 MEV PROTON CYCLOTRON FOR RARE ION BEAM PRODUCTION

Atanu Dutta[1,2,#], Animesh Goswami[1,2] and Arup Bandyopadhyay[1,2]

[1]*Variable Energy Cyclotron Centre,1/AF Bidhannagar, Kolkata 700064*

[2]*Homi Bhaba National Institute, Anushakti Nagar, Mumbai 400094*

Abstract

A 50 MeV 200 micro-Ampere Proton cyclotron is being designed in VECC to produce Rare Ion Beams (RIBs) for the ANURIB project [1],using ISOL (Isotope Separation On Line) post accelerator method. This will provide neutron deficient RIBs, using fusion evaporation reactions, and neutron rich RIBs, using fission reactions. The RIBs produced using thick targets will diffuse out, ionised in an online ion source, mass separated to select the RIB species of interest. The low energy RIBs (typically 1-1.5 KeV/u) will be further accelerated according to requirement of the experiments.

A volume type multicusp ion source will be used to produce negative hydrogen ions (H-) in CW mode. These ions will then be injected inside the cyclotron. A spiral inflector will be used to launch the ions in the central electrode geometry. A four-sector magnet with optimised hill profile will be used as the main magnet of the machine. Two triangular shaped RF cavity resonators connected in phase and situated at two opposite valleys will be used for accelerating the ions. These ions will be extracted, using carbon stripper, once they achieve the desired final energy. A switching magnet will be used to steer the beam towards the beamline.

This cyclotron will be operated for hydrogen ions (H-) at fixed frequency. It is possible to vary the energy of the extracted ions by adjusting the radial and angular position of the carbon stripper. Physics design of the main cyclotron magnet is underway. Maximum operating hill field, hill and valley gap, average magnetic field, axial and radial betatronic tune values, frequency error are the major parameters, which decide the optimum shape and size of any cyclotron magnet. In this paper, estimation of these parameters from hard edge calculation, as well as from three dimensional simulations, using a finite element based commercial software (OPERA) will be presented. Thicknesses of the iron return paths were adjusted in such a way that magnetic field inside the iron return path remains well below saturation magnetisation. Average magnetic field at the median plane of the cyclotron at different radii was optimised by shaping the pole profile in such a way that isochronism is maintained up to the extraction radius. Simulated result of this isochronous magnetic field will be presented in this paper. Static equilibrium orbit properties of the ion were analysed using Fortran based code GENSPEO[2,3] and which was used to control the pole profile. Another Fortran based code SPIRALGAP [4,5] was used to generate the central trajectory. Knowledge of this central trajectory will be used to design the central region of the cyclotron. Basic beam dynamical behavior based on these codes will also be presented in this paper.

ESTIMATION OF BASIC PARAMETERS

Operating frequency:

Operating frequency is one of the important parameters to fix the size of the pole tip for any cyclotron. As the designed particle revolution frequency increases, radius of the required energy also decreases. As a result, pole tip radius also decreases [Fig 1] thereby decreasing size of the magnet. Higher designed frequency makes the cyclotron compact. For 50 MeV H^{-}cyclotron, this dependence can be found out via following relation

$$radius(m) = \frac{15.56}{frequency\ (MHz)} \quad (1)$$

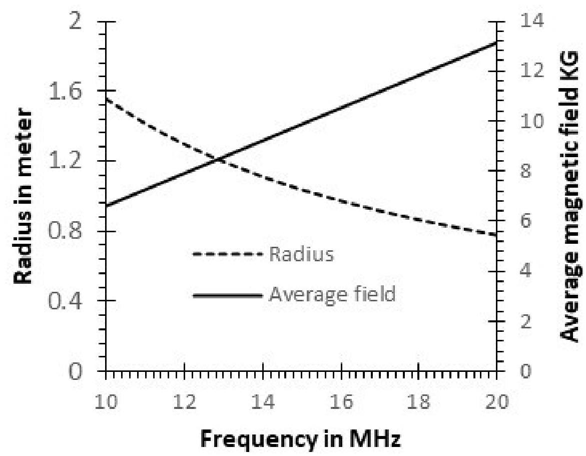

Figure 1: Dependence of extraction radius (for 50 MeV) and average magnetic field on particle revolution frequency.

Average magnetic field:

To support higher particle revolution frequency, average magnetic field should also be high [Fig 1]. Maximum hill field was chosen as 17 Kilo gauss.

$$Bavg(Kilo\ gauss) = 0.6576 * frequency(MHz) \quad (2)$$

Betatronic Oscillations:

Axial and radial betatronic oscillations for an azimuthal varying field cyclotron, without spiral, are estimated via following relations [6]

$$\nu_z^2 = -(\gamma^2 - 1) + F^2 \quad (3)$$

$$\nu_r^2 = 1 + \frac{r}{\langle B \rangle}\frac{d\langle B \rangle}{dr} + ... = \gamma^2 + ... \quad (4)$$

where F is the Flutter defined as

$$F^2 = \frac{< B^2 > - < B >^2}{< B >^2} \quad (5)$$

To avoid $2\nu_z = 1$ resonance, ν_z values kept either above 0.5 or below 0.5. We have chosen a value which is greater than 0.5 with a deep valley configuration, which essentially provides better focusing strength for high intensity beams and much room for RF cavity accommodation.

2D DESIGN OF CYCLOTRON MAGNET

Based on the hill field requirement, initial pole dimensions, return yoke dimensions and ampere turns were optimised in POISSON [7] maintaining iron field in the return yoke and pole cap well below saturation.

3D DESIGN OF CYCLOTRON MAGNET

2D parameters were then used in 3D simulation [Figure 2] using OPERA [8]. Hill pole profile was iteratively changed to control average magnetic field profile [Figure 3] to achieve frequency error [(w0/w)-1, w0 is the angular frequency of oscillating voltage and w is the angular frequency of the particle due to local magnetic field] within ±5.0E-4 [Figure 4] and phase error [Figure 5] within 20 degree[9,10]. Equilibrium Orbit code (GENSPEO) was used to generate frequency error. With respect to average magnetic field, hill and valley fields were chosen in such a way that vertical betatronic tune remains above 0.5 [Figure 6] and away from resonances [Figure 7].

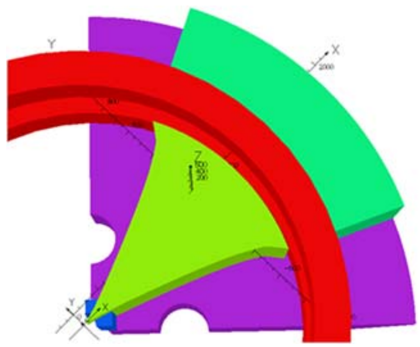

Figure2: Simulated model of the magnet

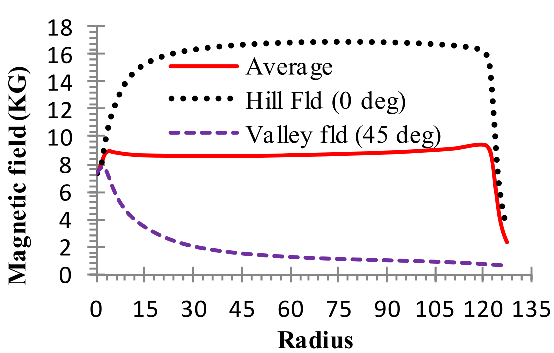

Figure 3: Optimised average field profile. Hill field and valley field at this optimized configuration.

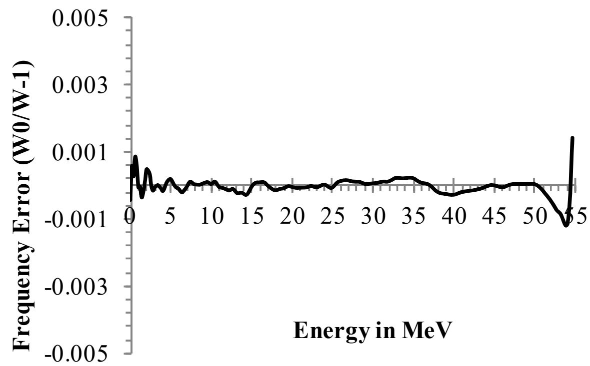

Figure 4: Frequency Error

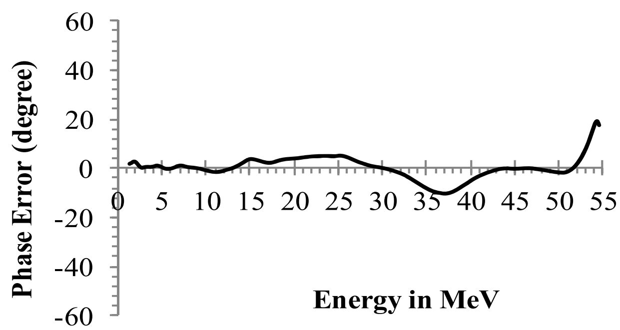

Figure 5: Phase Error

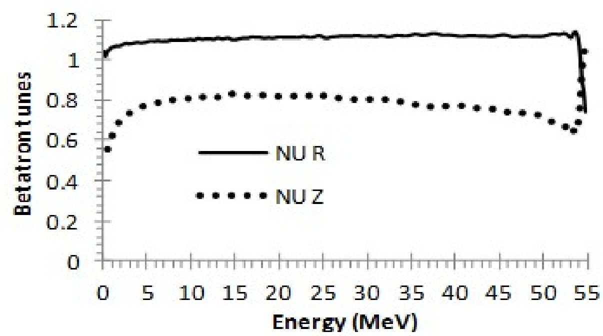

Figure 6: Variation of betatronic tunes with frequency

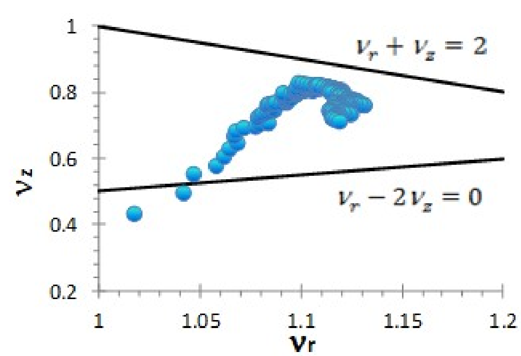

Figure 7: Location of betatronic tunes with respect to resonance lines.

Once required field properties were obtained, H- ion was tracked from lower radius of one of the hill centre till the extraction radius. Beam initial parameters were changed iteratively to find a centered orbit patterns [Figure 8] and minimum coherent oscillation [Figure 9] using SPIRALGAP code.

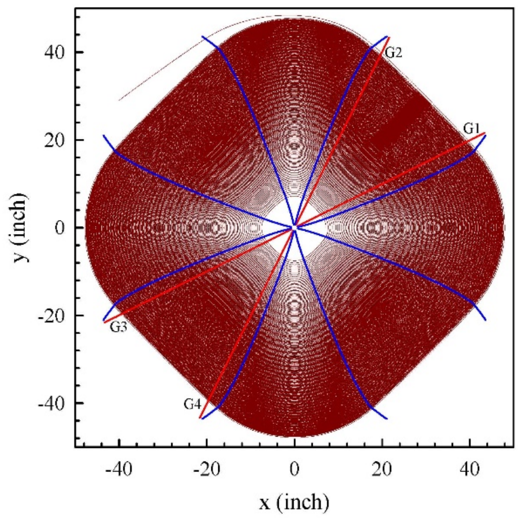

Figure 8: Accelerated orbit patterns

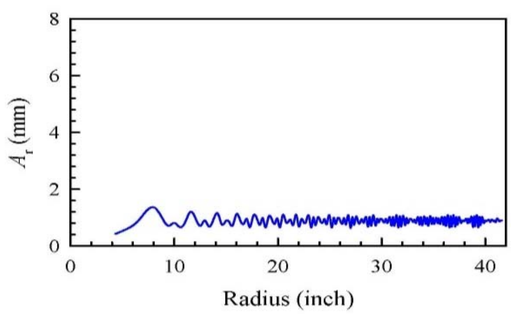

Figure 9: Coherent oscillation amplitude at different radius

SPECIFICATION

Based on the physics design calculation designed parameters are summarized in Table 1 and Table 2.

Table 1: Specification

Parameters	Values
Hill Gap (mm)	30
Valley Gap (mm)	1000
Hill field (Max)	17 KG
Valley field (approx.)	1 KG
Ion revolution frequency	13.5 MHz
Harmonic mode	4
Frequency of oscillating Voltage	54 MHz
Dee voltage	50 KV
No of dee	2

Table 2: Specification

Parameters	Values
Current density (A/mm2)	0.63
Ampere turns/coil	34713
No of coils	2
Coil ID	252 cm
Coil OD	290 cm
Width	19 cm
Height	29 cm
Magnet OD	386 cm
Magnet Height	180 cm
Iron Weight	100 Ton

DISCUSSION

The presented design of cyclotron was optimized for a lower revolution frequency of 13.5 MHz, and therefore, its size was on bit higher side. It is possible to optimize considering higher revolution frequency e.g., 16.25 MHz. In that case, its size will be compact. However, in that case, other complications arise during design stage. In future, a design based on higher frequency will be explored. Pole profile and valley depth will be finalized once RF cavity simulation is complete.

REFERENCES

[1] "ANURIB- Advanced national facility for unstable and rare ion beams" Arup Bandyopahyay et all PRAMANA 85, 505-515,2015
[2] GENSPEO NSCL, MSU, East Lansing, USA
[3] M M Gordon, Particle Accelerators Vol 16, pp 39-62 (1984)
[4] SPIRALGAP NSCL, MSU, East Lansing, USA
[5] M M Gordon, Nuclear instruments and methods 169 (1980) 327-336,
[6] J R Richardson "Progress in Nuclear Techniques and Instrumentation" (1965)
[7] POISSON/SUPERFISH
[8] OPERA (15R2)
[9] B Qin et al. Nuclear Instrumentation and methods in Physics Research A 620 (2010) 121-127
[10] IEEE Trans. NS.vol.56 no.5 2821-2827

CHARACTERISATION OF THE EFFECT OF UNBALANCING COIL ON THE DEVELOPED ION SOURCE

Himanshu Bisht[1], Mahima, Janvin Itteera, Kumud Singh, Sanjay Malhotra

Electromagnetic Applications and Instrumentation Division

Bhabha Atomic Research Centre, Mumbai, India

Email: hbisht@barc.gov.in

ABSTRACT

The effect of the unbalancing coil (UBC) on the indigenously developed magnetron sputtering based ion source was characterised by Langmuir probe and optical emission spectroscopy. In the balanced magnetron sputtering the magnetic field lines of magnetron confine plasma near the target. The introduction of the unbalancing coil distorts the magnetic field lines of traditional magnetron and form a closed trap for electrons between the unbalancing coil and magnetron which decrease the transverse field component. This limiting transverse mobility of electron leads to the extension of plasma volume along the axial direction [1]. The extension of plasma results in enhancement of the extracted current and also an improvement in ion to neutral atom ratio [2]. The plasma comprising of inert gas and sputtered metallic ions was ignited using glow discharge method and critical plasma characteristics of interest such as electron temperature, Debye length, electron density and ion density were mapped in the plasma volume and their dependence with discharge parameters were analysed in depth. Optimal magnetic field for extending the plasma for obtaining enhanced ion density was measured and ionisation states beyond first ionisation were not detected in the measured emission spectrum of the plasma. The absence of the higher ionisation states and an increased ion to atom ratio will result in an increased extracted ion current per sputtering target which will increase the efficiency of the developed ion source. The introduction of the UBC resulted in an increase in ion density in the vicinity of the probe which indicate increase in the plasma volume.

INTRODUCTION

Sputtering was introduced first in the year 1852. It was used for deposition of materials whose thermal evaporation is not possible but with the use of radio frequency waves now it can even be used for dielectric material target also. In a sputtering based ion source, a potential difference is created between the cathode and the anode (chamber wall and the substrate) which leads to ionisation of the neutral gas present inside chamber and plasma is ignited. The generated positive ions then accelerate towards the target at negative potential and if they have sufficient energy then an atom or ion is removed causing sputtering. The basic sputtering system suffers from the limitation of low ionization efficiency in plasma and low deposition rates which is eliminated by the introduction of magnetron sputtering methods. In magnetron sputtering the electrons are confined close to the target with the application of magnetic field lines parallel to the target surface causing higher ionization. Enhanced ionization efficiency results in denser plasma, higher sputtering and stable plasma at lower pressure and bias voltage as compared to conventional sputtering.

In a balanced magnetron sputtering all magnets have same strength resulting in all the field lines passing through the central magnet. This traps the electrons close to the cathode resulting in confinement of plasma close to the target. This confinement leads to poor ion flux at the extraction system and hence poor extraction current at applied extraction voltages. To improve extraction current the ion density have to be increased close to the extraction, this can be achieved by using the unbalanced magnetron sputtering. In unbalanced magnetron sputtering the field lines are modified such that all the field lines from outer poles are not terminated at the central pole thus some of the electrons escape which results in creation of ionized zone near extraction and hence enhanced ion density and penetration of plasma in that region.

The unbalanced configuration can be achieved in two ways, one by making the outer magnets weaker than the central magnet or by introduction of a solenoid coil. The second configuration has been used in this paper as the degree of unbalancing to be introduced can be controlled via the current which is not possible in the former configuration and hence can be optimized. When a solenoid coil is operated close to the balanced magnetron in polarity as shown in fig 1. The some of the magnetic field lines of outer pole terminate at the centre of solenoid thus forming a tunnel of field lines [3], the electrons precess around these field lines and reach the extraction region while ionizing the neutral atoms along the way. The effect of the solenoid coil on the developed ion source in this configuration has been characterized in this paper.

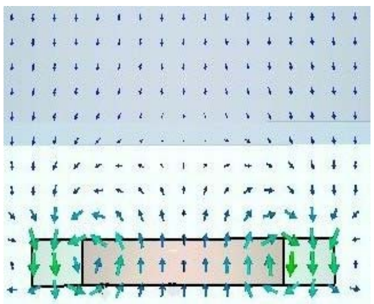

Figure 1: Magnetic field profile of the combined effect of balanced magnetron and solenoid coil simulated in CST

EXPERIMENTAL SETUP

The solenoid coil has inner diameter of 230 mm and consist of 1500 turns. It can sustain currents upto 4.5 A without cooling mechanism. The water-cooled magnetron consists of a central circular magnet surrounded by a ring of opposite polarity of equal strength of width 13 mm having peak axial magnetic field of 120 mT and the peak field achievable at the centre of the coil at 5A is 20 mT. Copper disc of diameter 76 mm and thickness 3mm was used as the sputtering target. Solenoid coil was externally mounted at 30 mm from the copper target such that its geometric centre matched with the centre of the target. The effect of coil on the ion source was then characterized for different solenoid field strength by varying the coil current for a chamber pressure of 8.5×10^{-3} mbar at a argon flow rate of 1.4sccm and sputtering voltage of 450 V.

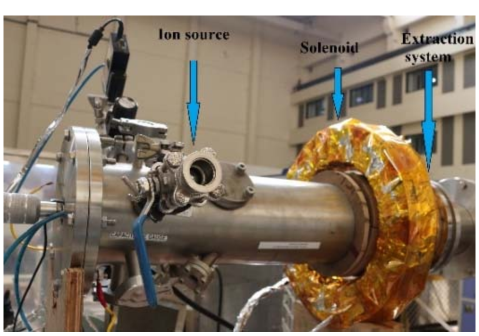

Figure 2: Setup

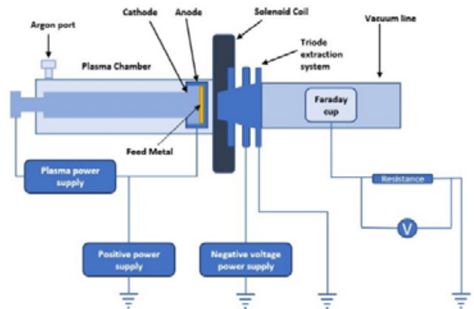

Figure 3: Schematic of the setup

CHARACTERISATION

Field Profile Characterisation

The knowledge of the magnetic field profile along the along the axis is important to understand the combined effect of the magnetron and the solenoid coil on the plasma and the sputtering process. The axial magnetic field component was measured using a Lakeshore gaussmeter with transverse type Hall probe and is shown in the figure 4. The polarity of the central pole of magnetron and the coil along the axis is opposite hence there is a sign change over in field strength at a point on axis known as null point and it dictates the radius of the sputtering region. By varying the magnetic strength of the solenoid null point distance from surface of the target can be varied and hence sputtering radius can also be changed. This change is sputtering radius can be utilised for better consumption of feed material.

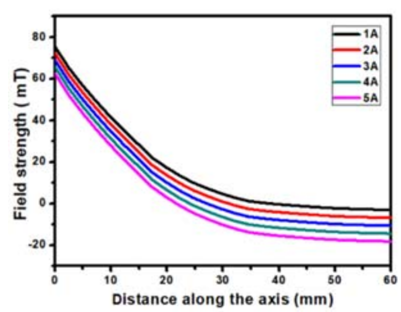

Figure 2: Variation of axial component along the axis for different magnet currents

Plasma characterisation

The plasma characterisation was done using the Impedans cylindrical air-cooled Langmuir probe assembly in single probe configuration with RF compensation using a cylindrical probe of diameter 6.5mm. The probe was placed at 30 mm from the surface of the target and various parameters such as ion density, electron temperature, Debye length etc. were determined from the measured VI characteristic of the plasma which gives the insight into the effect of the unbalancing caused by the solenoid coil.

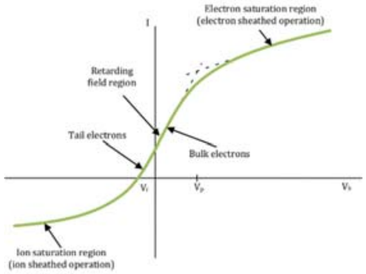

Figure 3 Typical I V characteristic of Plasma

Emission Spectrum of the Plasma

Optical emission spectrum of a gas gives the characteristic wavelength of atomic species present in it. The emission spectrum of the plasma was obtained in the optical range of the EM spectrum using Ocean Optics optical emission spectrometer in a wavelength range of 540nm to 640nm. The probe was attached on a glass window of the chamber. Probe was not directly placed inside the chamber due to the problem of copper film formation on the lens of the probe.

RESULTS

Typical Langmuir probe I-V characteristics are shown in Fig 5. The ion saturation region of I-V plot is used to determine the ion density using the equation.

$$N_i^2 = -\frac{4\pi m_i}{3A^2e^3}\left(\frac{\partial I_i^2}{\partial V}\right)$$

Where I_i is the ion saturation current, A_p is the surface area of probe, m_i is the ion mass, T_e (eV) is the electron temperature. The slope of the ln(I)-V curve between Vf (floating potential) and Vp (plasma potential) gives the electron temperature and is given by the equation

$$T_e = \frac{\partial V}{\partial \ln(I)}$$

Where I is the electron current.

Figure 6 shows variation of ion density with the solenoid current. This increase is due to the increase in electron temperature as is evident from the figure 6 which is due to the increase in Debye length with increase in the magnet current which results in increased ionisation of neutral atoms resulting in increased ion density. The decrease in the discharge current beyond 3 A (Figure 8) indicates that field of the solenoid is strong enough to distort the magnetron field and the magnetic field lines no longer form closed loop leading to decrease in the radial component of the magnetic field near the target due to which the electrons are able to escape to region beyond the target hence the electron density decreases suddenly which leads to a decrease in rate of sputtering as is clear from variation of Debye length with solenoid current in figure 7. The increase in Debye length is an indication of decrease in electron density with an increase in the current of the solenoid coil.

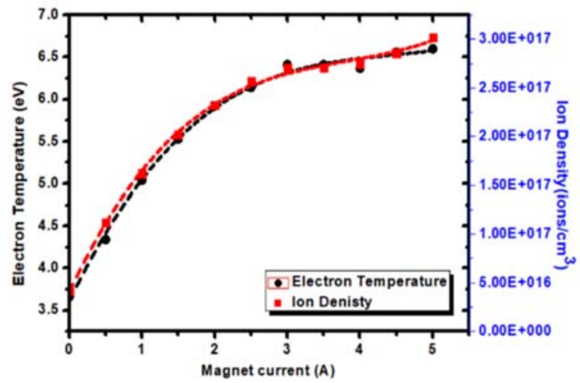

Figure 4: Variation of ion density and Electron temperature with magnet current

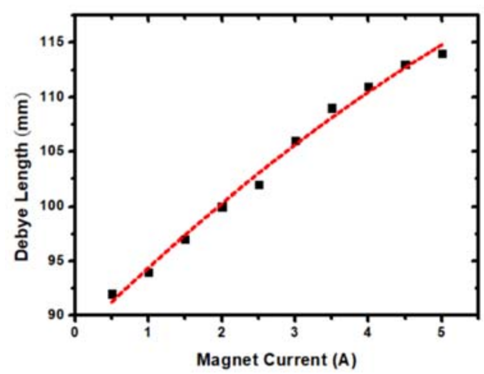

Figure 5: Variation of Debye Length with Magnet current

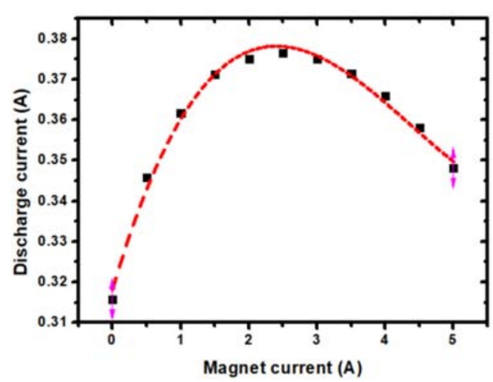

Figure 6: Variation of Discharge current with solenoid current

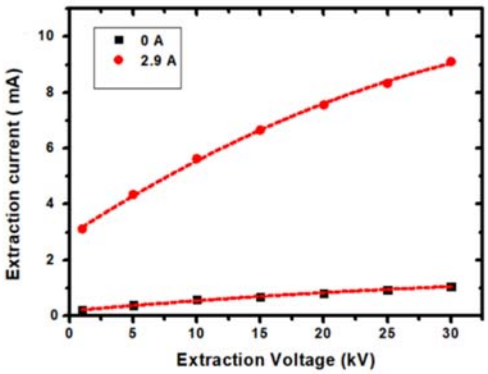

Figure 7: Variation of Extraction current with Extraction voltage for magnetron in balanced configuration and in unbalanced configuration

Due to the increase in the ion density in the region near extraction, a substantial increase in the extraction current was observed as compared to the balanced magnetron (figure 9).

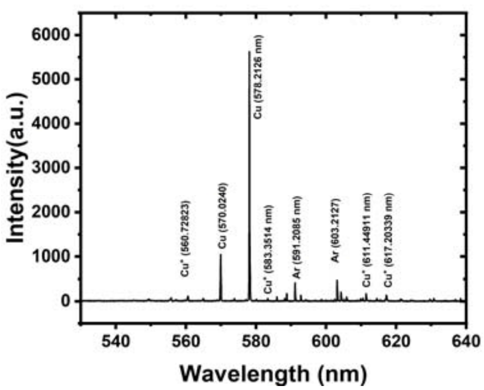

Figure 8: Optical Emission spectrum of plasma

The optical emission spectrum of the plasma is shown in figure 10. The characteristic peaks of the Ar and Cu along with Cu^{+} are clearly visible. But the prominent peaks of Cu^{+2} are missing in the observed spectral range which indicates that Cu^{+2} ions are present in a low fraction as compared to the Cu^{+}.

CONCLUSION

The effect due to introduction of solenoid coil in the indigenously developed ion source was characterized for different solenoid currents. It was observed that the increase in the solenoid current led to an increase in the ion density near the extraction region. This enhanced ion density resulted in higher extraction current as compared to balanced magnetron configuration. The introduction of the coil also led to increase in the discharge current which indicate increased sputtering rate for the same sputtering voltage and argon pressure.

ID:E7-146

REFERENCES

[1] Solov'ev, A. A., Sochugov, N. S., Oskomov, K. V., & Rabotkin, S. V. (2009). Investigation of plasma characteristics in an unbalanced magnetron sputtering system. *Plasma Physics Reports*, *35*(5), 399–408. https://doi.org/10.1134/s1063780x09050055

[2] Musil, J. (1998). Recent advances in magnetron sputtering technology. *Surface and Coatings Technology*, *100-101*, 280–286. https://doi.org/10.1016/s0257-8972(97)00633-6

[3] Komath, M., Mohan Rao, G., & Mohan, S. (1999). Studies on the optimisation of unbalanced magnetron sputtering cathodes. *Vacuum*, *52*(3), 307–311. https://doi.org/10.1016/s0042-207x(98)00304-2

[4] I.M. Hutchinson. Principles of plasma diagnostics. (Cambridge University Press, Cam-bridge, 1987) Chap. 3.

[5] F.F. Chen. Introduction to plasma physics and controlled fusion. Vol. 1: Plasma physics.2ndedition (Plenum Press, New York, 1984)

[6] Mona, Coat, V., & George. (2023, January 28). *The role of Un-Balanced Magnetron Sputtering*. VacCoat. Retrieved March 12, 2023, from https://vac-coat.com/blog/balanced-and-unbalanced-magnetron-sputtering/

VERTICAL PINGER MAGNET POWER SUPPLY FOR INDUS - 2

Yogesh Kelkar*, Lingam Srinivas, Rajesh Barothiya, Ulhas Karandikar, Yash Pal Singh
Accelerator Power Supplies Division, Raja Ramanna Centre for Advanced Technology, Indore

Abstract

A set of Pinger magnets is required to study linear and nonlinear beam dynamics in Indus-2. With these magnets, the beam can be excited vertically or horizontally, and the response to these magnets will be measured with BPMs. The half sine current pulse is generated by a highly underdamped LC circuit which is formed by HV capacitors and Vertical Pinger magnet which acts as an inductor. Power supply specifications were achieved with a low inductance, high voltage compliant pulser unit with Thyratron as a switch. The control unit, capacitor charger, thyratron auxiliaries, trigger unit were housed in 36U rack. The power supply was installed and commissioned in SS7 of Indus -2 (see Fig. 2) and is ready for beam dynamics experiments.

INTRODUCTION

Pinger magnet system consists of pulsed power supply and pulsed dipole ferrite core magnet which generates half sinusoidal magnetic field. A set of Pinger magnets namely Horizontal and Vertical magnets will be used to study linear and non linear dynamics of beam with the help of Beam Position monitors (BPM). Kick exerted by pinger magnet creates beam oscillations and the bunch motion is recorded with the help of BPM's.

MAGNETS SPECIFICATIONS

A single turn copper coil with Ni-Zn high frequency ferrite core material constitutes the magnet. A 2 mrad deflection in vertical direction is generated by 650 gauss magnetic field. This magnetic field is achieved at 5.5kA. To achieve better field uniformity & leakage flux magnet with window type geometry was chosen.

Table 1: Parameters of Vertical pinger system

Beam energy	2.5 GeV
Deflection angle (θ)	2.0 mrad
Inductance (L)	250 nH
Field uniformity ($\Delta B/B_0$)	$\pm 2 \times 10^{-3}$
Pole aperture (H × V)	106 mm ×56 mm
Peak current	5.5 kA
Current pulse width	946 ns
Pulse shape	Half Sinusoidal
HV Capacitance	150nF
LV Capacitance	500uF
Transformer Turns ratio	1:55
Charging Voltage –LV side	400V
Charging Voltage –HV side	15kV

*kelkar@rrcat.gov.in

THEORY OF OPERATION

The half-sine wave current pulse is generated by a pulsed circuit based on LC resonant discharge. The stored energy in the capacitor (C) will be switched by a HV switch (S) to the magnet inductance (L) as shown in fig 1.

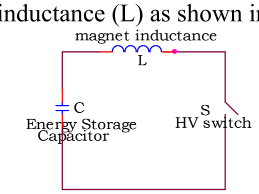

Figure 1: Pulser Schematic

Neglecting parasitic resistance and inductances, the peak current in the magnet is given by

$$I_{peak} = V_{Charging}\sqrt{\frac{C}{L}}$$

Equation 1

The half sine wave pulse period is given by

$$\tau = \pi\sqrt{LC}$$

Equation 2

SCHEME

The HV capacitor , switch assembly and magnet forms a highly underdamped resonant circuit which generates half sine current pulse in load. A previously charged HV capacitor is discharged in magnet load upon arrival of trigger pulse from the control systems which in turn triggers thyratron. The HV capacitors and thyratron are ground referenced and magnet is floating. The value of capacitance was calculated based on stray inductance, magnet inductance and pulse width specifications. The charging voltage is function of peak current and circuit inductances (including stray inductances) and capacitances. Reduction of stray inductance will reduce the HV charging requirement. In order to reduce inductance a coaxial Thyratron switch assembly was designed with low inductance, low ESL Capacitors were paralleled and all pulse forming network components were placed in closed vicinity. The HV capacitor is charged with command resonant charging scheme in which a low voltage capacitor is discharged in step up pulse transformer to generate HV at the secondary to charge PFN capacitor as illustrated in Fig. 1. A Voltage feedback loop around the lower capacitor allows it to be varied as per experimental requirements by varying reference voltage from control room.

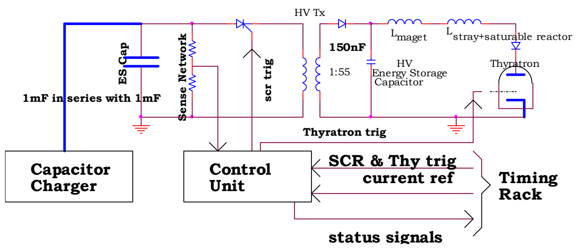

Figure 2: Power Supply Schematic

The switch has to handle 5.5kA peak current with di/dt of 17.27 kA/us at a PRR of 1 Hz with a blocking voltage of 15kV. Thyratron (CX1154) was chosen as a discharge switch as it meets all the requirements, but the switch is associated with two major problems, 1. Slow recovery characteristic, which leads to negative current in the load 2. Reverse arcing if reverse voltage exceeds ~7kV after anode pulse. To mitigate the above mentioned problems, a saturable reactor and diode stack (Fig. 3) was used in series with thyratron. The saturable reactor assistes in two ways[1]- 1. Reduces turn on losses by delaying collapsing anode voltage and rising anode current 2. Reduces initial and decaying di/dt which in turn controls thyratron clean up current. Jitter specifications were met with the help of regulated thyratron auxiliaries, single pulse and fast dV/dt trigger. The load current is characterised by specific feature such as 1. Stipulated peak current stability 2. Tight jitter specifications and 3. Small negative current in load.

Figure 3: Installed power supply in Indus-2 ring

Figure 4: Diode stack assembly

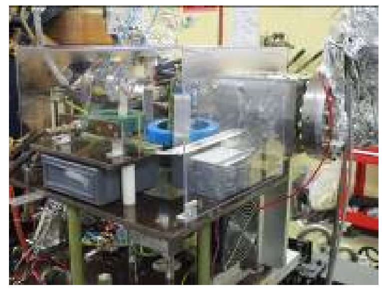

Figure 5: PFN and magnet assembly

TECHNICAL REALISATION

The low voltage capacitor is charged by RC charging scheme. The voltage of LV capacitor (500uF) is stabilized within ± 100 ppm. This LV capacitor when discharged into pulse transformer (1:55) to generate 15kV across yesha make HV capacitors bank (150nF).All the PFN constituents namely HV capacitors, pinger magnet and Thyratron are kept in close vicinity so as to reduce the stray inductance thereby reducing pulse width and charging voltage requirement.

MEASUREMENTS

The magnetic field measurements were carried out by search coil. The current was measured with Pearson make current monitor 110A with sensitivity of 0.1 Volt/Ampere and Tektronix make scope MDO3034 (as shown in Fig. 5). Dependence of charging voltage and output peak current is shown in Figure 6. The pulse width decreases as the charging voltage increases due to presence of saturable inductor in the pulse forming network path .

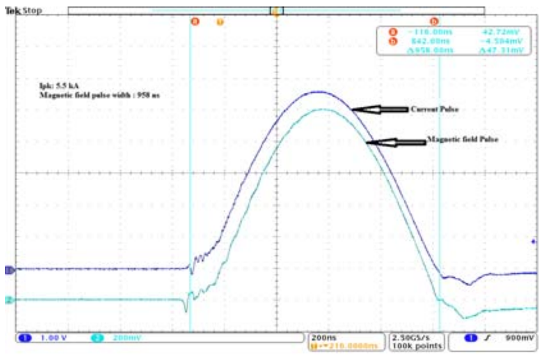

Figure 6: Current pulse and field waveforms

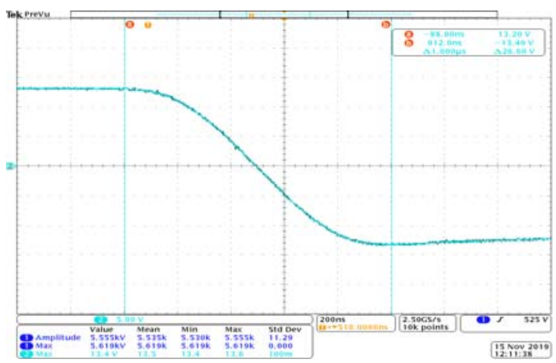

Figure 7: Voltage across HV Energy storage capacitor

The pulser will deliver 5.5kA peak current in load when HV Energy storage capacitor is charged to 15kV. At peak current the achieved current pulse width is 946 ns as shown in Figure 6 . The voltage of the capacitor is reversed due to an under damped circuit behaviour.

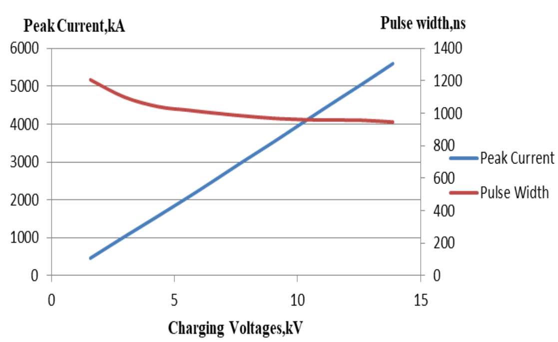

Figure 8: Variation of output current and pulse width wrt to charging voltage

The output current in the load varies linearly with the charging voltage (shown in Figure 8) as they bear linear relationship as mentioned in Equation 1. Pulse width increases with decreasing pulse current due to the non-linear V-I characteristics of the saturable reactor.

ACKNOWLEDGEMENT

The author sincerely thanks Sh Amresh Pandey, Sh Yogesh Raikwar and Sh Yunus Khan in recognition of technical assistance provided by them during development of power supply . We would like to thank Sh Renukanath, Sh M.D. Jha, Sh Chattar Singh who worked tirelessly towards the fabrication of transformers and inductors. Lastly, special thanks are due to Sh Deepchand, Sh G.H. Ansari, Sh Prabhu, Sh Milius Kujur and Sh Shankar Kumar Vishwakarma who assembled various components of the power supply and also installed the power supply in Indus-2 ring.

REFERENCES

[1] Y. P. Singh,U. Karandikar,R. Barothiya,Y.Kelkar, A.C. Thakutra and S. Kotaiah," Development of Indus-2 Kicker Power Supplies,InPAC2003,Indore, p.416

[2] M.Pont, N.Ayala, G.Benedetti, M.Carla, Z.Marti, R.Nuñez," A Pinger Magnet System For The Alba Synchrotron Light Source", ALBA-CELLS, 08290 Cerdanyola del Vallès, Spain

[3] Y. P. Singh, "Development, installation and commissioning of Verticle Pinger magnet power supply in Indus-2," Vol. 33 Issue 1 & 2, 2020, RRCAT newsletter

DESIGN AND DEVELOPMENT OF 125 A, 25 V POWER CONVERTERS FOR COMBINED FUNCTION CORRECTOR MAGNETS IN INDUS-1 STORAGE RING

Vineet Kumar Dwivedi†[1], B. Madhu[1], Manohar Koli[1], Alok Singh[1] and Mangesh Borage[1,2]
[1]Raja Ramanna Centre for Advanced Technology, Indore 452013, India
[2]Homi Bhabha National Institute, Mumbai 400094, India

Abstract

It is proposed to develop a set of eight combined function multipole magnets to facilitate closed orbit distortion (COD) correction. For chromaticity correction, sextupole coils of four magnets will be connected in series and energized by one power supply. Thus, in total two power converters of maximum output rating 125 A/25 V, with output current stability within ± 100 ppm are required. This is a new requirement for performance enhancement of Indus-1. The power converters are developed based on switch-mode, two-switch forward converter (TSFC) topology. So far, two power converters have been developed and tested. The paper reports the design details and test results including the stability data, and special test data.

INTRODUCTION

Due to the space limitation in the Indus-1 ring, a set of eight combined function multipole magnets is being developed to facilitate closed orbit distortion (COD) correction. Each magnet will produce four required magnetic field components, namely, sextupole component to correct the chromaticity, skew quadrupole component to reduce the coupling (between the horizontal and vertical planes), and vertical & horizontal dipole components for steering the beam in both the planes. For chromaticity correction, sextupole coils of four magnets will be connected in series and energized by one power supply. Therefore, two power converters of maximum output rating 125 A/25 V and stability of ± 100 ppm are required. This is a new development for performance enhancement of Indus-1.

The power converters are developed based on switch-mode, two-switch forward converter (TSFC) topology [1]. The converter is operating at 25 kHz switching frequency. IGBTs are used as switching devices. The main features of the new design are: high efficiency, smaller size, less cooling requirement, low audible noise, high stability, better maintainability, etc. The power converters are designed and developed in modular fashion. Each module is developed and tested separately. All the modules are integrated in cabinet. Open and closed loop testing at low as well as high power testing has been carried out. Apart from these functional tests, heat run test and special endurance tests, such as current cycling tests, etc., have been carried out. Stability for eight hours of continuous operation has been recorded to be well within the specification of ± 100 ppm.

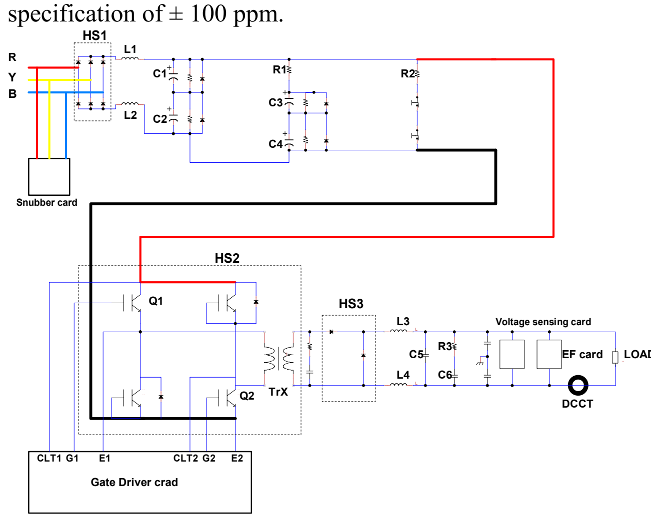

Fig.1: Schematic diagram of the power module.

THE POWER CONVERTER

The power converters are designed and developed in modular fashion. The power converter consists of three modules namely power module, breaker module and control rack. Each module has been developed and tested separately.

Power Module

A schematic diagram of the power module is shown in Fig. 1. The converter operates from 415 V, 3-phase ac mains. Three phase ac mains is rectified and filtered to get the intermediate dc-link voltage for the dc-dc converter. Switch *Q1*-*Q2*, transformer T_rX, diode module on HS9 and output L-C filter L_3, L_4, C_5, C_6, R_3 constitute TSFC stage. All switches Q_1 *and* Q_2 are insulated gate bipolar transistors (IGBT) operating at 25 kHz. Power converter is capable of providing 25 V, 125 A output. Various PCBs such as input current sensing cards for sensing transformer primary current, isolation amplifier card for sensing output voltage, IGBT driver card to drive IGBT switches are present in power converter module. All power semiconductor components and transformer is placed on heat sinks. Thermostats are placed on each heat sink for temperature interlock of heat sink. DCCT is placed on this module for sensing of output current. Power module is tested independently after wiring using test simulator and its functionality is ensured before integration into the power converter.

† email address: vineet@rrcat.gov.in

Breaker Panel

Breaker panel comprises of front-end circuit breakers and contactors along with auxiliary electrical devices such as circuit breaker, main and auxiliary contactor, timer relay, ac under voltage relay, inrush limiting resistors etc. Auxiliary contactor, along with the inrush limiting resistors, is used for limiting inrush current of capacitor. Terminal blocks are placed on breaker panel for termination of various connections from outside/inside such as single phase input, magnet water and temperature interlock, contactor on indication, fire interlock, etc. The function of breaker panel is to interface three phase ac line with the power module. In the event of fault, three phase supply will be interrupted through main contactor present in this breaker panel. Breaker panel is also tested separately with the help of test simulator before integration into the power converter.

Control Rack

The control rack is a 19-inch mounting rack which houses 5 cards namely auxiliary supply card, DCCT supply card, fault interlock card, control card and remote/local interface card. The function of control rack is to provide necessary control signals for proper functioning of power converter. The control card has precision electronic circuit for feedback control of output current and pulse-width-modulator that provides pulses of variable duty cycle to IGBTs. There are two loops in the control circuit: the inner voltage loop and outer control loop. Voltage loop is fast as compared to current loop. The bandwidth of voltage and current loop are 1 kHz and 35 Hz respectively. In order to improve the stability of the power converter, front-end electronics such as reference and feed-back amplifier, error amplifier, integrator etc. are kept in constant temperature environment. Oven is used to for this purpose. The temperature in the oven is maintained at 41 degree C. To ensure safety of the power converter and the magnet load, various internal and external signals are interfaced in the fault interlock card where they are compared with pre-set limits. These signals include over current, over voltage, ac under voltage fault, ac mains overload fault, magnet water fault, magnet over temperature fault, IGBT faults, load earth fault, DCCT supply failure fault, auxiliary supply failure fault, input over current fault etc. The remote interface card facilitates the operation of the power converter either in local mode or in remote mode. Auxiliary supply card provide various power supply such as ± 15V, ± 12V etc. to all the ICs present in control card, local remote card and fault card. DCCT supply card provides auxiliary supply to DCCT for its operation. Figure 2 depicts the photograph of power converter which shows all the three modules.

RESULTS AND DISCUSSION

Waveforms of voltage across IGBT switch and corresponding gate drive voltage are shown in Fig. 3. The output rectified voltage and overall output voltage is shown in Fig. 4. The output current of the power converter sensed by DCCT is logged for eight hours of operation to measure the output current stability. It is clear from the stability graph that the stability of the power converter is within ±100 ppm which is the required objective

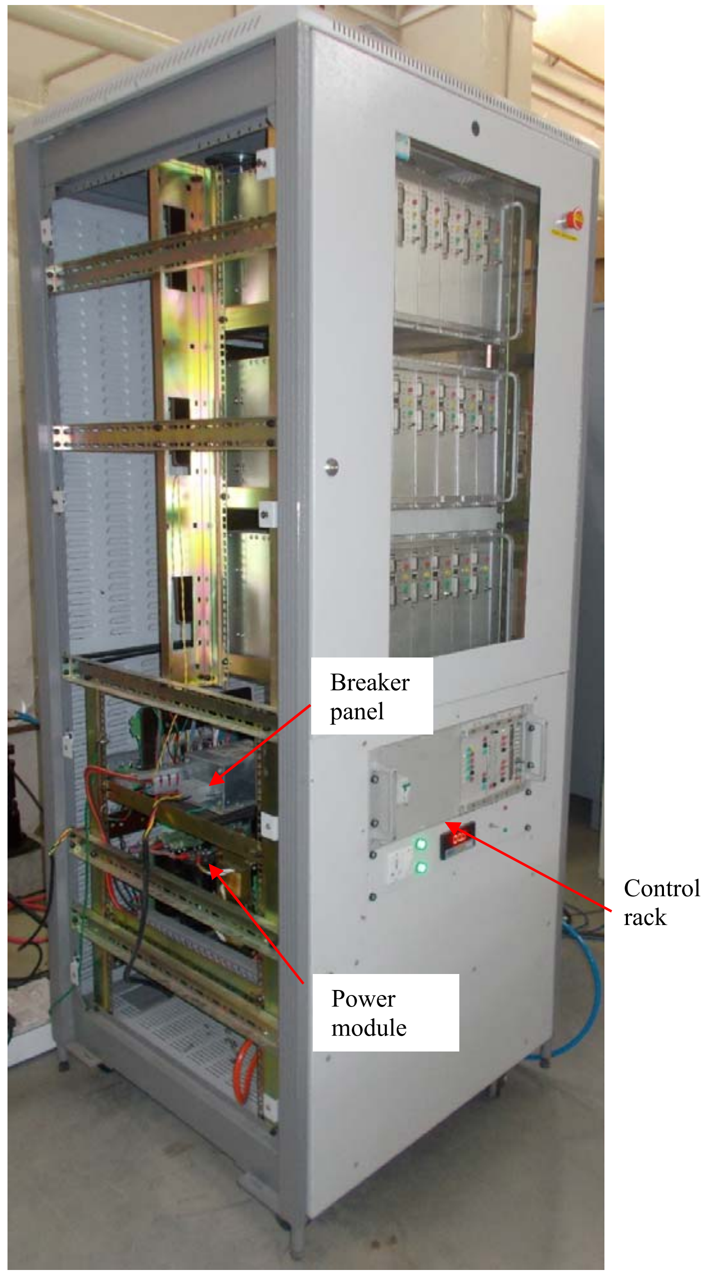

Fig.2: Photograph of the 125 A/25 V power converter

Rectified and output voltage is shown in Fig.4. Power converter has also a feature to prevent false tripping if there is sudden large-signal change in the reference. If there is large change in the reference, the voltage will be clamped at 25 V maximum [Fig. 5]. Bandwidth of the current loop has been measured practically to be approximately 35 Hz by applying small-signal step [Fig. 6]. Special endurance test has been carried out with power converters to simulate different operating modes of the power converter operation in slightly over-stressed conditions for accelerated testing. These tests help in identifying the weak links in the power converter during the laboratory testing itself, which helps in increasing the operational reliability of the power converters. The power converters are cycled to ensure magnet field repeatability. To induce cyclic electro-mechanical stress on various converter components, multiple cycles (typically forty cycles) of current from 5 % to 100 % of the rated current with current ramp rates much higher than those experienced during normal operation (typically 10-15 times) are carried out.

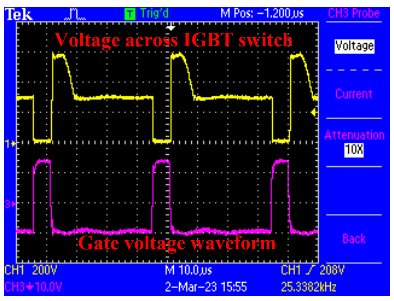

Fig.3: 1.Voltage across IGBT: Ch1 200 V/ div and 10 µs/div. 2. IGBT gate drive voltage: Ch3 10 V/div and 10 µs/div.

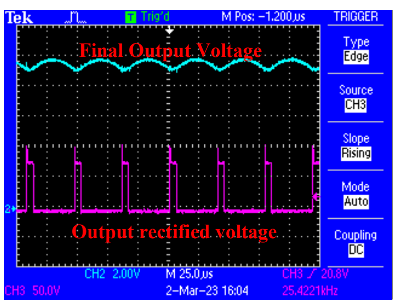

Fig.4: Key waveforms 1Output dc voltage: Ch2: 2 V/ div and 25 µs/div. 2.Output rectified voltage: Ch3: 50 V/div and 25 µs/div.

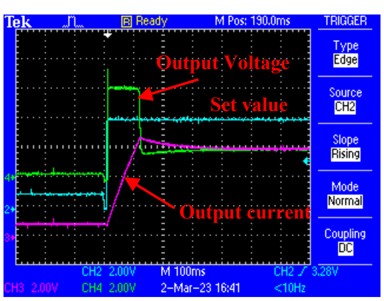

Fig.5: Large signal step test 1. Set value: Ch2: 2 V/ div and 100 m/div. 2. Output rectified voltage: Ch3: 2 V/div and 100 ms/div. 3.Output voltage: Ch4: 2 V/div and 100 ms/div.

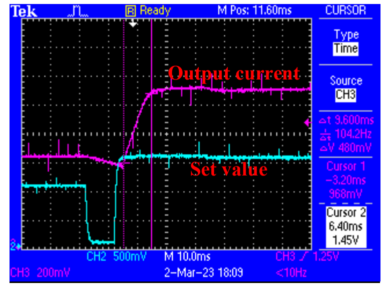

Fig.6: Small signal step test. 1. Set value: Ch2: 500 mV/ div and 10 ms/div. 2. Output current: Ch3: 200 mV/div and 10 ms/div.

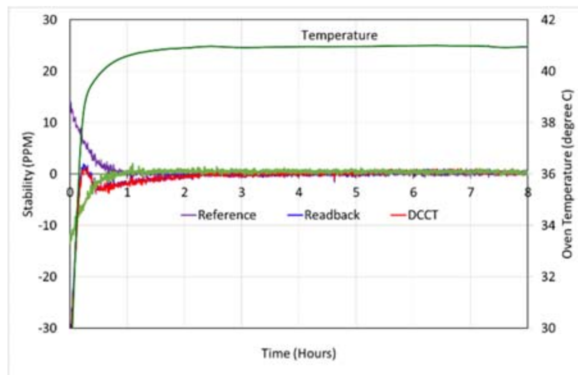

Fig.7: Output current stability for eight hours of continuous operation

The output current of the power converter sensed by DCCT is logged for eight hours of continuous operation for determining output current stability. Other logged signals are set reference, oven temperature etc. The stability graph is shown in Fig. 7. It is clear from the graph that the stability of the power converter is within ±100 ppm which is the required objective.

ACKNOWLEDGEMENT

The authors acknowledge the contribution of Shri P. Renukanath and his team for development of magnetic components, Shri Deepchand and his team for mechanical assembly of the power converter. Contribution of Shri S. K. Prajapati, Sh. V. W. Somkuwar and Sh. S. Mani at various stages of development and testing of the power converters is acknowledged.

REFERENCES

[1] Vineet Kumar Dwivedi, Alok Singh, Manohar Koli, Mangesh Borage and S. R. Tiwari “Design and development of new 20 kW power converters for quadrupole magnets in Indus-2”, Proc. of DAE-BRNS Indian Particle Accelerator Conference-2018 (InPAC-18) RRCAT, Indore, Jan-2018.

DESIGN AND SIMULATION OF UPGRADED 800 A, 140 V POWER CONVERTER FOR INDUS-1 DIPOLE MAGNET

Alok Singh#1 and Mangesh Borage[1,2]
[1]Raja Ramanna Centre for Advanced Technology, Indore 452013, India
[2]Homi Bhabha National Institute, Mumbai 400094, India

Abstract

The existing power converter for Indus-1 dipole magnet (800 A/140 V, ±100 ppm stability) is based on 12-pulse thyristor based rectifier scheme and is in operation for more than 25 years. It is planned to upgrade this power converter with technologically superior option based on switch-mode topology wherein five power converter modules operate in parallel with current sharing control, providing 4+1 redundancy. Each module consists of two stages of two-switch forward converter operating in Input Parallel Output Series (IPOS) configuration. This paper describes power converter architecture, highlight its features, presents design principle, layout details, and discusses simulation results.

INTRODUCTION

In Indus-1 synchrotron radiation source, four bending magnets are connected in series and energized by a single power converter with output ratings of 800 A/140 V and output current stability better than ±100 ppm. The existing power converter, based on 12-pulse thyristor based rectifier scheme [1], is in operation for more than two decades hence, most of the power components like magnetics, electromechanical components, electrolytic capacitors, etc. are reaching to their end of life. Maintaining spares for these components also becomes difficult as some of the components have become obsolete and retrofitting the available components in the running machine becomes difficult due to time and layout constraints. For these reasons, it is planned to develop a new power converter for the Indus-1 dipole magnet following switch-mode power converter scheme having smaller size, faster dynamic response, better power factor, better maintainability, etc.

DESIGN PRINCIPLE AND FEATURES

Power Converter Architecture

The new power converter is planned to be developed not as a single unit delivering 800 A / 140 V, but as an appropriate number of modules operating in parallel with current sharing control. As shown in Fig. 1, the power converter architecture consists of five 200 A / 140 V dc-dc power converter modules operating in parallel with 4+1 redundancy. In normal operation, when all the five modules are in healthy condition then each one operates at part load of 160 A to deliver maximum output current of 800 A. However, if any one module fails then the remaining four would share the load with each operating at its full rated capacity of 200 A. This N+1 redundancy will significantly increase the overall availability of power converter and reduce the machine down-time. The power converter operates on 3-phase 415 V, 50 Hz ac mains and all the five dc-dc modules share single ac-dc converter stage consisting of 3-phase diode rectifier and low pass filter as shown in Fig. 1.

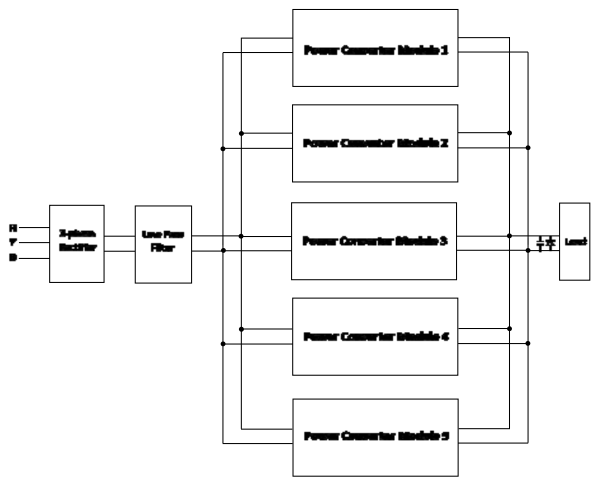

Figure 1: Power converter architecture

Topology and Salient Features

The new power converter is based on switch-mode topology which helps in achieving faster dynamic control, smaller size, lighter weight and improved power factor. Each power converter module consists of two stages of two-switch forward converter (TSFC) operating in Input Parallel Output Series (IPOS) configuration as shown in Fig. 2. This configuration has inherent load sharing capability and helps in distributed thermal management by equally distributing power losses between the two stages. Stresses in power semiconductor devices are also significantly reduced which helps in achieving high reliability. The two TSFC stages operate at switching frequency of 25 kHz in phase-staggered manner, thereby resulting in reduced ripple amplitude at the output along with frequency doubling. Similar module, rated for 20 kW maximum output power, has been used in new power converters for Indus-2 quadrupole magnets [2]. The design and layout of the power converter module is significantly updated to improve power density as well as maintainability.

#aloksingh@rrcat.gov.in

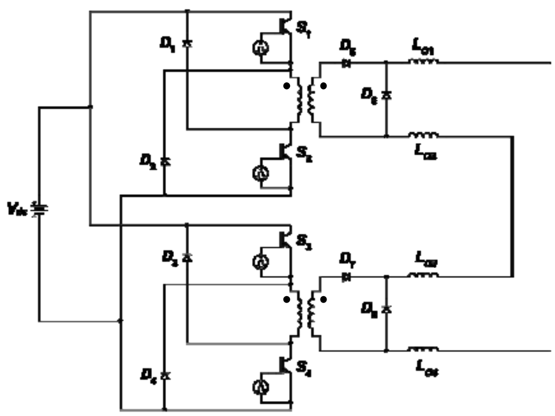

Figure 2: Schematic of each power converter module

The five power converter modules also operate in phase-staggered manner thereby, further reducing ripple amplitude in the final output and increasing the ripple frequency to 10 times of the switching frequency. Hence, a common output filter capacitor of low value can be used for all the five modules. Each module is equipped with a precision shunt made of manganin to sense the module current while a DCCT will be used to sense the total output current. In addition to this, an antiparallel diode is connected across the final output to freewheel the magnet energy whenever power converter becomes off.

Layout and Design Details

The layout of each power converter module is designed judiciously to achieve compactness, mitigate electromagnetic interference (EMI) and facilitate ease of maintenance. A high frequency filter is used at the input of each module to minimize variations in the dc link voltage due to flow of high frequency currents between TSFC stages and dc line. For EMI mitigation, distance between power circuit components carrying high frequency currents is kept minimum in order to minimize wiring lengths; signal wires and power cables are routed separately to the extent possible and overlapping, wherever required, is done at 90°; twisted and shielded pair of wires are used for routing feedback and gate drive signals. In addition to this, IGBTs and their driver cards are mounted in close vicinity.

Figure 3 shows the labelled photograph of a power converter module. A common high frequency filter capacitor bank of value 30 µF is used for both the TSFC stages in a module. For this, a compact assembly consisting of four IGBTs and three capacitors is fabricated on a water cooled heat sink as shown in Fig. 3. As shown in the figure, high frequency transformers of both TSFC stages are mounted on a single water cooled heatsink of size 450 mm x 450 mm x 10 mm to achieve compactness and simplify water cooling circuit. Each high frequency transformer is designed to have turns ratio of 5:2 and is made of 16 pairs of EE128.64.20 ferrite cores. Output filter inductors shown in Fig. 2 as L_{O1}, L_{O2}, L_{O3} and L_{O4}, respectively, have inductance of 35 µH each and are made of Metglas AMCC400 cores. The precision shunt and its amplifier card are shielded from stray magnetic fields using CRGO plates for achieving high signal to noise ratio. Thermostats are mounted on all heat sinks for over temperature protection. Infineon FF150R12RT4 IGBT modules are used as semiconductor switches while Vishay VSUD400CW60 ultra-fast soft recovery diode modules are used in the secondary rectifier circuit.

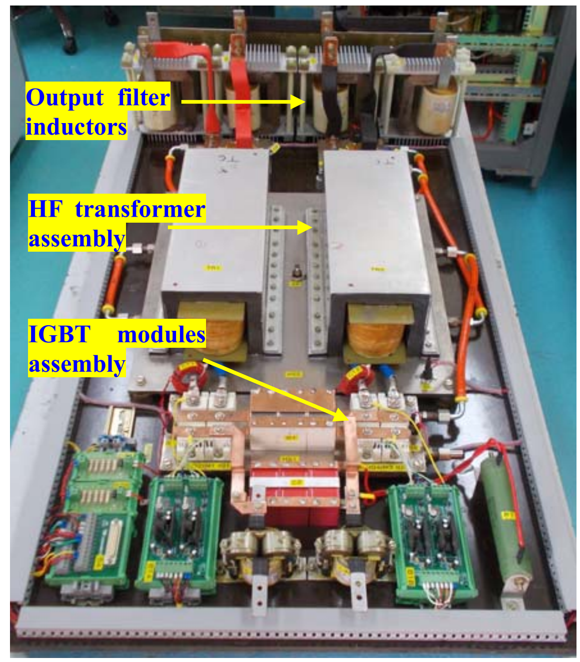

Figure 3: Labelled photograph of a power converter module

RESULTS AND DISCUSSION

Simulation studies are carried out using OrCAD PSpice Designer Software 17.2 for design validation. Figure 4 shows simulation results for a single power converter module consisting of two stages of TSFC operating in phase-staggered manner with duty ratio (D) of 0.75. In Fig. 4, the output of two TSFC stages are marked as “TSFC1 output” and “TSFC2 output”, respectively, while the overall module output is labelled as “Output of power converter module”. As shown in the figure, the output voltage of both TSFC stages contain ripple frequency of 25 kHz, which are phase-staggered by 180° or 20 µs to generate twice voltage at the output with reduced ripple amplitude and double ripple frequency of 50 kHz.

Figure 5 shows simulated output current waveforms of all the five power converter modules along with the final output voltage when each TSFC stage operates with duty ratio (D) of 0.35. In Fig. 5, output current of all the modules are labelled as “Module i output current”, where i = 1 to 5, and the final output voltage of the power converter is labelled as “Output voltage”. In simulation, ‘Module k+1’ is phase staggered by ‘Module k’ by 72° or 4 µs, where k = 1 to 4.

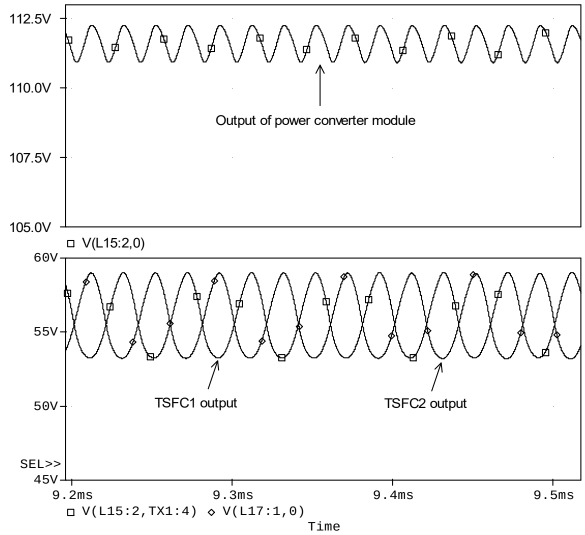

Figure 4: Simulated output waveform of a module with phase-staggered operation of two TSFC stages at D=0.75

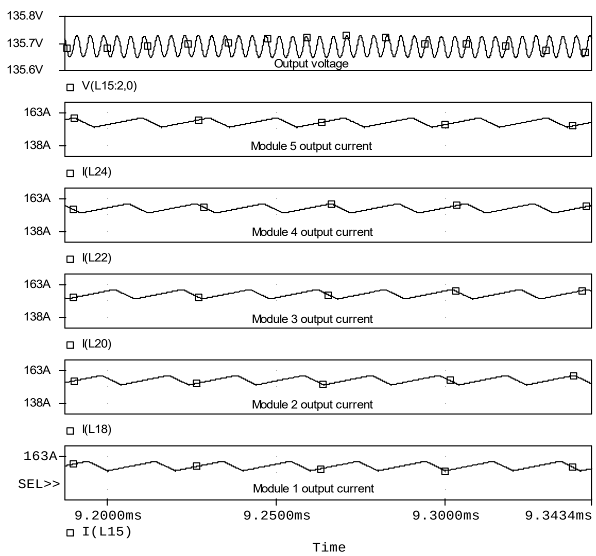

Figure 5: Simulated current waveforms of 5 modules with phase-staggered operation along with final output voltage

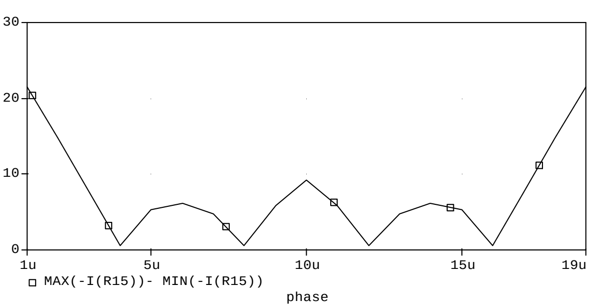

Figure 6: Variation in output voltage ripple for different phase-stagger values

As a result, ripple amplitude in the final output is reduced significantly and the ripple frequency increases to 10 times of the switching frequency, i.e., 250 kHz as shown in Fig. 5.

Figure 6 shows simulation results for variation in the ripple amplitude of the final output voltage of power converter with respect to phase-stagger (µs) between consecutive modules. As shown in the figure, the ripple amplitude is minimum when the value of phase-stagger is (*mT/2N*), where '*m*' is an integer, '*T*' is time period and '*N*' is the number of modules operating in parallel.

ACKNOWLEDGEMENT

The authors acknowledge the contribution of Shri P. Renukanath and his team for development of magnetic components, Shri Deepchand and his team for mechanical assembly of the power converter modules. Contribution of Shri S.K. Prajapati, Sh. V. W. Somkuwar, Sh. S. Mani and Sh. Bheemireddi Madhu at various stages of fabrication and wiring of power converter modules is acknowledged.

REFERENCES

[1] S.R. Tiwari, A.C. Thakurta, A.P. Thipsay, A. Pagare, M.L. Gandhi, T.N. Singh, Shyam Singh, S. Kotaiah, "Power Supplies for Indus-1", Asian Particle Accelerator Conference - 1998 (APAC-98), Tsukuba, Japan, Mar. 23-27, 1998.

[2] Vineet Kumar Dwivedi, Alok Singh, Manohar Koli, Mangesh Borage and S. R. Tiwari, "Design and Development of New 20 kW Power Converters for Quadrupole Magnets in Indus-2", Indian Particle Accelerator Conference-2018 (InPAC-18), RRCAT, Indore, India, Jan., 2018.

SIMULATION STUDIES ON SERIES CONNECTED FAST-RAMPED POWER CONVERTER MODULES FOR BOOSTER SYNCHROTRON

Pokharkar Rahul Rohidas[#,1,2], Abhishek Srivastava[1], Alok Singh[1], Mangesh Borage[1,2]
[1]Raja Ramanna Centre for Advanced Technology, Indore, 452013, India,
[2]Homi Bhabha National Institute, Mumbai, 400094, India

Abstract

In booster synchrotron, fast-ramped power converters (FRPC) are used for ramping up magnetic field at a fast rate. Studies reported in this paper are on a switch-mode FRPC with grid power control, which consists of DC link capacitor, two-switch forward converter (TSFC) as a front-end DC-DC converter for grid power control and a two-quadrant power converter (TQPC) for load current control. Circuit simulation of switch-mode converters for longer times (of the order of seconds) is computationally intensive and time consuming task for commercial simulation platforms. Therefore, simulation studies reported in this paper are carried out using equivalent circuit models of TSFC and TQPC. Effect of unequal input DC voltage of TQPCs on output voltages is presented for 2 series connected TQPCs. Simulation is performed to illustrate the energy flow between DC link capacitor and magnet.

INTRODUCTION

In booster synchrotron, magnetic field needs to be ramped up at a fast rate (typically within 100s of milliseconds) in synchronism with energy of charged particle. For this purpose, FRPCs are used, which are capable of operation in two or four quadrants, to energize series string of electromagnets. High peak power, having a large reactive component, needs to be handled by the power converter. Large reactive power fluctuations are undesirable as these causes various power quality issues, most notably the voltage flicker [1].

In large accelerators, electromagnets to be energized in series are large in numbers. The peak voltage encountered by power converter is prohibitively large during ramping. To minimize this voltage within feasible limits, the total number of magnets are divided into number of smaller sections of magnets in series and each section of magnets is energized by separate power converter. The power converter, depending on the power levels involved, itself may need to be developed not as a single unit but by connecting suitably rated modules in series.

The studies reported in this paper are done on FRPC which consists of DC link capacitor for energy storage purpose, TSFC and TQPC. TQPC is used for providing the required current to magnet load. TSFC is used to program the voltage across DC link capacitor in such a way that only active power is drawn from the source [2]. Circuit and block diagram of FRPC is shown in Fig. 1. AC-DC converter is connected to TSFC. TSFC control card and TQPC control card are used for controlling voltage output of TSFC and current output of TQPC, respectively.

EQUIVALENT CIRCUIT MODEL

Circuit simulations of switched-mode power converters operating at kilo-Hertz switching frequencies for longer time (of the order of seconds) is computationally intensive and time consuming task. Therefore, simulation studies are carried out using equivalent circuit models. While this method does not provide information on high-frequency parameters, it speeds-up the simulations to a great extent [3]. The studies reported in this paper are done on two FRPCs in series, for which equivalent circuit model of TSFC and TQPC are formulated.

Circuit averaging is popular technique for deducing power converter equivalent circuits. In this technique, power converter waveforms are averaged instead of averaging state equations of power converter. All the manipulations are carried out on the circuit diagram. Thus, the circuit averaging technique gives a more physical interpretation to the model [3].

Equivalent circuit model of TQPC

Circuit diagram of TQPC is shown in Fig. 1. S_1 and S_2 are IGBTs, D_5 and D_6 are diodes, L_1 is filter inductor, C_1 is filter capacitor. R_D and C_D are damping resistor and capacitor, respectively. For formulating the equivalent circuit model of TQPC, switch network is replaced with voltage and current source. This is done for obtaining a time invariant circuit topology. Then, converter waveforms

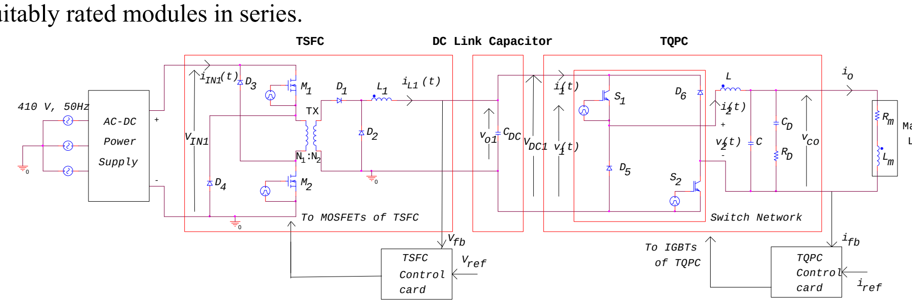

Figure 1: Circuit and block diagram of FRPC

#rahulpokharkar@rrcat.gov.in

are to be averaged over a switching time period to remove switching harmonics. The model obtained in this step is non-linear. Further, linear model is obtained from the averaged non-linear, time-invariant model. Small perturbation is introduced around DC operating point of averaged quantities and by introducing small perturbation and neglecting 2nd order terms, the model is obtained and is shown in Fig. 2. Where, variables with '~' denote small perturbations. V_{DC}, V_2, D, I_1 and I_2 are DC operating values.

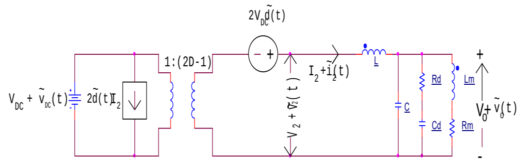

Figure 2: DC and small-signal AC model of TQPC [2]

Equivalent circuit model of TSFC

Circuit diagram of TSFC is shown in Fig. 1. M_1 and M_2 are MOSFETs. D_3, D_4 are diodes on primary side. D_1, D_2 are diodes on secondary side. TX represents the transformer with turns ratio N_1: N_2. D_F is the duty cycle. L_1 is the filter inductor. C_{DC} (DC link capacitor) is used as the filter capacitor. Equivalent circuit model of TSFC is formulated following the same steps as that for TQPC. The model obtained is shown in Fig. 3.

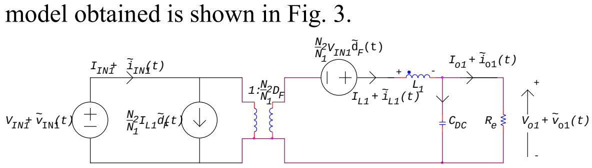

Figure 3: DC and small-signal AC model of TSFC

SIMULATION RESULTS

Equivalent circuit model simulation of two TQPCs in series is performed. This simulation is done in order to study the output voltages of individual and series connected TQPCs when fast ramping current is supplied by PCs to magnet load. It is assumed that fast ramping current to be supplied by PC is having lower and upper current value of 0 and 100 A, respectively. Input DC voltages to first and second TQPCs are denoted by V_{DC1} and V_{DC2}, respectively.

First, ideal case simulation is performed. Simulation circuit of equivalent circuit model of two TQPCs in series is shown in Fig. 4. It is assumed that $V_{DC1} = V_{DC2} = 50\ V$. Filter inductors and capacitors for both the TQPCs are $L_1 = L_2 = 80\ uH, C_1 = C_2 = 20\ uF$. Magnet load is assumed to have $R_m = 0.165\ \Omega, L_m = 54\ mH$. i_0 is output current, v_{c1} and v_{c2} are output voltages of individual TQPCs, v_{c0} is output voltage of series connected TQPCs. Type-2 compensator is used for controlling the output current [2]. Simulation waveforms of i_0, v_1, v_2 and v_0 under ideal case are shown in Fig. 5.

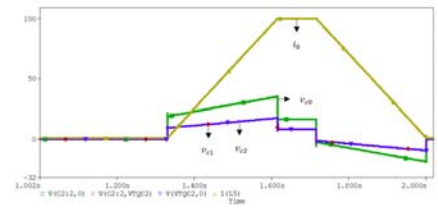

Figure 5: Simulation waveforms of i_0, v_{c1}, v_{c2} and v_{c0}

Effect of unequal input DC voltage

Practically, input DC voltages to both TQPCs will not be equal. Thus, effect of unequal input DC voltage ($\pm$ 10 % deviation) is studied with assumption that input DC voltage is $V_{DC1} = 55\ V$ and $V_{DC2} = 45\ V$. Simulation waveforms of i_0, v_{c1}, v_{c2} and v_{c0} are shown in Fig. 6.

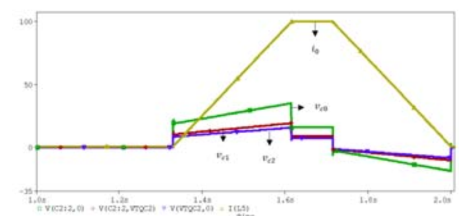

Figure 6: Simulation waveforms of i_0, v_1, v_2 and v_0 under unequal V_{DC} case

It can be observed from the simulation waveforms that v_{c1} is 1.1 and 0.9 times of output voltage in ideal case, respectively. This result emphasizes the importance of maintaining equal input DC voltages for two TQPCs.

Simulation for illustration of energy flow

Electrical equivalent of electromagnet is resistor and inductor in series. Energy flow is studied when fast-ramped current is supplied by PC to magnet load and simulation

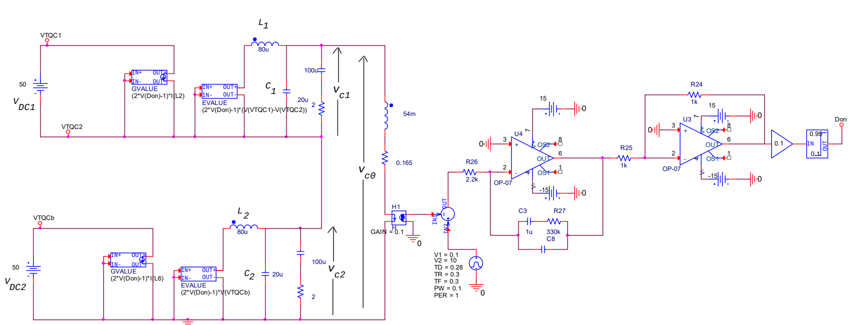

Figure 4: Equivalent circuit model simulation circuit of 2 TQPCs in series

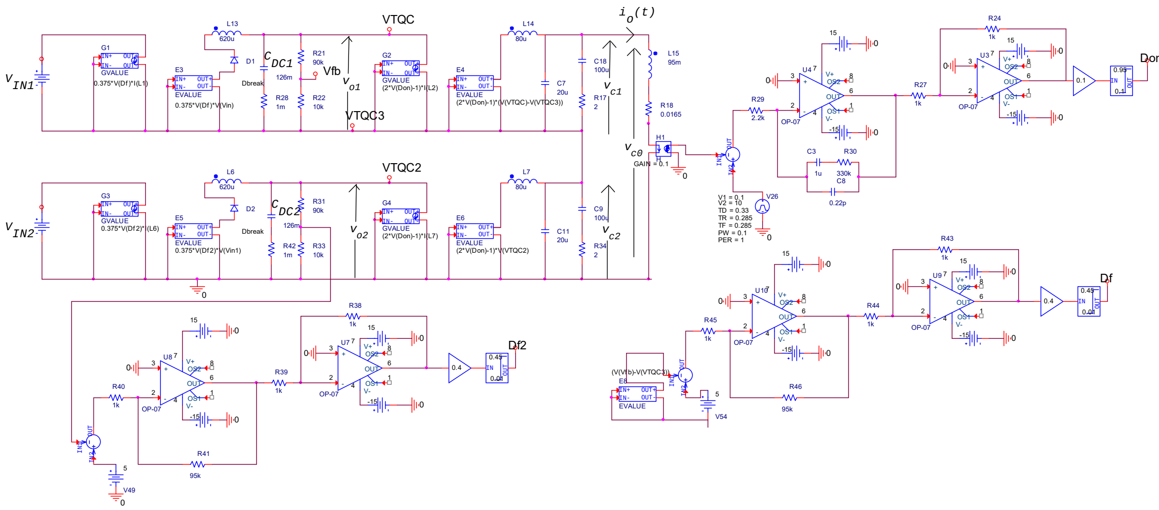

Figure 7: Equivalent circuit model simulation circuit of 2 FRPCs in series

circuit is shown in Fig. 7. Power is fed to the magnet load during ramp-up phase. Stored power in magnet is fed back to the source during ramp-down phase and stored in DC link capacitors C_{DC1} and C_{DC2}. Ideally, the active power is supplied by TSFC and the reactive power is supplied by DC link capacitor. Voltage across DC link capacitor ($v_{o1}(t)$) and current through inductor (magnet) ($i_o(t)$) are as shown in Fig. 8. V_1, I_1 and V_2, I_2 are values of $v_{o1}(t)$ and $i_o(t)$ at time t_1 and t_2, respectively. R_m and L_m are magnet resistor and inductance, respectively.

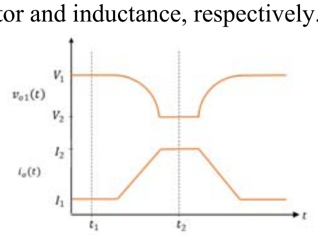

Figure 8: Waveform of $v_{o1}(t)$ and $i_o(t)$

Value of V_1 can be determined using (1).

$$V_1 = \sqrt{{V_2}^2 + \frac{L_m {I_2}^2}{2C}} \qquad (1)$$

Simulation is carried out in order to validate above equation and parameters considered are, $I_1 = 0$ A, $I_2 = 100\,A$, $L_m = 95.28\,mH$, $R_m = 0.0165\,\Omega$, $V_2 = 50\,V$. Simulation waveform of $v_{o1}(t)$, $v_{o2}(t)$ and $i_o(t)$ for $C_{DC1} = C_{DC2}$ = 126 mF is shown in Fig. 9.

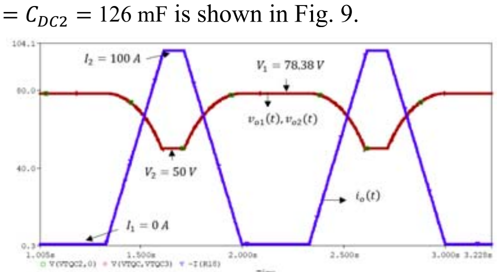

Figure 9: Simulation waveforms of $v_{o1}(t)$, $v_{o2}(t)$ and $i_o(t)$

DC link capacitor values are varied, V_1 is obtained by simulation and compared with V_1 obtained using (1) (table 1). It is clear from table 1 that V_1 from analytical matches closely with V_1 obtained from simulation.

Table 1: Values of C_{DC1}, C_{DC2}, V_1

$C_{DC1} = C_{DC2}$	V_1 (analytical)	V_1 (simulation)
126 mF	79.24 V	78.38 V
94.5 mF	86.84 V	85.78 V
63 mF	100.29 V	98.94 V

CONCLUSION

An overview of need and benefits of equivalent circuit model is presented. Equivalent circuit model is developed for TQPC and TSFC. Simulation for two PCs in series is performed when PC is supplying fast-ramped current to magnet load. Effect of unequal input DC voltage on output voltages of TQPCs is studied. This result emphasizes the importance of maintaining equal input DC voltages for two TQPCs. Further, simulation is carried out to illustrate the energy flow between DC link capacitor and magnet. The expression according to which energy flow takes place is verified.

REFERENCES

[1] J.F. Bouteille, "Power Converters for Cycling Machines", Proceedings CAS-CERN Accelerator School: Power converters: Baden, Switzerland, May 7-14, 2014.

[2] Abhishek Srivastava, "Analysis, design and development of fast-ramped, switch-mode power converter for inductive load", M.Tech. dissertation, Homi Bhabha National Institute, January 2022.

[3] Robert W. Erickson, Dragon Maksimovic, "Fundamentals of power electroncis", 2nd ed., Kluwer Academic publishers, 2004.

DEVELOPMENT OF HIGH-STABILITY TRUE-BIPOLAR POWER CONVERTERS FOR UPGRADED CLOSED ORBIT DISTORTION CORRECTION SCHEME IN INDUS-1 STORAGE RING

Manohar Koli[#,1], Bheemireddi Madhu[1], Vinod Kumar[1], Sanjay Kumar Prajapati[1], Vinod Somkuwar[1], Sundaram Mani[1], Pokharkar Rahul Rohidas[1], Abhishek Srivastava[1], Vineet Kumar Dwivedi[1], Alok Singh[1] and Mangesh Borage[1,2]
[1]Raja Ramanna Centre for Advanced Technology, Indore 452013, India
[2] Homi Bhabha National Institute, Mumbai 400094, India

Abstract

A set of eight combined function multipole magnets will be installed to facilitate Closed Orbit Distortion (COD) correction in Indus-1. To energize the horizontal and vertical corrector coils as well as the skew-quadrupole coil on these magnets, in all 24 high-stability, output-current-controlled power converters rated for output current of ±12 A and output current stability within ±100 ppm are required. These bipolar power converters need to have smooth zero-current-cross-over, with precise control while operating near zero. The paper discusses the design and development activities and salient results of these high-stability true bipolar power converters for upgraded COD correction scheme in Indus-1 storage ring.

INTRODUCTION

An upgraded closed-orbit-distortion (COD) correction scheme in Indus-1 storage ring will have new magnetic elements, better diagnostic devices, systems and capabilities to facilitate stable and repeatable operation of the machine. To produce skew quadrupole component to reduce the coupling (between the horizontal and vertical planes), and to produce vertical & horizontal dipole components for steering the beam in both the planes in these magnets, in all 24 high-stability, output-current-controlled, bipolar power converters rated for output current of ±12 A and output current stability within ±100 ppm are required. The power converter is based on the full-bridge converter whose design is standardized on a 6U, four-layer PCB. Five such power converter cards are housed in one 19-inch 6U rack. The prototype converter was first developed and tested rigorously Subsequently, series manufacturing of 30 power converter cards, that included spare power converters, was carried out with industry support.

THE POWER CONVERTER

The power circuit is based on four-quadrant, non-isolated, switch-mode power conversion scheme that uses MOSFETs operating at 50 kHz with unipolar PWM scheme [1]. With this scheme, the ripple frequency is doubled, that reduces size of filter components and facilitates miniaturization.

The overall block diagram of power converter is shown in Fig.1. This is basically a DC to DC full-bridge converter. The full-bridge converter consists of MOSFET switches (Q1 to Q4). These MOSFETs have low on-state resistance that reduces the conduction losses. The input DC-link electrolytic filter capacitor is placed near to the full-bridge to absorb high-frequency currents and reduce the overvoltage transients. The voltage generated by the bridge is filtered through high frequency inductors L1 and L2 and capacitor C4. Cd an Rd form the damping branch for the filter. Capacitors C2 and C3 are used for common-mode filtering. Thus the filter provides differential as well as common mode filtering.

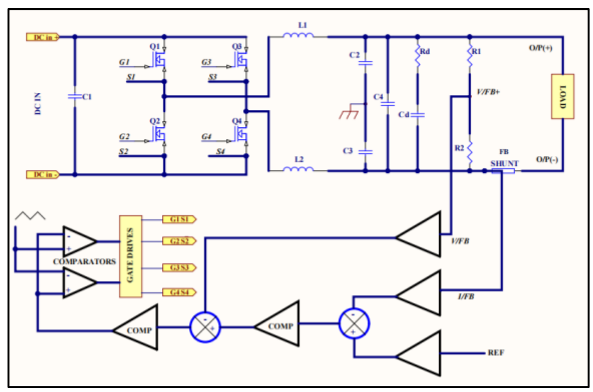

Fig.1: Block diagram of the power converter.

CONTROL CIRCUIT

The gate drive pulses for the MOSFET switches Q1 to Q4 have been generated by comparing the control voltage with triangular carrier signal. This control voltage is obtained from the feedback control loop. The feedback control has two loop architecture having outer current loop and the inner voltage loop. In the outer current loop, load current is sensed from the shunt resistor in voltage form. This sensed voltage is amplified by current feedback amplifier. Two current shunts have been incorporated: one for sensing the current for the current feedback loop and the other one to obtain current read back, to read and display the output current.

High stability precision potentiometers have been used for calibration and read the output current. Low drift ultra precision op-amps, metal film resistors and resistor arrays with ±15 ppm per Deg. C temperature coefficient, along with stable reference, have been used to achieve the required stability. All components of front end electronics

#manohar@rrcat.gov.in

have been placed in temperature controlled oven for constant temperature operation. Temperature of the oven is maintained at ~40 ºC and is kept stable within 1 ºC. The bandwidth of the inner current loop is ~35 Hz. The output of current loop acts as the reference for the inner voltage loop, which has the bandwidth of ~1.5 kHz for fast correction against the input voltage fluctuations.

The control voltage of the voltage control loop (and its inverted voltage) is compared with the triangular carrier signal generated by using function generator IC ICL8038 to generate four gate pulses suitable for unipolar PWM switching scheme. The gate pulses for switch Q1 and Q4 are generated by comparing control voltage with triangular carrier wave. Similarly, gate pulses for switch Q2 and Q4 are generated by comparing negative control voltage the triangular carrier voltage. Before applying to MOSFET, these gate pulses are fed to four driver ICs VO 3120, which is fed with isolated power supply generated by four ICs VLA106 15242.

Apart from the feedback loop, the control electronics also has circuit sections to perform power supply ON, OFF and RESET operation. Similarly, it has four channels for protection against abnormal operating conditions. The card has 12-T fascia panel fitted with LEDs and test points.

The power converter has the remote operation interface, which is provided through a 25-pin D-type connector. The power converter can be made ON, OFF, RESET. Similarly, status of the power converter can be monitored. The setting of the output current to be delivered by the power converter is done via analog programming in the range of -10 to 10 V. A readback signal is also provided in the same scale. In addition, another 15-pin D-connector is provided to monitor different internal signals of the power converter for diagnosis purpose, if required.

DEVELOPMENT STRATEGY

The power converter with its full-function power and control circuit is developed on one four-layer 6U sized PCB. The prototype converter was first developed and tested rigorously for long-duration continuous operation. Heat run test carried out for maximum rated power. Experimental results for the proto type have been captured in which long term stability, frequency response under different modes, namely, dc operation at positive/negative maximum current; cyclic bipolar operation with sinusoidal and triangular output currents, etc. Stepping resolution test have been carried out. It was planned to develop 30 power converters so that five power converter modules will be housed in one 6U. In all, six such racks are developed. In each rack, four power converter cards are used normally to feed the power to the load and one card is kept as spare, which ensures ease maintenance due to availability of on-site spare card.

For series manufacturing schematic diagram and bill of material (BOM) were finalized. Subsequently, series manufacturing of 30 power converter cards was carried out with industry support. For the testing of individual power converter cards, a detailed document providing testing guidelines was prepared to facilitate simultaneous testing of these cards on multiple testing setups. A test report template was also prepared for documentation of test results for individual cards. Similar test simulators and documents were also prepared to test the wiring correctness of the wired 6U racks independently.

TEST SIMULATORS

As these power converters normally operate in remote mode, a test simulator was developed for testing of these power converters in the local mode. The test simulator card is interfacing with power converter module through 25-pin D-connector. This card consists of local reference and it is generated from precision op-amp, ±15 ppm resistors and regulator IC LM 399. To make power converter ON and OFF push button switches are provided. The power converter ON and OFF status, remote mode status is provided on the simulator card by LED signals. Similarly, individual faults can be observed on test simulators by visual indications of LED. A RESET push button is provided to reset these faults. To monitor the load current, current reed back test points are provided. Also for the visual display of output load current, a DPM is provided. The stored energy of magnet load is absorbed in the dc-link capacitor. The design value of this capacitor is 60000 μF/100V.

Fig. 2 shows the overall set-up of for each power converter. A DCCT is provided on the test setup to monitor the output current for checking the calibration and stability of the output current. The test setup uses different instruments for various purposes. For better stability analysis, a highly stable Krohn-hite voltage source is used that has ±1 ppm stability.

The fully loaded power converter module is operated for continuous run for long time and data of reference, read back signal, DCCT output and oven temperature, etc. are monitored and logged at the interval of every 10 s using a multichannel data logger. Calibration and long term stability analysis has been done on the basis of these data readings.

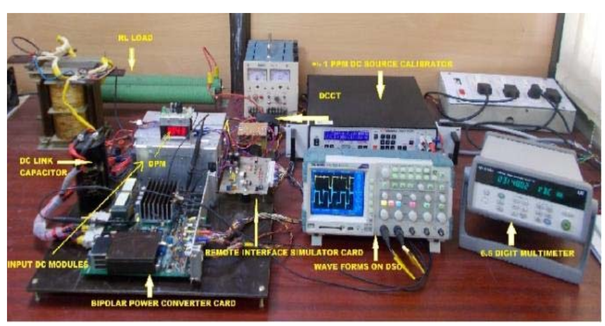

Fig. 2: Photograph of the test setup.

EXPERIMENTAL RESULTS

The photograph of one power converter card is shown in Fig. 3. Similarly, Fig. 4 shows the photograph of 6U subracks housing these cards. Each power converter card was subjected to extensive testing as per the testing guideline and the test results were recorded in the test report for each power converter card.

Fig. 3: Photograph of power converter card.

Fig. 4: Photograph of power converter racks.

Typical test results of the power converters are discussed in the following paragraphs. Fig.5 shows typical long-term stability measurements on one card. It can be seen that the power converter exhibits excellent stability performance. In place of showing the stability results by similar plots for all power converter cards, a histogram summarizing the stability of all thirty power converters is shown in Fig. 6, which confirms a repeatable stability performance in the batch of 30 power converters. The result of stepping resolution test performed on one power converter is shown in Fig. 7. The maximum error between set and actual current (as well as between set and readback current is observed to be less than ±10 ppm. The smooth zero-crossover capability of the power converter is tested and the results are shown in Fig. 8.

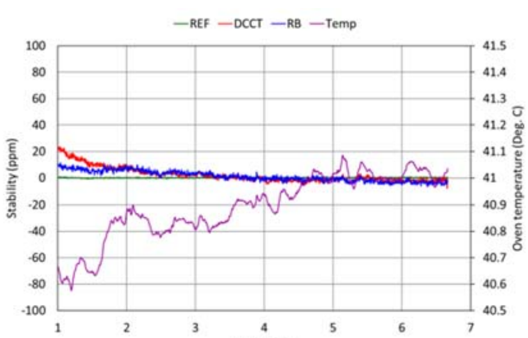

Fig. 5: Long term stability of one power converter

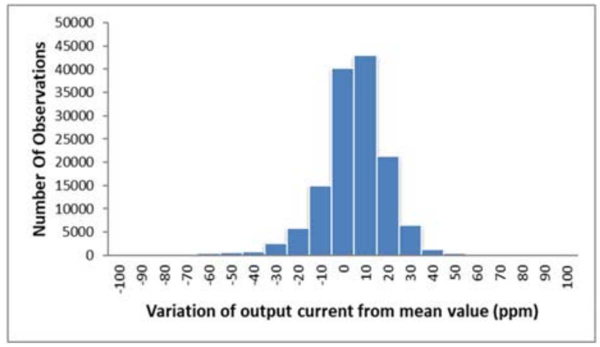

Fig. 6: A histogram showing long-term stability of 30 power converters.

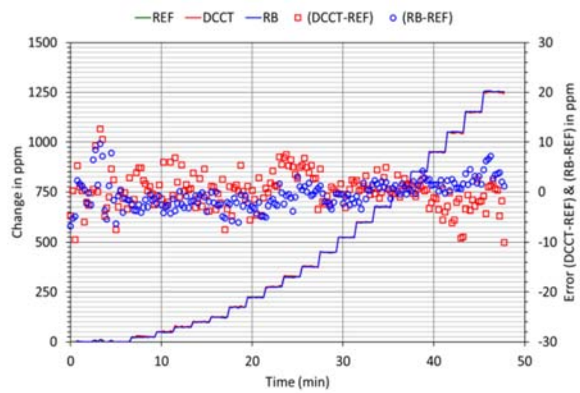

Fig. 7: Stepping resolution measured in 13.5 A set.

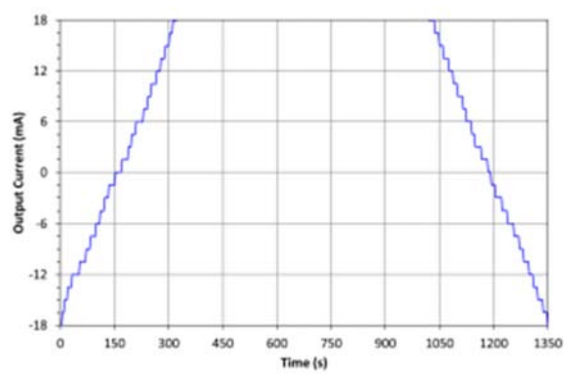

Fig. 8: Smooth zero-crossover of the output current.

ACKNOWLEDGEMENT

The authors acknowledge the contribution of Shri P. Renukanath and his team for development of magnetic components, Shri Deepchand and his team for mechanical assembly of the power converter.

REFERENCES

[1] Ned Mohan, T. Undeland and W. Robbins, "Power Electronics: Converters, Applications and design," 3rd New York: Wiley, 2007.

DESIGN AND DEVELOPMENT OF PULSE TRANSFORMER FOR PICO-SECOND ELECTRON ACCELERATOR KLYSTRON MODULATOR AT RPCD, BARC

Veeresh K Nayak*[1], Umesh Kale[2], B B Chaudhari[1], M C Rath[1]

[1]Radiation & Photochemistry Division, BARC, Mumbai, India- 400085

[2]Free Electron Laser & Utilization Section, RRCAT, Indore, India-452013

Abstract

The pulsed modulator for a 10MW peak power S-band RF system operational for a Pico-second Electron Accelerator at BARC as a part of Ultrafast Pulse Radiolysis [1,2] setup is being upgraded. The RF system consists of a 25MW S-band (2856MHz) Peak Power Klystron powered by a line-type modulator with a pulse transformer rated for 250kV, 250A, and 4.5us pulse width at a 10 Hz repetition rate. In a line-type modulator topology, the pulse transformer is an important component of the pulsed modulator because it not only matches the klystron impedance with the pulse forming network (PFN) for maximum power transformer but also results in a reduced charging voltage of PFN. For maximum power transfer and to reproduce the pulse shape at its input with minimum distortion, the pulse transformer should have very low leakage inductance and distributed capacitance and high magnetizing inductance [2]. These parameters affecting the pulse shape are the function volume enclosed between primary & secondary winding, the number of turns in the secondary winding, the volume of core employed and the maximum flux density of the core material. Optimization of these parameters is therefore important to arrive at an optimum design. In addition to the optimization of parameters, the design of a pulse transformer with a reset core (the transformer core held at negative saturation using DC bias current) and the cone bifilar winding further improves the pulse performance by reducing core volume, improving coupling coefficient between the windings and the volume enclosed between windings. Thus, the design of the pulse transformer is crucial for the modulator's performance. This paper discusses the design details – “core selection, bobbin design, mechanical design, electrical isolation, corona ring at high voltage end” – and operating results obtained during the testing of the pulse transformer with the Klystron.

INTRODUCTION

The development of Picosecond Electron Accelerator of 7MeV pulse energy for pulse radiolysis application at RPDC BARC requires ~ 12 MW pulsed RF power from klystron which needs electrical power in the form of high voltage pulses between its cathode and grounded anode repeating at 10Hz and 150Watts of input RF at its input rf port. The gain of klystron is ~ 50 dB while its efficiency is about 40%. Therefore, each pulse applied to the klystron terminals is of 4.5 us pulse duration with Peak pulsed voltage is 250kV, peak current of 250A A pulse transformer with the turn ratio of 1:14 has been designed to step up the high voltage pulse of 17.8kV generated from a pulse forming network (PFN), having characteristic impedance of 5Ω and to match characteristic impedance of PFN to that of klystron for maximum power transfer.

*veeresh@barc.gov.in

SPECIFICATIONS

Operating specification of the transformer shown in the table 1.

Table 1: Pulse transformer specifications

Parameter		**Value**
Secondary /Primary voltage (Nominal)	:	250kV/~18kV
Secondary/Primary current (Nominal)	:	250A/3.5kA
Turn Ratio	:	1:14
Pulse Repetition Rate	:	10Hz
Load (Klystron)/Source (PFN)Impedance	:	1000Ω/5Ω
Pulse width (Over 90% of nominal secondary voltage)	:	4.5us
Rise time/Fall time (10% to 90% of nominal secondary voltage)	:	<1us
Droop	:	2%
Over shoot	:	< 3%
Peak/ Average Power	:	65 MW/3.5kW
Polarity	:	Negative

CORE SELECTION

The selection of the proper core material is very important in pulse transformer design of a pulse transformer. In pulsed power applications, where the requirement of pulse shape is close to rectangular, the pulse transformer should have wide frequency spectrum with maximum bandwidth. Since the cutoff frequency of a pulse is a function of its distributed capacitance and leakage inductance, their values should be as low as achievable. In order to achieve maximum bandwidth, the core material with higher permeability, maximum saturation magnetic flux density (Bs) and high resistivity core material and low loss core is required. The core dimensions are also very important as the core size, shape, window length, cut-type and uncut-type core also play an important role. Higher window length required to maintain sufficient isolation space pace between turns to meet high voltage requirements, optimization is required to maintain fast rise time. Whereas higher resistivity of core material offers high resistance to eddy current i.e., low eddy current loss. Since the cut-core instead of closed type allows ease of the fabrication of tapered bobbins, windings with precise isolation, they are preferred. However, due to increased air gap there is small increase in leakage flux with results in increase in leakage inductance.

Based on above and commercially available common magnetic materials (silicon steel, Ferrite and Amorphous alloys), the CRGO Silicon steel closed-type oval shaped cores with window area (F x G :95 x181mm), having lamination thickness of 2mil and maximum saturation magnetic flux density (Bs) of about 1.5T are used for designing the design of pulse transformer.

The core of pulse transformer is made up of 4 sub-cores staked together as shown in the figure-1. Each sub core has a depth (D) of 1 5/8 inch and build up (E) of 2 3/8 inch resulting in a core area of 2489.9 mm2. The mean magnetic length is 793.7 mm. The figure-1 below shows the assembled cores for the pulse transformer.

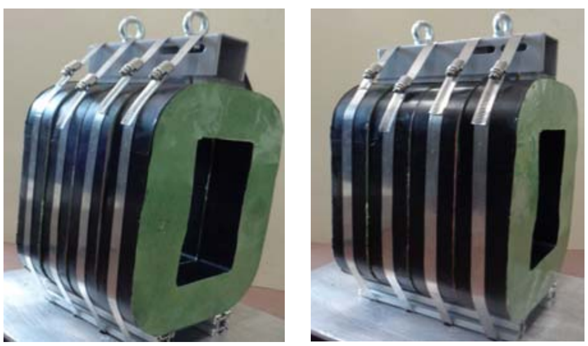

Figure 1: Assembled cores for Pulse Transformer.

ELECTRICAL DESIGN

Equivalent circuit methodology has been used for designing the pulse transformer in which circuit dis-create parameters are calculated based the core dimensions, winding design, isolation between primary and secondary windings etc. Figure-2 below shows a simplified equivalent circuit of a pulse transformer where Lp & Ls are primary and secondary magnetizing inductances, LL is leakage inductance referred to secondary side and CD is distributed capacitance. The core loss, winding resistances and non-linearity of the core has been ignored.

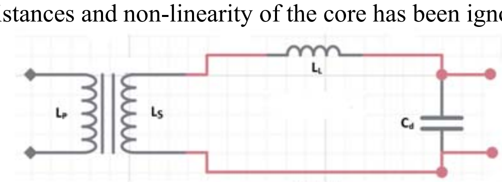

Figure 2. Simplified equivalent circuit of a pulse transformer

Based on the requirements of rise time and overshoot, the maximum permissible values leakage inductance and distributed capacitance was calculated. [3]

Considering damping ratio of 0.75 which corresponds to overshoot of 2% and rise time of about 1 us, the limiting values of LL and CD are ~655.58 µH and ~118.23 pF. Subsequently, based on the requirements of allowable droop, the minimum magnetizing inductance required was estimated to be 112.5mH for secondary turns of 82, primary turns 6, with cone winding configuration for 4 sub-cores. Since in cone winding topology the product of leakage inductance and distributed capacitance is lowest as compared to parallel and foil winding configurations [3,4,5], the cone winding topology was employed in which gape between primaries are secondaries is proportional to voltage gradient with the low voltage ends of both the windings are held at ground potential.

Finally, conductor dimensions of primary and secondary windings are calculated to carry total RMS current and skin depth requirements. There are two primaries are two secondaries wound in bifilar configuration. Each primary has six turns of 6 parallel 16AWG wires covering entire window height. Similarly, two secondaries each of 82 turns are wound using 20AWG wire with a teflon selves at the corner to provide an isolation of 3kV between turns. High voltage ends of each secondary has 31 mm of isolation with respect to grounded cores.

As pulse transformer in klystron modulator operates in unipolar pulse mode, the swing in flux is only in one direction. Therefore, to further reduce the volume of core, the cores are held at negative saturation using a DC bias current of ~10A. Figure 3(a) shows the fabricated pulse transformer without corona ring. Since even after providing sufficient isolation, near the high voltage points electric field lines are concentrated which lead to local corona discharges, high voltage ends guarded by corona rings. A carefully designed corona ring placed at the top of the secondary winding for electrical field line distribution as shown in Figure 3 (b).

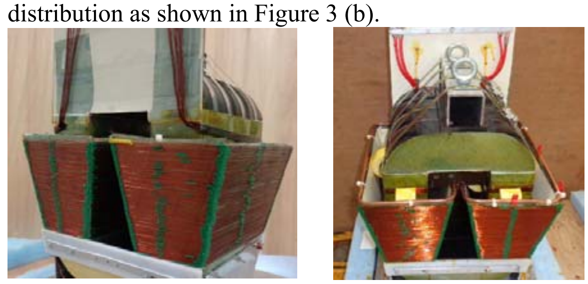

a b

Figure 3: a) Designed Pulse transformer without corona ring b) Designed pule transformer with corona ring.

MECHANIAL DESIGN

The mechanical design deals with the design and fabrication of components needed steel straps to fix the cores firmly on the base plate, support pulse transformer, capacitive potential divider, current transformer, installation of a 250kV isolation transformers to feed filament of the klystron floating at high voltage, fabrication of primary and secondary bobbin and provisions to handle pulse transformer for installing it with the klystron.

When the pulse transformer is installed with the klystron, various other auxiliary equipment's are needed to be installed with the transformer. A current transformer and a capacitive potential divider are essential for measuring pulse current and pulse voltage. Another important device is an isolation transformer to power klystron filament where the secondary voltage of pulse transformer is also connected. Since the transformer operates in reset mode, a biasing inductor is needed to pass DC current to primary windings which are connected to the source of primary pulse voltage. Figure-4 below shows the final pulse ttransformer final assembly ready for its high voltage tests.

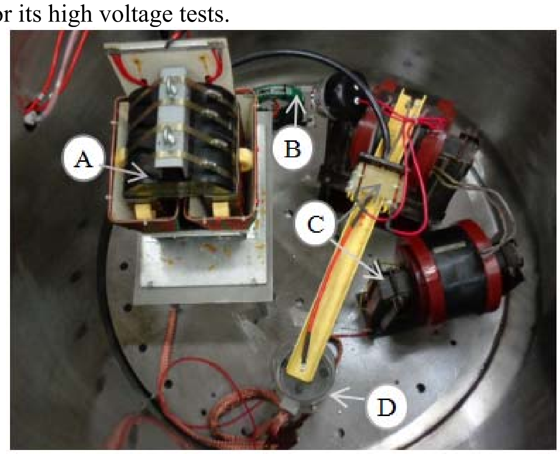

Figure 4: Pulse transformer final assembly. A) pulse transformer B) Current Transformer (CT) C) Klystron filament isolation transformer D) CVD.

EXPERIMENTAL RESULTS

Before starting high voltage tests, the magnetizing inductance of the pulse transformer was measured using a LCR meter of Hioki make. The measured value is 106.58 mH against the calculated value 111.54mH which is a close match. Measurements of basic parameters like turn ratio, winding resistances, leakage inductances were also carried out before installing the pulse transformer assembly with the klystron.

The typical high voltage pulse from pulse transformer with klystron 2171TH load is shown in figure-5.

Since the pulse at the primary of the pulse transformer itself has some droop and rise time, exact rise time and droop will be measured after optimizing the pulse shape from the PFN by tuning PFN inductors.

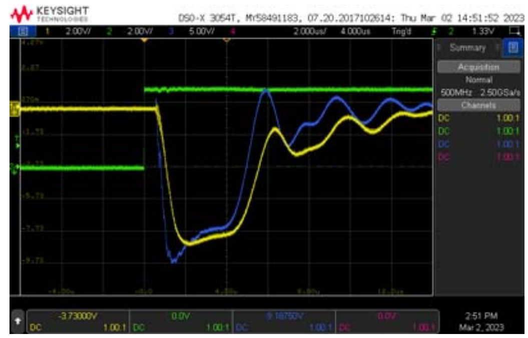

Figure 5: Measured output voltage waveform with klystron. Green-Trigger pulse, Blue: - CT pulse, Yellow: - Pulse transformer output high voltage pulse.

CONCLUSION

A pulse transformer using equivalent circuit methodology has been designed, developed and tested successfully with Thales TH2171 Klystron for Picosecond Electron Accelerator operation for pulse radiolysis application. A novel method to insulate secondaries for per turn voltage using Teflon sleeves were employed, which gave satisfactory results as predicted. The predicted value of magnetizing inductance agrees well with measured value. In addition, the estimated rise time of <1us achieved as seen in figure-5.

REFERENCES

[1] Marignier J-L, Waele V, Monard H, Gobert F, Larbre J-P, Demarque A, et al. "Time-resolved spectroscopy at the picosecond laser-triggered electron accelerator ELYSE", Radiation Physics and Chemistry. 2006;75:1024-1033. DOI: 10.1016/j.radphyschem.2005.10.020.

[2] AkhilPatel, Umesh Kale, P.Shrivastava ,K.K. Pant ,P. Nerpagar, Veeresh Nayak "6MW Peak power RF system for a Pulse Radiolysis facility" Proceedings of the VEDA-2017 Symposium

[3] D. Bortis, G. Ortiz, J.W. Kolar, and J. Biela "Design Procedure for Compact Pulse Transformerswith Rectangular Pulse Shape and Fast Rise Times", IEEE Transactions on Dielectrics and Electrical Insulation Vol. 18, No. 4; August 2011.

[4] M. Akemoto, S. Gold, A. Krasnykh and R. Koontz, "Pulse transformer R&D for NLC klystron pulse modulator," Digest of Technical Papers. 11th IEEE International Pulsed Power Conference (Cat. No.97CH36127), Baltimore, MD, USA, 1997, pp. 724-729 vol.1, doi: 10.1109/PPC.1997.679429.

[5] Glasoe & Lebacqz, "Pulse Generators" McGraw Hill, New York 1948.

Simulation and development of 650 MHz high power dummy coupler of superconducting RF cavity for Q_{ext} measurement

Kunver Adarsh Pratap Singh*, Vikas Rajput, P. Mohania, A. Mahawar, U. P. Pandey, R. Namdeo, D. Baxy, M. Lad, P. Shrivastava

RF Systems Division

Raja Ramanna Centre for Advanced Technology, Indore - 452 013, India

** email:adarshsingh@rrcat.gov.in*

Introduction

Superconducting RF cavities are formed using materials like niobium or Nb3Sn, which become superconducting at cryogenic temperatures. These cavities have a very high quality factor (10^{10}) and require qualification and testing at several stages before final use. Under the Indian Institutions' Fermi Lab Collaboration (IIFC), RRCAT is developing 5-cell, β0.92, 650 MHz SCRF cavities for Fermi Lab, USA. The external quality factor Q_{ext} of a cavity with a high power coupler is a critical parameter that must be measured before the cavity can be used. The high power coupler-to-cavity coupling factor is calculated from the measured Q_{ext}. As the actual high power coupler of the cavity is bulky & delicate and needs a Class 100 clean room for installation & measurement, a dummy coupler is being developed for Q_{ext} measurement of the cavity. For RF coupling and hence Q_{ext} measurement, the dummy coupler behaves like an actual high power coupler but does not require a clean room for installation. Dummy coupler measurement allows for the calculation of the SCRF cavity's power requirements during machine operation. This paper presents the simulation, analysis, development, and Q_{ext} measurement methods of a high power dummy coupler whose fabrication is in progress.

Description of coupler

The output impedance of the 650 MHz RF coupler (Fig. 1) is 105 Ω[4]. The output impedance of a real 650 MHz RF coupler is kept high to minimize/restrict the power loss in the outer conductor [4], as power loss on the outer conductor decreases the efficiency of the RF coupler. Goosefoot is provided for variable Q_{ext} values with respect to orientation angle. The cold part of the coupler also includes ceramic for vacuum requirements. After the output section, which is the cold part of the coupler, the warm part of the coupler is used for RF transmission. It consists of a waveguide to coaxial transition and a capacitor for dc biasing [1] to ensure mutipacting free operation during cavity powering.

The output impedance of the dummy coupler is designed to be the same as that of the actual 50 kW 650 MHz coupler. After that, the impedance of the coupler is transformed and matched to 50 ohms. Matching is necessary for obtaining accurate Q_{ext} value using vector network analyzer.

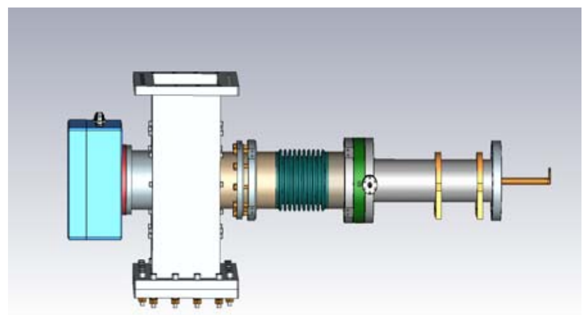

Figure 1: 50kW, 650 MHz RF coupler

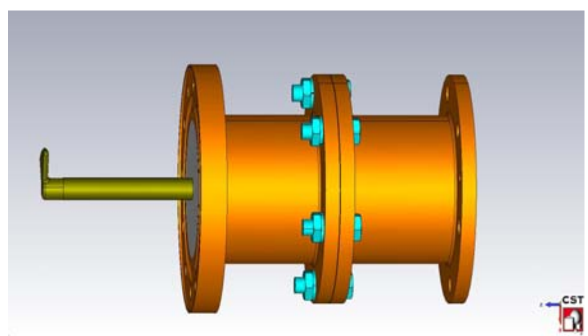

Figure 2: 650MHz RF dummy coupler which is equivalent to real coupler for Qext measurement.

Dummy coupler simulation

As the RF cavity sees only the centre conductor protruding into the cavity through the coupler port, only the output port structure is maintained like an actual coupler, and the rest of the dummy coupler is used to transform 105 Ohm to 50 Ohm [3]. The structure has been simulated using an electromagnetic simulation software called CST'. The results of the convergence study have been completed, and the results are as expected. The structure is resonant at 650 MHz, and the reflection loss is around -45 dB. The simulating structure also contains cavity port pipe for transmission measurement, as shown in figure 3. Simulation shows the negligible transmission loss from the input port to the SCRF cavity. This structure will provide very good cavity matching for RF transmission.

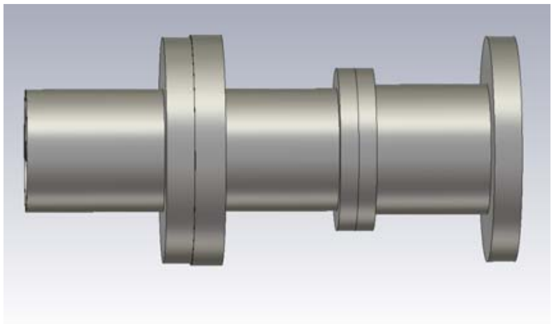

Figure 3: CST model used for dummy coupler simulation

Q_{ext} simulation

The real coupler for Q_{ext} has also been simulated. The inner conductor with goosefoot has been rotated 360° with a 30°step size, and Q_{ext} values have been computed using the software. Simulation data shows variation in Q_{ext} values with respect to inner conductor angles. The variation in Q_{ext} values at different angles is due to the asymmetry in the electric field distribution at the location of the coupler position, which is mounted on a beam pipe.

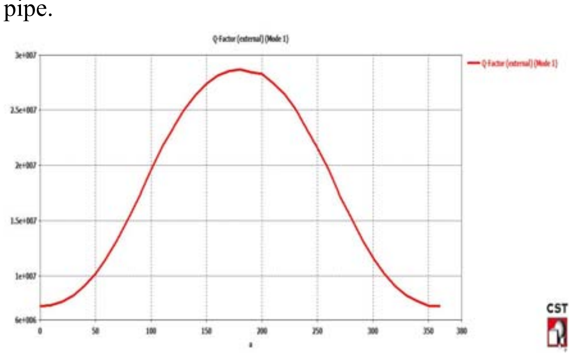

Figure 5: Simulated Qext values of 50 kW, 650 MHz coupler with respect to tip angle.

As we can see, the graph between Qext and angle is shown in Fig. 5. When goose foot is at 0° with respect to beam axis, it is sampling the maximum electric field, which is why at this position Q_{ext} is at its minimum. As goose foot is moved away from the beam axis, less electric field is available, so Qext value increases. At 180^0 coupler sees the minimum electric field, so the Q_{ext} value at this position is maximum. This curve is symmetric to the beam axis.

Measurement

After the fabrication of the dummy coupler, a dimensional inspection will be performed to verify the dummy coupler's geometry. The Q_{ext} values of the dummy coupler, which are expected to be close to those of a 50 kW high power coupler, will be measured. The Qext of the coupler will be measured using transmission methods. In this method, an additional antenna will be used for measurement using the transmission parameter method. The results of the measurement will be analysed and compared with the simulation data.

Transmission method of measurement:- Loss across the cavity with two couplers is given by:-

$$S_{21}(dB) = 10\log_{10}\frac{4\beta_1\beta_2}{(1+\beta_1+\beta_2)^2} \qquad [1]$$

For Qext measurement, we introduce a coupler that is critically coupled at room temperature to the cavity. so transmission loss across the cavity is due to the real coupler only.

$$S_{21}(dB) = 10\log_{10}\beta_2 \qquad [2]$$

So by measuring the transmission loss across the cavity for different angles of coupler tip, Q_{ext} values are calculated.

Figure 6: Q_{ext} measurement using transmission method of power coupler's quality factor with help of third coupler mounted on beam port in clean room.

Conclusion

A 650 MHz dummy coupler has been simulated for Qext measurement of 650 MHz 5 cell high beta SCRF cavities. The dummy coupler is being fabricated. After fabrication, Qext measurements will be performed. Measurement results for cavities B92-RRCAT-501, 503, and 507 will be compared.

Acknowledgments

The authors would like to thank Shri Akhilesh Rajak of RFSD and the colleagues of the Superconducting Cavity Manufacturing Section, RRCAT, for their support in coupler fitting and mounting.

REFERENCES:

[1] S. Kazakov et al., "**Design of 162.5 MHz CW main coupler for RFQ**", in Proc. 27th Linear Accelerator Conf. (LINAC'14), Geneva, Switzerland, Aug.-Sep. 2015, pp. 960-962.

[2] S. Kazakov et al., "**Status of 325 MHz main couplers for PXIE**", in Proc. 27th Linear Accelerator Conf. (LINAC'14), Geneva, Switzerland, Aug.-Sep. 2015, pp. 963-965.

[3]S. Kazakov, "**Design studies on LB650 & HB650 power couplers -simulation challenges and issues**", presented in the PIP-II Technical Workshop, December 10th, 2020.

[4] O. Pronitchev and S. Kazakov, "**Design of Main Coupler for 650 MHz SC Cavities of PIP-II Project"**, in Proc. North American Particle Accelerator Conf. (NAPAC'16), Chicago, IL, USA, Oct. 2016, pp. 121-123. doi:10.18429/JACoWNAPAC2016-MOPOB24

[5] Singh K.A.*, Rajput V.*, Mohania P.*, Namdeo R.K.*, Shrivastava P.* Design and simulation of the power and the pickup couplers for 5-Cell, Beta-0.92, SCRF cavity **InPAC-2018** , Indore, Jan., 9-12, 2018, p. ID-354

UPGRADATION, MODIFICATION AND RF TESTING OF LINE TYPE MODULATOR OF 7 MeV ELECTRON LINAC USED FOR PULSE RADIOLYSIS EXPERIMENTS AT RPCD, BARC

Madhu A Toley*[1], Sunil J Shinde[1], B B Chaudhari[1], Veeresh K Nayak[1]

[1]*Radiation & Photochemistry Division, Bhabha Atomic Research Centre, Mumbai, India- 400085*

Abstract

This facility was commissioned in 1986 which is based on a 7 MeV Linear Electron Accelerator (LINAC) procured from M/s Radiation Dynamics Ltd., UK.

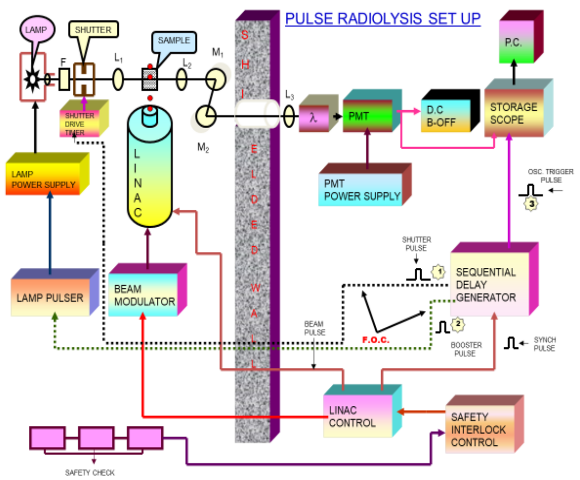

7MeV Electron LINAC for pulse radiolysis experiments [1] at RPCD, BARC is being upgraded for better dose stability and pulse to pulse electron beam energy stability. Nanosecond 7MeV electron LINAC modulator [2] is line type modulator, using a Pulse transformer rated to operate at 43kV, 100A, 2.6us pulse width at 50Hz repetition rate to generate 2MW peak power with a pulse-forming network (PFN) employing Hydrogen thyratron high voltage electrical switch. In conventional 3phase variac and step-up HT Transformer and rectifier-based power supply lacks the pulse-to-pulse stability in high voltage accuracy. Stability in high voltage power supply is crucial to achieve stable electron beam energy in every pulse. Therefore, high voltage power supply upgraded to constant current power supply (CC), the upgraded version of Line type pulse modulator has been tested for RF power with M5125, 2MW magnetron ~2998MHz. In the earlier version of LINAC modulator, the mains power from the 3-phase stabilizer is fed to the primary of the step-up transformer. The secondary voltage from the transformer is rectified by the bridge rectifier circuit. The high voltage (D.C.) thus generated is passed through the filter circuit. This voltage is used to charge the pulse forming network (PFN) through a charging choke and a charging diode. A high voltage thyratron tube is used to discharge the PFN voltage through the thyratron and primary winding of a pulse transformer (turns ratio 1:4.3) on applying a trigger pulses at the pulse to the grid of the thyratron, thereby generating 43 KV secondary terminal of the pulse transformer. This paper discusses the installation, commissioning and testing of 30 KV, 200 mA CC Power Supply in Main Modulator with all necessary modifications needed to incorporate the new power supply and restoration of all required interlocks in the system. Pulse to pulse stability reported in the specifications has been obtained with low noise when compared to earlier modulator.

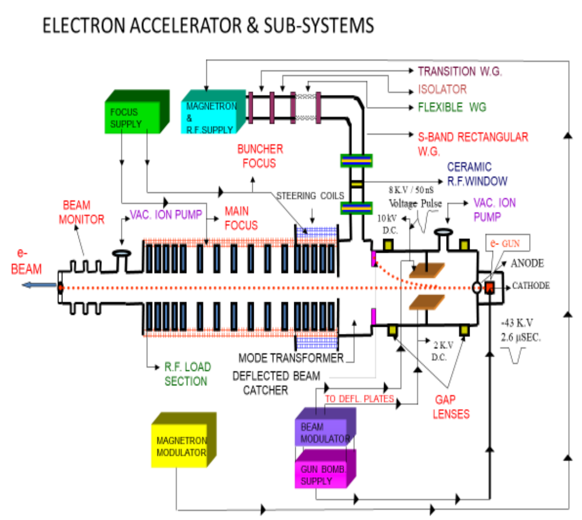

INTRODUCTION

The Pulse radiolysis facility based on 7MeV energy, nanosecond pulsed Electron Accelerator at RPDC BARC required approx. 2 MW/2998MZ pulse RF power from Magnetron. [2] The magnetron modulator contains the HV DC power supply, a pulse forming network, charging choke, series diode, inverse diode and Switch Thyratron with associated triggering unit and interlock circuitry. This paper presents the incorporation of 30kV/200mA constant current switch mode power supply (CC) by replacing the conventional HV DC power unit, installation and RF

*matoley@barc.gov.in

testing, restoring HV safety interlocks, pulse to pulse stability. Finally discusses the results and conclusion of upgradation and testing of modulator.

SPECIFICATIONS

Specification of the shown in the table 1.

Input Line Voltage	385 - 425V AC, 50Hz, Three Phase
Output Voltage	0 to 30kV DC
Output Current	0 to 200mA
Load Voltage Regulation	±0.05% of maximum voltage +500mV for full load change
Line Voltage Regulation	±0.05% of full voltage +500mV over specified input range
Load Current Regulation	±0.01% of max current ±100µA for full voltage change
Line Current Regulation	±0.05% of max current for ±10% input line change
Ripple	0.1% p-p +1 V_{rms}
Temperature coefficient	10ppm/ ºC Voltage or current
Stability	0.02%/hour after ½ hour warm-up for both voltage and current
Efficiency	90% at full load
Protections	Against overload, over current, short-circuit, Over temperature and arc
Special Protection	Capacitor charging power supply protection against back EMF

ADVANTAGE OF CONSTANT CURRENT HV POWER SUPPLY

The selection of a robust dc power unit is very important in modulator design. Parameters i.e. Stability, reliability, high order of protection against short circuit directly influence the performance of noise free response and size of the modulator. Advantages of the constant current HVDC switch mode power supply over conventional HVDC power supply are explained as under:

a. They have high order of line and load regulation of voltage and current.
b. Higher pulse to pulse stability, provides stable input voltage (43kV pulse) for magnetron. Thereby constant RF power gives stable beam energy and the delivered radiation dose from LINAC is more stable.
c. Very compact size, portability and availability of remote analog and ethernet interface.
d. Arc intervention feature that senses arc currents via a fast- acting current sense transformer. The purpose of the arc intervention circuitry is to prevent power supply damage from continuous, long term arcing.
e. Constant current power supply [3]has special protection against back EMF.
f. PFN charging using linear constant current power supplies produce better stability compare to resonance charging (HT transformer based system) scheme.

(a) (b)

Fig 1a & b, front and rear panel of CC HV power supply

Figure 1c: Front panel of power supply after installation in modulator system

MODIFICATIONS & INSTALLATION OF ADDITIONAL SAFETY FEATURES

It includes removal of components of linear HVDC power supply and installation of HVDC Switch mode power supply in the modulator system. Necessary modifications have been done and some additional safety features have been added, which are given as under:

a. Old system didn't have three-phase input supply voltage display. Now, for each phase, DPMs have been installed to continuously monitor the availability of three phase supply voltage.
b. CTs and 3 phase MCB have been installed in modulator unit to limit input current.
c. 100 kΩ/400W current limiting resistor has been added in series of the output voltage of new power supply.

In the existing modulator, if the thyratron is triggered, the PFN discharges through the pulse transformer primary producing a pulse of about 500 amps for about 2.6 µseconds.

$Q = CV$; $I.(t) = C.V$ where I is the charging current and t= charging time

$I(t) = 500 \times 2.6 \times 10^{-6}$ Sec; for 50pps, charging time 20msec

$I = 500 \times 2.6 \times 10^{-6}$ Sec/ 20×10^{-3} Sec; I= 65mA(theoretically)

Modulator DC power supply: 20kV/65mA

Considering continuous operation at 50pps, the DC power unit of 30kV/200mA rating was estimated for upgraded modulator.

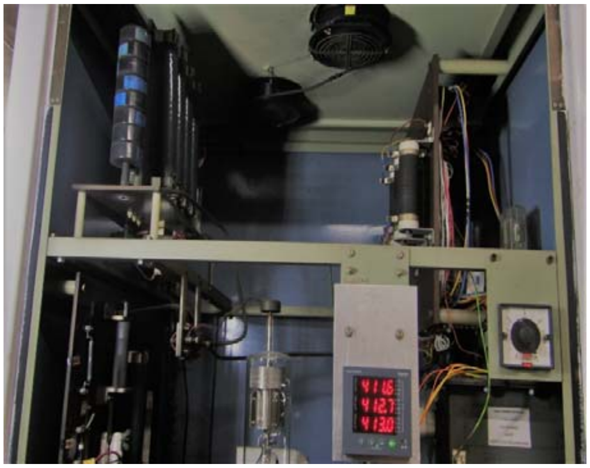

Figure 2: Installation of DPMs and CTs, MCBs in the modulator cubicle

RF TESTING AND EXPERIMENTAL RESULTS

Table 2: Pulse to pulse voltage stability testing of modulator

10 no. of e- beam pulses were given to check pulse to pulse voltage stability of Modulator	Variation in modulator supply voltage HVDC set @ 20kV	
	With existing linear HVDC power supply (kV)	With upgraded SMPS HVDC power supply (kV)
1	20.4	20
2	18.5	20
3	18.0	20
4	19.0	20
5	20.5	20
6	20.8	20
7	19.0	20
8	21.0	20
9	19.5	20
10	19.5	20

Above table shows the comparison between existing and upgraded modulator voltage stability parameter. With upgraded system the voltage was found to be rock steady at 20kVdc, whereas in the existing conventional HT transformer based modulator, voltage was varying between 18 kV to 21kV.

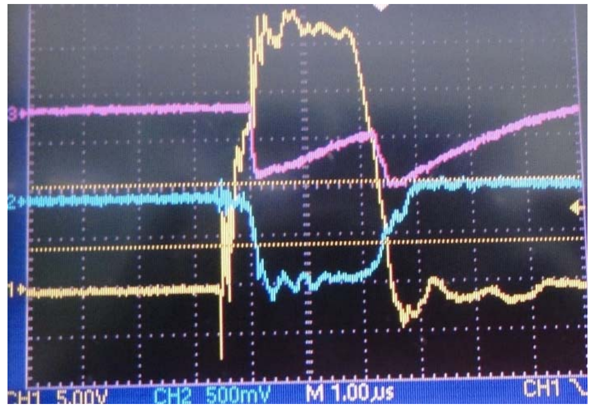

Fig 3a: Measured output pulses; yellow-Magnetron pulse current, blue- e- beam pulse, pink- reflected rf power

Fig 3b: blue 20 kV pulse, yellow- trigger pulse for thyratron trig. drive, pink- grid pulse of thyratron

CONCLUSION

In this paper, upgradation of LINAC modulator for high order of pulse to pulse stability, restoring of modulator safety interlocks and incorporation of additional safety circuits was discussed. Stability was achieved as per the specified parameters, e- beam dosimetry (Table 2) was carried out and results were found to be ok, as per the old scheme. LINAC is continuously in operation with upgraded and modified modulator for pulse radiolysis application.

REFERENCES

[1] "Pulse Radiolysis and Computational Studies on a Pyrrolidinium Dicyanamide Ionic Liquid: Detection of the Dimer Radical Anion", Laboni Das, Rahul Kumar, Dilip K. Maity, Soumyakanti Adhikari,Surajdevprakash B. Dhiman, James F. Wishart, *J. Phys. Chem. A, 122, 3148−3155*, [2018]

[2] The Radiation Dynamics Super X Linear Acclerator for Pulse Radiolysis. (Technical Information Manual)

[3] Glasoe & Lebacqz, "Pulse Generators" McGraw Hill, New York 1948between 18 kV to 21kV.

SIMULATION OF TRANSVERSE SINGLE BUNCH INSTABILITIES IN HBSRS BOOSTER SYNCHROTRON

Abdurrahim[#] and Pradeep Kumar
APSUD, Raja Ramanna Centre for Advanced Technology, Indore - 452013 (M P), India

Abstract

There is a proposal to design a booster synchrotron as a pre injector for top up injection of beam energy 6 GeV in a High Brilliance Synchrotron Radiation Storage ring. In the booster synchrotron, the energy of the beam coming from LINAC will be ramped from injection energy of 200 MeV to 6 GeV. At injection energy, in booster synchrotron, even at lower stored current in a bunch, the motion of electrons may become unstable due to the transverse single bunch instabilities. In this work, simulation studies are carried out to find the effect of transverse single bunch instabilities on beam motion in booster synchrotron. We have considered the resistive wall impedance as an input impedance. Particle tracking is carried out to find the effect of transverse instabilities on beam centroid motion and also on beam emittance. Particle tracking is also carried out considering different positive chromaticities to control the effect of transverse single bunch instabilities on beam motion. The effects of lattice nonlinearities on beam instabilities are also studied after including the nonlinearities in the one turn transfer map. As the beam energy ramping starts in the booster synchrotron, the radiation damping becomes strong, therefore, a simulation is also carried out to study how the ramping process influences the beam centroid motion as well as the emittance, in presence of resistive wall impedance.

INTRODUCTION

The HBSRS booster is designed to accelerate the electron beam energy from 200MeV 6 GeV. The circumference of this ring is 868.633 m, which is divided into 86 unit cells. There are total 1448 rf buckets to store the beam. A 200 MeV LINAC will be used as an injector for the booster. The optical functions (horizontal and vertical beta functions and the horizontal dispersion function) in a unit cell are shown in Figure 1, while the key parameters of the booster synchrotron are listed in table 1 [1].

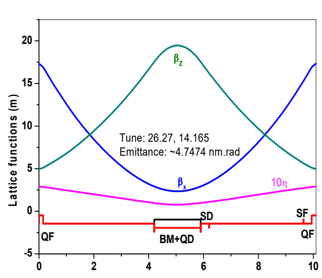

Figure 1: Optical functions of the HBSRS booster in a unit cell

Table 1: HBSRS Booster synchrotron parameters

Parameters	Value
Energy	0.2 – 6.0 GeV
Circumference	868.633 m
Revolution time	2.897 µs
Betatron tunes (x, z)	26.270 14.165
Natural chromaticity (x, z)	-34.017, -20.824
Natural emittance (ε_x)	5.27 pm.rad @ 200 MeV 4.75 nm.rad @ 6 GeV
Momentum compaction factor	6.029×10^{-4}
RF frequency	499.75 MHz
Harmonic number	1448
Repetition rate	1-2 Hz
Damping times (x, z, s)	122, 190, 132 s @ 200 MeV 4.52, 7.05, 4.89ms @ 6 GeV

TRANSVERSE SINGLE BUNCH INSTABILITIES

In order to find the threshold of single bunch charge in booster, study and simulation of transverse single bunch instability is essential. There are two main transverse single bunch instabilities, which limit the stored current, one is Transverse Mode-Coupling Instability (TMCI) and another one is head–tail instability. The effect of beam instabilities are more severe at lower beam energies, therefore, it is very important to study and simulate the above instabilities at injection energy. The vacuum chamber of the booster synchrotron is made with small aperture. In this case, the contribution of resistive wall impedance becomes significant to total impedance. Therefore, initially resistive wall impedance has been taken as impedance model for particle tracking. The geometrical impedances of the vacuum chamber components will be included for simulation in the future. The aperture of the chamber at different locations in the ring is given in table 2.

Table 2: Chamber aperture at different locations

Element	Aperture
Dipole	±13 mm, circular
Quadrupole	±18 mm, circular
Rest of the ring	±18 mm, circular

The aperture at the location of the dipole is chosen relatively smaller to achieve the required field. The resistive wall impedance of the chamber (stainless steel) is calculated analytically [2] considering the radius of the circular cross mentioned in table 2.

[#] arahim@rrcat.gov.in

$$\frac{Z_T^{rw}}{C} = \frac{Z_0 c^2}{\pi} \frac{2}{(i+sign(\omega))b^3 c\sqrt{2\sigma_c Z_0 c|\omega|}} \quad (1)$$

Here C: circumference of the ring, c: speed of light, σ_c: conductivity of the chamber material, Z_0: free space impedance, b: radius.

The calculated resistive wall impedance with frequency is shown in Figure 2. It will be the same for horizontal as well as vertical planes

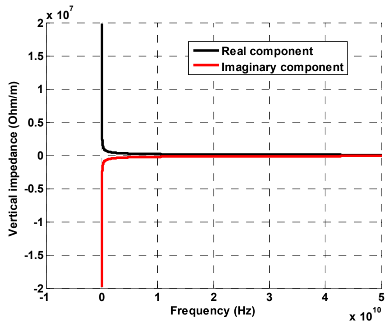

Figure 2: Resistive wall impedance of booster synchrotron vacuum chamber

Particle tracking at injection energy

Gaussian bunch is generated considering a beam coming from 200 MeV LINAC with the initial emittance of 60 nm-rad in the horizontal and vertical plane. The bunch length of the incoming beam is 5.2ps, however, the energy spread is 0.5%. Particle tracking is performed with 100000 macro-particles for 200000 turns at different chromaticities. As it is known that the head–tail instability does not get excited at zero chromaticity. Therefore, at this chromaticity, only the transverse mode coupling instability (TMCI) will limit the current in a single bunch. Using the linear one turn map in the ILMATRIX element of elegant code [3, 4], particle tracking is performed. The Fast Fourier Transform (FFT) of the centroid oscillations is carried out. From the FFT results, it is found that with the current 0.23mA, beam motion becomes unstable in the vertical plane. The vertical beam spectrums obtained from FFT are shown in Figure 3(a) and Figure 3(b) for the current of 0.1mA and 0.23mA respectively. From the spectrum, it is found as the current increases the vertical head-tail modes 0 and -1 approach each other and merge at the beam current of 0.23mA (Figure 3(b)) and as a result growth in vertical centroid oscillation as well as vertical emittance is observed and are shown in Figure (4a & 4b).

As the chromaticity increased to [2 2] in the linear lattice, beam centroid oscillation and emittance in both planes blows up even at 0.1mA of stored current in a single bunch. It is due to the excitation of higher-order head tail modes in both the transverse planes.

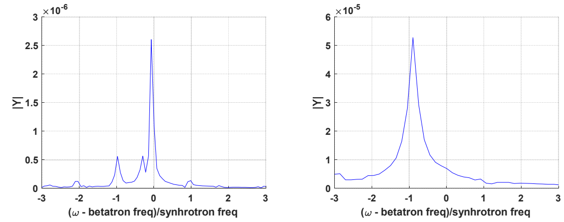

(a) (b)

Figure 3: Vertical head tail modes at (a) 0.1mA and (b) 0.23mA. Both the modes merges at 0.23mA

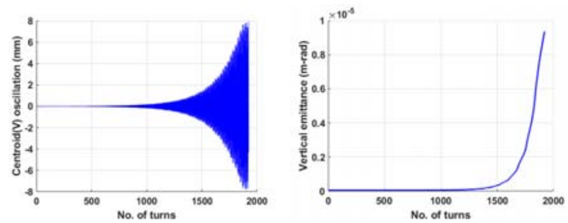

(a) (b)

Figure 4: (a) Vertical centroid oscillation and (b) growth in vertical emittance at 0.23mA

Particle tracking is also performed including the lattice nonlinearities in one turn transfer map at chromaticity [0 0]. The nonlinear terms include the second order momentum compaction factor, first and second order amplitude dependent tune shifts, first and second order amplitude dependent path length difference, and the second and third order chromaticities. The analysis of tracking results reveal that the lattice nonlinearities help in stabilizing the beam motion. Beam motion is now stable at 0.23mA, it becomes unstable at 0.5mA as it can be seen in Figure (5a & 5b). Hence threshold increases by 0.27mA in presence of lattice nonlinearity.

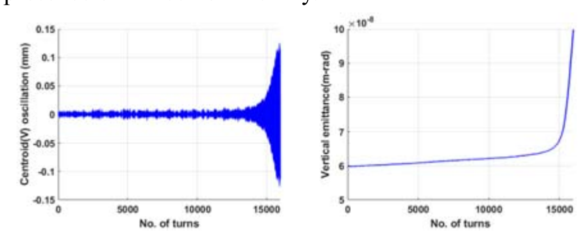

(a) (b)

Figure 5: (a) Vertical centroid oscillation and (b) growth in vertical emittance at 0.5mA

Effect of chromaticity with nonlinear lattice

Particle tracking is carried out with different chromaticities set by the sextupoles. Effect of lattice nonlinearities are included in one turn transfer map. The tracking results for the current of 0.5mA with the chromaticities [2 2], [3 3] and [4 4] are plotted and shown in Figure 6. It can be seen in Figure (5 & 6) that for the beam current of 0.50mA, the unstable vertical centroid oscillation at [0 0] chromaticity becomes stable after increasing the chromaticities. Moreover, the rate of growth in emittance reduces as we increase the chromaticity.

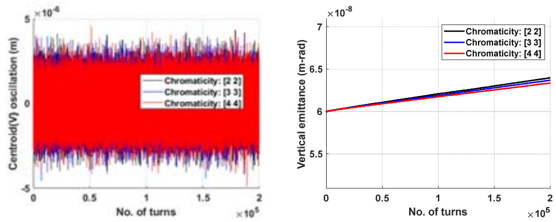

(a) (b)

Figure 6: (a) Vertical centroid oscillation and (b) growth in vertical emittance at 0.5mA for chromaticities [2 2], [3 3] & [4 4]

For the chromaticity [2 2], the beam motion is stable up to 0.6 mA. After this current, beam motion becomes unstable.

Effect of beam energy ramping on centroid oscillation and emittance

In the booster synchrotron, beam energy will be ramped from 200MeV to 6 GeV. As the energy increases, the damping process due to synchrotron radiation becomes fast. It helps in stabilizing the beam oscillation. Particle tracking is carried out to study the effect of the ramping process on vertical centroid motion and emittance.

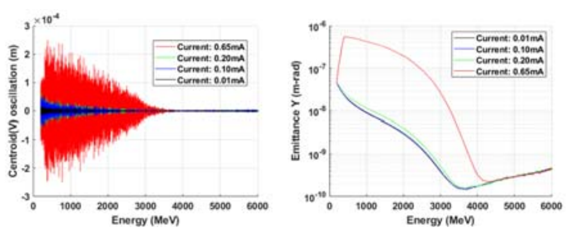

(a) (b)

Figure 7: (a) Vertical centroid oscillation during beam energy ramping (b) Variation of vertical emittance during ramping

Tracking is performed for the lattice with the chromaticity [2 2] and including the nonlinearity. Tracking is carried out for 500ms considering the 1 Hz ramp repetition rate. After analysis of the tracking results, it is found that for a very small current of 0.01mA, the vertical emittance, which is almost equal to natural emittance, decreases monotonically up to 3.6 GeV (~296 ms) because of the stronger synchrotron radiation damping during beam energy ramping. After the beam energy 3.6 GeV, there is an increase observed in the vertical emittance due to dominating effect of quantum fluctuation in the horizontal plane. The increase in vertical emittance arises from the increase in horizontal emittance (coupling: 10%). As we increase the current, an increase in emittance is observed up to 4.5 GeV (~360 ms), after that emittance overlaps with natural emittance. It indicates that after the beam energy 4.5 GeV, the effect of impedance becomes negligible as compared to SR damping effect. For the current of 0.65 mA, there is significant growth in vertical emittance as well as in centroid oscillation (Figure 7(a & b)). If the current is further increased, there is emittance blow up, which ultimately results in a partial beam loss.

CONCLUSION

Particle tracking is performed using elegant code, to simulate the effect of transverse single bunch instabilities on beam motion in booster synchrotron at injection energy as well as during beam energy ramping. The resistive wall impedance of the chamber is considered as an input impedance for simulation. Analysis of particle tracking reveals that the nonlinearity of the lattice helps in stabilizing the beam motion. With the nonlinearity in the lattice, at injection energy, the beam motion is stable up to 0.6 mA for the chromaticity [2 2]. The results of particle tracking during beam energy ramping indicate that if we store the current more than 0.65 mA in a single bunch, there is emittance blow up, which leads to beam loss.

The above current thresholds achieved from the simulation results may change or reduce further, as in the future, we include the geometrical impedance along with the resistive wall impedance of the HBSRS booster synchrotron chamber.

ACKNOWLEDGEMENT

We are highly thankful to computer division for providing the computing facility and support. We are also thankful to the Dr. Tapas Ganguli Head APSUD, for their kind support and motivation to publish the work.

REFERENCES

[1] V K Meena, AA Fakhri and AD Ghodke, “On-axis injection scheme for booster synchrotron of high brilliance synchrotron radiation source”, InPAC- 2022

[2] Ryutaro Nagaoka, Karl L. F. Bane, “Collective Effects in a Diffraction Limited Storage Ring”, Journal of Synchrotron Radiation, June 2014, Vol. 21, pp 937-960.

[3] M. Borland, “Elegant: A Flexible SDDS-Compliant Code for Accelerator Simulation”, Advanced Photon Source LS-287, Sep 2000.

[4] H. Xu, Y. Peng, N. Wang, “Studies of transverse single-bunch instabilities in booster synchrotrons”, Nuclear Inst. and Methods in Physics Research, A 2019, Vol. 940, pp 313–319.

STUDY OF ON-AXIS LONGITUDINAL BEAM INJECTION IN STORAGE RING OF HIGH BRILLIANCE SYNCHROTRON RADIATION SOURCE (ID: E1-219)

Saroj Kumar Jena* and Ali Akbar Fakhri
Accelerator Physics and Synchrotrons Utilization Division,
Raja Ramanna Centre for Advanced Technology, Indore-452013

Abstract

A High Brilliance Synchrotron Radiation Source (HBSRS) based on storage ring is being planned based on multi bend achromat lattice with strong quadrupole and sextupole magnets to achieve ultra-low beam emittance. These strong non-linear magnets with even small errors may significantly reduce the dynamic aperture of the storage ring lattice as compared to a 3rd generation light source. Thus, this configuration generates a great challenge for the beam injection by conventional 4 kicker scheme. To relax the dynamic aperture requirement in transverse plane, on-axis longitudinal injection scheme is studied. In this injection scheme, a bunch is injected in the longitudinal plane with suitable energy and time offset, with respect to the stored bunch. This injected bunch gradually merges into the stored bunch through synchrotron radiation damping phenomena. For this, a very fast dipole kicker with a pulse length shorter than the bunch spacing is required to keep stored bunches undisturbed. With the help of this kicker, the off energy injected beam is placed on the dispersive orbit of the storage ring, which is longitudinally separated from the stored beam. Appropriate placement of the kicker demands a phase advance of an odd multiple of $\pi/2$ from the injection point and finite dispersion in horizontal plane. In this paper, the feasibility of longitudinal injection scheme for the storage ring of HBSRS is studied and reported. For this, the optimum placement of the kicker is chosen according to the availability of space in the lattice and injected beam energy offset is chosen according to the available momentum acceptance of the storage ring.

INTRODUCTION

A project of high brilliance synchrotron radiation source (HBSRS), a future fourth-generation light source is being envisaged which will consist of a 6 GeV electron storage ring, full energy booster synchrotron and 200 MeV Linac. The design lattice for storage ring of HBSRS is based on multibend (7 BA) achromats to achieve ultra-low beam emittance of 150 pm rad [1]. Conventional 4 kicker injection scheme and pulsed sextupole injection scheme have been studied for this lattice. In future, further lowering of beam emittance using concept of longitudinal gradient bend and anti-bend magnets in the lattice is being envisaged. As a consequence to this design, the transverse dynamic aperture may further shrinks and hence off-axis beam injection may become difficult. Therefore, the feasibility of on-axis longitudinal injection scheme is studied, that does not require higher value of dynamic aperture in transverse plane. In the longitudinal injection scheme, the electron bunches from booster are injected with an offset in both phase and energy than the circulating bunches in storage ring [2 & 3]. In this process, an injected bunch is kicked transversely on-axis between two circulating bunches by a short-pulse dipole kicker. The main function of the kicker is to place the off energy injected beam onto the dispersive orbit of storage ring. Since the storage ring will be operated in the top-up mode, where frequent beam injection atop the stored beam is done, pulse length of injection kicker is required to be less than the spacing between adjacent bunches to keep the stored beam undisturbed. With 500 MHz RF, the kicker pulse width is required to be less than 2 ns which is quite challenging but achievable using stripline kicker [4 & 5]. Future light sources, HEPS, SOLEIL upgrade, and SLS 2.0 [4-6] have proposed the longitudinal injection scheme to enable beam injection into reduced transverse dynamic aperture of the storage ring. The parameters relevant to this study for the storage ring of HBSRS are listed in Table I. Fig. 1 shows the optical functions of the storage ring.

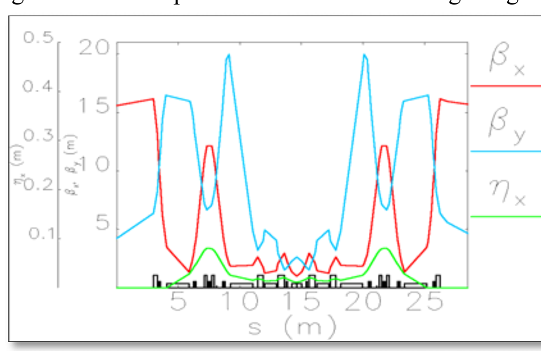

Figure 1: Lattice function of HBSRS storage ring (one unit cell)

TABLE I. Parameters of HBSRS storage ring

Parameter	Value
Beam energy	6 GeV
Beam current	200 mA
Circumference	911.4 m
Number of unit cell	32
Horizontal emittance	150 pm rad
Betatron tune (x,y)	76.15, 27.2
Momentum compaction factor	0.00012
Energy loss per turn	2.375 MeV
RF frequency	500 MHz
Harmonic number	1520

*s_jena@rrcat.gov.in

The motion of electron beam in longitudinal plane is described by following two difference equations

$$\varphi_{n+1} = \varphi_n + \frac{2\pi h\eta}{\beta^2 E}\,\Delta E_n \quad \dots (1)$$

$$\Delta E_{n+1} = \Delta E_n + eV_0\,(\sin\varphi_n - \sin\varphi_s) \quad \dots (2)$$

$$\varphi_s = \pi - arcsin\left(\frac{U_0}{eV_0}\right) \quad \dots (3)$$

where h is harmonic number, η is slip factor, E is the beam energy, V_0 is the RF voltage, U_0 is the energy loss per turn for nominal energy particle, φ_n is phase of the beam when it passes the RF cavity n^{th} time and φ_s is the synchronous phase. This above equations are true for on momentum particle. The energy loss per turn for off momentum particle is approximated as [2]

$$U\left(\frac{\Delta E}{E}\right) = U_0\left(1 + \frac{\Delta E}{E}\right)^3 \quad \dots (4)$$

In presence of energy dependent synchrotron radiation loss, the longitudinal phase space gets modified and resembles the shape of a "golf club," whose shaft extends towards the neighboring RF bucket [7]. This is shown in Fig. 2, considering the parameters of storage ring. This modified phase space allows capture of injected beam at the expense of slightly higher injection energy.

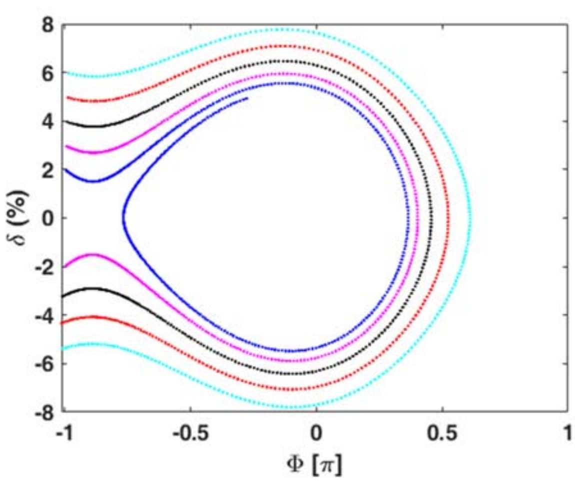

Figure 2: Motion in longitudinal phase space in presence of synchrotron radiation damping.

Since in this injection scheme, the injected beam has energy and time offset, this results in a large synchrotron oscillation amplitude. Thus it is important to accurately estimate the momentum acceptance of the storage ring and this is shown in Fig. 3. This figure shows that, tolerable off momentum particle of 3 % can be injected into storage ring.

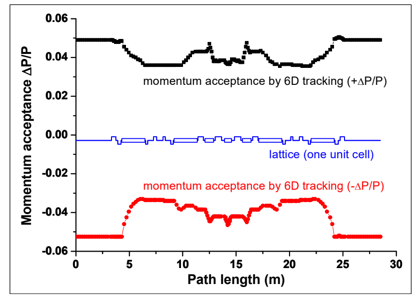

Figure 3: Momentum acceptance of storage ring

LONGITUDINAL INJECTION

In this scheme, the injected beam is separated longitudinally from the stored beam and a transverse kick is imparted by a pulsed dipole kicker to place the off energy injected beam in the corresponding dispersive orbit of storage ring. Thus, dipole kicker shall be placed at finite dispersion and suitable location also demands of a phase advance of an odd multiple of π/2 from the injection point (IP). As per the space availability in the lattice, this kicker is placed between 2^{nd} and 3^{rd} bending magnet of first unit cell, at a distance of 11.2 m from IP, where the phase advance from IP is 266^0 and dispersion and its derivative are η_x=0.018 m and η_x'=0.009. The injected beam is launched into storage ring at the IP with transverse displacement and optimized angle in horizontal plane (x, x') = (-6 mm, -0.2mrad) and 3 % energy offset. The incoming angle of the particle is optimized using simulation code, with objective of achieving minimum kicker strength and well matching of injected orbit with the dispersive orbit. Fig. 4 shows the single particle trajectory of injected beam for the kicker OFF and ON condition. It is seen from the figure, with an optimized kicker strength of 0.64 mrad, the injected orbit nearly coincides with the dispersive closed orbit of the storage ring.

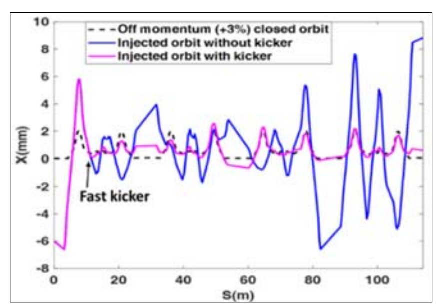

Figure 4: The injected beam trajectory with and without the dipole kicker and off momentum closed orbit

TABLE II. Parameters of the injected beam

Parameter	Value
Beam energy	6 GeV
Horizontal emittance	5 nm rad
Coupling	1 %
Bunch length	12 ps
Energy spread	1.24×10^{-3}

For the multi-particle tracking, simulation was carried out using particle accelerator code, ELEGANT [8]. Table-II presents the parameters of injected bunch which are assumed from the booster design. With these parameters, an injected bunch of 1000 particles is generated. This bunch is injected into storage ring with an energy offset of +3% and a time offset of −1 ns with respect to a circulating bunch, which corresponds to middle of two successive circulating bunches. The injected bunch is tracked for 10000 turns along the storage ring lattice with the kicker strength of 0.64 mrad. The synchrotron radiation (SR) damping time in longitudinal plane is 11.16 ms, corresponding to 3671 turns and SR damping time in horizontal plane corresponds to 3111 turns. The phase space result in every 200 turns for longitudinal and horizontal plane is shown in Fig. 5 and 6 respectively. It is observed from Fig. 5, off energy injected beam gets damped and finally merged with stored bunch. The injected beam effectively got confined in longitudinal and transverse acceptance of the ring in the whole injection process. This confirms that, even if the dynamic aperture reduced to 3 mm in horizontal plane, the longitudinal injection can be successfully carried out.

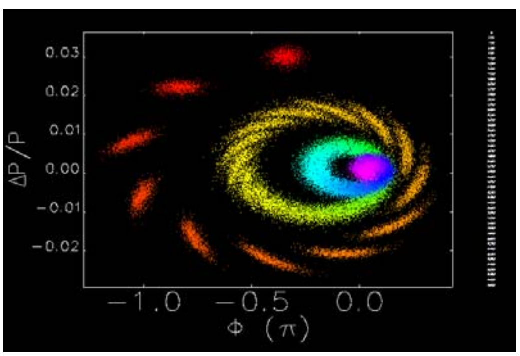

Figure 5: For injection bunch, phase space in longitudinal plane up-to 10000 turns. The origin of phase corresponds to synchronous phase. Different color represents particle in every 200th turn and magenta color shows particles merged with stored beam

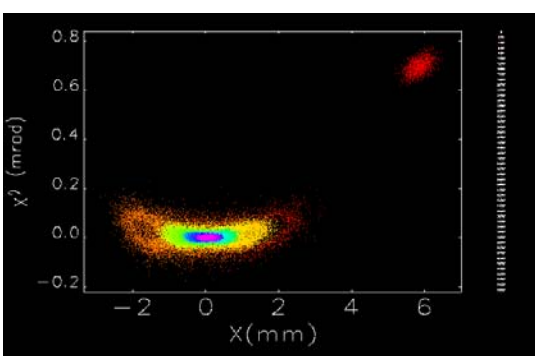

Figure 6: For injection bunch, phase space in horizontal plane at maximum dispersion, upto 10000 turns. Different color represents particle in every 200th turn and magenta color shows particles merged with stored beam

CONCLUSION

The longitudinal injection scheme is currently under study for the storage ring of HBSRS and preliminary simulation results shows capture of the injected beam which is transferred to storage ring acceptance in energy and time by a dipole kicker using transverse kick. The major challenge in such longitudinal injection scheme is the design of the ultrafast pulse kicker of pulse length < 2 ns for 500 MHz RF, which needs a state of art technology. Development of such kicker system with pulse length of nano-second regime is in advanced stage elsewhere in the world.

ACKNOWLEDGMENTS

The authors wish to acknowledge the support of computer center for providing computing facility Kshitij-5 cluster for the usage of simulation code ELEGANT. The authors would also like to thank Dr. Pradeep Kumar for the fruitful discussion.

REFERENCES

[1] A. D. Ghodke, et al., “Physics design study for proposed high brightness synchrotron radiation source (HBSRS) in India, in Proceedings of InPAC-2019

[2] M. Aiba, M. Böge, F. Marcellini, Á. Saá Hernández, and A. Streun, “Longitudinal injection scheme using short pulse kicker for small aperture electron storage rings”, Phys. Rev. ST Accel. Beams, 2015, Vol 18, pp 020701

[3] Shichang Jiang and Gang Xu, “On-axis injection scheme based on a triple-frequency rf system for diffraction-limited storage rings”, Phys. Rev. Accel. Beams, 2018, Vol. 21, pp110701

[4] L. Wang, J.H. Chen, H. Shi, G.W. Wang, N. Wang, Z. Duan, S.K. Tian, L.H. Huo, P. Liu, “A novel 5-cell strip-line kicker prototype for the HEPS on-axis injection system”, Nucl. Instrum. Methods Phys. Res., Sect. A, 2021, Vol 992, pp165040

[5] M. Paraliev, M. Aiba, S. Dordevic, C.H. Gough, A. Streun, “Development of fast and super-fast kicker system for SLS 2.0 injection”, in Proceedings of IPAC 2021, Brazil, pp 2889

[6] M.-A. Tordeux, et al., “A novel injection scheme using R.F. manipulation for SOLEIL upgrade”,in proceedings of ESLS RF SOLEIL Nov. 2018

[7] Peter Kuske, Ji Li, and Masamitsu Aiba, “Longitudinal acceptance measurement at an electron storage ring”, Phys. Rev. Accel. Beams, 2020, Vol. 23, pp030701

[8] M. Borland, "elegant: A Flexible SDDS-Compliant Code for Accelerator Simulation", Advanced Photon Source LS-287, September 2000

DESIGN STUDIES ON SOLID-STATE RF POWER SYSTEM FOR 10MEV RE-CIRCULATING HIGH POWER ACCELERATOR (RHPA)

M. K. Jain#, R. K. Deo, Gaurav Kanyal, M Lad, RRCAT, Indore-452013

Abstract

Design & development work of realizing 3x50kW, 107.5MHz solid-state RF power system for exciting coaxial accelerator cavity of 10MeV/30kW RHPA in in-phase multi-port excitation mode, is taken up as an alternative to tetrode-based RF power systems used in single-port excitation mode for this application [1,3]. Important sub-systems required for a 50kW/107.5MHz RF output: - compact 1.6kW/107.5MHz RF amplifier modules, simultaneously matched 32:1 RF combiner at 50kW output level, and 50dB coaxial/microstrip-line directional coupler, are designed & developed. Effect of phase & amplitude variance among the power-waves at accelerator-cavity feed-port, coupled to 3x50kW RF outputs for multi-port excitation of the cavity, is studied. Realized with suspended strip lines and Gysel network topology in axially symmetric multi-layer configuration, the simultaneously matched 32:1 combiner as designed, does not require junction circulators at the outputs of the amplifier modules. Coaxial line to microstrip-line backward coupled-lines directional-coupler structure is integrated with the solid-state amplifier modules chassis. This paper gives a brief description of the design, satisfactory performance and progress made in the realization.

INTRODUCTION

In view of uncertainty in availability of suitable high power tetrode tubes due to out-phasing from regular production; alternatively, RF power system based on solid-state devices is considered as required for feeding the coaxial accelerator cavity of 10MeV/30kW RHPA, at resonance frequency of 107.5MHz, proposed for industrial application. In this respect, design & development work of realizing 3x50kW RF power outputs based on LDMOS devices is taken up, as required- to develop 700kV of peak RF voltage across the cavity in median azimuthal plane resulting in a cavity copper-losses **P_c** of ~95kW, to transfer 30kW RF power **P_b** to the electron beam, and to have 1dB margin in available power for dynamic operation.

RF SYSTEM CONFIGURATION

Multi-port excitation of the accelerator cavity at a resonance RF frequency of 107.5MHz was considered to transfer 150kW RF power to accelerator-cavity by means of three, loop-coupled, axially symmetric, 50Ω 6-1/8" EIA coaxial feed-ports, each one driven by a 50kW/50Ω output through 60kW/107.5MHz Y-junction circulator. In scheme, outputs from 32 nos. of 1.6kW/107.5MHz RF power amplifier modules, based on MRFX1K80H LDMOS devices, are to be combined with help of simultaneously matched 32:1 RF power combiner for having a 50kW/50Ω RF O/p. With simultaneously matched combiner, output of 1.6kW/107.5MHz amplifiers module are directly connected to the 32:1 combiner, without using circulator which otherwise is required for stabilizing operating load to amplifiers O/p against possible variations of that, caused due to phase & amplitude imbalance that may be existing among amplifier O/p being combined [2]

MULTI-PORT EXCITATION OF CAVITY

Considering lumped-element parallel resonance model of the cavity under resonance, S-parameter model of the cavity under the three-port-excitation mode is expressed by equation *1c &1d*. Thereby, reflection coefficient Γ_i at a feed-port and variation in cavity voltage V_c, due to an imbalance in amplitude & phase among RF *I/p* (a_j) coupled to the cavity feed-ports, is deduced by eq. *1a* & *1b*. In our case, value of cavity coupling coefficient $\boldsymbol{\beta_i}$ for each of the feed-port is ~1.3/3. For stabilizing cavity voltage within ±2% and phase 2º and reflection losses less than 1%; maximum, imbalance among all three RF *I/p* should be less than be *±0.5dB* & *±5º*. Coupling of beam to the accelerator cavity is expressed as $\beta_o = {P_b}/{P_c}$; R_{sh} and Z_o represent cavity shunt impedance and feed-port impedance respectively.

$$\Gamma_i = -1 + \frac{(2\beta_i)}{(1+3\beta_i+\beta_o)} \times \frac{1}{a_i}\sum_{j=1}^{3} a_j\,; \qquad \ldots\ (1a)$$

$$V_c = \sqrt{\left({R_{sh}}/{\beta_i Z_o}\right)} \times \frac{(2\beta_i)}{(1+3\beta_i+\beta_o)} \times \sum_{j=1}^{3} a_j \qquad ..(1b)$$

$$S_{ji} = -1 + \frac{2\beta_i}{(1+3\beta_i+\beta_o)}; \quad (i,j) \in [1,2,3]; i = j \ \ldots\ (1c)$$

$$S_{ji} = \frac{2\beta_i}{(1+3\beta_i+\beta_o)}; \qquad i,j \in [1,2,3]; i \neq j \qquad \ldots\ (1d)$$

With multi-port excitation, as expressed by eq.1b, the accelerator cavity serves as RF power combiner; thus, avoiding requirement of high-power combiner at 150kW RF output level, required otherwise. The operation with three numbers of feed-ports, is found to be optimum considering the following: - stable operation of coupling loop, ease of RF tuning and voltage regulation in the cavity, and optimum design of *N*-way simultaneously matched RF power combiner at 107.5MHz.

32:1 RF POWER COMBINER

A 32:1 RF power combiner matched at all ports is realised in form of axially symmetric multilayer structure, shown in fig 3, using suspended strip-lines and Gysel topology for implementation. Analytically, common-mode power-waves from the inputs are added at the 50Ω output-port; but odd-mode power waves, as arises due to any amplitude & phase imbalance among inputs, are diverted to 50Ω ballast-ports to be absorbed there, resulting in no reflected-waves. Therefore, if there is imbalance in phase and

#Email: mkjain@rrcat.gov.in

amplitude among amplifier outputs being combined, they operate under matched load even without incorporating circulators at their outputs. This simplifies overall layout and avoid circulator insertion losses helping in improving combining efficiency.

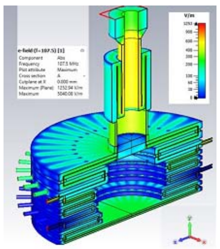

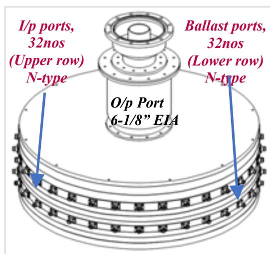

Figure 1a: 3DFull wave simulation with CST MWS; (1b): True 3D CAD drawing of the combiner structure for fabrication.

Performance

3D full-wave EM simulation of the combiner was carried out on *CST MWS* for evaluation and optimization of its performance in terms of S-parameters and *E*-field & *H*-field values at 50kW operating power level. The results are shown in figure 1a and 2. Parameters of I/p-port matching S_{ii} and isolation between input-ports $S_{ji,}$ are better than 30dB and 40dB respectively over a band width of ±7MHz. Similarly, variance in the coupling factor between output to input is less than ±0.02 over a nominal value of 15.05dB. Output port matching is found to be better than 30dB over a band width of ±2.5MHz at 107.5MHz operating frequency.

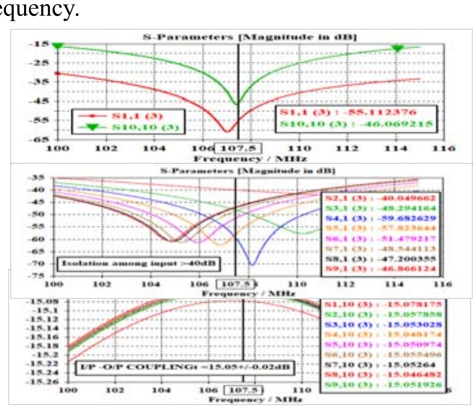

Figure 2:(a) I/p & O/p port matching.

(b) Isolation among I/p-ports(c) I/p-O/p coupling.

Reflection coefficient at an input-port, $\Gamma_{i,}$, caused due to amplitude & phase imbalance in the combining RF inputs, and effect of that on combining efficiency, are evaluated with help of equation 2 deduced from S-parameter analysis of the network model. For a variance of ±1dB & ±10º in amplitude and phase among all I/p's, combining efficiency and input-port reflection-coefficient are found to be ≥ 98% and <0.02 respectively, as depicted in figure 3 for various combinations of input excitations.

$$\Gamma_i = \frac{b_i}{a_i} = S_{io} \times b_o \times \Gamma_o + \sum_{j=1}^{32} S_{ij} \times a_j \ldots (2a)$$

$$\frac{\boldsymbol{P_o}}{\sum_{i=1}^{32} \boldsymbol{P_i}} = \frac{(\boldsymbol{b_i})^2}{\sum_{i-1}^{32} (\boldsymbol{a_i})^2} = \left(\frac{\sum_{i=1}^{32} \boldsymbol{S_{oi}} \times \boldsymbol{a_i}}{(\boldsymbol{1} - \boldsymbol{\Gamma_o} \times \boldsymbol{S_{11}})}\right)^2 \times \frac{\boldsymbol{1}}{\sum_{i=1}^{32} (\boldsymbol{a_i})^2}. \quad (2b)$$

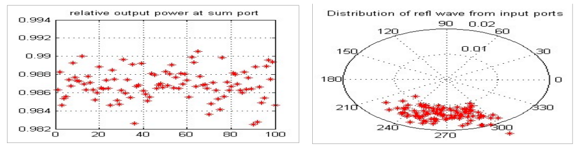

Figure 3: reflection coefficient at I/p-port and relative o/p power at sum port at all combinations of I/p- variance of ±1dB & ±10º.

1.6KW/107.5MHz AMPLIFIER MODULE

The 1.6kW/107.5MHz RF power amplifier, based on MRFX1K80H LDMOS device and designed to operate in class B push-pull configuration, is shown in figure 4 as developed and has following features-

Figure 4: Integrated assembly of 1.6kW/107.5MHz RF amplifier and 50dB directional couplers at I/p and O/p.

- Input & output matching circuit takes the form of planar transformer balun, made on Teconic make substrate RF-35, helping to minimise module-to-module variation in phase-delay and power gain as desired for minimizing RF combining losses.
- Box-type water-cooled copper heat sink was used for compact, and light weight design of the amplifier. Circuit PCB and the box-type copper heat-sink are housed suitably on Aluminium-chassis, doing away with heavy single copper plate design amplifier chassis & water-cooled heat-sink.
- LDMOS is mounted on the heat-sink with an interface of thin layer of Liquid metal in between; providing high thermal conductivity and good electrical contact between them, and also enable easy replacement of the device in case of a failure. This helped in limiting the device-case temperature below 65°C; thus, getting larger safe margin from max rated value of the device temperature to operate with in case of a transient overload.
- Circulator is not required at the amplifier o/p for connecting to a I/p of RF combiner as realized. Variations in phase and amplitude among combining inputs will be less.
- Coaxial/microstrip 50dB directional-couplers is part of amplifier chassis at I/p and O/p, thus avoiding connector junctions and RF losses at high-power level.

Design and Simulation of planar balun

Method of moment technique of AXIEM simulator is used to extract port parameters of both input and output planar balun transformers. These results are then used in AWR simulator to calculate return loss of matching networks. Return loss variation over frequency is graphically represented in Figure 5 for input matching networks.

Return loss is calculated, when gate and drain side of matching networks are terminated with conjugate values of loaded gate impedance and drain loading impedance (as mentioned in Table 1) respectively.

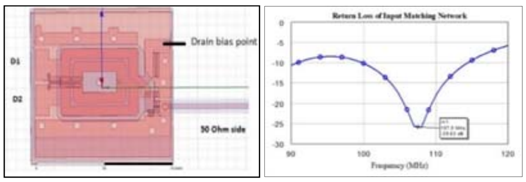

Figure 5: AWR CAD model and response of I/p network.

RF Amplifier performance

High power test on the RF power amplifier is carried out for evaluating its performance at high power level and for testing its ruggedness against possible RF overload. The satisfactory outcome of the test results is shown in table 1.

Table 1: Parameters of performance test as measured.

S. No.	Parameter	Value	Unit
1.	RF output power	1.6	kW
2.	Drain Voltage	62	V
3.	Operating frequency	107.5	MHz
4.	Power gain at 1.6 kW	≥ 25	dB
5.	Efficiency at 1.6 kW	≥ 70	%
6.	Harmonic distortion at 1.6 kW	≤ -24	dB
7.	Input return loss	≤ -22	dB
8.	Max LDMOS case Temp. (Inlet water temp 25º C)	≤ 65	º C
9.	Drain loading impedance(Ω)	3.35 + j3.95	
10	Gate Loading impedance(Ω)	3.19+j4.69	

Figure 6: Measured performance of the amplifier

1.6kW/50dB Coupler and performance

50dB directional couplers (DC) is part of Aluminium amplifier-chassis for through-line monitoring of forward and reflected power at 1.6KW power level for the cause of RF power monitoring, and protection. Main line of the DC is in form of coaxial line having Ø8mm centre conductor which is coaxially located along 16x16 mm bore made in the amplifier chassis; microstrip auxiliary line is coupled to main-line through a slot designed for required design-parameters. Performance of Directional-coupler is measured in terms of S-parameters as shown in figure 7, and at high power level with through-line RF monitoring of RF output from the RF amplifier; getting directivity and coupling factor >28dB and 50.1dB respectively at 107.5MHz as required.

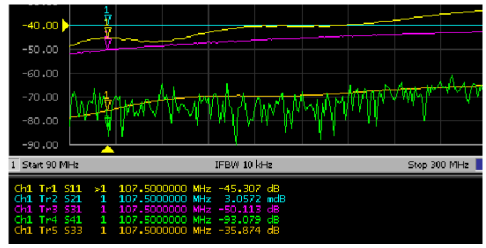

Figure 7: S-parameters of the Directional coupler as measured for its characterization.

CONCLUSION

Multi-port feeding of the accelerator cavity with 3X50kW/50Ω RF outputs is investigated to serve the accelerator cavity as RF power combiner at high power level of 3X50kW as desired. A suitable scheme for realising 50kW/50Ω RF output with operating frequency band of 107.5±0.2MHz using LDMOs devices is presented based on the 32:1 RF combiner as developed. A 32:1 RF combiner, matched at all ports, is realised in form of axially symmetric multi-layer structure using suspended strip-lines and Gysel topology. Operation with this combiner, RF amplifiers need not have circulators at their outputs as the combiner offers matched load to all the amplifier modules in presence of phase & amplitude imbalance among their RF outputs, or when some amplifiers have failed. This simplifies overall layout and avoid insertion losses as caused by circulators, helping in improving combining efficiency. A 1.6kW/107.5MHz RF power amplifier, based on MRFX1K80H LDMOS device is developed with good module to module repeatability as required for efficient RF power combining and with lower operating case-temperature of LDMOS for having reliable operation. The amplifier has 1dB operating margin over 1.6kW o/p level. Coaxial/microstrip 50dB DC is integrated with amplifier chassis at I/p and O/p, thus avoiding connector junctions and so RF losses at high-power.

ACKNOWLEDGEMENTS

Authors acknowledge contribution of all the team members of HPRFL as made in assembly and testing work. Authors are thankful to IAD, RRCAT for the support as received in mechanical design and fabrication. Authors are thankful to GD, PAG for encouragement and support.

REFERENCES

[1] Y. Jongen etc.," The Rhodotron, a new 10 MeV, 100 kW, accelerator", Nuclear Instruments and Methods in Physics Research B79 (1993) 865-870 North-Holland.

[2] A. Jain, etc., High-power solid-state RF amplifier for proton accelerator, Rev. Sci. Instrum. 79 (2008).

[3] M. K Jain etc.,"Design and Development of tetrode based RF power system for RHPA", InPAC 2019.

DEVELOPMENT OF A PROTOTYPE FAST-RAMP POWER CONVERTER WITH GRID POWER CONTROL

Abhishek Srivastava[1,*], Mangesh Borage[1, 2], Alok Singh[1]
[1]Raja Ramanna Centre for Advanced Technology, Indore 452013, India
[2]Homi Bhabha National Institute, Mumbai, 400094, India

Abstract

In Indus Accelerator Complex, booster synchrotron is used to boost the energy of electrons to the desired levels required to fill Indus-1 and Indus-2 storage rings respectively. Presently, the series connected main windings of dipole and quadrupole magnets in the booster are energized by a single power converter, which is based on 12-pulse thyristor controlled rectifier scheme. However, despite meeting the present requirements, existing booster magnet power converter scheme has certain limitations and since it is in operation for many years, the power converter is also due for up gradation in near future. Therefore, this paper discuss the development of a new prototype power converter that will bring many advantages since it will be based on switch-mode power conversion technology with grid power control.

This paper presents the development and testing of a prototype fast-ramped power converter with grid power control that delivers 100 A trapezoidal current with a ramp rate of 350 A/s, followed by simulation and experimental results.

INTRODUCTION

Booster magnet power converter (PC)

With the booster synchrotron at the Indus Accelerator Complex (IAC), RRCAT Indore, low-energy electrons coming from microtron are boosted to energies of 450 MeV and 550 MeV respectively for injection into Indus-1 and Indus-2. Booster ring consists of six dipole, six quadrupole focusing and six quadrupole defocusing magnets, whose main windings are connected in series, forming a circuit with a total resistance (R_m) and inductance (L_m) of nearly 0.265 Ω and 0.265 H, respectively. As of now, a 12-pulse thyristor based PC scheme, as shown in Fig. 1, is used to power these series-connected electromagnets [1], [2].

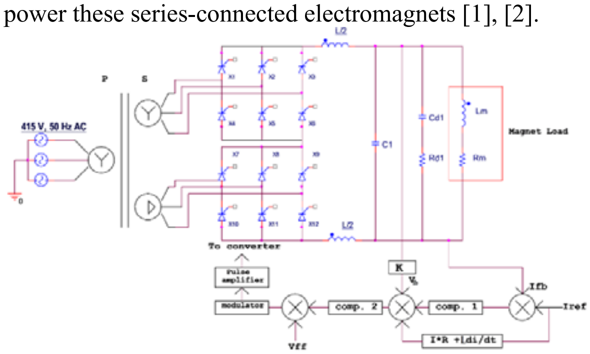

Figure 1: Present scheme of Booster magnet PC.

*asrivastava@rrcat.gov.in

As the energy of electrons increases, so does the output current of the PC (load current). When this load current flows through these electromagnets, which is trapezoidal in nature having a maximum value of about 700 A with a ramp rate of 2000 A/s and a repetition rate of 1 Hz, a bipolar voltage profile is obtained across the load. Figure 2 depicts this.

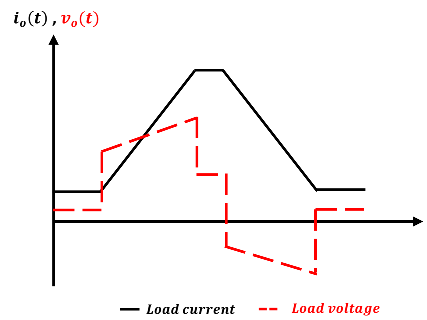

Figure 2: Load current and voltage of Booster magnet PC.

Limitations in the present scheme of the Booster magnet PC

It is obvious from Figure 2 that a two- or four-quadrant PC may be deployed in a ramping system. These PCs allow power to flow in both directions, from source to load and vice versa. Existing PC has a two-quadrant design. As power is delivered to the load during ramp-up, some of it is dissipated by the resistor and some is stored by the inductor and this stored power is fed back to the source during ramp-down time. As an example, data obtained from the IAC, RRCAT shows that this power fluctuation is around 740 kVA while average power dissipation is only 42 kW. Various power quality issues arises due to this power fluctuation such as voltage flicker etc.

The existing PC scheme is able to meet the specified requirements. However, it poses certain limitations such as operation at low power factor and voltage flicker due to repetitive power fluctuations. Further, as the power converter scheme has inherent slow dynamic response, a control scheme that has multi-loop feedback and feed forward control is used to achieve the desired tracking accuracy. Being operational over many years, the power converter is also due for up gradation in near future. Therefore, it is planned to develop a new power converter using switch-mode power conversion technology with grid power control which is the topic of this paper.

NEW SCHEME

A switch-mode based technology is investigated in this section to overcome the limitations of the existing PC scheme. As the operating frequency of switch-mode PCs is in the kHz range, so the response will be inherently fast and will ensure the tracking accuracy, possibly leading to a simple loop configuration. As previously stated, voltage flicker is caused by power fluctuations between the source and the load. Therefore, if the energy that the magnet was feeding back to the source during ramp-down can somehow be stored, then again when energy is required during ramp-up, this stored energy can be used and mains will supply only resistive losses [3]. This requires the installation of an energy storage system between the source and the load. Fig. 3 demonstrates what an electrical layout would look like if the information discussed so far here in this section was put together.

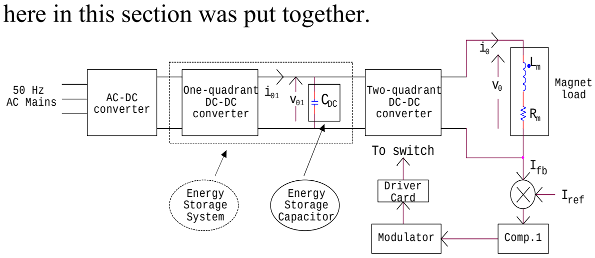

Figure 3: The new PC scheme.

This topology use two dc-dc converters interfaced with a capacitor bank, C_{DC} as shown in Fig. 3. To regulate the load current and facilitate two-quadrant operation, a two-quadrant dc-dc converter (TQC) is deployed at the output with a single control loop architecture. An intermediate energy storage system is installed. This system consist of an energy storage capacitor (C_{DC}) and a two-switch forward converter (TSFC) which is a one-quadrant dc-dc converter. Under the assumption that all the losses will be supplied from the mains, the energy between the L_m and C_{DC} system is conserved. Let at a particular time t_1 the voltage across the C_{DC} and current flowing through L_m is V_1 and I_1 respectively then energy stored in L_m and C_{DC} system at time t_1 is given by Eq. 1.

$$\frac{1}{2}L_m I_1^2 + \frac{1}{2}C_{DC}V_1^2 \qquad (1)$$

As per energy conservation, this stored energy will be equal to the energy stored in L_m and C_{DC} system at any point of time. Therefore,

$$\frac{1}{2}L_m I_1^2 + \frac{1}{2}C_{DC}V_1^2 = \frac{1}{2}L_m i_o(t)^2 + \frac{1}{2}C_{DC}v_{01}^2(t) \qquad (2)$$

$$v_{01}(t) = \sqrt{V_1^2 - \frac{L_m}{C_{DC}}\left(i_o(t)^2 - I_1^2\right)} \qquad (3)$$

Eq. 3 is the voltage across the C_{DC}. If C_{DC} follows the voltage profile obtained from Eq. 3, for the desired load current as shown in Fig. 4, then only resistive losses will be supplied from the mains. A voltage loop can be deployed to obtain this type of voltage profile across the C_{DC}. With this modification, an updated version of the discussed new PC scheme is shown in Fig. 5.

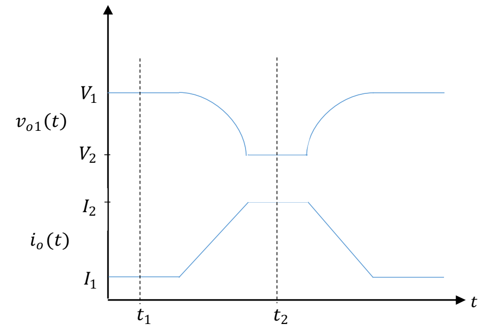

Figure 4: Waveform of current through magnet inductor and voltage across capacitor bank.

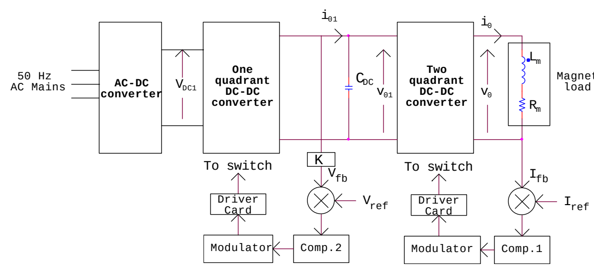

Figure 5: Updated PC scheme.

PROTOTYPE DETAILS

As a first step in the developmental process of this new technology, a prototype PC with grid power control was design and developed. The important specification are summarized in Table 1.

Table 1: Margin Specifications

S.No.	Parameter	Value
1.	L_m	54 mH
2.	R_m	0.165 Ω
3.	I_{omax}	100 A
4.	Slope	350 A/s
5.	Flat top duration	100 ms
6.	*f*	1 s

A detailed steady-state and small-signal analysis of TQC and TSFC is carried out. Designing of these PCs was very challenging as the converter duty cycle was modulating continuously to provide the time varying load current and voltage. Hence, all the other parameters depending upon the duty cycle, was also varying cyclically. Calculation of these cyclic variations is important to know peak, average and rms values of various quantities since they directly affect ratings of components, thermal design, etc. Therefore, a step by step design flow diagram for time varying load conditions is evolved. The analysis and design of these converters are detailed in [4], [5].

SIMULATIONS AND EXPERIMENTAL RESULTS

To verify the analytical results and validate the design calculations, TQC and TSFC were simulated in OrCAD PSpice Designer software 17.2. The results obtained from the simulations were then compared with the theoretical results. Fig. 6 and Fig. 7 show a comparison between calculated and simulated output voltages for TQC and TSFC at different duty cycles [4], [5].

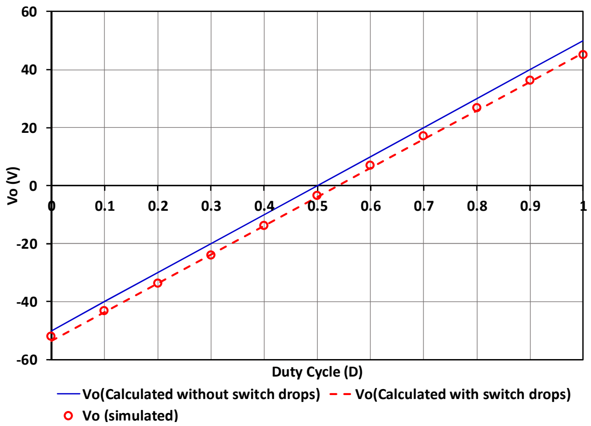

Figure 6: Variation of output voltage of TQC with respect to duty cycle.

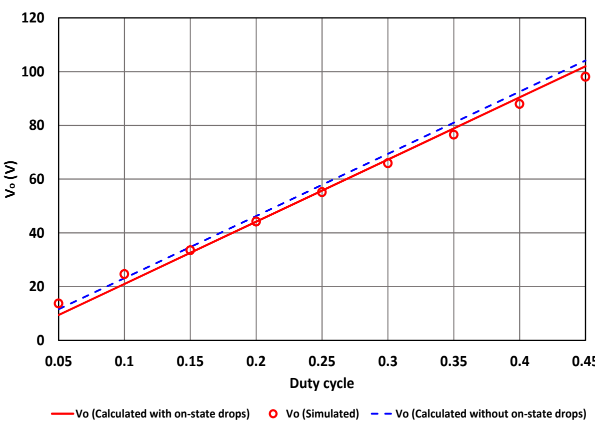

Figure 7: Variation of output voltage of TSFC with respect to duty cycle.

Once the simulation results verified the analytical design equations an experimental prototype was developed whose photograph is shown in Fig. 8. Here, a 3-phase transformer is used to power the AC-DC converter whose output is acting as the input for the TSFC. The output of the TSFC is the input to the TQC.

The experimental prototype is tested to verify the theoretical findings. Experimental waveforms shown in Fig. 9 gives the waveforms of output voltage and output current of TQC and TSFC respectively. From the experimental waveforms it can be seen that, when the C_{DC} is following the desired voltage profile (CH-1) then the current (CH-4) coming from the TSFC (i.e. from mains) is positive i.e. mains is supplying only resistive losses.

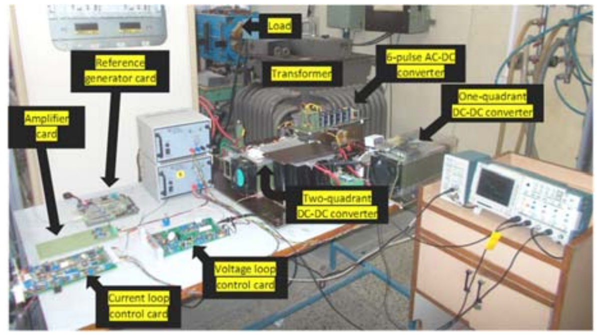

Figure 8: experimental prototype of FRPC.

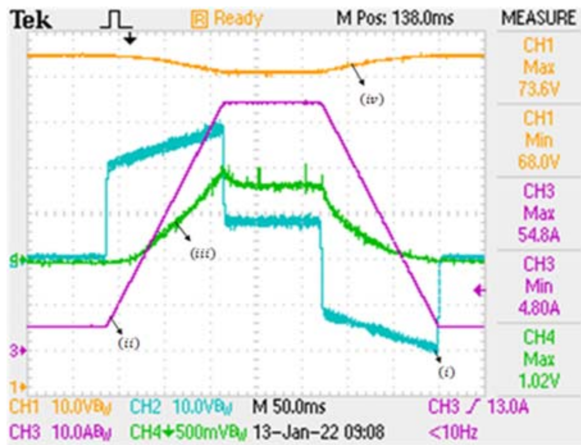

Figure 9: Experimental waveforms of prototype PC showing ramping rate (i) v_o, 10 V/div, (ii) i_o, 10 A/div, (iii) i_{o1}, 5 A/div, (iv) v_{o1}, 10 V/div, x-scale: 50 ms/div

ACKNOWLEDGMENT

The assistance of Mr. S. Mani, Mr. Vinod Somkuwar, Mr. Sanjay Kumar Prajapati in development of the prototype converter, preparation of test set-up and during the testing is acknowledged. The author also acknowledge the contribution of Shri P. Renukanath and his team for development of magnetic components.

REFERENCES

[1] Indus Accelerator Complex (IAC), RRCAT, Indore; https://www.rrcat.gov.in/technology/accel/isrf_index.html

[2] Pagare Anand et al., "Modifications in booster dipole magnet, power supply," Proceedings of the DAE-BRNS Indian particle accelerator conference-2003.

[3] Burnet, J.-P., "Requirements for Power Converter," CERN Accelerator School: Power Converters, Baden, Switzerland, 7-14 May 2014.

[4] Srivastava A. et al., "Steady-State Analysis and Design of Two-Quadrant, Switch-Mode, Fast-Ramped Power Converter for Electromagnets in Particle Accelerators," 2021 National Power Electronics Conference (NPEC), 2021, pp. 1-6,doi:10.1109/NPEC52100.2021.9672504.

[5] Srivastava A. et al., "Analysis and Design of Two-switch Forward Converter for Time-varying Load Conditions," Indian Particle Accelerator Conference (InPAC), VECC, Kolkata, Mar., 22-25, 2022.

Remote Monitoring system for high-temperature Vacuum Furnace

Manoj Kumar T.K.[1*], A.N. Takke[1], J.N. Karande[1], M.E. Sawant[1], A.A. Shinde[1], S.P. Singh[1], S.Pal[1]

R. Palit[2] and V. Nanal[2]

[1]PLF, Tata Institute of Fundamental Research, Mumbai 400005

[2]DNAP, Tata Institute of Fundamental Research, Mumbai 400005

** manoj@tifr.res.in*

Abstract

A custom-built high-temperature vacuum furnace has been installed at TIFR in the Pelletron Linac Facility (PLF) for heat treatment of Niobium resonator cavities. During the heat treatment, crucial parameters like vacuum and temperature need to be monitored continuously to ensure the safe and secure operation of the vacuum furnace. For this purpose, a remote monitoring system is designed and developed using Espressif ESP-32 development board. Further, the monitoring of auxiliary support systems like chilled water temperature is also important to avoid accidental malfunctioning and prevention of the job damage. These parameters from the system, are transmitted through the android-based telegram messenger application. Additionally, an alert message is generated and sent to the operator group, if the parameters exceed the set values.

INTRODUCTION

Vacuum furnaces are used to carry out annealing, brazing and heat treatment with high consistency and low contamination. A high temperature vacuum furnace has been installed at TIFR in the Pelletron Linac Facility (PLF) for heat treatment of Niobium resonator cavities [1]. The furnace is designed to operate at 1200° C with a vertical hot zone 600 mm diameter and 1000 mm height. During the heat treatment the vital parameters like vacuum at different zones and chilled water temperature needs to be monitored continuously. Intelligent monitoring systems are playing a major role in present day to day activities. IoT is playing a vital role in the design and development smart and intelligent systems in industrial applications. ESP-32 is an IoT capable microcontroller which can be used to build smart data acquisition systems [2]. An Arduino based remote monitoring system is designed and developed using ESP-32 to access the parameter values from the vacuum furnace and transmit the data to a Telegram messenger group. The telegram app can be easily installed on a smart phone. Whenever the parameters breach the threshold level, an alarm is generated and sent to the operator group for promptly taking timely remedial action to resolve the issue.

SYSTEM DESIGN

The remote monitoring system is developed around the Espressif ESP-32 development board. ESP-32 is a low cost, low power System On Chip (SoC) 32-bit microcontroller and works well with the arduino IDE, an open source software development tool. ESP-32 is equipped with digital I/O lines, multichannel 12-bit Analog to Digital Converter (ADC), Wi-Fi and Bluetooth connectivity. These features make ESP-32 a powerful device to develop automation and monitoring devices easily and efficiently. Figure 1 shows the photo of the Espressif ESP-32 development board.

Figure 1: Espressif ESP-32 development board.

During the heat treatment operation, vacuum level of the furnace and chilled water temperature needs to be monitored very closely to ensure secure operation of the system. There are four vacuum gauges deployed at different zones in the vacuum furnace. The readings are available locally at the Pfeifer Maxiguage™ [3] pressure measurement and control unit and on the PC. The developed remote monitoring system collects the real time process parameters and transmits to an operating group created using the telegram application, which can be easily installed in the mobile phone. Figure 2 shows the block diagram of the ESP-32 based remote monitoring system.

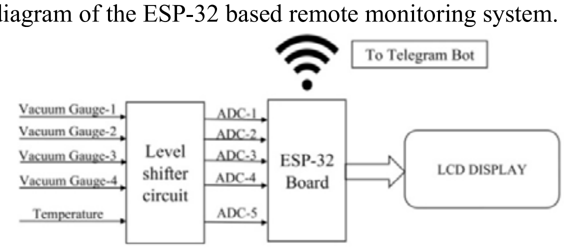

Figure 2: Block Diagram of ESP-32 based remote monitoring system

The analogue voltages equivalent to the pressure value is available in the control I/O connector provided in the Maxiguage unit. These analogue values relating to the four gauges are connected to a level shifter network and scaled proportional to the actual parameter value. The ESP-32 ADC can accept a maximum voltage level of 3.3 V with 12-bit resolution. These signals are filtered and fed to different channels of the ADC for digitization. Figure 3 shows the photograph of the level shifter and filter card. The chilled water temperature is measured with PT-100 sensor and its output is also level shifted and fed to one of the ADC channels for processing.

Figure 3: Level shifter and filter card with ESP-32 development board.

The ESP-32 is programmed to digitise the various analogue parameters available at the input. The formula given in the vacuum guage datasheet is incorporated in the ESP-32 programming to reconstruct the actual pressure parameter values. These process parameters are locally displayed on the LCD screen. The ESP-32 is programmed to connect to the Wi-Fi router and connects to the user through the telegram app. The process parameters are sent to the operator group in telegram app and can be monitored remotely. Telegram app can be easily installed in the smartphone (Android and iPhone) or computer (PC, Mac and Linux). Telegram app allows to create bots. Users can interact with these bots by sending messages, commands and inline requests. The bots can be controlled using HTTPS requests to Telegram Bot API. An operator group is created in the telegram app and the bot is also added to the group. The ESP-32 is programmed with the bot token ID and group chat ID to enable the two-way communication between the ESP-32 and the telegram app. Whenever, the process parameters breach the set points the ESP-32 sends an alarm to the operator group. The alarm is repeated at a specified time interval till is gets acknowledged. The process parameters can be obtained by sending relevant command from the group and the ESP-32 will send back the instantaneous parameter values. The remote monitoring system works on a 5 V, 1 A AC to DC power adapter available in the market. Figure 4 shows the developed remote monitoring system for the vacuum furnace.

Figure 4: Remote monitoring system board for vacuum furnace.

RESULT & SUMMARY

The remote monitoring system using ESP-32 development board is designed and developed and tested with the Vacuum Furnace installed in PLF. The level shifter and filter circuits are wired on a general purpose PCB along with ESP-32 development board. The system is interfaced with the vacuum furnace and it functioned as per the expectation. The alarm message and the acknowledgement of the alarm by the user is shown in figure 5. As this is a general design, this scheme can be used to monitor the parameters of any LINAC sub systems or other crucial equipments.

Figure 5: Left panel shows the alarm generated by the remote monitoring system. Right panel shows the telegram screen shot of alarm acknowledgement and systems response.

ACKNOWLEDGEMENT

We express our gratitude to all LINAC staff for rendering their support as and when required.

REFERENCES

[1] Shinde A. A, Pal. S, Karande J.N, Dhumal P, Rozario C, Nanal Vandana, Pillay R.G. **"**Vacuum furnace: design, installation and commissioning**",** Proceedings of the eighth DAE-BRNS Indian particle accelerator conference-2018, ID359.

[2] https://www.espressif.com/en/products/socs/esp32.

[3] https://www.mpi-hd.mpg.de gerda/ tg04_technical/ manuals/bg805186be_b_web.pdf.

PROPOSED CLOSED ORBIT CORRECTION SCHEME FOR INDUS-1 STORAGE RING

V. K. Meena†, Suraj Prakash and Riyasat Husain
Accelerator Physics and Synchrotron Utilization Division
Raja Ramanna Centre for Advanced Technology, Indore-452013

Abstract

Indus-1 synchrotron radiation source is a 450 MeV, 125 mA electron storage ring, emitting synchrotron radiation from mid-IR to soft X-rays with a critical wavelength of ~ 61 Å, and operational at RRCAT. Its injector system consists of a 20 MeV Microtron as a pre-injector and a 450 MeV Booster Synchrotron as an injector, providing an electron beam for injection into the Indus-1 storage ring. Simulation results of the present closed orbit correction scheme for Indus-1 indicate poor closed orbit correction at beam position monitors (BPMs) in the vertical plane and at the dipole centre in both planes, from which the beamlines are connected to tap the photons. In view of this, two closed orbit correction schemes are proposed with different configurations of BPMs and correctors in terms of their locations and numbers. Simulation studies have been carried out for correction efficiency for both the schemes considering various quadrupoles and dipoles alignment error sets, and maximum corrector strengths required for correction are evaluated. Based on the simulation results, a closed orbit correction scheme has been finalized, which is efficient in controlling the closed orbit at all the BPMs and at the dipole magnet positions. In this paper, the results of the simulation studies are presented for existing and proposed closed orbit correction schemes for the Indus-1 storage ring.

INTRODUCTION

The Indus-1 storage ring is operated mainly for tapping the synchrotron radiation from bending magnets [1]. The combined function lattice consists of 4 unit cells. Each unit cell accommodates one bending magnet (BM) with a field index of n=0.5 and two quadrupole doublets (a pair of quadrupole focusing (QF) and quadrupole defocusing (QD)). To correct the natural chromaticity of the ring one sextupole focusing (SF) and one sextupole defocusing (SD) are also used. Each unit cell has a 1.3 m long straight section (S). Two such straight sections are used for beam injection; one section accommodates the septum magnet and the other diametrically opposite to it accommodates the pulsed kicker magnet. In the remaining sections, one accommodates a RF cavity and one available for diagnostics devices. In addition, for orbit measurement 4 BPMs are installed and for orbit correction 3 correctors in the horizontal plane (CHs) and 3 correctors in the vertical plane (CVs) are installed independently and 4 CHs are integrated with BM. The optical function and layout of one unit cell and, the present orbit correction scheme are shown in Fig. 1 and the main parameters of the Indus-1 storage ring lattice are mentioned in Table 1, respectively [2].

† vkmeena@rrcat.gov.in

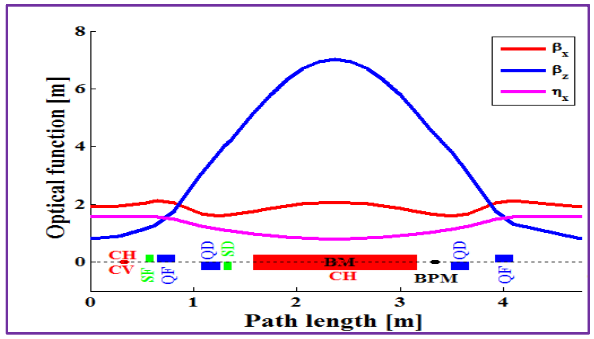

Figure 1: Optical function of one unit cell of Indus-1 lattice. The solid rectangular boxes represent bending magnet (red), quadrupole magnets (blue) and sextupole magnets (green) and position of the BPMs (black sphere) and correctors (red sphere) also indicated.

Table 1: Main parameters of Indus-1 storage ring

Parameter	Value
Beam energy	450 MeV
Beam current	125 mA
Circumference	18.97 m
Betatron tune	1.602, 1.466
Bending magnet (B, n, l)	1.5 T, 0.5, 1.57 m
Horizontal emittance (ε_x)	190 nm-rad
Critical wavelength (λ_c)	61.38 Å
Harmonic number	2
Natural chromaticity (ξ_x, ξ_y)	-0.89, -1.87
Beam size (σ_x, σ_z)	700, 120 µm

The closed orbit distortion (COD) is mainly generated from the magnetic field errors and axial rotation errors of dipoles, and misalignment errors of dipoles and quadrupoles. Due to the higher value of COD, the efficiency of beam injection and reduction rate of beam lifetime and photon flux etc. come into the picture. If the beam goes off-centre in the sextupoles, these will generate feed-down effects. Therefore, correction of COD is mandatory to keep the electron beam at the design orbit. In this paper, an initial study of the present orbit correction scheme is carried out. After that new orbit correction schemes are studied and evolved by distributing BPMs and correctors over the ring. The COD before and after correction for all the schemes are compared at BPMs and at dipole positions. Based on the simulation studies, a scheme with 8 correctors and 8 BPMs is finalized. The required maximum strengths of correctors are also estimated.

CLOSED ORBIT DISTORTION

Any unwanted dipolar kick generates distortion in the ideal orbit. The effect on the orbit due to smaller error is defined as COD w.r.t. ideal orbit, it is given by [3]

$$z_{co}(s_j) = \frac{\sqrt{\beta_{zmax}(s_j)}}{2\sin\pi\nu_z}\sum_{i=1}^{N}\theta_i\sqrt{\beta_{zi}(s_i)}\cos\left(\pi\nu_z - \left|\psi_z(s_j) - \psi_{zi}(s_i)\right|\right) \quad (1)$$

where $z(s) = x \text{ or } y$ represents horizontal and vertical plane, ν_z is the betatron tune of the ring, and (β_i, ψ_i) and (β_j, ψ_j) are the beta function and the phase function for the θ_i dipolar kick and j^{th} BPM respectively, and $z_{co}(s_j)$ is the orbit distortion at the j^{th} BPM due to θ_i kick of the i^{th} element in horizontal and vertical plane respectively.

The origin of θ_i is given by

$$\theta_i = \left(\frac{\Delta B}{B}\right)_i \theta_B \quad \text{for the dipole field error} \quad (2a)$$

$$\theta_i = (\Delta\phi)_i \theta_B \quad \text{for the dipole rotation error} \quad (2b)$$

$$\theta_i = (kl)_i \Delta z_i \quad \text{for quadrupole misalignment} \quad (2c)$$

where $\left(\frac{\Delta B}{B}\right)_i, \Delta\phi_i \text{ and } \theta_B$ are the magnetic field error, rotation error and bending angle of i^{th} dipole magnet and $k_i, l_i \text{ and } \Delta z_i$ are the strength, length and misalignment of the i^{th} quadrupole magnet.

Thus, COD is the overall effect of all the dipolar field errors discussed above and given by eqn. (2). Hence, rms orbit at any point in the lattice can be obtained by the following equations

$$x_{rms}(s) = \frac{\sqrt{\beta_{xmax}(s)}}{2\sqrt{2}\sin\pi\nu_x}\left\{(\Delta x)^2\sum_i (kl)_i^2\beta_{xi} + \left(\frac{\Delta Bl}{Bl}\right)^2\sum_i \theta_B^2\beta_{xi}\right\}^{\frac{1}{2}} \quad (3)$$

$$y_{rms}(s) = \frac{\sqrt{\beta_{ymax}(s)}}{2\sqrt{2}\sin\pi\nu_y}\left\{(\Delta y)^2\sum_i (kl)_i^2\beta_{yi} + (\Delta\phi)^2\sum_i \theta_B^2\beta_{yi}\right\}^{\frac{1}{2}} \quad (4)$$

Closed Orbit Correction

The measurement of the COD is carried out by the BPMs and the correction is carried out by the dipole correctors. The corrector-to-BPM orbit response matrix (ORM) is a vital piece of information for both closed orbit correction and linear optics analysis. The basic format of the response matrix equation is

$$z = R\theta \quad (5)$$

where column vector z contains the orbit shift produced by incremental change θ in the corrector magnets. The elements of the response matrix, between BPMs and correctors, are given by

$$R_{ij} = \frac{\sqrt{\beta(s_i)\beta(s_j)}}{2\sin\pi\nu}\cos\left(\pi\nu - \left|\psi(s_j) - \psi(s_i)\right|\right) \quad (6)$$

The strength of the corrector magnets is computed by solving the linear equation as following

$$\theta = -R^{-1}z \quad (7)$$

where R^{-1} is the pseudo inverse response matrix (RM).

New Closed Orbit Correction Schemes

For COD measurement, four old BPMs located near BMs and four new BPMs located between QF and SF are considered. Similarly, for COD correction, four old correctors integrated with BMs for the horizontal plane are considered. In addition to this, for correction scheme-A, four new correctors for the horizontal plane and four new correctors for the vertical plane are integrated with the SFs and SDs respectively. Similarly for correction scheme-B, eight new correctors for horizontal and vertical planes are integrated with the SFs and SDs simultaneously. The tentative arrangements of the BPMs and correctors in one unit are shown for both scheme-A and scheme-B in Fig.2.

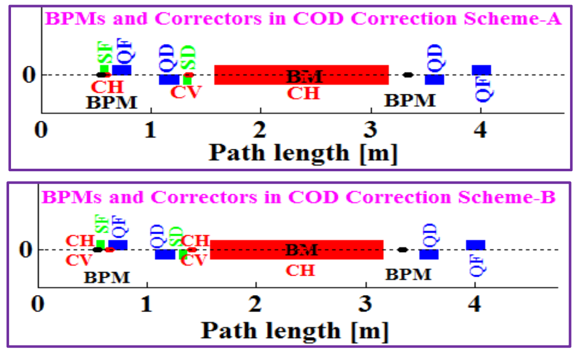

Figure 2: Configuration of BPMs and correctors in correction scheme-A and scheme-B.

RESULTS AND DISCUSSION

COD Correction with Present Scheme

To simulate the COD correction, a program is developed in MATLAB using Accelerator Toolbox [4]. Misalignment errors of quadrupoles and dipoles, magnetic field errors of dipoles and rotation errors along the beam axis of dipoles are generated for a Gaussian distribution truncated at 3σ and, which are mentioned in Table-2 [2].

Table 2: Errors setting in simulation

	Δx	Δy	$\Delta\phi$	$\Delta B/B$
	μm	μm	μrad	
BM	100	100	200	$5 * 10^{-4}$
QD & QD	100	100		

These error settings are applied in the storage ring lattice to generate uncorrected COD. The simulation of uncorrected COD was performed iteratively by applying errors amplitude randomly truncated at 3σ for 1000 machines. This simulation is carried out with the natural chromaticity in both transverse planes. By this, uncorrected orbit max~ [4.3, 5.3] mm and rms ~ [1.5, 1.3] mm in the (x, y) plane are generated. Using the present COD correction scheme, COD is corrected to max ~ [3.4, 5.4] mm and rms ~ [0.8, 0.9] mm respectively. Using the pseudo inverse of RM, the max strength of the corrector is estimated to be ~ [2.4, 3.7] mrad in respective planes.

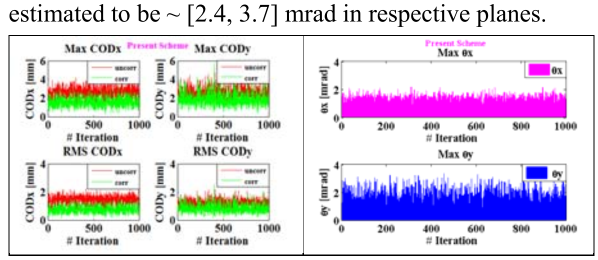

Figure 3: Max and rms COD before and after correction and max required strength of correctors

† vkmeena@rrcat.gov.in

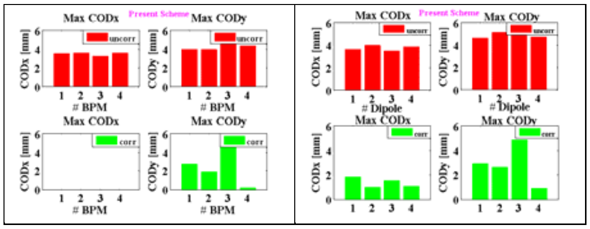

Figure 4: max COD uncorrected and corrected at BPM and at dipole locations using present correction scheme

COD correction with scheme-A and Scheme-B

In COD correction scheme-A, for orbit measurement in transverse plane 8 BPMs (4 old and 4 new BPMs) and, for orbit correction 8 CHs (Integrated on BMs and SFs) in horizontal plane and 4 CVs (Integrated on SDs) in vertical plane are considered, which is shown in upper part of Fig. 2. Using this correction scheme, uncorrected max ~ [4.3, 5.3] mm and rms ~ [1.5, 1.3] mm in (x, y) planes are reduced to max ~ [0.2, 1.1] mm and rms ~ [0.03, 0.26] mm respectively, after correction. Using the pseudo inverse of RM, the max strength of the corrector is estimated to be ~ [2.7, 1.6] mrad in respective planes.

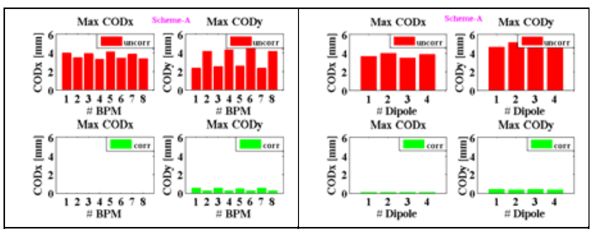

Figure 5: max COD uncorrected and corrected at BPM and at Dipole locations using correction scheme-A

In COD correction scheme-B, for orbit measurement in transverse plane 8 BPMs (4 old and 4 new BPMs) and, for orbit correction 12 CHs (Integrated on BMs, SFs and SDs) in the horizontal plane and 8 CVs (Integrated on SFs and SDs) in the vertical plane are considered, which is shown in the lower part of Fig. 2. Using this correction scheme, uncorrected orbit max ~ [4.3, 5.3] mm and rms ~ [1.5, 1.3] mm in (x,y) planes are reduced to orbit max ~ [0.4, 1.2] mm and rms ~ [0.09, 0.28] mm respectively, after correction. Using pseudo inverse of RM, the max strength of the corrector is estimated to ~ [2.4, 2.4] mrad in the respective planes.

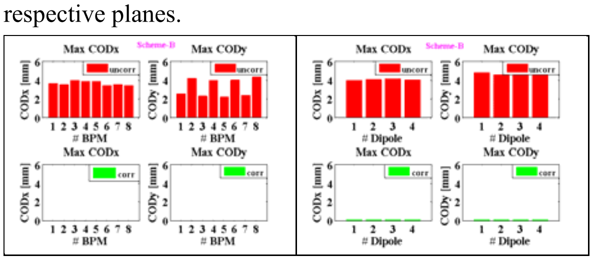

Figure 6: max COD uncorrected and corrected at BPM and at Dipole locations using correction scheme-B

In addition to this, performance of COD correction schemes are summarised in Table-3.

Table 3: Performance of COD correction schemes

Max COD	**@BPM** Δx	Δy	**@Dipole** Δx	Δy	**@Kick** $\Delta\theta_x$	$\Delta\theta_y$	**Correction Scheme**
	(mm)		(mm)		$(mrad)$		
Uncorr	4.3	4.7	4.3	5.3	-	-	-
Corr	~0	4.5	1.1	5.6	2.4	3.7	Present
Corr	~0	0.6	0.2	0.1	2.7	1.6	Scheme-A
Corr	~0	~0	0.2	0.1	2.4	2.4	Scheme-B

Corrector strengths

In order to estimate required strength of horizontal and vertical corrector magnets, CODs are generated and corrected for error settings mentioned in Table-2 for 1000 random machines. The strength of the corrector magnets for orbit correction scheme-A and scheme-B are shown on the left side and right side in Fig. 7 respectively.

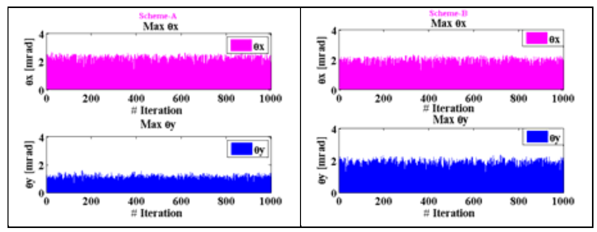

Figure 7: Strength of corrector for scheme-A & scheme-B

CONCLUSION

The study of a closed orbit correction scheme has been carried out for 450 MeV Indus-1 storage ring. Simulation results indicate that the present closed orbit correction scheme shows poor closed orbit correction at BPMs in the vertical plane and at the dipole centre in both planes. To overcome this, two orbit correction scheme-A and scheme-B have been studied. Based on the simulation studies, the scheme-B in 8 correctors integrated on sextupoles, and 8 BPMs: four at old locations and four at new proposed locations, is finalized. In simulations, it was found that scheme-B is more efficient in controlling the closed orbit at all BPMs and at the dipole magnet positions, from which the beamlines are connected to tap the photons. In addition, the max strength of the corrector is estimated to be ~ [2.4, 2.4] mrad in the respective planes, which is reasonable to achieve with normal conducting magnet technologies.

REFERENCES

[1] G K Sahoo et al, Commissioning of Indus-1 storage ring, EPAC (2000).

[2] A D Ghodke et al, The closed orbit distortion and its correction in Indus-1, International Conference on Synchrotron Radiation Sources (1992).

[3] Y Jin et al, A study of Closed Orbit Distortion and their correction for APS, (1987).

[4] A Terebilo et al, Accelerator modelling with MATLAB accelerator toolbox, PAC (2001)

† *vkmeena@rrcat.gov.in*

MODELLING AND SIMULATION OF TEMPERATURE STABILIZATION SYSTEM FOR VOLTAGE REFERENCE TO BE USED IN PRECISION MAGNET POWER SUPPLY

S. V. Pratihast[1*], Anindya Roy[1], S. Pal[1,2],
[1]Variable Energy Cyclotron Centre, Department of Atomic Energy, Kolkata-700064, India
[2]Homi Bhabha National Institute, Mumbai-400088, India

Abstract

Voltage reference IC is a crucial component present in the controller of the high-precision current regulated power supplies used in particle accelerators. These power supplies are used to power the electromagnets required for desired beam dynamics. However, varying environmental factors such as changes in ambient temperature can cause output voltage of the reference voltage IC to drift from its ideal characteristic. In this paper, we describe a novel method for temperature stabilization of the voltage reference IC in indigenous power supplies being developed to replace imported power supplies. We developed a SIMULINK based electrical equivalent model of the thermoelectric system that utilizes a thermoelectric module working on the Peltier effect. Suitable closed-loop control algorithms such as PI, ON-OFF, and ON-OFF with an integrator are implemented and optimized controller parameters for dynamic and steady-state control parameters. The modelling, simulation, and analysis of results are described in detail in this paper.

INTRODUCTION

The voltage reference used in precision magnet power supply is typically designed to maintain a stable voltage output over a wide range of temperatures and other environmental conditions [1]. Despite the internal compensatory circuitry present in the voltage reference, there is still a residual temperature coefficient associated with it. The residual temperature coefficient is the amount by which the output voltage of the voltage reference varies with changes in temperature, even after the internal compensatory circuitry has been applied. This coefficient can cause an unwanted drift in the output voltage. To address this issue, a temperature stabilization system was required for the voltage reference. This paper demonstrates a temperature stabilization system for the voltage reference which is modelled and simulated using SIMULINK.

The study is divided into three main sections: system modelling, implementation of various control algorithms, and control system analysis. In the system modelling section, the parameters for the final control element (a Peltier module) and the temperature sensor (an IC-based temperature sensor) were modelled using SIMULINK. In the control algorithms section, different closed-loop control algorithms were applied to the model to design the temperature stabilization system. Finally, in the control system analysis section, the results obtained from the simulation were analysed using control theory to know the theoretical feasibility of the system.

SYSTEM MODELLING

Before implementing an actual temperature stabilization system for the voltage reference, it was necessary to simulate the control system to determine optimal parameters, such as the operating current for a Peltier module. SIMULINK, a simulation tool provided by MATLAB, is a powerful tool for designing and testing such control systems [2]. Due to the unavailability of Peltier module blocks in SIMULINK, an electrical equivalent model of the Peltier module was designed. In the past, many researchers have modeled thermal systems using lumped electrical equivalent parameters [3]. One such paper focused on modeling the Peltier module using electrical equivalent parameters as listed in Table 1.

Table 1: Electrical Equivalent of Thermal Parameters

Thermal Parameter	Electrical Parameter
Heat	Charge
Rate of Heat Flow	Current
Temperature	Voltage
Thermal Conductance	Electrical Conductance
Heat Capacity	Electrical Capacitance

The heat flow in the designed thermoelectric system is governed by several thermodynamic equations such as Fourier’s law of conduction, the Peltier effect, and Joule’s law of heating [4]. However, for ease of calculation, the contribution of the Thomson effect and heat transfer due to radiation and convection has been neglected. The thermoelectric module is a device with two sides, the hot side and the cold side, where the Peltier effect causes one side to cool down as it absorbs energy and the other side to heat up as it releases energy. The heat flow between the two sides is governed by Fourier’s law of conduction, where heat from the hot side flows to the cold side through a resistance that represents the thermal resistance of the module as shown in Figure 1. To simplify the model, it is assumed that in steady-state conditions, half of the joule heat generated will flow into the hot side and the remaining half into the cold side. This assumption allows for an easier calculation of the heat flow and enables the design of a more efficient temperature stabilization system.

*sv.pratihast@vecc.gov.in

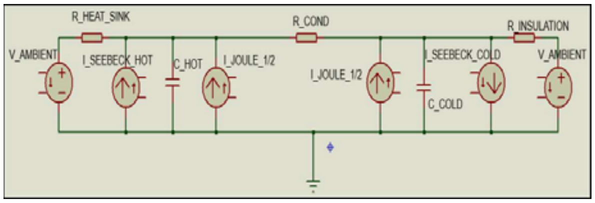

Figure 1: Thermoelectric Model of Peltier Module

Once the electrical equivalent model of the thermoelectric module is established, the next step is to incorporate the parameters of the temperature sensor IC and voltage reference. The parameters that were taken into consideration include the heat generated due to the self-heating of ICs, the dimension of the ICs, the thermal resistance of their packages, and the temperature coefficient of the voltage reference. These parameters were added to the model to get a more realistic simulation of the system. In the designed thermoelectric system, the model included a connection between the hot side of the module and a heat sink with low thermal resistance, allowing for the dissipation of heat into the surrounding environment. On the other hand, the cold side of the module was connected to the ambient temperature through a high resistance, which represented the insulation of the chamber containing the voltage reference.

In order to represent the effect of varying ambient temperatures in the model, a controlled voltage source is used. This voltage source generates a voltage signal based on the desired signal provided by the signal builder block of the SIMULINK. By doing so, the varying ambient temperature is simulated in the model, and its effect on the thermoelectric module can be studied. The use of a controlled voltage source adds a level of flexibility to the model, allowing for the simulation of different ambient temperature conditions and the study of their impact on the performance of the thermoelectric system. The generation and absorption of Peltier heat and the generation of heat due to Joule heating were represented by controlled current sources. The temperature coefficient of the voltage reference was also taken into account, with a value of 1 ppm/ºC being used in the model.

CONTROL ALGORITHM

The simulation results obtained by different closed-loop control approach is presented in this section. Initially, a PI (Proportional Integral) control algorithm is implemented in SIMULINK using suitable blocks [5]. Subsequently, the On-Off control algorithm is applied, followed by the implementation of the RC circuit-based on-off control algorithm.

Proportional Integral Control

The first step involved implementing a PI-based closed-loop control algorithm using SIMULINK blocks. The proportional and integral gains were manually tuned by taking into account the static and dynamic aspects of the control system, such as settling time, rise time, steady state error, and overshoot. As the process variable to be controlled was temperature, which varies slowly, a derivative control action was not employed, as it would have induced unwanted oscillations in the system response. A proportional controller alone would not have been effective in eliminating the steady-state error, thus necessitating the inclusion of an integral action. To address the practical constraints on the current supplied to the module, a current limiter was designed using SIMULINK blocks that restricted the current to ±0.5 Amperes. The overall view of the control system is depicted in the Figure 2.

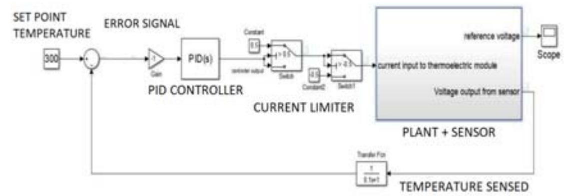

Figure 2: PI based Closed Control Loop

ON-OFF

This section will discuss the implementation of an ON-OFF control algorithm with built-in hysteresis for the system as shown in Figure 3. The option to implement an ON-OFF control algorithm was considered, and if successful in restricting temperature fluctuations within 1ºC with fewer components, a PI-based controller will not be required for the design.

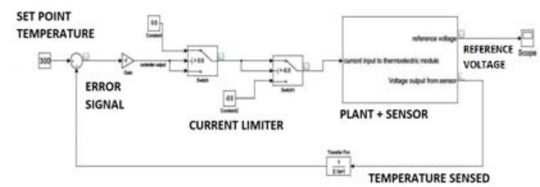

Figure 3: ON-OFF based Closed Control Loop

ON-OFF along with Integrator

The implementation of ON-OFF control in the system gave satisfactory results, except for one issue. The fast switching of the MOSFET resulted in a high rate of change of current through the TEC Module, which limited the hysteresis band. If the hysteresis band was set below a certain value, the closed-loop control would fail to maintain the temperature within the desired range due to overshoot. To reduce the rate of change of current through the thermoelectric module, a simple RC circuit (integrator) was added in cascade with the controller. The schematic diagram in the Figure 4 shows the overall design.

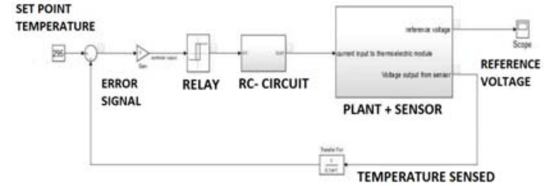

Figure 4: ON-OFF with Integrator based Closed Loop Control

The appropriate values of R and C were selected to design the R-C circuit according to the desired time constant. The voltage reference output was ultimately stabilized with significantly reduced fluctuations, comparable to that of the PI-based design.

OBTAINED PLOTS AND ANALYSIS

The Figure 5 depicts the plot of cold side temperature variation over time, which demonstrates the positive effect of the RC circuit in reducing the rate of temperature variation. Figure 6 depicts that the operating current of 0.5 Ampere is sufficient for the amount of heat load to be managed by Peltier Module.

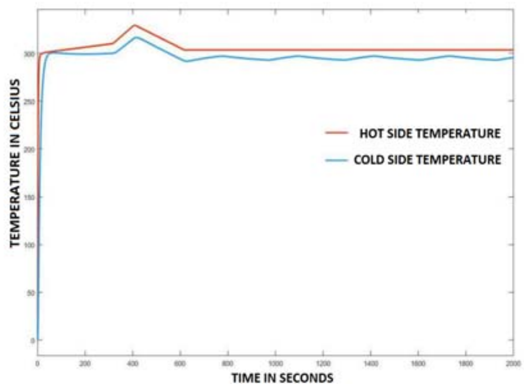

Figure 5: Temperature vs Time plot for ON-OFF with RC Control Loop

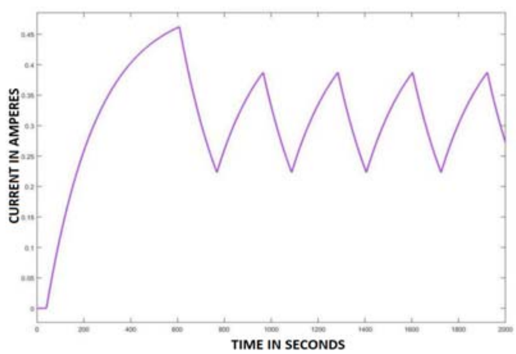

Figure 6: Current drawn by Peltier Module

The voltage reference output was ultimately stabilized with significantly reduced fluctuations. The plot in Figure 7 shows the voltage reference output over time.

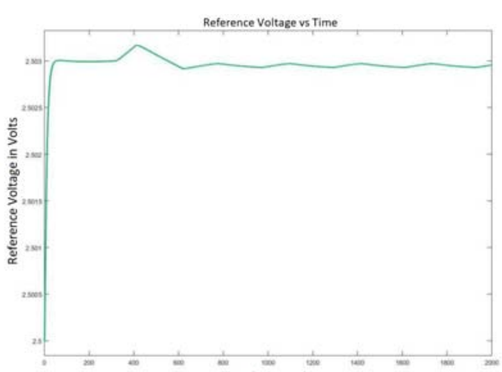

Figure 7: Voltage Reference Output vs Time

The Bode plot, available as a tool in MATLAB, was used for control system analysis. The Bode plot depicted in the Figure 8 shows that the gain margin and phase margin of the system is infinite, indicating that the system is inherently stable in theory. The entire system is comprised of two states, namely cold side heat capacitance and hot side heat capacitance.

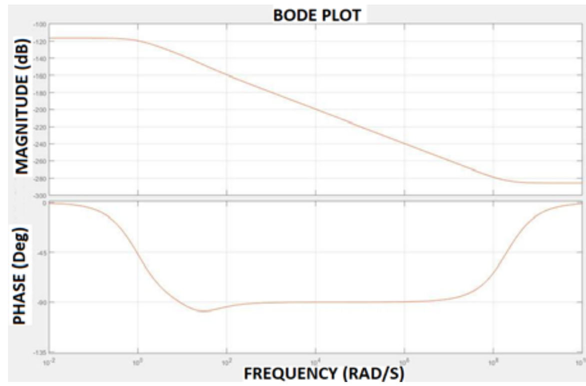

Figure 8 Bode Plot

CONCLUSION

The analysis of simulation results, provided valuable feedback about theoretical feasibility, optimum controller design and operating current of the Peltier module. The use of control theory ensures that the system is stable, precise, and operates at optimal performance.

The aim was to minimize the drift in the output voltage due to the residual temperature coefficient of the voltage reference. Overall, the study provides a detailed and comprehensive approach to developing a temperature stabilization system and highlights the importance of modeling and simulation in optimizing its performance. The techniques and methods presented in this paper could be applied in other applications where temperature stabilization is necessary, and the results could help guide the development of future voltage references with greater stability and precision.

REFERENCES

[1] S. Bandyopadhyay, M. Das, *et al.*, “Regulation scheme for precision magnet power supply,” in *Asian Particle Accelerator Conference*, pp. 669–670, 2007.

[2] Simulink Documentation, “Simulation and model-based design,” 2020.

[3] C. Alaoui, “Peltier thermoelectric modules modeling and eval- uation,” *International Journal of Engineering (IJE)*, vol. 5, no. 1, p. 114, 2011.

[4] D. Zhao and G. Tan, “A review of thermoelectric cooling: materials, modeling and applications,” *Applied thermal engi-neering*, vol. 66, no. 1-2, pp. 15–24, 2014.

[5] E. Mujčić, U. Drakulić, and M. Škrgić, “Closed-loop tem-perature control using matlab@ simulink, real-time toolbox and pic18f452 microcontroller,” in *Advanced Technologies, Systems, and Applications*, pp. 301–310, Springer, 2017.

DEVELOPMENT OF PINGER MAGNETS FOR INDUS-2 ELECTRON STORAGE RING

Prashant Pareek#, Vinod Gaud, Karan Singh, S. Senthil Kumar, T. Veerbhadraiah, Brahmanand Sisodia, K. Sreeramulu and S. N. Singh

Raja Ramanna Centre for Advanced Technology
Indore-452013, INDIA

Abstract

Pinger magnets are used to find important linear and nonlinear dynamic characteristics of the beam by exciting betatron oscillations of the stored beam in horizontal and vertical planes. Two such magnets (a horizontal and a vertical pinger magnet) were developed and installed in Indus-2 (2.5 GeV) electron storage ring. These magnets are required to produce a half sinusoidal magnetic field pulse *of less than* 1μs *duration* with *spa*tial *magnetic field* uniformity better than 2×10^{-3} in the good field region (GFR). This paper discusses the design, simulation, fabrication and pulsed magnetic characterization of these magnets.

INTRODUCTION

The Indus-2 is a synchrotron radiation source of 2.5 GeV energy and 200 mA stored beam current, operating in round the clock mode. Pinger magnets are developed and installed in Indus-2 to probe the linear and nonlinear dynamics of beam. These pulsed dipole magnets are used to excite betatron oscillations. These oscillations are captured turn by turn using BPMs installed over the entire storage ring. The captured data is used to calculate betatron tunes, betatron function, dynamic aperture etc. of the lattice [2]. The major parameters of pinger magnets are given in table 1.

Table 1: Major parameters of pinger magnets.

Parameters	Horizontal Pinger	Vertical Pinger
Beam energy	2.5 GeV	2.5 GeV
Deflection angle	1.5 mrad	2.0 mrad
Peak magnetic field	596 G	650 G
Field uniformity	2×10^{-3}	2×10^{-3}
Good field region	± 10 mm	± 10 mm
Magnetic field pulse width and shape	≤ 1μs (Half sine)	≤ 1μs (Half sine)
Pole gap	56 mm	106 mm
Magnet core length	200 mm	236 mm
Peak Current (I_{peak})	2.7 kA	5.5 kA
Inductance (L)	565 nH	250 nH

ppareek@rrcat.gov.in

MAGNET DESIGN

The first goal of designing these magnets was to achieve the required spatial field uniformity. Along with it was also required to keep the inductance of the magnet and associated leads below a cetratin value so as to be able to get the required field pulse width (< 1μs).

To achieve the above goals, a window shaped geometry with Ni-Zn ferrite core and single turn copper coil was chosen [1]. Schematic cross-sectional view of both the magnets are shown in figure 1.

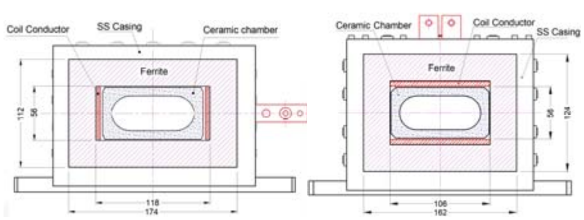

Figure 1: Schematic cross sectional view of horizontal and vertical pinger magnets.

Simulations have been carried out with Opera 3D Elektra solver [3]. Simulated field distribution in horizontal pinger magnet is shown in figure 2.

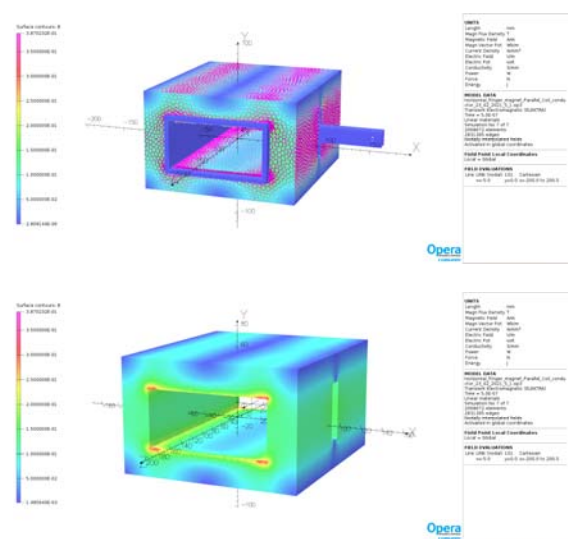

Figure 2: Simulated magnetic field distribution in horizontal pinger magnet.

The electrical conductivity of copper coil is taken in simulation to include the effect of eddy currents on magnetic field uniformity. Coil end terminal's profile is optimized to improve field uniformity and reduce terminal inductance. The obtained simulated field uniformity is better than 2×10^{-3} over the good field region.

MAGNET DEVELOPMENT

The magnet core is fabricated using Ni-Zn ferrite blocks. Ferrite blocks were cut and ground to required dimensions using diamond cutting and grinding wheel. Achieved tolerance on length & width is ± 0.1 mm, flatness and parallelism of the blocks are within 0.01 mm. By assembling these blocks, the pole gap accuracy is achieved within ± 0.02 mm.

The single turn excitation coil is fabricated using ETP copper and insulated with self-adhesive Kapton tape to avoid electrical breakdown (short) between coil & ferrite core. Outer casing of magnet is fabricated from SS 304L.

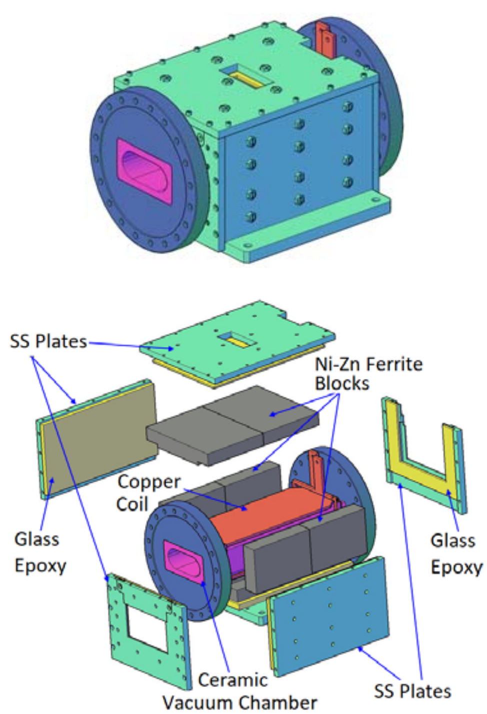

Figure 3: 3D and exploded view of vertical pinger magnet.

The ferrite core and copper coil conductors are precisely assembled into the SS casing around the ceramic vacuum chamber. The inner surface of ceramic vacuum chambers of horizontal and vertical pinger magnets are coated with Ti having average coating thickness 587.4 nm and 690 nm respectively. MACOR spacers are incorporated between coil window and stainless steel end plates to avoid arcing between them. Glass epoxy sheets are incorporated between ferrite core and stainless steel casing. The whole magnet body is isolated from the magnet stand by inserting 8 mm thick Teflon sheet between them. Special Teflon bushes are used for isolating mounting bolts with stand. 3D and exploded view of vertical pinger magnet is shown in figure 3.

PULSED MAGNETIC FIELD MEASUREMENTS

Pulse magnetic field measurements of pinger magnets with and without Ti coated ceramic vacuum chamber were carried out using 14-bit digitizer system and search coils. Two types of search coils namely, point coil and long single turn integrated PCB coil are used for point and integrated field measurements. Measurement setup and pulse wave forms are shown in figure 4 and figure 5.

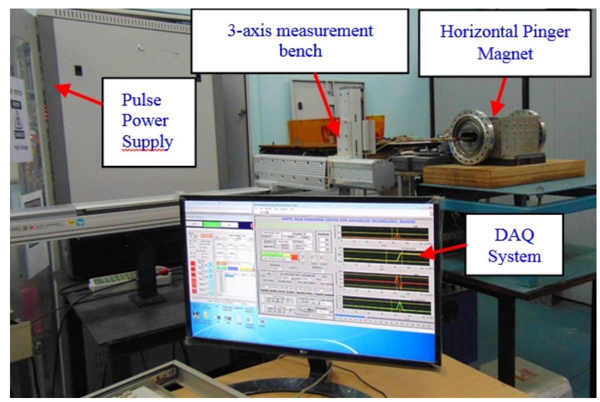

Figure 4: Pulsed magnetic field measurement set-up.

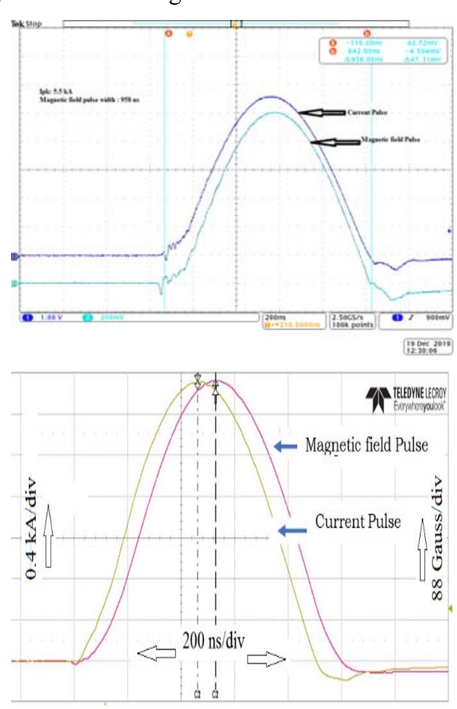

Figure 5: Current and magnetic field waveforms of vertical and horizontal pinger magnets.

The measured field uniformity of the magnets are shown in figure 6 and figure 7. The achieved magnetic field uniformity along pole width and pole gap is better than 2 x 10^{-3} in good field region for both the magnets.

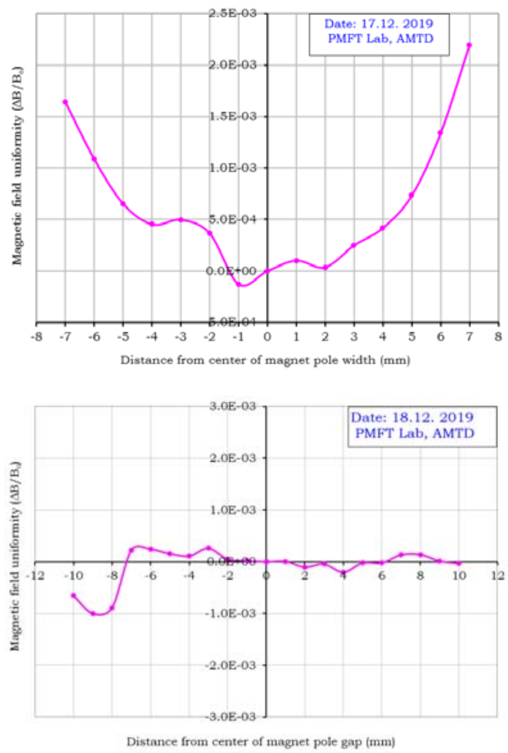

Figure 6: Magnetic field uniformity of vertical pinger magnet along pole width and pole gap.

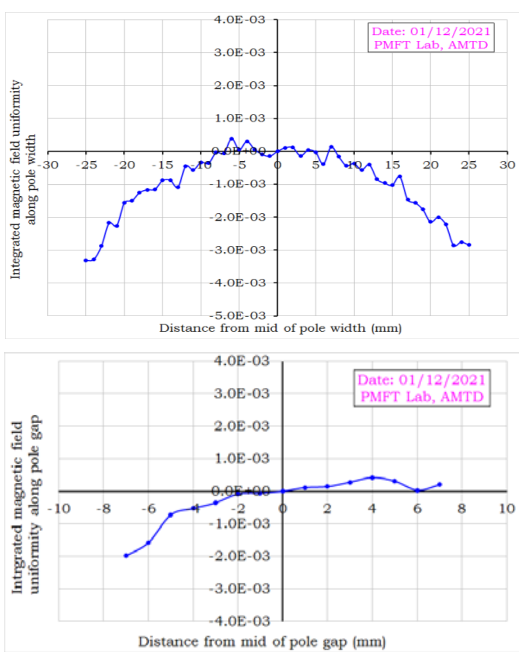

Figure 7: Magnetic field uniformity of horizontal pinger magnet along pole width and pole gap.

The pinger magnets are installed in Indus-2 ring. Photographs of installed pinger magnets are shown in figure 8. The magnets were energized to excite betatron oscillations and turn by turn data of beam using beam position monitors (BPM) were collected from which preliminary information related to the linear beam optics was extracted [2].

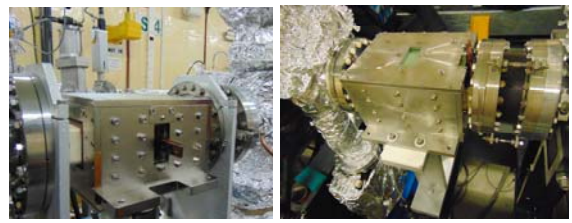

Figure 8: Photograph of installed horizontal and vertical pinger magnets in Indus-2 ring.

CONCLUSION

We were able to meet the required field uniformity of better than 2×10^{-3}. By keeping the magnet inductance low, we could also get magnetic field pulse of less than 1 µs (948 ns & 958 ns). The measured effective magnetic length of horizontal and vertical pinger magnets are 219 mm and 250 mm respectively. The magnets are installed in Indus-2 ring and are being used for beam dynamics experiments.

ACKNOWLEDGMENT

We would like to thank Shri T. A. Puntambekar, Director, Electron Accelerator Group, RRCAT for his motivation during development and installation of pinger magnets. We would also like to thank Shri A.D. Ghodke, Dr. Riyasat Husain, Shri Deepak Kumar Tyagi and Shri Pradeep Kant for scientific and technical discussions. Technical support of Shri Lalchand Ghongde is greatly acknowledged.

REFERENCES

[1] Gangopadhyay Sampa, Pareek Prashant, Singh Yash Pal, Tyagi Deepak Kumar, Vikas, Yadav D.P., Yadav Surendra, Puntambekar T.A. "Pinger Magnet System in Indus-2", RRCAT Newsletter - Issue 1, 2022

[2] Deepak Kumar Tyagi, Riyasat Hussain, Pradeep Kumar and A.D. Ghodke "Analysis of Turn by Turn BPM data at Indus-2 electron storage ring", InPAC-2022, March 22-25, 2022

[3] Opera 3D (Elektra solver), Version 18R2, COBHAM.

PRELIMINARY SIMULATION STUDIES ON CLOSED ORBIT CORRECTION IN HBSRS STORAGE RING

Suraj Prakash*, V. K. Meena and Riyasat Husain
Raja Ramanna Centre for Advanced Technology, Indore, 452013

Abstract

A high brilliance synchrotron radiation source (HBSRS), a 6 GeV and kilometre scale electron storage ring, is proposed at RRCAT, Indore. A preliminary commissioning simulation study of HBSRS storage ring is presented mainly addressing the issues related to closed orbit distortion. Results indicate that the final corrected closed orbit with various sets of alignment and power supply calibration errors can be achieved to meet the performance and design goals of HBSRS.

INTRODUCTION

The baseline magnetic lattice of HBSRS storage ring is designed using hybrid seven-bend achromat concept to achieve 150 picometer-rad (pm rad) beam emittance [1]. Further optimization studies are being carried out to enhance the performance of HBSRS storage ring lattice. In the lattice very strong quadrupoles are employed leading to very large natural chromaticities and require very strong sextupoles for its correction. However, strong sextupoles introduce high non-linearity in the machine, which degrade**s** the dynamic aperture and beam lifetime even in ideal design. In practical HBSRS storage ring, these will be further degraded because of various imperfections in magnets [2, 3]. Even in some cases beam injection and first turn beam circulation will be difficult to achieve [3]. The usual sources of machine imperfection are alignment and multipole errors in a magnet. In presence of strong quadrupoles and sextupoles the lattice becomes more sensitivity to alignment errors compared to third generation light sources (3GLSs). This puts emphasis on the need for realistic modelling of HBSRS storage ring to find limits on tolerable errors and development of efficient beam orbit and optics correction, so that rapid commissioning can be ensured [2, 4].

In this paper we present a preliminary commissioning simulation study and performance results in the form of statistical analysis of data for 200 sets of machine imperfections in HBSRS storage ring. For these studies, we have used a simulated commissioning package [4], which is widely used now a days for all ultra-low emittance storge ring simulated commissioning studies.

ERRORS AND SIMULATION SETUP

The HBSRS storage ring consist of 32 sections or super-periods. A schematic of one super-period is shown in Fig. 1, which shows distribution of optical function, distribution of different magnets, physical aperture, and girders. Some selected parameters of lattice are presented in Table 1. A total of 320 combined function dipole corrector magnets (CMs) which are capable of kicking electron beam in both transverse planes and 320 beam position monitors (BPMs) suitable for turn-by-turn beam position evaluations are assumed for efficient correction. RMS errors in different elements are assigned according to the value as given in Table 2 (taken from [2, 4, 6]), in which each error source follows a Gaussian distribution truncated at $\pm 2\sigma$.

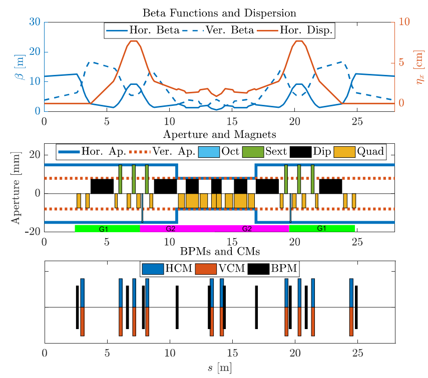

Figure 1: (Top) Distribution of beta and dispersion functions. (Middle) Distribution of different magnets, physical aperture, and girders G1 & G2 within one cell. In the horizontal pane the physical aperture is ± 15 mm except in the middle section where it is ± 8 mm and in the vertical it is ± 8 mm everywhere. (Bottom) Distribution of CMs and BPMs within one cell for trajectory/orbit correction.

Table 1: Selected lattice parameters of HBSRS

Parameter	Value
Natural horizontal emittance ε_x	150 pm rad
Tunes ν_x / ν_y	76.15 / 27.20
Natural chromaticity ξ_x/ξ_y	-109 / -80
Corrected chromaticity ξ_x/ξ_y	+4 / +4
$\beta_{x,y}$ at straight section	12 m, 3 m

Performance of uncorrected HBSRS storage ring lattice: For the realization of effect of alignment and calibration errors in different elements before any correction of trajectory/orbit, particle dynamics studies have been carried out in presence of all errors such as

* sprakash@rrcat.gov.in

misalignments, calibration errors, etc. in the model. This provides a good approach to compare the difficulties with 3GLSs.

Table 2: RMS errors considered in the model

Error Type	rms value	Error type	rms value
Girder Trans. offsets	50 μm	BPM Trans. Offset	100 μm
Girder rolls	100 μrad	CM offset	100 μm
Section Trans. offset	50 μm	CM Cal. Error	5%
Dipole Trans. offset	60-100 μm	BPM Cal. Err.	5%
Quadrupole Trans. offset	60-85 μm	BPM noise (TBT)	25 μm
Sextupole Trans. offset	60 μm	BPM noise (CO)	1 μm
Octupole Trans. offset	80 μm	CM limit	0.5 μrad
Magnet Long. offset	500 μm	Cavity Freq. offset	250 Hz
Roll in Mag., BPM & CM	200-500 μrad	Cavity Volt. offset	0.5 %
Magnet Cal. error	0.05 %	Phase error	90 °

Trans: Transverse, Cal. : Calibration, Mag. : Magnet, Long.: longitudinal TBT: Turn-by-turn, CO: Closed orbit

In this study, all the errors from Table 2 are scaled by the same multiplicative scaling factor; which means an error scaling factor of 1 corresponds to the nominal errors. For each lattice realization, we have calculated the closed orbit existence as shown in Fig. 2, mean of rms closed orbit deviation (COD) and the beta function distortion $\Delta\beta/\beta$ which are shown in Fig. 3 for 200 error realization. These studies are performed in presence of physical aperture in the model.

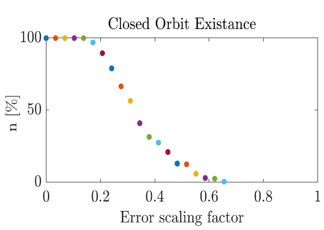

Figure 2: The fraction of lattice realization at which the COD exists.

At about 15 % of the nominal error amplitude, the closed orbit exists in nearly 100 % of the cases and exponentially drops to zero at an error scaling factor of 0.6. The closed orbit existence is calculated with AT findorbit6() function and COD is supposed to exist if this function successfully converged to a solution [4]. The fraction of lattice realization for which COD exist, the mean of rms CODs and mean of rms beta-beat have been calculated. It can be inferred from Fig. 3 that though the deviation of COD is small the beta-beat is very large because of amplitude dependent tune shifts. For the machines like HBSRS storage ring the beta-beat is only allowed up to 4-5%.

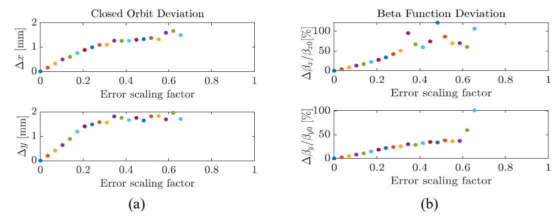

Figure 3: (a) mean of rms of closed orbit deviation and (b) mean of rms beta beat before correction.

SIMULATED COMMISIONING STUDIES

There are two goals of simulated commissioning studies of HBSRS storage ring lattice; (i) validation of lattice design and correction schemes which provides the specification of error tolerance, and (ii) it helps for the preparation of actual machine commissioning [4]. Our motive is to develop an automated trajectory/orbit for a given set which can be applied to a statistically large number of populations of lattice-error realizations. For a given number of populations, the performance of lattice is evaluated by studying the dynamics. The results are presented in terms of cumulative distribution function (CDF). For a large machine like HBSRS storage ring multi-particle and multi-turn tracking takes a considerable amount of time. In order to generate meaningful results for a variety of error assumptions in HBSRS storage ring, a distribution of 100 particles is considered. Since, during the initial commissioning stages we merely want to steer the beam to achieve first turn beam circulation**,** strong sextupole, octupoles and RF cavities are switched OFF because they will introduce orbit dependent multipoles. A bunch distribution of 100 particles having static and random injection errors is injected into HBSRS storage ring and beam loss is observed for 200 set of machine imperfections. From Fig. 4, it can be seen that for 90% of the cases beam gets lost within 5 sections. It necessitates the development of correction schemes to achieve first turn beam circulation and subsequently achieve beam accumulation, and ultimately correct the COD.

First turn trajectory correction (beam threading): It has been described earlier, that the beam is lost within the 5 sections/ super-periods in HBSRS storage ring. Therefore, establishing one turn transmission using a feedback-like iterative trajectory correction approach is the first step in correction chain [4]. We have used a relatively large regularisation parameter α equal to 50 to get the inverse of 1-turn trajectory response matrix and correction is performed. After correction, full beam transmission over one turn in HBSRS storage ring is achieved. The next step is to obtain two-turn transmission. This is achieved by "stitching" the second turn BPM readings to the first turn BPM readings. Initially, only a small number up to 12 BPMs located within two sections is used. Once the beam transmission is established through the full second turn, we included all BPMs in the feedback-like iterative correction algorithm to minimize overall BPM reading. Finally, BPM readings in the first turn are considered to define reference trajectory for the BPM readings in the second turn. We call it multiturn correction. This procedure corrects the machine to a state having period-one orbit and beam circulate to a large number of turns as shown in Fig. 4. At this point, the beam loss is due to tune shift as large chromaticities are not corrected. Therefore, next step is to switch ON the sextupole magnets.

Sextupole ramp: As large natural chromaticities are limiting factor for beam transmission which also degrade the multi-turn BPM readings [4], therefore, turning on the sextupoles are necessary. The sextupoles are ramped up in steps of 1/20 of their nominal strength and previously described multi-turn trajectory feedback is applied to maintain period one orbit. This increases the overall beam transmission significantly (~100 turns) as shown in Fig. 4.

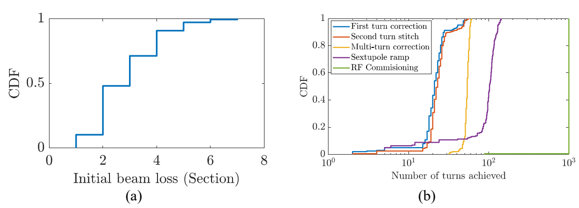

Figure 4: (a) Beam transmission without any correction, (b) beam transmission after various correction steps.

After chromaticity correction, next step in the correction chain is to turn on cavities to restore the electron beam energy. However, at this point of commissioning the storage ring is not in the operation and thus rf frequency and phase of RF cavity should be corrected such that injected beam can be launched longitudinally on the closed orbit. A detail explanation can be found in [2, 4].

Energy and phase correction: The correction routine uses the fact that because of dispersion, turn-by-turn (TBT) variation of energy will result in a TBT variation of horizontal BPM readings. Therefore, difference of average horizontal value of BPM readings of all BPMs between two turns will be a measure of gain or loss of energy of the bunch. For correction, rf phase of cavity is changed in steps within $\pm\pi$ and for each step the BPM readings are evaluated over 30 turns which is small compared to synchrotron tunes ~212 turns. The variation of average horizontal TBT BPM is calculated as a function of rf phase and fitting of a sine function is carried out. Here synchronous phase is calculated by identifying zero crossing of fitted data [4]. For a well corrected rf phase, rf frequency is corrected in a similar way by calculating mean of TBT horizontal BPM variation for 100 turns as a function of a frequency change within ± 1 kHz. Fitting of straight line to the data is carried out and synchronous frequency is calculated by identifying zero crossing of fitted data [4]. The rms phase and rms energy error which were initially 110 ° and 0.52%, respectively are corrected to 1.6° and 0.18 %, respectively. From Fig.4, it can be seen that beam circulates more than 1000 turn after RF correction which indicates that beam accumulation is achieved and beam based alignment (BBA) and COD correction can be performed.

Pseudo BBA: After successfully storing beam a pseudo-BBA is performed which reduces the offsets in BPMs with respect to nearby quadrupole to 50 μm rms in the model. In future iterations of the commissioning simulation, we will include real BBA procedure in detail. The rms closed orbit deviation at this point of correction is 300-450 μm and 200-300 μm in horizontal and vertical plane, respectively and need to be corrected.

Closed Orbit correction: After performing the pseudo-BBA, an orbit response matrix is measured and COD correction is performed. For COD correction the α is initially chosen 40 and orbit correction is performed and for further reduction of rms orbit α is reduced in subsequent correction steps. It is found that in 90% of the lattice error realization, the COD is reduced below 140 μm rms in horizontal and less than 100 μm rms in vertical plane as shown in Fig. 5. Also, CMs strengths are below 400 μrad.

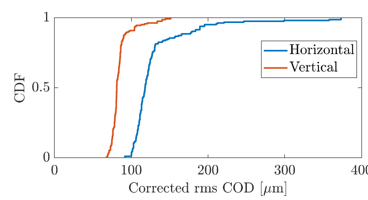

Figure 5: The COD after correction.

CONCLUSION AND FUTURE STUDIES

For 200 sets of machine imperfection**s**, we successfully achieved first turn beam circulation for 100% cases and for 95% of error sets, the simulation code ran successfully. Final corrected rms COD closely meets the machine requirements. In future, further simulation studies for optics and coupling correction will be performed.

REFERENCES

[1] R. Husain, A. D. Ghodke, "Physics design study for proposed high brightness synchrotron radiation source (HBSRS) in India", Proceedings of InPAC, 2019.

[2] V. Sajaev, Physical Review Accelerators and Beams 22, 040102 (2019) and references therein.

[3] V. K. Meena et al., "Alignment tolerances of the quadrupole magnets and closed orbit correction scheme in low emittance storage ring", Proceedings of InPAC, 2019.

[4] T. Hellert et al., Physical Review Accelerators and Beams 22, 100702 (2019) and references therein.

[5] V. K. Meena et al., "Strategy for first turn beam circulation in high brilliance synchrotron radiation source", Proceedings of InPAC 2022.

[6] ESRF-EBS storage ring technical report, 2018.

DEVELOPMENT OF B-H CURVE MEASUREMENT SYSTEM USING ROWLAND RING METHOD

Niraj Chaddha[1,2,*], Siddharth V. Pratihast[1,2], Ankur Agrawal[1], Uttam Bhunia[1,2], V. K. Khare[1], Jayanta Debnath[1,2], Malay Kanti Dey[1,2], Anindya Roy[1], Arup Bandyopadhyay[1,2], Sarbajit Pal[1,2]
[1]Variable Energy Cyclotron Centre, 1/AF Bidhan Nagar, Kolkata - 700064
[2]Homi Bhabha National Institute, Anushaktinagar, Mumbai – 400094

Abstract

The design of an iron-dominated magnet, especially for particle accelerators, beamlines, spectrometer, and other allied areas largely depend on the correlation of the magnetization curve or relative permeability in terms of magnetic flux density (B) and magnetic field strength (H) (B-H or μ_r-H data) of the magnetic steel used. The pole profile of accelerator magnets such as cyclotron main magnet and beam line magnets like dipole magnets, quadrupole magnets, etc. are optimized considering a particular grade of magnetic steel or its B-H curve. However, the B-H property of magnetic steel largely depends on its composition and metallurgical process of heat treatment. Even if one follows a stringent metallurgical process of steel ingot production, it is very difficult to predict its magnetic performance unless measured. Using the wrong B-H data of the ferromagnetic core during magnet design has a huge impact on the design performance of accelerators in terms of field quality. Therefore, it is essential to use measured B-H data to ensure the magnetic performance as desired. The conventional Rowland ring method that employs primary and secondary windings on a toroidal core has been used for B-H curve measurement.

This paper discusses an experimental setup for the characterization of different magnet cores by measuring their magnetization (B-H) curves. Different ferromagnetic materials e.g. ferrite, silicon iron, mild steel, etc. have been used to cross-verify the measured data. During the testing process, a precision current source is used to produce the magnetizing force (H) in the primary coil of a toroidal electromagnet. A Precision Digital Integrator (PDI) is used to measure and record the B-H loop data. One channel of the PDI records the instantaneous current in the primary coil whereas the second channel integrates the time-varying voltage signal, developed across the secondary coil. A detailed calibration method is used to find the relation between the Volt-second (V-s) value and the integrated counts obtained from the PDI. The dimensional parameters of the coil are used to calculate the magnetic field intensity B from the measured V-s value and the magnetizing force H from the instantaneous current in the primary coil. The obtained B-H data will be compared with the standard data used in FEA software like OPERA, ANSYS, etc. for different grades of iron steel commonly used for accelerator magnets. The details of the measurement set-up, the calibration method for V-s calculation, and the measured data will be described in this paper.

INTRODUCTION

The measurement of the B-H curve is a fundamental tool to evaluate ferromagnetic materials and is essential in the design and development of electromagnetic devices. B-H curve analysis also parameterizes the magnetization curve for application in mathematical modelling of transformer cores, eddy current generation and magneto-modulation probes [1, 2].

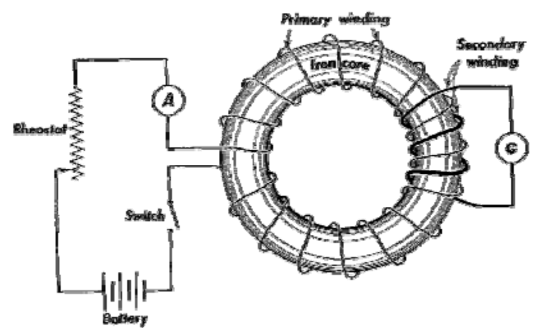

Figure 1: Conventional Rowland Ring Method [4]

A conventional method to obtain a B-H curve uses a Magnetization Curve Tracer [3]. This device portrays the B-H curve on a calibrated screen of a cathode-ray oscilloscope. In this method, the specimen of the material under test is inserted into the bore of the pick-up coil and the magnetizing coil is energized. The induced voltage in the pick-up coil is proportional to the rate of change of the flux density in the specimen. This voltage, with adjusted phase and amplitude, along with the energizing voltage across the magnetizing solenoid is applied to the deflection plates of oscilloscope. By choosing proper amplification factors, the operator can obtain an accurate B-H curve on the oscilloscope screen.

In this paper, we present a system using the Rowland ring method, aiming to enhance the accuracy and reliability of B-H curve measurements. The proposed system has the potential to improve the understanding of the magnetic behaviour of materials, leading to the development of better electromagnetic devices.

* nchaddha@vecc.gov.in

MEASUREMENT SYSTEM

Among the various methods used for measuring the B-H curve, the Rowland ring method [4] stands out for its accuracy and simplicity.

This method (see Fig. 1) involves a toroidal shape magnetic core, known as the Rowland ring, with primary and secondary coils. When a time varying current is applied to the primary coil, it induces a magnetic flux in the core, and in turns induces a voltage across secondary coil. The Magnetizing force H(t) is directly proportional to the current in the primary coil i(t) with number of turns in the primary coil N_p and inversely proportional to mean length of the magnetic path I_m. This mean length can be derived with the help of inner and outer radius r_1 and r_2. The magnetic field B(t) is proportional to the integration of the induced voltage in the secondary coil $v_s(t)$, number of turns in the secondary coil Ns and area of the secondary loop A_s.

$$H(t) = \frac{N_p}{l_m} i(t)$$

$$l_m = \frac{\pi(r_2 - r_1)}{\ln\left(\frac{r_2}{r_1}\right)}$$

$$B(t) = \frac{\varphi}{A_s} = \frac{1}{N_s A_s}\int_0^T v_s(t)dt$$

Hardware

The schematic (see Fig. 2) shows the components and measurement methodology of the system.

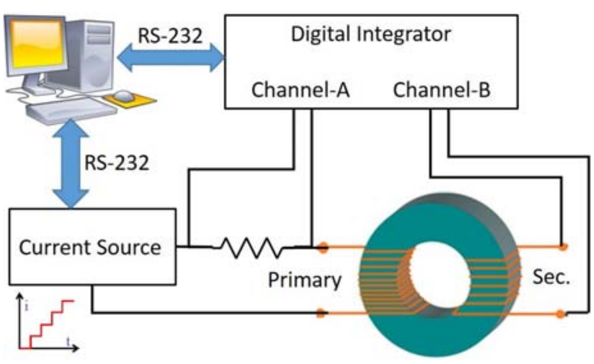

Figure 2: Schematic of the Measurement System

A toroidal ring of Silicon steel with 92 primary turns in one layer and 340 secondary turns in 3 layers have been used for the first set of measurement. Keithley make model 2400 Source Meter has been used to feed current to the primary coil in linear staircase form, ranging from -1A to 1A in various step sizes.

The induced voltage of the secondary coil is typically very small, in order of micro to milli volts, and accurate integration of this voltage signal is crucial for measuring the magnetic flux with high precision. In this regard, a Precision Digital Integrator (see Fig. 3) from Metrolab, (PDI-5025) is used to integrate the induced voltage of the secondary coil.

Another channel of this instrument was used to measure the current in the primary coil by measuring the voltage drop across a series resistor. This instrument offers an accuracy in order of 100 ppm which certainly improves the reliability of the measurements.

A detailed calibration method was followed to convert the cumulated counts of the PDI to integrated voltage (in volt-second). A set of fixed voltages were given to the PDI channels for various integration time at different channel gains. The integrated counts of the PDI are internally adjusted according to the gain of the channel. The analysis has provided a multiplication factor in terms of counts per volt-second.

The Digital Integrator instrument has very low noise though the integration effect makes is substantial to a final error values in 1-2%. To resolve this issue, consequent scans are taken without changing the current in the primary coil. This provides the integrated value of the instrument noise. This volt-second data is then subtracted from the actual scan data to get a result, having error, less than 1% for the final analysis, considering the error in calculating the current through a voltage drop.

Software

A Graphical User Interface (GUI) has been developed for interfacing with the current source and Precision Digital Integrator (see Fig. 3) The software controls the current source and sets the desired current sweep in format of a linear staircase. The Initial and final current values with a step size is given by the user. This information is communicated to the current source to generate the staircase output.

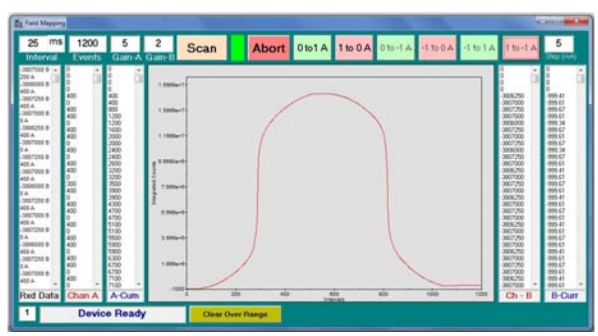

Figure 3: Graphical User Interface

The software communicates with the PDI through serial link to set the integration parameters such as the integration time and gain. The software also monitors the output of the digital integrator to ensure that it remains within the specified range. In case of an overflow condition or a data transmission fault, the software generates an error message and stops the measurement.

The software monitors the current value corresponding to each integration segment. The software initiates the data acquisition process by triggering the current source to generate a current sweep. The integration process starts in synchronisation with it. The software stores the acquired data from two channels with a time stamp and other relevant information like gain of channels, integration time step etc. in a text file. A graph, corresponding to current vs. integrated counts is displayed to have a primary visual verification of the scanned data. The stored data is used for offline analysis to get the B-H curve and other parameters.

RESULT

A toroidal shape silicon iron magnet was taken for the test sample. The maximum current of the sourcing instrument is ±1A and the initial analysis shows that the magnet is not saturating at this current hence another current source with higher capacity is required. A crossover distortion in the region of +50mA to -50mA was observed in the current source, causing a glitch in the induced voltage in the secondary coil. This glitch, many a times, caused the overrange error in the PDI. This problem was taken care by applying a low pass filter at the output of secondary coil, though a detailed analysis will be required to study it's effect on the other parts of the scan.

The final scan of the magnet sample is shown in Fig.4. The plotting of the received data forms a non-symmetric curve. The B-H loop was shifted in the either side of Y-axis. It was later analysed that the scan was starting from zero current and sweeping between -1A to +1A but as the measurement cycle starts with a test scan of the current sweep to estimate the integration time, the magnetism in the coil was not zero for a fresh scan from zero current. It is proposed to start the scan from negative saturation and then sweep up to positive saturation current. The median axis can be obtained by the principle of symmetry. A symmetry correction of the obtained data shows that the measurements obtained using this system are in good agreement with theoretical predictions, indicating that the system is capable of providing accurate measurements of the magnetic properties of materials.

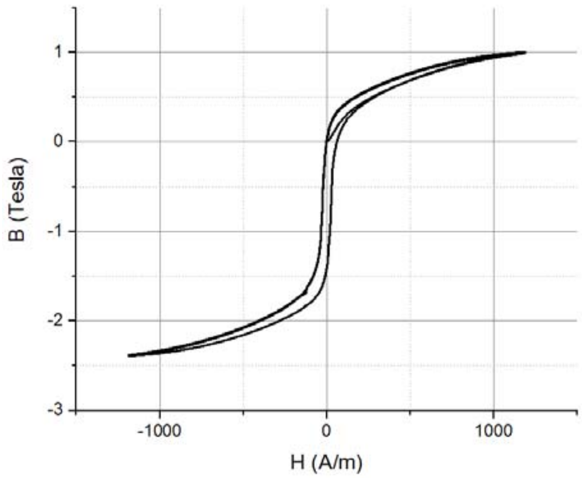

Figure 4: Problem with initial B-H curve

CONCLUSION

The B-H curve measurement system using the Rowland ring method has successfully developed. The experimental results demonstrate that a symmetry correction will produce accurate and reliable results, with a high level of precision and repeatability. Also another instrument with higher current capacity is required to drive the magnet to saturation.

We are planning to perform the measurement on different magnetic materials to study their properties and suitability for the electromagnets for accelerator applications.

REFERENCES

[1] F.C. Trutt, E.A. Erdelyi and R.E. Hopkins, "Representation of the Magnetization Characteristic of DC Machines for Computer Use", IEEE Trans. PAS 87 (1968) 665.

[2] G.F.T. Widger, "Representation of magnetisation curves over extensive range by rational-fraction approximations" Proc. IEE 116 (1969) 156.

[3] B. B Young, "A B-H Curve Tracer", Journal of the Franklin Institute, Volume 254, Issue 1, July 1952, Pages 61-63.

[4] Henry Semat, Robert Katz, "Physics, Chapter 33: Magnetic Properties of Matter", University of Nebraska.

EFFECT OF WEHNELT POTENTIAL ON THE BEAM PARAMETERS OF A 20 KEV STRIP TYPE DC ELECTRON GUN AND ITS INITIAL BEAM TRIALS

Monika Rana[1], Pramod R[2], V. Sriharsha[3], B.K. Sindal[3], Sujata Joshi[3], D.P. Yadav[3]
[1]Accelerator Physics and Synchrotrons Utilisation Division
[2]Industrial Accelerator Division
[3]Ultra High Vacuum Technology Section
Raja Ramanna Centre For Advanced Technology, Indore, India

Abstract

Photon absorbers (crotches) are used to absorb unused heat of synchrotron radiation emitted in a storage ring and their performance is interlocked with machine operation. It is planned to test these crotches in laboratory under vacuum environment using electron beam from an electron gun as an equivalent thermal power source. The physics design of a 20 keV/100 mA thermionic, DC electron gun delivering rectangular beam of power density 11 W/mm^2 at a throw distance of 300 mm for the above work had been reported previously using CST particle studio to test photon absorbers by Monika Rana et al. [1]. In the present work, we report the simulation studies that have been carried out for studying the effects of Wehnelt potential on the beam parameters and subsequent to the fabrication of this gun as per the design specifications, the preliminary results of beam trials in the laboratory with a crotch are summarized.

INTRODUCTION

An electron gun is a current controlled device whose beam current can be controlled by varying the temperature of the cathode. This method of controlling beam current is very sensitive to the heating current of the cathode and hence it is difficult to maintain stable beam current in the temperature dependent region of the electron gun. In order to obtain a stable beam current, the electron gun is converted into a voltage-controlled device by applying negative bias to the Wehnelt. The bias voltage acts as a beam current adjustable shutter that controls the emitted current density from the cathode surface and footprint of the beam size on the crotch surface for a fixed throw distance. The emitted current is finally limited by the geometrical perveance of the gun. To test crotches of different dimensions at a fixed throw distance, beam size needs to be varied which can be done by varying the wehnelt voltage keeping all the other geometrical parameters unchanged. In the beginning, we are planning to test functional performance of crotches of dimensions 3 mm x 60 mm which are to be installed in the vacuum chamber of the dipole magnets using electron beam from 20 keV electron gun. To test these crotches, physics design of 20 keV, thermionic, DC electron gun delivering rectangular beam has already been carried out using CST particle studio [1]. Figure 1 shows the evolved geometry of Wehnelt and anode of the gun. The design parameters of the gun are listed in table 1.

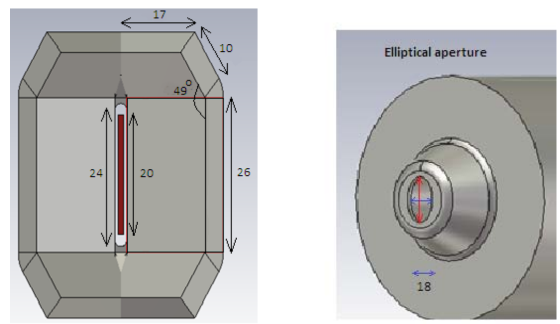

Figure 1: Evolved geometry of Wehnelt and anode [1]

Table 1: Parameters of the gun for testing crotches

Parameters	Values
Type	Thermionic, DC, Triode
Energy	20 keV
Beam Current	100 mA
Geometrical perveance	45.25 nano pervo
Throw distance	300 mm
Beam size at throw distance	3 mm x 60 mm
Cathode to anode distance	18.75 mm

In the present simulation the requirement of bias voltage to the Wehnelt is optimised to vary the beam current from 50 mA to 100 mA from the gun. Further, the effect of bias voltage on the beam sizes in both the planes have been optimised to produce the desired beam size at the throw distance of 300 mm. The gun has been fabricated and preliminary beam trials have been carried out in the laboratory with a crotch. This paper will also report the measured data of beam current variation with the Wehnelt bias voltage. Fabrication details of the electron gun will be reported separately [2].

SIMULATION

In the simulation, a strip thoriated tungsten of dimension 1 mm x 20 mm is used as an emitting surface

[3]. The gun is designed to deliver rectangular beam of size 2.5±0.5 x 55±5 mm at 300 mm from the cathode at 100 mA with negative bias to the Wehnelt, where crotch is to be placed for testing. It is a triode gun which delivers 130 mA beam current without bias when operated in space charge region. The effect of bias on emitted current and beam sizes in both the planes is carried out using CST particle studio (PS). It is a three-dimensional code to analyze charged particle dynamics in 3D electromagnetic fields and is extensively used for parametric analysis of the gun designs. Parameter sweep dialog has been used which offers an efficient way to perform several simulations with different structure parameter values. For each simulation, previously specified results are stored. Then template based post-processing is used to visualize all calculated and monitored results [4].

Beam current control

Non-relativistic electron beams are inherently defocusing in nature, hence, a focusing electrode (Wehnelt) with negative potential relative to the cathode is placed in front of the cathode in the beam direction to focus and control the electron beam. With increasing negative bias, the beam current decreases due to reduction in space charge forces in the beam. A more negative voltage on the wehnelt will repel more of the electrons emitted from the cathode, so fewer get through to anode, reducing the beam current [5].

Figure 2 shows the variation of beam current with increasing negative bias voltage as simulated using CST-PS.

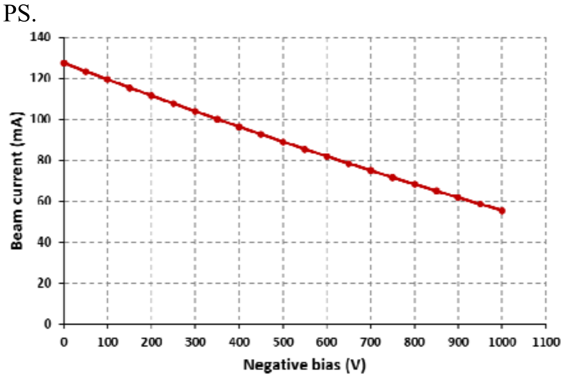

Figure 2: Effect of negative bias on beam current.

Beam size control

With increasing negative bias, the space charge forces decrease which results in reduction in beam size in both horizontal and vertical planes. Hence, the Wehnelt acts as a convergent electrostatic lens. However, since the beam size in horizontal plane is very small, it starts increasing with negative bias after attaining beam waist. This is because, at higher negative bias, longitudinal electric field in the gun decreases. In the optimized geometry, beam waist of the beam shifts toward anode with rising negative potential at the fixed throw distance. This results in increase in beam size with rising negative potential.

The variation in horizontal and vertical beam size with bias at a location of 300 mm from the cathode is shown figure 3 and 4 respectively.

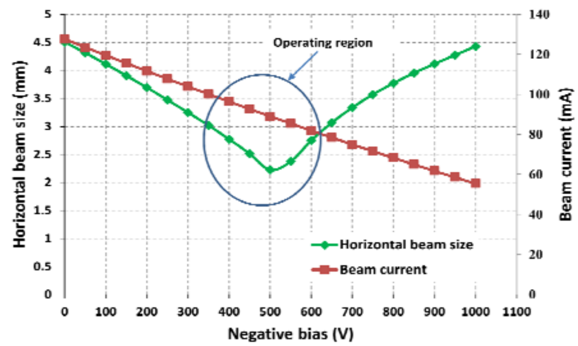

Figure 3: Effect of bias on horizontal beam size.

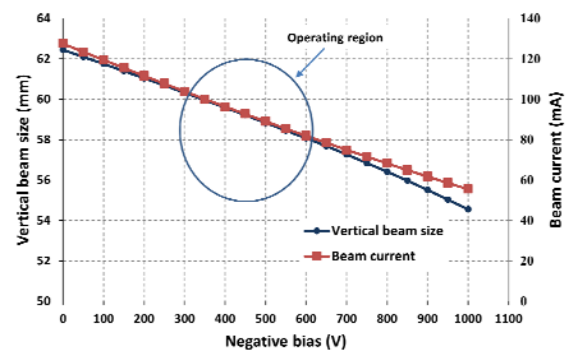

Figure 4: Effect of bias on vertical beam size.

MEASUREMENTS

The evolved geometry of anode and wehnelt of the gun have been fabricated within 20 µm tolerance as shown in figure 5. The beam current from the gun is sensitive to the position accuracy between cathode and anode. The components of the guns are assembled within ±100 µm of positional accuracy with the help of rotary indexing head and dial gauge. Packing shim was placed to maintain flatness and distance between anode plate and cathode and measured with Vernier depth gauge. The entire gun test setup has been installed in a suitable radiation shielded hutch made of lead.

Figure 6 shows the photograph of experimental set-up of electron gun in the hutch. The functional performance (estimation of sagging at high temperature) of 20 mm/0.7 mm diameter pure tungsten used as cathode has been studied separately in an independent set-up at 10^{-6}-10^{-7} mbar. The cathode is heated using a DC power supply which is floated at -20 kV using 50 kV isolation transformer. The vacuum in the set-up is maintained in the range 10^{-6}-10^{-7} mbar using turbo molecular pump and a Sputter ion pump. The initial beam trial is carried out at 20 kV acceleration with full negative bias voltage and maximum heating current so as to get few mA beam currents from the gun in the beginning. Gradually, bias is reduced to increase the beam current from the gun for conditioning. The beam current from the gun is measured on the crotch by electrically isolating it from rest of the assembly.

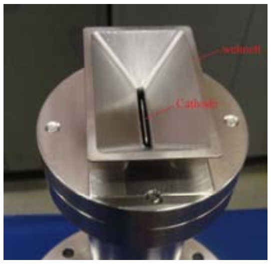

(a)

(b)

Figure 5: Photograph of fabricated (a) Wehnelt and cathode, (b) anode plate with elliptical aperture.

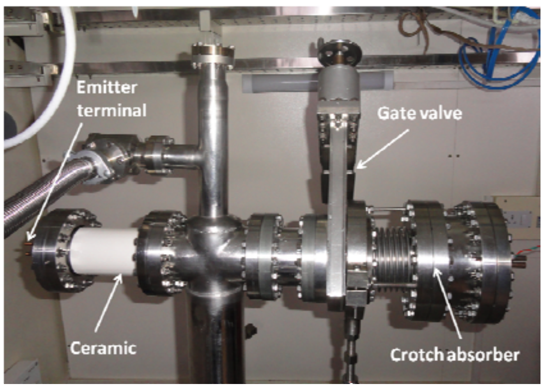

Figure 6: Photograph of the mechanical assembly of the electron gun for testing crotches.

At cathode heating power of 225 W and Wehnelt voltage of -100 V, beam current of 100 mA is measured on the water-cooled crotch. At the rated beam power of 2 kW, the radiation survey is carried, radiation level was found close to background level inside as well as outside the hutch. Figure 6 shows the plot of variation in beam current with accelerating voltage for with bias voltages 50V and -100 V.

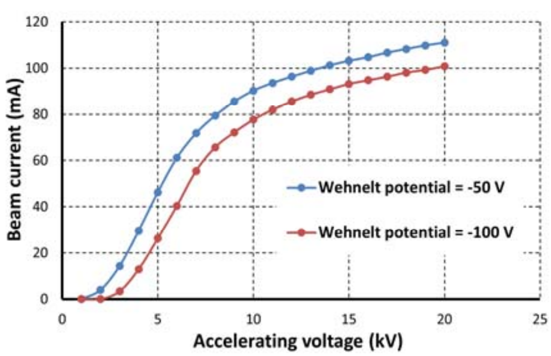

Figure 6: Variation in beam current with accelerating voltage for wehnelt voltage of -50 V and -100 V.

CONCLUSION

A 20 KeV/100 mA triode electron gun has been designed and developed. Initial beam trials have been carried using water cooled crotch in the laboratory at the rated power. We have observed the footprint of electron beam on the crotch which is placed at a distance 300 mm from the gun.

ACKNOWLEDGEMENT

We would like to express our sincere gratitude to Dr. Tapas Ganguli for his keen interest, expert comments and valuable suggestions in writing this paper. We would like to acknowledge Shri Manish Kumar Singh and Shri Deepak Mishra for useful discussions in overcoming issues faced in CST simulations. We would like to thank colleagues of Ultra High Vacuum Technology Section for their support.

REFERENCES

[1] Monika Rana, Pramod R, A.D. Ghodke, B.K. Sindal, Sujata Joshi and D.P. Yadav, "Simulation of a 20 keV/100 mA Strip Electron Gun for Testing Photon Absorbers", in Proc. Indian Particle Accelerator Conf. (InPAC), VECC, March 2022.

[2] V. Sriharsha*, B. K. Sindal, Vijay Singh Bais, Pramod R, Monika R, Utpal Chaterji, B. N. Sisodia, Vishnu Pandey, Sujata Joshi, D. P. Yadav, Purushottam Shrivastava, "Development of a 20 keV, 2 kW DC strip type electron gun system for testing photon absorber of indus-2 SRS", in Proc. Indian Particle Accelerator Conf. (InPAC), BARC, March 2023.

[3] S.V. Venkateswaran, R. Pramod and S.C. Bapna, "Development of 151x5 mm^2 strip electron gun to test for Indus-2", in Proc. Indian Particle Accelerator Conf. (InPAC), 2003.

[4] CST Particle Studio, "Workflow & Solver Overview", 2017.

[5] M.Hoseinzade, A.Sadighzadeh, "Design and numerical simulation of thermionic electron gun", arXiv preprint arXiv: 1509.06363, 2015.

UPGRADATION, MODIFICATION & TESTING OF HIGH D.C. CURRENT POWER SUPPLIES USED FOR MAIN FOCUS AND BUNCHER FOCUS COILS OF 7MeV ELECTRON LINAC USED FOR PULSE RADIOLYSIS EXPERIMENTS AT RPCD, BARC

Sunil J Shinde*[1], Madhu A Toley[1], B B Chaudhari[1], Veeresh K Nayak[1]

[1]*Radiation & Photochemistry Division, Bhabha Atomic Research Centre, Mumbai, India- 400085*

Abstract

Nanosecond 7MeV Electron LINAC [1,2] was procured in 1986 from Radiation Dynamics Ltd., UK for carrying out experiments in Radiation Chemistry [2]. It was commissioned .in 1986 at Mod.labs. BARC. Since then, it has been working however due to aging of components, modifications were done as per the required specifications. It is being upgraded for better dose stability and pulse to pulse electron beam energy stability. In this accelerator, the RF waves tend to defocus the beam and this effect is counteracted by strong solenoid focusing fields generated when 200 Amp DC Current flows through Buncher focus coil and Main focus coil. Therefore, very stable high current DC power supply is required for pulse-to-pulse electron beam energy and dose stability in single shot mode operation and also in repetitive mode operation of the electron LINAC. Thus, power supplies have been upgraded with Constant Current SMPS based programmable high current DC Power Supply.

New programmable DC Power Supply having input voltage three phase, 50 Hz and Output 0-15 V DC & Output Current 0-400 A DC is installed, commissioned and tested successfully with the Accelerator. All necessary modifications needed to incorporate the new Power Supply were carried out and interlocks in the system were restored properly. Earlier version of these Power Supplies were based on conventional transformer and thyristor circuits.

This paper discusses the power supplies up gradation for focus coils, interlocks incorporation for safe and stable operation, and the performance result i.e., reduction in noise, energy stability, current regulation and efficiency.

INTRODUCTION

In this Linear Electron Accelerator [1,2], electrons emitted from an electron gun are initially focused by a gap lens into a deflection chamber and via another gap lens into the accelerating waveguide. These electrons are accelerated to an energy of 7 MeV by an axial field associated with an electro-magnetic wave travelling down a disc loaded circular waveguide (corrugated waveguide). The acceleration takes place in a high order of vacuum. The accelerating field is obtained from radio-frequency power produced by a magnetron which is operated in short pulses supplied to it by modulator. The RF waves tend to defocus the beam and this effect is counter acted by strong solenoid focusing fields. Two solenoids focusing coils, one 20 cm long Buncher coil and the other 130 cm long Main Focus coil are fitted directly around the vacuum envelope. The coils are wound with rectangular section tube, internally water-cooled, and are of the low voltage high current type. The electron beam accelerated in the waveguide require focussing to get a sharp beam at the exit window.

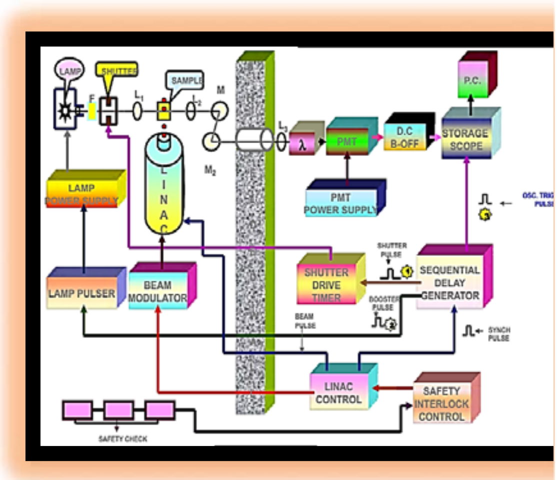

Figure 1: Pulse Radiolysis Facility using Electron LINAC

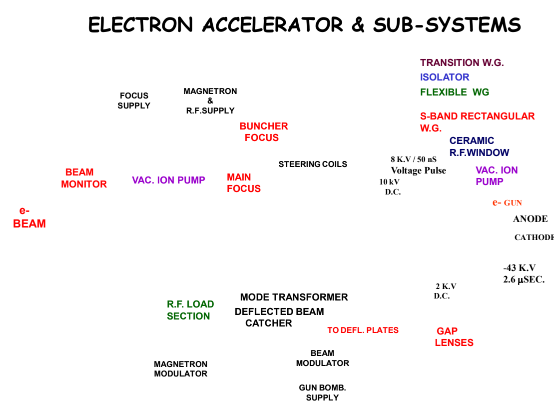

Figure: 2 Electron Accelerator & Sub-systems

Table 1: Specifications of Electron Linear Accelerator

	Parameter	Description
1.	Output Beam	Electron
2.	Electron energy	7 MeV
3.	Energy spread	± 0.4 MeV
4.	Pulse Width (nsec)	Peak current (mA)

**sjsindia@barc.gov.in*

	25, 50, 100, 200, 500, 2000	900, 400, 200, 150, 90, 70
5.	Pulse repetition Rate	1)12.5 -50pps; in steps of 12.5pps, 2) Single shot
6.	Beam diameter	3mm at exit window
7.	Magnetron	RF Frequency: 2998MHz RF power: 2 MW Peak, 2 KW avg
8.	Focus coil current	Buncher: 200 A, Main: 200 A
9.	Vacuum	10^{-7} torr

The focus cubicle supplies very stable high DC Current to both Main Focus coil and Buncher Focus coil. These coils require 200 Amp. DC current from closed loop Constant current switched mode power supply. Previously old Power Supply employed a transformer, rectifier, LC filter (big size components) and a phase angle thyristor controller bridge circuit. Due to aging of components, frequently maintenance of the Focus Power Supply units had to be carried out. Then also, variation in the load current was observed due to which getting dose stability was difficult. To overcome this problem, New Power Supply units for Buncher and Main Focus coil were procured, tested and commissioned successfully, all machine interlocks were retained for safety of the accelerator machine.

Figure 3: New Focus Power Supply Units

Figure 4: Rear Side of New Power Supply

Features of the new Switched mode DC Constant current Power Supply units are as follows: -

Designed for long life at full power, Protected against all overload and short circuit Conditions, Excellent dynamic response to load changes, 0-5V analogue programming, voltage and current monitor, voltage sensing, 10 turn pots for voltage and current, parallel and series operation, rack mountable, pre-set voltage and current, Interlock with electron LINAC.

Figure 5: Connection of Focus Coils in Machine

To maintain interlock of the machine with this new Power Supply units, additional circuit with Relay contacts are used in series with other machine interlocks like Mains supply, Water, Vacuum, Air (Dry iolar Nitrogen gas pressure), Time Delay, all in series for safe operation of the Accelerator. New Focus Power Supply units with interlocks were tested with machine ON and found to be working satisfactorily. At load of, 200 Amp. DC current flowing through focussing coils, regulation, stability, and ripple were measured. Finally, dose delivered by the machine was measured and found to be very stable compared with dose variation [3] existed when old power supplies were used for focusing coils.

Table 2: Specifications of New High DC Current Power Supplies for Focussing Coils

S. No.	Parameter	Description
1.	Input Voltage	Three Phase, 380-480 V AC, 50 Hz
2.	Output Voltage	0 – 15 V DC
3.	Output Current	0 – 400 A DC
4.	Output Power	6000 Watt
5.	Active power factor correction PF	0.98 (at 100% load)
6.	Analog programmable	0-5 V (on both voltage and current)
7.	Efficiency	85% or better at full load
8.	Load Regulation	CV: ≤2.5 mV, CC: ≤24 mA
9.	Line Regulation	CV: ≤0.5 mV, CC: ≤4 mA
10.	Ripple & noise	CV: ≤1 mV rms CC: ≤ 100 mA rms
11.	Temp. Coeff. Per °C	CV: ≤40 ppm, CC: ≤60 ppm
12.	Output voltage & current stability	CV: ≤50 ppm, CC: ≤100 ppm
13.	Programming speed	≤ 3.5 ms (10 -90%) of voltage at full load

14.	Input output Insulation	3600 Vrms
15.	Meter Scale	3.5 digit
16.	di/dt of load step	5 A/µS
17.	Recovery time 50-100% load step	< = 130 µs
18.	Max. deviation	< = 340 mV
19.	Indicators	Voltage meter, Ampere meter, AC-Fail, DC-Fail, Over Temperature, Remote – Shutdown, Remote-CV, Remote-CC, Output On, CV-limit, CC-limit, CV- and CC- mode
20.	Remote Monitoring	Digital Panel Meters to remotely monitor output Voltage and Current
21.	Cooling	Low noise blower, fan speed adapts to temperature of internal heat sink.
22.	Operation	Series & Parallel with Master slave
23.	Protection	Overload, Short Circuit, Over Temperature, Phase loss
24.	Operating temperature	-20 to + 50ºC

When old Power Supplies were used for Focus coils and if current value is set to 170 Amp., actual currents flowing through coils were varying from 161 Amp. to 179 Amp. over the period of ten hours of machine operation. Also, maintenance of old circuit, discrete components was time consuming affecting badly machine ON time. Now when new power supplies are used for Focus coils, if current is set to 170 Amp., it will remain same i.e., 170 Amp. for continuous 10 hours of machine ON operation without any problem.

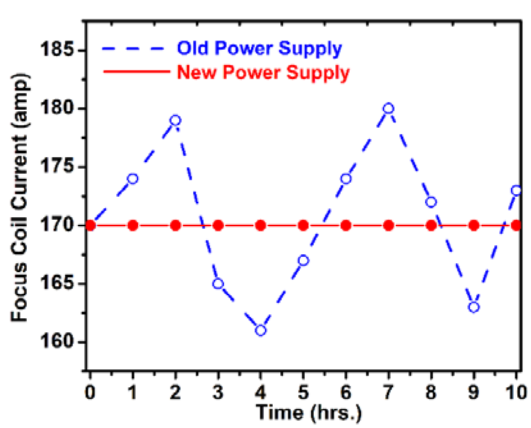

Figure 6: Current variation vs time

CONCLUSION

New Constant Current DC Power Supplies for Buncher Focus Coil and Main Focus Coil in LINAC were procured as old Power supplies were not functioning properly. New Power supplies were installed, tested and commissioned successfully in LINAC machine retaining all machine interlocks for safe operation of LINAC machine. Performance of the machine is improved; dose is also constant. New Power supplies are giving maintenance free service and working satisfactorily in the last five years.

REFERENCES

[1] The RADIATION DYNAMICS SUPER X Linear Accelerator for PULSE RADIOLYSIS. (Technical Information Manual)

[2] M.C. Rath, V. Gawandi, T. K. Ghanty, H. Mohan and T. Mukherjee " Pulse radiolytic reduction studies of 1,4,4a,8a-tetrahydro-1,4-methano-naphtha-5,8-dione (HMND): effect of tertiary structure.", *RAes. Chem. Intermed., 30, 2004, 579-593.*, [2004]

[3]M.A.Toley, S.J.Shinde, B.B.Chaudhari and S.K. Sarkar " Electron Energy Device For LINAC based Pulse Radiolysis Facility of RPCD" BARC Report External, BARC/2015/E/009

DEVELOPMENT OF BEAM POSITION BASED INTERLOCK SYSTEM FOR INDUS-2

R. Jain*, A. C. Holikatti, S. Yadav, L.K. Babbar, B. B. Sonawane, P. Fatnani, T. A. Puntambekar
Beam Diagnostics Section / Beam Diagnostics & Coolant Systems Division
Raja Ramanna Centre for Advanced Technology, Indore - 452 013, India
* email: rahuljain@rrcat.gov.in

Abstract

Indus-2 operates at 2.5 GeV and current up to 200 mA with three Insertion Devices (IDs) namely U1, U2 and U3 to get high intensity photon beam. This high intense photon beam can cause thermal damage to vacuum chamber, if electron beam orbit is deviated from its normal orbit due to any subsystem of machine or parameter of it, is misbehaving. For the safety of vacuum chamber, an interlock system has been developed and deployed in Indus-2. Beam Position Indicators (ID-BPIs) are installed at the entry and exit of each IDs to measure the beam positions in the vacuum chamber. The ID-BPIs generate 'beam cross-over' signals when the beam crosses the safe beam position limits. The cross-over signals are used as inputs to the interlock system to trip the RF stations of Indus-2 and consequently dumps the beam. The development and deployment of the interlock system is presented in this paper.

INTRODUCTION

Indus-2 (2.5 GeV, 200 mA) is a Synchrotron Radiation Source (SRS) at RRCAT, Indore. Three Insertion Devices (IDs) have been installed in Indus-2 ring to have high intensity Synchrotron Radiation (SR) beam. The first two are planer undulators, namely U1, U2 and third one is Advanced Planer Polarized Light Emitter (APPLE) also called as U3. Normally the electron beam in Indus-2 revolves closely around the user orbit, and the SR produced in the IDs passes through the vacuum chamber without any obstruction. Any deviation of the electron beam due to variations in magnet power supplies, phase change of RF system or any other subsystem of machine or parameters of it, are misbehaving, may cause the SR beam to hit the vacuum chamber. This direct interaction of the SR beam from IDs with the vacuum chamber results in the excessive spot heating, which may damage the chamber walls. For the safety of ID vacuum chamber, a beam position based interlock system has been developed and deployed in Indus-2. Beam Position Indicators (ID-BPIs) [1] are installed at the entry and exit of each ID to measure the beam positions in the vacuum chamber. The ID-BPIs in Indus-2 are four-button electrode type and based on the principle of electrostatic pick-ups. The scheme of beam position measurement in Indus-2 is shown in figure 1. As shown in the figure, beam position measurement electronics [2] unit takes four beam pickup signals of a ID-BPI as inputs and process them to calculate beam positions. The beam positions are calculated using difference over sum method (refer equation 1).

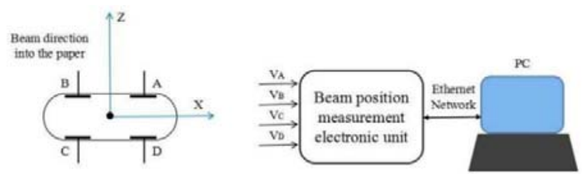

Figure 1. Indus-2 beam position measurement scheme

$$X = K_X\left[\frac{(V_A+V_D)-(V_B+V_C)}{\Sigma}\right]$$
$$Z = K_Z\left[\frac{(V_A+V_B)-(V_C+V_D)}{\Sigma}\right] \qquad (1)$$

Where:
V_A, V_B, V_C and V_D are the four pick up signals.
$\Sigma = V_A+V_B+V_C+V_D$ is beam intensity/sum signal
K_X and K_Z are proportional constants in X and Z planes respectively.

Each ID-BPI electronics has been embedded with a server and provide beam position data over a TCP/IP network connected to control room PC. In addition, these ID-BPIs also generate 'beam cross-over' signals when the beam crosses the safe beam position limits. The limits are set in the digital beam position measurement electronics of ID-BPIs.

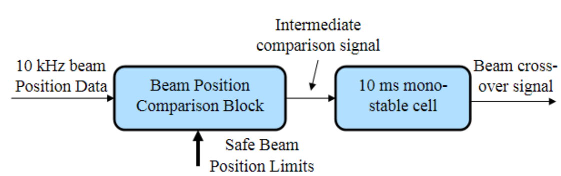

Figure 2. Cross-over signal generation

The cross-over signals are used as inputs to the interlock system which generate an interlock signal to dump the beam through RF. A schematic diagram of cross-over signal generation is shown in figure 2.

SYSTEM DESCRIPTION

The developed interlock system is modular. For each ID, an interlock module has been developed which takes in the beam cross-over signals from the ID-BPIs and status signal of the position of jaws of the corresponding ID. When the jaws of an ID are moved inwards for high intensity SR based experiments, a 'jaws close status' signal is asserted and the corresponding interlock module gets enabled. In this condition, if the 'beam cross over' is detected in the associated ID interlock module, an 'ID-BPI interlock' signal is generated. The interlock signal is opto-isolated open collector type signal.

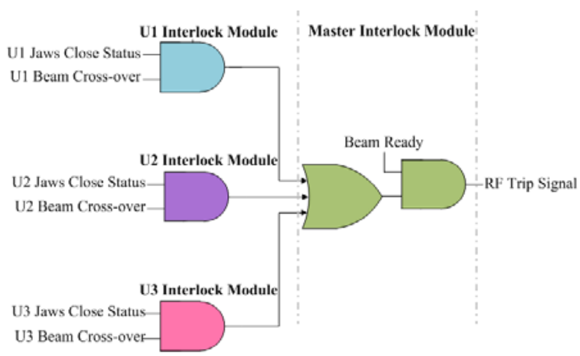

Figure 3: Logic diagram of beam position based interlock system

For each ID, there is a dedicated interlock module. A separate master interlock module, takes in the 'ID-BPI interlock' signals of each ID and qualifies them with the 'beam ready' (beam at 2.5 GeV and available for user) status signal. When the interlock conditions are met, an 'RF trip signal' is generated from the master interlock module to dump the beam immediately. A logic diagram of the beam position based interlock system is shown in figure 3 and its truth table is given in table 1. The status of interlock signals from all the interlock modules are provided for logging of the events on the Indus server. The interlock system sends RF trip signal in less than 300 μs to the RF system to dump the beam.

Table 1: Truth table of the Interlock System

Beam Ready	U1/U2/U3 Jaw Close Status	Any of ID-BPIs Beam Cross-over	RF Trip Interlock
0	X	X	0
1	0	X	0
1	1	0	0
1	1	1	1

A detailed system block diagram of beam position based interlock system for Indus-2 is shown in figure 4.

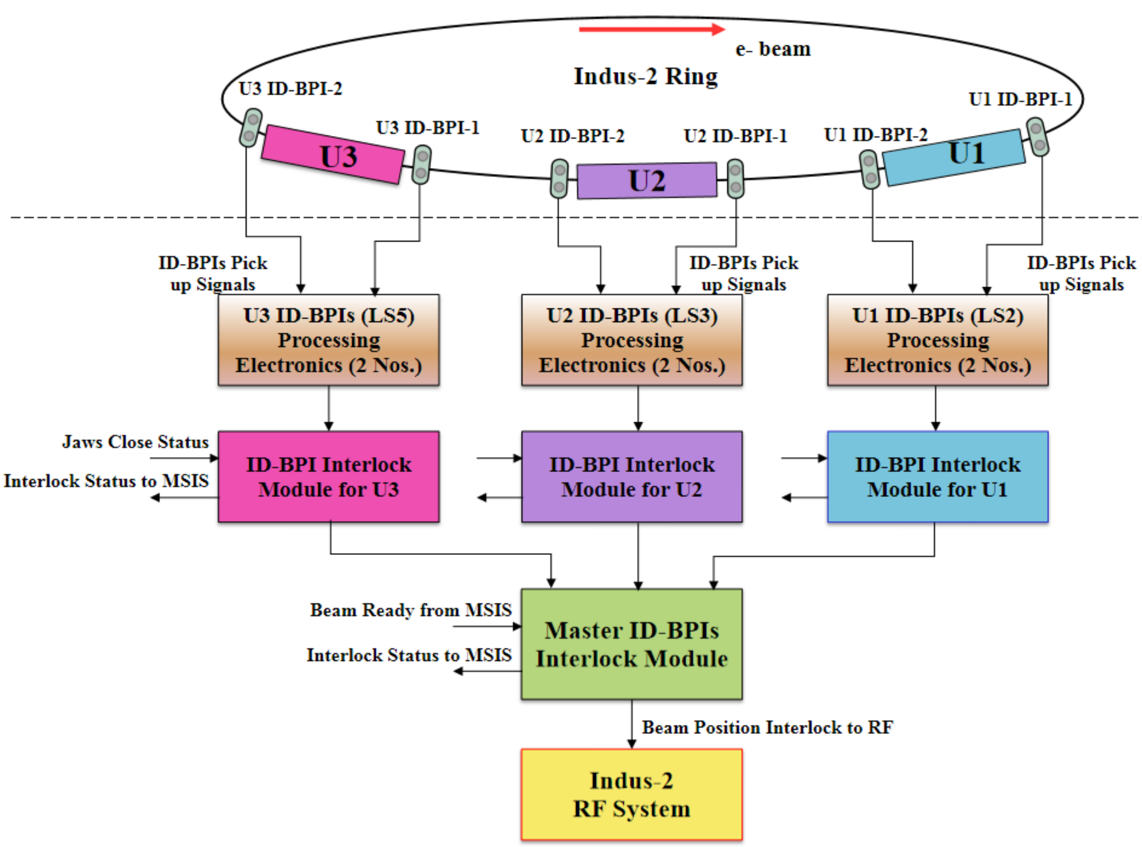

Figure 4: Block diagram of beam position based interlock system for Indus-2

As shown in the figure, the beam position measurement electronics of ID-BPIs at both sides of an ID, monitor the beam positions and generate 'beam cross-over' signals when the beam crosses the safe beam position limits.

FIELD TESTING AND RESULTS

The beam position based interlock system has been developed and deployed in Indus-2. The 6 nos. of ID-BPI electronics, developed interlock modules corresponding to each ID and a master interlock module have been installed at the equipment gallery of Indus-2. The required no. of cables to transport RF and digital signals have been laid and tested.

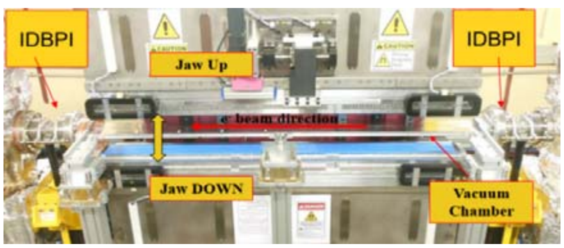

Figure 5: Photograph of installed Undulator U3 and its ID-BPIs

A photograph of installed U3 ID-BPIs in Indus-2 ring is shown in figure 5. In figure 6, a photograph of equipment rack where U3 ID-BPI electronics and its interlock module are installed, is shown.

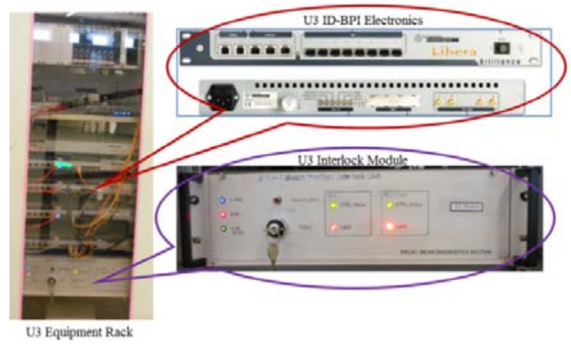

Figure 6: Photograph of equipment rack where ID-BPI electronics and U3 interlock module is installed

An application program has been developed on MATLAB platform which configures the electronics of all the six ID-BPIs over TCP/IP interface and sets the safe beam position limits. The software acquires and displays the real time beam positions of ID-BPIs along with set beam position limits on the developed GUI. The available margin of the real time beam positions to the set position limits are also displayed on the GUI. The set margins on the user beam orbit is ±1000 micron in X-plane and ±200 micron in Z-plane. A screenshot of the GUI to acquire ID-BPI beam position data is shown in figure 7. As shown in the figure, the GUI displays beam position margins to the set beam position limits quantitatively and graphically both.

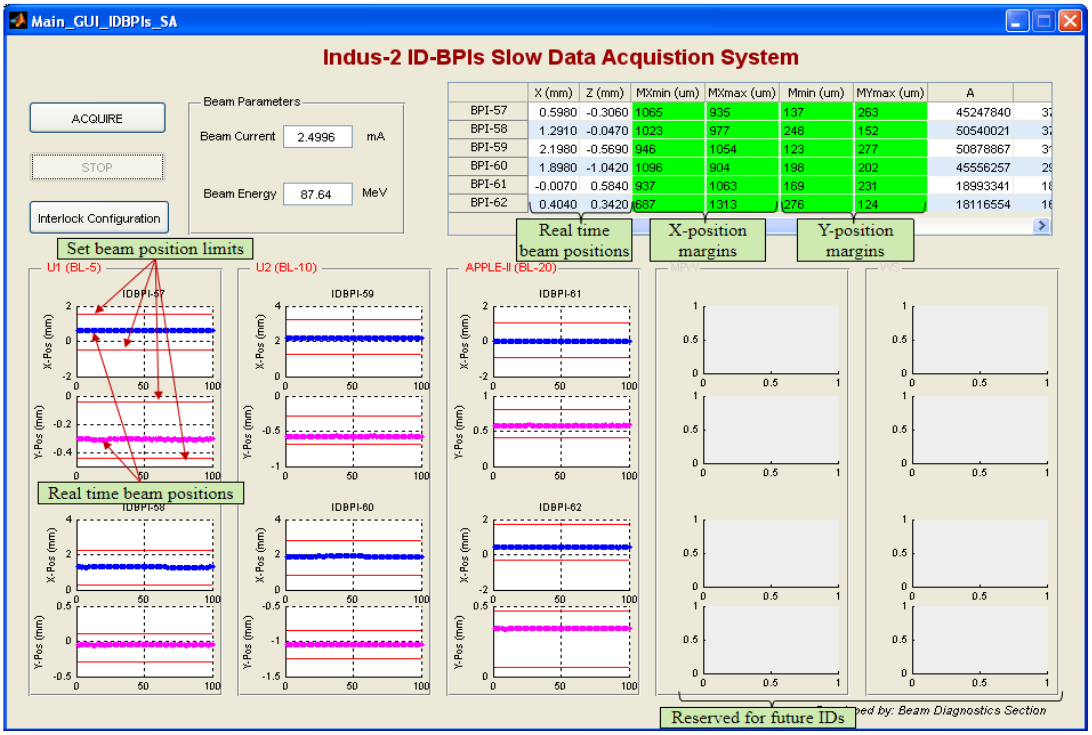

Figure 7: Screenshot of GUI to acquire ID-BPI beam position data

A GUI pop-up window to configure the safe beam position limits is shown in figure 8.

Figure 8: Screenshot of GUI window to configure the safe beam position limits in the ID-BPI electronics

For the qualification of the interlock system, low beam current (~ 20 mA) is filled in Indus-2 at injection energy and all the ID-BPIs are set with the appropriate margin. The jaws of an undulator are moved inwards and strength of an upstream steering magnet is varied to shift the beam position intentionally. As soon as the beam crosses the safe beam position limits, a beam killing event is observed as shown in figure 9. The procedure is repeated for each undulator to qualify the corresponding ID-BPI electronics and the interlock module.

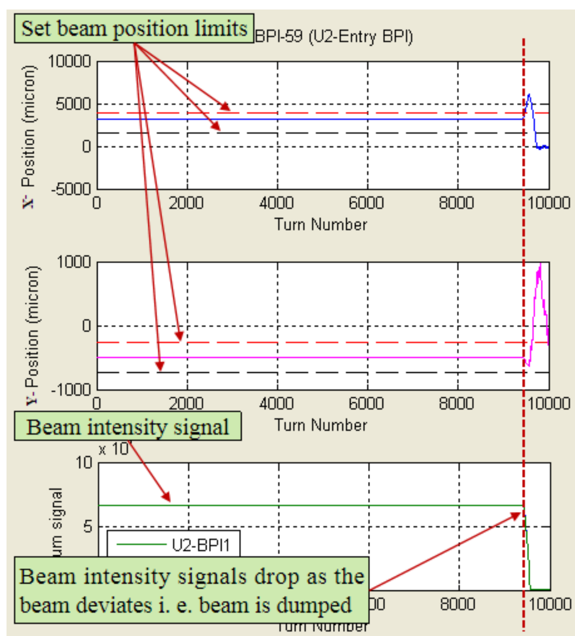

Figure 9: Screenshot showing beam killing event as the beam crosses the safe beam position limits

There is a Machine Safety Interlock System (MSIS) panel in the main control room, on which the interlock event is latched, as shown in figure 10. The event is cleared remotely by the shift crew for the fresh beam filling in Indus-2. In addition, the status of interlock signals from all the interlock modules of the system are provided for logging of the events on the Indus server.

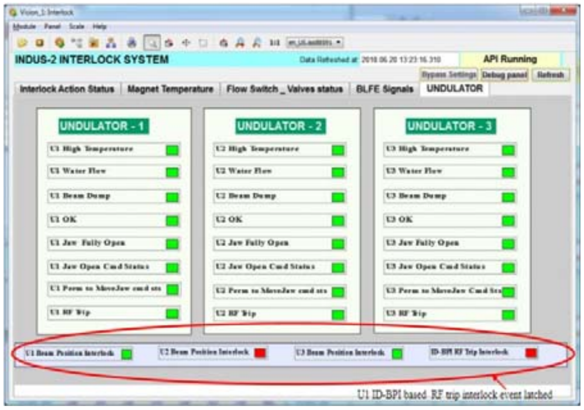

Figure 10: Screenshot showing U2 ID-BPI interlock event (GUI developed by ACSD)

CONCLUSION

In this paper, development and deployment of the beam position based interlock system for Indus-2 has been presented. The developed interlock system sends the interlock signal in less than 300 µs to the RF system to dump the beam if the beam position crosses the safe limits. The status of interlock signals from all the interlock modules are logged on the Indus server. The developed system also has the scalability to accommodate the two future IDs in Indus-2

ACKNOWLEDGMENTS

The authors would like to thank Shri V. S. Yadav for his support in assembly, installation and testing of the interlock modules. Authors are also thankful to Shri Narendra Kumar (RFSD) and Shri A. M. Gupta (ACSD), RRCAT for their involvement during the beam experiments.

REFERENCES

[1] Babbar L.K., Kumar Mukesh, Yadav D.P., Upadhyaya B.N., Sridhar R., Puntambaker T.A., “Mechanical design, development, and installation of ultra high vacuum compatible beam position indicators for insertion devices in Indus-2”, DAE-BRNS Indian particle accelerator conference; Mumbai (India), 21-24 Dec 2015

[2] https://www.i-tech.si/products/libera-brilliance-3/

DEVELOPMENT OF A 20 keV, 2 kW DC STRIP TYPE ELECTRON GUN SYSTEM FOR TESTING PHOTON ABSORBER OF INDUS-2 SRS

V. Sriharsha*, B. K. Sindal, Vijay Singh Bais, Pramod R, Monika R, Utpal Chaterji, B. N. Sisodia, Vishnu Pandey, Sujata Joshi, D. P. Yadav, Purushottam Shrivastava#, RRCAT, India.

Abstract

A 20 keV, 2 kW DC triode thermionic emission strip type electron gun is designed with tungsten cathode of size dia. 0.7 mm x length 20 mm, producing strip electron beam foot print of size 3 mm x 60 mm. The electron gun system is developed to extract desired beam current of 100 mA at average power density of 14.5 W/mm^2 at water cooled photon absorber surface for its qualification testing. In Synchrotron Radiation Sources (SRSs), photon absorbers are used to absorb unused synchrotron radiation (SR) power emanating from bending magnets. In next generation SRS, the SR power density to be absorbed by such devices is in the range of 10-100 W/mm^2. Such photon absorbers, being designed indigenously, need to be tested with an alternative power source simulating identical power density. To meet this requirement, an indigenous test setup is developed with electron gun depositing heat load in vacuum environment on water cooled photon absorber as thermal power source. This paper describes design, development, manufacturing, hardware architecture and initial optimization of test set up parameters for desired beam power density.

INTRODUCTION

In Indus-2 SRS facility, electron beam is accelerated from 550 MeV to 2.5 GeV under ultra high vacuum (UHV) environment using RF cavities, bending magnets (BM) and various magnetic components. The SR power emanating from BMs and insertion devices installed in this SRS facility is tapped from 0°, 10° and 15° down stream beam line ports of BM for experimental use. Photon Absorbers (PA) are installed in between two respective ports to absorb unused SR and reduce photon induced desorption (PID) as a result of SR material interaction. These low conducting water (LCW) cooled oxygen free high conductivity (OFHC) copper PA are efficiently designed to transfer SR heat to flowing water sink. The average SR power density absorbed by a typical PA is ~14.5 W/mm^2. For machine safety, temperature of each PA is monitored by thermocouple mounted on atmospheric side of PA. The SR power density to be absorbed by such devices in next generation SRS will be in range of 10-100 W/mm^2. An indigenous test set up comprising electron beam as thermal power source is developed to evaluate and qualify PA with simulating identical power density under vacuum environment. The design, development and experimental results of test set up are detailed in next sections.

*sriharsha@rrcat.gov.in
Proton Accelerator Group, RRCAT.

DESIGN OF ELECTRON GUN

A DC electron gun is designed to test PA with simulating identical power density using electron beam as thermal head load with following attributes [1] shown in Table 1. Pure tungsten (99.7% W) of Ø 0.7 mm is used as cathode in thermionic emission type electron gun. Initially, experiments were conducted to characterize cathode for evaluating its maximum operating temperature and emission current using Richardson-Dushmann equation [2]. The characteristic plot is shown in Figure 1.

Table 1: Electron Gun Specifications

Parameter	Specification
Type of electron gun	DC electron beam
Mode of heating	Direct heating, thermionic emission
Cathode material	Pure Tungsten, Ø 0.7 mm
Beam footprint	Strip type (55 mm±0.5 mm)x(2.5 mm±0.5 mm)
Beam power	20 keV, 2 kW at 100 mA
Operating pressure	<1E-06 mbar

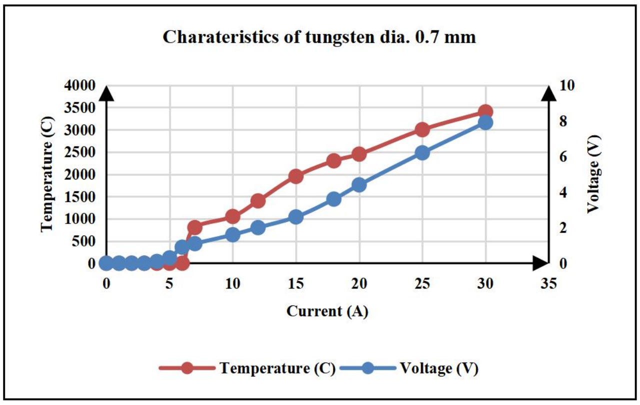

Figure 1: Transfer characteristics of tungsten depicting its temperature and non-ohmic resistance against current.

DEVELOPMENT OF ELECTRON GUN BASED TEST SET UP

Multiport UHV chambers were designed as per guideline of ASME section VIII Division-1 and fabricated using AISI 316L. Multiport UHV chamber connected with ceramic chamber combinedly houses electron gun assembly, SIP 140 l/s for pumping, right angle UHV valve for initial evacuation and gauge for pressure measurement. Adjacent multiport UHV chamber is used for assembled PA assembly as target for electron beam extracted from electron gun and another 140 l/s SIP is used for its evacuation as shown in Figure 2. UHV chamber of PA assembly was kept electrically isolated with connecting chamber for incident current measurement. After fabrication, chemical cleaning and electropolishing were carried out, cathode sub assembly was mounted on ceramic chamber using UHV compatible electrical feed-through inside a tubular assembly with desired concentricity and straightness with wehnelt as shown in Figure 3(b). The wehnelt assembly was specifically machined with desired accuracy and surface finish using AISI 316L with its multiple features like slanting focusing walls and rectangular slit to house cathode in single piece using CNS milling followed by EDM wire cutting process. The cathode was assembled and aligned inside rectangular slit of wehnelt maintaining equidistant with all four side with accuracy of ±100 µm as shown in Figure 3(a) . Similarly the focusing anode plate was mounted with desired accuracy. After assembly of all the components leak detection was carried out using Helium Mass Spectrometer Leak Detector (HMSLD) for leak tightness <1E-10 mbar-l/s.

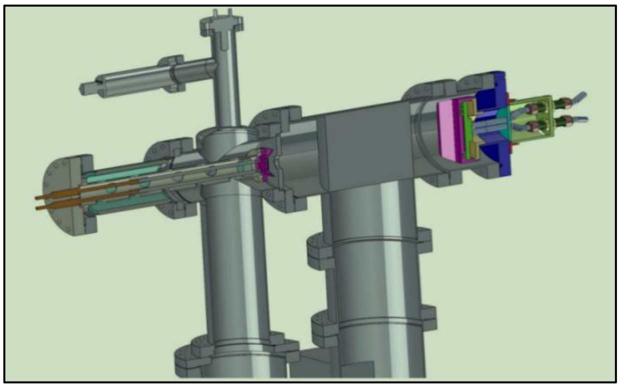

Figure 2: Cross sectional 3D view of developed electron gun test set up

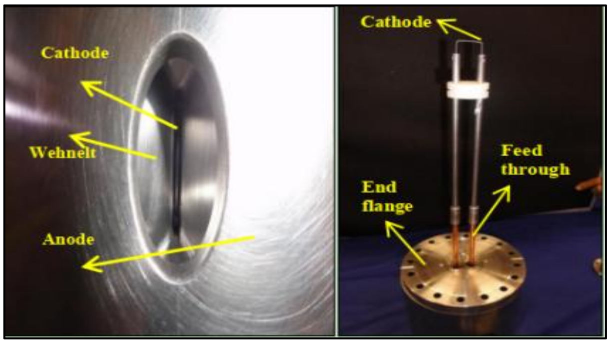

Figure 3: (a) Internal view of cathode, wehnelt and anode with precision alignment, (b) Assembly of tungsten cathode (0.7 mm Ø, 20 mm long) on HV end flange

For the extraction of electron beam from cathode with sufficient beam energy, application of high potential difference between cathode and anode is essential. A 20 kV, 5A DC power supply[3] is used to extract electron beam from cathode. A 2 kV DC power supply at wehnelt is used as electrostatic lens to control the beam shape and throw distance. A 10 V, 40 A DC power supply is used for heating cathode for thermionic emission of electrons. Both wehnelt and heating power supplies are floated at 20 kV (negative) using isolation transformer and housed in HV deck as shown in Figure 5. The entire test set up is installed in 1 mm thick lead sheet sand witched with 3 mm thick mild steel radiation shield hutch which is designed and fabricated for dose rate of <1 µSv/h to occupational workers as shown in Figure 4.

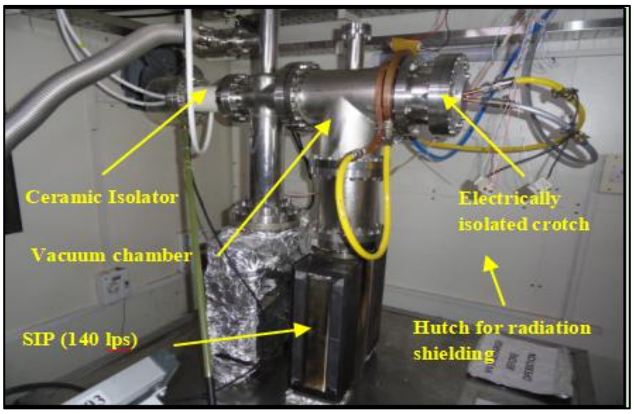

Figure 4: Fully assembled 20 keV, 2 kW DC electron gun installed in radiation shielded hutch

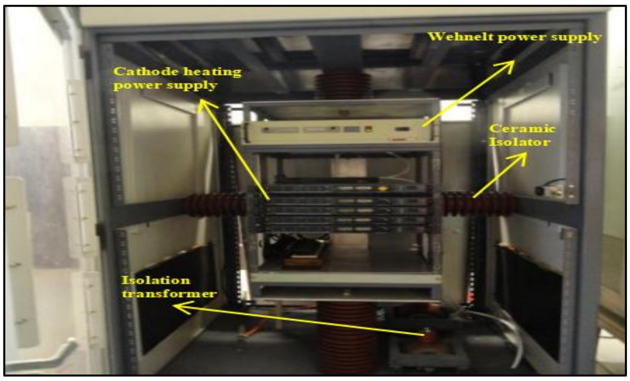

Figure 5: High Voltage deck housing wehnelt and cathode heating power supplies

EXPERIMENTAL ANALYSIS

Prior to starting actual experiment, cathode degassing is done by heating it sufficiently. For HV conditioning, the HV level is increased gradually to 20 kV at a step size of 1 kV without electron beam. For safety of equipment, over current and over voltage trip limits are set in event of any discharge or spark. To measure extracted beam current, PA is isolated from grounded anode using epoxy bushes shown in Figure 4. After all conditioning, cathode heating power is sufficiently increased to extract beam current, there by optimizing heating power supply and wehnelt power supply. Experiments are conducted repeatedly to note down precise findings, their plots are shown in Figure 7 & 8. Eventually, A 2 kW (20 keV, 100 mA) electron beam was deposited on water cooled PA at 225 W of cathode heating power and when wehnelt is at -100 V as shown in Figure 6. The temperature on rear side of of PA is measured to be 38 °C at 20°C of chilled water at flow rate of 8 lpm. Low conductivity water (LCW) circuit with electric isolation is used for facilitating the measurement of e-beam current incident on PA surface. Experiments are continued till the beam current is in steady state due to pressure dynamics caused by electron induced desorption i.e., 2E-5 mbar & 6E-7 mbar at SIP currents of 55 mA & 20 mA respectively as shown in Figure 9.

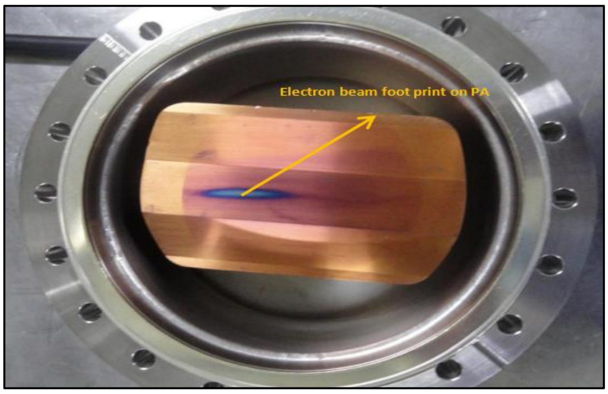

Figure 6: Specimen OFHC copper Photon absorber installed on end flange showcasing beam power foot print at 20 keV, 100 mA.

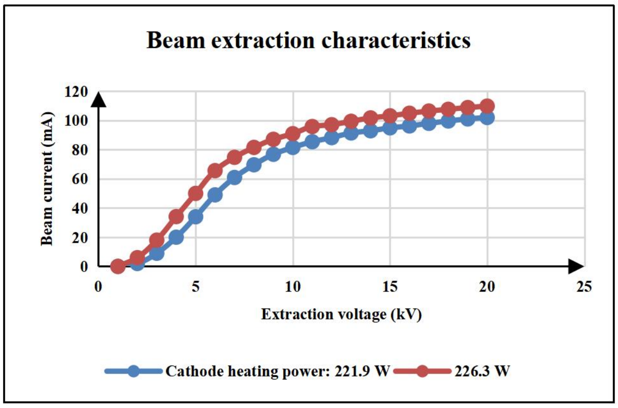

Figure 7: Beam current extraction characteristics.

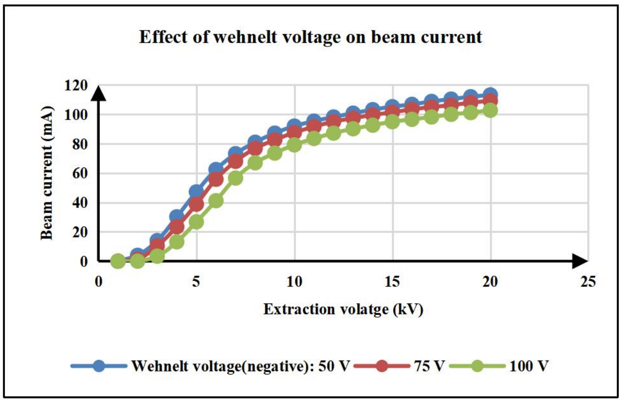

Figure 8: Variation in beam current at PA with change in wehnelt voltage

CONCLUSION

A 20 keV, 2 kW DC strip type thermionic emission electron gun is successfully designed and developed to extract 100 mA of beam current which is incident on OFHC copper photon absorbers at a throw distance of 300 mm. This development is important contribution for upcoming accelerator projects.

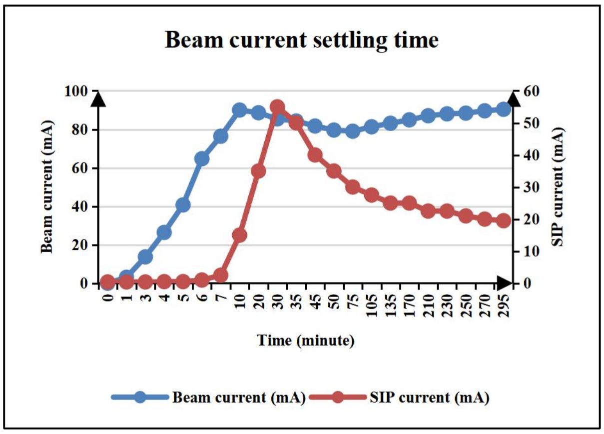

Figure 9: Settling time in beam current on account of pressure dynamics due to ESD.

ACKNOWLEDGEMENTS

We would like to express our sincere gratitude to Shri D. Y. Deokar, Shri Vipin Rajbar, Shri T. R. Meena, Dr. G. Haridas and Shri Vijay Bhardwaj, RRCAT. Colleagues of UHVTS, RRCAT deserves our gratefulness for their direct or indirect support.

REFERENCES

1. Monika Rana, Pramod R, A.D. Ghodke, B.K. Sindal, Sujata Joshi and D.P. Yadav, "Simulation of a 20 keV/100 mA Strip Electron Gun for Testing Photon Absorbers", in Proc. Indian Particle Accelerator Conf. (InPAC), VECC, March 2022.
2. Hosseinzadeh, M., & A.Sadighzadeh (2015). Design and numerical simulation of thermionic electron gun. arXiv: Accelerator Physics.
3. M. K. Badapanda & P. R. Hannurkar (2008) Klystron Bias Power Supplies for Indus-2 Synchrotron Radiation Source, IETE Journal of Research, 54:6, 403-412, DOI: 10.4103/0377-2063.48630

DARK CURRENT CALCULATION IN SRF ELLIPTIC CAVITIES

Ram Prakash[1,2#], Arup Ratan Jana[1], Vinit Kumar[1,2]
[1]Proton Accelerator Group, Raja Ramanna Centre for Advanced Technology, Indore
[2]Homi Bhabha National Institute, Mumbai.

Abstract

This paper investigates the phenomenon of dark current build-up in the medium and high energy accelerating sections of a 1 GeV pulsed H^- linac. Dark current refers to the formation of current due to highly energetic field-emitted electrons in RF cavities (due to high electric fields on the cavity surface), which escape through the cavity beam pipe and may potentially harm accelerator operations. The study begins by calculating the trajectory of these electrons under the influence of electromagnetic fields inside the β_g=0.61 (mid beta) and 0.81 (high beta) elliptic cavities, with a comparison of the dark current emission behaviour of these two classes of cavities. The next step involves tracking the dark current electrons in the corresponding mid- and high-beta cryo-modules in 3-dimensions, using a particle tracking program. Simulations show that for our case, most of the dark current electrons get lost inside the linac, and therefore cannot build-up, resulting in an overall amplification factor of zero.

INTRODUCTION

Dark current is a phenomenon that occurs in RF cavities, where field-emitted electrons from regions of very high electric field (~ 10^4 MV/m) on the cavity surface undergo acceleration and exit through the beam pipe [1]. Such a high electric field on the cavity surface results from the large field enhancement factor caused by irregularly shaped contaminants [2], that may remain on the surface, even after undergoing a rigorous processing procedure. The dark current electrons attain significant kinetic energy in the cavity, after exiting the cavity's beam pipe, they can reach even higher energies when passing through downstream or upstream elliptic cavities [3]. Highly energetic dark current beam can be detrimental to accelerator operation, and this phenomenon can limit the maximum operable acceleration gradient of a superconducting RF (SRF) accelerator by producing significant amount of X-rays [4][5]. In this paper, we have studied the process of dark current buildup in the medium and high energy accelerating sections of a 1 GeV H^- pulsed linac that is being designed at RRCAT [6] for the envisaged Indian Facility for Spallation Research (IFSR). For this purpose, we developed Python based computer programs for analyzing the motion of charged particles in two dimensions (2D) inside the elliptic cavities where they are generated, and in three dimensions (3D) for tracking these particles further in the other cavities and transport lines. Here, we calculated the electromagnetic (EM) field, using the code SUPERFISH [7], and imported it to our self-developed program. Drawing from our experience with particle tracking simulations for β_g = 0.92 elliptic SRF cavities [8], we decided to truncate the location of possible emission sites near the iris region. This approach enabled us to reduce the total simulation size for trajectory calculations in the medium (*i.e.,* β_g = 0.61) and high beta (*i.e.*, β_g = 0.81) elliptic cavities. When the dark current propagates through these sections of the linac, it may get amplified with the help of contributions from the several elliptic cavities installed in these sections, and it may also be reduced due to transverse kicks by the quadrupole triplet magnets and the EM field of the RF cavities. As a result of these two competitive processes, for the case that we have studied, all the dark current electrons gets lost inside the cryo-module before they reach the cry-module exit. Therefore, the dark current does not build-up in the mid and high beta accelerating sections, and an overall amplification factor for the dark current is zero, for the case that we have studied. This paper is organized as following. The next section details the methodology for particle tracking inside the elliptic cavity and presents a comparison of results for particle tracking in β_g = 0.61 and 0.81 elliptic cavities. The subsequent section describes the 3-D particle tracking calculations in the linac, and the paper concludes with a summary of our findings.

PARTICLE TRACKING INSIDE THE ELLIPTIC CAVITY

This section outlines the methodology used for particle tracking in elliptic cavities and describes the obtained results. The relativistic form of Lorentz's equation of motion [9] was numerically solved in 2D, using the leap-frog method. The EM fields were obtained from the SUPERFISH code. For more information on the particle tracking scheme one can refer to our earlier work in Ref. 10. To perform these calculations, the elliptic cavity was provided with several emission sites having an assumed density of 3000 emitters per square meter, uniformly distributed on its surface. Particle emission was considered to occur in bursts after every 5 degrees during a full RF cycle. These parameters are directly adopted from our earlier work [8], where we conducted a detailed optimization study to perform particle tracking calculations in the β_g = 0.92 elliptic SRF cavities. Following this reference, we decided to limit the maximum radial distance of the emission sites near the iris region to a maximum value of 180 mm for β_g = 0.61 cavity and 90 mm β_g = 0.81 cavity, in order to save computation time. The particles were assumed to be

#rprakash@rrcat.gov.in

emitted perpendicular to the surface of the cavity, with kinetic energy equivalent to the Fermi energy of niobium, which is approximately 5.3 eV. The trajectory of these emitted particles was traced until they collided with the cavity surface. Thereafter, no subsequent secondary emission of the electrons was considered in this analysis. The above mentioned methodology was used for particle tracking in the β_g = 0.61 and 0.81 elliptic cavities at their respective design acceleration gradients of 15.5 MV/m and 18.5 MV/m. The results obtained from these calculations are summarized in Table 1. It can be seen that β_g = 0.61 cavities exhibit lower number of emitted macro-particles per RF cycle, in comparison to the β_g = 0.81 cavities. This can be attributed to the longer length of the β_g = 0.81 cavities that gives rise to a larger surface area with higher value of electric field. However at the same time, due to the longer length of the β_g = 0.81 cavities, particles emitted from any of the irises have a higher probability of striking the cavity surface and getting lost. Consequently, despite higher number of particles are emitted from the iris region of β_g = 0.81 cavities compared to β_g = 0.61 cavities, a smaller fraction of the particles escape through any of the beam pipe.

Table 1: Comparison of particle tracking calculations for β_g=0.61 and 0.81 elliptic cavities.

Type of Elliptic cavity →	βg = 0.61	βg = 0.81
Acceleration Gradient E_0T	15.5 MV/m	18.5 MV/m
Emission sites at iris region (emitted macro-particles per RF cycle)	3082 (221904)	645 (46440)
Particles escaping through the beam pipe per RF cycle a. Right end b. Left end	 1844 1787	 1355 1110
	Total: 3631	1465
Maximum Energy of particle exiting the cavity	~5.2 MeV	~9.6 MeV
Escape time for the particles created in one RF cycle	~3.38 RF cycles	~2.6 RF cycles

We have plotted the energy spectrum of the dark current electrons in the β_g = 0.61 elliptic cavity in Fig. 1, which shows a prominent peak at around 3 MeV. It is worth noting that the energy spectrum obtained from particle tracking results of the β_g = 0.92 elliptic cavity showed the presence of five distinct peaks, corresponding to contributions from the five irises of the cavity. Specifically, the peak with the smallest energy was formed by the iris closest to the beam pipe, while the peak with the largest energy was formed by the iris farthest from the beam pipe. Since the electrons quickly become relativistic, they find good synchronization with the cavity structure for β_g = 0.92 case, and particles emitted from different irises get accelerated by distinctly different amount. However, in the case of β_g = 0.61, only one peak is observed because although the field emitted electrons quickly become relativistic, they are in relatively poor synchronisms with fields in β_g=0.61 cavities. These electrons undergo synchrotron oscillation in phase space, with only few electrons achieving maximum energy, while exiting the cavity. A similar behaviour was observed in the energy spectra of particles exiting the beam pipe of the β_g = 0.81 elliptical cavity, where two distinct peaks were observed. However, unlike in Fig. 1, where the peaks corresponding to particles leaving from the left and right sides of the beam pipe are the same, in this case, they were different. This needs to be further investigated.

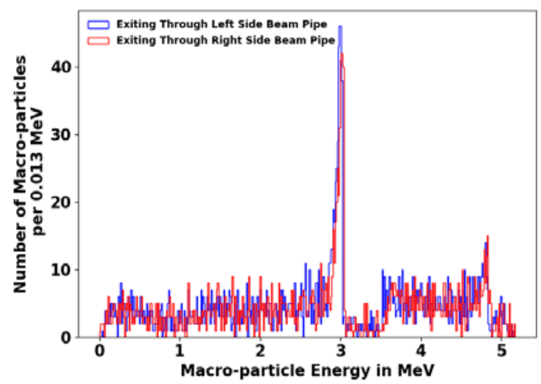

Figure 1: Energy spectrum of the dark current electrons emitted from the βg = 0.61 elliptic cavity obtained from the numerical calculations performed at the design acceleration gradient *i.e.* 15.5 MV/m.

PARTICLE TRACKING IN THE MID- AND HIGH BETA CRYO-MODULES

The particles that exit the cavities flow along with the main H^- beam through the linac. We performed particle tracking calculation for these particles, as they escape through downstream cavities and quadrupole magnets. It is important to note that the quadrupole magnets may kick the dark current electrons out of the plane, necessitating a shift from 2D to 3D particle tracking. We therefore converted the final coordinates of the outgoing particles from the earlier 2D tracking calculations to 3D by assigning a random azimuthal position and zero azimuthal velocity. Additionally, the EM field in the elliptic cavity was converted from 2D to 3D. Since each cavity operates at a different gradient, and is independently phased, we performed 2D particle tracking for cavities at various acceleration gradients. Thereafter, for 3D particle tracking, the cavity phase for H^- from earlier linac simulations was adjusted for the electron beam. For 3D particle tracking in the linac, we developed an in-house code that is compatible with the Cartesian coordinate system for tracking particles in 3D. This code was used to track particles in both the mid and high beta sections of the 1 GeV H^- linac. Previously, a baseline lattice design for the linac was developed [6]. In the medium beta section of the linac, the H- beam energy is increased from ~170 MeV beam to ~ 480 MeV. Our baseline design includes 12 cryomodules, each containing three elliptic cavities. A quadrupole triplet is placed between two cryomodules to provide transverse focusing for the H- beam. The high beta section, which further accelerates the beam to ~ 1 GeV, consists of six cryomodules, each containing six high beta elliptic cavities. Similar to the medium energy section, quadrupole triplets are used for transverse focusing of the beam in this section as well.

The particle tracking was performed in the mid- and high- beta section cryo-modules. Figure 2 displays the number of absorbed and surviving particles as a function of longitudinal distance as these particles traverse through the drift, downstream cavities, and quadrupole triplet magnets in the mid-beta cryo-module. As the beam propagates through the linac, the downstream cavities keep contributing more particles, leading to an increase in the total number of particles. However, upon reaching the first quadrupole magnet, most of the beam strikes the linac aperture, and only a few particles remain, which are subsequently lost in the next quadrupole. The upstream dark current electrons also pass through strongly focussing quadrupoles and subsequently get lost. These results indicate that the entire dark current beam is lost in this cryo-module. This behaviour was seen in all the cryo-modules of the mid-beta section. Further, a similar analysis was performed for high-beta section cryo-modules. Result for one of the cryo-modules is presented in Fig. 3. The analysis indicates that dark current macro-particles are lost in the drift space immediately after they are generated in the cavity. As a result, we can conclude that the dark current amplification factor in the mid- and high-beta sections of the linac is zero, and therefore, dark current build up is unlikely to occur in this case.

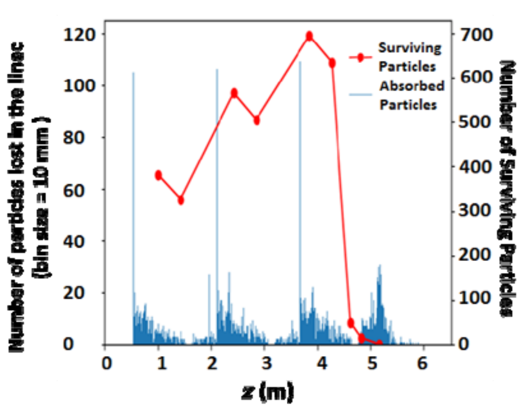

Figure 2: The particle loss along the mid-beta cryo-module longitudinal distance.

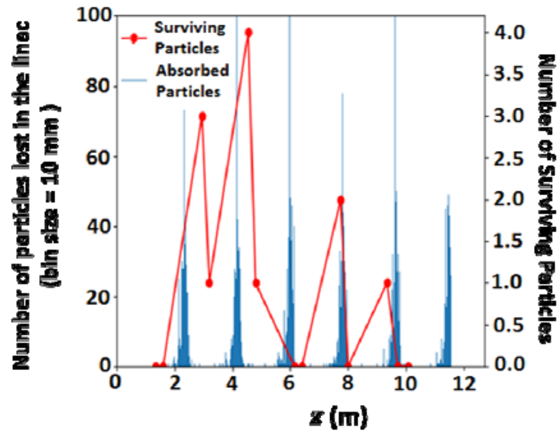

Figure 3: The particle loss along the high-beta cryo-module longitudinal distance.

CONCLUSIONS

In conclusion, our study showed that the mid-beta cavities may emit more dark current compared to the high-beta cavities. Since the electrons are ~ 1838 times lighter than the H-, the electrons receive a strong kick from the quadrupole magnets. This prevents the build-up of dark current in both mid- and high-beta sections of the linac. Therefore, the overall amplification factor for dark current is zero, indicating that the dark current issues are unlikely to occur in our design of 1 GeV H- linac. Though the outcome of this study is intuitive, it reinforces the fact that the dark current electrons will not pose a problem for our H- linac design.

ACKNOWLEDGEMENTS

Co-authors would like to acknowledge Shri Purushottam Shrivastava for constant support and encouragement.

REFERENCES

[1] H. Padamsee, J. Knobloch and T. Hays, Ithaca: John Wiley and Sons, Inc., 1998.

[2] D. Biswas, *Physics of Plasmas,* vol. 25, p. 043105, 2018.

[3] C. Xu *et. al.* in *North American Particle Accelerator Conference (NAPAC 2016)*, Chicago, IL, 2016.

[4] V. Volkov, *Physical Review Special Topics- Accelerator and Beams ,* vol. 13, p. 084201, 2010.

[5] K. L. F. Bane *et. al. Physical Review Special Topics - Accelerator and Beams,* vol. 8, p. 064401, 2005.

[6] A. R. Jana et. al. Nuclear Instruments and Methods in Physics Research Section A, vol. 942, p. 162299, 2019.

[7] K. Halbach *et. al.Particle Accelerators,* vol. 7, pp. 213-222, 1976.

[8] R. Prakash et. al. (to be published).

[9] D. J. Griffith, Introduction to Electrodynamics, Prentice Hall, 2009.

[10] R. Prakash *et al. Nuclear Instruments and Methods in Physics Research A,* vol. 867, pp. 128-138, 2017.

DEVELOPMENT OF TRANSFER FUNCTION MEASUREMENT SYSTEM FOR ELLIPTICAL HIGH BETA SUPERCONDUCTING RF DRESSED CAVITY

K. K. Singh*[1], V. K. Jain[2], D. V. Ghodke[1], Vijendra Prasad[1], Sanjay Chouksey[2] and Purushottam Shrivastava[3]

[1]*Proton Linac Development Division*
[2]*Superconducting Cavities Development Division*
[3]*Proton Accelerator Group*
Raja Ramanna Centre for Advanced Technology, Indore

Abstract

RRCAT is developing elliptical high beta dressed superconducting RF cavity for domestic as well as international projects. Due to high quality factor, superconducting RF cavities are very sensitive to external vibrations. In order to check the performance of superconducting RF cavity towards external vibrations, transfer function measurement system has been developed.

This paper describes development of transfer function measurement system. Developed system excites the cavity by a set of sinusoidal signals through piezo-actuators. These piezo actuators are part of cavity tuning system. Cavity response to these excitations is measured by change in phase by RF measurements system. Developed system consists of function generator and piezo-driver for set of sinusoidal signal generation and phase detector for cavity response measurement. Change in phase is digitalized by NI based DAQ system. FFT of the phase signal gives transfer function of the dressed cavity. The transfer function measurement system is mounted with 5-cell 650 MHz dressed cavity. The setup is initially tested on a rotary fixture and tested for 1 Hz to 500 Hz piezo excitation. During this test, two most strong mechanical modes were observed at 231 Hz and 460 Hz and no mechanical modes were observed below 100 Hz. The results are compared with FE analysis results which show a close matching of the excited modes.

INTRODUCTION

Elliptical Multi-cell SCRF cavities are essential for the future superconducting proton linear accelerator at RRCAT and are also deliverable to Fermilab, USA under Indian Institutes Fermilab Collaboration (IIFC). These cavities are very sensitive to any small perturbation due to their narrow bandwidth. Small perturbations generated from cryo-flow induced vibrations, vacuum pumps, AHU, motors etc. Due to narrow bandwidth of the cavity, significant power may be reflected from the cavity. Which will affect the accelerator operation. In order to avoid resonance with external vibrations, superconducting RF cavities are designed to have mechanical resonance frequency above 100 Hz because frequencies of the external sources are laying below 100 Hz [1,2]. The mechanical resonance frequency of the cavity depends on its material of construction, design, type of mounting/ support, tuner stiffness etc. In order to find out 1st mechanical modes FE analysis is also carried out which showing that for tuner stiffness greater than 40 kN/mm, 1st longitudinal mechanical mode is above 100Hz [3]. To measure/ verify the mechanical modes of the superconducting RF cavity, transfer function measurement system is developed. The developed system is tested at room temperature.

SCHEME FOR TRANSFER FUNTION MEASUREMENT

Elliptical 5-cell 650 MHz β = 0.92 superconducting dressed RF cavity has been taken for transfer function measurements. The cavity is assembled with piezo-actuator along with lever tuner. Transfer function measurement system consist of control PC, function generator, piezo driver, dressed RF cavity, RF signal generator, RF amplifier, phase detector and NI based DAQ system. Scheme for transfer function measurement is described in Fig.1.

Function generator has been programmed for generating sequence of sinusoidal pulses (10 Vpp). The sinusoidal pulses are amplified by piezo driver (40 Vpp 1A) and drive the piezo actuators. Piezo-actuator excite the cavity with sequence of sinusoidal pulses. An RF signal generator is used to fed low level RF power to the cavity. Phase difference between transmitted signal from cavity and input signal is monitored. As cavity is excited with sequence of sinusoidal pulses, change in phase is observed. Change in phase signal is amplified for further processing. The amplified phase signal is digitalized by National Instruments based 16 bit- data acquisition system. Fast Fourier Transform (FFT) of the phase signal gives transfer function of the dressed cavity.

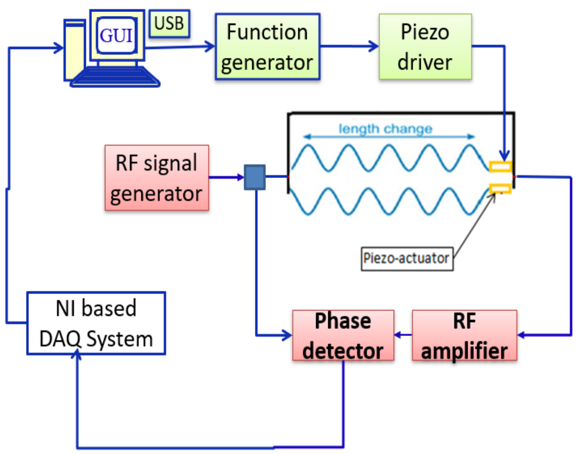

Figure 1: Scheme for transfer function measurement.

EXPERIMENTAL SETUP

Figure 2 shows experimental setup for transfer function measurement. 5-cell 650 MHz superconducting dressed cavity assembled with tuner and piezo-actuator is shown in the figure. Control rack consist of function generator, piezo driver and RF measurement setup. RF measurement setup includes RF signal generator (IFR 2025) for feeding low level RF power to cavity through RF port as shown in figure, RF amplifier, phase detector (AD8302) for measuring phase difference between transmitted and input signal and 16-bit NI based data acquisition card (PXIe-6361) for digitalizing phase signal. Calibration of phase detector is carried out by applying the DC voltage to piezo actuator and measuring the change in phase signal [4] and comparing this phase signal with phase measured in vector network analyser at same piezo voltage.

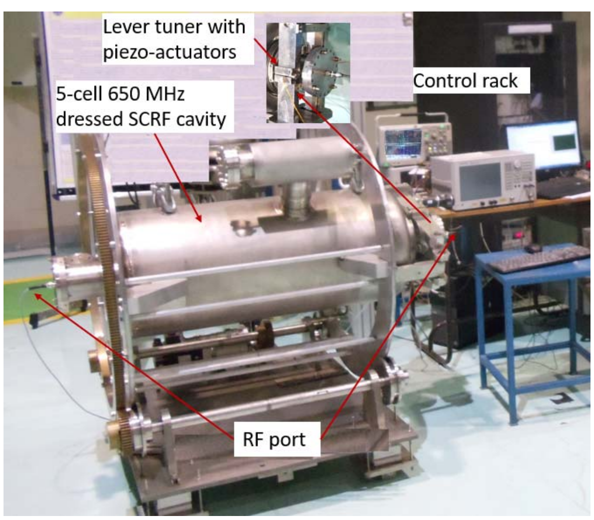

Figure 2: Experimental Setup for transfer function measurement.

GUI is developed on PC for controlling sinusoidal pulse parameters generated from function generator. Developed GUI is shown in Fig.3. GUI has feature for selecting function generator channel, waveform function, amplitude, DC offset, frequency, phase level and impedance. Continuous and burst mode are also selectable from the developed GUI.

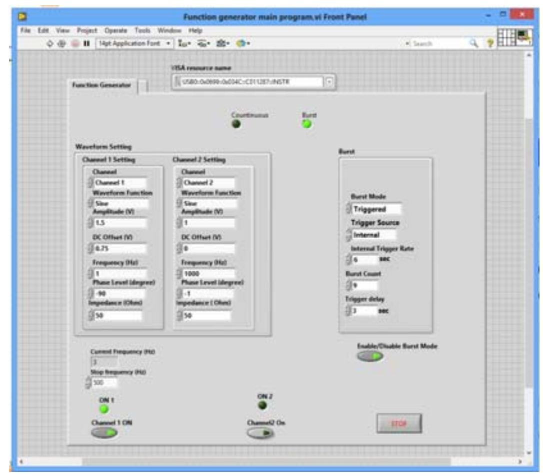

Figure 3: GUI for function generator control.

Data acquisition card PXIe-6361 (16 bit, 2MS/s, 2 analog outputs, 32 analog input) is programmed in LabView for acquiring phase signal at sample rate 10ksample/sec. Developed GUI is shown in Fig.4 for channel setting of PXI card, for timing setting (sample rate, number of samples taken), for plot of acquired data and for Fast Fourier Transform (FFT) of acquired data. LabView program is done for saving the acquired data in text format for further processing.

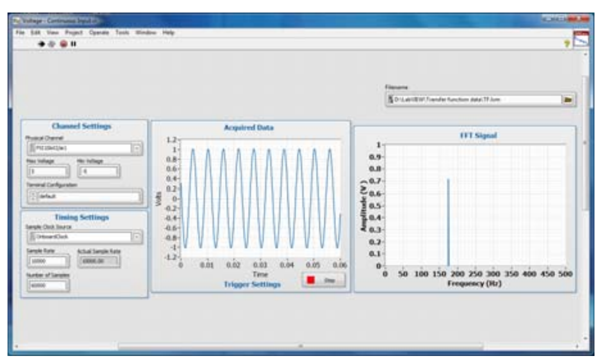

Figure 4: GUI for data acquisition and FFT calculation.

RESULTS

The transfer function measurement system is interfaced with 5-cell 650 MHz dressed cavity. The setup is tested on a rotary fixture. A sequence of sinusoidal pulse (3 second ON at 1Hz, 3 second OFF, 3 second ON at

2Hz….) is applied to piezo actuators from 1 Hz to 500 Hz. Drive signal amplitude is kept at 40V peak to peak. FFT, as shown in Fig.5, of acquired phase data is calculated using developed software. It is found that two most strong mechanical modes were observed at 231 Hz and 460 Hz and no mechanical modes were observed below 100 Hz.

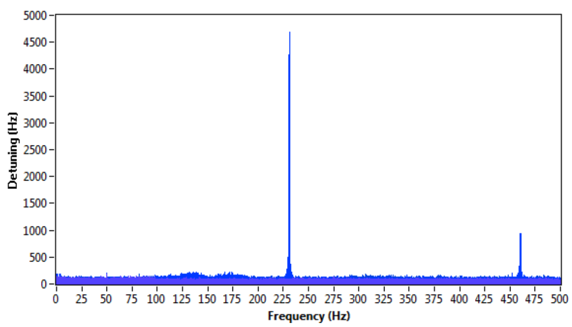

Figure 5: Fast Fourier Transform of phase signal.

CONCLUSION

Transfer function measurement system has been designed and developed. Developed system is assembled with 5-cell, 650 MHz, β =0.92 elliptical superconducting RF cavity and tested at room temperature. During testing cavity is excited with sequence of sinusoidal pulses and phase response of the cavity is measured. LabView based software is developed for function generator control, phase signal data acquisition and FFT calculations. During measurements no mechanical modes are found below 100 Hz. Transfer function measurement has to be done for every superconducting RF cavity before its qualification. So, this development is an important millstone towards superconducting cavity qualification.

ACKNOWLEDGEMENT

We are thankful of Shri R. B. Adbol, Shri Vinesh Kumar Verma Shri Umakant Shrivastava and Shri Maloth Suresh for their important role in the assembly and testing of this transfer function measurement setup. The author also would like to appreciate the help received from Shri Sanjay Kumar Singh, Shri Bharat Kumar Arya and all the members of PLDD during various stages of development.

REFERENCES

[1] Yu. Pischalnikov et. al, “Performance of the 650MHz SRF Cavity Tuner for PIP II Project”, in Proc. 19th Int. Conf. on RF superconductivity (SRF2019), Dresden, Germany, July 2019, pp.652-655.

[2] A.N. Other, “Microphonics simulation and parameters design of the SRF cavities for CiADS, in Proc. 10th Int. Particle Accelerator Conf (IPAC - 2019), Melbourne, Australia, pp 2903-2905.

[3] V. K. Jain et.al, “650 MHz Elliptical Superconducting RF Cavities for PIP-II Project” in Proc. North American Particle Accelerator Conference 2016, Chicago IL USA, Oct 2016, pp 859-886.

[4] https://www.analog.com/media/en/technical-documentation /data-sheets/ad8302.pdf

DESIGN METHODOLOGY FOR FORMING TOOL OF SCRF CAVITIES

*Nitin Nigam1, S Mandle1, N K Sharma1, G V Kane1, Vijendra Prasad1, Purushottam Shrivastava2
1Proton Linac Development Division
2Proton Accelerator Group
Raja Ramanna Center for Advanced Technology, Indore

Abstract

RRCAT is involved in the design and development of various superconducting RF (SCRF) cavities for high energy proton accelerator. SCRF cavities have a very high-quality factor and are very sensitive to any dimensional changes. These cavities are generally fabricated by deep drawing and it is very difficult to achieve the required tight tolerances due to spring-back, thickening, and thinning.

Using finite element analysis, die and punches have been designed to get the RF profile that is very close to the required profile for SR011 spoke cavity. The main components of the cavity are, end wall, spoke and shell. These components are manufactured by the deep drawing of thin sheets of niobium. This paper will elaborate on the procedure to estimate the spring-back, thinning, thickening and other forming parameters for the End Wall using finite element method. Based on the forming simulations, the profile of die and punches has been varied iteratively to get the RF profile of the formed component close to the design profile.

INTRODUCTION

Various SCRF niobium cavities will be required for the proposed high energy proton accelerator at RRCAT. SCRF cavities have a very high quality-factor and are very sensitive to any dimensional changes. These cavities are generally fabricated by deep drawing of the niobium material, and it is very difficult to achieve the required tight tolerances due to spring-back, thickening, and thinning. A methodology has been developed to design the forming tool for SCRF cavities.

SCRF cavities are fabricated using thin sheets of niobium. The methodology to design the forming tool has been explained with the example of forming of theend wall for SR011 cavity. All the FEM simulations have been done using Altair Hyper-Form software. Tthickening, thinning, and spring-back have been estimated from the forming simulations and clearances were defined between die and punches accordingly. The final forming tool design conforms to the required RF profile of the end wall and also requires a lower tonnage requirement for forming.

SIMULATION MODEL AND MATERIAL ASSIGNMENT

Figure-1 depicts the forming simulation model for the end wall. It depicts different forming tools such as blank holder, punch & die and blank. Radius The radius of the end wall is 226.4 mm, and the height is 59.2 mm. The physical dimensions of the end wall have been taken based on 2K operational temperature and the cavity will be fabricated at room temperature. All the dimensions have been scaled based on the thermal contraction of niobium to get room-temperature dimensions.

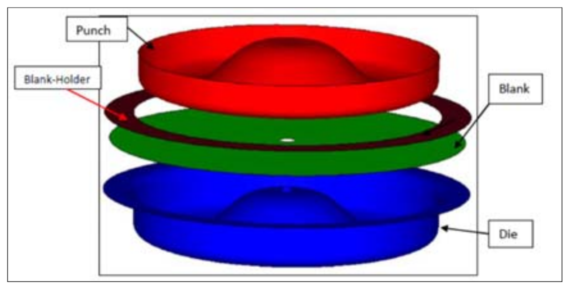

Fig.1:- Simulation model showing forming tool and blank.

The end wall will be fabricated using 3.15 mm thick niobium sheet. The blank material was defined byHill orthotropic material model. This model is applicable only to shell elements. Figure-2 shows the plastic strain vs. stress for niobium. Stiffness of die, punch and binder is much higher as compared to stiffness of blank. Hence, rigid material was defined for die, punch and binder during simulation.

Fig.2 :- Plastic strain vs. Stress for Niobium.

*nitin@rrcat.gov.in

INITIAL FORMING SIMULATION

First, the blank size was estimated using Hyper-Form one step analysis module. Mid surface of the actual component was modelled to develop the initial blank. The developed blank was a circular disc with an outer diameter of 522 mm with an extra trimming margin of ~5 mm. Trimming margin includes weld shrinkage & trimming. Punch, die & blank holder was modeled, and meshed using rigid shell elements to save computation time. This assumption holds true as the thickness/stiffness of blank is quite small as compared to the stiffness of the forming tool. Niobium material property (measured stress strain curve) was assigned to blank. Uniform 3.15 mm gap has been defined between die and punch that is equal to sheet thickness of niobium without any clearance. Proper clearance will be provided after 1st iteration of forming simulation based on thickening and thinning. During the simulation, only the flow radius was varied to get a better formed end wall. Decreasing the flow radius increases thinning, and increasing the flow radius increases wrinkle formation. An optimum flow radius was chosen, which gave good forming results. The results for the final iteration of forming simulation have been discussed below.

Figure-3 shows the developed strain on the formed end wall. The maximum strain was found to be 20%, which is well below the maximum % elongation of the niobium material, which is 40%.

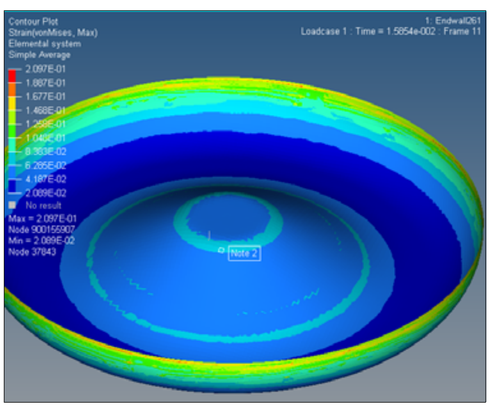

Fig.3:- Developed strain on the end wall

Figure-4 shows thinning and thickening after forming simulation of the end wall. The maximum thinning was found to be ~10%, which is acceptable based on experience gained during the forming of the half cells for the 650 MHz 5-cell SCRF cavity [3].

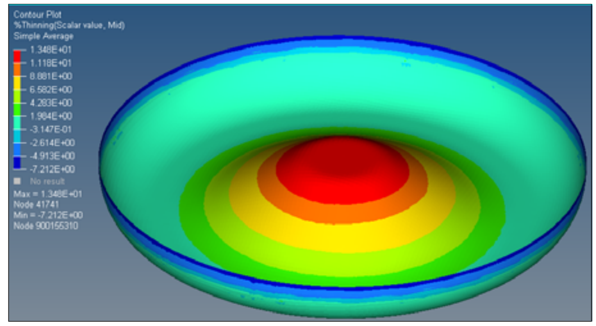

Fig.4:- Thinning and thickening of end wall after forming.

Based on thinning and thickening of the material, variable clearances need to be defined for the final forming simulation. From figure-5, thinning is ~12% at point 1 and gap between die & punch is 3.15 mm. The formed component conforms to the die profile, although it need to conforms the punch profile, as the punch surface is the RF surface. The gap between die and punch need to be reduced from 3.15 mm based on 12 % thinning at this location. At point 2, thinning is very small, and the formed component conforms to punch profile. There is no need to alter clearance between die and punch at this location. At point 3, ~5% thickening is observed, it will increase the force required to form the end wall. So, at this location, more clearance needs to be defined.

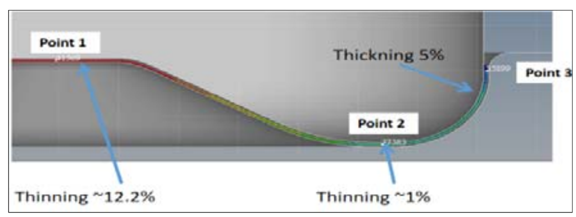

Fig.5:- Thinning and thickening of the end wall.

Figure-6 shows the tonnage requirement for forming the end wall. Due to thickening at the equator, tonnage required to form end wall increases drastically at the end of forming. The end wall is planned to be formed using a 120-tonne forming press, which would be incapable of forming it completely. So, more clearance needed to be defined at the location of thickening.

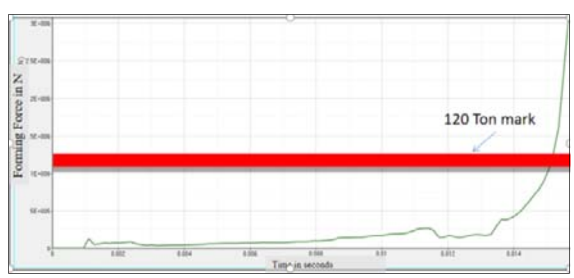

Fig.6:- Tonnage requirement for forming the end wall.

Forming is a highly non-linear phenomenon. During forming, the material deforms beyond its yield point plastically. After removal of forces, the material recovers some of its strain equal to the elastic strain. This recovery after forming is called spring-back. Spring-back analysis was performed after the forming analysis of the end wall.

Figure-7 shows the deformed end wall after spring-back simulation. The estimated deformations are with respect to the ideal model of end wall. Spring-back is higher at the equator location.

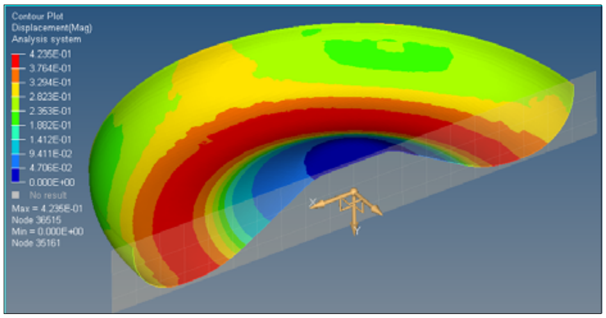

Fig.7:- Deformation distribution after Spring-back.

Figure-8 shows height of the formed component after spring-back. The estimated height was found to be 58.7 mm, which is higher than the actual height that is 59.2 mm. Only the height of the end wall has been compared, as this is the most affected dimension from spring-back. Die and punches needed to be designed to compensate for the spring-back.

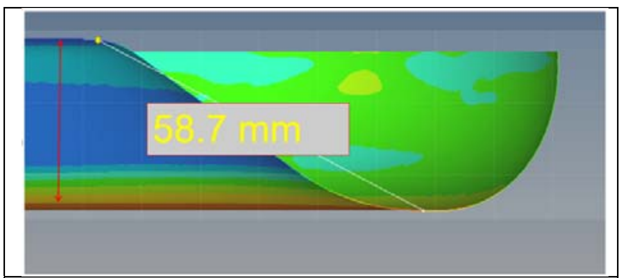

Fig.8:- Height of the formed end wall after spring-back.

FINAL FORMING SIMULATION

Based on the initial forming simulations, changes have been made to the die and punch. Based on spring-back, the profiles of the die and punch have been modified. Clearances have been changed between die and punch based on thinning and thickening, keeping the punch profile unchanged as it decides the RF side. The final forming simulation was performed, and the results are discussed below.

Thinning and thickening are nearly the same as in the initial simulation. The tonnage requirement on the updated die and punch has been reduced due to the larger clearance provided at the location of thickening. Figure-9 shows that less than 50 tonnes are required to form the end wall, which is less than the maximum available tonnage of the press machine available at our lab.

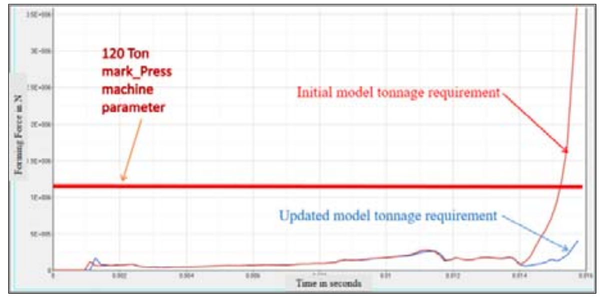

Fig.9:- Comparison of tonnage requirement for initial and final simulation.

A spring-back simulation was performed after forming simulation. Figure-10 shows that the height of the formed component is 59.22 mm, which is very close to the required height of 59.2 mm. Also, the profile of the formed component matched within 100 microns.

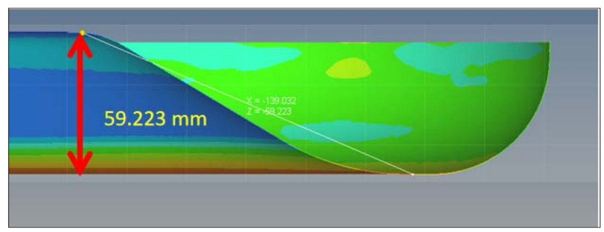

Fig.10:- Height of the formed component after spring-back.

CONCLUSION

Methodology to design a forming tool for SCRF cavities has been developed. The complete procedure has been explained using the design of the forming tool for the end wall of SR011 cavity as an example. Similar methodology can be used to design other components of SR011 cavity, and other cavities for the high energy proton accelerator.

REFERENCES

[1] N. Nigam, A. Chaturvedi, N. K. Sharma, G. V. Kane and S. C. Joshi, "Forming Simulation for Components of Low beta Spoke Resonator", in InPAC-2018 held at RRCAT, Indore.

[2] Mukesh Kumar Pal, Rahul Gaur and Vinit Kumar, "Electromagnetic design of 325 MHz superconducting single-spoke resonators for Indian Facility for Spallation Research", Pramana 96 article number: 69, Journal of Physics 2022.

[3] M. Bagre, T. Maurya, A. Yedle, A. Puntambekar, S.C. Joshi et al, "Development of 1.3 GHz Nine-cell SCRF cavity", InPAC-2015 held at TIFR-BARC, Mumbai.

POWER COMBINING TOPOLOGY FOR CW 32 kW-650 MHz SOLID STATE RF AMPLIFIER INSTALLED AT HORIZONTAL TEST FACILTY (HTS), RRCAT (ID: A2-286)

Alok Kumar Gupta*, Akhilesh Jain, Mahendra Lad
SSRFAS/RFSD, RRCAT, Indore - 452013, INDIA

ABSTRACT

For characterization and qualification of superconducting RF cavities at HTS facility, RRCAT, a 32 kW-650 MHz CW water-cooled Solid-State high power RF Amplifier (SSPA) has been designed, developed and deployed. Fully dressed, high beta, elliptical, super conducting RF cavity AES-010, from Fermilab, USA was tested at HTS facility, RRCAT successfully with the help of this SSPA. RF output power of 32 kW from SSPA is obtained by combining two nos. of 16 kW SSPAs using a lossless, junction type, 2-way RF Power Combiner with power handling capacity of 70 kW. This Power Combiner has two inputs and one output in EIA 6-1/8" rigid coaxial line interface. To achieve 16 kW of RF output from single SSPA Rack, 48 nos. of 500-watt solid state RF amplifier modules have been combined by novel 48-way RF Power Combining-Power Dividing Structures at 650 MHz. These lossless structures are based upon radial power combining/dividing topology. This paper discusses detailed RF design methodology including design of input impedance matching sections, design of shorting stub for amplitude compensation, thermal management, and RF measurements for the 70 kW 2-way RF Power Combiner, 48-way RF Power combiner and 48-way RF Power Divider.

INTRODUCTION

SSPA technology has numerous advantages over their counterpart i.e. traditional vacuum tubes namely absence of high voltage, graceful degradation, modular and scalable architecture, cleaner RF power and higher reliability. In RRCAT, various SSPAs have been designed and developed indigenously [1][3][6]. Four nos. of CW 60 kW-505.8 MHz SSPAs have been deployed in INDUS-2 and running in round the clock mode for more than past ten years. 150 kW-325MHz pulsed RF SSPA have been developed for energizing Radio Frequency Quadrupole (RFQ). 32kW and 40 kW-650 MHz CW SSPAs were also developed as a in kind contribution to FERMILAB, USA for R&D phase of PIP-II project. Recently, 32 kW-650 MHz CW SSPA has been also deployed at HTS facility, RRCAT for characterization of superconducting RF cavities. As RF output power from single RF MOSFET device is quite moderate (of the order of hundreds of watts only) development of compact, low loss, cost effective and efficient RF power combining

Figure 1: 48-way RF Power Combiner at 650 MHz

Figure 2: 48-way RF Power Divider at 650 MHz

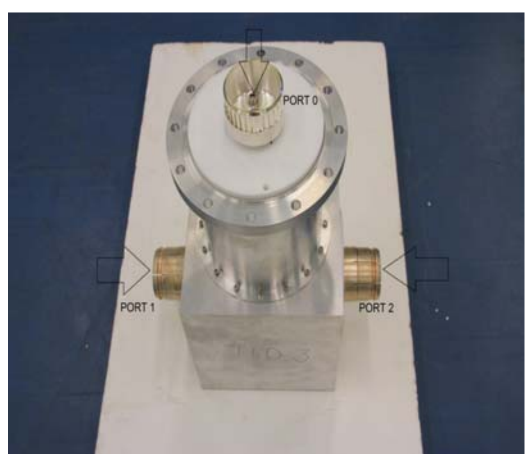

Figure 3: 70 kW-650 MHz, 2-way RF Power Combiner

* alok_gupta@rrcat.gov.in

DESIGN

Several symmetrical, lossless and radial power combining and power dividing RF structures have been reported by us at different frequency of operations up to 16 nos. of input/output ports [4][5][7]. Asymmetrical RF power combining-power dividing RF structures with 40 nos. of input/output ports for pulsed RF applications were also reported for 150 kW-325 MHz SSPA system [2]. Asymmetrical RF power combiner and RF power divider with 48 nos. of input/output ports have been successfully developed and characterized for CW 32 kW-650 MHz with efficient water-cooling mechanism.

Being an asymmetrical architecture, coupling coefficients of both EM planes (24 nos. of RF inputs on either side of radial line) were matched in amplitude by altering EM field suitably in one side of radial line. Size of radial line was also optimized to achieve maximum junction impedance with 48 nos. of 50-ohm inputs/outputs. Cascaded stepped impedance matching sections were designed for matching of radial line junction to system impedance of 50 ohm for wider band match. The 48-way power combiner has output on 6 1/8-inch coaxial line interface and has 48 nos. of RF inputs on N-type connectors. 48-way RF power divider has its inputs as well as output at N-type connector. Complete 3-dimensional RF structures for the 48-way RF power combiner and power divider were modelled in ANSYS make High Frequency Structure Simulator (HFSS) and optimized for return loss better than 30 dB with bandwidth better than 20 MHz. It has been also ensured that phase offset between coupling coefficients of both EM planes remains identical for 48-way power combiner as wells for 48-way power divider. Hence, by using 48-way power divider and power combiner in cross fashion, power combing efficiency better than 97% has been successfully achieved in 32 kW-650 MHz SSPA system. 70 kW, 2-way RF power combiner at 650 MHz is a lossless, symmetrical and junction type architecture with inputs as well output on 6 1/8-inch coaxial line interface. Shape of junction of two inputs has been designed to ensure smooth transition of impedances with optimum distance from outer conductor to ensure minimum electric field at corners. Compact impedance matching sections have been designed to match the junction impedance to system impedance of 50 ohm with minimizing weight and maximizing bandwidth of the RF structure. Complete 3-dimensional structure of 2-way RF power combiner has been modelled in HFSS and optimized for return loss better than 30 dB.

For efficient heat removal from centre conductor of 48-way RF power combiner and 70 kW, 2-way RF power combiner, centre conductor has been physically shorted with outer conductor with help of a shorting stub. A water cooled heatsink has been fitted at the location of shorting stub with suitable bolts. In this way, heat generated at centre conductor flows towards outer conductor with water cooled sink. Substantial decrease in temperature of centre conductor have been observed with this water-cooling mechanism ensuring increased life span and higher reliability for these RF structures.

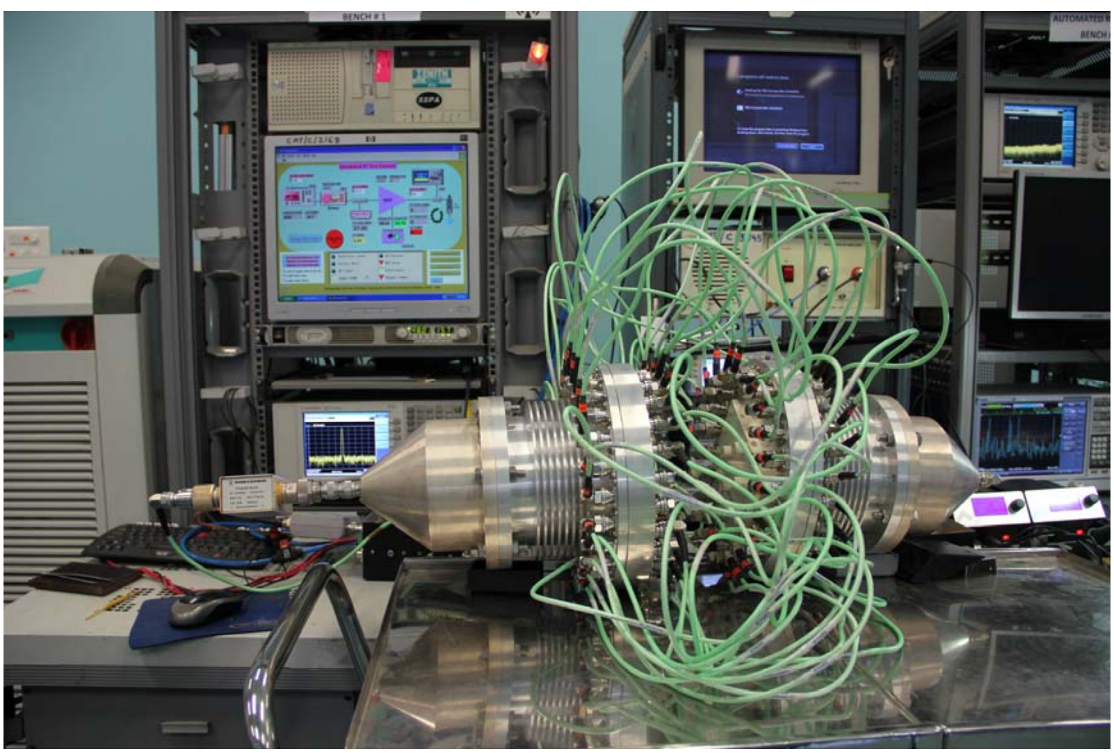

Figure 4: Insertion loss measurement setup for 48-way RF power combiners assembly at high power

MEASURED PERFORMANCE

48-way RF power combiner and 48-way RF power divider structures were successfully fabricated and characterized using Rohde & Schwarz (R & S) make vector network analyser (VNA) ZNB-4. Output port for 48-way RF power combiner and input port for 48-way RF power divider has been designated as Port zero (0). Coupling coefficients (sN0, N=1 to 48) were also measured for both these structures and tabulated in Table-1 and Table -2 for power combiner and power divider respectively. To measure insertion loss for these RF structures, two nos. of 48-way RF power combiners were connected back-to-back in cross configuration with the help of 0.75 m coaxial RF cables. R & S make NAP power sensor were deployed at both ends of the assembly. 500 watt of RF power was fed to one end of this divider-combiner assembly as shown in Fig.4. Difference in readings of these power sensors gives us the insertion loss of complete assembly. Insertion loss of RF cables is subtracted (i.e. 0.25 dB) from this value to get the insertion loss of RF power combiners. S-parameters of the 70 kW, 2-Way RF power combiner were also measured with the help of VNA and have been tabulated in Table-3.

Table 1: s-parameters of 48-way RF Power Combiner

Sr. No.	s-parameters	Magnitude (dB)	Phase (degree)
1.	s00	-21.5	16.2
2.	sN0 (N= 1 to 24)	16.92±0.1	60.4±0.9
3.	sN0 (N= 25 to 48)	16.75±0.1	114.7±0.5

Table 2: s-parameters of 48-way RF Power Divider

Sr. No.	s-parameters	Magnitude (dB)	Phase (degree)
1.	s00	-20.2	37.1
2.	sN0 (N= 1 to 24)	16.95±0.1	50.9±0.8
3.	sN0 (N= 25 to 48)	16.78±0.1	105.2±0.6

Table 3: s-parameters of 2-way RF Power Combiner

Sr. No.	s-parameters	Magnitude (dB)	Phase (degree)
1.	s00	-24.6	86.3
2.	s10	-3.12	-28.1
3.	S20	-3.09	-26.9

CONCLUSION

70 kW 2-way RF power combiner, 48-way RF power combiner and 48-way RF power divider structures at 650 MHz were designed, realized, and characterized as a part of 32 kW-650 MHz SSPA system. Excellent amplitude and phase symmetry have been measured between input/output ports for these structures, which is an absolute necessity for efficient power combining. 70 kW 2-Way RF power combiner have exhibited return loss better than 24 dB. Return loss better than 20 dB was measured for 48-way power combiner as well as 48-way RF power divider structures. Insertion loss less than 0.1 dB was measured for 48-way power combiner, ensuring power combing efficiency to be better than 97%. Measured RF performance is in good agreement with theoretical and simulated results for all these RF structures. Successful development of these compact and cost-effective RF structures has ensured that wall plug efficiency and spatial layout of 32 kW SSPA remains within the constraints, as desired for our particle accelerator programs

REFERENCES

[1] Akhilesh Jain, Deepak Kumar Sharma, Alok Kumar Gupta, kriti Pathak and Mahendra Lad. “High-power solid-state amplifier for superconducting radio frequency cavity test facility” Rev. Sci. Instrum., Vol. 92, no. 034704, p. 1-11, Mar. 2021.

[2] Alok Kumar Gupta, Akhilesh Jain, Ravi Kant Patel and Joseph Tharayil “Design and development of 40-port coaxial line based radial power combiner at 325 MHz” Indian Particle Accelerator Conference INPAC 2018, RRCAT Indore, Jan., 9-12, 2018.

[3] Akhilesh Jain, Deepak Kumar Sharma, Alok Kumar Gupta, kriti Pathak and Mahendra Lad. “150 kW Pulse Solid State Amplifier for Radio Frequency Quadrupole Application” IEEE Transactions on Nuclear Science, Vol. 57, no. 11, p. 2303-2310, Nov. 2020.

[4] Alok Kumar Gupta, D.K. Sharma, Akhilesh Jain, and M.R. Lad “Power combining scheme for 50 kW pulsed Solid Sate RF power amplifier unit at 325 MHz”, in InPAC 2015.

[5] Akhilesh Jain, Alok Kumar Gupta, D.K. Sharma, P. R. Hannurkar, and S.K. Pathak “Design and analysis of high power radial multiway combiner”, International journal of Microwave and Wireless technology, Vol. 06, Issue 01, Feburary 2014.

[6] Akhilesh Jain, P. R. Hannurkar, D. K. Sharma, A. K. Gupta, A.K. Tiwari, M.Lad, and R. Kumar, P.D. Gupta and S.K. Pathak “Design and characterization of 50 kW solid-state RF amplifier” International Journal of Microwave and Wireless Technologies, vol. 4, no. 6, p. 595 603, Dec 2012.

[7] Alok Kumar Gupta, Deepak Kumar Sharma, Akhilesh Jain, and P. R. Hannurkar, “High Power, lossless, rigid line 2-Way RF power Combiners”, INPAC 2011.

STUDY AND DEVELOPMENT OF VARIOUS DISSIMILAR METAL JOINTS OF SUPERCONDUCTING RADIO FREQUENCY CAVITIES

Syed Moulali[1], Vijaya Kumar V[1], Tilak Maurya[1], Ashish Singh[1], Ajay Yedle[1], Manish Bagre[1], P Ganesh[2], Vikas Jain[1], Sanjay Chouksey[1], Purushottam Shrivastava[3],
[1]Superconducting Cavities Developement Division, [2]LMPD Division, [3]Proton Accelerator Group, Raja Ramanna Centre for Advanced Technology, Indore, India.

Abstract

The Superconducting Radio Frequency (SCRF) cavities are a prominent element of the modern linear proton accelerators. The SCRF bare cavities are fabricated mostly with high RRR Niobium (Nb), and except the flanges and transition spools, were made of Niobium-Titanium (Nb-Ti) material. The vessel for dressing/jacketing of the cavity, is fabricated from Titanium (Ti). For joining the Nb cavity to the Ti vessel, a transition material of Nb-Ti is used in between the two dissimilar materials. The welding of Nb to Nb-Ti and Nb-Ti to Ti material were challenging for developing a desired weld joint of these dissimilar materials. This is mainly due to wide difference in the material thermal properties between Nb and Ti. The developments of these joints were carried out in EB and TIG by optimizing the EB and GTAW heat source offset to make stable joints. This paper describes the study of these dissimilar material's metallurgical compositions, development & optimization of EB welding, TIG welding parameters, micrographs of the weld joints, fusion zone composition and hardness etc.

INTRODUCTION

RRCAT is developing high beta (HB) 650 MHz five-cell cavities for PIP-II project under Indian Institution and Fermilab collaborations (IIFC). The bare niobium cavities were fabricated using an in-house EBW machine and the jacketing was carried out by TIG welding in a controlled environment glove box. A schematic of the bare five-cell cavity is shown in the Fig. 1. The helium vessel was fabricated with Ti. The alloy of Nb-Ti was used in the bare cavity, due to its mechanical properties and as a transition between the Nb and Ti materials to make joints of Nb to Nb-Ti and Nb-Ti to Ti. Also, these dissimilar materials have close co-efficient of linear expansion and so will not generate high mechanical stress, during cavity cool down from 300K to 2K. These materials have complete solubility to each other as per phase diagram [1]. If the concentration of the weld zone of Nb-Ti to Nb is not homogenous, a small dissipation in the weld could be heat it up above the critical temperature. This depends on the Nb concentration in the Nb-Ti. Also, if Nb content becomes below 40% in weld joint composition, it may form an inter metallic phase in the weld joint composition. The inter metallic leads to low ductility/toughness. In order to retain the joint properties, composition as close to the base metal, proper welding techniques are need for the development of these dissimilar metal weld joints. A large no of experiments were conducted on the samples to optimise and develop the dissimilar metal joints followed by micrograph studies of weld fusion zones for compositional variation of Nb-Ti and Ti diffusion in Nb grain boundaries by using Energy Dispersive X-ray Spectroscopy (EDX). The hardness was also measured on HV 0.2 scale across the fusion zone to parent metal.

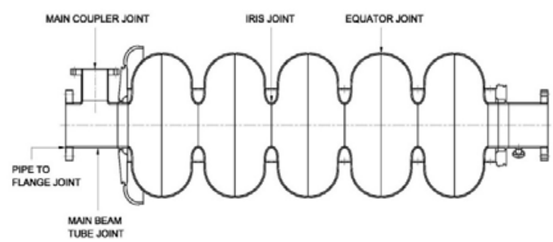

Figure 1: Bare five-cell SRF cavity

MATERIAL AND WELD JOINTS

The dissimilar materials were Niobium (RRR > 300), Nb45% -Ti55% and Ti-Gr-2. The materials properties of these materials are shown in Table 1 [2].

Table 1: Material properties

Properties	Nb	Nb- 55 Ti	Ti Gr-2
Melting point (^{0}C)	2447	1900	1668
Density (g/cc)	8.57	5.7	4.51
Thermal Conductivity (W/m-K)	54	10	16.4
Specific heat (J/g-°C)	0.26	0.427	0.523
Co-efficient of liner expansion (μm/m-°C)	7.3	9.03	8.9
Diffusivity (mm/s^2)	23.8	14	9
Tensile strength (MPa)	110	546	344

The large difference in melting temperatures and thermal conductivity makes a challenge for developing a good welded joint of these dissimilar metals. Which can lead to highly asymmetric thermal fields in the weld region. In order to obtain a symmetric weld, the beam should have an offset toward the metal with the higher melting point.

* msyed@rrcat.gov.in

The study was conducted on test coupons of Nb, Nb-Ti and Ti weld joint configurations similar to the actual bare and dressed cavity joints, as shown in Fig -2. The welding of all the joints were carried out in the in-house RRCAT 15kW EBW machine [3]. The integration of components of the dressed cavity (Nb-Ti to Ti) were performed by TIG welding in a glove box with controlled atmosphere having O_2 < 20PPM and relative RH in PPM level [4].

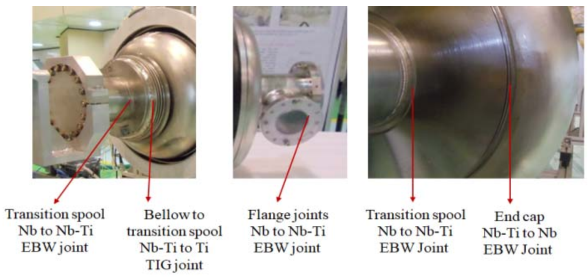

Figure 2: Dissimilar metal joints in SRF cavity.

EXPERIMENTAL SETUP WELDIGN PROCEDURE

Samples of Nb to Nb-Ti, Nb-Ti to Ti of 4 mm thickness with butt joint were prepared. The EB welding was carried out changing the beam off-set as shown in the Fig-3. The EB welding was performed at 110kV and welded standard procedure of tacking, seal pass and full welding pass form. The seal weld is approx. half of full weld current and it act as a pre-heat in the metal weld joint.

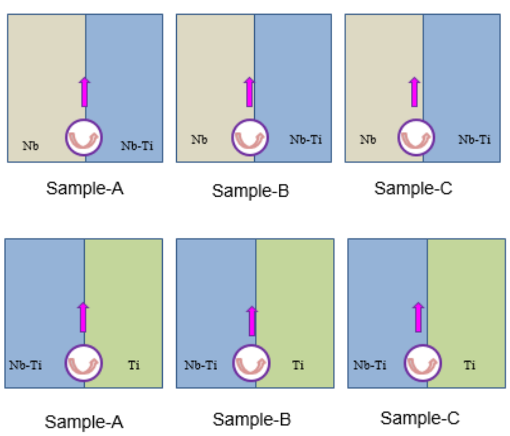

Figure 2: EB weld joint and beam offset for Nb-Nb-Ti joint (top) and NbTi -Ti joint (bottom)

The beam offset details are as shown in Table 2. S_A-0 indicates sample-A: 0-beam exactly on the joint.

Table 2: Heat source offset comparison

Metal joint	Process	Heat source offset on samples (S) in "mm"
Nb to Nb-Ti	EBW	S_A- 0, S_B- 0.2, S_c- 0.5 in Nb
Nb- Ti to Ti	EBW	S_A- 0, S_B- 0.15, S_c- 0.3 in Nb
Nb-Ti to Ti	TIG	towards Nb-Ti side 0.3 mm

The TIG welding of Nb-Ti to Ti falls under the category of pressure boundary joint and weld as per code [5]. Hence, Ti-Gr2 filler metal was used. During welding TIG torch was kept towards in the Nb-Ti side along with the filler resulting melting of the filler and parent metal. The joint configuration of the sample was single bevel with root gap of 0.5 mm. Which simulates the bellow to transition joint on the cavity as shown in Fig. 2.

MACROGRAPH STUDY

Micrographs of the welded samples were prepared by EDM wire-cut from the weld section followed by mechanically polishing. After polishing, cross sectional images of the weld joint acquired with microscope. The images are as shown in the Fig. 3.

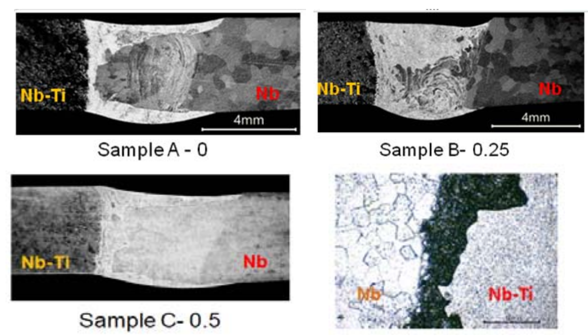

Figure 3: Macrographs of weld joints sample A to C and View of Heat affected zone Nb side of Nb-Ti to Nb.

Samples A, and B show partial melting of Nb in to Nb-Ti and sample C shows the homogeneous mixture of Nb in Nb-Ti metal. The micro graphs of the images of the Nb-Ti to Ti joint are as shown in Fig. 4.

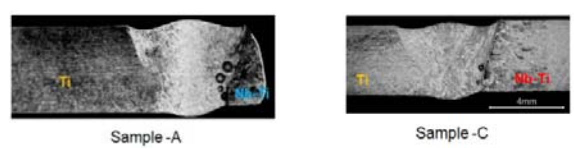

Figure 4: EB welding joint of Nb-Ti to Ti

The sample A shows weld porosity near the fusion zone line near the fusion zone line on the Nb-Ti side (dark circles). The sample-C shows complete fusion of Nb-Ti with Ti. The macroscopic image of the TIG welded joints shows the three distinct layer of complete fusion zone without any defects as show in Fig-5.

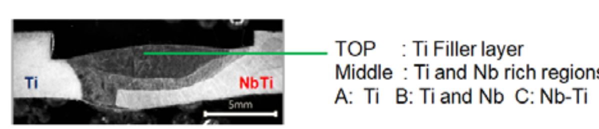

Figure 5: TIG welding joint of Nb-Ti to Ti

SEM- EDX STUDY

The SEM-EDX elemental characterization is also performed in weld fusion zones for composition of the Nb, Ti and Ti diffusion in the grain boundaries of Nb in all the dissimilar metal joints of Nb to Nb-Ti, Nb-Ti to Ti. The Images are acquired with help of SEM and selected scan area covering the heat affected zones (HAZ) on the Nb side. No titanium contamination is measured on the Nb side of the weld for all the samples analysed. The results and scan area of one of the joint of Nb to Nb-Ti sample-c is shown in the Fig-6.

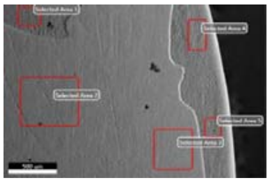

eZAF Smart Quant Results

Element	Weight %	Atomic %
NbL	48.7	32.9
TiK	51.3	67.1

Figure 6: EDX image and composition

The composition variation in the weld fusion zone in samples of Nb- Nb-Ti with 0, 0.25 mm offset and Nb-Ti to Ti 0, 0.15 mm was observed. The EB beam offset of 0.5 mm in Nb- Nb-Ti and 0.3 mm offset in the Nb-Ti to Ti joints shows a homogeneous composition. Similarly, in the TIG welding samples, fusion zone was analysed in all the three layers and it was found that Nb concentration ranged from 20-25% as shown in Fig-7. Also the elemental composition performed for a selected scan area covering the HAZ on the Nb side of Nb to Nb-Ti joint. No titanium trace contamination is measured on the Nb side of the weld in all the analysed samples.

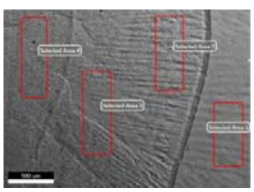

eZAF Smart Quant Results

Element	Weight %	Atomic %
AlK	0.0	0.1
NbL	24.6	14.4
TiK	75.4	85.5

Figure 7: EDX image and composition

HARDNESS STUDY

The Vickers hardness test was performed with 200g weight ($HV_{0.2}$) on the samples of weld fusion zone.

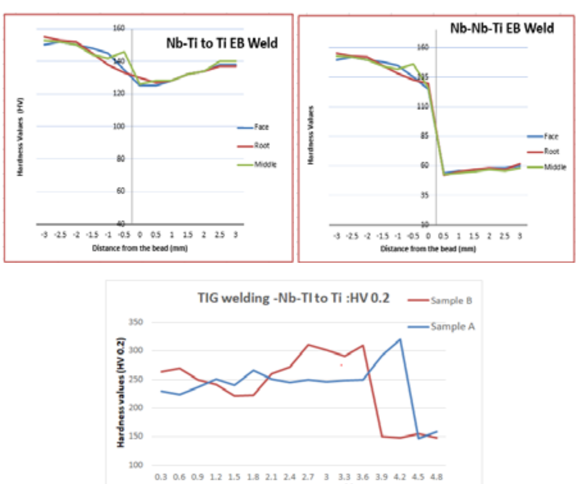

Figure 8: Microhardness of EB and TIG welding samples.

We measured the micro hardness of the samples across weld area to parent material below the face of weld fusion zone, middle of the weld fusion zone, and root of the fusion zone. The plots of the all the samples are as shown in Fig -8. The hardness of the Nb to Nb-Ti joints in all the samples varyed in the range of 120-55 HV in fusion zones and for Nb-Ti to Ti in the range 130-140 HV and the hardness was close to the parent materials. Similarly, the measured hardness of the centre of the of fusion zone of Nb-Ti to Ti of TIG welding samples ranged from 147-300 HV.

CONCLUSION

The welding process of the different material associated with five-cell bare cavity and dressed/jacketing joints was developed in EB and TIG welding. The beam offset plays a vital role in making sound weld joint. It has been observed that micrographs and SEM-EDX analysis shows that the beam offset of 0.5 mm towards Nb in Nb-Nb-Ti produces homogeneous composition in the fusion zone and retain the parent material properties. Similarly, in Nb-Ti to Ti the beam offset of 0.3 mm towards Nb-Ti side make a homogeneous composition and a defect free joint. When TIG samples were welded in control environmental glove box of Nb-Ti to Ti by using Ti filler, the TIG torch towards Nb-Ti side makes a defect-free joint. Seven numbers of five-cell 650MHz bare cavities have been successfully welded using these techniques. All the bare cavities were leak tested at liquid nitrogen temperature and qualified for a vacuum leak rate of 1E-10 mbar l/s. It is demonstrated that the all the weld joints were safe at cryogenic temperatures.

ACKNOWLEDGEMENT

We would like to express my sincere thanks to Mr. Abhijit Chowdhury, Smt. Rashmi Singh, P Ram Shankar, Mr. P. Kamble, Mr. Anuj Kumar, Mr. Raju Adbol, Mr. Salilesh Maratha for their technical support.

REFERENCES

[1] Matthias Bonisch thesis "Structural properties, deformation behaviour and thermal stability of martensitic Ti-Nb alloys.
[2] ATI Wah chang USA for material properties
[3] Manish, V Jain, S. Moulali et.al "Fabrication Experience of five-cell HB 650 (β=0.92) Bare SCRF cavities" InPAC 2019
[4] Vikas Jain, M. Bagre, S. Moulali "Progress on HB 650 MHz superconducting cavity dressing and its infrastructure" InPAC 2019.
[5] Moulali et.al. "Dressing Joint Qualification of High Beta 650 MHz five-cell SCRF cavity", proceedings of DAE-BRNS2022.ASME Boiler & Pressure Vessel Code.
[6] N. Valverde Alonso, S. Atieh, I. Aviles Santillana et.al "Electron beam welding and vacuum brazing characterization for srf cavities" Proceedings of LINAC2014, Geneva, Switzerland.

THERMAL CHARACTERISTICS AND FREQUENCY TUNING METHODOLOGY FOR 325 MHz RFQ STRUCTURE

N. K. Sharma, Anurag Chaturvedi, G.V. Kane, Vijendra Prasad, Purushottam Shrivastava
Raja Ramanna Center for Advanced Technology, Indore

Abstract

RRCAT is involved in the development of a 3 MeV, 325 MHz Radio Frequency Quadrupole (RFQ) structure for high energy proton accelerator. During operation, Radio Frequency (RF) induced heating results in temperature rise, deformations and subsequent frequency shift from designed value. A water cooling scheme is designed to dissipate RF heat from RFQ structure. Beside heat removal, cooling water will also be used to tune the cavity frequency close to the designed value. Detailed three dimensional multi-physics finite element analyses of RFQ structure have been carried out for various duty factors. Parametric studies are performed to investigate the effect of cooling water temperatures on RFQ frequency. Based on thermal characteristics of RFQ, the cooling water temperatures will be adjusted to achieve the designed frequency during steady state operation. Results of numerical studies and frequency tuning methodology for RFQ are presented in the paper.

INTRODUCTION

A four vane integrated 325 MHz, 3 MeV RFQ structure has been designed to serve as a front end component for H^- injector linac. RFQ is an extremely effective structure following ion source, which is capable of performing beam bunching, focusing and imparting acceleration simultaneously.

MULTIPHYSICS SIMULATIONS

Three dimensional multi-physics simulations have been performed to design a water cooling scheme for RFQ structure. Flowchart for proposed multi-physics simulation methodology has been shown in fig. 1.

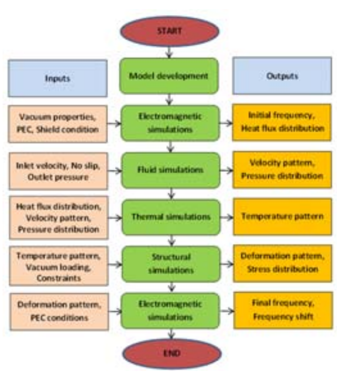

Fig.1: Multi-physics Analysis Methodology

#navneet@rrcat.gov.in

Model Development

Three dimensional model of RFQ has been developed within ANSYS code using ANSYS Programming Development Language (APDL) scripts. Total length of RFQ is 3.48 m, which has been divided in three segments of nearly equal lengths. Each segment consists of 16 cooling channels, 8 on vanes and 8 on cavity walls. Fig. 2 shows the model developed for second segment of RFQ structure.

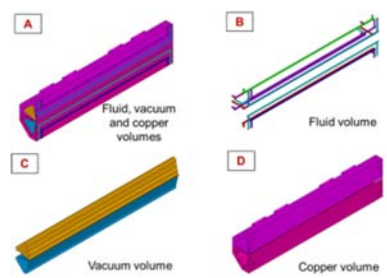

Fig.2: Model Development

Electromagnetic Simulations

High frequency electromagnetic simulations have been performed for vacuum volume of RFQ structure. During simulations, relative permittivity and relative permeability for vacuum are defined as unity. The Perfectly Electric Conductor (PEC) and shielding conditions have been applied at vacuum-RFQ walls interfaces. Magnetic field contours for RFQ are shown in fig. 3. RFQ frequency and quality factors have been evaluated as 324.988 MHz and 10340 respectively.

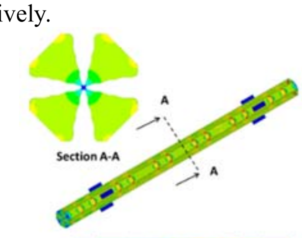

Fig.3: Magnetic Field Distribution

Fluid Simulations

Computational Fluid Dynamics (CFD) simulations have been performed for fluid volume of RFQ structure. Flow velocities of 2.0 m/s with inlet water temperatures of 20 ^{0}C and zero gauge pressure outlet conditions are applied for cooling channels. Mass and momentum equations have been solved using Semi-Implicit Method for Pressure Linked Equations (SIMPLE) algorithm.

Velocity and pressure profiles along cooling channels have been evaluated. Pressure distribution for cooling channels is shown in fig. 4. Maximum pressure drop has been evaluated as ~18kPa.

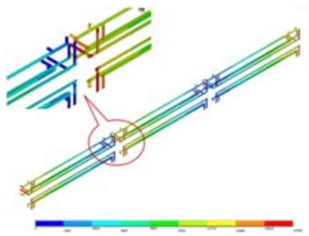

Fig.4: Pressure Distribution

Thermal Simulations

Heat fluxes from electromagnetic simulations and velocity and pressure profiles computed from fluid simulations are applied as inputs for thermal simulations. Resultant temperature profiles for RFQ are shown in fig.5. Maximum temperature of RFQ has been evaluated ~ 21.7 °C close to the vane cut back regions.

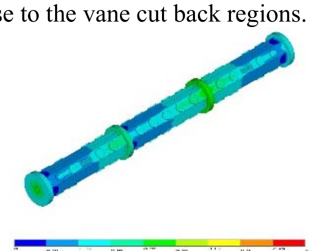

Fig.5: Temperature Distribution

Structural Simulations

Temperature results computed from thermal simulations have been applied as input loads for structural simulations. Beside thermal loads, the vacuum loading is also applied on RFQ surfaces. Resultant displacements for RFQ are shown in fig. 6. Maximum displacement has been evaluated as ~29 μm for RFQ structure.

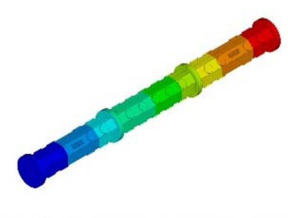

Fig.6: Displacement Pattern

Based on displacements computed from structural simulations, the cavity geometry is updated to model deformed geometry. Electromagnetic simulations for updated geometry are performed and frequency shift with respect to initial frequency has been evaluated as ~ -15 kHz. Frequency shift will be minimized by adjusting cooling water temperatures predicted by tuning methodology.

FREQUENCY TUNING METHODOLOGY

Shifts in cavity frequency can be attributed to various aspects, which can be summarized by eq. 1.

$$\Delta f_{cavity} = \Delta f_{fab.} + \Delta f_{tuner} + \Delta f_{power} + \Delta f_{water} \qquad (1)$$

Frequency shifts due to fabrication and assembly errors are nullified by inserting slug tuners inside RFQ cavity. Based on the low power RF measurement results, slug tuners are machined to provide specific tuner insertion depth and assembled with RFQ structure. Once the tuning is completed, the $(\Delta f_{fab.} + \Delta f_{tuners})$ contribution would be zero for frequency shift. Therefore, the frequency shift now may be defined as,

$$\Delta f_{cavity} = \Delta f_{power} + \Delta f_{water} \qquad (2)$$

Three dimensional multi-physics simulations for frequency shifts have been carried out at different duty factors. The variation is evaluated linear in nature and can be represented with eq. 3.

$$\Delta f_{power} = -1.38 \text{ DF} - 11 \qquad (3)$$

In above expression, Δf_{power} represents the shift in RFQ frequency due to RF power and DF is the duty factor (%) for RFQ operation.

Multi-physics simulations have also been carried out to explore the impact of cooling water temperatures on frequency shift. It has been evaluated that RFQ frequency varies linearly with cooling water temperatures. RFQ frequency sensitivity with cooling water temperatures can be expressed by eq. 4 and eq. 5 respectively.

$$\partial f / \partial T_V = -29.94 \text{ kHz/°C} \qquad (4)$$

$$\partial f / \partial T_W = 24.71 \text{ kHz/°C} \qquad (5)$$

In these expressions, $\partial f / \partial T_V$ indicates the change in RFQ frequency when vane water temperatures are varied and wall water temperatures are kept constant. Similarly, $\partial f / \partial T_W$ presents the change in RFQ frequency when wall water temperatures are adjusted and vane water temperatures are kept constant.

The change in RFQ frequency can be brought about in a predictable manner by varying vane and wall water temperatures. The change in cavity frequency by varying cooling water temperatures can be defined as,

$$\Delta f_{water} = (T_V - T_{VR})(\partial f / \partial T_V) + (T_W - T_{WR})(\partial f / \partial T_W) \qquad (6)$$

Parameters with "R" subscript present the reference values for vane and wall water temperatures. In our case the values for T_{VR} and T_{WR} are 20 ^{0}C.

Substituting expressions from eq. 3 and eq. 6 in eq. 2,

$$\Delta f_{cavity} = (-1.38 \text{ DF} - 11) + (T_V - T_{VR})(\partial f / \partial T_V) + (T_W - T_{WR})(\partial f / \partial T_W) \qquad (7)$$

Based on eq. 7, vane and wall water temperatures can be adjusted to attain near about zero frequency shift using following three options.

$$T_V = T_{VR} - \frac{1}{(\partial f/\partial T_V)}[(T_W - T_{WR})(\partial f/\partial T_W) - (1.38\,DF + 11)] \quad (8)$$

$$T_W = T_{WR} - \frac{1}{(\partial f/\partial T_W)}[(T_V - T_{VR})(\partial f/\partial T_V) - (1.38\,DF + 11)] \quad (9)$$

$$T_V = T_W = \frac{1}{\left(\frac{\partial f}{\partial T_V}+\frac{\partial f}{\partial T_W}\right)}\left[\frac{\partial f}{\partial T_V}T_{VR} + \frac{\partial f}{\partial T_W}T_{WR} + (1.38\,DF + 11)\right] \quad (10)$$

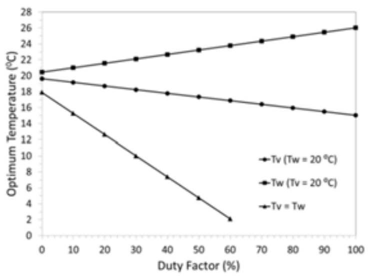

Fig.7: Optimum water temperatures for various duty factors

Optimum values of vane and wall water temperatures for three options have been shown in fig. 7. However, with the change in cooling water temperatures, the deformations in RFQ cavity may increase. These deformations may result a significant impact on RFQ accelerating and focusing functions. Therefore, among three alternatives, the preferred approach would be that only, which results minimum deformations for RFQ cavity. Deformations produced in RFQ cavity for 3% duty factor operation are shown in fig.8. It can be concluded from results that changing vane water temperatures with constant wall water temperatures will result least deformations in RFQ cavity and therefore will be utilized for frequency tuning.

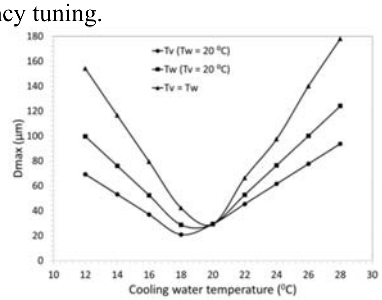

Fig.8: Deformations with change in cooling water temperatures

VALIDATION

Benchmarking of multi-physics simulations for RFQ has been performed with experiments. A cold model of RFQ segment in aluminum was designed, manufactured and assembled for testing. Measurements have been performed to assess the impact of cooling water temperatures on frequency shift. The test set up utilized for measurements is shown in fig. 9.

Fig.9: Experimental setup for frequency sensitivity measurements

Vane water temperatures are varied from 14 ^{0}C to 26 ^{0}C and cavity frequency has been measured for each case. 3-D multi-physics simulations have been carried out for evaluating frequency shift in RFQ with change in vane water temperatures. Fig.10 shows comparison of experimental and simulation results for frequency sensitivity of RFQ with cooling water temperatures.

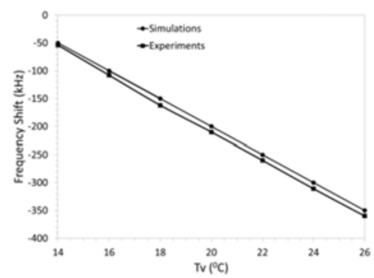

Fig.10: Comparison of simulations and experimental results for frequency shift

CONCLUSIONS

A water cooling scheme has been designed for 325 MHz, 3 MeV RFQ structure. Apart from heat removal, water cooling will be utilized to restore the resonating frequency of RFQ during high power operation. A frequency tuning strategy has been developed and ideal cooling water temperatures which results close around zero frequency shift have been evaluated. Benchmarking of results has been carried with experiments conducted on a prototype RFQ structure.

REFERENCES

[1] N. K. Sharma, C. P. Paul, S. C. Joshi, G. V. Kane and A. Chaturvedi, “Coupled 3D multiphysics analysis of 325 MHz ISNS RFQ structure”, Nuclear Instruments and Methods in Physics Research Section A: Accelerators, Spectrometers, Detectors and Associated Equipment, 2019, 937, 59-71

[2] N. K. Sharma, C. P. Paul, S. C. Joshi, G. V. Kane and A. Chaturvedi, “Multiphysics Analysis for Thermal Management of a 3 MeV, 325 MHz Radio Frequency Quadruploe Accelerator for Indian Spallation Neutron”, Journal of Electromagnetic Analysis and Applications, 2019, 11, 55-78

RF CHARACTERIZATION OF 32 kW AND 40 kW, 650 MHz SOLID STATE RF POWER AMPLIFIERS

Kriti Pathak*, Deepak kumar Sharma, Alok kumar Gupta, Akhilesh Jain and Mahendra Lad

Raja Ramanna Centre for Advanced Technology, Indore, M.P., India - 452013

Abstract

This paper presents RF characterization and high-power RF measurements of 32 kW and 40 kW amplifier systems working at 650 MHz which are developed under R& D phase, as deliverables to Fermi Lab, USA. These amplifiers were characterized and tested for required specifications at rated RF power on dummy load. These high-power amplifiers comprise around hundred numbers of power amplifier modules; similar numbers of directional RF power sensors, 48/64-way power dividing and combining structures, cooling water distribution system, RF protection unit, electrical power sub-system etc. Along with these, control and interlock sub-system is there to ensure proper functioning of various sub-systems. Both 32 kW [1] and 40 kW amplifiers are realized in the form of two racks, outputs of which are combined to achieve the rated power. Divide and combine strategy is followed in both the amplifiers wherein the input RF is divided and fed to individual racks. Each rack of 32 kW amplifier consists of forty-eight numbers of 500 W power amplifier modules and outputs of these are combined using a 48-way RF power combiner. In 40 kW amplifier, 64-way RF power combiner is used. Measurement sequence includes cold testing, output measurement set up calibration at 1 kW RF power and eventually high-power testing [2]. In cold testing different checks like water leakage check, electrical testing, assembly and integrity check and control and interlock functionality check are performed. High power testing includes amplifier gain and efficiency measurement, spectral response measurement, bandwidth measurement, group delay measurement and radiation mapping. This measurement sequence is followed for individual racks first. After optimizing output power of individual racks, outputs of these racks are combined using a 2-way RF power combiner and high-power testing is performed along with the configuration of alarm and trip limits for RF power and amplifier heat-sink temperature. Developed amplifiers were tested in pulsed mode also and suitable pulsed RF measurements were carried out. In addition to these tests, amplifiers performance was observed for increased inlet cooling water temperature as per requirement of Fermi Lab specifications. Spectral response of both these amplifiers was measured where the harmonic content was found below -30 dBc and spurious below -55 dBc. Radiation mapping in the complete amplifier zone within a distance of 1 m from the amplifier was carried out with radiation maxima inside the rack within prescribed safety limits. Amplifiers were tested and characterized successfully at rated power with AC to RF efficiency better than 40 %.

* kpathak@rrcat.gov.in

INTRODUCTION

Particle accelerators are used worldwide in R&D, medical and industrial applications. SSRFA, owing to various advantages over its vacuum tube counterpart, are being used extensively in these accelerators. RRCAT, DAE has collaborated with Fermi Lab, USA for Proton Improvement Plan-II (PIP-II). PIP II plan aims to build 800 MeV superconducting (SC) linear accelerator (LINAC) which will provide powerful, high-intensity proton beams to carry out the laboratory's experiments for particle physics research. RRCAT will be designing and developing large numbers of 40 kW and 70 kW solid-state RF power amplifiers at 650 MHz for use in low-beta and high-beta elliptical (LB650 & HB650) structures respectively [3].

Figure 1: 40 kW SSRFA installed in Fermi Lab

One 32 kW RFPA and one 40 kW RF power amplifier (see Fig. 1) have already been supplied to Fermi Lab which are being used in their cryo test facility. 40 kW SSRFA comprises two 20 kW amplifier units (Master and Slave unit), each of which consists of a 64-way RF divider and combiner, 20 PA modules (4x500 W), 40 directional power sensors; along with some other requisites. Both these units are similar except for the RT controller and control hardware which is placed in the Master unit only. The final power of 40 kW is achieved by combining outputs of both these 20 kW units with the help of a 2-way high power combiner (see Fig. 2).

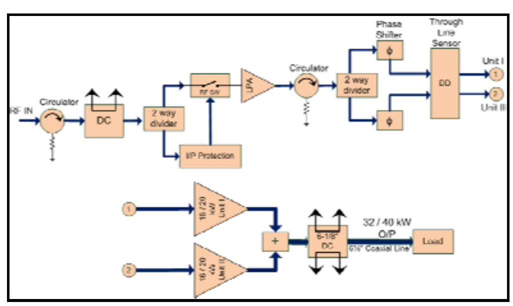

Figure 2: Block diagram showing 32 kW/40 kW SSRFA architecture

The combined signal thus obtained, is passed through a 6-⅛″ dual directional coupler (DC) for RF power measurements. The RF drive input to each of the 20 kW units is provided by a low-level protection and driver unit. In each unit, the output ports of the 64-way radial divider are connected to the input of the respective 500 W power amplifiers (PA), using flexible coaxial cables (see Fig. 3). The amplified signals, from a cluster of 64 PAs, are fed to the 64-way combiner, through dual-channel power sensors. These sensors are meant for directional power measurement of each PA. Being a dual channel each sensor serves two PAs. One 500 W PA (identical to other PAs) is used as a driver in each of the 20 kW units.

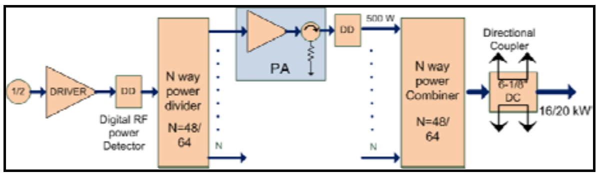

Figure 3: Block diagram of 16 kW/20 kW unit

The 32 kW SSRFA is similar in architecture except for the 64-way radial divider/combiner which is replaced by 48-way radial structures. Here the two 16 kW units will be combined to generate 32 kW output.

To evaluate the RF performance of the developed SSRFA, various measurements have been performed which will be described in detail in this paper.

MEASUREMENT PROCEDURES

Different types of measurements were performed on the amplifiers, which are categorized as *non-RF measurements and RF measurements*.

Non-RF Measurements

These measurements include the following checks:

- *Visual inspection*: All the electric AC/DC wire/plug connections, water valves and RF cabling connections are checked.
- *Water leakage test*: Water connections are checked for any leakage and required flow rate (80 lpm in each unit) is maintained.
- *Electrical testing*: AC/DC connections continuity is checked followed by insulation testing.
- *Control system configuration*: It includes the software installation in the RT controller followed by loading of system configuration and executable files. Preliminary configuration of Alarm/Trip limits for amplifier powers/heatsink temperatures. Dual channel digital directional sensors which are meant to measure amplifier forward and reflected powers are assigned with unique IDs once they are mounted in the amplifier units at designated places. Additionally, the microcontroller units (MCUs) in the control PCBs are assigned unique IDs.
- *Functionality testing*: In this test the contactors are made ON sequentially and their corresponding DCPS status are checked.
- *Control Interlock testing*: Check the status of all the interlocks in GUI panel. Functionality of Front Panel Control PCB (FPC) and UI switches is checked. Interlocks functionality is ensured by using external interlock test board.

RF Measurements

These include the *low power and high-power RF measurements* carried out on both the units individually followed by RF testing of complete amplifier. In low power RF testing, first the RF chain is tested for any missing or faulty RF connection. The 20 kW amplifier unit is then tested for 1 kW RF output in order to calibrate the output measurement set up comprising 6-1/8” directional coupler (DC), RF cable, attenuator and power detector.

After this calibration, high power RF testing is performed where the input RF power to the 20 kW unit is swept at 650 MHz to get rated output power with simultaneous monitoring of specified parameters like amplifier gain, heatsink temperatures, reflections at different stages in amplifier etc. In case of any module or component failure, same is replaced followed by repetition of previous step. When rated output power is achieved for the individual unit, following tests are performed in addition to the power sweep test:

- *Bandwidth measurement*: Amplifier gain performance is observed in desired band of frequencies. 3 dB BW is beyond ± 2 MHz.
- *Spectral Response measurement*: Harmonics and spurious signal levels are measured at the output.
- *Pulsed measurements*: Amplifier is tested in pulsed mode at 50 Hz pulse repetition frequency (prf) and pulse width ranging from 500 µs to 6 ms.
- *Radiation profile measurement*: Due to the presence of tens of kilowatt of RF power, it is mandatory to measure the RF radiations and make sure these are well within the occupational safety limits. Complete amplifier zone mapping of radiation is performed where the radiated power density as well as RF field strengths are measured near different components in the amplifier.

After optimizing individual 20 kW units, outputs of these units are combined via a 2-way power combiner and 6-1/8” high power DC. Amplitude and phase of inputs of these units are tuned using phase shifters to compensate for any phase differences in the input feed path of the two units. The output measurement set up consisting of high-power DC (placed at the final output) is calibrated at 1 kW output level. Input RF power to the 40 kW amplifier is swept to get the rated output with simultaneous fine tuning of phase shifters thereby optimizing return loss at the output. Parameters like power and temperature alarm/trip limits are reconfigured. This is then followed by spectral response and radiation profile measurements for the complete amplifier system. Additionally, amplifier performance is also observed for coolant water increased temperatures up to 34 °C as per the Fermi TRS requirements.

RESULTS AND DISCUSSION

Both 32 kW and 40 kW SSRF amplifiers were tested and characterized for required specifications at rated RF power on dummy load. Measured results for both the amplifiers are quite similar and therefore 40 kW amplifier performance is mostly discussed throughout this paper to better utilize the space constraints. Table 1 below shows the TRS requirements for 40 kW RF amplifier along with the measured performance.

Table 1: Measured performance of 40 kW SSRFA

Sr. No.	Test Parameter	Fermi Lab TRS	Measured Performance
1.	RF Power output	≥ 40 kW	40 kW
2.	AC to RF output efficiency at 40 kW output	≥ 40 %	40.4%
3.	Bandwidth at 3dB	≥ ±2 MHz	> ±2 MHz
4.	Harmonic Response	Better than - 25 dBc	2nd harmonic = -40 dBc 3rd harmonic = -48 dBc
5.	Spurious Response	Better than - 55 dBc	Better than - 68 dBc within 2 GHz Span
6.	Radiation level at 1 m from amplifier	< 1 mW/cm2	0.005 mW/cm2

AC to RF output efficiency achieved at 40 kW output is around 40.4 % owing majorly to the RF losses in LDMOS, RF cables at the output of 500 W amplifiers and DC bias power supplies. Amplifier gain peaks near rated output and saturates slightly with further increase in input power. Thus it can be seen (in Fig. 4) that the amplifier operates linearly as the saturation is well below 1 dB compression point. Efficiency improves with increasing input power as can be seen in Fig. 4.

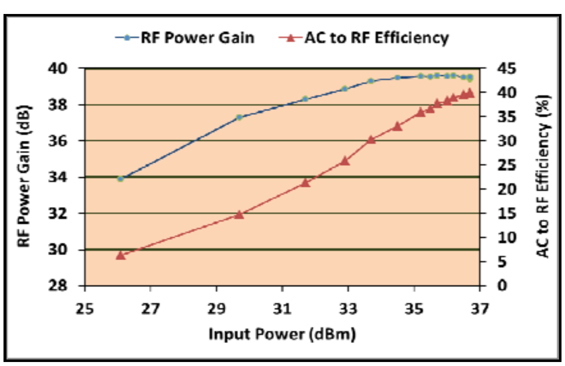

Figure 4: 40 kW SSRFA gain and efficiency variation with input power

In this zone the individual 500 W amplifiers approaches their optimum operation range. Measured harmonic response is better than - 40 dBc and - 48 dBc for second and third harmonic respectively as shown in Fig. 5 below.

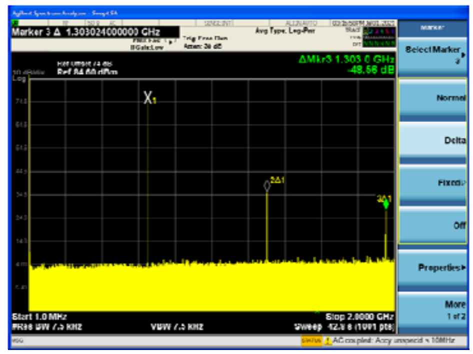

Figure 5: Harmonics at amplifier output as seen on Spectrum Analyzer

Spread in outputs of 128 numbers of the 500 W PAs is also observed which is around ±55 W referenced to average forward output of 375 W. This tight spread is achieved through strict control of insertion phase and gain of individual PA which helped in maximizing combining efficiency at the output. Radiated power density measured around the amplifier at a distance of 1 m with all the doors closed is around 0.005 mW/cm^2 which is well below the occupational safety limit of 1.2 mW/cm^2 at 650 MHz. Radiation maxima developed is around 2.2 mW/cm^2 near the combiner inside 20 kW amplifier unit. Pulsed measurements are also carried out for both the amplifiers wherein pulse rise time and droop for 6 ms pulse width is around 275 ns and 0.01 dB respectively in 40 kW SSRFA.

ACKNOWLEDGEMENTS

Authors gratefully acknowledge the kind support and constructive feedback of Joseph Tharayil, Varun Bhalla and Ravi kant Patel in this work.

REFERENCES

[1] A. Jain, D.K. Sharma, A.K. Gupta, K. Pathak, M. Lad M, "High-power solid-state amplifier for superconducting radio frequency cavity test facility", in Review of Scientific Instruments, Mar. 2021, Vol. 92, no. 034704, p. 1-11.

[2] A. Jain, D.K. Sharma, A.K. Gupta, K. Pathak, N. Kumar, "Operational Experience of High-Power Solid-State Amplifiers Deployed at RRCAT" in Indian Particle Accelerator Conference (InPAC-2022), VECC Kolkata, Mar., 22-25, 2022

[3] 40 kW, 650 MHz Amplifier Technical Requirements Specifications, FNAL TC No. ED0005489 and Sangam No. DAE334.

Design and development of unipotential Electrostatic focusing element for heavy metal ion beam isotopes

Vikas Tiwari, Janvin Itteera, Kumud Singh, Himanshu Bisht, Mahima and Sanjay Malhotra
Electromagnetic Applications and Instrumentation Division,
Bhabha Atomic Research Centre, Mumbai
E. mail: vikast@barc.gov.in

Abstract
A magnetron sputtering based ion source has been developed for concentrating isotopes of medical significance on the principle of electromagnetic separation of momenta. The ion optics of high-current beams is as critical as a high current ion source for efficient beam transmission up to the ion beam collector. Thermal velocity distribution, convex plasma meniscus and space charge forces cause divergent ion beams. Beam focusing at the exit of ion source is important to increase the beam transmission and decrease the loss at the entry slit. A divergent ion beam can be focused either by magnetic viz. solenoid or electrostatic focusing elements. A unipotential electrostatic element (Einzel lens) is used for effective radial focusing of Lutetium ion beam. The Einzel lens is a variant of the immersion. An Indigenous electrostatic element for high current ion source for Electromagnetic Isotope separation experimental facility has been designed with SIMION and CST particle studio code. Various geometrical design parameters, focusing properties and fabrication for proper alignment of three coaxial hollow cylindrical lens are discussed in this paper.
The optimized geometry was selected for development. The effects of different particle beam parameters such as initial size and energy distribution on the performance of the proposed lenses are investigated. Einzel lens for ~1mA of extracted current of Heavy ion beam was designed, developed and installed in the beam line and its operational parameters were measured.

INTRODUCTION
Electrostatic lens is widely used in charged particle optics in lower energy region i.e., less than β=0.14, where they are more effective than magnetic lenses. Magnetic elements focusing properties depend on mass to charge ratio and energy of ion beam but electrostatic elements focusing depend on energy of ion beam and independent of mass of beam. The exciting features of these lenses, such as their small size, relatively low power consumption, fast response times, and fabrication simplicity have made them suitable choices for many applications in low energy region. It consists of three colinear tubes, with the middle tube elevated to high potential. The Einzel lens consists of two immersion lenses in series. The Einzel lens is the best choice for the systems which need to the focusing without changing the energy of the both sides of the lens. This paper presents the design, construction, and characterization of the Einzel lens.

Theory of beam focusing action
Assume outer cylindrical electrodes are at same potential and middle one at elevated or lower potential with respect to outer electrode. There are four zones in the lens out of these two zones support radial focusing and others support defocusing. When energetic ion beam enters in decel -accel mode inside lens then kinetic energy of ion beam deceases in radial focusing zone while it increases in radial defocusing zones hence overall focusing effect dominate over defocusing.

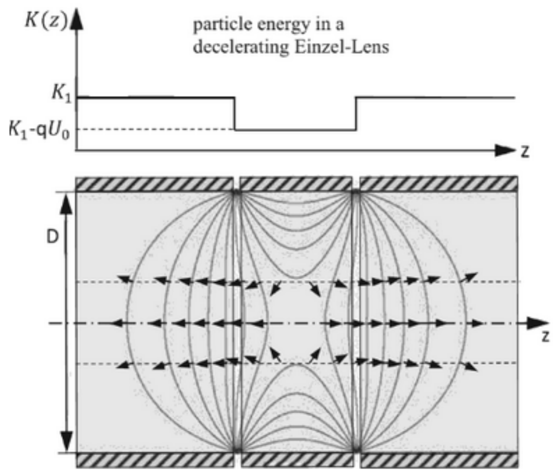

Figure 1: Reduced energy in central focusing zone

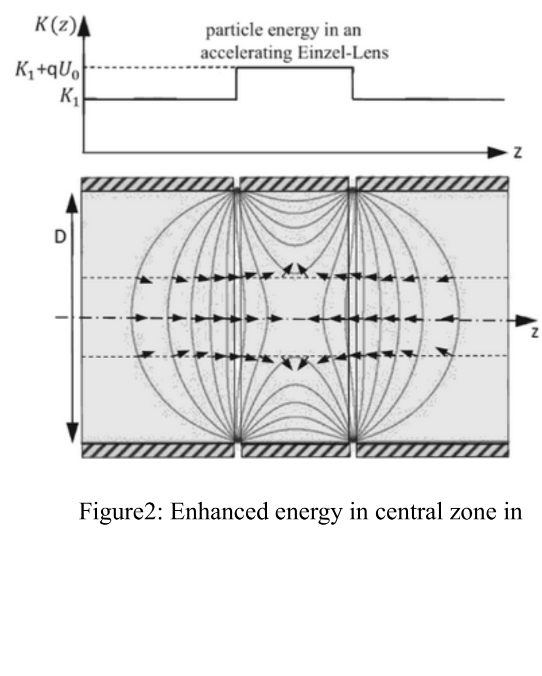

Figure2: Enhanced energy in central zone in

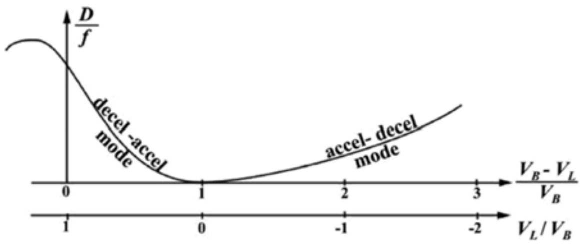

Figure 3: lens focusing power in two modes of operation

Chromatic aberration is reduced in accel- decel mode of operation at higher velocity of beam inside the lens. Spherical aberration is also reduced as beam tend to travers close to central axis.

Interaction of charge particle in electrostatic field

Suppose charged particle(+q) is accelerated through a uniform field between the equipotential planes denoted P_1 and P_2. The spaces to the left of P_1 and right of P_2 are field free and have the potentials V_1 and V_2. The potentials are counted from where the charged particles have zero energy so that their kinetic energy inflight direction at any point in space with the potential V_i is qV_i

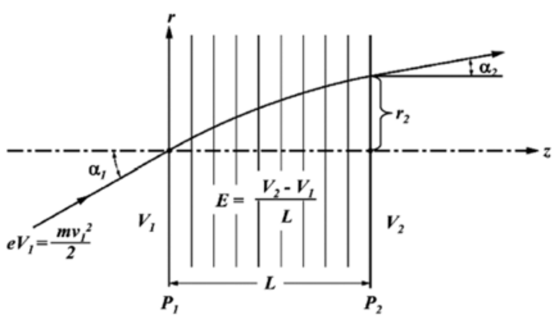

Figure 4: optical correspondence of charged particle electric field

In this simple case, the differential equations of motion can be integrated and resultant motion of the particle in the z–r-coordinate system as a function of time t is:

$$\frac{sin\alpha_1}{sin\alpha_2} = \sqrt{\frac{V_2}{V_1}}$$

Note that in the above relation is independent of distance L. If one could compress the field to an infinitely narrow double-layer with the potentials V_1 and V_2 on either side, one would have the exact analogue to the refraction of light at the interface between two media with the refractive indices n_1 and n_2, where the familiar law of refraction is valid. This reveals that in electrostatic optics, the square root of the potential plays the role of the refractive index n, whilst in light optics, sharp interfaces determine overall refractive index, however, in particle optics, refractive index undergoes gradual transitions. Another key remarkable difference with immense practical significance in electrostatic optics, for any given geometry of the electrodes, refractive is tunable with varying electrostatic potentials.

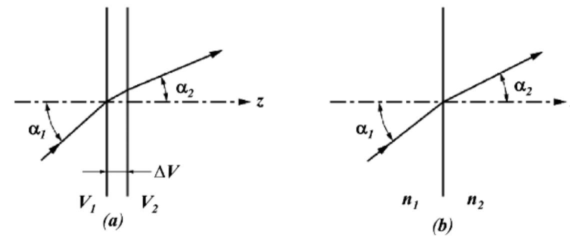

Figure 5: Refraction of charged particle trajectories (a) compared to that of light (b)

Description of the Einzel lens

Beam line consists of ion source, extraction system electrostatic focusing element, bending magnet and collection system at the end. Lens is designed with commercial electromagnetic codes for various aperture size, length of the electrodes and their gap. Focal length of lens is dependent on beam enery and applied potential at central electrode. It is also validated with beam dynamics simulation. However, the above lense suffers from inherent spherial aberrations due to the reducing focal length transversely by fringe fields. This results in different focal length for particle at different transverse locations. Longer Focal length will be experienced by smaller beam size and vice versa.

the electric lines of forces start from positive elevated central electrode and finishe at ground electrodes(figure6). Radial component of electric field depicted

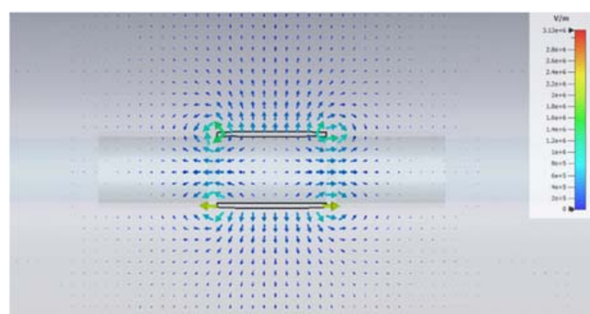

Figure 6: Vector plot of Electric field distribution

Ion beam trajectory is depicted in figure 7. Kinetic energy of ion beam remains constant but inside lens kinetic energy first decreases because ions move in opposite direction of electric field between first and second electrode and then increases to initial value

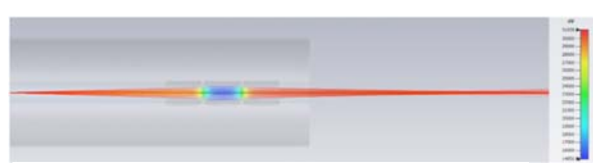

Figure 7: Ion beam trajectory passing through

CAD model and fabricated lens is depicted in Figure 8 &9. Gap between electrode is insured by small Teflon spacer rod. Outer support rings having radius 80mm and thickness 10 mm fit precisely in the beam line. Extruded parts of electrode are provided for Teflon spacer rod.

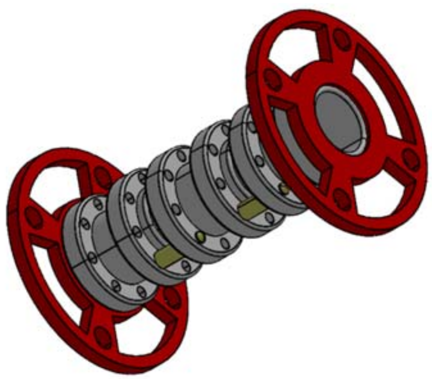

Figure 8: CAD model of Einzel lens

Figure 9: Designed Einzel lens

Table1: Summary of designing parameters

Short description of parts of lens	**Parameter value**
Length along beam line	229mm
Maximum input beam diameter	42mm
Central electrode potential	14kV @31.6keV
Axial distance between electrode	6.4mm

MEASUREMENT RESULTS

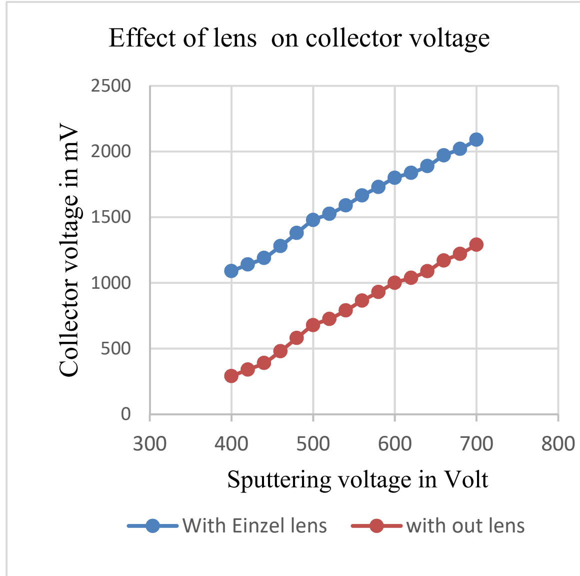

Figure 10: Collector voltage vs sputtering voltage

Argon plasma is confined by magnetic field. Magnetic field is generated behind the target in ion source chamber. Path length of electron increases which in turn insure more and more ionization. When optimize electrode voltage is applied in extraction system ion beams emerges out. Einzel lens reduces beam transmission loss (Figure 10) by providing radial electric field.

CONCLUSIONS

Fabricated Einzel lens has been successfully tested in ion beam line to get enhanced ion current at beam collection plate and Focal length of designed lens as function of ion beam energy is also validated.

References

1.O. Sise, M. Ulu, and M. Dogan, "Multi-element cylindrical electrostatic lens systems for focusing and controlling charged particles," Nuclear Instruments and Methods in Physics Research A, vol. 554, pp. 114-131,2005.

2. A. Adams and F. Read, "Electrostatic cylinder lenses II: Three element Einzel lenses," Journal of Physics E: Scientific Instruments, Feb. 1972.

3.Helmut Liebl “Applied charged particles optics.2008”

4. Jack E. Manuel, Szabolcs Z. Szilasi, Dustin Phillips, Alexander D. Dymnikov, Tilo Reinert, Bibhudutta Rout, Gary A. Glass. “Design and construction of an electrostatic quadrupole doublet lens fornuclear microprobe application”

5. Harmann wolnick, “Optics of charged particles.2021”

EFFECT OF Dy SUBSTITUTION AT Nd SITES IN MELT-SPUN Nd-Fe-B PERMANENT MAGNET RIBBONS

S. K. Dey[1], G. Sinha[2] and S. Aich[1*]

[1] Department of Metallurgical and Materials Engineering, IIT, Kharagpur, WB, PIN-721302,

[2] Department of Atomic Energy, RRCAT, Indore, MP, PIN-452013,

Abstract

In this study the effect of adding Dy as an alloying element to the Nd-Fe-B magnetic system was evaluated by preparing the samples via melt-spinning process. Ribbons of Composition $Nd_{2-x}Dy_xFe_{14}B$ (x=0 and 0.6) were synthesized, keeping the wheel speed at 30 m/s. Thereafter the ribbons were studied by various characterization techniques such as X-Ray diffraction, FE-SEM imaging and SQUID measurements at 6T. It was found that Dy addition increased the Max. Energy product 2-fold while the Coercivity values increased 4 times. The increased coercivity by Dy addition is attributed to the segregation of Dy at the interface between the matrix phase and the grain boundary phase which opposes the nucleation on reverse domain during demagnetization.

INTRODUCTION

New materials and techniques are being used to attain extremely high magnetic fields in permanent magnet-based accelerator magnets that may offer a viable alternative to their conventional electromagnetic counterparts for many applications, especially where strong gradients, low power consumption and less radiation damage are needed [1], [2]. Rare-earth magnets are characterized by high energy product $(BH)_{max}$, high intrinsic coercivity (H_{ci}) and reasonably high remanence (B_r). The temperature dependencies of the parameters $(BH)_{max}$, magnetic remanence (B_r or M_r) and intrinsic coercivity (H_{ci}) are critical factors in electric machine design and performance. Sm-based and Nd-based magnets are commonly used rare-earth (RE) alloys. In addition, an increase in magnetic properties while decreasing the temperature makes RE alloys suitable for cryogenic applications [3]. Nd-based alloys have high remanent field/energy values than Sm-based alloys but they have a lower coercivity. However, recent studies stated that the coercivity of Nd alloys could be improved by Dy or Tb diffusion or grain boundary diffusion without loss of remanence or significant reduction in remanence[4]. The process of melt-spinning aids the enhancement of magnetic properties because of the nano-crystalline grains formed in this process. The higher wheel speed corresponds to a greater cooling rate and finer grains which in turns increases the max. energy product [5]. The melt- spun ribbons develop nano-structure as a result of rapid solidification which enhances its properties as compared to the bulk samples. Moreover, the Nd-Fe-B melt-spun ribbons form an in-situ nano-composite with Alpha-Iron and $Nd_2Fe_{14}B$ phase, with the former being a soft magnetic phase while the latter being a hard magnetic phase. The exchange coupling between the soft and the hard magnetic phases helps in a significant increase of the remanence value. The Nd-rich phase surrounds the grains of the Nd-Fe-B and it helps to increase the Intrinsic coercivity by reducing the exchange interaction between the hard magnetic phases [6]. Grain size calculation from the electron microscopy images of the rapidly solidified ribbons reveals that the Nd-Fe-B grains are smaller than the critical size for single domain. Hence, it can be said that the Nd-Fe-B melt-spun ribbons are made up of single domains which in turn increases the coercivity values [7]. Theoretical studies by first-principle calculations have suggested that keeping Nd:Fe ratio less than 30:70 in Nd-Fe alloys have resulted in ferromagnetic behavior at room temperature [8].

MATERIALS

High purity rare-earth elements Neodymium (Nd), Dysprosium (Dy), and high purity Iron (Fe) and Boron (B) have been used to synthesize $Nd_2Fe_{14}B$ and $Nd_{1.4}Dy_{0.6}Fe_{14}B$ alloys. Each material was procured from Sigma-Aldrich with high purity (99.9% purity).

EXPERIMENTATION

The experimentation consists of making ingots of the above mentioned compositions by vacuum arc melting followed by melt-spinning of the ingots to obtain the rapidly solidified melt-spun ribbons. Ingot alloys are synthesized using an ultra-high-vacuum arc-melting furnace (TIG). UHP grade argon was purged and melting was done in Argon atmosphere. These ingots are melted repeatedly (each with four times) to assure proper mixing and good homogenization of the alloy during arc-melting process. These ingots were then melt-spun with a wheel speed of 1650 rpm to obtain the melt-spun ribbons. The ribbons were then characterized by X-ray diffraction, SQUID and FE-SEM imaging.

RESULTS & DISCUSSION

X-Ray Diffraction Analysis

Figure 1 shows X-ray diffraction pattern of the melt-spun ribbons having composition $Nd_2Fe_{14}B$ and $Nd_{1.4}Dy_{0.6}Fe_{14}B$. From the XRD pattern of $Nd_2Fe_{14}B$ it can be seen that the peaks strongly match with the phases $Nd_2Fe_{14}B$ and B, while there is a weak matching with Nd_2Fe_{17} phase also. These matchings were confirmed by the ICSD 98-005-4924, ICSD 98-061-2521 and ICSD

98-010-6661, respectively from the standard database. The peaks of Boron indicate its precipitation which helps to increase the Coercivity values as it precipitates around domain walls and reduces the domain wall motion. From the XRD pattern of $Nd_{1.4}Dy_{0.6}Fe_{14}B$ we can see that majority of the peaks are matching with the phase $Nd_2Fe_{14}B$, while some of the peaks match with Dy_2Fe_{17} also. The matchings were confirmed by the ICSD 98-005-4924 and ICSD 98-062-9587, respectively. The presence of Dy_2Fe_{17} peak confirms the Dy substitution at Nd sites. The crystal structure was confirmed as tetragonal. The lattice parameters are given in the following table (Table-1).

Table 1: Lattice Parameters and crystal structures.

Composition	**a Value (in Å)**	**c value (in Å)**	**c/a ratio**	**Crystal Structure**
$Nd_2Fe_{14}B$	8.63	9.266	1.07	Tetragonal
$Nd_{1.4}Dy_{0.6}Fe_{14}B$	8.706	12.04	1.38	Tetragonal

From the table 1 we can see that the c/a ratio of both the compositions are more than 1, indicating elongated anisotropic crystals. The c/a ratio of the crystals of composition $Nd_{1.4}Dy_{0.6}Fe_{14}B$ is more than the c/a ratio of the crystals of composition $Nd_2Fe_{14}B$ which shows that $Nd_{1.4}Dy_{0.6}Fe_{14}B$ composition has higher shape anisotropy.

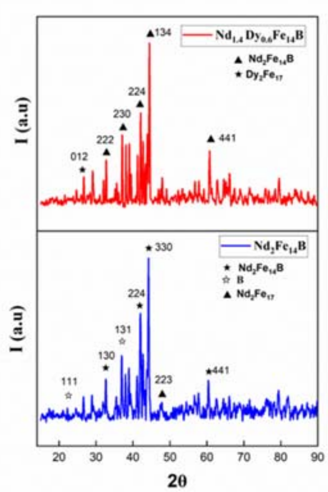

Figure 1: XRD plot of the melt-spun ribbons of composition $Nd_2Fe_{14}B$ and $Nd_{1.4}Dy_{0.6}Fe_{14}B$.

Microstructural Analysis

Melt-spun ribbons generally show different microstructures on two different sides of the ribbons. Melt-spinning is a rapid solidification technique which leads to the formation of some dendritic type structures. The added advantage is that in this technique we can form the nano-crystalline, even sometimes amorphous structures upon the controlling cooling rates that can be controlled by changing the wheel speed of the rotating copper wheel. In the figure 2(a) we can see the surface morphology of the wheel side of $Nd_2Fe_{14}B$ melt-spun ribbons. Irregular shaped grains were observed and there are hardly any equiaxed grains. This is in line with the fact that during rapid solidification mostly irregular grains are formed. Presence of some fused grains are also observed there. This feature attributes to the amorphous phase formation as a result of rapid solidification. Being the wheel side surface, the heat transfer rate at that side is also higher as compared to the free side, so we can get nano-crystalline or sub-micron structures. Figure 2(b) represents the free side (opposite to the wheel side) morphology of the same ribbon, where we can see a very different kind of grain morphology. At the free side it can be observed that the grains are slightly regular in contradiction to the irregular shaped grains observed in the wheel side. The grains are cubical in shape where slight traces of dendrite arms can be seen inside these grains. The difference in grain morphology can be related to the difference in the heat exchange rates for both sides of the ribbons. Figure 2(c) and 2(d) show the surface morphology of the Dy-added melt-spun ribbons. It is very interesting to note that upon Dy addition the grain morphology also changed. In figure 2(c) the image of wheel side surface of the melt-spun ribbon, we can see dendritic morphology clearly with the dendritic arms. In $Nd_2Fe_{14}B$ ribbons we could see the irregular morphology of the grains but cannot clearly see the dendrites. The dendritic structure enhances the magnetic properties due to higher anisotropy. Also, in the wheel side surface, as the ribbon surface touches the rotating copper wheel, the grains are having tendency to be elongated along the spinning direction. Figure 2(d) gives the free side surface image of the $Nd_{1.4}Dy_{0.6}Fe_{14}B$ ribbons. The dendritic structure is not visible here rather we can see highly irregular shaped grains having some kind of branches that contains almost equiaxed sub-grains. The absence of perfect dendritic structure on the free side of the ribbons can be due to the slight decrease of the heat exchange rate. However, the irregular shaped grains can be observed in both the cases, which is indicative of its rapid solidification. From SEM images we could roughly estimate the size of the grains. The grain size for different compositions and different sides of the ribbon surfaces are given in the Table-2. The exact estimation of the grain size is very difficult here, because of the presence of the agglomerated (sometimes fused) structure. The grain size reported here mostly indicates the size of the agglomerated feature (consisting of multiple grains), rather than a single grain size. From the table we can conclude that ultrafine grains are formed on the wheel side of the ribbons for both the compositions. It is interesting to note that grain sizes are also different on the free side of the ribbons, where the grain sizes are in the sub-micron domain. This again relates back to the difference in the heat exchange rate between the melt and the sink (which is copper wheel in case of *melt-spinning*).

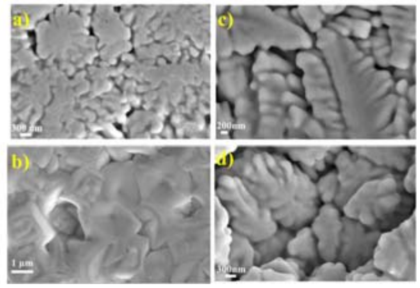

Figure 2: Field Emission Scanning Electron (FE-SEM) Micrographs of the melt spun ribbons. (a) FESEM image of wheel side of $Nd_2 Fe_{14}B$ ribbons, (b) FESEM image of free side of $Nd_2 Fe_{14}B$ ribbons, (c) FESEM image of wheel side of $Nd_{1.4} Dy_{0.6} Fe_{14}B$ ribbons, (d) FESEM image of free side of $Nd_{1.4} Dy_{0.6} Fe_{14}B$ ribbons.

Table 2: Average Grain size

Composition	Ribbon Surface	Grain Size
$Nd_2 Fe_{14}B$	Wheel side	296.53 nm
$Nd_2 Fe_{14}B$	Free side	1.65 µm
$Nd_{1.4} Dy_{0.6}Fe_{14}B$	Wheel side	416.33 nm
$Nd_{1.4} Dy_{0.6}Fe_{14}B$	Free side	659.34 nm

Magnetic Properties

The figure 3 shows the hysteresis plots of the melt-spun ribbons of composition $Nd_2Fe_{14}B$ and $Nd_{1.4}Dy_{0.6}Fe_{14}B$. We can clearly see from the hysteresis plots that the addition of Dy as an alloying element has significantly enlarged the area under the hysteresis plot indicating a very good enhancement of the magnetic properties. Though, we can see that there is not much difference in the remanence value but the intrinsic coercivity shows a major improvement upon Dy addition. The remanent magnetization was measured as 68.96 emu/g for $Nd_2Fe_{14}B$ while for $Nd_{1.4}Dy_{0.6}Fe_{14}B$ composition it was measured around 69.79 emu/g. The intrinsic coercivity values as measured from the hysteresis loops were 2.44 kOe for $Nd_2Fe_{14}B$ and 8.15 kOe for $Nd_{1.4}Dy_{0.6}Fe_{14}B$ ribbons.

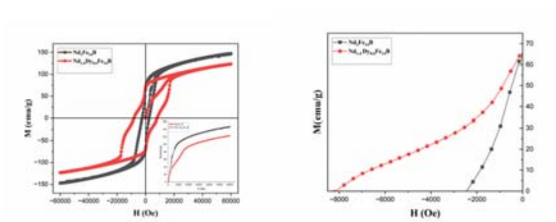

Figure 3: Hysteresis loop of the melt-spun ribbons with the initial magnetization curve as inset and Demagnetization curve of the melt-spun ribbons.

The significant enhancement of the intrinsic coercivity value upon the Dy addition, can be attributed to the higher c/a ratio of the crystals as observed in the case of Dy-added melt spun ribbons which indicates higher anisotropy that helps in increasing the intrinsic coercivity values. Also, as discussed in microstructural analysis the ribbons of the composition $Nd_{1.4}Dy_{0.6}Fe_{14}B$ had dendritic morphology which can be correlated to the enhancement of the coercivity. The maximum energy product $\{(BH)_{max}\}$ is also increased upon Dy addition. The $(BH)_{max}$ value as calculated for the melt-spun ribbons of the composition Nd_2Fe_{14} B was 2.67 MGOe while for the composition $Nd_{1.4}Dy_{0.6}Fe_{14}B$ it was calculated to be 4.62 MGOe.

However, it was also observed that the magnetization of the ribbons having $Nd_2Fe_{14}B$ composition was slightly higher as compared to the ribbons with $Nd_{1.4}Dy_{0.6}Fe_{14}B$ composition.

CONCLUSIONS

Melt-spun ribbons with composition $Nd_2Fe_{14}B$ and $Nd_{1.4}Dy_{0.6}Fe_{14}B$ were synthesized by maintaining the wheel speed at 1650 rpm. The as-spun ribbons were studied for crystal structure, microstructure and magnetic property correlation upon addition of Dy as an alloying element. It was found that on Dy addition the magnetic properties, like intrinsic coercivity and maximum energy product values showed significant improvement. The microstructural study reveals the presence of dendritic grain morphology in case of Dy-added melt-spun ribbons. The enhancement of magnetic properties in case of Dy-added melt-spun ribbons can be correlated to the formation of the dendritic grains as well as the increment in c/a ratio. Hence, Dy addition certainly plays an important role in improving the magnetic properties of the melt-spun Nd-Fe-B ribbons.

REFERENCES

[1] J. Chavanne *et al.,* Prospects for the use of Permanent Magnets in Future Accelerator Facilities, Proceedings of the 5th Int. Particle Accelerator Conf. IPAC2014 (2014) 6 pages.

[2] R. Qiu *et al.*, Radiation damage of Nd2Fe14B permanent magnets at 2.5GeV electron accelerator, Nuclear Instruments and Methods in Physics Research Section A: Accelerators, Spectrometers, Detectors and Associated Equipment. 594 (2008) 111–118.

[3] S. Sugimoto *et al.*, Current status and recent topics of rare-earth permanent magnets, J. Phys. D: Appl. Phys. 44 (2011) 064001.

[4] L. Zhou *et al.*, Dy gradient and coercivity in grain boundary diffusion processed Nd-Fe-B magnet, Journal of Rare Earths. 35 (2017) 559–566.

[5] A. Manaf *et al.*, Enhanced magnetic properties in rapidly solidified Nd-Fe-B based alloys, Journal of Magnetism and Magnetic Materials. 101 (1991) 360–362.

[6] M.A. Al-Khafaji *et al.*, The effect of phase constitution on the magnetic structure of nanophase NdFeB alloys observed by magnetic force microscopy, Journal of Magnetism and Magnetic Materials. 188 (1998) 109–118.

[7] H.C. Hua *et al.*, Microstructure of melt-spun NdFeB magnet, Materials Letters. 7 (1988) 65–67.

[8] A. Sakuma *et al.*, Magnetism of Nd–Fe films as a model of grain boundary phase in Nd–Fe–B permanent magnets, Appl. Phys. Express. 9 (2016) 013002.

*Corresponding Author Email
saich@metal.iitkgp.ac.in

DESIGN, DEVELOPMENT AND CHARACTERIZATION OF THREE ELECTRODE ION BEAM EXTRACTION SYSTEM FOR MAGNETRON SPUTTERING ION SOURCE

Mahima#, Himanshu Bisht, Janvin Itteera, Vikas Tiwari, Kumud Singh, Sanjay Malhotra
Bhabha Atomic Research Centre, Mumbai

Abstract

Ion extraction systems are crucial beam handling component for ion beam formation at the exit of an ion source. It determines the beam properties such as ion current and beam quality. Primary requirement of an ion extraction system is to optimize the beam focusing for desired beam current and energy with low emittance and high perveance. Electrode shaping and design optimization shall focus on maximizing the number of ions extracted with low divergence and minimize the losses on various electrodes to enhance the electrical efficiency and lengthen the lifetime of the electrodes. A three-electrode extraction system is designed for extraction of Lutetium ion beam at the exit of a magnetically confined ion source for electromagnetic isotope separation experimental facility. Optimization parameters like separation between electrodes and the aperture diameter of extraction and screening electrode were investigated in addition to influence of space charge on beam quality. Numerical analysis of electrodes was done in SIMION software to optimize geometrical parameters to maximize beam current while minimizing the divergence of beam. Trajectory simulations were performed for charged particle dynamics. Formation and shape of plasma meniscus near extraction electrode aperture is discussed. Plasma meniscus serves as a source of ions, therefore factors affecting its shape are investigated. Interaction of ion emission current density and space charge limited current density is mainly responsible to determine the shape of plasma meniscus [1]. For different shapes of plasma meniscus e.g., concave, convex and flat, beam trajectory was estimated using numerical simulations. Beam size and divergence were also assessed. Triode extraction system with features for precise alignment was developed as alignment of the electrodes is a key parameter for performance of the extraction system. Thermal management of the extraction system has been incorporated in the design to limit the rise of the operating temperature of the electrodes resulting in increased lifetime. The developed extraction system is integrated with the beam line of electromagnetic Isotope separator. High Voltage conditioning of electrodes was done to obtain stable operation of extraction system. Beam parameters are determined using wire scan method. Experimental results are summarized and analyzed.

INTRODUCTION

In the case of space-charge-limited surface-emitted electrons, there is a perfect solution (Pierce Geometry [2]) for providing a parallel electron beam accelerated from the cathode set-up along with measured results are discussed. However, for the plasma ion sources it does not provide a perfect solution, as the ions do not start from a fixed surface, but from plasma with varying starting conditions. According to Bohm's law, extractable ion current density J_i from a plasma boundary is given by [3]:

$$J_i \approx 0.6 n_+ \, e \sqrt{\frac{2kT_e}{M_i}} \qquad (1)$$

Where n_+ is ion density at the plasma boundary, k is Boltzmann constant, T_e is electron temperature, e is electron charge. Also, the maximum achievable extracted current density J_{scl} under space charge limited conditions from a plasma boundary is given by [4]:

$$J_{scl} \approx \frac{4}{9}\varepsilon_0 \sqrt{\frac{2q}{M_i}} \cdot \frac{V^{1.5}}{d^2} \qquad (2)$$

Where V is the acceleration voltage, ε_0 is the permittivity of free space, d is the extraction gap. The meniscus formed at the plasma surface depends on the plasma density and the applied electric field and can be classified as a) convex, b) planar, and c) concave. In the case of convex meniscus beam is under focused, and hence significant number of ions are lost. This results in secondary emission of the electrons and sputtering of the electrodes surface. This existence of convex meniscus can be attributed to may be high plasma density in comparison to space charge density. A planar meniscus is the optimum meniscus shape since it well suited and matched condition between the extraction field and the plasma density for the maximum ion beam extraction i.e. the plasma density is approximately equal to the space charge density. It is obtained by proper variation of the applied electric field and the plasma density. A concave meniscus is formed due to a high extraction field and a low plasma density i.e. the plasma density is less than the space charge density. In this condition, the beam is over focused and then it diverges strongly, which leads to the hitting of the surface of the electrode [4].

The perveance 'P' of the ion beam is defined as,

$$P = \frac{I_i}{V^{1.5}} \qquad (3)$$

#mahima@barc.gov.in

NUMERICAL DESIGN & MODELLING

A three-electrode system basically consists of plasma, screening and ground electrode. The purpose of screening electrode is to provide negative potential barrier for electrons so that they are not attracted towards plasma potential and thus space charge compensation in the ion beam is maintained. The electrodes are modelled in SIMION software as shown in Fig. 1. Using a finite difference method, SIMION uses the potentials of electrode points to calculate the potential of non-electrode points [3]. Once all three electrodes are designed and defined within a potential array, SIMION solves the Laplace equation, $\nabla 2V = 0$.

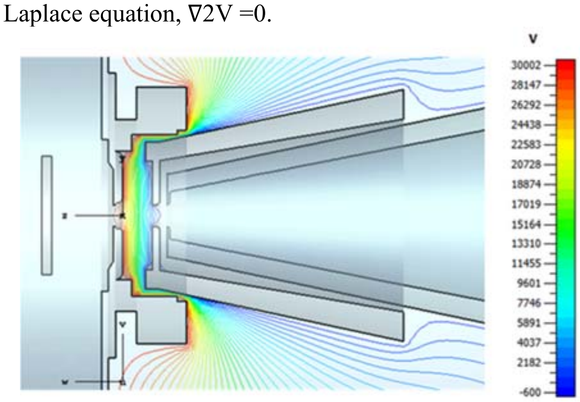

Fig. 1 Potential lines distribution in the electrode gap.

Beam trajectory simulations were performed for Lutetium ions. Ion emission surface is defined with 10,000 particles having initial energy of 1.5 eV. A model for the extraction electrodes is used to simulate the possible plasma boundary curvatures resulting due to change in an extraction potential with a constant plasma density. The voltage applied to the plasma-electrode was +30 kV, screening electrode at -600V and the decel-electrode on ground potential. The voltage applied to the accel-electrode was varied and optimized to accomplish the suitable shapes of the plasma boundary curvatures, shown in Fig. 2 to 4.

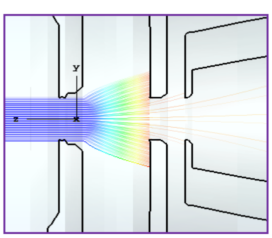

Fig. 2 Convex meniscus

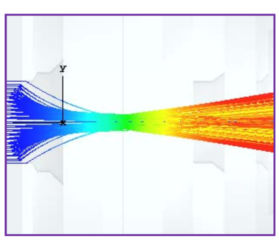

Fig. 3 Concave meniscus

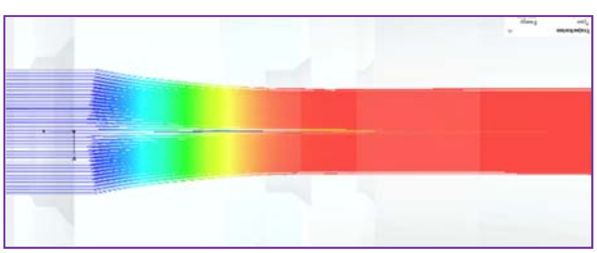

Fig. 4 Flat meniscus trajectory

SIMULATION RESULTS

For optimization of extraction gap and aperture radius, various simulations are performed and beam parameters are evaluated. Beam current density is taken $20 A/mm^2$. Emittance is estimated at 250 mm away from the extraction electrode aperture. Fig. 5 shows variation in rms emittance for different values of extraction gap. It is found that minimum beam emittance is obtained at extraction gap value of 12 mm. Similarly, rms emittance plot for various extraction aperture is given in Fig. 6 and minimum beam emittance is obtained at aperture of 4.5 mm.

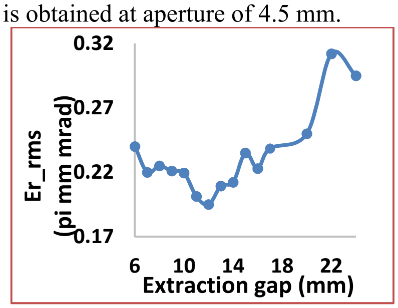

Fig. 5 Influence of extraction gap on beam emittance

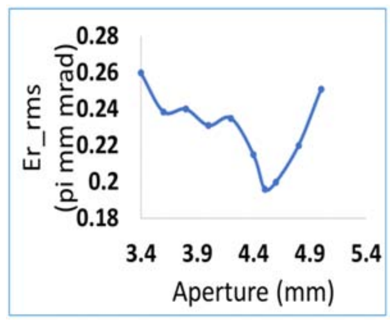

Fig. 6 Influence of aperture on beam emittance

DEVELOPMENT

A 3D model of extraction electrodes system was prepared with optimized design variables and cross-sectional view is shown in Fig. 7. Fig. 8 shows developed and assembled three electrode extraction system. It has been integrated with ion source in EMIS beam line and High voltage conditioning has been performed and stable operation has been achieved.

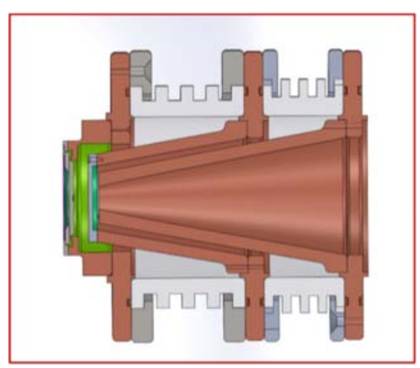

Fig. 7 Design model

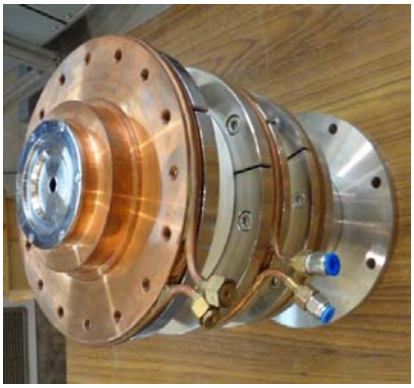

Fig. 8 Developed three electrode system

Measurements Results & Summary

Experiments are performed on integrated electrodes system and extracted current values were recorded with plasma electrode voltage for obtaining I vs V characteristics. The resulting plot is summarized in Fig. 9. Also, beam parameters are determined using wire scan method with an array of 18 parallel wires placed at exit of extraction electrode (250 mm away). The spacing between wires is 1 cm and wire diameter is about 0.4 mm. The voltages induced in each wire due to intercepted ions were measured. The optimum operational parameters for specified plasma parameters were 9kV plasma voltage, -1kV screening electrode voltage, 1.5 mA extraction current with a FWHM of 20 mm.

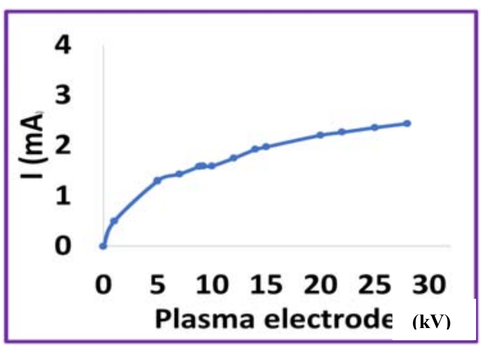

Fig. 9 Extracted I vs V characteristics

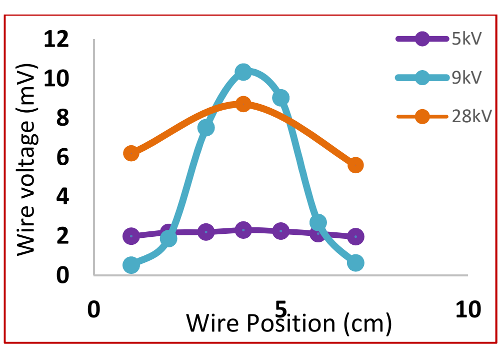

Fig. 10 Wire scan results

The beam size was observed to vary with plasma voltage because of change in shape of plasma meniscus. Also, the optimum extraction voltage varies with plasma parameters du to variation in plasma density. Experiments are going on and extraction system exhibited a stable operation for longer duration.

REFERENCES

[1] A. Forrester, Ion Beams Fundamental of Generation and Propagation, New York: Wiley, 1988.

[2] J. R. Pierce, Theory and Design of Electron Beams, London: Van Nostrand, 1949.

[3] M. M. Abdelrahman, G. A. Helal and O. A. Moustafa, "SIMION Calculations for the Triode Extraction System," *International Journal of Theoretical and Mathematical Physics*, pp. 122-129, 2012.

[4] A. Septier, Focusing of charged particles, New York: Academic press, 1967.

[5] B. A. Soliman, "Simulation of ion beam extraction and focusing system," *Chinese Physics C (HEP & NP,* vol. 35, no. 1, pp. 83-87, 2011.

STUDY OF CUMULATIVE BEAM BREAKUP INSTABILITY IN SPOKE RESONATOR SECTION OF A 1 GeV PULSED H$^-$ LINAC

*Mukesh Kumar Pal[1,2] and Rahul Gaur[1,2]
[1]Proton Accelerator Group, Raja Ramanna Centre for Advanced Technology, Indore
[2]Homi Bhabha National Institute, Mumbai

Abstract

Beam instabilities due to the higher order modes (HOMs) have been a concern for the superconducting (SC) linacs worldwide. Due to HOMs, the beam breakup instabilities (BBU) can occur in transverse and longitudinal planes. In this paper, we present a study of cumulative transverse BBU instability for the single spoke resonator (SSR) section for a 1 GeV pulsed H$^-$ linac designed at RRCAT for the envisaged Indian Facility for Spallation Research (IFSR). For this, the difference equations for transverse position and angle of beam bunch due to deflecting mode of cavities are solved for SSR sections. Numerical simulation indicates that cumulative transverse BBU instabilities are not a concern in the spoke section for the 1 GeV pulsed H$^-$ linac. Moreover, effects of the frequency, frequency spread, and R/Q value of the HOMs on the cumulative BBU have been studied, which are also presented in the paper.

INTRODUCTION

The baseline lattice design and beam dynamics study for a 1 GeV pulsed H$^-$ linac along with component error/failure study has been performed recently [1-3]. The linac will comprise of five superconducting (SC) sections to accelerate the 3 MeV beam to 1 GeV. Amongst five SC sections, first three are single spoke resonator (SSR) sections, named as SR0, SR1 and SR2 sections, which are designed at β_g of 0.11, 0.21, and 0.42, respectively, where β_g is geometric β [1]. Whereas, last two superconducting sections are 5-cells elliptic cavity sections, designed at β_g of 0.61 and 0.81, respectively. The SR0, SR1 and SR2 sections will boost the energy of beam from 3 MeV – 12 MeV, 12 MeV – 45 MeV and 45 MeV - 168 MeV, respectively. The lattice period for SR0, SR1 and SR2 with length of their elements is shown in Fig.1.

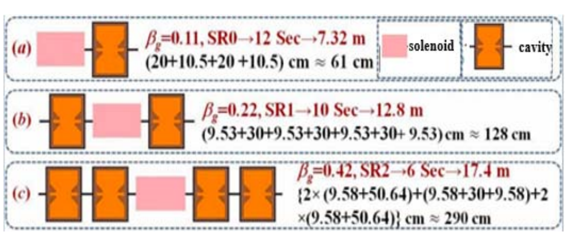

Figure 1: Lattice period for SR0, SR1 and SR2 sections.

Beam breakup (BBU) instability due to Higher Order Modes (HOMs) may arise in long SC linacs in transverse as well as longitudinal plane, which can be of regenerative type or cumulative type [4, 5]. The regenerative BBU occurs in a single multicell structure, where the cells are strongly coupled electromagnetically. Here, a dipole mode gives a transverse kick to an on-axis particle to make it off-axis during its travel in the cavity, which regenerates the dipole mode and enhances its strength further. On the other hand, the cumulative BBU dominates in case of a linac, which consists of an array of electromagnetically independent cavities. Here, an off-axis bunch generates deflecting mode in the cavity, which gives a transverse kick to the following bunches, and the transverse displacement of a bunch may grow as it moves downstream in the linac. We present a study of cumulative transverse BBU instability for the SSR section of a 1 GeV pulsed H$^-$ linac, along with the effect of frequency, frequency spread, and *R/Q* value of the HOMs on this instability, in this paper.

BEAM BREAKUP DIFFERENCE EQUATIONS FOR SSR SECTION

Gluckstern *et al* [6] derived BBU difference equations for relativistic electron beam, in case of a linac, which consists of identical cavities placed on axis with periodicity L. Using Ref. [6], we have derived BBU difference equations for the SSR section of 1 GeV linac, where solenoid and cavity are considered as drift space and thin lens, respectively. The equations of beam displacement x and angle θ during beam transport from N^{th} cavity centre to $(N+1)^{\text{th}}$ cavity centre are [6],

$$\begin{pmatrix} x_M^{N+1} \\ \theta_M^{N+1} \end{pmatrix} = \begin{pmatrix} M_{11} & M_{12} \\ M_{21} & M_{22} \end{pmatrix} \begin{pmatrix} x_M^{N+} \\ \theta_M^{N+} \end{pmatrix}, \qquad (1)$$

$$x_M^{N+} = x_M^N, \qquad (2)$$

$$\theta_M^{N+} = \frac{p_x^+}{p_z^+} = \frac{\beta_N \gamma_N}{\beta_{N+1}\gamma_{N+1}} \theta_M^N + \frac{R_1}{\beta_{N+1}\gamma_{N+1}} \sum_{l=0}^{M-1} s_{M-l}\, x_l^N, \qquad (3)$$

where, x_M^N and x_M^{N+} are displacements of M^{th} bunch just before and after the action of N^{th} cavity, respectively, and M_{11}, M_{12}, M_{21} and M_{22} are transport matrix elements. The quantity γ_N is the relativistic energy parameter of the beam upon entry to N^{th} cavity. Here, $R_1 = \frac{Ze^2\Gamma}{2m_0\beta c}$, and wake-function $s_{(M-l)} = e^{-\frac{(M-l)\omega\tau}{2.Q_l}} \sin((M-l)\omega\tau)$, where $\Gamma = \left(\frac{R}{Q}\right)_\perp \frac{\omega^2}{c^2}$, m_0 is the rest mass of H$^-$ ion, Ze is charge per microbunch (here, 47.4 pC), and ω, τ, Q_l and $\left(\frac{R}{Q}\right)_\perp$ are angular frequency, time interval between two bunches, loaded quality factor and transverse shunt impedance to unloaded quality factor ratio of most prominent deflecting HOM, respectively. Equation (1) serves as the basis for numerical simulations of the BBU problem.

*mukeshp@rrcat.gov.in

A subroutine to solve difference equations of transverse BBU was written in MATLAB and benchmarked with the example case discussed in Ref. [6]. Results obtained from subroutine are found to be same to those presented in Ref. [6]. Figure 2 shows the result of transverse beam centroid displacement calculated by the subroutine for the example case of Ref. [6]. Here, parameter $M_{12}\ R_1/\gamma = 2.88 \times 10^{-3}$, $\omega\tau/2\pi = 1.846$ and $Q_l = 10^3$, whereas all the bunches enter to the first cavity has an offset of 1mm.

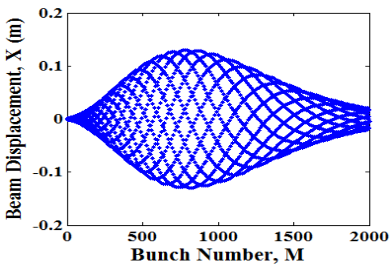

Figure 2: Plot of transverse beam centroid displacement at the end of 30th cavity for the example case of Ref. [6].

From HOM analysis of SSR cavities, performed using EM code CST-MWS [7], the deflecting HOMs with maximum value of R/Q were identified, which are listed in Table 1. The Q_l -value of these HOMs was taken to be ~ 10^3 - 10^7 [8].

Table 1: Deflecting HOMs with maximum value of R/Q for SSR and their corresponding frequency.

S.N.	Cavity	R/Q (Ω)	f_{HOM} (MHz)
1	SR0	0.62	805.30
2	SR1	0.95	728.69
3	SR2	3.10	1706.95

The beam centroid displacement was calculated at the end of SR2 section for the worst case scenario of SR0, SR1 and SR2 sections, where we have taken the most prominent HOMs, as depicted in Table 1. Figure 3(a) and 3(b) show the displacement of the first 2000 bunches after SR2 section, in the case when all bunches entered the first SR0 cavity at an offset of 1 mm from the axis, while $Q_l = 10^3$ and 10^7, respectively. Figure 3(c) shows the displacement of the first 2000 bunches after SR2 section for the case when the first bunch entered the first SR0 cavity at an offset of 1 mm from the axis with $Q_l = 10^7$ (Displacement of 1st bunch is not shown in the figure).

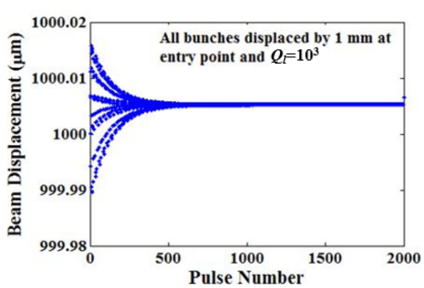

3(a)

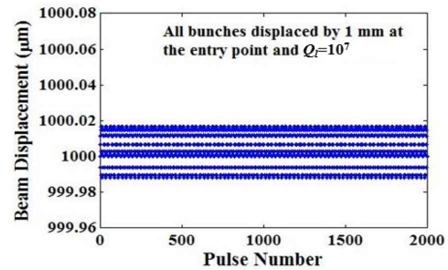

3(b)

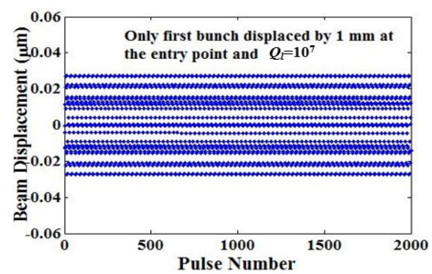

3(c)

Figure 3: Displacement of the first 2000 bunches at the end of the SR2 section for different cases.

The study shows that beam displacement due to cumulative BBU in SSR section is negligible. The reason is the low R/Q value of deflecting HOMs of SSR cavities. We have observed that the maximum bunch displacement increases almost linearly with R/Q value on log-log plot.

It is also observed that as the succeeding bunches are displaced farther from the beam axis, the maximum bunch displacement reduces slightly, which can be seen by comparing Fig. 3b and Fig. 3c.

EFFECT OF HOM FREQUENCY ON BBU

To identify the frequency of dangerous deflecting HOMs in SSRs of 1 GeV linac, the transverse integro-differential BBU equation [8] is solved. The steady state solution of the transverse integro-differential BBU equation in the case of delta function bunches [8] (assuming coasting beam and no focusing) is,

$$x_\infty(N) = x_0 cosh\left[N\sqrt{\frac{\varepsilon.\omega\tau\left(\frac{l}{L}\right)^2 P_R(\omega\tau)}{4}}\right] \tag{4}$$

where, N is the number of cavities in linac, x_0 is the beam displacement before entering the first cavity, and x_∞ is the beam displacement at the end of linac. Here, $\varepsilon = \frac{1}{2}\frac{<I>Ze}{p}\frac{\Gamma}{\omega}\frac{l^2}{L}$ is BBU strength, where $<I>$ is average beam current, l is one period length, L is length of linac, and p is the momentum.

The resonance term $P_R(\omega\tau)$ is expressed as,

$$P_R(\omega\tau) = \frac{\sin(\omega\tau)}{sinh^2\left(\frac{\omega\tau}{4.Q_l}\right) + sin^2\left(\frac{\omega\tau}{2}\right)} \tag{5}$$

In the worst case scenario, assuming R/Q = 0.62 Ω, $Q_l = 1 \times 10^7$, $<I>$ = 1.0 mA, $p = 0.4 \times 10^{-19}$ kg.m/sec and x_0 =

1 mm, the calculation for transverse beam bunch displacement was performed in the frequency span 325 MHz - 1700 MHz for SR0 section. The length of a period l and of the SR0 section L was taken to be 0.61 m and 7.32 m, respectively. Resonances occur, when the condition $\omega\tau = 2n\pi(1 \pm \frac{1}{2Q_l})$ [9] is satisfied, which is shown in Fig. 4. Here, deflecting factor, X is the ratio of beam displacement at the end of linac to beam initial displacement.

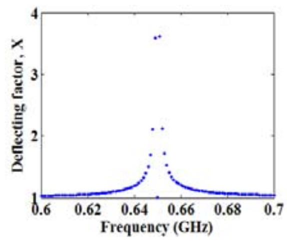

4(a)

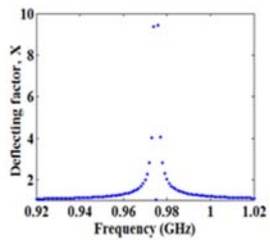

4(b)

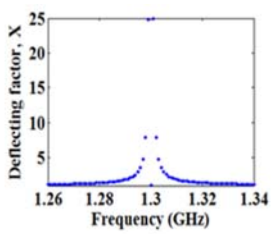

4(c)

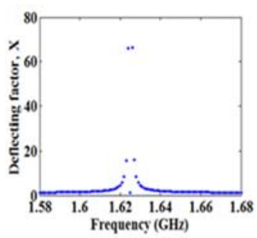

4(d)

Figure 4: Transverse deflecting factor at the end of SR0 section as a function of HOM frequency.

From this study, it is clear that the HOM frequency should not be an integer multiple of beam bunch frequency, *i.e.*, 325 MHz. From HOM analysis of SSR section of 1 GeV linac, performed using CST-MWS code, it is found that no HOM is lying near to these resonance locations.

The calculation of threshold current, which is defined as the beam current that produces deflecting factor of 2.0 at the end of SSR section, was carried out using following formula [9],

$$< I > = \frac{2p}{Q_l . e .} \frac{c^2}{\left(\frac{R}{Q}\right)_\perp \omega} \frac{l}{L^2} ln^2 \left(2 \frac{x_\infty}{x_0}\right) \qquad (6)$$

The threshold current is calculated to be 10.7 mA, 7.2 mA, and 2 mA in SR0, SR1, and SR2 sections, respectively, at Q_l value of 10^7, which is higher than the average beam current of 1 mA in case of the 1 GeV H^- linac.

EFFECT OF HOM FREQUENCY SPREAD ON BBU

During the fabrication process of cavities, there is always a possibility of fabrication error in cavity, due to which the frequency of a particular HOM varies from cavity to cavity. We studied the effect of HOM frequency spread on BBU in the worst case of f_{HOM} = 1.6251 GHz, where the deflecting factor was found to be maximum (Fig. 4). Moreover, we assumed $Q_l = 1.0 \times 10^7$, R/Q = 100 Ω, and uniform frequency spread [9]. Using the formula for wake-function $s_{(M-l)}$ in case of uniform frequency spread [10],

$$s_{(M-l)} = e^{-\frac{(M-l)\omega\tau}{2Q_l}} \sin((M-l)\omega\tau) \frac{\sin\left(\frac{\Delta\omega}{2\omega_0}(M-l)\omega\tau\right)}{\left(\frac{\Delta\omega}{2\omega_0}(M-l)\omega\tau\right)} \qquad (7)$$

the average beam displacement was calculated at the end of SR0 section. In case of uniform frequency spread of ±0.2, ±0.5, ±1.0 and ±5.0 MHz, with 500 statistical runs, the calculated average beam displacement is shown in Fig. 5.

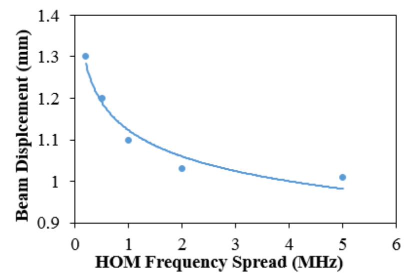

Figure 5: Beam displacement at the end of SR0 section with HOM frequency spread.

It is clear from Fig. 5 that the transverse beam displacement reduces as the HOM frequency spread increases, which shows that HOM frequency spread stabilizes the beam against BBU instability in linac.

CONCLUSION

In this paper, we have presented numerical calculations which indicate that cumulative BBU is not a major concern in SC SSR sections of the 1 GeV pulsed H^- linac. As the HOMs frequencies in SSR sections are far away from the harmonic of the beam bunch frequency, BBU instability is not enhanced in these SC sections. Further, the study of longitudinal cumulative BBU instability for the SC SSR section of the 1 GeV H^- linac is currently underway.

REFERENCES

[1] A. R. Jana and V. Kumar, *Nucl. Instrum. Methods Phys. Res. A* 942, 162299 (2019).
[2] R. Prakash *et al*, RRCAT Report, RRCAT/2021-06 (2021).
[3] M. K. Pal *et al*, RRCAT Report, RRCAT/2021-08 (2021).
[4] T. P. Wangler, RF Linear accelerators, 2nd edn, Wiley-VCH Verlag GmbH & Co. KGaA, Weinheim (2008).
[5] A. R. Jana and V. Kumar, *IEEE Transactions on Applied Superconductivity*, **24** (2014) 3500216.
[6] R. L. Gluckstern *et al*, Proc. of *Particle accelerators* 1985, Vol. 16, pp. 125-153.
[7] CST Studio Suite 2022, www.cst.com.
[8] C. L. Bohn and J. R. Delayen, Proc. of *Linear accelerator conf. 1990*, Albuquerque, New Mexico, USA.
[9] D. Jeon *et al*, *Nucl. Instrum. Methods Phys. Res. A* 495 (2002) 85-94.
[10] C. L. Bohn and J. R. Delayen, *Physical review A*, vol. 45 (1992), 5964-5993.

FPGA BASED DIGITAL I/Q DEMODULATOR FOR LLRF CONTROL SYSTEM AT RIB FACILITY IN VECC

Shantonu Sahoo[1,2] *, Anindya Roy[1], Hemendra Pandey[1,2]

[1]*Variable Energy Cyclotron Centre, 1/AF Bidhannagar, Kolkata-700064, INDIA*
[2]*Homi Bhabha National Institute, Training School Complex, Anushakti Nagar, Mumbai-400094, INDIA*

Abstract

The RF system is one of the crucial component of a Linear Accelerator. The low level RF (LLRF) control system plays an important role in maintaining the proper phase and amplitude of the RF voltage inside the accelerator cavity. A LLRF control system consists of three components namely I/Q demodulator, PID controller and I/Q modulator, out of which I/Q demodulator is responsible for measurement of phase and amplitude of the RF input. In our present design we have developed a fully digital IQ demodulator for 1.3 GHz RF superconductive cavity which is being used in the electron linear accelerator (e-LINAC) beamline at the RIB facility in VECC. In this paper we will discuss in details about the hardware implementation and performance criteria of the digital IQ demodulator.

INTRODUCTION

Radioactive Ion Beam (RIB) facility at VECC, Kolkata consists of a series of linear accelerating cavities [1]. All these cavities require RF power with precise amplitude and phase. The RF power is responsible for the acceleration of the ion beam to higher velocity. Thus, the phase mismatch between RF voltage and ion beam may result in transmission losses. The low level RF (LLRF) control system plays an important role in maintaining the proper phase and amplitude of the RF voltage inside the accelerator cavity. Traditionally, conventional amplitude-phase control is being used at RIB facility in VECC [2], which has inherent limitation due to interdependency between amplitude loop and phase loop. Thus I/Q (In-Phase and Quadrature) based LLRF control system is being developed at VECC. The I/Q demodulator is the first and the most crucial part of I/Q based LLRF control system. It is responsible for measurement of the phase and amplitude of the RF pickup signal from the cavity and thus calculating the amplitude error and phase error from the desired set values respectively. Initiatives have been taken earlier for implementation of I/Q demodulator with conventional analog RF components [3]. But the analog technique is susceptible to noise, drift and other inherent errors that can degrade the I/Q Demodulator performance. Recent advances in high-speed analog-to-digital converters allow the I/Q demodulator to be implemented digitally, greatly reducing these errors [4].

Fig.1 shows a simplified block diagram of the control and tuning mechanism for the 1.3 GHz RF cavity in RIB. The 1.3 GHz RF pickup signal from the cavity is first down-converted to an Intermediate Frequency (IF) of 113 MHz using a Local Oscillator (LO) of 1187 MHz. The Digital IQ demodulator computes the I and Q components of the pickup signal using a sampling clock of desired frequency which is derived from a global reference clock of 113 MHz. Subsequently the phase and amplitude errors are calculated which are minimized using a PID control loop inside the LLRF control block. The corrected IF signal is again up-converted to 1.3 GHz RF signal and fed to the cavity after proper amplification.

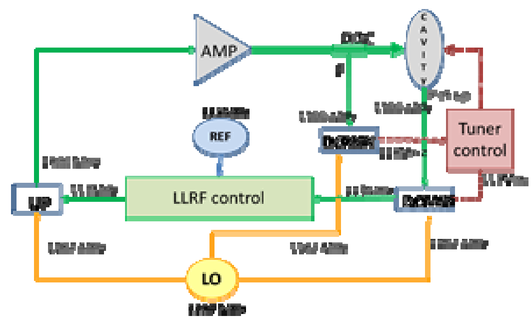

Fig. 1: Block diagram of 1.3GHz RF cavity tuning in RIB

IQ DEMODULATION SCHEME

The conventional analog I/Q demodulator, shown in Fig. 2, uses two matched demodulator circuits to convert the RF input signal directly to analog I and Q signals which are subsequently converted to digital data. The main disadvantage of this scheme is that, the parallel nature of the analog I and Q legs needs to be closely matched for accurate I/Q measurements. Also, the quadrature phase shift must be exactly 90° at all frequencies. This nature of the conventional analog I/Q detector makes it susceptible to errors associated with gain matching, DC offsets, quadrature phase errors, carrier leakage, and impedance matching.

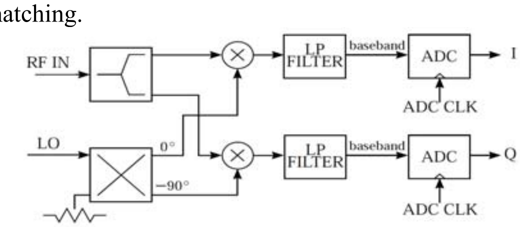

Fig. 2: Conventional IQ demodulator

Due to the above mentioned errors, we are currently developing digital I/Q demodulator that inherently improves performance. Fig. 3 shows the block diagram of the I/Q demodulator implementation for RIB. Within this implementation, the RF input is down converted to an IF of 113 MHz by mixing the RF with a 1187 MHz LO. The resulting signal is bandpass filtered to remove the high-frequency component that results from mixing and also limit the signal bandwidth to avoid aliasing.

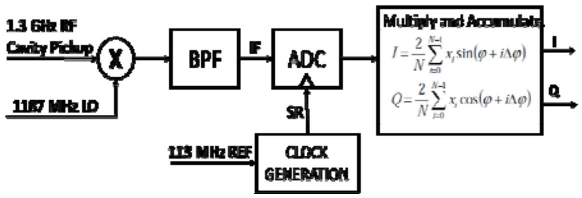

Fig. 3: Digital IQ Demodulator

The 113 MHz IF output is sampled with an analog-to-digital converter (ADC) operating at a suitable sampling rate (f_s) which is derived from the global reference clock of 113 MHz. In theory [5] there are two popular techniques which decides the f_s as follows:

1. IQ Sampling: $f_s = 4\ f_{IF}$
2. Non-IQ Sampling: $f_s = \frac{N}{M}\ f_{IF}$

The IQ Sampling has the advantage that it offers a very low latency and doesn't require a multiplication with rotation matrix in order to compute the I and Q components. On the other hand, IQ sampling requires a high speed ADC ie. 452 MHz in our case. In Non-IQ sampling technique N samples are taken during M periods of IF signal, therefore IF signal and sampling rate must fulfil a condition: $N \cdot f_{IF} = M \cdot f_s$ (M, N – integer numbers). Therefore, the latency is M/f_{IF}. I and Q can be calculated from the following equations:

$$I = \frac{2}{N}\sum_{i=0}^{N-1} x_i \sin(\varphi + i\Delta\varphi)$$

$$Q = \frac{2}{N}\sum_{i=0}^{N-1} x_i \cos(\varphi + i\Delta\varphi)$$

Due to non-availability of high-speed ADC, we have used Non-IQ Sampling Technique in our case with N=4 and M=5. This results in f_s = 90.4 MHz. A comparative study has also been done with different values of M and results have been shown in Test and Results section.

HARDWARE IMPLEMENTATION

A 16-Bit, 250 MSPS Analog-to-Digital Converter (ADC) with a 1.6 GHz Voltage Controlled Oscillator (VCO) based clock multiplier and a Zynq-7000 SoC (System on a Chip) based development kit is used for hardware implementation of the I/Q demodulator. The Zynq 7000 SoC is selected for our application to take advantage of the software programmability of the Advanced RISC Machine (ARM) processor and hardware programmability of the Field Programmable Gate Arrays (FPGA) on a single chip.

Fig.4 shows a simplified block diagram of the hardware implementation. ZC-702 FPGA development kit is used as the baseboard which connects to the ADC board through FPGA Mezzanine Card (FMC) port. It may be noted that the sampling rates shown in the block diagram represent the maximum capability of the ADC module and not the implementation. The ADC board contains the VCO based clock generator circuit which is used to generate desired ADC clock which is used for actual implementation. It is based on selected M and N parameters for non-IQ Sampling ($f_s = \frac{N}{M} f_{IF}$) as described in the previous section. Fig.5 shows the block diagram of clock generator unit which is based on AD9517 IC from Analog devices. The N and M parameters are configured by changing the registers of AD9517 from FPGA through SPI communication. Fig. 6 shows the actual image of the hardware with IF and ref signals given from function generator.

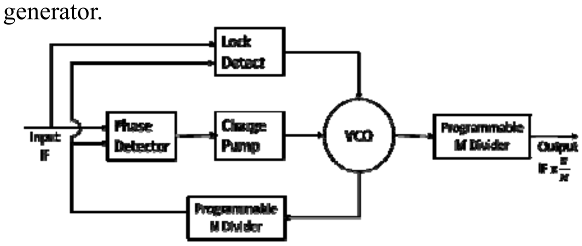

Fig. 5: Clock Generator Unit

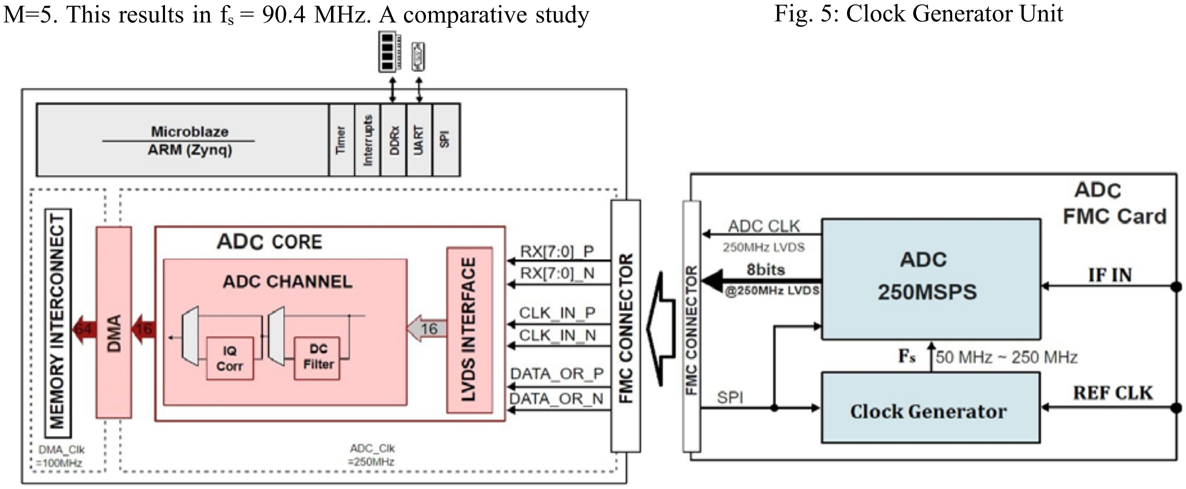

Fig. 4: Block diagram of the hardware implementation on FPGA Board

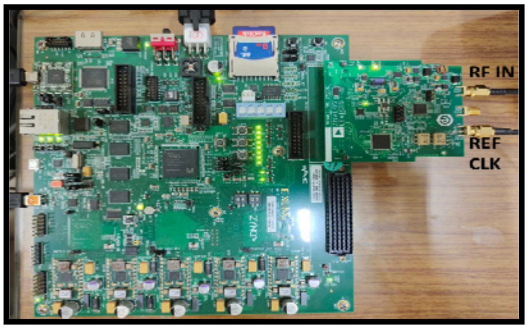

Fig. 6: FPGA Board with ADC and Clock Generator

SOFTWARE

A LabVIEW based DAQ system is also developed for data acquisition and configuration of the I/Q demodulator. The software interfaces the FPGA board through Universal Asynchronous Receiver Transmitter (UART) communication. The GUI (given in Fig. 7) features the provision for start and stop of acquisition along with online display and logging of input signal, I and Q component and computed phase and amplitude using the following equation:

$$\text{Amplitude} = \sqrt{(I^2 + Q^2)}$$

$$\text{Phase} = \tan^{-1}\left(\frac{Q}{I}\right)$$

Fig.7: Labview GUI for Data Acquisition

TEST AND RESULTS

The digital IQ demodulator has been tested and calibrated for phase and amplitude measurement. In this scheme, the reference clock and IF input signal with a constant phase and amplitude of 30° and 0 dBm have been generated from AFG3000 arbitrary function generator. Phase and amplitude stability are computed using the standard deviation of 8192 data-points acquired for different sampling frequencies (for N = 4 and M = 3,5,7,9 and 11) (plot given in Fig. 8). The phase and amplitude stability for N=4, M=5 (that is selected for our design) is less than 0.025° and 0.0003 V respectively.

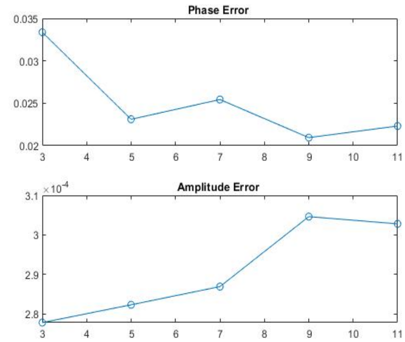

Fig.8: Phase and Amplitude errors for different M

The IQ demodulator has been calibrated for full scale region of amplitude and phase variation i.e. from -20 dBm to 10 dBm of amplitude variation and -180° to 180° of phase variation. Fig.9 shows the phase calibration plots i.e. the variation of measured I, Q, phase and amplitude with change of input phase from -180° to 180°.

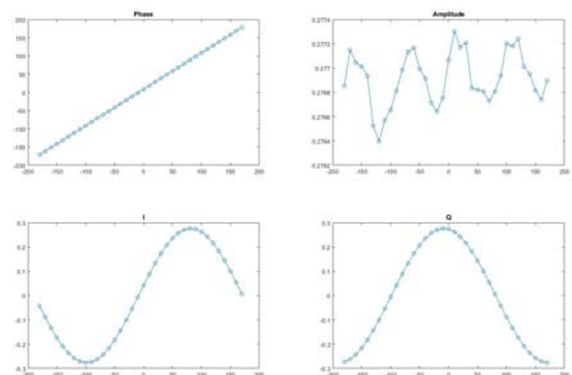

Fig.9: Phase Calibration plots

REFERENCES

[1] S. Dechoudhury, et.al, “Design and development of a radio frequency quadrupole linac postaccelerator for the Variable Energy Cyclotron Center rare ion beam project”, Review of Scientific Instruments, (2010)

[2] T.K. Mandi, et.al, “Design and development of LLRF control system for RF transmitters operated at 37.8 MHz”, Indian Particle Accelerator Conference (2019)

[3] P. P. Nandy, et.al, "Development of EPICS Enabled Analog I-Q Based Low Level RF Control System," International Conference on Electronics, Materials Engineering & Nano-Technology, Kolkata, (2021)

[4] Sigit Basuki Wibowo, et.al, “Digital low level RF control system for the International Linear Collider”, Physical Review Accelerators and Beams 21, (2018)

[5] C. Ziomek and P. Corredoura, "Digital I/Q demodulator," Proceedings Particle Accelerator Conference, Dallas, TX, USA (1995)

DEVELOPMENT OF A COMPUTER PROGRAM FOR DESIGN OF DIODE TYPE ELECTRON GUN

*Mukesh Kumar Pal[1,2], Arup Ratan Jana[1,2] and Vinit Kumar[1,2]
[1]Proton Accelerator Group, Raja Ramanna Centre for Advanced Technology, Indore
[2]Homi Bhabha National Institute, Mumbai

Abstract

For designing an electron gun, the EGUN software [1] is commonly used by the accelerator physics community. To understand the physics as well as the simulation procedure of electron gun, and also to develop the capability to add new features in the design calculations, an indigenous MATLAB [2] based computer program is being developed at RRCAT. The Poisson equation inside the electron gun is solved for an appropriate axisymmetric boundary, and the five-point difference technique is used to calculate the voltages at grid points for a specified domain. Ray optics approach is used to evolve the electron dynamics, for which the relativistic equation of motion is solved in cylindrical coordinates, using 4th order Runge-Kutta method. For the calculation of perveance, we follow a method indicated in EGUN software. The indigenous program is benchmarked with the code EGUN for case study of 90 keV electron gun design. The voltage distribution, ray positions, current per ray, pervenace and beam parameters, as calculated using the indigenous program are found to be in close agreement to the results obtained using EGUN.

INTRODUCTION

For designing an electron gun, several computer codes, such as EGUN [1] and CST particle tracking solver [3] *etc.* are commercially available, which simulate the physics of electron gun. EGUN is two-dimensional (2D) software that simulates axisymmetric structures, whereas CST is three-dimensional (3D) software. EGUN is old software and commercially available since 1990's. EGUN has been widely used by the accelerator community to design electron gun. Simulating the beam dynamics in an electron gun is of somewhat different nature compared to that in downstream accelerating structures. This is because in an electron gun, the beam formation takes place; and the space charge field seen by an electron, and hence its dynamics depends on the overall distribution of charge between the cathode and the anode, which in turn depends on the electron dynamics. This problem thus needs to be solved in a self-consistent manner. After the beam is formed in the electron gun, and it enters downstream in the accelerator, the beam dynamics needs to evolved, taking the space charge field for a nearly known charge distribution of the formed beam. Manual of the EGUN software describes the procedure for several calculations, such as calculation of voltages on grid points and ray tracing in the space inside the gun structure, calculations of charged density on grid points and beam emittance calculations, *etc*.

However, as we found, in the manual, the procedure for perveance calculation is not described in detail with adequate clarity. Reference is however provided to a paper [4, 5] for detailed methodology. Another point of confusion is the different values of beam emittance obtained in the output, while running different submodules of this EGUN code. Hence, to add more clarity and confidence to our present understanding, an indigenous MATLAB based computer program is developed, and benchmarked with the code EGUN for case study of 90 keV electron gun design.

In the next section, we have described the procedure for calculation of voltage on grid points inside electron gun geometry, with an appropriate boundary condition. The obtained results are compared with EGUN simulation and discussed. The electron dynamics and calculation of charged density on grid points are presented and discussed in the following section. We have also discussed how the self-consistent charge distribution between the cathode and anode in electron gun is obtained. In the last section, the procedure for calculation of perveance and different beam parameters *e.g*., beam emittance is discussed, and the results obtained using the in-house developed program are compared with EGUN results. The further scope of upgrades is also discussed in the paper.

VOLTAGE CALCULATION INSIDE ELECTRON GUN GEOMETRY

A typical geometry of diode type electron gun, depicting the boundary surfaces for solving the electrostatic problem is shown in Fig. 1. Boundary surfaces comprise of electrode surfaces, *e.g*., cathode and anode electrode where voltage is specified. Normally, cathode is considered to be at zero potential and anode at positive potential *e.g*., +90 kV. Boundary surface may also contain regions, where the normal derivative of potential is zero, as shown in Fig.1.

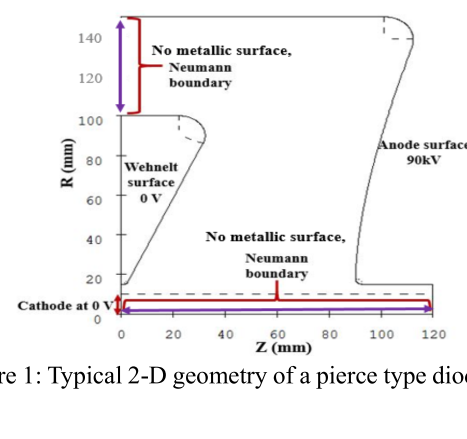

Figure 1: Typical 2-D geometry of a pierce type diode gun.

*mukeshp@rrcat.gov.in

For a case study, a typical Pierce type [6] axisymmetric 90 kV gun geometry is considered. Geometric schematic of the gun is shown in Fig. 1. We now give a brief description of the methodology used in the program. Variables Z and R represent the longitudinal and transverse coordinates, respectively. To obtain the potential inside this axisymmetric zone, Poisson equation, $\nabla^2 V = -\frac{\rho}{\varepsilon_0}$ is solved in this two-dimensional variable space, with appropriate boundary conditions. In order to calculate voltage at the grid points for a specified domain, the five-point difference technique is used, using which, Voltage $V_{i,j}$ at the grid points (i,j) [1], shown in Fig. 2(a), is obtained as follows:

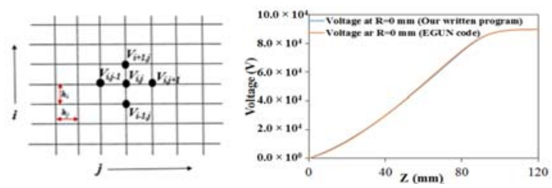

2(a) 2(b)

Figure 2: (a) Voltage at grid points (i,j) and (b) axial voltages obtained using our program as well as using EGUN.

$$V_{i,j} = \frac{1}{4}\left[\left(\left(1-\frac{1}{2(i-1)}\right)V_{i-1,j} + \left(1+\frac{1}{2(i+1)}\right)V_{i+1,j} + V_{i.j-1} + V_{i,j+1} - \frac{1}{i}\frac{\rho_{i,j}}{\varepsilon_0}\right)\right]. \quad (1)$$

Here, (i,j) denotes the indexes of grid along Z and R axes, respectively, $\rho_{i,j}$ is charge density on (i,j) grid. Based on our discretization, the geometrical mesh indexes, i and j are varied from 2 to 149 and 2 to 119 respectively. In this discretization, the two mesh dimensions h_i and h_j are scaled to unity, which helps us to represent the maximum extent of the axial and radial coordinates of this geometry using the two dimensionless quantity Z_{max} and R_{max}, respectively. Here, to obtain the voltage at the non-grid points, we have adopted the method as described by *Z. Jomaa* and *C. Macaskill* [7]. Figure 2(b) shows the on-axis voltage obtained using our program as well as using EGUN. The values of potential obtained using indigenous developed program and EGUN software are found to be in close agreement within 1 %. Equipotential lines calculated using our program, as well as the same generated using EGUN is shown in Fig. 3(a) and Fig. 3(b) respectively.

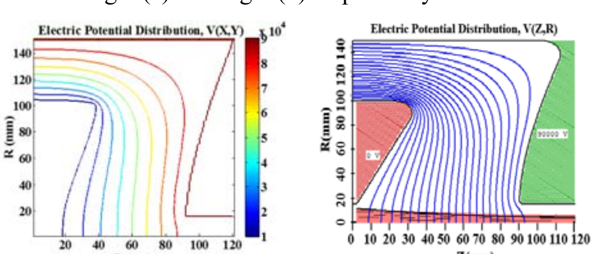

3(a) 3(b)

Fig. 3: (a) equipotential line by our developed program, and (b) equipotential line generated by EGUN code.

Note that these calculations are done after evolving the profile of beam charge density in a self-consistent manner, the procedure for which is given in remaining sections of the paper.

ELECTRON DYNAMICS AND CALCULATION OF CAHRGE ON GRID POINTS

Similar to the approach taken in EGUN, in our indigenous program also, the ray optics approach is used to evolve the electron dynamics, for which the relativistic equation of motion is solved in the axisymmetric geometry, using 4th order Runge-Kutta method [1]. In the cylindrical coordinate system, the three equations of motion for the longitudinal, radial and azimuthal directions are [1]:

$$\ddot{z} = \frac{e}{m}(1-\beta^2)\left[-E_z\left(1-\frac{\dot{z}^2}{c^2}\right) + \frac{\dot{z}.\dot{r}}{c^2}E_r + \frac{\dot{z}\dot{\alpha}}{c^2}E_\varphi - \dot{r}B_\varphi + \dot{\alpha}B_r\right], \quad (2)$$

$$\ddot{r} = \frac{e}{m}(1-\beta^2)\left[-E_r\left(1-\frac{\dot{r}^2}{c^2}\right) + \frac{\dot{z}.\dot{r}}{c^2}E_z + \frac{\dot{r}\dot{\alpha}}{c^2}E_\varphi + \dot{z}B_\varphi + \dot{\alpha}B_z\right] + \frac{\dot{\alpha}^2}{c^2 r}, \quad (3)$$

$$\ddot{\alpha} = \frac{e}{m}(1-\beta^2)\left[-E_\varphi\left(1-\frac{\dot{\alpha}^2}{c^2}\right) + \frac{\dot{z}.\dot{\alpha}}{c^2}E_z + \frac{\dot{r}\dot{\alpha}}{c^2}E_r + \dot{z}B_r + \dot{r}B_z\right] - \frac{\dot{r}\dot{\alpha}}{c^2 r}, \quad (4)$$

where, $\beta = v/c$, v and c are velocity of electron and light respectively. E_z, E_r, E_φ, B_z, B_r and B_φ are electric and magnetic fields in respective directions. $\dot{z}$, $\dot{r}$ and $\dot{\alpha}$ are longitudinal, transverse and azimuthal velocity components, respectively, e/m is charge to mass ratio of electron and r is position of electron ray is transvers direction. For axisymmetric system, E_φ is zero, E_z, E_r are generated by differtiating the voltage on grid points, i.e., $E_z(i,j) = -[V(i,j+1)-V(i,j)]/h_j$ and $E_r(i,j) = -[V(i+1,j)-V(i,j)]/h_i$, B_z, B_r are taken zero (assuming no externally applied fields). The magnetic field B_φ due to axial electron beam current I of a ray is given by $B_\varphi = \frac{\mu_0}{2\pi}\frac{I}{r}$ for r larger than the ring radius of the ray. These equations have time as independent variable, whereas, to obtain beam parameters at the end, we have converted the output in spatial coordinate. The initial value of transverse and azimuthal velocity are taken to be zero, whereas the longitudinal velocity is taken to be $v_z = \sqrt{\frac{2e(V_3-V_1)}{m}}$, here V_1 and V_3 are the respective voltages at cathode surface and at two grid step ahead towards the longitudinal direction. To set the initial transverse positon of each ray, and their fractional current, i.e., the current value assigned per ray, we have opted the same method, as in the software EGUN [1].

A self-consistent charge distribution between the cathode and anode is evolved iteratively. In the first run, calculations are performed without space charge, *i.e.*, the case, where Poisson equation simply converts into Laplace equation, and is solved with the help of five-point deference method, and particle tracking is performed, starting from cathode to anode. After that, charge distribution is obtained at each of the grid points, and in the next run, potential profile is reconstructed by solving Poisson equation, followed by an update of electron dynamics in the presence of space charge. In each of these iterative steps, charge density is estimated by calculating $\frac{J(r_i)}{v_z} = \frac{I(r_i)}{A.v_z}$, where $J(r_i)$ is current density and v_z is longitudinal velocity component, I is current per ray and A is area of ring $2\pi r_i \times h_i$ square mesh units. Here, r_i is transverse position of rays in the discretized geometry. After each iteration, the charge density profile on the grid points, is rationalised according to their inverse of the distances from the nearby ray (or rays). Repeating these sequences for few iterations, finally, a self-consistent charge distribution is obtained. In this example case, the tracing of 50 rays at 1.0 A current for 90 kV gun is carried out using our program, as shown in Fig. 4(a). The obtained beam profile is benchmarked with EGUN generated profile which is shown in Fig. 4(b). The charge density on grid points obtained from our program and EGUN are shown together in Fig. 4(c). Although not large, but deviations are there in the density profiles as obtained from our program and EGUN, which may be because of slight deviations obtained in the ray positions calculated numerically in these two codes. Deviations in the positioning of the rays also results in deviations in calculating current per rays using our program as well as using EGUN. Flow chart of our program for electron gun design is shown in Fig. 4(d).

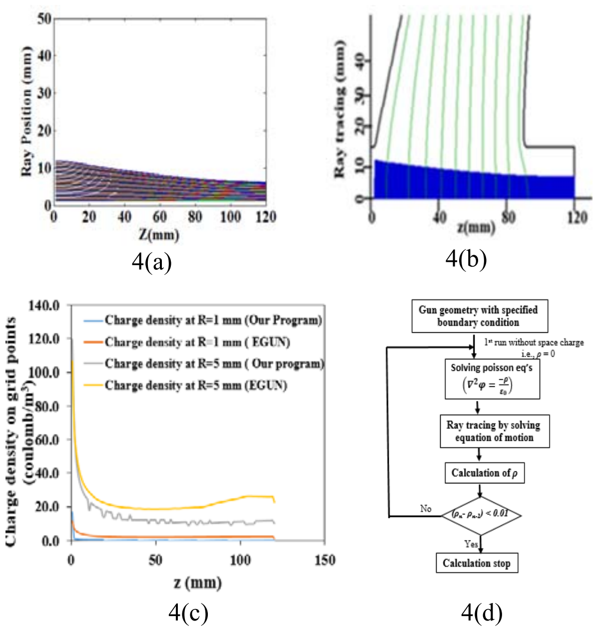

Figure 4: (a) Ray tracing by our program, **(b)** Ray tracing by EGUN, and **(c)** charge density calculation by both codes and (d) flow chart of our program for electron gun design.

CALCULATION OF PERVEANCE AND BEAM EMITTANCE

Like EGUN, our written program also calculates the beam parameters, and the perveance at any fixed axial position, *e.g.*, at the output of the electron gun. To calculate space charge limited current and perveance values, we adopted the same procedure as described in EGUN manual and Ref. [4, 5]. The perveance, P is defined as,

$$P = \frac{I}{V^{3/2}}, \tag{5}$$

where, I is the converged space charge limited beam current for a voltage V. Following for the example case of 90 kV gun, our code calculates space charge limited current and perveance values as 2.741 A and 0.1015 μP, respectively, whereas, from EGUN these values are found to be 2.822 A and 0.1045 μP, respectively.

RMS beam emittance is calculated by the formula [1],

$$\varepsilon_{rms} = [< X^2 >.< X'^2 > - < X.X' >^2]^{1/2} \tag{6}$$

where, <.> represents weighted average, X denotes the x coordinate of the ray, and a weight proportional to its current is given to each ray. Using our program, for the case of 1.0 A beam, ε_{rms} is obtained as 2.22 π.mm.mrad, rms beam size σ_x, twiss parameters β and α are obtained as 3.27 mm, 4.86 m/rad and 5.75 respectively. For comparison, these values are also calculated from EGUN for the same output current as 2.28 π.mm.mrad, 3.55 mm, 5.53 m/rad and 4.98, respectively.

Results obtained from both of these codes are also compared for the perveance limited case. Here, the resulting ε_{rms}, σ_x, β and α values from our code are found to be 8.11 π.mm.mrad, 5.19 mm, 3.32 m/rad and -10.92 respectively, whereas, the code EGUN calculates these values as 6.61 π.mm.mrad, 6.79 mm, 6.99 m/rad and -22.64, respectively.

CONCLUSION

A MATLAB based computer program is developed for simulating diode type, axisymmetric electron gun. Developed code self consistently calculates voltage on grid points inside gun geometry, in presence of electron beam current. The program calculates ray positions, current for each ray, and performs ray tracing. Calculation of charge density on grid points, perveance, space charge limited current as well as beam emittance is also performed. The results obtained from our indigenous program has been benchmarked with the code EGUN, for an example case of a 90 keV Pierce type electron gun. Although, most of the results obtained from our program are comparable with those obtained using EGUN, yet small deviations are observed, particularly in the ray position and charge density calculation. This will be analysed further. In future, we will extend this work for triode and generalized gun case also.

REFERENCES

[1] https://www.slac.staford.edu/pubs/slac-r-331.pdf.

[2] MATLAB 2014a v 8.3.

[3] CST Studio Suite 2022, www.cst.com.

[4] I. Langmuir, Phys. Rev. 21, 419 (1923).

[5] I. Langmuir and K. B. Blodgett, Phys. Rev. 22, 347 (1923).

[6] J.R. Pierce, Journal of Applied Physics, vol. 11, no. 8 pp. 548–554, 1940.

[7] Z. Jomaa *et. al.*, ANZIAM J. 45(E) ppC713-C728 (2004).

A REVIEW OF CALCULATION OF EMITTANCE GROWTH FOR SOME COMMON CASES IN ACCELERATOR PHYSICS

Vinit Kumar[#1] and Amalendu Sharma, Raja Ramanna Centre for Advanced Technology, Indore
[1]also at Homi Bhabha National Institute, Mumbai

Abstract

Emittance is one of the crucial parameters in charged particle beam dynamics, and one of the key concerns while designing an accelerator is to control its growth. Although the phenomenon of emittance growth is complex, approximate formulas for quantifying it can be derived for some cases. In this paper, we present a review of such formulas, and present simple derivations, starting from scratch. We have considered the cases, where forces are linear, such as beam transport in a skewed quadrupole, an ideal solenoid and an ideal RF cavity. Under thin lens approximation, formulas are also derived for the cases with nonlinear forces, such as beam transport through sextupoles, and also due to nonlinear space charge forces. Approximate formulas are also derived for the case of field errors in magnets. Such formulas are useful for estimating and controlling the emittance growth while designing an accelerator.

INTRODUCTION

Emittance is defined in many ways in accelerator physics. Fundamentally, it is defined as the area/volume occupied by the beam in phase space [1], and physical picture given by this definition is very useful, while visualizing its evolution. Since the phase space of a charge particle beam is in general six-dimensional (6D), we define the 6D emittance, which is the volume occupied by the beam in 6D phase space. Liouville theorem states that if the beam evolves due to time-independent conservative forces (for which Hamiltonian is a constant of motion), the phase space volume occupied by the beam, *i.e.*, the 6D emittance remains constant [1,2]. Note that this is true even if the forces are nonlinear [1]. We often take the projection of 6D volume onto 2D transverse/longitudinal phase space, and get an area in the phase space, which is defined as the projected transverse/longitudinal emittance [3]. In the absence of coupling between motions in different dimensions, the Hamiltonian is decoupled and the projected emittance also remains conserved, as the beam evolves [3]. This is not true if coupling is present.

For mathematical analysis, rms emittance is more useful, which is defined as the determinant of beam matrix. The beam matrix is in general a 6 × 6 matrix, and we define 6D rms beam emittance, as the determinant of this matrix [4]. If the beam transport is linear, *i.e.*, governed by first order transport matrix alone, it can be shown that the determinant of beam matrix is conserved, and thus 6D rms emittance is conserved, as the beam evolves [4]. Again, we define 2D rms emittance, *i.e.*, transverse/longitudinal rms emittance, as the determinant of 2D beam matrix corresponding to motion in each of the three dimensions. The 2D rms emittance remains conserved if the beam transport is linear, and there is no coupling [4]. Note that the rms emittance is not conserved if the force is nonlinear, even if it is conservative and time-independent [5]. This is unlike what happens to phase space area/volume in this case.

The trans./long. rms emittance ε_ζ is given by [5]

$$\varepsilon_\zeta{}^2 = \langle\zeta^2\rangle\langle\zeta'^2\rangle - \langle\zeta\zeta'\rangle^2, \tag{1}$$

where ζ denotes x, y or z, which are the displacements relative to reference particle, " $'$ " denotes derivative with respect to independent variable s that denotes the displacement of the reference particle along the beam axis, and $\langle\cdots\rangle$ denotes average over all particles in the bunch. It can be easily shown by taking the s-derivative of Eq. (1) that the rate of growth of ε_ζ is given by

$$\frac{d\varepsilon_\zeta^2}{ds} = 2\langle\zeta^2\rangle\langle\zeta'\zeta''\rangle - 2\langle\zeta\zeta'\rangle\langle\zeta\zeta''\rangle. \tag{2}$$

Equation of motion, including the case when the particle undergoes longitudinal acceleration is given by [6]

$$\zeta'' + \frac{\gamma'}{\beta^2\gamma}\zeta' + C_\zeta\frac{\gamma'}{\beta^2\gamma} = \frac{F_\zeta}{\gamma\beta^2 mc^2}, \tag{3}$$

where β is the particle speed in unit of speed of light c in vacuum, $\gamma = 1/\sqrt{1-\beta^2}$, m is rest mass of the particle, $F_\zeta$is the force acting on the particle along the ζ-direction, $C_\zeta = 0$ for $\zeta = x, y$ and $C_\zeta = 1$ for $\zeta = z$. Here, the second term on the left side of Eq. (3) is the damping term, which is introduced due to relativistic effect. Using Eqs. (2) and (3), it can be easily shown that in case of beam acceleration, $\beta\gamma\varepsilon_\zeta$, defined as the normalized rms emittance, remains conserved, if the forces F_ζ are linear, and there is no coupling. Note that if we define emittance in terms of trace space area, then in order to keep the phase space area conserved, we need to define the normalized longitudinal rms emittance as $\beta\gamma^3\varepsilon_\zeta$ [5]. This is because during the particle acceleration in the longitudinal direction, effective mass for the transverse dynamics is given by γm, whereas for the longitudinal dynamics, it is given by $\gamma^3 m$ [5].

In this paper, we discuss the calculation of growth in rms emittance for some of the common scenarios in accelerator physics, and develop a physical understanding, using the phase space picture. For performing all the calculations, we assume a cold beam with zero emittance at the input with $\zeta' = 0$ for all the particles, and calculate the rms emittance that builds up. In each case, we find out how the trajectory and its slope

[#]vinit@rrcat.gov.in

evolve and then use Eq. (1) or (2) to find the growth in the emittance.

EMITTANCE GROWTH DUR TO LINEAR COUPLING

When a cold beam passes through a thin skew quadrupole of normalised integrated strength k and exits, $x' = ky$ and $y' = kx$. Assuming that the input beam has no correlation in x and y, *i.e.*, $\langle xy \rangle = 0$, we get $\varepsilon_{x,y} = k\sigma_{x0}\sigma_{y0}$ at the exit, where σ_{x0} and σ_{y0} are the initial rms beam size in x and y, respectively. Same result has been obtained in Ref. 7. Evolution of the beam in the phase space is shown in Fig.1, and the area of the phase space is $4\pi k\sigma_{x0}\sigma_{y0}$ for uniform upright elliptic beam at input. Note that the 4D rms emittance, as well as the volume in 4D phase space however remain zero. As the beam further propagates after exiting the skew quadrupole, $\sigma_x^2 = \sigma_{x.0}^2 + k^2\sigma_{y,0}^2 s^2$ and $\sigma_y^2 = \sigma_{y.0}^2 + k^2\sigma_{x,0}^2 s^2$, which is consistent with $\varepsilon_{x,y} = k\sigma_{x0}\sigma_{y0}$. It is interesting to note that if we rotate the coordinate system by -45° such that the skew quad becomes a normal quad, and denote the new coordinates by (X, Y), we get $\sigma_X^2 = \left(\frac{\sigma_{x,0}^2}{2} + \frac{\sigma_{y,o}^2}{2}\right)(1+ks)^2$ and $\sigma_Y^2 = \left(\frac{\sigma_{x,0}^2}{2} + \frac{\sigma_{y,o}^2}{2}\right)(1-ks)^2$, which expectedly implies zero emittance since the beam waist has zero size.

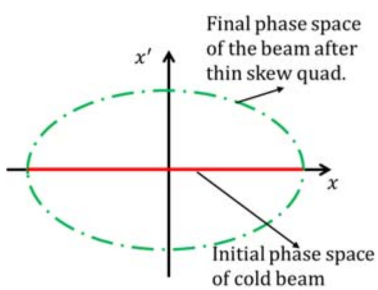

Figure 1: Evolution of a cold beam in phase space, as it passes through a thin skew quadrupole.

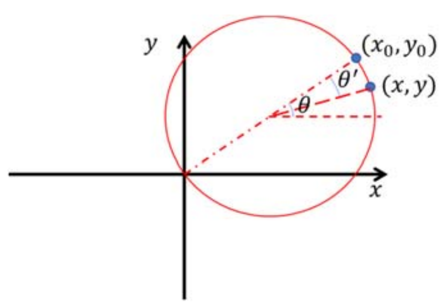

Figure 2: Trajectory of a particle inside solenoid. Solenoid axis is along z-direction, passing through origin.

Next, let us discuss the evolution of emittance due to coupling as the beam propagates in a solenoid. The trajectory of a charge particle that enters a hard-edge solenoid at (x_0, y_0) can be easily derived using Fig. 2 [8], where it is illustrated that on the xy plane, the particle moves in a circle passing through its initial location and the origin, with cyclotron frequency ω_c. Trajectory is given by $x = \frac{x_0}{2}\left(1 + \cos\frac{\omega_c s}{v}\right) + \frac{y_0}{2}\sin\frac{\omega_s s}{v}$, $y = \frac{y_0}{2}\left(1 + \cos\frac{\omega_c s}{v}\right) - \frac{x_0}{2}\sin\frac{\omega_s s}{v}$ and the slopes x' and y' can be easily derived by taking the s-derivative of trajectory. Here, v is the longitudinal speed of the particle. Using this, Eq. (1) gives us the following equation for evolution of emittance of an axi-symmetric beam of initial rms beam sixe σ_0, inside the solenoid due to x-y coupling:

$$\varepsilon_{x,y} = \frac{\sigma_0^2}{4}\frac{\omega_c}{v}\left(1 + \cos\frac{\omega_c s}{v}\right). \tag{4}$$

Note that immediately after the beam enters the hard-edge solenoid, at $s = 0$, it gets an azimuthal kick, and develops an emittance, known as the Busch emittance [3]. Inside the solenoid, the emittance evolves, as described by Eq. (3). Finally, when the beam exits the hard edge solenoid, it gets another azimuthal kick, and the emittance vanishes thereafter. Note that the coupling however vanishes in a frame rotating with Larmour frequency, and thus in that frame, there is no emittance growth seen inside the solenoid. Emittance is thus different in different frames of reference. After the beam exits the solenoid, the Larmour frame stops its rotation, thus becomes equivalent to the laboratory frame, and emittance is zero in both the frames, which gives a consistent picture.

EMITTANCE GROWTH DUE TO TIME DEPENDENT RF FIELD

Under paraxial approximation, a particle passing through an RF cavity (excited with standing wave of TM_{010} mode) experiences linear transverse forces, and under hard edge model for the RF cavity, it experiences net transverse force only at the edges [9]. The transverse kick at the entry/exit edge is given by $r' = \mp \frac{qE\sin\phi_0}{2\beta^2\gamma mc^2} r$ [10], where E and ϕ_0 are the amplitude and phase of is the electric field, when the particle enters/exits the cavity, and '-'/ '+' sign is for entry/exit edge. Since different particles in a bunch experience different amount of transverse kick, the beam develops a transverse emittance at the entrance, as given by

$$\varepsilon_{x,y} = \frac{qE}{2\sqrt{3}\beta^2\gamma mc^2}\sigma_{x,y}\Delta\phi|\cos\phi_m|, \tag{5}$$

where it is assumed that at the entrance, the particle phases are uniformly distributed between $\phi_0 - \Delta\phi$ and $\phi_0 + \Delta\phi$, and $\Delta\phi$ is small such that contribution of only the first order terms in $\Delta\phi$ is taken, while deriving the expression for emittance growth. For a prebuncher cavity, if a particle gets a focusing kick at the entrance, it gets a defocusing kick at the exit, resulting in a net defocusing kick that gives rise to an emittance, given by

$$\varepsilon_{x,y} = \omega\frac{qEL}{2\sqrt{2}\beta^3\gamma mc^3}\sigma_{x,y}^2, \tag{6}$$

for a DC beam, where L is the effective length of the prebuncher cavity. After passing through the pre-buncher, the phase space occupied by the beam looks like a bow tie, as shown in Fig. 3, and the phase space area is $8\sqrt{2}$ times the rms emittance for a uniform beam.

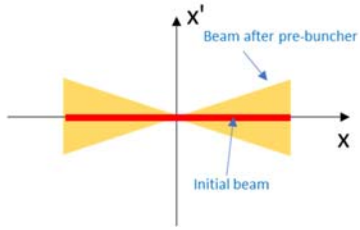

Figure 3: Phase space of the initial beam and beam after pre-buncher.

EMITTANCE GROWTH DUE TO NONLINEAR MAGNET

We now discuss the case of emittance growth in sextupoles magnets [11, 12], *i.e.*, inherent nonlinear magnets. In accelerators, nonlinear magnets always couple the betatron motion in x and y plane. For understanding the effect of nonlinearity on the emittance growth, again we consider a cold beam is entering a thin sextupole magnet. In a thin sextupole magnet, the particles get kick, as given by $x' = -\frac{S}{2}(x^2 - y^2)$ and $y' = Sxy$ in horizontal and vertical plane, respectively. Here, S is the integrated normalized sextupole strength. Due to coupling, when a cold beam passes through a sextupole, its phase space evolves from a straight line to a shape having non-zero area, and hence non-zero emittance. In case of a horizontal sheet beam at input, the phase space evolves from a straight line to curved line with zero area, but it still develops an rms emittance. Expression for the emittance of a cold azimuthally symmetric beam after it exits the sextupole is given by

$$\varepsilon_x = \frac{S}{2}\sqrt{\langle x^2\rangle\langle x^4\rangle + \langle x^2\rangle\langle y^4\rangle - 2\langle x^2\rangle\langle x^2y^2\rangle}, \tag{7}$$

$$\varepsilon_y = S\sqrt{\langle y^2\rangle\langle x^2y^2\rangle}. \tag{8}$$

For a given initial density distribution of the beam, obtaining different order moments, above expression can be evaluated. Assuming uniform round beam of rms size σ at entrance, the emittance after exit from the sextupole magnet is obtained as

$$\varepsilon_{x,y} = \frac{2}{\sqrt{6}}S\sigma^3. \tag{9}$$

Assuming an initial bi-variate Gaussian beam distribution in x and y, for the axi-symmetric case, we obtain $\varepsilon_{x,y} = S\sigma^3$, and the same result has been obtained be Emma [11], however there is some difference between our result and Ref. 11 for non-axisymmetric case. Similar methodology can be used to estimate emittance growth due to higher order nonlinearities, such as octupoles, decapoles *etc*.

EMITTANCE GROWTH DUE TO NONLINEAR SPACE CHARGE

We illustrate the calculation of emittance growth due to nonlinear space charge for a beam with 4D waterbag distribution, where the charge density ρ has a parabolic distribution given by $\rho = \rho_0\left(1 - \frac{r^2}{r_b^2}\right)$. Here, ρ_0 is the on-axis charge density and the beam is assumed to be hard edge with a radius r_b. For this case, it can be shown using Gauss's law that $E_r = C_0\left(r - \frac{r^3}{2r_b^2}\right)$, where $C_0 = \frac{I}{\pi\varepsilon_0\beta c r_b^2}$, I is the beam current and ε_0 is the permittivity of free space. Expression of $E_x(= E_r\cos\theta)$ and $E_y(= E_r\sin\theta)$ can be explicitly written in rectangular coordinates as

$$E_x = C_0\left(x - \frac{x^3}{2r_b^2} - \frac{xy^2}{2r_b^2}\right), \tag{10}$$

$$E_y = C_0\left(y - \frac{y^3}{2r_b^2} - \frac{x^2y}{2r_b^2}\right). \tag{11}$$

It is clearly seen that there is a coupling associated with octupole nonlinearity in the field. When a cold beam represented by a straight line in trace space experiences this coupling, it evolves into a shape with non-zero area, because for a given value of x, there may be multiple values of x', due to different possible values of y. This gives rise to an emittance.

Let us now analyse the evolution of beam trajectory, assuming that the beam density distribution is rigid, *i.e.*, not evolving with time. The radial equation of motion under the influence of the radial electric field E_r and azimuthal magnetic field $B_\theta = \frac{v}{c^2}E_r$, due to space charge, is given by

$$r'' = \frac{2K}{r_b^2}\left(r - \frac{r^3}{2r_b^2}\right). \tag{12}$$

Here, $K = \frac{eI}{2\pi\epsilon_0\beta^3\gamma^3 mc^3}$ is generalized perveance of the beam. After traveling a small distance Δs, change is r' can be written as $r''\Delta s$, and the growth in ε_r^2, defined as $\langle r^2\rangle\langle r'^2\rangle - \langle rr'\rangle^2$ can be evaluated, which gives the following equation for the growth rate of ε_r:

$$\frac{d\varepsilon_r}{ds} = \frac{K}{r_b^4}\sqrt{\langle r^2\rangle\langle r^6\rangle - \langle r^4\rangle^2} = \frac{K}{6\sqrt{5}}. \tag{13}$$

Although we have assumed the radial distribution of charge density to be rigid in the above calculation, in reality, due to the space charge force, the radial distribution of charge density will evolve, with its peak shifting away from the axis initially, and then shifting back towards the axis and so on, giving rise to a kind of plasma oscillation. The emittance growth rate also oscillates and it effectively saturates in one fourth of plasma period [8]. Consequently, the expression for growth in emittance due to space charge force in this case is given by [8]

$$\varepsilon_{x,y} = \frac{K}{12\sqrt{5}}\frac{\lambda_p}{4} = \frac{\pi}{24\sqrt{15}} r_b \sqrt{\frac{eI}{2\pi\epsilon_0\beta^3\gamma^3 mc^3}}. \quad (14)$$

Note that here we have used the relation $\varepsilon_{x,y} = \varepsilon_r/2$ for round beam. Also, we have used the expression $\lambda_p = 2\pi r_b/\sqrt{3K}$ for 4D waterbag distribution, which is derived by straightforward generalization of the corresponding formula for uniform distribution in terms of the equivalent rms beam size.

The methodology described above can be easily extended to any arbitrary charge distribution.

EMITTANCE GROWTH DUE TO FIELD ERROR IN MAGNETS

Finally, we discuss the case of emittance growth due to field error in magnets. Here we consider two cases – first, the random field error in the good field region of a dipole magnet, and second, the random gradient error in the good field region of a quadrupole magnet. Although these magnets are linear, emittance growth occurs because the errors are random [13]. Consider a case, where a group of parallel trajectories enters an ideal hard edge sector type magnet in a way, so that all the trajectories have angular deflection around θ after the dipole magnet, *i.e.*, bending angle is θ, and all trajectories after the magnet will undergo linear focusing. However, due to random field error, different trajectories will have an additional random angular deflection $\Delta x'$. In this case, for an individual particle, $\Delta x' = \Delta\theta$. Here $\Delta\theta$ is a random kick, which will be different for different particles, depending on their position. Therefore, on exit from this dipole magnet, a cold beam will develop an emittance given by

$$\varepsilon_x = \left(\frac{\Delta B}{B}\right)_{rms} \sin\theta\, \sigma_x. \quad (10)$$

Here, $(\Delta\theta)_{rms} = \left(\frac{\Delta B}{B}\right)_{rms} \sin\theta$. Note that this expression is derived, assuming that the particle is experiencing the same error field throughout its trajectory, which is a strong assumption. For a realistic case, a statistical analysis with trajectory simulations, using point to point field distribution in the magnet volume should be performed to evaluate the emittance growth.

In case of random gradient error in a quadrupole magnet, different trajectories will have different slope change, *i.e.*, $\Delta x' = (k + \Delta k)x$. Here, Δk is random, uncorrelated with x, and has a mean value of zero. For this case, the emittance is given by the following expression

$$\varepsilon_{x,y} = \left(\frac{\Delta k}{k}\right)_{rms} k\sigma_{x,y}^2. \quad (15)$$

SUMMARY

We would like to emphasize that although we have assumed a cold beam at the input, in reality, the input beam will have a finite emittance. However, the results obtained in this paper can be generalized for this case by adding the input beam emittance and the emittance growth calculated for the cold beam in quadrature, to obtain the final beam emittance.

To summarise, we have discussed the calculation of emittance growth for a variety of cases. Although a vast literature exists on this topic, it is hoped that the review presented in this paper will be useful for developing an easy understanding of the topic. Some interesting and useful topics that are left out here are: emittance growth due to coherent and incoherent synchrotron radiation, Intra-Beam Stripping, wakefield *etc*.

ACKNOWLEDGMENTS

One of us (VK) would like to thank Bruce Carlsten for introducing this topic to him during US Particle Accelerator School in 2005. We would also like to thank an unknown reviewer for useful suggestions.

REFERENCES

[1] J. D. Lawson, The Physics of Charged Particle Beams, Clarendon Press, Oxford, Second Edition (1988).
[2] A. H. Sørensen, "Liouville's theorem and emittance", in CERN Accelerator School: General Accelerator Physics (CERN, Switzerland) 1988, pp. 18–36.
[3] V. Balandin, W. Decking and N. Golubeva, Proceedings of IPAC (2013) 1904.
[4] U. Uriot and N. Pichoff, "Tracewin documentation", CEA Internal Report CEA/DSM/DAPINA/SEA/2000/45, 2011.
[5] Thomas P. Wangler, RF Linear Accelerators, WILEY-VCH, Verlag GmbH & Co. KGaA, 2nd Ed. (2008)
[6] C. K. Allen and N. Pattengale, "Theory and technique of beam envelope simulations", Los Alamos National Laboratory Internal Report LA-US-02-4979, 2002.
[7] David H. Dowell, Feng Zhou, and John Schmerge, Phys. Rev. Accel. and Beams, 21 (2018) 010101.
[8] Vinit Kumar, American Journal of Physics, 77 (2009) 737.
[9] Kwang-Je Kim, Nuclear Instrum. and Methods in Phys. Res. A 275 (1989) 201.
[10] V. Kumar and A. Sharma, Proceedings of InPAC (2018) 776.
[11] Paul Emma, Proceedings of 32nd international FEL conference (2010).
[12] David H. Dowell, "Correcting Emittance Growth Due to Stray Sextupole Fields", Sep. 2018 (https://arxiv.org/abs/1810.00086).
[13] Ji Qiang, Nuclear Instrum. and Methods in Phys. Res. A 948 (2019) 162844.

THREE-DIMENSIONAL ELECTROMAGNETIC SIMULATIONS OF A CONSTANT GRADIENT TRAVELING WAVE ACCELERATING STRUCTURE INTEGRATED WITH RF COUPLERS

R. Dhingra[#1], V. Kumar[1]and N.S. Kulkarni, Proton Accelerator Group, RRCAT, Indore
[1]also at HBNI, Mumbai

Abstract

An S-band Constant Gradient (CG) Traveling Wave (TW) accelerating structure has been designed [1] for the injector linac of a High Brilliance Synchrotron Radiation Source (HBSRS), to accelerate the 15 MeV electron beam to 200 MeV. Since different cells are designed independently using a 2D EM code SUPERFISH [2], it is prudent to perform end-to-end three-dimensional (3D) electromagnetic (EM) simulation of TW linac section, integrated with input and output RF power couplers, to confirm that the design works as desired, in totality. With this aim, 3D EM simulations have been performed using frequency domain solver module of 3D EM computer code CST-MWS [3]. Error and tuning studies have also been performed for random errors in cell radius and fixed error in output coupling iris, using Steele's bead-pull perturbation technique [4]. An in-house developed tuning program has been used for tuning this linac in simulation environment.

INTRODUCTION

A storage ring based High Brilliance Synchrotron Radiation Source (HBSRS) is envisaged at RRCAT with ultra-low beam emittance (150 pm-rad), very high brilliance, and wide photon energy range [5]. A baseline design has been evolved for this project, which includes an injector linac, comprising a 90 keV electron gun, and a Standing Wave buncher section with energy of ~15 MeV. The electron beam will then be accelerated to 200 MeV, using four traveling wave CG accelerating sections. The energy of the electron beam will be further increased to 6 GeV in a booster synchrotron, and finally stored in a storage ring, where it will emit synchrotron radiation in bending magnets and insertion devices. In this paper, we present the three-dimensional EM simulation studies of a single TW accelerating section, integrated along with RF power couplers. The geometrical error and tuning studies that have been performed using 3D code CST-MWS are also discussed.

STRUCTURE DETAILS

The TW accelerating structure for the injector linac of HBSRS project is a disk-loaded structure, with design frequency of 3 GHz. It is designed with four sections, each having a length of 3.793 m. Each section will consist of 114 regular cells, with β_p (phase velocity of operating electromagnetic mode in unit of speed of light in vacuum) of each cell as 0.999 [1]. As the structure is CG type, the cell radius and aperture radius are varied for each cell, such that a constant electric field profile is obtained along the linac length, in the absence of beam. The cell-to-cell variation in cell inner radius is 4-8 µm, while the cell-to-cell variation in aperture radius is 16-33 µm. Note that this is the variation between any two consecutive cells, and is desired to ensure the constant field profile. The RF power will be fed into the structure through an input RF power coupler, and the remnant power at the end of the structure will be sent to a matched load through an output power coupler. The power coupler will consist of a coupling iris, and a tapered waveguide that connects the iris to the WR-284 transmission line. The cell-to-cell variations in geometrical dimensions, as obtained through design calculations performed using SUPERFISH [2], have been explicitly considered in the 3D CST-MWS model, and it has been observed that the RF characteristics of the integrated accelerating structure are satisfactory. Further, fabrication and brazing may introduce geometrical errors (which could be up to few tens of microns), and we have shown in this paper that these are easily correctable by tuning the linac. The results of these studies are given in this paper.

3D ELECTROMAGNETIC SIMULATIONS

The frequency domain solver of CST-MWS has been utilized to perform 3D EM simulations of TW accelerating section that includes explicit consideration of the finite resistivity of copper. Figure 1 illustrates the schematic of the complete linac, which is integrated with both input and output RF power coupler.

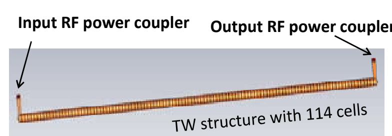

Figure 1: Full-length integrated 3D model.

Ideal Structure: No error case

Polar plots of complex ΔS_{11} have been generated for various RF frequencies. Here, ΔS_{11} is the difference in reflection coefficient, in the presence and absence of bead at different locations on the linac axis. As $\Delta S_{11} \propto E^2$, the complex electric ($E$) field data is used to generate these plots. Four such representative plots are shown in Fig.2. A perfect flower-like pattern is obtained at 3 GHz, which is the signature of tuned linac in laboratory. The graphical representation in Fig. 3(a) illustrates the variation of average phase advance per cell as a function of source frequency. The figure highlights a data point corresponding to a frequency of 3 GHz, where the phase

[#]rinky@rrcat.gov.in

advance per cell is 119.93^0. The phase error at this frequency is $\pm 3^0$, which is shown in Fig. 3(b). In Fig. 4 (a), the reflection coefficient (S_{11}) is plotted as a function of frequency, and the corresponding value is -36.4 dB at 3 GHz, indicating a power reflection of 0.02%. For the entire frequency range that was investigated, S_{11} is less than -25 dB and Voltage Standing Wave Ratio (VSWR=1+|S_{11}|/1-|S_{11}) is less than 1.12, indicating that the power reflection is kept at a level less than 0.03%. Figure 4(b) shows the transmission coefficient (S_{21}) as a function of frequency. At a frequency of 3 GHz, the value of S_{21} is -4.4 dB. It implies that in the absence of beam, the remnant RF power at the output coupler end is 36.3%, which is close to the analytical value of 34.13%.

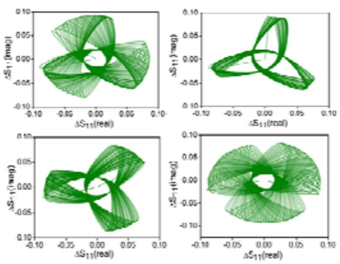

Figure 2: Polar plot of ΔS_{11} at frequency of 2999.9 MHz (top left), 3000 MHz (top right), 3000.1 MHz (bottom left) and 3000.2 MHz (bottom right).

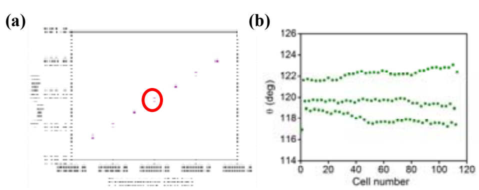

Figure 3: (a) Average phase advance versus frequency (b) Phase advance versus cell number at 3 GHz.

Figure 5 shows the magnitude of normalized on-axis electric field (E) amplitude along the linac length at frequency of 3GHz. The plot exhibits 114 peaks representing each cell center, and 115 dips corresponding to each iris location. We observe that peak of electric field amplitudee remains nearly constant in CG structure, in contrast to a Constant Impedance (CZ) structure, where it decays along the length.

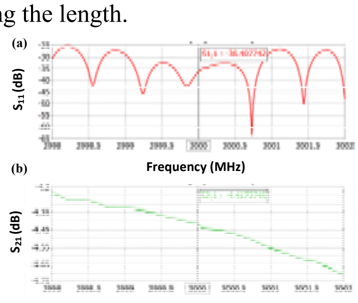

Figure 4: (a) Reflection coefficient versus frequency (b) Transmission coefficient versus frequency.

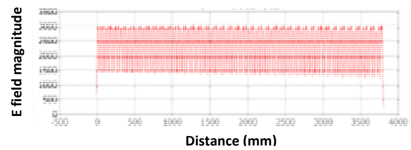

Figure 5: On-axis electric field magnitude versus distance.

Error and Tuning Studies

Random errors have been introduced in the cell radius (see Fig. 6(a)), such that the maximum detuning in cell frequency is +3 MHz. Additionally, an error of -600 μm is introduced in the output coupling iris. Tuning process of the linac has been performed in simulation environment, utilizing the non-resonant bead-pull perturbation technique. In order to consider the RF characteristics of various cells in CG structure, the electric field magnitude has been normalized as [6] $E_n=T_n/(\alpha_n r_{sh,n})^{0.5}$, where T, α and r_{sh} are transit time factor, attenuation coefficient per unit length and effective shunt impedance per unit length, respectively, and the subscript 'n' refers to the cell number. The tuning of the output coupler is accomplished using last two cells of the linac [6], in such a way so as to create a backward wave that counteracts the impact of the reflected wave resulting from the error in coupling coefficient (beta mismatch). Figure 6(b) depicts the phase advance per cell, before and after tuning. The phase advance error is reduced from $\pm 42^0$ to $\pm 2^0$, with the exception of one point, where it is $+6^0$. The average phase advance per cell is improved from 123.4^0 to 120^0, which is the intended design value.

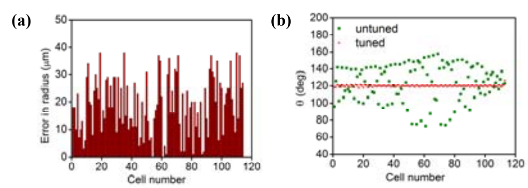

Figure 6: (a) Cell-wise error in cell radius (b) Phase advance per cell (before and after tuning) at 3 GHz.

Figure 7 and 8 illustrate the results of un-tuned and tuned linac, respectively. Tuning has led to an improvement in reflection coefficient from -11.4 dB (see Fig. 7(a)) to -33.3 dB (see Fig. 8(a)), indicating a reduction in power reflection from 7.2% to 0.05%. The three-fold pattern in polar plot of reflection coefficient that was lost in un-tuned linac (see Fig. 7(b)) has been reinstated after the tuning process (see Fig. 8(b)). Figure 7 (c) shows that geometrical errors result in significant deviations in the magnitude of electric field. Tuning process restores the constant field profile by mitigating these deviations (see Fig. 8(c)). For the un-tuned linac, local reflections are substantial, with maximum imaginary component of -0.18 (see Fig. 7(d). For the tuned linac, these reflections are nearly zero for most of the points, except at two points, as depicted in Fig. 8(d).

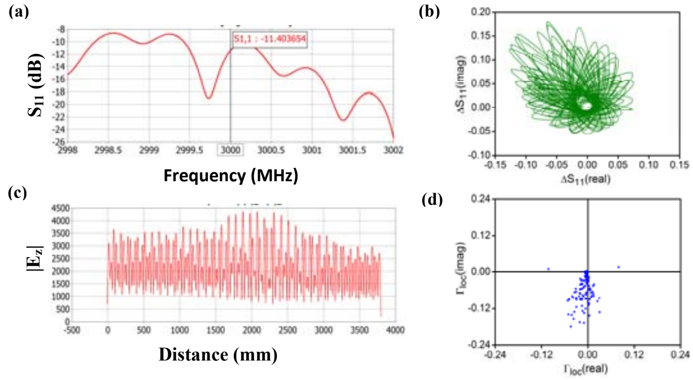

Figure 7: (a) Reflection coefficient versus frequency (b) Polar plot of ΔS_{11} (c) Magnitude of on-axis electric field versus distance (d) Imaginary component versus real component of local reflection coefficient, for the un-tuned linac. Plots (b), (c) and (d) correspond to RF frequency of 3 GHz.

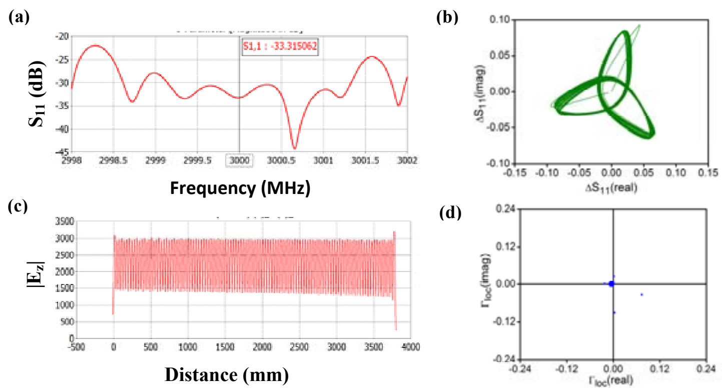

Figure 8: (a) Reflection coefficient versus frequency (b) Polar plot of ΔS_{11} (c) Magnitude of on-axis electric field versus distance (d) Imaginary component versus real component of local reflection coefficient, for the tuned linac. Plots (b), (c) and (d) correspond to RF frequency of 3 GHz.

CONCLUSION

Through the integrated three-dimensional simulations of linac, the 2D design of cells and RF power coupler design for a CG-type TW linac has been validated. The RF power coupler design is generally designed using Kyhl's method [7], considering only the coupling cavity and the adjacent cell of the linac. Tuning methodology has been explicitly tested in simulation environment, using an in-house developed tuning code, for the case of errors in cell radius and output coupling iris. Such studies are useful for assessing the behaviour of linac under various fabrication error conditions, determining manufacturing tolerances, and for testing the tuning algorithm prior to its implementation in laboratory.

ACKNOWLEDGEMENT

Author (RD) would like to thank Smt. Parul Arora and Shri P.K. Jana for sharing the geometrical dimensions of the linac cells and the RF power coupler respectively, for performing the integrated 3D EM simulations.

REFERENCES

[1] P. Arora, N.S. Kulkarni and V. Kumar, "Physics design studies for accelerating section of 200 MeV injector linac for High Brilliance Synchrotron Radiation Source", in *Proc. of Indian Particle Accelerator Conference (InPAC 2019)*, IUAC, New Delhi, Nov 2019, ID-275.

[2] SUPERFISH, Free Distribution Code, LANL.

[3] CST Studio Suite 2014, www.cst.com.

[4] C. Steele, "A nonresonant perturbation theory", IEEE Trans. Microwave Theory Tech. 14 (1966) 70.

[5] A.D. Ghodke et al, "Preliminary beam dynamical considerations for High Brilliance Synchrotron Radiation Source", RRCAT Internal Report, 2017-10.

[6] J.Shi, A. Grudiev, and W. Wuensch, "Tuning of X-band traveling-wave accelerating structures", Nucl. Instrum. Meth. A 704 (2013) 14.

[7] E.P. Westbrook, "Microwave impedance matching of feed waveguides to the disk-loaded accelerator structure operating in the 2pi/3 mode", SLAC-TN-63-103, 1963.

DESIGN AND CONSTRUCTION OF AN ISO CLASS-4 CLEANROOM FACILITY FOR SCRF CAVITY PROCESSING AND ASSEMBLY

Ambar Vohra*, B K Rawlani, Raju John, Sanjay Singh, Vimal P Jharware, S Suhane,

S Raghavendra, G. Parchani, P. Shrivastava

Abstract

At RRCAT, a programme has been initiated for development and production of Superconducting Radio Frequency (SCRF) cavities and infrastructure development for cavity string assemblies for future high power pulsed superconducting proton accelerators. After fabrication, SCRF cavities needs to be inspected, processed and assembled under controlled environmental conditions. For achieving the controlled environment, an ISO Class-4 cleanroom as per ISO 14644 Part-1[1] has been planned and constructed at RRCAT. The cleanroom is intended for SCRF cavity processing activities which include High Pressure Rinsing (HPR), component & hardware preparation, assembly, evacuation and vacuum leak testing.

The paper highlights the layout planning, salient design features & construction details, check points at various stages and validation of the cleanroom facility for SCRF cavity processing.

INTRODUCTION

Development of SCRF cavities is an important accelerator technology to provide efficient, high current and high gradient accelerating structure for nearly all major high duty proton/ H- accelerator projects around the world. The proposed superconducting proton linac for the Indian Spallation Neutron Source Project would require a large number of multi-cell superconducting cavities. The superconducting cavities are being developed under (IIFC) mutual collaboration between RRCAT (Indian Institute) and Fermilab (USA).

The final processing of SCRF cavities has a stringent condition requiring cleanroom environment during HPR and assembly of SCRF cavities.

Figure 1 shows general layout of clean room. The overall dimension of the cleanroom is 3.80 m x 10.00 m and height is 4.50 m for ISO class-4 cleanroom and 4.20 m for rest of the cleanroom.

Based on functional classification entire cleanroom has been divided in two zones: -

Service Zone: This includes room no. R1 - Ante Room, R2 - Gowning Area, R3 - Ante Room and R4 - Air Shower. The rooms in this area have cleanliness of level ISO Class - 6 & 8. These rooms provide barrier to avoid direct exposure of ISO - class 4 room to outside environment. They also provide mobility and space for carrying out services like gowning of personals as per cleanroom Standard Operating Procedure, buffer zone for cavity, storage of cleanroom accessories etc.

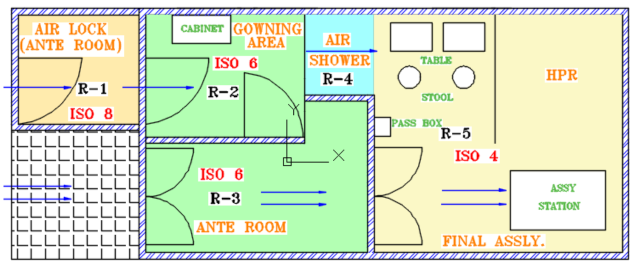

Figure 1: Schematic plan of ISO Class-4 Cleanroom

Processing Zone: In this room assembly and High Pressure Rinsing of SCRF cavities is carried out. Room no. R5 - Assembly and HPR Room is designated for this work. The room has ISO Class-4level of cleanliness.

DESIGN OF CLEANROOM

The cleanroom has been partitioned into various cleanliness zones from ISO class 8 to ISO class 4 cleanliness levels. The cleanroom has been designed to achieve following parameters: -

- Cleanliness (Particulate Concentration)
- Temperature and Relative Humidity
- Velocities / Air changes per hour
- Air Pressure Differential across rooms

Considering the design requirement of filter coverage in the range of 87-99% in ISO Class 4 area, the ISO class 4 area has been designed based on plenum concept to maximize the filter coverage. Terminal HEPA (H-14 as per EN-1822) and ULPA (U15 as per EN-1822) filters have been installed within plenum in series to achieve desired cleanliness (refer Figure 2).

Table 1: General design parameters of the cleanroom

Description	Unit	Specification
Outside design conditions		
Location	Area	Indore, Madhya Pradesh
Summer	ºC	41.1 DBT /25 WBT

*ambarv@rrcat.gov.in (**ID:E8-320**)

Monsoon	ºC	32.2 DBT / 27.7 WBT
Winter	ºC	10 DBT / 7.2 WBT
Inside design conditions		
RH	%	50 ± 5
Temperature	ºC	22 ± 2
Pressure	Pa	Cleaner areas are at higher pressure (around 5-10)
Occupancy	Nos.	3 Persons
Equipment Load	KW	2
Diversity Factor	No.	0.6
Exhaust Air	CFM	0
Air Changes Per Hour	ACPH	As mentioned in below Table 2
Light intensity	Lux	~ 500 Lux
System Type		Ducted with plenum concept

Air flow rate has been maintained in different rooms to achieve desired cleanliness. Two nos. Air Handling Unit (AHU) have been deployed to achieve air flow rate as mentioned in Table 2. The details of the AHUs is as follows: -

- AHU – 1 – 20000 CFM – dedicated for ISO class 4 room.
- AHU – 2 – 5500 CFM – catering ISO class 6 and class 8 rooms

Table 2: Air changes rate and Filter coverage Details

S. No.	Class	Air changes ACPH	Physical Filter Coverage (%)	Effective Filter Coverage (%)
1	4	> 500	92	85
2	6	170	38	35
3	8	40	10	9

Following systems have been incorporated in the cleanroom to ensure swift and safe working: -

- Facility monitoring and control system
- Fire Detection and suppression system
- Air shower and dynamic pass box to reduce contamination without compromising personnel circulation
- VFD based Dx type AHU
- Air tight view panels for communication

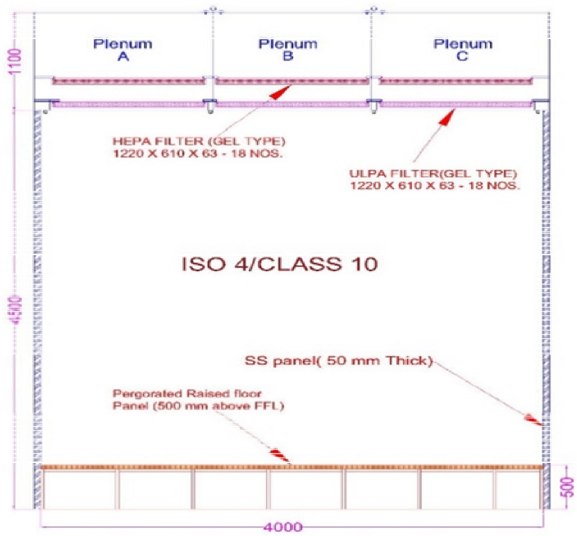

Figure 2 : Sectional elevation of Plenum type design for ISO class 4 area with three plenums viz. A, B and C

CONSTRUCTION, PLANNING AND MANAGEMENT

The cleanroom construction process must be carefully managed to ensure that the environment is not contaminated during the construction process. This involves the use of temporary walls, filters, and other measures to control contamination. The construction process must also be closely monitored to ensure that the specifications of the cleanroom are met. Figure 3 depicts typical construction process followed for constructing cleanrooms.

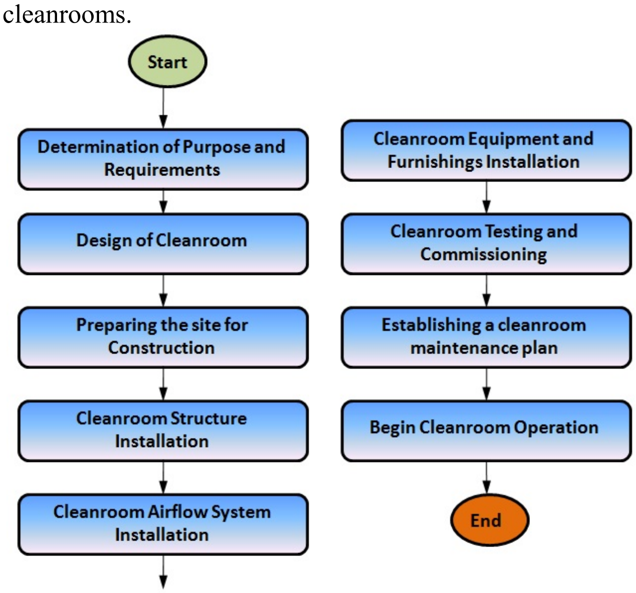

Figure 3: Construction process of cleanroom

TESTING AND VALIDATION

The cleanroom has been tested as per ISO – 14644 – Part – 3. Following parameters have been tested for validation of the cleanroom: -

1. Air-borne particle count
2. Airflow test
3. Air pressure difference test
4. Installed filter system leakage test
5. Airflow direction test and visualization
6. Temperature and Humidity test
7. Recovery test
8. Containment leak test
9. Illumination level measurement

Light scattering airborne particle counter (LSAPC) used for the test had a flow rate of 2.38 litre / min. The sampling time at each location was taken as 10 min for ISO class 4, class 6 and class 8 rooms to get a sampling volume of 28.30 litre.

The recovery time of the cleanroom is 30 minutes. The cleanroom has been validated as per ISO 14644 Part-3 and results obtained for particle count shows consistent performance of the cleanroom. As shown in Table 3 we have been able to achieve one class higher cleanliness as compared to the intended class of the cleanroom at all locations i.e. at ISO class 4 location we are getting results of ISO class 3 level of cleanliness.

Table 3 : Actual results obtained in particle count test

Concentrations (particles/m3) for particles equal to and greater than the considered sizes						
Particle size	**≥0.1 µm**	**≥0.2 µm**	**≥0.3 µm**	**≥0.5 µm**	**≥1 µm**	**≥5.0 µm**
HPR room Average	**508**	**109**	**26**	**5**	**2**	**0**
ISO Class 3 limit	1,000	237	102	35	-	-
ISO Class 4 limit	10,000	2,370	1,020	352	83	-

Figure 4 : Some photographs of the testing of cleanroom

COMMISIONING

The commissioning of the cleanroom took place in March 2022 when the cleanroom was handed over to the user. The testing was carried out in two occupancy state viz. as-built and at-rest.

Figure 5 : Cavity rinsing process inside cleanroom

CONCLUSION

Challenges encountered during execution and the measures taken to overcome those challenges are listed below: -

1. **Tendering and documentation** – Elaborate study was carried out during initial stage to derive the specifications of the work so as equal opportunity is available to all the bidders.
2. **Space constrains** - Use of filter in series inside the plenum, optimization of ducting work.
3. **Complexity and interlinking of work** - Adequate planning and sequencing of activity, analysing and designing the junction points between different services.
4. **Quality Control** - Special test procedures were adopted to ensure requisite quality of work.
5. **Maintenance** - To consistently maintain the class of cleanroom maintenance plan was prepared concurrently.

REFERENCES

[1] ISO 14644 - Part - 1:2015 - Classification of air cleanliness by particle concentration

[2] ISO 14644 - Part - 4: Design, Construction, and Start-up

[3] ISO 14644 - Part - 3: Test Methods

[4] IS - 800 - General construction in steel – code of Practice

OPTIMIZATION OF OPERATING PARAMETERS OF ECR PROTON SOURCE IN PULSED MODE

Manish Pathak[1,2,a], Praveen Mohania[1], S. K. Jain[1,2], Rekhya Naika[1], Rohit Mishra[1], D. V. Ghodke[1], Vijendra Prasad[1], D. Baxy[1], M. Lad[1], Purushottam Shrivastava[1]

[1]Proton Accelerator Group,
Raja Ramanna Centre for Advanced Technology, Indore-452 013, India
[2]Homi Bhabha National Institute, Training School Complex, Anushakti Nagar, Mumbai-400 094, India

Abstract

An electron cyclotron resonance (ECR) ion source operating at microwave frequency 2.45 GHz was designed and developed at RRCAT. The source was re-commissioned and operated in CW mode (magnetron - adjustable up to 2 kW). Ion beam current is extracted using three-electrode extraction geometry and is measured using water cooled standard pneumatic controlled Faraday cup. CW proton beam current up to 8 mA at 25 keV beam energy was extracted. This source has been now modified and upgraded to operate in pulsed mode. For this, a RF source has been designed and developed indigenously based on solid state RF pulsed amplifier of 1 kW (peak power), 2.45 GHz, pulse width 1-5 ms, duty factor up to 10% and integrated with the ion source. The hydrogen plasma has been obtained by varying pulsed RF power, solenoid current and hydrogen gas flow to investigate the optimized operating parameter of the source. The reflected power behaviour was also studied at the different operating parameters and minimized using triple stub tuner. This paper presents the optimization of operating parameters of ECR proton source for the extraction of pulsed proton beam current.

INTRODUCTION

The sub-systems of high power pulsed proton linac are being developed at RRCAT, Indore. In this direction, the first step is to build a high current pulsed proton source as an injector. The electron cyclotron resonance (ECR) source is being widely used as proton current source in CW mode as well as in pulsed mode. RRCAT has developed its own ECR ion source working at 2.45 GHz microwave frequency. CW proton beam current up to 8 mA at 25 keV beam energy was extracted and characterized [1, 2]. This source has been now modified and upgraded to operate in pulsed mode in-house developed solid state RF pulsed amplifier of 1 kW (peak power) [3]. The pictorial image of in-house developed ECR pulsed proton source is shown in Figure 1. In ECR source, plasma is produced by matching the cyclotron frequency of an electron in a DC applied magnetic field with the applied microwave frequency. The major subsystems of the ECR ion source are, plasma cavity, vacuum system, electromagnets for confinement of the plasma, microwave system for the coupling/transfer of the microwave power to the plasma cavity, multi-electrode geometry for beam extraction, plasma characterization tool, beam diagnostics devices, etc. Since the gas pressure/flow, RF power, solenoid current (magnetic field) are crucial for the operation of an ECR source. Therefore, optimisation of these becomes necessary to obtain desirable operational parameter for reliable and smooth operation of the source.

Figure 1 : Pictorial image of an in-house developed ECR pulsed proton source

Optimization of operating parameter:

Optimization of gas pressure & flow:

A 3D CAD model of ECR proton source chamber was built in COMSOL geometry window using multiphysics module (shown in Figure 2). Built model has a different sub chambers in line like WR-284 wave guide, plasma cavity, triode extraction geometry and multiport vacuum chamber for beam diagnosis. One high speed Turbo Molecular Pumps (TMP) of capacity 550 l/s is coupled to the extraction chamber through DN100CF port for pumping the purged hydrogen gas. Hydrogen Gas in ion source is purged through a flow line of diameter 4 mm. Flow of hydrogen gas in chamber was varied from 0.1 SCCM to 5 SCCM (Standard Cubic Centimeters per Minute). The above model is simulated in 3D COMSOL multiphysics to get required pressure value in extraction chamber to optimize the RF power coupling for different purging rate. The hydrogen gas pressure on chamber wall at 0.5 SCCM gas flow rate is shown in Figure 3.

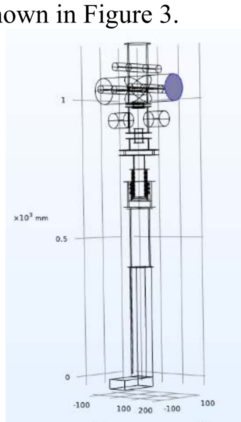

Figure 2 : 3D CAD of ECR proton source chamber

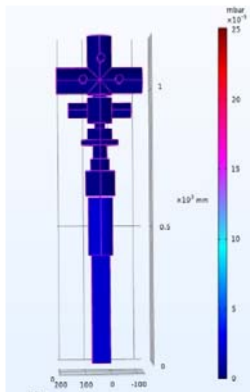

Figure 3 : Hydrogen gas pressure on chamber wall at 0.5 SCCM gas flow rate

Optimization of plasma intensity

An experiment was performed for behavioral study of plasma discharge intensity with respect to variation of hydrogen gas pressure, solenoid current and pulsed RF power. The hydrogen plasma discharge was obtained at different pulsed RF power for different inlet hydrogen gas flow 0.1 to 5 SCCM. The gas pressure was measured at extraction chamber due to non-existence of vacuum port in plasma cavity, as it is floated at high voltage at the time of beam extraction. First initial significant intensity of glow of discharge was observed at a pulsed RF power of 20 W at neutral gas pressure of 4.2×10^{-5} mbar. The plasma glow images were captured using CMOS camera in trigger mode, initiated by pulse electrical trigger fed by RF driver amplifier from RF generator. The captured images were processed in LabVIEW based GUI application for different pulsed RF power (10-850 W), gas pressure/flow (0.1-5 SCCM) and solenoid current to get the information about average plasma intensity as shown in Figure 4.

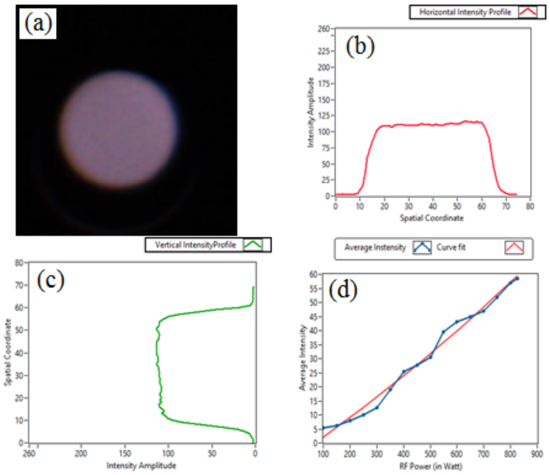

Figure 4 : (a) Plasma image captured from extraction aperture (b) Horizontal intensity variation (c) Vertical intensity variation (d) Average intensity variation w.r.t. to pulsed RF power

Optimization of solenoid current

Solenoid coils are used for the plasma generation and confinement. Our system has capability to generate the off-resonance, flat field and mirror field configurations by varying the solenoid current. To get the proton beam current, flat field configuration is produced by using three water cooled solenoids coils (M1, M2, and M3). The coils are energized independently with the use of three independent dc power supplies. The ECR resonance condition must be satisfied where microwave is introduced to the plasma. This helps to produce homogeneous and high density plasma. For 2.45 GHz frequency the required magnetic field is 875 G. Current variations in solenoids vary the structure of resonance surface as well as plasma discharged intensity. Different combination of current for M1, M2, and M3 gives variation in plasma discharge parameter. The arrangement of solenoid coil with plasma cavity and waveguide is shown in Figure 5.

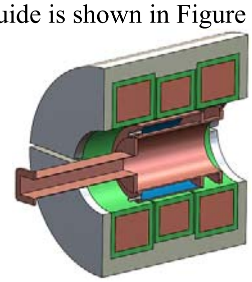

Figure 5 : The arrangement of solenoid coil with plasma cavity and waveguide

Optimization of pulsed RF power

The pulsed RF power is fed through coaxial adapter to waveguide and coupled to plasma cavity via rectangular open ended waveguide (WR-284). The microwave power transfer line consists of isolator, directional coupler, triple stub tuner, microwave window and high voltage DC break. The directional coupler is used for the measurement of forward and reflected RF power. The directional coupler was calibrated for the pulsed forward and reflected power measurements and mV signal was recorded using digital storage oscilloscope. The hydrogen plasma discharge was obtained by varying pulsed RF power from 10-850 W by using attenuators ranging from 1 to 6 dB and forward and reflected power are recorded on a digital storage oscilloscope. The RF power is optimised by minimising the reflected power using slight variation in solenoid current and hydrogen gas flow. The recorded waveform of measured forward and reflected power on a digital storage oscilloscope is shown in Figure 6.

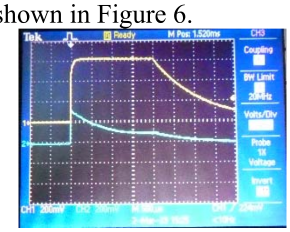

Figure 6 : Recorded waveform of measured forward (yellow in colour) and reflected power (cyan in colour) on a digital storage oscilloscope

Optimization of electrode voltage

A triode geometry based ion beam extraction system has been used for proton beam current extraction. It has three electrodes plasma electrode (PE), extraction electrode (EE) and ground electrode (GE). The PE is floated at high voltage, equivalent to beam energy for singly charged ions, EE is biased at negative potential to control the beam emittance and to suppress the accelerated electrons and GE is biased with zero voltage. The PE, EE and GE have an aperture of 5, 8 and 10 mm respectively. The source/plasma electrode is biased with positive (+) 60 kV DC power supply, and suppressor/extraction electrode is biased with negative (-) 10 kV DC power supply. The extracted beam current is measured using standard water cooled 1.5 kW Faraday cup. Extraction electrode voltage is changed to optimise the proton beam current at specified source voltage/energy. A current shunt of 100 ohm across Faraday cup is used and pulsed voltage waveform is recorded using digital storage oscilloscope to evaluate the proton beam current. The recorded waveform of measured beam current on a digital storage oscilloscope is shown in Figure 7.

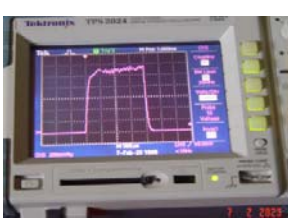

Figure 7 : Recorded waveform of a measured pulsed proton beam current on a digital storage oscilloscope

RESULTS AND DISCUSSIONS

The present Electron Cyclotron Resonance source has been optimised to maximised extracted pulsed proton beam current using in-house built solid state pulsed power amplifier. To get the required pressure in plasma cavity, flow of hydrogen gas in ion source chamber is simulated using COMSOL multiphysics. The simulation results are shown for hydrogen gas pressure distribution over the ECR chamber. The required pressure of ~ 1-2 × 10^{-5} mbar in extraction chamber has been obtained through controlled gas injection at 0.5 SCCM. It was seen that by processing the glow image of plasma indirect estimation of plasma density can be done, which are useful for higher beam current extraction studies. It has been also found that solenoid current plays a very crucial for plasma discharge. The following current combination of solenoid magnets M1 (7.6 V/45 A), M2 (7.4 V/45 A) and M3 (6.2 V/45 A), produces stable discharge for flow range between 0.1-5 SCCM. It is observed that reflected pulsed RF power changes with pressure and solenoid current. Up to some limit power requirement increases with gas pressure and then it gets saturate at fix values of solenoid current. It was found that extraction electrode voltage is crucial for optimisation of beam current. With all the above optimisation, a 10 mA, 35 keV stable pulsed ion beam current of 2 ms and 2 Hz is extracted at -1.67 keV extraction voltage. The source is now being tested continuously for different duty factor with varying pulsed RF power, solenoid current and gas flow.

CONCLUSION

ECR ion source has been indigenously developed at RRCAT and in operation in CW and pulsed mode. 8 mA CW proton beam current extracted at 35 keV beam energy and 10 mA pulsed (2 ms, 2 Hz) ion beam current extracted at 35 keV beam energy.

REFERENCES

[1] S. K. Jain, Akhilesh Jain, P. R. Hannurkar, and S. Kotaiah, "Characterization of Plasma Parameters, First Beam Results, and Status of Electron Cyclotron Resonance Source", Review of Scientific Instruments 78, 053301 (2007).

[2] S. K. Jain, M. Tayyab, S. Bagchi, J. A. Chakera, P. A. Naik, "Characterization of Proton Beam Emission from an Electron Cyclotron Resonance Ion Source", Nuclear Instruments and Methods in Physics Research A 708, 51-55 (2013).

[3] Praveen Mohania et al, "Design and Development of 1 kW Pulse RF Amplifier with Integrated Power Meter and Pulse Generator for ECR Proton Source", this conference

[a]mkpathak@rrcat.gov.in

Electromagnetic Design of Bending magnets for LBNF beamline

Janvin Itteera, Kumud Singh, Sundar Rajan S, Mahima, U G P S Sachan, Vikas Tiwari, P K Rai , Sanjay Malhotra

Bhabha Atomic Research Centre, Mumbai-85

Abstract

The Long baseline neutrino facility shall use the primary proton beam(60-120GeV) from the MI-10 section of the main injector at FNAL for high energy physics experiments. The high energy proton beam shall be directed to interact with solid target to produce mesons which will be subsequently focused by magnetic horns onto a decay pipe where they decay into muons and neutrinos [1]. The paper shall present the electromagnetic design of these bending magnets using Opera TOSCA software. 2-D Shimming of the pole faces were carried out to achieve the desired magnetic field uniformity within the good field region. Magnetic field estimates were sampled in the good field region to calculate the higher order harmonics coefficients of the magnetic field.

INTRODUCTION

Bending magnets are typically defined by their beam rigidity which is the product of magnetic field induction(B_0) and the radius of curvature(ρ_0) of the charged energetic projectile. In case of proton beam, rigidity is as follows [2,8]:

$B_0.\rho_0 = \frac{1}{300}\sqrt{E^2 + 2E.E_0}$ (T.m)

Wherein E_0 is the rest mass energy(938MeV) and E is the beam kinetic energy and C=3 x10^8 m/s.

Magnetic field homogeneity in the interaction region and the consistency of the effective magnetic length throughout the entire range of operation are the key design challenges involved. Moreover, these magnets were envisaged to be interoperable with main injector magnets and within the compliance of the existing power supplies. The electromagnetic design was carried out extensively to optimise these parameters with iterative changes on the largely iron dominated magnets.

ELECTROMAGNETIC DESIGN

Pole tip profile

The magnet integral required to steer the beam is exceptionally large due to the high beam rigidity of 120GeV proton particle through the given the desired beam lattice. This demands presence of 1.6T over an effective interaction length of 4m, to achieve the desired integral field of 6.68T-m[2,3].

In iron dominated magnets, infinitely wide flat pole is the ideal boundary conditions for perfect dipole. Empirically, following expression indicates the minimum optimized pole width required to achieve the desired dipole field uniformity in the interaction region[8].

$$\frac{a}{h} = -0.14ln\frac{\Delta B}{B} - 0.25$$

Wherein 'a' refers to the pole overhang beyond the good field region, h is the half pole gap. Optimized pole width has certain projections at the pole tip to enhance the transverse uniform field region at the center of the air gap. The pole faces need to be profiled to achieve the desired field homogeneity throughout the interaction region. Due to their large lengths, these magnets can be largely considered a quasi-2D system [3].

2D modelling was carried out using TOSCA software with appropriate symmetry and boundary conditions. Fig.1 shows the field plots in the iron yoke.

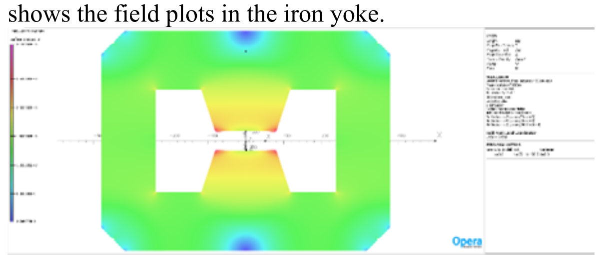

Fig 1.0: Magnetic field profile in the iron yoke.

The dipole magnetic field distribution within good field region of 25mm diameter is shown in Fig-2.

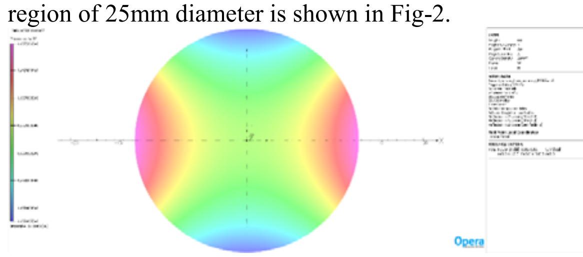

Fig 2: Dipole Homogeneity in the Good Field region @ nominal field of 1.658T

The quality of the pole profile was assessed by studying its sensitivity to the field uniformity with degradation in the magnetic properties of the ferromagnetic materials.

Harmonic Analysis

Harmonic analysis was carried out at the good field region of diameter 25 and 50mm to evaluate the relative field quality with reference to the dipolar field.

Fig. 3 illustrate the relative field non homogeneities contributed by various multipole components at various operating dipole field levels.

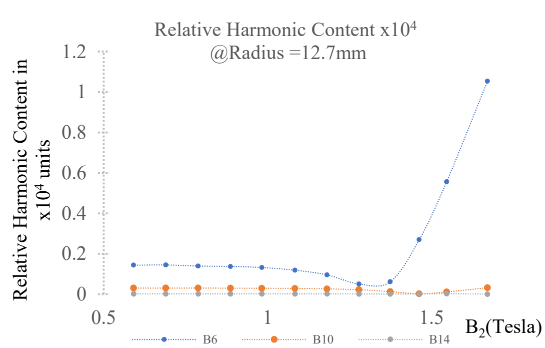

Fig 3: Multipole profile at 12.7mm radius

B_2 and B_6 refers to the dipole and sextupole components respectively(2n nomenclature used in this paper). Harmonic analysis was also carried out at 50.4mm diameter throughout the operational range of the magnet and is shown in fig 4.0.

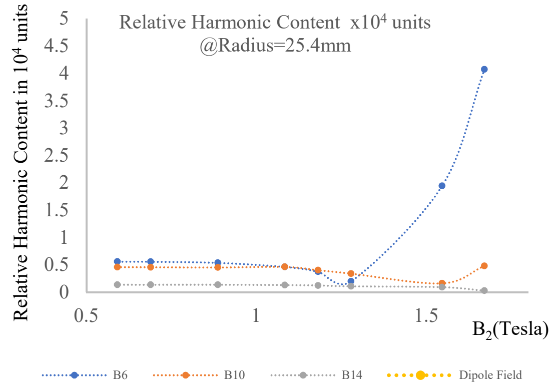

Fig 4: Harmonic field profile at radius of 25.4mm

It is known fact that sextupole is the dominant systematic error in H-type dipole magnet. Therefore, it was found prudent evaluate the relative dependence of sextupole and other higher order modes transversely. This is shown in fig. 5.

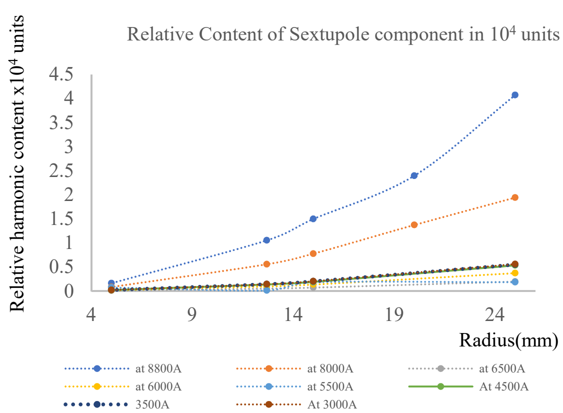

Fig-5: Transverse dependence of various relative harmonic content at various currents

As evident from the above curves in figure-5, at lower current, sextupole errors are relatively close which is attributable to the pole tips magnetized well below the saturation region. At higher currents, magnetization of pole tips gradually approaches the saturation region leading to deterioration of the field homogeneity. This effect is more pronounced at larger transverse radius

Similar analogy is applicable for field uniformity and is shown in fig. 6. The pole tip chamfers have been designed adequately to immunize field profiles from varying magnetisation properties attributable to sourcing from different production batches of magnetic steel, often limited by capacity of the mill. The design efficacy was evaluated based by imposing a 10% degradation in magnetic field intensity (A/m) of the B-H properties and calculating the field homogeneity. Negligible decline(<1%) in the field homogeneity was observed.

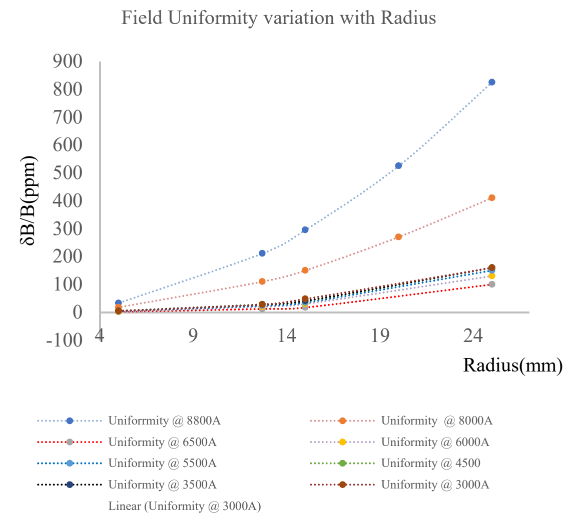

Fig 6: Transverse Dependence of field homogeneity at different excitation levels

Electromagnetic design of end packs

The critical design element of the end pack is the constancy in the effective length of the magnet which determine bending angle of the beam[4,6,7]. The effective length (L_{eff}) is defined as:

$$L_{eff} = \frac{\int By.dl}{B_{y0}}$$

Wherein, B_y is dipole magnetic field (T) and B_{y0} is the central dipole field (T), with the integral computed along the reference beam trajectory.

Fringe field at the magnet ends play a vital role in the above integral and their variations arising from core saturation are the main design concern. In a typically sharp edge terminations, the pole saturates prematurely resulting in the decrease of the integral and consequently lower effective edge. This is overcome, by means of beveled ends, chamfers or specially designed rogowski profile for minimal core edge saturation. The end packs have negligible contributions towards the overall integral field homogeneity, as they are predominated by the results of the 2-D analysis. We have adopted a beveled stepped edges with terminations contoured along a modified rogowski profile and is shown in fig. 7.

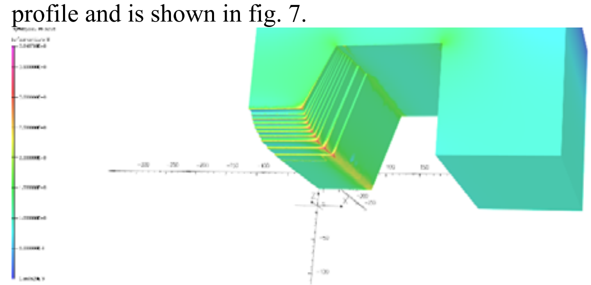

Fig 7: A quarter model of the end packs

The variations in the effective length were computed for various excitation levels and shown in fig. 8.

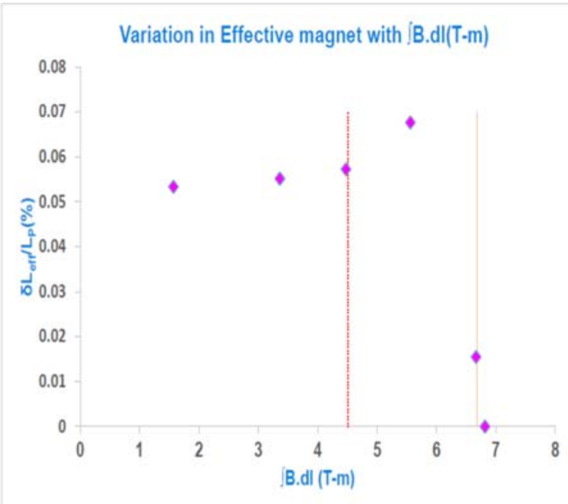

Fig-8: Dependence of the effective length along the operating range

The field variations(inhomogeneity) is expected to be well within 0.04% considering the achievable tolerances on the lamination's stampings and the electromagnetic design. The normalized sextupole component was computed along the reference beam trajectory at the entrance of the magnet and is shown in the fig. 9. It may be remembered that as beam advances in to the magnet along the reference path, normalized sextupole experienced by the particle approaches the 2-D analysis values.

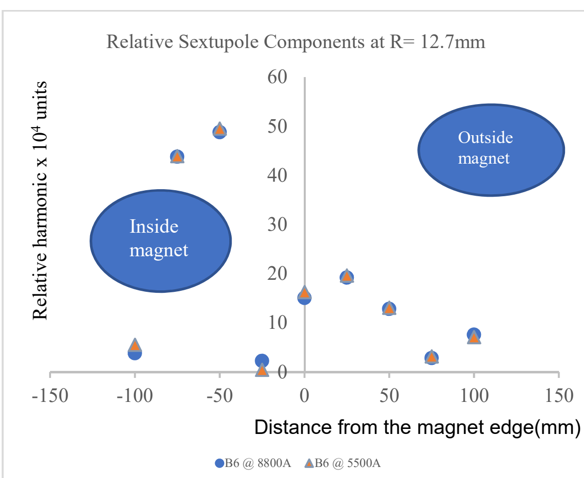

Fig 9: Variation of the sextupole components along the reference beam trajectory

SUMMARY

Electromagnetic design has been completed. The overall uniformity of better than 0.02% has been achieved in the good field region of 25mm diameter. The end pack has been optimized to limit the sextupole component in its proximity and control variation in effective magnetic length, which is found to remain within 3mm in the operational regime.

REFERENCES

1. Design of the LBNF beamline, FERMILAB-CONF-16-163-AD
2. Main Injector Technical Design Handbook, November 1995
3. Main Injector Dipole Magnet: 2D Field Computations, MI-0036, Jean –Francois Ostiguy
4. Design and Measurements of prototype Fermilab Main Injector Dipole End packs, D. J Harding et al, IEEE-1993
5. The Design and manufacture of the Fermilab Main Injector Dipole Magnet, B.C Brown et al, EPAC, 1992.
6. Design considerations and prototype performance of Fermilab main injector dipole, D. J Harding Et al, IEEE-1991
7. Magnet End design: The main injector dipoles, Jean-Francois Ostiguy, IEEE-1991
8. Iron Dominated Electromagnets - Design, Fabrication, Assembly and Measurements, Jack Tanabe, SLAC-R-0754, June 2005

REMOTE CONTROL APPLICATIONS FOR OPERATION OF HYDROGEN NEGATIVE ION SOURCE

Rohit Mishra[1], Kuldeep Kumar Singh, Rajnish Kumar, Manish Pathak, D. V. Ghodke, and Vijendra Prasad

Proton Accelerator Group,
Raja Ramanna Centre for Advanced Technology, Indore - 452013, INDIA

Abstract

To control, operate and optimize negative hydrogen ion source parameters remotely, a GUI based control applications have been developed in LabVIEW. A high voltage deck for the ion source houses instruments viz. mass flow controller, 13.56 MHz based RF ignitor, 10kV/1A pulsed extraction power supply, 2 MHz RF source for main plasma generation etc. These instruments have RS-232/485 and ethernet digital communication ports. The high voltage deck instruments are communicated through duplex fiber optic converter. The ground side instruments are high voltage acceleration power supply, turbo molecular pumps, roughing pumps, vacuum gauges, beam current measuring instruments etc. Communication ports of both, the ground side instruments and high voltage side instruments, are interconnected though ethernet switch to computer. A LabVIEW based GUI has been developed to control and monitor the operation of these instruments. The developed control application features supports in optimizing the performance of ion source by varying different parameters like gas flow rate, 2 MHz RF power, extraction voltage at different acceleration potential etc. The developed user interfaces have been successfully used for generation of negative hydrogen pulsed ion beam current of 26 mA at 50 kV energy up to repetition rate of 50 Hz with pulse width of 2 ms. This paper presents the brief description of remote operation of ion source using designed control application, GUI and high voltage optical isolation communication architecture.

INTRODUCTION

Pulsed RF ion source has been developed at RRCAT for extracting negative hydrogen ion beam from high intense hydrogen plasma. To accomplish it, external cylindrical RF antenna coil is used to inductively couple RF energy into plasma chamber. The generated plasma and extraction sub-systems delivers negative hydrogen ion beam current up to 26 mA with 2 ms pulse width at pulse repetition rate of 2 Hz to 50 Hz with rms emittance of 0.25 π mm-mrad and energy of 50 keV, at the exit of ion source. Three electrode extraction geometry has been used for ion extraction as shown in Figure 1.

To operate the high voltage ion source system remotely and to optimize the system performance, control system becomes an essential part of the ion source. All the floating high voltage side devices are optically networked with the low voltage side electronic devices. Installed electronic devices and power supplies have in-built microprocessor controller which provides LAN interface or RS-232/RS485 serial interface. RS232/RS485 to Ethernet converters are used to bring uniformity in communication interfaces.

Computer based control system was developed for controlling and monitoring all the device parameters. Graphical User Interfaces (GUIs) are developed for each device in LabVIEW software. LabVIEW and Java software applications are written to collect and log time series data in text files for offline analysis.

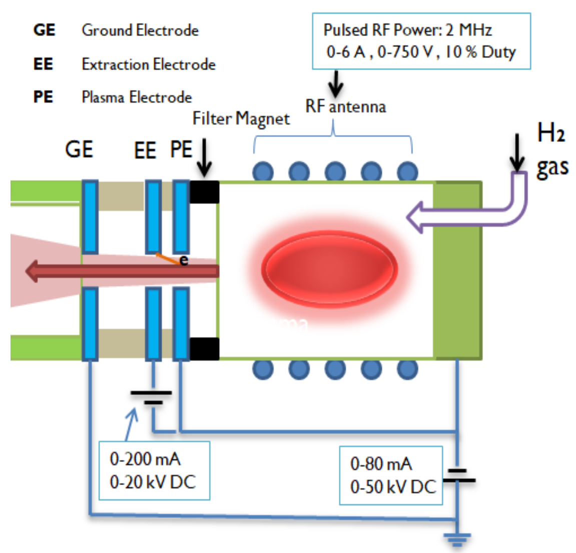

Figure 1: RF Ion Source Architecture.

GUI DESIGN AND CONTROL ARCHITECTURE

Figure 2 represents the control architecture used to network all the ion source devices. The devices are arranged as per the requirement into high voltage platform (floated at -50 kV potential) and low voltage platform. To remotely communicate and control the devices, high voltage optical isolated communication channel is established using fibre to Ethernet converter.

In order to assist the user of the ion source to control the operation, several GUI were designed which were interfaced with the designated device. These GUIs independently control and monitor the associated device. The designed GUI for each device is successfully tested for long hours of operation.

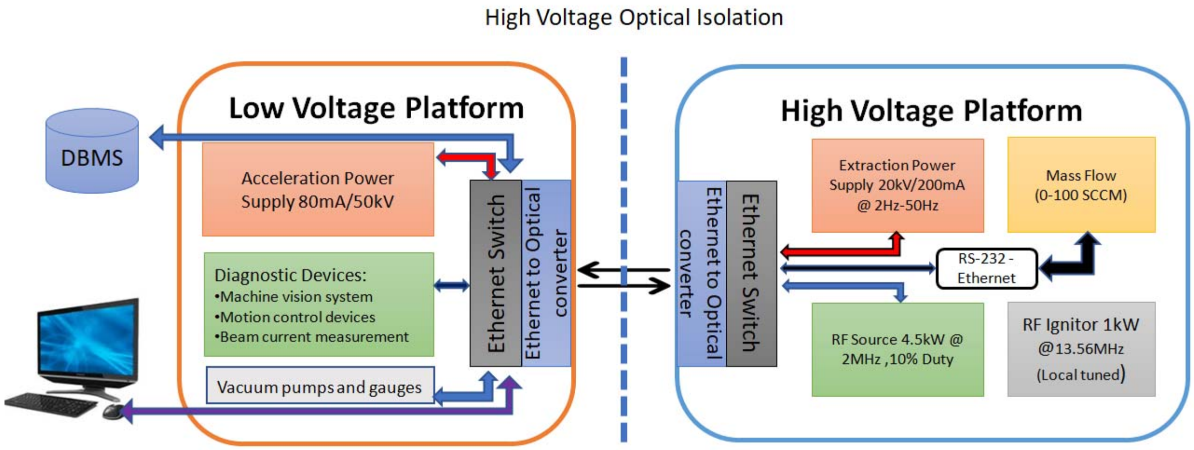

Figure 2 : RF Ion Source Control System Architecture

GUIs and Control Design Features:

Considering the device and human safety, GUIs were governed with operational restriction of parameter range and safety interlocks. Following list of features were implemented in the background GUI coding of each device:

- In-built LAN interface is preferred for communication with devices to implement uniformity and easy management.
- Serial RS232/485 to Ethernet converters are used if device does not support LAN interface.
- Particular Standard Commands for Programmable Instruments (SCPI) commands are used in LabVIEW programming to communicate with devices.
- SCPI commands are communicated on value change event basis.
- LabVIEW ® 2019 software is used to develop GUIs for remote controlling and status monitoring.
- Standalone touch screen based device control GUIs has been developed for devices with initial one time configuration using microcontroller based embedded system.
- The control system is scalable in its operation.
- Status monitoring of door interlock and temperature based interlock has been developed.
- GUI for machine vision system, multiple power supply system, mass flow system, water chiller system, vacuum system, standalone timing system, digital storage oscilloscope, function generator etc. has been developed.
- Database system has been installed and networked with ion source control system.

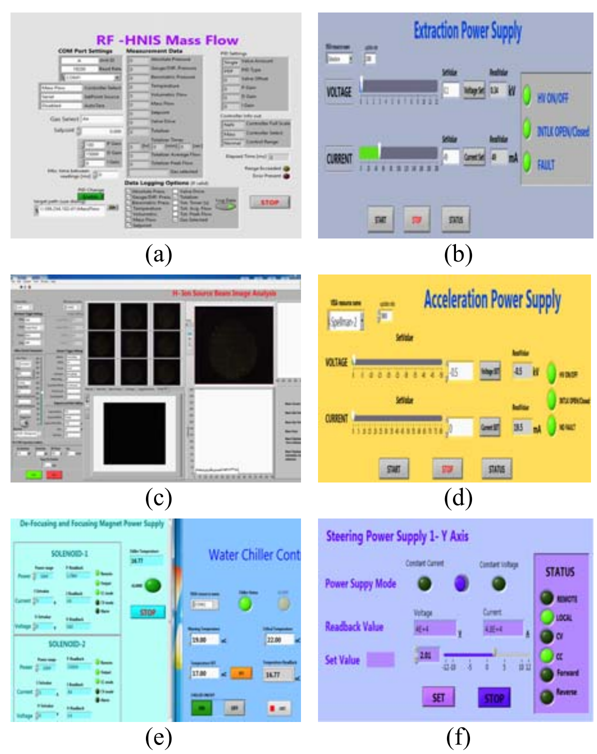

Figure 3 : Images of GUI of sub-systems of ion source developed (a) Mass flow controller, (b) Pulsed extraction power supply, (c) Camera configuration and beam image analysis, (d) Acceleration power supply,

[1]rohitmishra@rrcat.gov.in

(e) LEBT focusing and defocusing power supply control and water chiller, and (f) LEBT steering bipolar DC power supply.

- Database schema has been created to log the ion source parameters time series data.
- Java applications are written to interface database system for data logging.
- Arduino based stepper motor control hardware and its control GUI has been developed in LabVIEW for ion beam current measurement using Faraday cup.

CONCLUSION AND FUTURE SCOPE

Developed GUIs supports the operator in controlling and monitoring the ion source. Also by varying the control parameters, the user optimizes the quality of the beam and improves the performance of the ion source. The control system has been successfully tested in real environment for long hours. There exists further scope of improvement in replacing the relay and embedded system based interlock system with PLC based interlock safety system. Also one time configuration devices like reference trigger timing system, RF ignitor standalone system will be integrated to main control network with LAN interface.

REFERENCES

[1] Saurabh Srivastava, Anirban De, Sabyasachi Pathak, "**Control Architecture of Prototype Ion Source Power Supplies for MC18 at VECC**", Indian Particle Accelerator Conference (InPAC-2022), at Variable Energy Cyclotron Centre, Kolkata, India, 22-25 March 2022.

[2] Rohit Mishra, Kuldeep Singh, Sunil Kumar Jain, D. V. Ghodke, Vijendra Prasad, "**Development of Time Synchronized Beam Image Acquisition and Characterization Application for Hydrogen Negative Ion Sources**", Indian Particle Accelerator Conference (InPAC-2022), at Variable Energy Cyclotron Centre, Kolkata, India, 22-25 March 2022.

[3] H. M. Kewlani, P. Roychowdhury, D. P. Chakravarthy, L. Mishra, S. H. Gharat, K. C. Mittal, **"Electron Cyclotron Resonance Ion Source Control System**", PCaPAC-2012, 04-07 December 2012 at Variable Energy Cyclotron Centre, Kolkata, India.

[4] M. Eguiraun, I. Arredondo, M. Campo, J. Feuchtwanger, G. Harper, S. Varnasseri, "**ISHN Ion Source Control System Overview and Future Developments",** Proceedings of IPAC2011, San Sebastian, Spain, WEPC153

DEVELOPMENT, FRINGE FIELD OPTIMIZATION & CRYOGENIC QUALIFICATION OF PRE-SERIES 6T CONDUCTION COOLED MAGNET ASSEMBLIES FOR HIGH INTENSITY PROTON ACCELERATORS

Kumud Singh, Janvin Itteera, Mahima, Vikas Tiwari, Himanshu Bisht, Sanjay Malhotra, S B Howal, M.C Fanade, R K Jalan and R R Singh
Electromagnetic Applications and Instrumentation Division,
Bhabha Atomic Research Centre, Mumbai-400094.

Abstract

Medium beta cryomodule for High Intensity Proton accelerator envisages using superconducting solenoids as transverse focusing elements. Electromagnetic, thermal and mechanical design of the compact magnet assemblies equipped with focusing solenoid, corrector coils and active shielding coils has been carried out at Bhabha Atomic Research Centre (BARC) [1&2]. With the transition to a new superconducting magnet technology based upon conduction cooling, it is important to have a quantitative understanding of the stability limits and the quench behavior so that magnets can be effectively protected [2]. A cryogenic test stand using closed cycle cryocooler was designed & developed for cryogenic qualification of conduction cooled magnets [2, 3]. Axial magnetic field mapping for integral field strength calculation and fringe field measurement demands a clear bore for magnetic field probe placement. The test stand is equipped with warm bore for scanning of the field in magnet aperture. Warm section and the cold portion of the current leads in the test stand have been optimized to reduce steady state heat in-leaks as well as dynamic heat load during ramping. Cryogenic test stand is being used for quench training, ramp rate testing and axial magnetic field mapping of the conduction cooled magnet at various excitation currents. 6T pre-series superconducting solenoid magnet assembly has been integrated with the test stand and tested for its performance. Cool down and warm up rates were measured as well as peak temperature of first stage and second stage heat sink plates were recorded during magnet quench. This paper reports the design, assembly, and commissioning of the cryogenic test facility, and presents results of the test performed on the pre-series magnet assemblies.

INTRODUCTION

The use of superconducting solenoids as focusing elements in medium-energy sections of superconducting proton linacs is becoming a standard practice in accelerator technology because these provide sufficiently strong axially symmetric focusing while using relatively small longitudinal real estate.

Spatial constraints requisite the focusing lenses to provide main focusing field and horizontal and vertical correction fields for the beam centroid in same magnet package. Additionally, the fringe magnetic field requirements at the cavity surface needs to be minimized to avoid increase in the cavity surface resistance due to trapped flux. To meet these requirements, the magnet assembly has been designed to consist of main coil, two active shielding coils and four steering coils. The design has been optimized for maximization of focusing field strength and minimization of fringe magnetic field at the cavity surface within the limiting spatial and electrical constraint.

ELECTROMAGNETIC DESIGN

Analytical as well as Parametric studies using FEM simulations were carried out for the geometry of the main and the bucking coils, the type and size of superconducting strand, and the number of turns in the windings. Electromagnetic and quench design for these magnets was done using Opera TOSCA software. Table 1. lists down the main functional requirement of magnet derived from beam optics simulations.

Table 1: Margin Specifications

Sr. no	Parameter	Specified	Unit
1.	Focusing strength $\int B_z^2\ dl$	4.5	T^2m
2.	Nominal current	< 100	A
3.	B_{max} at cavity Surface	<10	G
4.	Bending strength	5	mT-m
5.	Effective length of solenoid (FWHM)	≤ 180	mm
6.	Maximum current in the dipole correctors	< 50	A

Main coil is designed to provide the solenoidal field for focusing, while active shielding coils are placed in a Helmholtz arrangement to buck the fringe field at cavity surface. The bucking coils are wound concentrically to the main coil and are located at the axial each ends. Dipole corrector coils used for correcting for the beam centroid shift in corrector mode and skew quadrupole components in quad mode. The space between the bucking coils is used to bring all current leads out of the lens.

Active shielding lens was designed & optimized for SSR cryomodule iteratively by varying the ID, OD, length and axial position of the main coil and bucking coil. Figure 1 shows the axial field profile of the magnet assembly with only main coil (black curve) and with main coil & bucking coils (red curve). Field in the vicinity of and on the surface of SSR cavity walls was minimized.

Practical limit to the level of this field is set by possible quenches in SRF cavities that can result in degradation of cavity performance after quenching, so the magnetic field generated by magnetic elements inside cryomodule must be sufficiently small to limit the degradation [5]. Figure 2. shows the field levels on the cavity surface, Bucking coil selection has been done to minimize field at the desired location . Figure 3. shows the minimum B field locations for various configurations of bucking coil. ID and OD of the Bucking coil was varied within the range of +/- 5mm. 4 magnet assemblies were developed for design validation.

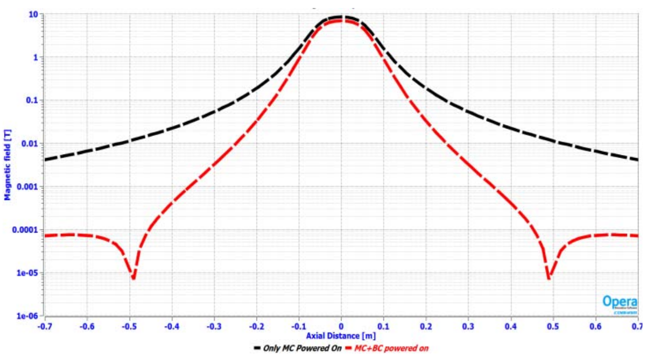

Figure 1:Axial magnetic field (|B|) profile of the SSR Focusing lens with and without shielding coil

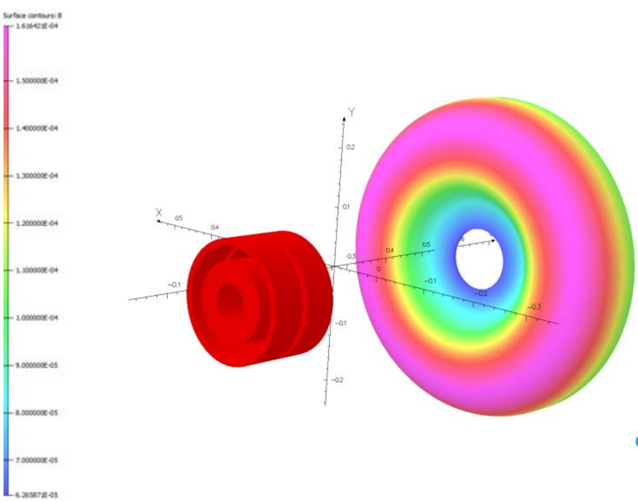

Figure 2: Magnetic field strength on the SSR cavity surface

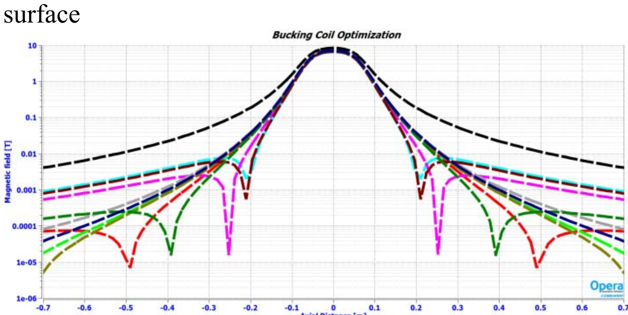

Figure 3. Minimum field location optimization for different bucking coil configuration

TEST AND MEASURMENTS

Developed magnet assemblies were tested in a cryocooler based test stand. Axial field mapping and detailed thermal tests were carried out during cryogenic testing of the magnet assemblies. Fig 4 shows the photograph of the magnet assembly integrated with test cryostat and Figure 5. shows the measured axial field map. Temperature sensors and voltage tap data was measured for recording the quench characteristic of the magnet assembly. Some of the temperature sensors were observed to be showing higher readings which was attributed to incorrect anchoring of the CERNOX sensors as shown in Figure 6. Hence the quench data was compared with voltage tap acquisition.

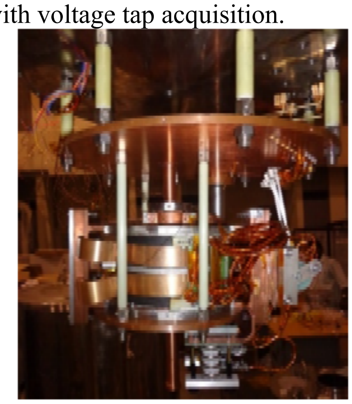

Figure 4. Magnet integrated with cryogenic test stand

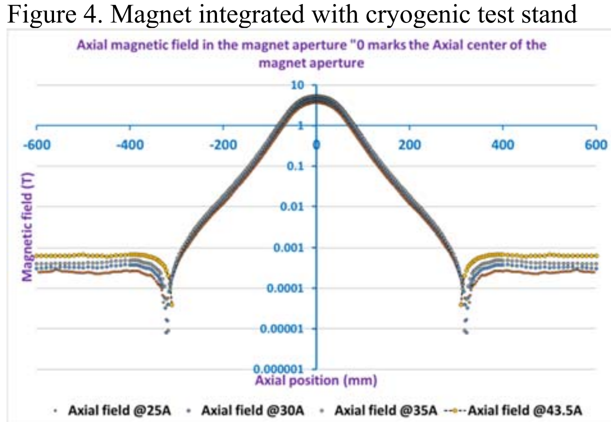

Figure 5. Measured axial field profile of the magnet assembly

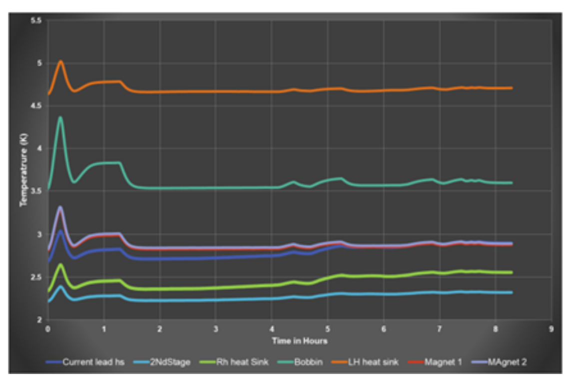

Figure 6. Measured Temperature rise during quench of the magnet assembly

Hysteresis measurement

Hysteresis affects the instantaneous value of the field generated in magnet aperture and makes it dependent on the powering history. Figure 7. shows the measured hysteresis effect for the main solenoid. It is therefore important to know how the hysteresis in order to control the magnets.

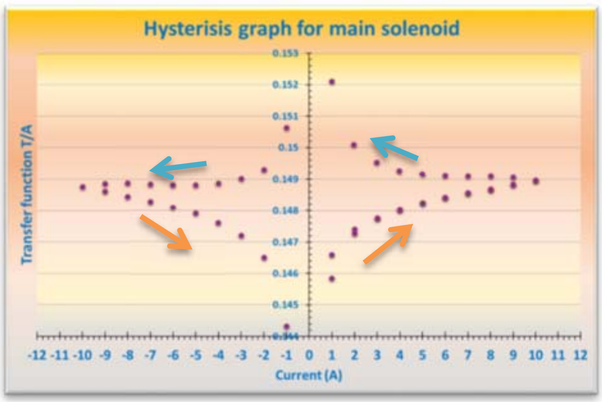

Figure 7. Measured Transfer function of main coil during ramp up (orange arrow) and ramp down (Blue arrow)

Fringe field measurements

The minimum field location (Fringe field) is extremely sensitive to main coil & bucking coil dimensions. Figure 8. shows the measured field profile on two of the developed magnet assemblies. The variations between various magnet assemblies are attributed to slight dimensional variations in the ID and OD of BC coils. Variations have been recorded for specifying tolerances (+/-0.2 mm) for series magnet fabrication.

Cool down of magnet assembly

Cool down and warm up rates were measured for the assembled magnets in the cryogenic test stand. Cool down of each of the magnet assembly takes about 48 hours consistent with the static heat load and heat capacities of cold mass. Figure 9. shows the partial cool down graph of the magnet assembly.

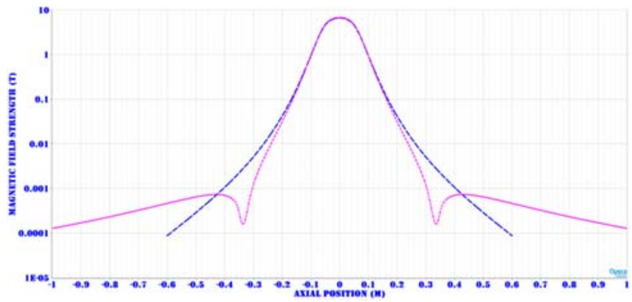

Figure 8. Measured Axial field profile of two magnet assemblies

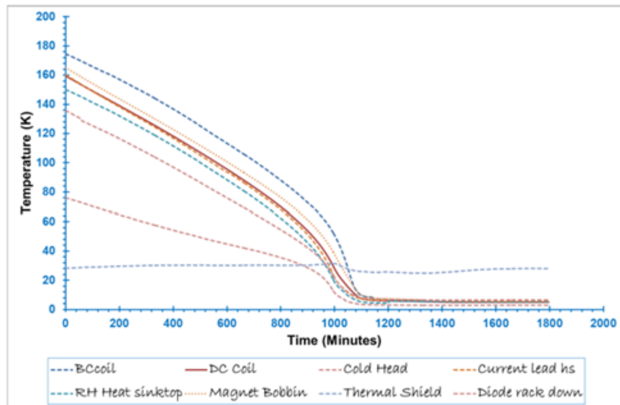

Figure 9. Partial cool down curve for the magnet assembly

RESULTS

Conduction cooled magnet assemblies for medium beta cryomodule for high intensity proton accelerator has been built and qualified in indigenously developed cryogenic test stand. Initial pre-series magnet assemblies have been qualified for various performance parameters like Integral focusing strength calculated from the measured axial field map, fringe fields on cavity surface, nominal operating currents. Further testing and characterization is in progress for detailed radial field measurements at cavity location. Completion of detailed quench characterization and ramp rate dependence tests will be useful for thermal design validation of the magnets for the cryomodule.

REFERENCES

[1] Kumud Singh, Janvin Itteera, Sanjay Malhotra - Final design Report “Cold magnets for PIP-II SSR Cryomodule”. (Published and uploaded in Fermilab Document database for PIP-II project, August 9th 2020)

[2] Wilson, M., “Superconducting Magnets”, Oxford University Press, New York, 1986, pp. 98-99

[3] Battelle, “Handbook on Materials for Superconducting Machinery, Metals and Ceramics Information Center”, Columbus Laboratories 1977, pp.8.1.2-5

[4] P. Brindza, E. Sun, S. Lassiter, and M. Fowler “Cryostat design and analysis of the superconducting Magnets for jefferson lab’s 11 gev/c super high Momentum spectrometer”, AIP Conference Proceedings 1218, 957 (2010)

[5] T. Khabiboulline, D. Sergatskov, and I. Terechkine, “SSR1 Cavity Quenching in the Presence of Magnetic Field,” FNAL TD note TD-12-007, June 2012

DESIGN STUDIES FOR A PILL BOX TYPE ACCELERATING STRUCTURES WITH BEAM PORTS AND COUPLING LOOP USING ANALYTICAL AND PERTURBATION TECHNIQUES

Tushar Dave[1,2], Shankar Lal[1,2], Arvind Kumar[1] and K. K Pant[1]
[1]Raja Ramanna Centre for Advanced Technology, Indore, Madhya Pradesh-452013, India
[2]Homi Bhabha National Institute, Training School Complex, Anushaktinagar, Mumbai-400094, India

Abstract

Radio-Frequency (RF) cavities are employed in accelerating facilities to play different roles: as pre-bunchers, bunchers, accelerators, deflectors etc. The important RF properties that qualify these cavities are their resonant frequency (f_0), Quality factor (Q_0), Shunt impedance (R_{sh}) and the accelerating electric field (E_z) to be supported by the structure. Making a functional RF cavity requires openings for the electron beam propagation through it, vacuum pumping and coupling of RF power. The simplest RF cavity that can be designed precisely by employing analytical formulae is a pill-box type cavity without any openings. A freely available RF code like SUPERFISH can be employed to design an azimuthally symmetric RF cavity with the beam ports on axis [1]. However, the presence of openings on its side walls for vacuum pumping or for RF coupling, or for RF pickup, cannot be treated analytically, and usually require design codes normally not available freely.

A simple accelerating structure like a single cell pill-box type pre-buncher with a coupler loop, can be designed by employing analytical formulae of a pill-box, with perturbation techniques to determine the effect of port openings on its resonant frequency. Analytical formulation can also be employed to design RF power coupling and pickup loops to achieve the desired RF coupling coefficients for the structure.

In this paper, the design and development of a prototype, single cell, pill-box type, S-band pre-buncher resonant at 2856 MHz will be discussed. An Aluminum prototype has been built and systematic studies have been performed to study the agreement between the designed RF properties and those measured using a Vector Network Analyzer (VNA). The perturbation in resonant frequency due to presence of ports for beam propagation, RF coupling and RF pickup, and the design of a RF coupler loop to achieve a desired RF coupling coefficient is also discussed. Predictions from the analytical studies are compared with measurements made on an Aluminum prototype. The implications of mounting an RF coupler loop on the cylindrical wall versus on a side wall adjacent to a beam port will also be discussed, considering the deployment of such structures as part of injector linac system with air-core solenoids. The study is motivated by the ongoing design of an injector linac system for a proposed Tera Hertz Free Electron Laser (THz-FEL) [2].

INTRODUCTION

The designed injector system of the proposed THz-FEL at RRCAT comprises a thermionic electron gun followed by a Sub-Harmonic Pre-Buncher (SHPB), a Fundamental Frequency Pre-Buncher (FPB), an Accelerating Buncher (AB) and a linear accelerator (linac). The electron bunches of ~1ns (FWHM) will be generated using a 90 keV thermionic electron gun and compressed to ~20 ps by passing through a 476 MHz SHPB and a 2856 MHz FPB. These 90 keV electron bunches will subsequently be passed through a 2856 MHz AB to compress to ~10 ps and accelerate up to ~4 MeV and finally accelerated up to 7-13 MeV by a 2856 MHz linac [2]. The electron bunches repeat at ~29.75 MHz within a macro pulse of 5-10 µs. THz-FEL radiation will be generated by passing the relativistic electron bunches of through an undulator placed inside an optical cavity [2].

All injector linac system components for the THz-FEL are proposed to be developed in-house, and the design studies related to the development of a single-cell, pill-box type FPB cavity resonating at 2856 MHz is presented in this paper.

ANALYTICAL STUDIES

The geometrical dimensions and important RF parameters of a pill-box cavity operating in TM_{010} can be determined analytically by solving Maxwell's equations with appropriate boundary conditions [3]. The resonance frequency (f_0) of a pill-box cavity is given as $f_0 = 2.405c/2\pi R$, where 'c' is the speed of light and R is the radius of the cavity.

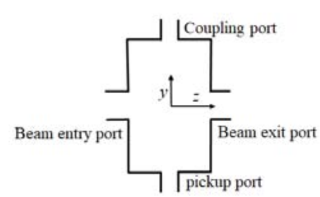

Figure 1: 2D Schematic diagram of a pillbox cavity with ports.

But an RF cavity employed in an accelerator has ports for beam propagation, RF power coupling and RF pickup as shown in Fig.1. The presence of these ports affects the f_0 of the pill-box cavity, which is difficult to determine analytically. However, the effect of port openings can be determined by employing perturbation techniques, and the perturbations can also be compensated during design.

Effect of ports openings on resonance frequency

The presence of port openings modifies the boundary conditions locally leading to variation in the RF parameters of the cavity, mainly in the f_0. Using Slater's perturbation theorem, Gao has given an analytical formula for variation in f_0 of an RF cavity due to a port opening as [4]

$$\frac{\Delta f}{f_0} = \left(\frac{\Delta U_e}{U}(1 - e^{-2\alpha_1 z}) - \frac{\Delta U_m}{U}(1 - e^{-2\alpha_2 z})\right), \quad (1)$$

where U is the total stored energy in the cavity, ΔU_m and ΔU_e are the variations in the magnetic and electric energies, α_1 and α_2 are the attenuation coefficients. Once the variation in the resonance frequency is known, the desired f_0 can be found by using equation 1.

Determination of geometrical dimensions of a pill-box cavity with ports

The geometrical dimensions of a pill-box type FPB cavity of axial length of 27.63 mm ($\beta\lambda/2$, where β is the speed of particle, λ is the wavelength of EM field), resonating at 2856 MHz with on-axis beam entry and exit ports of 20 mm diameter and ports for RF power coupling and pickup of 10 mm diameter on its cylindrical surface is determined by using analytical formula discussed in the previous sub section. The presence of beam ports increases the f_0 by 50.208 MHz while the presence of RF ports reduces the f_0 by 3.4 MHz. Therefore, to achieve a f_0 of 2856 MHz with all the ports, the unperturbed pill-box should have a f_0 of 2809.192 MHz. For an accelerating gap voltage of 10 kV, important geometrical dimensions of the FPB are summarized in Table 1.

Table 1: The important RF parameters and geometrical dimensions of the FPB without ports predicted by analytically.

Parameter	Values
Cavity Radius (R)	40.85 mm
Resonant Frequency (f_0)	2809.192 MHz
Power Dissipation (P_{diss})	94.68 W
Quality Factor (Q_0)	10236.88
R_{sh}/Q_0	254.58 Ω

DESIGN OF RF POWER COUPLING AND PICKUP LOOPS

Considering the operating frequency and power levels, loop type RF power coupler and pickup loop are designed for the FPB [5]. The fraction of input RF power coupled to a cavity is defined in terms of the RF coupling coefficient (β) as [3] $P_c = 4\beta P_{in}/(1+\beta)^2$, which is maximum for β=1 (also known as critical coupling). For an RF source coupled to a cavity through a loop, the β is given as [6]

$$\beta = \frac{2\pi^2 f_0^2 A^2 B^2 \cos^2\theta}{Z_w P_c}, \quad (2)$$

where B is the amplitude of magnetic field in the cavity at location of the loop for an unperturbed cavity, A is area of the loop, θ is the angle between A and B, Z_w is the characteristic impedance of the transmission line and P_c is the power dissipation in the cavity. The values of B and P_c can be determined either analytically or from SUPERFISH simulations. The loop area for β=1 for the FPB is 5.53 mm^2.

Sometimes the accelerating electric field in a cavity is monitored by employing a pickup loop. The typical value of pickup power required for signal processing is ~3 dBm which can be achieve by using a pickup loop area of 1.76×10^{-2} mm^2. Since it is impractical to make such a loop, the pickup loop is made of slightly larger size and value of β is adjusted by varying θ.

VERIFICATION OF ANALYTICAL DESIGN BY SIMULATION STUDIES

To verify the analytical design, a pill-box cavity with beam ports is modeled in SUPERFISH with the same radius of 40.85 mm. The resonance frequency (f_0) predicted by SUPERFISH is 2846.23 MHz which is 2859.4 MHz in analytical estimation. This difference may be due to perturbation in the magnetic field at beam ports, which is ignored in analytical estimation. The variation in the resonance frequency is compensated by changing the cavity radius to 40.66 mm. As the estimated reduction in f_0 due to RF ports is ~ 3.4 MHz, it is expected to achieve f_0= 2856 MHz with all the ports.

DEVELOPMENT AND TUNING OF AN ALUMINUM PROTOTYPE

Based upon analytical and SUPERFISH studies, an aluminum prototype of the FPB is developed as shown in Fig.2. The RF parameters of the prototype are measured using a VNA.

Figure 2: Components of the aluminum prototype.

The effect of beam ports on RF parameters of the cavity is studied by machining beam ports of different radii. The variation of the f_0 with the beam port radius is shown in Fig.3. The analytical results are agreeing well with the simulation and the measured values for beam port upto 5 mm, while it start deviating for larger radii, which may be due to variation in the magnetic field at the location of beam ports, which is ignored in analytical estimation. The variation in RF power coupling coefficient (β) for different loops sizes is also studied. The variation in β with loop size is shown in Fig .3 (b). The prototype is finally tuned to 2856.746 MHz with β=1.11. The summary of estimated and measured RF parameters is given in Table 2. The difference in estimated and measured values of β could be due to machining errors, leading to lower the value of B^2/P_c as compared to that is taken form SUPERFISH simulation (see equation 2).

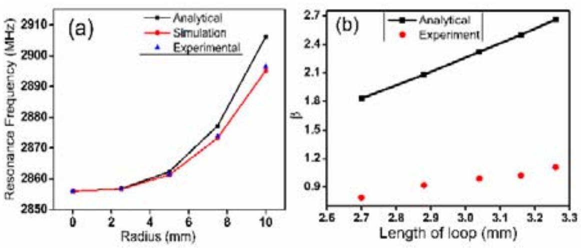

Figure 3: Variation in: (a) resonance frequency with radius of beam ports and (b) RF power coupling coefficient with loop size.

Table 2: Summary of RF parameter of the FPB.

Parameter	Measured	Analytical	SFISH[1]
R (mm)	40.65	40.65	40.65
f_0 (MHz)	2856.746	2867.595	2857.343
Q_0	7537.678	--	--
β	1.11	2.66	--
R_{sh}/Q_0 (Ω)	239.85	--	--

[1]SUPERFISH with beam ports + including effect of RF ports

MOUNTING OF COUPLER LOOP ON THE CYLINDRICAL V/S ON A SIDE WALL

The FPB will be employed in the injector system of a THz-FEL with solenoids employed for electron beam focusing. To avoid a possibility of interference of the RF coupler and pickup loop fittings with solenoids, mounting the RF power coupler on side wall of the cavity adjacent to a beam port as shown in Fig. 4, is studied. A comparison of the perturbation in resonant frequency due to 10 mm diameter aperture on the cylindrical wall and on the side walls to mount the loops is shown in Table 3. The required area of the loops required to achieve critical coupling in the two configurations is also shown in Table 3. Both the configurations are similar, and the choice can depend purely upon the configuration of the injector system.

Table 3: The change resonant frequency and area of the loop for cylindrical wall and side wall.

Parameter	Cylindrical wall	Side wall
Δf_0	-1.704 MHz	-1.862 MHz
Area of the loop	5.53 mm^2	4.98 mm^2

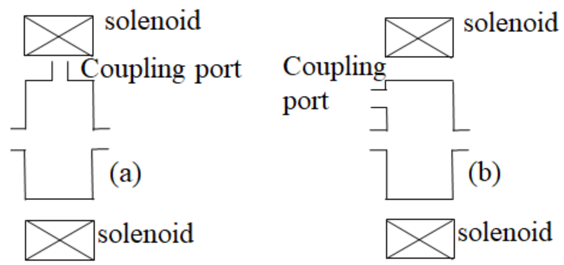

Figure 4: (a) 2D schematics of coupling port on cylindrical wall of FPB, (b) 2D schematics of coupling port on a side wall of FPB

CONCLUSION

A pill-box type, S-band FPB with beam, RF power coupler and pickup ports is designed using analytical formulae and perturbation techniques. Based upon the inputs generated, an aluminium prototype is developed and tuned. The analytical design values are very close to the experimental results. Feasibility of mounting the RF power coupler on end walls of the FPB from practical considerations is also studied. The dimensions of RF power loops and effects on resonance frequency are similar to those for a coupler mounted on cylindrical wall of the cavity. Therefore, the RF power coupler could be mounted either on the cylindrical surface or on the end wall, depending upon interference with elements of the THz-FEL injector system.

ACKNOWLEDGEMENT

The authors would like to thank to Shri R.K. Pandit for his assistance in RF measurements, and Shri S.K. Gupta for his help in preparing the mechanical drawings. Thanks, are also due to Shri R.B. Bhowate for his support in preparing the FPB prototype for measurements and to colleagues from the LCDFS, RRCAT for machining of the prototype.

REFERENCES

[1] Young, James H. Billen and Lloyd M., “Poisson Superfish”, Los Alamos National Laboratory, 2006.
[2] R.S. Saini et.al, “Design Studies for a THz-FEL at RRCAT”, in Proceedings of InPAC, IUAC, New Delhi, 2019.
[3] T. P. Wangler, “Principles of RF Linear Accelerators”, John Wiley & Sons, 1937.
[4] J. Gao, “Analytical Formulae for the Resonant Frequency Changes due to Opening Apertures on Cavity Walls”, NIMA 437-443, 1992.
[5] D. Alesini, “Power coupling”, CERN Accelerator School, Denmark, 2010.
[6] Shankar Lal and K. K. Pant, “Study of the effect of loop inductance on the RF transmission line to cavity coupling coefficient”, RSI vol. 87, p. 8, 2016.

AUTO-CONFIGURABLE CLOCK DIVIDER FOR DIGITAL LOW-LEVEL RADIO FREQUENCY SYSTEM OF INFRARED FREE ELECTRON LASER

Ekansh Mishra, Dheeraj Sharma, Nitesh Mishra, Pritam S. Bagduwal, Pankaj Gothwal, Nitesh Tiwari and Mahendra Lad, RFSD, RRCAT, Indore (M.P.)-452013.

Abstract

Digital Low Level Radio Frequency (DLLRF) system is developed and deployed in Infrared Free Electron Laser (IRFEL) at RRCAT, Indore for controlling the amplitude and phase of Radio Frequency (RF) signal inside the Sub-Harmonic Pre-Buncher (SHPB) cavity, within the required limits (±0.1% for amplitude and ±0.1° for phase) [1]. Various synchronized RF signals are required for operation of DLLRF and sub-systems of IR-FEL. Signals such as clock (95.2MHz) to Analog-to-Digital Converter, signal (23.8MHz) for Local Oscillator (LO) frequency (499.8MHz) generation, signal (2856MHz) to Linear Accelerator (LINAC), signal (476MHz) for Electron Gun etc. are being generated for operation of IR-FEL. For proper operation, all these RF signals must be synchronized in nature that is achieved by deriving these RF signals using a master clock and programmable multichannel clock divider. These signals are generated by changing/programming the division ratio of different channels of clock divider. RF signals are generated using Analog Devices/#AD9516 based programmable clock generator in IRFEL. Since, AD9516 chip is volatile in nature, all the essential settings (division ratio, output levels etc.) are erased out after power to the chip is turned off. Each time power to chip is turned on; AD9516 has to be programmed via the Graphical User Interface (GUI) provided with the board for working of the DLLRF system. An automated solution has been developed for programming of clock divider that configures DLLRF system automatically, without any manual programming. Automatic programming is carried out by a Raspberry Pi (RPi) that is installed and commissioned along with the AD9516 based board. RPi programs the board by sending the data frames to AD9516 through Serial Peripheral Interface (SPI). A script has been developed in python that automatically executes after RPi boots and all the essential settings (stored in a database on RPi) are being transmitted through SPI to program the AD9516. Two GUIs (remote and local) has also been developed in Python for changing the division ratios and other essential settings. Remote GUI runs on a window that sends command through Ethernet and local GUI runs on Raspberry Pi. GUIs used to modify the division ratios and updated ratios are also stored in the database simultaneously. Updated division ratios are used for the configuration at the time of powering of the chip. This system for automated configuration will be installed in DLLRF system of IR-FEL at RRCAT, Indore. Old scheme, updated/new design scheme, algorithm and result of auto-configurable clock divider for DLLRF system will be described in detail in the paper.

INTRODUCTION

An infrared free electron laser (IR-FEL) is a kind of laser that uses the free-electron laser principle to generate coherent infrared light. Unlike traditional lasers, which rely on stimulated emission from a population of atoms or molecules, an IR-FEL generates light by accelerating electrons to relativistic speeds and sending them through a series of alternating magnetic fields. As the electrons move through the fields, they emit photons of infrared light, which can be amplified and focused into a high-intensity beam for various scientific experiments.

Figure 1 shows the scheme used to generate infrared light. A 90keV beam is generated in an e-gun and then bunched in a Sub-Harmonic Pre-Buncher (SHPB) cavity. The bunched beam is then further energized by the bunching section and Linear Accelerator (LINAC), reaching energies of 4 and 15-20MeV respectively. The beam is transported to the undulator where lasing occurs.

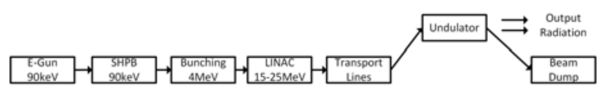

Figure 1: Layout Schematic of IR-FEL.

A 476MHz Pulsed Digital Low Level Radio Frequency system has been installed and commissioned in the IR-FEL to generate the pulsed field inside the SHPB. This DLLRF system requires various synchronized signals, including Clock to Analog-to-Digital Converter (ADC) for In-phase and Quadrature (I/Q) sampling, signal for the generation of Local Oscillator (LO) frequency, and timing signals. Synchronized clocks are generated by a multichannel programmable clock divider chip (AD9516), with division ratios determined according to the DLLRF system design. To generate synchronized clocks, an evaluation board of AD9516 (14-Output Clock Generator Integrated Circuit) is utilized. However, AD9516 is a volatile chip, meaning that all the division ratios and essential settings are erased once power to the board is turned off. To address this issue, a standalone, compact, and non-volatile memory-based solution has been developed in-house. This solution is now used for programming EVAL-AD9516-0 (AD9516 Evaluation board), which configures the DLLRF system for an automated and contactless start-up.

RF SYSTEM

The RF system of the IR-FEL consists of multiple subsystems. Figure 2 shows a general schematic of the RF system of the Sub-Harmonic Pre-Buncher (SHPB) of the IRFEL. It includes an RF source, Low Level RF (LLRF), RF power detection, RF protection system, RF amplifier, and transmission line components. To increase the low output power of the RF generator, RF is amplified using an amplifier or a combination of multiple amplifiers before being fed into the cavity. The RF cavity produces a large accelerating/voltage gradient that accelerate the electrons. While RF cavities are generally used for providing energy, the SHPB cavity is used for bunching the electron beams. A circulator and a directional coupler are used between the amplifier and the cavity for protection and RF power measurement, respectively. Multiple interlocks are present at various stages to ensure safe operation.

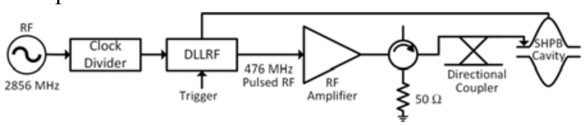

Figure 2: Schematic of RF system of SHPB of IR-FEL.

476MHZ PULSED DLLRF SYSTEM

The SHPB of IR-FEL requires amplitude and phase stability of 0.1% and 0.1°, respectively. To maintain a stable field inside the cavity, a DLLRF system is used. The DLLRF system monitors the field inside the cavity and ensures that the amplitude and phase are corrected within the desired range. It is important to note that the DLLRF system of the IR-FEL operates in pulsed mode. To enable the DLLRF system to work efficiently in pulsed mode, an algorithm using fast adaptive feed forward is used.

Figure 3 exhibits the schematic of the DLLRF system for the SHPB of IR-FEL, which operates on pulsed I/Q detection and correction. The pulsed RF is generated by triggering from a signal generated by a multi-channel pulse and delay generator. I/Q values are detected using digital I/Q sampling, where the down-converted RF signal (23.8MHz) is sampled using a synchronized clock signal (92.5MHz). The RF signal is down-converted before sampling to avoid the use of a very high-speed ADC. Signal down-conversion is carried out by mixing 499.8MHz and 476MHz signals. All generated signals must be synchronized with each other, which is achieved by deriving the RF signal with the help of a clock divider. Phases of generated signals are always in sync with each with each other by utilization of SYNC function of the clock divider. System also generates various synchronized signals for auxiliary systems such as e-gun, LINAC etc.

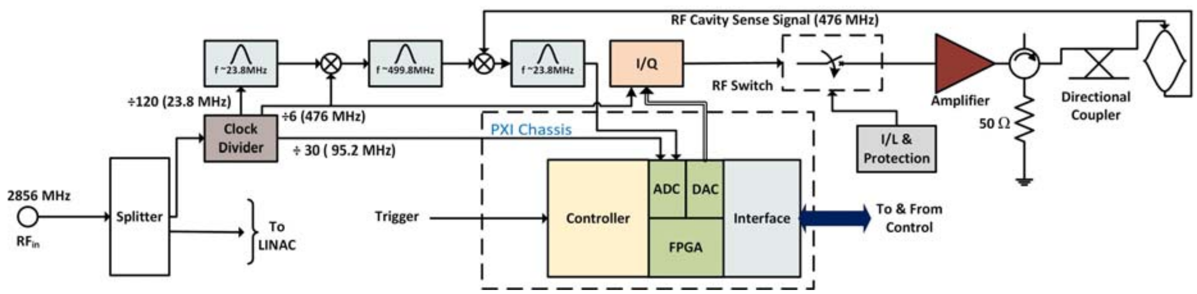

Figure 3: 476MHz Pulsed DLLRF System of SHPB of IR-FEL

LO AND CLOCK GENERATION

The synchronized LO and clock generation scheme is illustrated in Figure 4. An RF signal of 2856MHz is split using an RF splitter, and one of the signals is directed to the clock divider. The clock divider then divides the signal by 6, 30, and 120 times, generating signals of 476MHz, 92.5MHz, and 23.8MHz, respectively. The 92.5MHz signal is used for digital I/Q sampling, while the signals of 476MHz and 23.8MHz are employed for the LO signal for down-conversion. The clock divider used in the system is the Evaluation board Eval-AD9516, a 14-channel clock divider that is programmed through the AD9516 Evaluation software via USB. The clock divider uses multiple cascaded dividers to generate the required output signals. Levels of output can be settable to either CMOS or LEVPECL, depending upon the requirements.

Firstly, the input signal of 2856MHz is given to the VCO divider, which divides the input signal by 6 and generates a 476MHz signal. This 476MHz signal is further divided by 5 and 20 to generate the desired output signals of 92.5MHz and 23.8MHz, respectively. Additionally, one of the dividers is bypassed and a divide by 1 setting is used to take out the 476MHz signal.

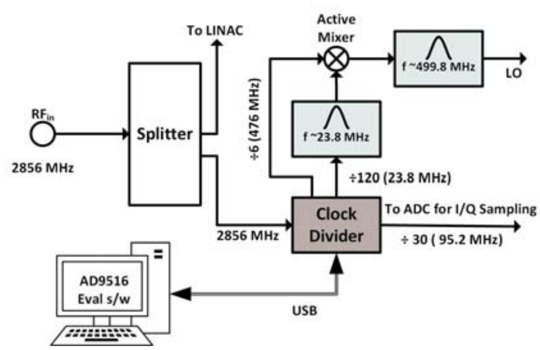

Figure 4: LO and Clock generation.

A screenshot of the AD9516 Evaluation software, which is used to program the clock divider, is shown in figure 5 to display the typical settings of IR-FEL.

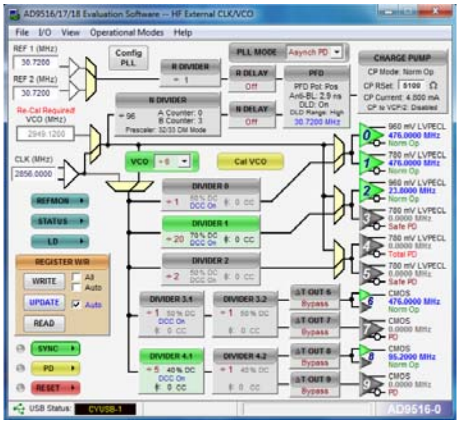

Figure 5: Clock setting of IR-FEL .

AD9516 is a volatile chip and all the essential settings and division ratios are erased once power is turned off, programming of the chip is required every time the power is turned on for the DLLRF system start-up.

AUTO-CONFIGURED CLOCK DIVIDER

A solution has been devised for automated and contactless start-up of the system.

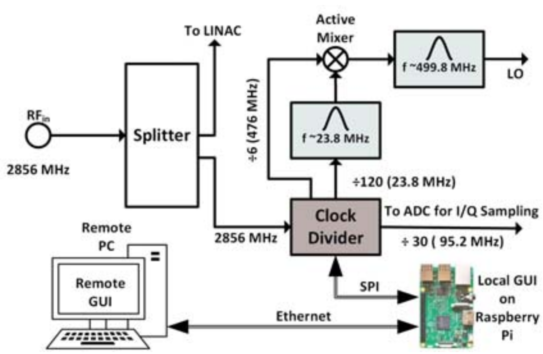

Figure 6: LO and Clock generation for auto start-up.

The AD9516 is programmed through the Serial Peripheral Interface (SPI) via a GUI developed in Python, which runs on a Raspberry Pi. The system has been intgreated with an evaluation board, and the layout schematic is shown in Figure 6. Programming of the board can be carried out in both local and remote modes. An application has been developed in Python that runs on Windows for configuration in remote mode through Ethernet. The developed system automatically configures the clock divider that auto starts the DLLRF system power is turned on. The developed system has been tested with the Evaluation board of AD9516.

The observed phase noise reaches a remarkable level of better than -120dBc/Hz. To filter out multiple harmonics produced by the clock divider, a band pass filter with a stop band attenuation of ~40dB at ±20MHz and a return loss better than 18dBc is utilized. By utilizing this clock divider, the DLLRF provide a phase stability within ±0.1°. Furthermore, the amplitude of the clock divider remains stable with input changes of approximately 10dB, achieving an amplitude stability of ±0.1%. Achieving high spectral purity is crucial for the performance of the system, the absence of these essential stabilities result in the inability of IR-FEL to generate laser emissions.

To develop the Python program, various Python libraries/modules were utilized, such as OS, time, socket, json, spidev, Tkinter, etc. The division ratios/settings are sent to AD9516 through SPI, and data is stored on the local drive. Spidev is used for SPI communication, json is used for storing and transferring data, and Tkinter is used for GUI development. The program is written in such a way that every time the Raspberry Pi boots or power to the Pi is turned on, the script is automatically executed, which recalls the old value from the locally stored database and sends it to AD9516 through SPI for configuration. Local and remote operation through Ethernet is carried out via sockets. Local and remote GUIs are developed via Tkinter. The GUI developed is shown in figure 7. Once the "send" button is pressed, updated division ratios are sent to AD9516, along with updating/overwriting the data in the database.

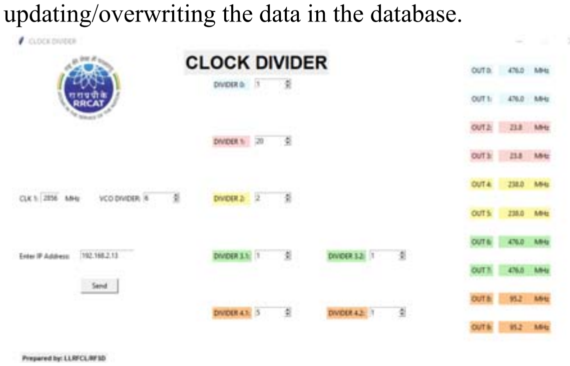

Figure 7: GUI developed for Clock divider.

CONCLUSION AND FUTURE WORK

After successfully integrating Raspberry Pi along with the Evaluation board, the auto-configuration of the clock divider has been demonstrated. The system will be installed in IR-FEL, and human intervention should be significantly reduced. The results of this development will also aid in supporting the development of indigenous standalone boards for various accelerators.

ACKNOWLEDGEMENT

The authors are grateful to Shri D. Suresh, Shri Sudarsan Kishan, and Shri Manikandan M. for their help and support with various technical and experimental requirements. The authors would also like to thank Shri Rishal Gedam for his help in the development of the GUI.

REFERENCES

[1] K.K. Pant, et al., “First Lasing in an infrared fee electron laser at RRCAT, Indore”, Current Science, Vol. 114, no. 2, Jan 2018, pp. 367-373A. Name and D. Person, Phys. Rev. Lett. 25 (1997) 56.

ELECTROMAGNETIC SIMULATION OF 107.5 MHZ CO-AXIAL RF CAVITY AND ITS HIGHER ORDER MODE IDENTIFICATION.

Deepak Kumar Mishra□, Divya Purohit, Subhajit Dutta, Pankaj Kumar and Jishnu Dwivedi
Industrial Accelerators Division, RRCAT, Indore, India

Abstract

RRCAT has developed and installed 10 MeV, 6kW Linac at ARPF for bulk radiation processing. This is the first step on the roadmap for reaching on industrially viable level of electron beam power for bulk processing. For economic viability, the electron beam power of 100 KW or higher is required for radiation processing applications. The next step on this roadmap include increasing the beam power to 30-50 KW level. Accelerator schemes making use of a large single cavity for repeated acceleration can work in cw mode and are capable of providing very high beam power with well defined energy and narrow energy spread. Considering this fact an electrodynamic design of 107.5 MHz coaxial recirculating cavity was carried out.[1][2] In this paper we will be presenting optimized shape of the □/2 coaxial resonant cavity obtained form electromagnetic simulation and identification of its higher order modes.

INTRODUCTION

The ionizing radiation are widely used in a lot of industrial applications such as cross linking of polymers, processing of thermo shrinkable products, medical disposals sterilization, food preservation, etc. Radiation treatment of very large volumes of material require an economical, reliable and powerful radiation source. Re-circulating electron accelerators have demonstrated reliable operations that could meet the most strenuous industrial demands[5]. The practical advantages of re-circulating electron accelerator include very high beam power capabilities at high efficiency, low energy spread, good control on beam energy and ready compliance to regulatory requirements of maximum electron energy. This type of accelerator is capable of steady state operation and inherent multi energy operation. Apart from this, the re-circulating accelerator offers the advantages like suitability to multiple RF source options including solid state amplifier (particularly suitable for our situation), large dose range, ease of maintenance, overall reliability. This type of accelerator is suitable for X-ray mode of irradiation which gives very high dose uniformity and is considered a superior radiation processing source.

THE RF CAVITY

The design of re-circulating RF cavity at 107.5 MHz was undertaken using Superfish and CST studio suite. The main criteria of design was to optimize the effective shunt impedance keeping in mind the synchronous condition and provision for placing the dipole magnets for bending the beam after getting accelerated in the cavity.

The expression for transit time factor for relativistic electron is given as, [3][4]

$$TTF = \frac{S_i(\theta_2) - S_i(\theta_1)}{\ln R_2 / R_1} \qquad \text{--------(1)}$$

Where □□ (□) is the sink function, □2 = $\frac{2\pi R_2}{\lambda}$ and □1= $\frac{2\pi R_1}{\lambda}$

The shunt impedance is give as,

$$Z_s = \frac{8\pi}{\rho_s} \ln^2 \frac{R_2}{R_1} \left(\frac{\lambda}{8} \left(\frac{R_2 + R_1}{R_2 R_1} \right) + \ln \frac{R_2}{R_1} \right)^{-1} \qquad \text{--(2)}$$

The synchronous condition is given as,

$$2R_2 + D = \lambda \qquad \text{---(3)}$$

The various symbols used in equations 1, 2 and 3 are as shown in figure no.1

Where □□ is the skin effect resistivity. For copper, □□ = 2.51 × 10^{-7} □ $^{1/2}$. During the transit in the gap electric field
do not remain constant. So the useful parameter is effective shunt impedance □□・□□□^{2}.

In the design of a cylindrical RF cavity, the frequency is indeed primarily determined by the height of the cavity rather than the inner and outer diameters of the conductors. The height of the cavity sets the resonance condition for the desired frequency.

Once the outer radius of the cavity, R_2, is chosen based on specific criteria of equation 3, the inner radius can be determined to maximize the effective shunt impedance. This choice helps optimize the cavity's performance and efficiency.

Other parameters of the cavity, such as the shape of the end caps or the shape of inner conductor were optimized to increase the effective shunt impedance, which directly impacts the cavity's effectiveness in accelerating particles.

* deepak@rrcat.gov.in

To adjust the frequency of the cavity, the height is modified. Overall, the height of the cavity determines the frequency, while the choice of inner and outer diameters, as well as other cavity parameters, is optimized to enhance the effective shunt impedance and overall performance.

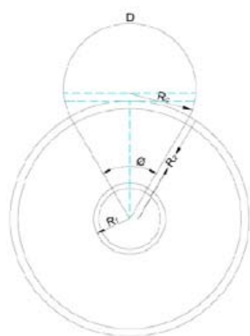

Figure 1: Cross sectional view of the coaxial cavity.

OPTIMIZED DIMENSIONS OF RF CAVITY

The figure below shows the optimized dimensions of recirculating RF cavity.

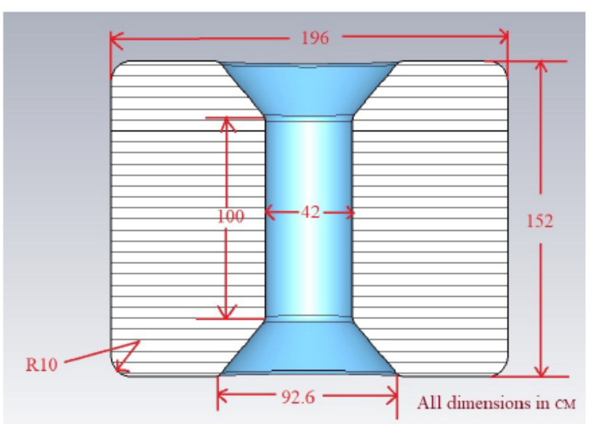

Figure 2: Optimized cavity Dimensions.

The RF parameters for fundamental mode of the cavity are tabulated in table 1.

Table 1: RF parameters of fundamental mode

Parameter	Value	Unit
Resonant Frequency	107.507	MHz
Quality Factor	55968	-
Shunt Impedance	15.83	MΩ
R/Q	282.87	Ω

HIGHER ORDER MODE IDENTIFICATION

HOMs can degrade the beam quality by causing beam breakup, beam halo, or beam emittance growth. These effects arise due to the coupling of HOMs with the beam, leading to energy spread or transverse perturbations. HOMs can cause energy loss in the RF cavity. This can happen through different mechanisms such as ohmic losses in the cavity walls or wakefield effects induced by the HOMs. Energy loss can limit the overall efficiency of the cavity. HOMs can destabilize the cavity operation. If the amplitude of the HOMs exceeds certain thresholds, it can lead to instabilities such as beam break-up or cavity detuning. These instabilities can affect the beam performance and the overall operation of the accelerator. To mitigate the negative effects of HOMs, several techniques are employed, including: RF cavity design optimization to minimize HOM content. HOM couplers or damping materials to absorb or dissipate HOM energy. Beam diagnostics and feedback systems to monitor and control the beam behavior in the presence of HOMs. Active control systems to suppress HOMs and maintain cavity stability. A study was undertaken to identify the various higher order modes of the optimized cavity. Higher order modes are parasitic to the performance of RF cavity. The Higher order modes are needed to be suppressed if the same is excited some how by the beam. For making a provision for higher order suppression an advance knowledge of various modes supported by the cavity are required. A comparative study was under taken using Superfish and CST studio suite to identify the various Higher order modes supported by the cavity.

Figure 3 and 4 below shows the filed pattern of fundamental TEM1 mode simulated by Suerfish and CST respectively.

Figure 5 shows the field pattern simulated by CST and Superfish for TM011 mode.

Various TEM and TM modes were identified during this simulation. The modes identified are tabulated in

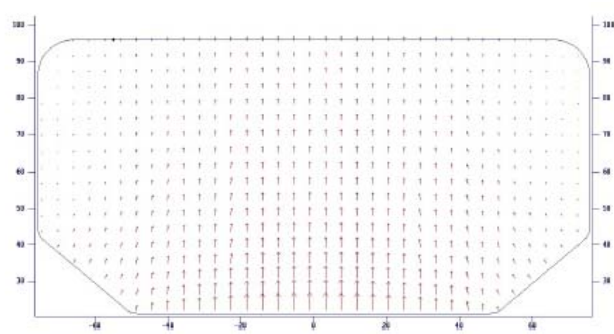

table 2.

Figure 3: Electric Field simulated by Superfish for fundamental mode .

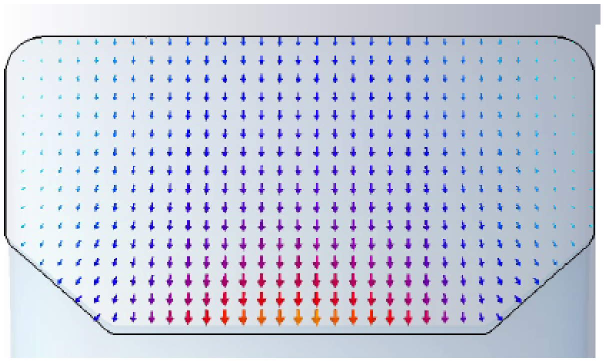

Figure 4: Electric Field simulated by CST Studio Suite for fundamental mode

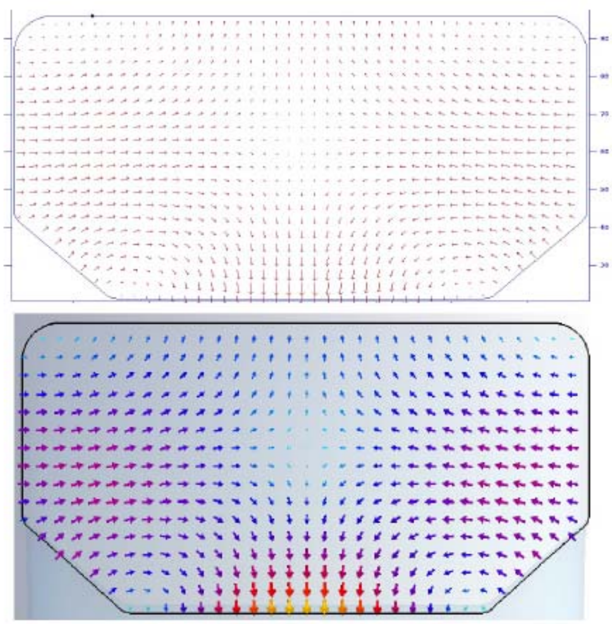

Figure 5: Electric Field simulated by the two codes for TM011 mode.

Table 2: RF parameters of fundamental mode

MODE	Superfish MHz	CST Studio Suite MHz
TEM1	107.507	107.506
TEM2	216.856	217.440
TEM3	313.556	314.882
TM010	194.022	192.919
TM011	233.155	233.512
TM012	301.629	302.799

Figure 6 shows the field calculated by CST for TEM3 mode.

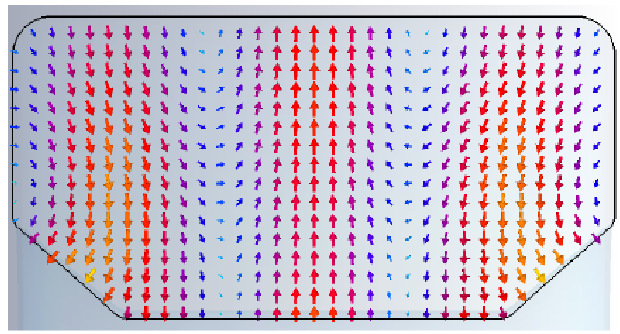

Figure 6: Electric Field simulated by CST formTEM3 mode.

CONCLUSION

The design of re-circulating RF cavity has been done for 107.5 MHz. The various higher order modes supported by the cavity have been identified. Few higher order modes have been reported in this paper.

REFERENCES

[1] Deepak Kumar Mishra et al, Design of half wavelength coaxial resonant cavity for electron acceleration, InPac 2019.

[2] Deepak Kumar Mishra et al, Preliminary study of half wavelength coaxial resonant Cavity operating in fundamental mode for electron Acceleration, . InPac 2018.

[3] Iraj Jabbari et al.,Design study of double-layer beam trajectory accelerator based on the Rhodotron structure Nuclear Instruments and Methods in Physics Research A828(2016) 72–80.

[4] J. Pottier. “A new ty-pe of RF electron accelerator: the Rhodotron”. Nucl. Instr. Meth. Phys. Res.. Vol B40/41. Pp 943-945, 1989

[5] Y. Jongen et al., The Rhodotron, a new 10 MeV, 100 kW, CW metric wave electron accelerator, Nucl. Instrum. Meth. B 79 (1993) 865.

FINAL COMMISSIONING OF THE HIGH-POWER RF SYSTEM FOR CONDITIONING OF THE RF PHOTOCATHODE GUN AT HIGHER FIELD GRADIENT

B.K. Sahu *, Ashish Sharma, P. Patra, J. Karmakar, B. Karmakar, M. Aggarwal, S.Venkataramanan, P. Singh, Y. Mathur, S.K. Saini and S. Ghosh

Inter-University Accelerator Centre, New Delhi.

Abstract

Delhi Light Source (DLS), a compact, pre-bunched Free Electron Laser facility is being commissioned at IUAC. This facility is expected to produce electron beam of maximum energy up to 8 MeV by a 2.6 cell normal conducting RF photocathode gun operating at 2860 MHz for pulse operation up to 4 µs duration with estimated field gradient of 110 MV/m. The high-power RF system for the gun consists of a solid-state pulsed modulator-based Klystron system rated for 25 MW peak RF power for the desired pulse duration at 50Hz repetition rate. The RF System was installed and tested up to full rated power with a vacuum based waveguide system connected to water cooled matched load. When the matched load section was replaced with the actual RF gun, the RF power was limited up to 1 MW for RF conditioning of the gun due to high value of the reflected power during conditioning in absence of the high-power Circulator [3]. In place of high vacuum-based Circulator as planned initially, SF_6 Gas based circulator is now installed in the waveguide system. After installation of the Circulator the RF conditioning of the photocathode gun could be carried out at high RF power level. The VSWR is found to be better than 1.1 for the entire 4µs pulse duration and RF gun could be conditioned at high field gradient up to 65 MV/m to produce 4.5 MeV electron beam using a nanosecond UV laser beam.

INTRODUCTION

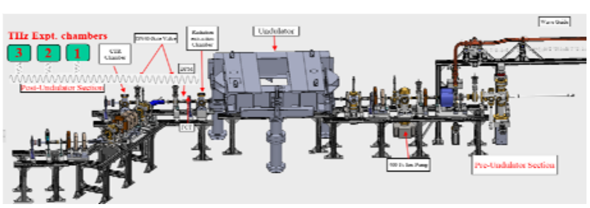

Figure.1. 3-D overview of the Free Electron Laser based Delhi Light source facility at IUAC

Delhi Light Source (DLS), a compact, pre-bunched Free Electron Laser facility [1] is being commissioned at IUAC and recently production of 4.5MeV electron beam is demonstrated using the 2.6 cell normal conducting RF photocathode gun [2]. Once fully operational, the facility will be producing electron beam of energy of ~ 8 MeV to generate THz radiation in the range of 0.18-3 THz. The main beamline components apart from RF system are shown in Fig. 1. The RF source for the system consists of Klystron and solid state modulator operating in pulsed mode for a maximum duration of 4µs. The system is rated for 25MW of peak RF power for the operation of RF Gun. During initial phase of installations of RF system, the RF gun could not be conditioned beyond 1 MW of RF power due to high reflected power during the conditioning process of the Gun in the absence of RF circulator. Finally, the problem was solved by installing a high-power RF isolator to condition the RF Gun at higher power level. The final stage of installation of high-power RF system along with RF conditioning at higher power level is presented in detail.

.

FINAL COMMISIONING OF HIGH-POWER RF SYSTEM

The high-power RF system for DLS is meant to power the 2.6 Cell normal conducting photo cathode based electron gun operating at 2860 MHz [3]. The system consists of a Thoshiba make klystron operating in pulsed mode using a solid-state modulator of Scandinova make with a maximum power rating of 25MWfor a duration of 4 µs (max) with repetition frequency up to 50 Hz.

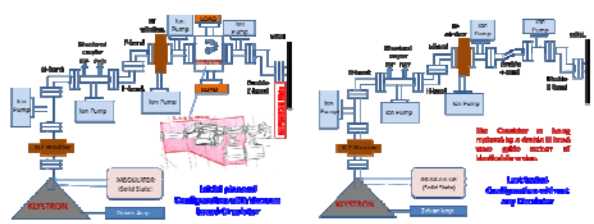

Figure.2. Block diagram of high power RF system along with earlier installed system for RF conditioning

The RF distribution system used to transport RF power to the Gun consists of vacuum based WR284 waveguide system to avoid any contamination of semiconductor photo cathodes to be used during operation. As per intial plan, this included straight sections, E and H-bends, directional couplers, RF windows and pumping sections having Merdinian/SLAC type flange connector along with high Power Isolator consisting of vacuum based circulator and load. However, the RF isolator could not be installed due to technical problems associated with fabrication of such a high-power Vacuum based circulator and hence the isolator section was replaced with a double H bend of identical dimension. After conditioning the RF system with a matched load, the matched load was replaced by the photocathode based RF Gun and the RF conditioning continued to generate electric field inside the gun. As it was realized that RF conditioning beyond 1MW is not possible without VSWR protection, a SF_6 based isolator was later installed to withstand higher values of reflected power.

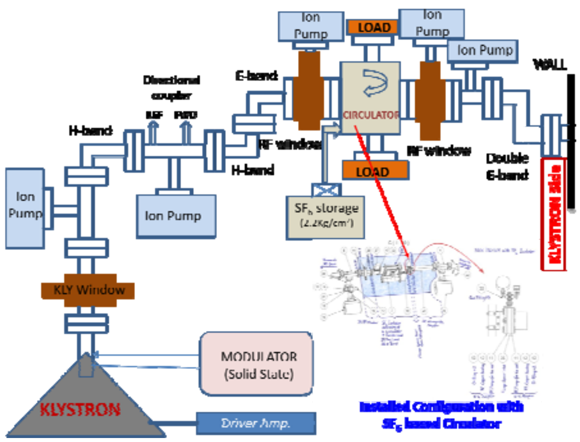

Figure.3. Block diagram of complete installed high power RF system with SF6 based RF isolator

To accommodate the new isolator, necessary design changes were made in the RF delivery system. One WG pump section with ion pump has been removed and the RF window before this WG pump section is now being used to separate the vacuum part and the SF_6 part. After the RF window, a WG adapter having SLAC male flange on the input side towards the RF window and a CPR284F flange at the other end is used along with Grooved-Grooved flange adapter (G-G flange adapter), the flange spacer inlet and another G-G flange adapter for installation of the SF_6 isolator, consisting of circulator, ferrite load, H-bend, and dry load. An arc detector is installed with fibre optic cable to interlock the system against any arc detected inside the isolator. At the output of the isolator a G-G flange adapter and additional new RF window is installed. This RF window has CPR284F flange at the input side which is pressurized with SF_6. The vacuum side has SLAC female flange and mates with the old part of the WG system. Before the input of the isolator, the flange spacer inlet is placed. This component allows for filling of SF_6 into the WG. The gas filling kit is placed at the orifice on the flange spacer inlet. It has a filling nipple for 6mm plastic tube, followed by a needle valve that secures the pressure inside the WG and can be opened to fill more pressure inside the WG. An analogue pressure gauge clearly indicates the WG pressure and a digital pressure gauge indicates the WG pressure with digits. The digital pressure gauge also contains a monitor function and outputs a voltage proportional to the WG pressure to the pulse modulator.

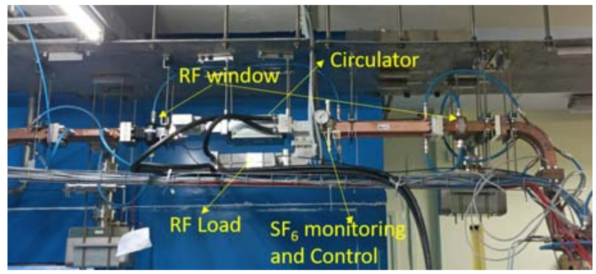

Figure.4. View of the installed SF6 based Isolator with existing Wave Guide section

In case the pressure drops below a pre-set lowest limit the pulse modulator will interlock and cannot be started again until more SF_6 has been filled inside the WG through the filling nipple and the needle valve. Manual filling ensures that only very tiny amounts of SF_6 can leak from the WG and not from the filling system or SF_6 bottle.

RF CONDITIONING OF PHOTO-CATHODE GUN

After the installation of the SF_6 based isolator, RF conditioning of the entire waveguide section continued with the RF photo cathode gun. The resonance frequency of the gun was tuned to 2860 MHz by setting up the temperature of the precise water chiller to 35^0C within an accuracy of ±0.05 ºC. The forward port of the directional coupler just before the cavity and reflected port of the isolator are being used for RF monitoring during conditioning. VSWR interlock is armed with forward and reflected power taken from the directional coupler just after the klystron and digitized using the inbuilt RF digitizer of the modulator. Initial load matching was done by optimizing the position of the photocathode plug using vacuum manipulator at the entrance of the gun. The VSWR interlock conditions are always maintained well within the specified limit of the Klystron during conditioning and relaxation given in the VSWR software interlock during earlier RF conditioning due to impedance mismatch was withdrawn. The frequency of the RF Gun was continuously tracked with the master oscillator frequency to minimize the reflected power during conditioning. The high-power conditioning was started with a low pulse duration of 1 µs up to 5 MW of RF forward power initially at 10Hz repetition rate and then pulse duration was increased in steps to condition the RF Gun up to desired 4 us pulse duration. The dark current was monitored during RF conditioning using a commercial faraday cup used for continuous dc beam operation and lock in amplifier. Beam Viewer Camera was also used to see the profile on the YAG screen. BPM have also been installed and used to see the position of laser induced electron beam. Various interlock limits are set for protection of RF gun against beam loading. Typical observation of forward power, Reflected power and cavity pickup during conditioning at 5 MW of RF forward power is shown in Fig. 5.

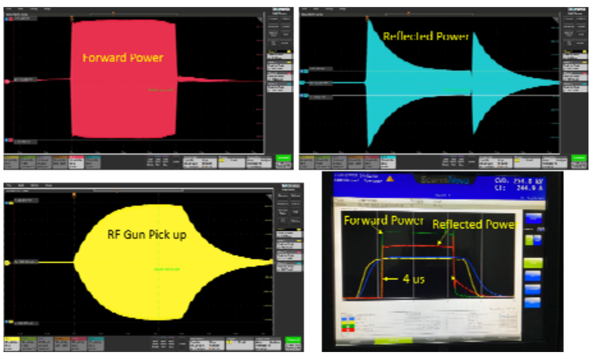

Figure.5. Measurements at both the directional couplers during RF conditioning

The Electric field generated in the RF gun as well as estimated energy of the electron beam at the given forward power level is estimate as shown in Fig. 6. In order to calibrate verify the Electric field generated in the Cavity the Energy measurement of the photo electron beam generated at different RF forward power levels is done using a dipole magnet. The measurement was found to be as per the estimate within 10% variation.

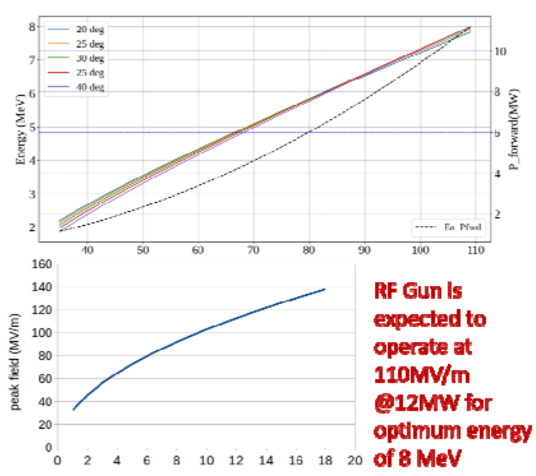

Figure.6. Estimation of Electric field and Electron beam Energy at different RF forward power level

As RF Gun is expected to deliver 8 MeV of photo-electron beam, The RF conditioning should be completed up to 12MW of forward power. Similar steps starting with lower pulse width are being repeated for condition the RF Gun up to the desired RF forward power level.

RESULTS AND DISCUSSIONS

The installation of SF_6 based Isolator has enabled us to condition the RF Gun at high RF power to increase the field gradient up to 65 MV/m for desired pulse length of 4µs. RF Conditioning of the photo cathode gun is still continued to reach the desired electric field of 110Mv/m. RF Gun is conditioned up to 10 MW of forward power for 1.2 µs pulse duration and pulse width is now gradually being increased up to 4 µs. The Electric field generated inside the RF Gun has been verified with the measurement of energy of produced by the laser induced electron beam up to 4.5 MeV at 4 MW of RF Forward power. As the final goal is to produce electron beam energy up to 8 MeV for production of THz radiation ranging from 0.18-3 THz, the conditioning will be continued up to 12 MW of RF forward power along with the measurement of energy of the produced electron beam using the nanosecond UV laser.

ACKNOWLEDGEMENT

The authors would like to acknowledge the help received from Prof. T. Rao of BNL, USA during different stages of the RF conditioning and electron beam production. The authors would like to acknowledge the help received from Prof. J. Urakawa, Dr. A. Aryshev of KEK, Japan and Prof. Yang from Waseda University, Japan on various occasions. Technical support and assistance received from M/S Scandinova systems during the entire installation process is highly acknowledged. Encouragement and support received from Prof. A. C. Pandey, Director, IUAC is very much appreciated.

REFERENCES

[1] S. Ghosh et. al, Nuclear Instruments and Methods in Physics Research B 402,(2017) p. 358-363

[2] S. Ghosh et. al, "Commissioning Status of the IUAC-DLS facility" Proceeding of this conference InPAC 2023

[3] B.K. Sahu et. al, " RF system for the Free Electron Laser based Delhi Light Source", in Proceedings of Indian Particle Accelerator Conference (InPAC 19), IUAC, NewDelhi, November 2019.

[4] B.K. Sahu et. al, "High Power RF Conditioning of the photocathode gun for IUAC_DLS", in Proceedings of Indian Particle Accelerator Conference (InPAC 22), VECC, Kolkatta, March 2022

UNSCENTED KALMAN FILTER AS SC CAVITY DETUNING ESTIMATOR

R. T. Keshwani[1], S. Mukhopadhyay[2], R. D. Gudi[3], Gopal Joshi[2]
[1]Research Scholar HBNI, BARC, Mumbai, [2]Sr. Prof. HBNI, BARC, Mumbai, [3]Prof. IIT Mumbai

Abstract

In an operational accelerator, value of cavity detuning needs to be known for tuning and tracking of cavity resonance frequency. As direct sensor/s for detuning are not available, often model of RF cavity is employed to infer or estimate its value from available measurements. Dynamics of Model of RF Cavity is linear in case of normal conducting cavity, thus methods of linear estimation suffice. However, the model is nonlinear in case of Superconducting cavity necessitating use of non-linear estimators. In this paper Unscented Kalman filter, a well-known estimator for non-linear system is described followed by its application as estimator for RF cavity detuning. Modelling & Simulation results are presented.

INTRODUCTION

In an operational accelerator, resonance frequency (f_r) may shift w.r.t. operational RF frequency (f_{RF}). The difference $2\pi(f_r\text{-}f_{RF})$ is referred as detuning $\Delta\omega$. Its value forms important performance parameters of RF cavity. However, it is not a directly measurable parameter. Continues time state space (CTSS) model of RF cavity is employed to estimate $\Delta\omega$ from measured inputs and outputs of cavity.

$$\frac{d}{dt}\begin{bmatrix} V_r(t) \\ V_i(t) \end{bmatrix} = \begin{bmatrix} -\omega_{1/2} & -\Delta\omega \\ \Delta\omega & -\omega_{1/2} \end{bmatrix}\begin{bmatrix} V_r(t) \\ V_i(t) \end{bmatrix} + \begin{bmatrix} R_L\omega_{1/2} & 0 \\ 0 & R_L\omega_{1/2} \end{bmatrix}\begin{bmatrix} I_r(t) \\ I_i(t) \end{bmatrix} \;\&\; \mathbf{z}(t) = \begin{bmatrix} 1 & 1 \end{bmatrix}\begin{bmatrix} V_r(t) \\ V_i(t) \end{bmatrix}$$

The CTSS model is used to obtain stochastic discrete state space model of system (with discrete time index k) for assumed state noise with covariance matrix $\mathbf{Q}_k$ and measurement noise with covariance matrix $\mathbf{R}_k$ and appropriate sampling time. Here, at time instant t, states $V_r(t)$ and $V_i(t)$ are measured from cavity pick up signal while $I_r(t)$ and $I_i(t)$ from cavity input signals. Parameters $\omega_{1/2}$ and R_L are cavity half bandwidth and loaded resistance. $\Delta\omega$ is cavity operational parameter. In case of normal conducting cavity, above model suffices the purpose of $\Delta\omega$ estimation. However, in case of superconducting (*SC*) cavity, Lorentz force detuining (*LFD*) also affects $\Delta\omega$ depending on mechanical time constant τ_m, *LFD* constant k_{LFD} and E_{ACC} field inside cavity. Thus, $\Delta\omega$ is now function of t denoted as $\Delta\omega(t)$ as time varying detuning (*TVD*).

$$\frac{d}{dt}\Delta\omega(t) = -\frac{1}{\tau_m}\Delta\omega(t) + \frac{2\pi}{\tau_m}k_{LFD}E_{ACC}^2(t) \qquad (1)$$

$E_{ACC}(t)$ field is related to $V_r(t)$ *and* $V_i(t)$ by relation $E_{ACC}^2 = V_r^2 + V_i^2$. The dependence of $\Delta\omega(t)$ on square of $E_{ACC}(t)$ leads to nonlinear system dynamics. Any linear estimator used to estimate parameters of a nonlinear system leads to incorrect estimate value. The measurement $\mathbf{z}(t)$ is often assumed to be corrupted by gaussian noise which when propogated through a nonlinear system, changes to non-gaussian noise leading to incorrect $\Delta\omega(t)$ estimated denoted as $\Delta\hat{\omega}(t)$. In order to avoid such issues, it is recommended to use estimator comensurate with system dynamics. Although Kalman filter has been reported for this purpose [1], the *UKF* is better alternative due to non linearity involved herein. Though comparatively simpler approaches like extended *KF* (*EKF*) [3, 4] are available, they suffer from serious limitations of divergence issues [3]. In this papers authors present application of Unscented Kalman filter (*UKF*) as $\Delta\omega(t)$ estimator.

UNSCENTED KALMAN FILTER

UKF addresses the general problem of estimating the states of a discrete-time controlled process that is governed by the non-linear stochastic difference equation [2]. Rather than states obtained by linearization around operating point (as in case of *EKF*), it relies on better approximation using unscented transformation (*UT*). In general, the probability distribution (*pdf*) function cannot be described by a finite number of parameters and most practical systems employ an approximation of some kind. It is conventionally assumed that the distribution is Gaussian at any time. Thus only first two moments of *pdf* i.e, the mean and variance are considered while addressing an estimation problem with *UKF*. *UKF* [3,6] makes use of the fact that it is easier to approximate a probability distribution than it is to approximate an arbitrary nonlinear function or transformation. The *pdf* of the states (and parameters) is approximated by a sample chosen appropriately. The sample points are propagated using the nonlinear state space model, and the state estimates and its error covariance matrix are computed using the corresponding sample statistics. Consider a nonlinear system with state space model at discrete time instant k.

$$\mathbf{x}_{k+1} = f(\mathbf{x}_k, \mathbf{u}_k, \mathbf{w}_k, k)$$

With a measurement given by,

$$\mathbf{z}_{k+1} = g(\mathbf{x}_{k+1}, \mathbf{u}_{k+1}, k) + \mathbf{v}_{k+1}$$

Here f and g are nonlinear functions of state equation and output equation respectively, $\mathbf{x}_k$, $\mathbf{u}_k$ and $\mathbf{z}_k$ are states, system input and measurement matrices respectively. $\mathbf{w}_k$ represents white noise matrix representing model uncertainty while $\mathbf{v}_k$ represents measurement noise matrix. *UKF* carries out state estimation of such a nonlinear system by representing first two moments of

.

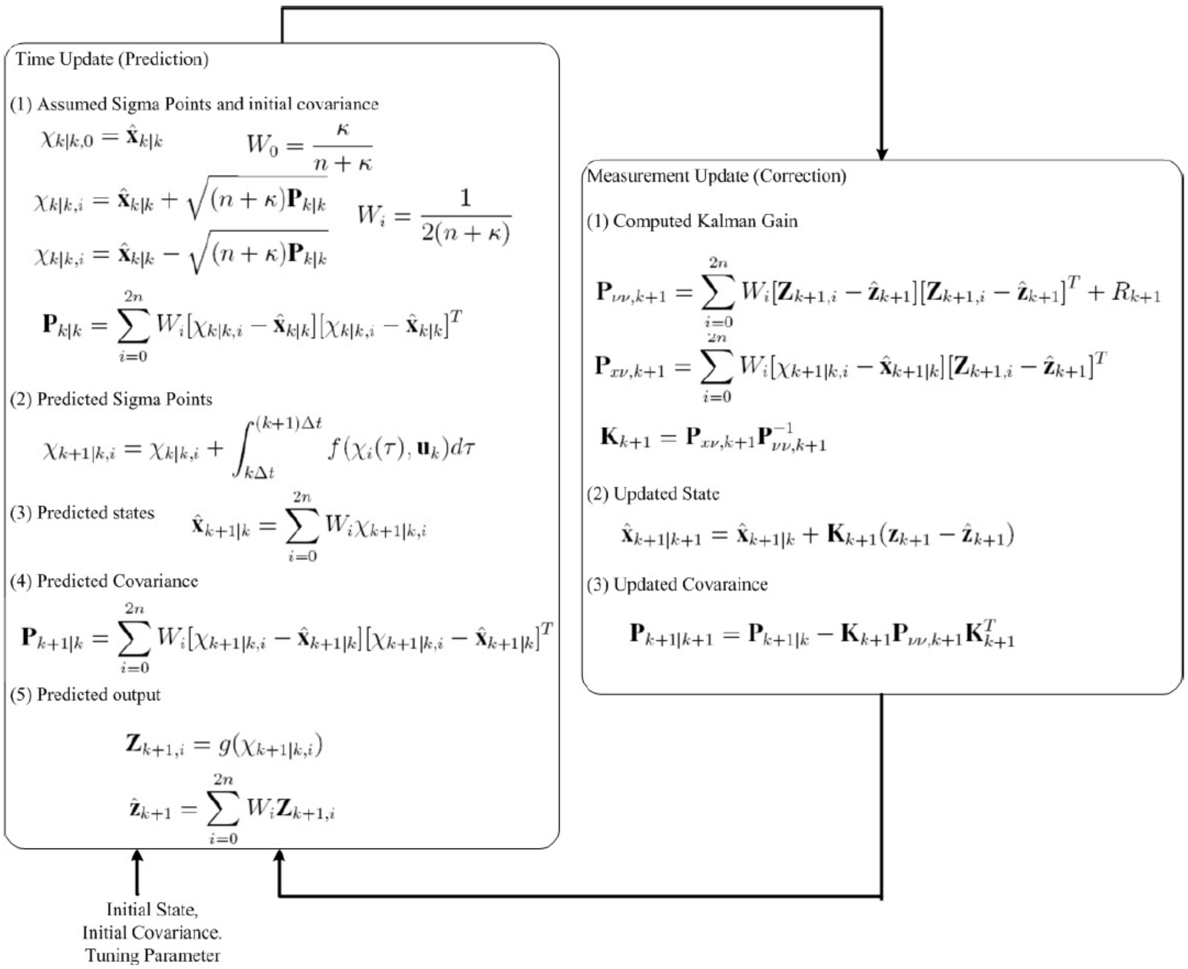

Figure 1: Steps used in *UKF* operation.

underlying *pdf* using $2n$ (n is no of states) sigma points with appropriate weight W_i of i^{th} sigma point. From initial state, covariance & tuning parameter κ, sigma points χ are defined. This is followed by predicting values of states, covariance and outputs at k^{th} instant. Kalman gain $\mathbf{K}_{k+1}$ is computed. As soon measurement is available, state matrix and its error covariance is updated.

APPLICATION OF *UKF* AS *TVD* ESTIMATOR

Estimation of predicated states and covariance is carried out from given input sequences $I_r(k)$ and $I_i(k)$ and parameters of cavity (R_L, $\omega_{1/2}$ and $\Delta\omega$), for assumed noise model (which is formed from $\mathbf{w}_k$ and $\mathbf{v}_k$ and hence value of *TVD* is estimated as a third state. Tesla cavity parameters have been assumed in model. It has f_r =1.3 GHz, R_L= 1.3 Gohm, $\omega_{1/2}$ =216 Hz. As mentioned in [5] the cavity model has input in terms of mA as generator and beam induced current (I_r and I_i) while its output V_r and V_i is of order of MV. On arrival of measurement, the state values are upated hence *TVD*. Figure 2 shows the *UKF* estimated sigma points from noisy measurements **Z**. **Z** calculated from sigma points is much cleaner than noisy **Z** signal input to *UKF* algorithm.

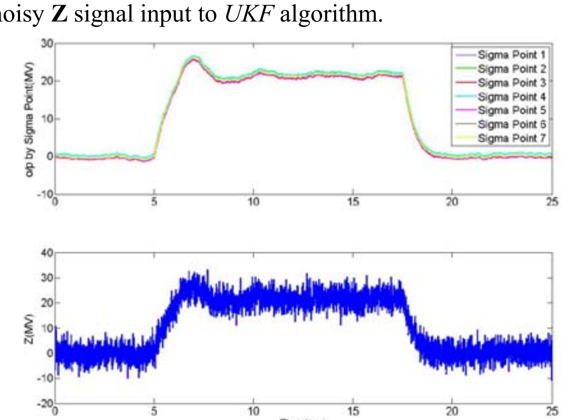

Figure 2: Estimated output by sigma points from noisy measurement **Z.**

From states estimated by *UKF*, *TVD* $\Delta\omega(t)$ is available using discerte version of Eq. (1) and is shown in figure 3. The states estimated for pulsed RF cavity operation is represented in state plane of V_r versus V_i as shown in figure 4. Both figure 3 and figure 4 also show the states and $\Delta\omega(t)$ estimated by *UKF* as well as *EKF*. Though *EKF* and *UKF* show similar estimates, *EKF* is not recommended as it suffers from divergence issues. However, advantages offered by *UKF* comes at high computational costs and high implementation complexity involved. Unlike *EKF*, in addition to computation of states and their error covanriance, during operation of *UKF*, one has to keep computing sigma points too as it is essential to capture structure of underlying noise*pdf* by these sigma points. This important feature of *UKF* helps propagation of noise through non-linear system, which otherwise could have lead to incorrect estimates of states. Figure 5 shows the *UKF* estimated covariances for state error. For properly tuned *UKF*, elements of covariance matrix **P** achieve steady state values depending on assumed tuning parameters $\mathbf{R}_k$ and $\mathbf{Q}_k$. $\mathbf{Q}_k$ is obtained from knowledge of process model while $\mathbf{R}_k$ depends on uncertinities posed by sensing and measurement system.

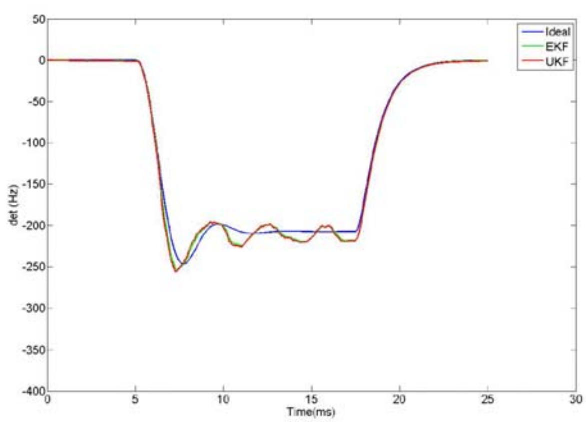

Figure 3: Estimated *TVD* by *EKF* and *UKF*.

CONCLUSION

The main focus of this paper has been to assess performance of *UKF* as estimator of *SC* cavity *TVD* under non-linear systems formulation via simulation studies. It is concluded that estimated states of *SC RF* cavity are close to true states i.e to value of states in absence of noise. Sigma points in *UKF* formulation help capture the first two moments of underlying *pdf* of noise. Due to nonlinear dependence of *TVD* on E_{ACC}, the dynamical model governing cavity behaviour is nonlinear. Due to non linearity of model, a model based on *UKF* is expected to give better estimation results compared to that based on discrete *KF*. The advantages offered by *UKF* are at cost of higher computational burden on system used for estimator implementation.

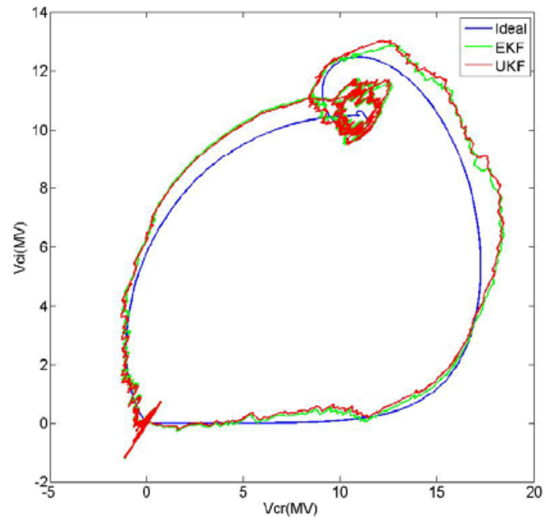

Figure 4: Estimated V_r versus V_i in state plane.

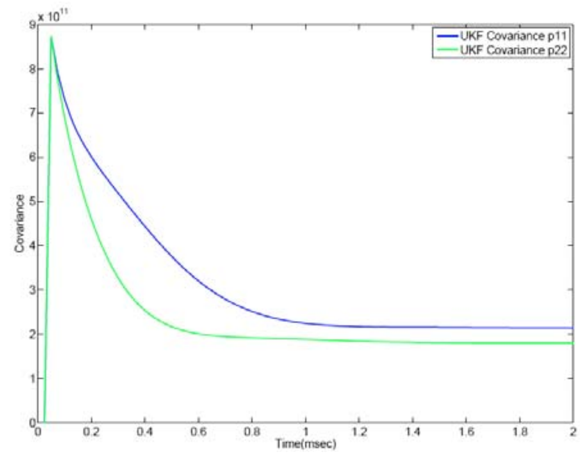

Figure 5: *UKF* estimated covariances.

REFERANCES

[1] Ushakov, A., Echevarria, P., and Neumann, A., “Developing Kalman filter based detuning control with a digital SRF CW cavity simulator”, (2018).

[2] Stark, H. and Woods, J.W., Probability, Statistics, and Random Processes for Engineers,” Pearson, (2011).

[3] Vachhani, P., Rengaswamy, R., Gangwal, V., and Narasimhan, S., “Recursive estimation in constrained nonlinear dynamical systems,”, AIChE journal, 51(3), (2005).

[4] B.Patel, S., S.Mukhopadhyaya, A.P.Tiwari, “ Estimation of reactivity and delayed neutron precursors concentrations using a multiscale extended kalman filter”, Annals of Nuclear Energy, 111:666–675, (2018).

[5] Schilcher, T., Vector sum control of pulsed accelerating fields in lorentz force detuned superconducting cavities. PhD Thesis, (1998).

[6] Romanenko, A., Santos, L. O., and Afonso, P. A. F. N. A., “Unscented Kalman Filtering of a Simulated ph system”, Ind. Eng. Chem. Res., (43):7531–7538, (2004).

STATISTICAL METHODS FOR ASSESSMENT OF RF AMPLIFIER LINEARIZATION

R. T. Keshwani[1], S. Mukhopadhyay[2], R. D. Gudi[3], Gopal Joshi[2]
[1]Research Scholar HBNI, BARC, Mumbai, [2]Sr. Prof. HBNI, BARC, Mumbai, [3]Prof. IIT Mumbai

Abstract

In design of particle accelerators, solid state RF power amplifier linearization has been one of the challenging areas. Among various available techniques, digital predistortion based on least square estimation is one of the promising approaches. Design of such an estimator needs fitting a suitable model exhibiting inverse characteristics of that of *SSRFPA*. For assessment of goodness of fit, one has to often resort to statistical methods based on linear regression concepts. Once problem is formulated as linear regression, many design issues may be seen from different perspective. This paper applies concepts of linear regression to least square estimation to obtain confidence interval estimates, goodness of fit, etc for models fitted to *SSRFPA* and *DPD* input output characteristics.

INTRODUCTION

Linearization of *SSRFPA*[1] by using its inverse input output (I/O) characteristics in technique of digital predistortion (*DPD*) [2] involves, placing an inverse transfer function block in series with it. The success of this method of linearization depends on accuracy of coefficients obtained while characterization of *SSRFPA*. I/O of *SSPA* is fitted with model of form of Eq. 1.

$$y = \sum_{i=0}^{M} h_i x^i \quad \ldots\ldots\ldots \quad (1)$$

From model of *SSRFPA* or *SSPA*, least square estimation (*LSE*) is then used to model of *DPD*. Assessment of model of *DPD* for its effectiveness as linearizer is also one of important design step before using *DPD* in practice. There is need to assess goodness of fit of model to I/O data provided to linearizer. To achieve this objective, linear regression concept is used in this paper. It leads to interesting estimates such as confidence interval (*CI*) estimates and R^2 measures. Here, it is applied to linearizer build using Saleh model [2] for *SSPA*. As *SSPA* models are well documented in literature, they won't be discussed due to space limitation.

Simple linear regression is a statistical method that allows summarizing and studying relationships between two continuous (quantitative) variables. One variable, denoted as *x*, is regarded as the predictor, explanatory, or independent variable. The other variable denoted by *y* may be considered as the outcome/ response/ dependent variable. Other terms used frequently are predictor/response to refer to the variables encountered. In deterministic relationships between two variables, the equation/s exactly describes the relationship between the two variables. In statistical relationship, the relationship between two variables may not be perfect and some uncertainty may be involved. The paper aims at assessing this uncertainty in model parameters using few related concepts outlined in linear regression literature for data science. Authors have published *LSE* of *DPD* parameters in [3]. Note that *DPD* is unaffected by related issues like homoscedasticity, multivariate normality, etc.

LINEAR REGRESSION FOR *DPD* MODEL

In general, various *LSE* methods are used to solve a linear regression (*LR*) problem. Above mentioned problem of finding model parameters of *SSPA* and/or *DPD* may be viewed under *LR*. In application of finding fitting parameters for *SSPA* I/O & *DPD* I/O, designers usually seek answers to below questions:

1) Number of parameters needed for arriving at ideal model of *SSPA* or *DPD* I/O.
2) Value of modelling error w.r.t. to true response of given I/O data and ways/methods/means to reduce it.
3) Amount of confidence that can be associated with each model parameter and list least significant parameter/s.
4) Goodness of fit of model output to experimentally obtained outputs and ways to quantify it with aim to choose among competing models.
5) Number of readings over I/O range of *SSPA* to obtain reasonably accurate model
6) Over a full I/O range, effect of resolution or spacing between readings.

To answer these questions, one has to be understand *LSE* under purview of *LR*. In *LR* exercise, measures are obtained from errors (called R^2 measure) and confidence intervals (*CI*) are defined (using statistical hypothesis testing) for parameters to assess goodness of fit (*GOF*) for obtained model. The simplest of the *LR* problem is where one regresses a variable *y* on to a variable *x* each for j^{th} reading upto *n* (sample size) for model parameters θ. Thus,

$$y_j = \theta_1 x_j + \theta_0 + e_j \quad \ldots..(2)$$

In *LSE*, one finds best estimate of θ_0 and θ_1 that minimizes performance index J given by,

$$J = \sum_{j=1}^{n} (y_j - \hat{y}_j)^2$$

Here, $\hat{y}_j$ is model estimated y for its corresponding j^{th} reading. The collective minimization or optimization procedure leads to below unique solution for Eq. 2 and equations for estimated random variable parameters for mean of y ($\bar{y}$) and mean of x($\bar{x}$). To avoid confusion, it is mentioned that: (x_j , y_j) are pair j^{th} reading of I/O obtained from *SSPA*, ($\hat{x}_j , \hat{y}_j$) are pairs of j^{th} I/O fitted by *LSE* model while ($\bar{x}$, $\bar{y}$) is pair of mean of I/O. Then,

$$\hat{\theta}_1 = \frac{S_{xy}}{S_{xx}} \;\; \& \;\; \hat{\theta}_0 = \bar{y} - \hat{\theta}_1 \bar{x}$$

$$\text{where, } S_{xy} = \sum_{j=1}^{n} x_j y_j - \frac{1}{n} (\sum_{j=1}^{n} x_j)(\sum_{j=1}^{n} y_j)$$

$$\text{and } S_{xx} = \sum_{j=1}^{n} x_j^2 - \frac{1}{n} (\sum_{j=1}^{n} x_j)^2$$

Note that S_{xy} and S_{xx} quantities depend only on I/O data.

Hypothesis tests using the CI approach

One needs the sampling distribution of $\hat{\theta}$. For distribution of $\hat{\theta}$, it is assumed that error e_j has Gaussian distribution. $\therefore \hat{\theta}_m \in N(\theta_m , \sigma^2_{\hat{\theta}_m})$; m=0.1

A standard result available in *LR* literature for variance s_e^2 of residual error e characterization is,

$$s_e^2 \equiv \hat{\sigma}^2 = \frac{1}{n-2} \sum_{j=1}^{n} e_j^2 = \frac{SSE}{n-2}$$

Note that we define sum square total (*SST*), sum square error (*SSE*) and sum square residual (*SSR*) from $\hat{y}$, y_j and $\bar{y}$. Construction of *CI*s of parameter needs using *t*-statistic with (*n*-2) degrees of freedom:

$$T_m = \frac{\hat{\theta}_m - \theta_m}{\hat{\sigma}_{\hat{\theta}_m}} \in t(n-2) \; ; m\text{=0,1}$$

$100(1-\alpha)^2$% *CI* for parameter θ_1 is obtained from *t*-test :

$$\theta_1 \in \hat{\theta}_1 \pm t_{\alpha/2}(n-2) \frac{s_e}{\sqrt{S_{xx}}}$$

For parameter θ_0 , one carried out *t*-tests for:

$$\theta_0 \in \hat{\theta}_0 \pm t_{\alpha/2}(n-2) \frac{s_e}{\sqrt{\frac{1}{n} + \frac{x}{S_{xx}}}}$$

Model fitting is a variance decomposition explained by analysis of variance (ANOVA) identity. It is interpreted that variance in y is due to variance in x and variance in e.

$$\text{i.e, } \sum_{j=1}^{n} (y_j - \bar{y})^2 = \sum_{j}^{n} (\hat{y}_j - \bar{y})^2 + \sum_{j}^{n} (y_j - \hat{y}_j)^2$$

i.e, SST=SSR+SSE. ANOVA helps to define below mesaures of goodness of fit:

R^2 measures: $R^2 = 1 - \frac{SSE}{SST}$ with $0 \le R^2 \le 1$

Adjusted $R^2 = 1 - \frac{SSE/(n-M-1)}{SST/(n-1)}$

SIMULATIONS TO ASSES GOODNESS OF *LSE* MODEL USING *CI* AND R^2 MEASURE

Saleh model *SSPA* amplitude I/O data was used for fitting in using single regression case by *LSE*. Objectives of simulations are:

(1) To assess minimum no. of coefficients needed to model I/O.

(2) Asses effect of no. of fitted coeff. on *SSE*, *SSR* and *SST*.

(3) Effect of total no. of data points in I/O on model and errors.

(4) Asses confidence on each coefficient value.

(5) Asses *DPD* model obtained for a given *SSPA* model. To accomplish these objectives below was carried out. I/O data end point was fixed to keep amount of nonlinearity as constant across different cases considered. Two cases were considered:

Case I (Saleh model with resolution of 0.1 with n=100): Linear, quadratic, cubic polynomial model and so on were fitted using *LSE* to *SSPA* I/O. Eq. 1 gives,

For M=1 case, $y = h_0 + h_1 x^1$

For M=4 case, $y = h_0 + h_1 x^1 + h_2 x^2 + ... + h_4 x^4$

Figure 1 shows the values of coefficients $h_0, h_1 .... h_4$ for cases M=1...4. Most important observation is, as M is increased, the value of each coefficient changes. It is quite obvious, as terms in Eq. 1 are highly coupled to each other. Outcomes from figure 1 can be used to asses, which coefficient contributes least significantly to y and may be discarded. For cases considered, for each case using known true y, $\hat{y}$, *SSE*, *SSR* and *SST* were calculated and from them R^2 measure was calculated. For obtaining figure 1, *t*-statistic test on mean of estimated coefficients was formulated to indicate *CI* of that particular estimated coefficient. It was found that, linear polynomial has largest *SSE* as it is well known that Saleh model for *SSPA* has high nonlinearity. R^2 measure is far below unity indicating erroneous fit. When higher order polynomials of order of 2 and 3 were fitted, the *SSE* went down and R^2 enhanced closed to 1 for case of

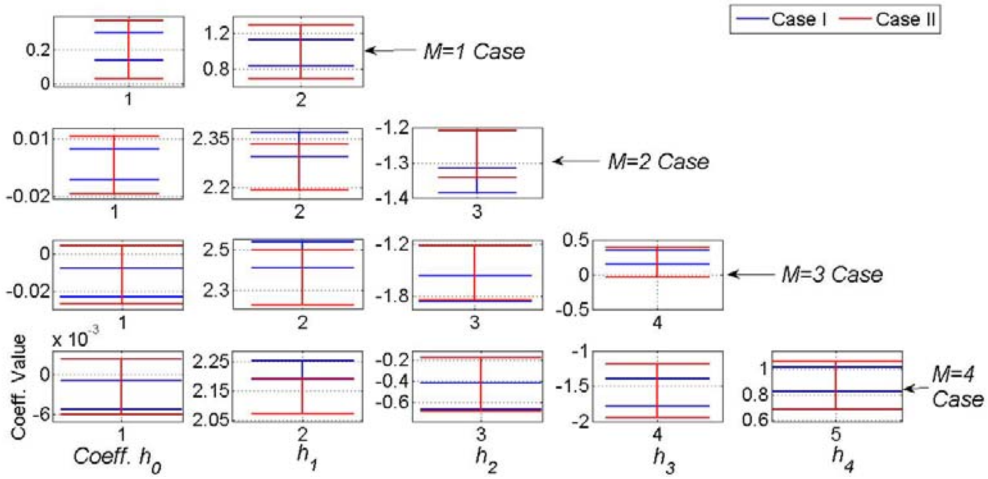

Figure 1. Effect of *M* and data resolution on *CI* of estimates.

M=3. Thus it as concluded (Table 1) for this case that cubic polynomial (*M*=3) gives a reasonable fit.

Table 1: Outcomes for Case I

M	*SSE*	*SSR*	*SST*	R^2	Adj. R^2
1	1.057	8.2052	9.2619	0.8859	0.8847
2	0.0045	9.2574	9.2619	0.9995	0.9995
3	0.0022	9.2597	9.2619	0.9998	0.9998
4	1:412e-4	9.2618	9.2619	1	1

Table 2: Outcomes for Case II

M	*SSE*	*SSR*	*SST*	R^2	Adj. R^2
1	0.2644	2.2056	2.470	0.8929	0.8883
2	0.0009347	2.469	2.4701	0.9996	0.9996
3	0.0005972	2.4695	2.4701	0.9998	0.9997
4	3.062e-05	2.4700	2.4701	1	1

Case II (Saleh model with resolution of 0.4 with *n*=25): Resolution of I/O data points was reduced by factor of 4 as compared to that in case I, the outcomes were assessed. It is concluded (Table 2) that *M*=3 and *M*=4 are sufficient no. of terms in polynomial model. Comparison of case I and case II data for *CI* of parameter estimates was carried out. It was observed that: (1) For all polynomial orders (*M*), the *CI* width is higher for case II compared to that for case I. Higher *CI* width implies more variance and lower confidence in value of parameter estimates giving lower confidence on overall model. This implies that one has to carefully select resolution of readings while conducting experiments. (2) Mean values of estimated parameters are changed by some amount due to resolution change. (3) Coeff.1 i.e h_0 in Eq. 1 is close to zero in case of cubic to 4th order polynomial as data from Saleh model I/O ranges from 0 to 1 only. For case of linear polynomial, h_0 value is not close to zero indicating erroneous fit to I/O data. It is insisted by various authors that any data fitting or regression carried out by *LSE* must be followed by such analysis of error, measures and *CI* of estimated parameters before making use of modelled I/O data for practical application. Case I to Case II outcomes after *LSE* were compared to see difference in values of R^2 and adjusted R^2 as function of *M*. For Case I and II, R^2 and adjusted R^2 were compared.

(1) It is seen that as *n* increases, R^2 decreases. Larger *n* gives more value of *SSE* reducing R^2.

(2) For a given *n*, as *M* is increased, R^2 increases due to reduction in *SSE*. Adjusted R^2 also increases, but not as high as R^2 as its getting penalized for increase in *M*.

CONCLUSION

Concept of *LR* could be used to look at *LSE* problem from error analysis perspective. The amount of error served as guide for R^2 measure and also for selection of appropriate no. of coefficients in *SSPA*/*DPD* model. In order to build confidence on model, *CI*s are found as useful tools. Values of *CI* help in choosing no. of total readings and their resolution while acquiring data during model building exercise for application of *SSPA* linearization using *DPD*.

REFERANCES

[1] A. Johanssan and R. Zeng, “Challenges for the low level RF design for ESS,” pp. 460–462, 01 2011.

[2] H. Ku and J. Kenney, “Behavioral modeling of nonlinear RF power amplifiers considering memory effects,” IEEE Transactions on Microwave Theory and Techniques, vol. 51, no. 12, pp. 2495–2504, 2003.

[3] R. T. Keshwani, S. Mukhopadhyay, R. D. Gudi, Gopal Joshi, “Digital Predistortion technique for RF power amplifier linearization: Modelling and Simulations,” Indian Particle Accelerator Conference 2022 (Inpac’22), March 22, VECC, Kolkata.

DEVELOPMENT OF PROTOTYPE LLRF SYSTEM FOR 18 MEV MEDICAL CYCLOTRON

#Shubham Tripathi, Vikash Sahoo, Balkrishna Arora, Swarnendu Thakurta, Surajit Ghosh, Aditya Mandal, Sudeshna Seth, Sumit Som
Variable Energy Cyclotron Centre, Kolkata

Abstract

A low-level RF (LLRF) has been designed for the 18 MeV Medical Cyclotron (MC-18), which will be used to deliver the requirements of medical radiopharmaceuticals in and around Kolkata. The LLRF system is used to feed the RF cavity having frequency of 65.6 MHz with the controlled amplitude of RF. A prototype LLRF system operating at 65 MHz is designed to stabilize acceleration voltage and control the resonance of the cavity. LLRF system broadly consists of a Dee Voltage Regulator (DVR), Spark Detector, Ripple Detector, Interlock Protection System, and tuner control system. The RF amplitude is designed to be controlled by PI feedback control for keeping the voltage stability of the cavity within 0.1%. Spark detector will stop the RF power input to the amplifier within 1us as soon as the voltage in the cavity dips. Furthermore, the testing results and simulation of the LLRF prototype has been presented.

INTRODUCTION

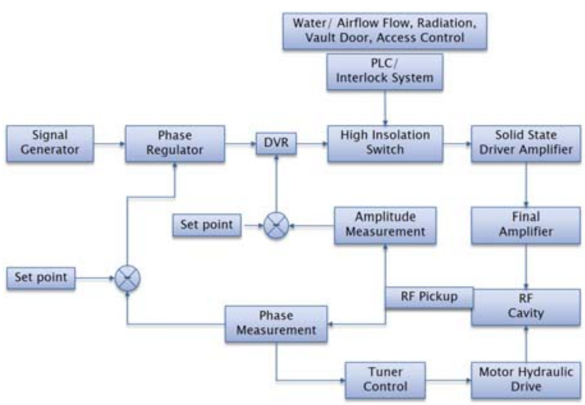

Figure 1: Typical block diagram of LLRF

Figure 1 shows basic block diagram of LLRF system. LLRF is a system that controls the RF field inside the accelerating cavities; it mainly controls amplitude and phase of electric field and also includes frequency control operation along with interlock and protection system for RF cavities. Table 1 shows the RF system specifications for MC-18 [1].

Table 1: RF System specifications for MC-18

RF Cavity parameters	**Specification**
Frequency	65 MHz
Dee Voltage	30-50 kV
Quality Factor	5000-6000
Shunt impedance	85 kΩ – 100 kΩ

In present paper, amplitude control, spark detector, ripple detector, interlock and protection system and resonance frequency control operations are discussed.

COMPONENTS OF LLRF

Dee Voltage Regulator

Dee voltage regulator (DVR) is the amplitude control module which is realised using PI controller and RF modulating circuit. Feedback of the cavity is taken with capacitive divider circuit to bring it at low level and given to DVR after passing through peak detector. Control system generates error signal after comparing it with set point, which is given to PI control logic (realised using analog components) whose output is multiplied by RF to feed the power into cavity. Figure 2 shows the control unit for amplitude control. There are two modes of operation for this system: Tune mode and Run mode. Tune mode is an open circuit system used for conditioning of the cavity during tuning operation, whereas Run mode is a feedback control system which keeps the Dee voltage stable during run time. Current system provides Dee voltage stability upto 0.1%.

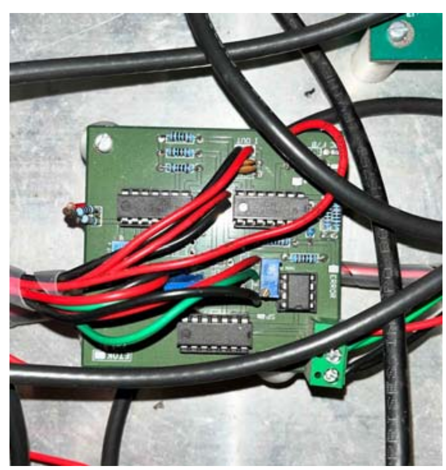

Figure 2: Control unit for amplitude control

Figure 3 shows step response of control unit for different integral constant, represented by RC values, in PI

#s.tripathi@vecc.gov.in

controller. Here the cavity is approximated by a Low Pass Filter (for resonant frequency of 65 MHz and Q = 6000) [2][3].

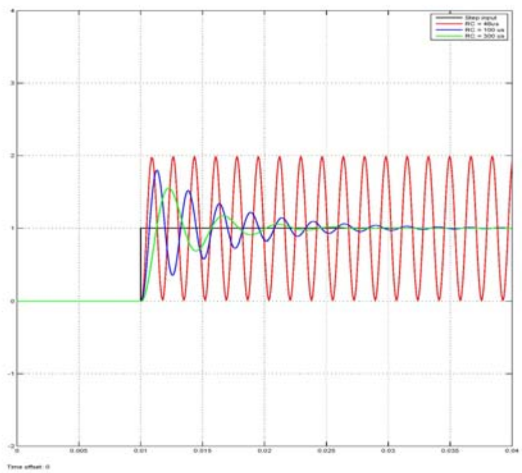

Figure 3: MATLAB Simulation of control unit

Spark Detector

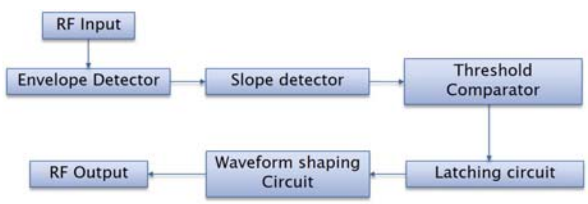

Figure 4: Basic block diagram of Spark Detector

Figure 4 shows the basic block diagram of spark detector. For spark detection in RF signal, firstly, the envelope has to be extracted; thereafter slope of the envelope is compared with the threshold slope, below which no action will be taken. Once a spark is detected, a pulse is generated with the help of a waveform shaping circuit such that output gets low instantaneously and then gradually starts increasing after some time. This output is modulated with RF to give final input to the amplifier. The circuit is fabricated as shown in Figure 5, and results

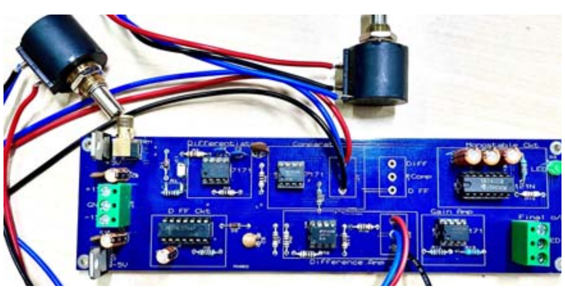

Figure 5: Spark detector unit

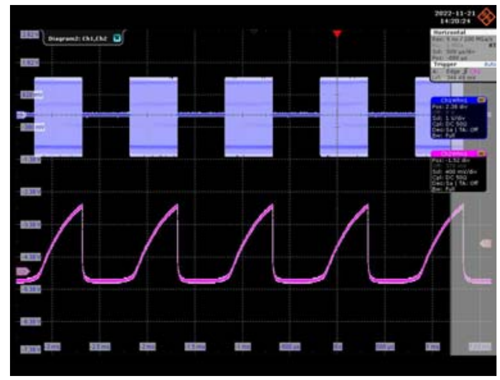

Figure 6: Spark detector output

as shown in Figure 6, indicate that spark detection occurs within 1us and RF output is switched off within 5us.

Interlock and Protection System

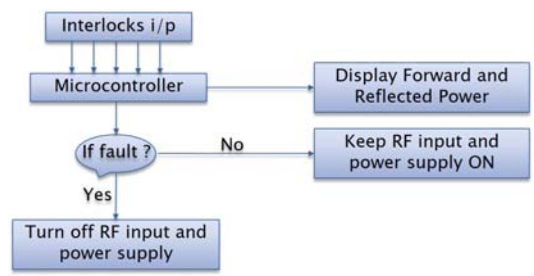

Figure 7: Basic working of Interlock and Protection unit

Figure 7 shows the basic Interlock and protection system. It is a microcontroller based system which continuously checks the potential free contacts of the interlock inputs and turns off the RF switch and power supply whenever it detects any fault. This unit also houses power measurement unit for forward and reflected RF power. Power measurement unit is based on ZX47-40-S+, which is an RF to DC convertor and this DC value is calibrated using microcontroller for the actual system requirements. Accuracy of the designed measurement system is within 2%. Figure 8 shows the designed interlock and protection unit.

Figure 8: Interlock and protection unit along with power measurement results

Tuner control system

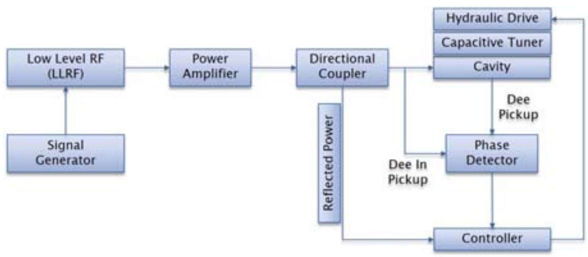

Figure 9: Block diagram of Tuner control system

Figure 9 shows the basic block diagram of tuner control system. This is a fine tuning system based on comparing the phase of the Dee pickup and Dee in pickup. At resonance, the phase difference between the two signals should be zero degree, i.e. the system is purely resistive. In case of detuning , the phase difference is measured using AD8302 based phase detector and this error is used to drive the DC motor which is connected with variable capacitance plates, hence tuning the system. A prototype tuner control system is shown in Figure 10.

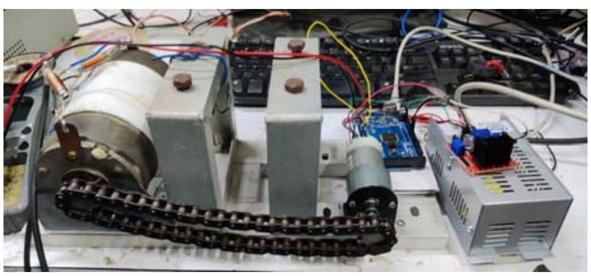

Figure 10: Prototype tuner control system

Ripple Detector

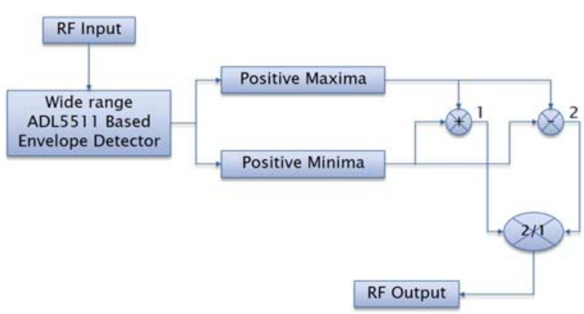

Figure 11: Block diagram of Ripple detector unit

Figure 11 shows the ripple detector unit, which is used to measure the residual modulation in Dee voltage. Here, ripple signifies the modulation index in the input RF wave. Ripple is detected by extracting the envelope of the input wave (realised using ADL5511 based envelop detector), followed by finding the positive maxima and positive minima of the envelope. These two signals are further operated to detect the final ripple. Logic for positive minima detection is shown in Figure 12. The fabricated system, as shown in Figure 13, measures ripple from 0 - 5%.

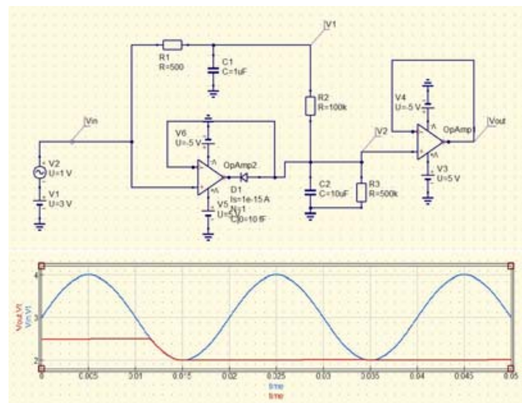

Figure 12: Positive minima detection for ripple detector

Figure 13: Ripple detector unit

CONCLUSION

The different components of prototype LLRF system for medical cyclotron have been presented. The designed systems have been tested for the results shown above and further tests and refinement is in progress. The design is being further improved for better integration among different components and with other units of cyclotron through wired communication .

REFERENCES

[1] MC18 Design Report: RF System _MCP18_DBR

[2] R. Garoby, "Low level RF and feedback," in CERN PS/RF Note; see http://cdsweb.cern.ch/record/328252/files/ps-97-034.ps.gz

[3] Michael John O'Farrell, "Low level radio frequency control of RIA superconducting cavities," MSc thesis, Michigan State University, 2005

DESIGN, DEVELOPMENT AND COMMISSIONING OF SERIES REGULATOR BASED HIGH VOLTAGE REGULATED SCREEN GRID POWER SUPPLY FOR VECC K-130 ROOM TEMPERATURE CYCLOTRON KOLKATA

Sabyasachi Pathak[2], Anirban De[2], Vipendra Kumar Khare[1], Mrinal Kanti Ghosh[1] and Sajjan Kumar Thakur[1]
[1]Variable Energy Cyclotron Centre, DAE, Kolkata-64, India

[2]also at Homi Bhabha National Institute

Abstract

A novel scheme incorporating SCR based AC voltage control type pre-regulator followed by in-house developed step-up transformer and solid-state series regulator has been designed and developed. This was done to replace the older vacuum tube based power supply with a compact and rugged solution for the existing system. The design includes the development of an analog control system for the pre-regulator as well as a dual loop control architecture for the output voltage regulation of the said power supply. The multiple inner current loops ensure equal current sharing of the individual series pass elements as well as better control dynamics in terms of overcurrent protection of the load (EIMAC 4CW150000). Low output storage energy, better line ripple rejection, better line and load regulation etc. were also the major concerns during the design, development and optimization of the control scheme. The power supply additionally features protection against overcurrent, over-temperature, mains fault etc. and also provision for remote interfacing with the existing supervisory control system for upgradation of the power supply with minimum shut-down time of the system. This paper reports the design of the power converter stage, control system modelling, controller design, and the important results obtained at various stages of the development.

Keywords—Room Temperature Cyclotron, LCW, Solid State RF Power Supply

INTRODUCTION

K130 Room Temperature Cyclotron (RTC) of Kolkata has been operating uninterruptedly for four decades. The old Burle 4648 water-cooled tetrode-based 250kW RF Amplifier tube has been replaced with Eimac 4CW150000E water-cooled tetrode tube [1]. The new amplifier requires four power supplies for DC biasing of the tube. These are Anode Power Supply (APS), Screen-Grid Power Supply (SGPS), Control-Grid Power Supply (CGPS) and Filament Power Supply (FPS) [2]. The older vacuum tube based SGPS for Burle tube was rated at 1.2kV, 1A. Though it was a rugged design it had limitations in terms of size, requirement of forced low conductivity water (LCW) cooling, limited regulation and stability and also the rating was insufficient for the new tube.

The new SGPS is solid-state based linear power supply that overcomes the above limitations by incorporating triac based pre-regulator that regulates the voltage across the series regulator and thus limits the power loss in the series element, improving efficiency. Lesser power loss also allows use of forced air-cooling, reducing component counts and failure points with respect to forced LCW cooling which was essential in case of the old vacuum tube-based power supply. A comparison between the old and the new power supply is given in table 1 below.

Table 1: Comparison of old and new power supply

Parameters	Specifications	
	Old P/S	**New P/S**
Rating	1.2 kV, 1A	1.5 kV, 2A
Topology	Vacuum tube based linear power supply	Solid state based linear power supply along with triac controlled pre-regulator
Cooling	Water cooled	Air cooled
Dimension (mm)	1200X1800X1000	600X1200X700
Efficiency	65%	81%
Regulation	0.1%	<0.05%
Maintenance	Difficult	Easy

The power converter topology, control architecture, testing procedures and the results achieved are reported in the following chapters.

POWER CONVERTER TOPOLOGY

The power supply derives its power from AC three phase mains and converts to DC voltage regulated output in the range of 0-1.5kV with maximum output current up to 2A. The required and achieved specifications of the power supply are given in table 2.

The power circuit (refer to Fig. 1) consists primarily of a 3ø triac-based pre-regulator followed by step up transformer, passive rectifier along with capacitive filter and finally a series regulator incorporating MOSFET bank as series pass element.

Table 2: Power Supply Specifications

Parameters	Specifications	
	Required	Achieved
Output Voltage (Vo)	1-1.5 kV	0-1.5 kV
Output Current (Io)	2 A	2A
Line & Load Regulation	0.06 %	<0.05 %
Ripple (peak to peak)	0.07%	<0.05%
Stability	500ppm/ºC	300ppm/ºC

Pre-Regulator

The pre-regulator is designed incorporating the conventional 3ø AC voltage control technique with the resistive load being replaced with a transformer isolated 3ø uncontrolled full-wave rectifier. The schematic is given in Fig 2. Here R_7 is the equivalent resistance of series regulator along with the load i.e. 775Ω (referring to Fig. 1, adding max allowed voltage drop of MOSFET bank, 50V max output voltage rating from table 2).

Triacs are fired with respect to respective zero-crossing of the primary side phase voltages.

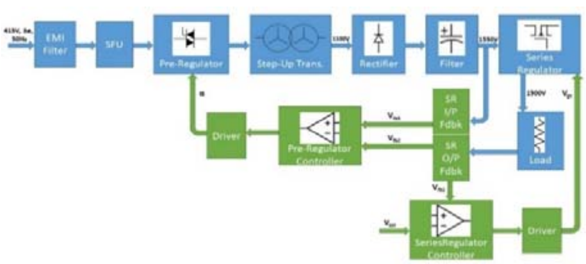

Figure 1: Block diagram of the power converter

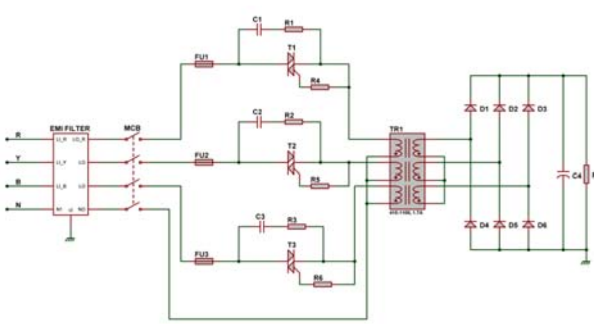

Figure 2: Schematic of 3ø pre-regulator

The purpose of the pre-regulator is to regulate the voltage drop across the series-regulator in order to reduce the continuous operational loss in the series pass elements which in turn increases the overall efficiency, reduces cooling requirement and the overall size of the converter. The pre-regulator controller in Fig. 1 regulates this voltage drop.

The ratings of the major components are estimated using the basic governing equations 1 to 5 [3,4].

Unregulated capacitor bank, $$C_4 = \frac{1}{12\sqrt{2}R_7 f * \text{R.F.}} \quad (1)$$

Secondary full-load line voltage, $$V_{sl} = \frac{(V_I)max}{\sqrt{2}} \quad (2)$$

Secondary full-load line current, $$I_{sl} = \frac{2.5}{3} I_o \quad (3)$$

Transformer output power, $$Q = \sqrt{3} V_{sl} I_{sl} \quad (4)$$

Primary full-load line current, $$I_{pl} = \frac{V_i I_o}{\sqrt{3} V_{pl} * \eta * P.F.} \quad (5)$$

Here, f is line frequency i.e. 50 Hz, I_O is final output current which is equal to input current of the series regulator, V_{pl} is primary line voltage, η is the efficiency of the transformer and the rectifier combined, R.F. is the desired ripple factor in the input side of the series regulator (considered 0.2% assuming 20dB ripple rejection in series regulator) and P.F. is the power factor from the primary side of the transformer (typically 0.8). It is to be noted that equation 3 is an empirical relation assuming diode rms current is 2.5 times of average load current owing to the charging effect of the capacitor bank.

Series Regulator

The rectified and filtered DC voltage, V_I is fed to a series regulator, shown in Fig. 3, to generate the final voltage regulated output which will be fed to amplifier screen grid. The load is parallel equivalent of output bleeder resistance and actual RF load including amplifier side RF filter and bleeder. For simplicity of analysis, the equivalent load, R_{11} is considered to be a resistor of 750Ω from the full rating of the power supply given in table I. The power supply was initially tested with a dummy resistive load before integrating to actual load.

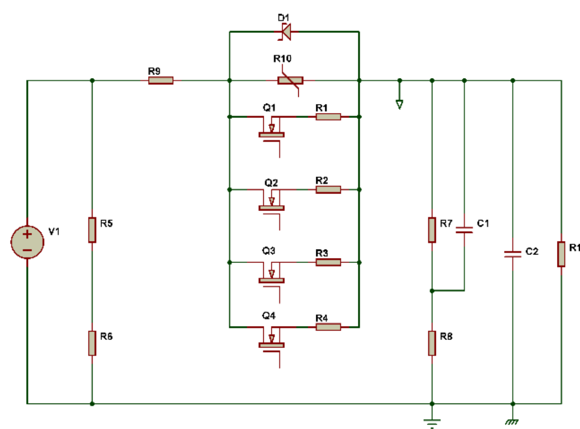

Figure 3: Schematic of series-regulator

A bank of 4 nos. MOSFETs connected in parallel is used as series pass element to share the power dissipation and current amongst individual MOSFETs. Resistors R_1 to R_4

are used to sense the MOSFETs' currents which are then used in internal current regulator which equalizes the current through each of them. It is to be noted that the series-regulator controller in Fig. 1 is a cascade control system comprising of outer voltage regulator which regulates the final output voltage and 4 nos. of inner current regulators which regulate the individual MOSFET current and also act as MOSFET driver. The inner regulator block is floating at high voltage since source side of MOSFET is at high voltage.

CONTROL SCHEME

Referring to Fig. 1, essentially there are two control systems, 1. pre-regulator control and 2. series-regulator control. The manipulated variable in the former is the firing angle α for which theoretical control bandwidth limit is 50Hz owing to the modulator IC that generates two 180° shifted firing pulses for each 50Hz cycle. Firing angle, α is dependent on input control voltage V_{C1} as shown in Fig. 4. Therefore, the practical bandwidth of pre-regulator controller is taken as one-fifth of the above theoretical limit i.e., 10Hz.

Whereas considering the linear series regulator there is no theoretical limit in ideal cases but considering the practical limitations i.e., bandwidth of controller op-amps, MOSFET parasitic effects etc. the bandwidth of series-regulator (outer loop) is taken as 3kHz which is 10 times of the maximum possible frequency of the periodic line voltage disturbances and ripples i.e., 300Hz (ignoring the higher order harmonics).

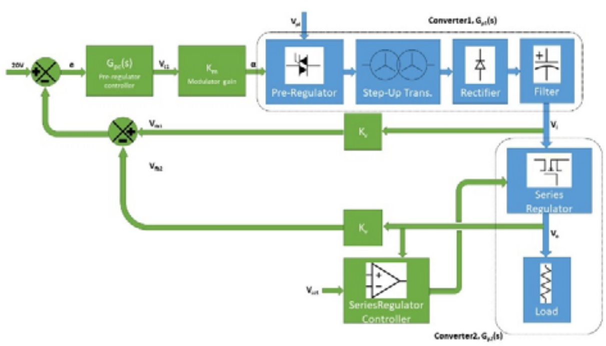

Figure 4: Block diagram of the control systems

The control systems in Fig. 4 are non-linear and they are not independent. In order to derive linear and independent models a small signal analytical model is considered where small perturbations [Δα, Δv_{pl}, ΔR] around the operating point [α, V_{pl}, R] is considered [5]. Now, since changes in V_o are very fast compared to the slower dynamics of converter1 the linearized model around the above operating point resolves into Fig. 5.

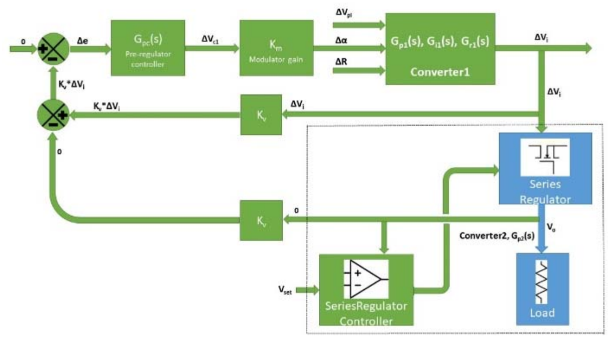

Figure 5: Block diagram of linear model of pre-regulator

Following assumptions are made while deriving the transfer function $G_{p1}(s)$,

- The leakage inductances of the transformer being small, the pre-regulator operates in discontinuous current mode i.e., the inductor current resets before next commutation. Therefore, inductance has no play in the dynamics of the time averaged model [6,7].
- $C_4 = C_i$
- $R_7 = R_i$
- Diodes $D_{1\text{-}6}$ are ideal.
- At steady state α is within $\left[\frac{\pi}{3}, \frac{\pi}{2}\right]$

Therefore,

$$G_{p1}(s) = \frac{\Delta V_i(s)}{\Delta \alpha(s)} = \frac{K_1}{1+sR_iC_i} \quad (6)$$

$$K_1 = \frac{\delta V_i}{\delta \alpha} \quad (7)$$

A linearized model of the series regulator involving outer voltage control loop and inner current control loops (two out of four) are shown in Fig. 6. The transfer functions $G_{p21}(s)$ to $G_{p24}(s)$ are derived from the high frequency small signal model of MOSFET (shown in Fig. 7). Required parameter in Fig.7 can be found in MOSFET datasheet and external circuit values. Considering the MOSFETs to be identical the current controllers $G_{ic1\text{-}4}(s)$ are designed considering gain crossover frequency at 30kHz (10 times higher than outer voltage loop) and phase margin more than 45°. From the known values of plant transfer function, current controller and the feedback ratios the voltage controller $G_{vc}(s)$ is also designed.

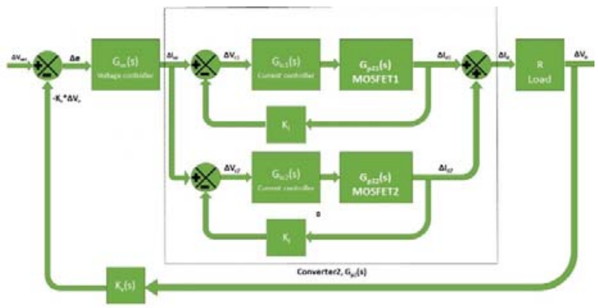

Figure 6: Block diagram of linear model of series regulator

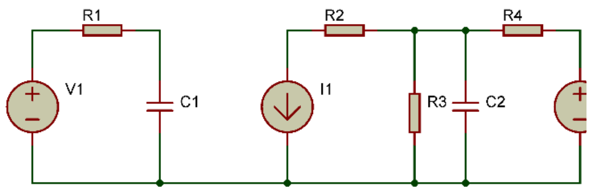

Figure 7: High frequency equivalent model of MOSFET

TEST RESULTS

After the final assembly of the power supply in was tested with a dummy load in following steps,

1. The prerugulator part is tested in open loop while the series regulator is bypassed. Then it is tested in closed loop while regulating the output voltage.
2. Then the series regulator is connected and the drop across it is set at 20V and power supply is tested in closed loop at no load and full load.

The scope results showing voltage ramp up, no load to full load voltage transient and transformer primary voltage of one phase along with sync pulse and traic gate pulse are given below.

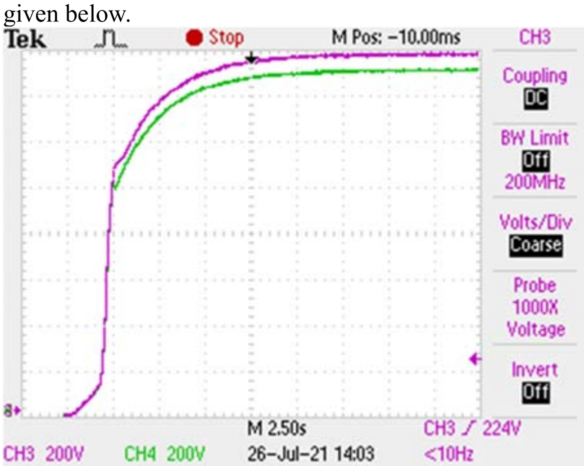

Figure 8: Series regulator input(purple) and output(green) voltage vs time when turning the PS ON

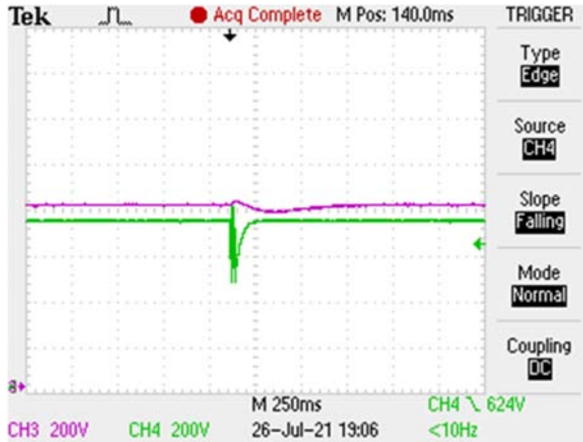

Figure 9: No load to full load transient of series regulator input(purple) and output(green) voltage

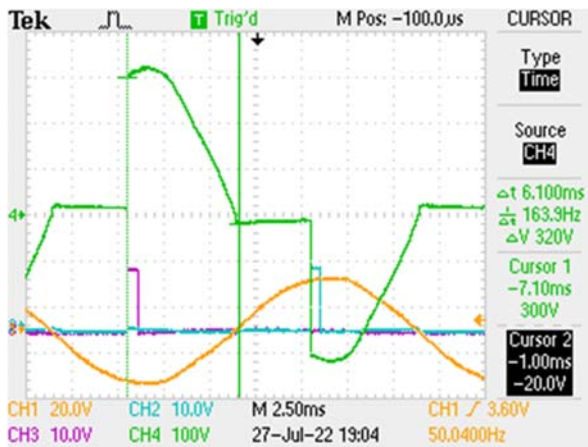

Figure 9: Transformer primary voltage(green), sync voltage(yellow) and triac control gate pulse (purple, blue)

After testing with dummy load the power supply was installed with actual load and field testing was done. Now it is currently running round the clock with the RF system. The pictures of the assembled and installed power supply are given below.

Figure 9: Pictures of the power supply

REFERENCES

[1] Surajit Ghosh, Aditya Mandal, Sudeshna Seth, S. K. Manna, U. S. Panda and Sumit Som, "Design and development of high powerRF amplifier for 88 in. room temperature cyclotron at Variable Energy Cyclotron Centre (VECC), Kolkata," Review of Scientific Instruments, December 2020.

[2] Aditya Mandal et al., "Up-gradation of radiofrequency system for the K-130 Room Temperature Cyclotron," Indian Particle Accelerator Conference, December 2020.

[3] P.S. Bimbhra, Power Electronics, 5th ed., Khanna Publishers.

[4] M.E. Van Valkenburg, "Network Analysis", 3rd ed. PHI, 2009.

[5] Sabyasachi Pathak, Anirban De et al., "System Modelling And Digital Controller Design For Per-Formance Analysis Of A Phase-Shifted Full Bridge Series Resonant Converter," Indian Particle Accelerator Conference 2018.

[6] Christophe P. Basso, "Switching Mode Power Supplies", BPB Publications.

[7] Abraham I. Pressman, Keith Billings, and Taylor Morey, "Switching Power Supply Design,"McGraw Hill.

DEVELOPMENT OF TEST STAND FOR PERFORMANCE EVALUATION OF HIGH VOLTAGE PFN CAPACITORS

T.Reghu, V.Mandloi, Akhil Patel, J.K.Mulchandani, M.Acharya, Y.Wanmode, Divya Purohit, Prem Baboo, M.Lad , P.Shrivastava , RRCAT, Indore, M.P. ,India
Ravindra K. Sharma, Vivek Sanadhya, V. Kurariya, Anuradha Mayya, BARC, Mumbai, India.

Abstract

The pulse forming network (PFN) capacitors of the HV pulsed modulators are required to be capable of simultaneously handling the high voltages, high peak and RMS currents, and high repetition rates. Proper testing and qualifying the capacitor's performance for their peak design values is crucial for such applications. The manufacturers (OEM) generally do not have the facilities for testing the capacitors at high peak currents and voltages at high repetition rates. OEM conducts usual tests of viz capacitance, peak voltage, leakage current, peak current, equivalent series resistance (ESR) and equivalent series inductance (ESL). ESR parameter directly indicates the loss within the capacitor. The measured ESR and ESL values are highly affected by the measurement test set up and do have large measurement errors. Local industries are not equipped with set up for testing of energy storage capacitors for high repetition rate applications. Also, direct loss calculation based on the inference of the test data may lead to wrong conclusion. Hence, a test stand has been designed and developed at RRCAT for the performance evaluation of high voltage PFN capacitors at parameters very close to real application parameters. The test stand operates at maximum charging voltage, peak current and repetition rate of 25 kV, ~800 A and 400 Hz, respectively. The design, construction details and results of the test stand will be discussed in the paper.

INTRODUCTION

The PFN capacitors are very important component of a conventional line type HV klystron modulator topology. Amongst the various topologies of pulsed modulators, line type is still very widely used modulator scheme for fixed pulse width, and high average power modulator applications [1,2]. In such applications, The PFN capacitor goes through severe electrical stress due to repetitive charge and discharge cycles. During charging cycle they are subjected to high voltages and during discharge cycle they are subjected to very high currents. Additionally, they are also subjected to regular voltage reversals (up to 10%) and occasional 100 % reversals. The major loss mechanism in PFN capacitor is heat generation due to dielectric losses and conductor losses. The equivalent series resistance (ESR) of the capacitor directly represents the dielectric loss. The measurement of ESR using differential method is very tricky and has large measurement errors. In differential measurement method of ESR, the measurement can be a relative value and not very useful for the absolute calculation of the power loss. In order to measure heat loss or temperature rise of the capacitor, it is required to test the capacitors at actual charging and discharging cycles of peak voltages and currents for high repetition rates. In order to perceive this, a test stand has been designed and developed for the performance evaluation of high voltage PFN capacitors at parameters very close to the real application parameters

DESCRPTION

The test stand consists of a HV capacitor charging power supply (CCPS), thyratron based switching unit and resistive load as shown in Fig.1. The CCPS linearly charges the "capacitor under test (CUT)" to the desired voltage. The CCPS has the output voltage and current capability of 25 kVmax and 1.44 A respectively. The supply is based on high voltage, high frequency switched, DC-DC converters using series L-C resonant topology [3]. There are four modules of HV DC-DC converter modules and all modules are connected in series to get 25 kV output. Each unit generates isolated 6.25 kV output. The DC-DC converter modules are based on IGBT based full bridge topology employing series resonant scheme. The switching frequency of the DC-DC converter is chosen as ~10 kHz. The ferrite cored high frequency transformer transforms the high frequency, low voltage to high voltage. Subsequently by the use of high frequency rectifiers it is rectified to get DC current. A resistor –diode combination has been connected across the CCPS to protect the output rectifiers of CCPS against voltage reversal of CUT. Upon command, the CCPS charges the CUT to the desired value and the stored energy in the CUT is discharged to the resistive load using a HV switch unit. The HV switching unit consists of a hydrogen thyratron (CX1154) and associated grid drive unit to turn on the thyratron switch. The CX1154 is a 40 kV hydrogen thyratron capable to handle 3 kA peak and 2 A average current. A readymade thyratron driver unit MA2709 has been used to generate triggering pulses to the thyratron. Low cost heating elements have been used to construct the resistive load. The test stand serves as a qualification set up of PFN capacitors for loss estimation close to real parameters before its usage in the modulator. The test stand operates at maximum charging voltage, peak current and repetition rate of 25 kV, ~800 A and 400 Hz, respectively.

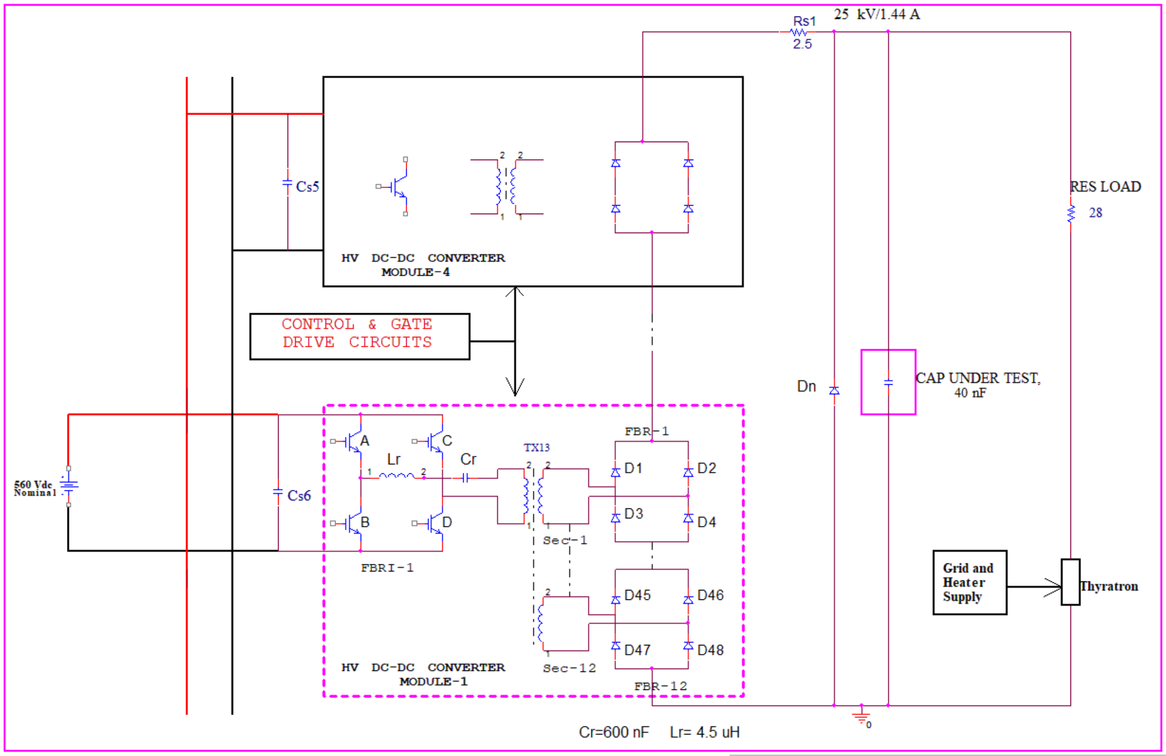

Figure 1: Simplified block diagram of the test stand

Fig.2 Photograph of a 25 kV CCPS unit

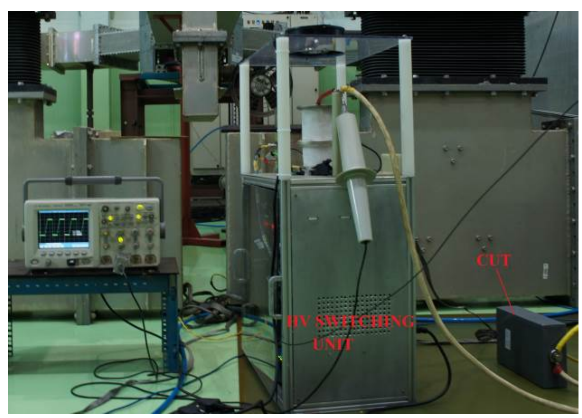

Fig.3 View of HV switching unit and "CUT"

The Fig. 2 shows the photograph of the 25 kV CCPS Fig. 3 shows the view of the high voltage switching unit and capacitor under test (CUT). Fig .4 shows the Voltage waveform across the capacitor under test (CUT) at 400 Hz pulse repetition rate (PRR). The voltage waveform has been measured using M/s Tektronix make high voltage probe. Fig. 5 shows the discharge current waveform through the CUT. The current is measured using Pearson make current transformer (CT). It is to be noted that the peak current and pulse width are ~760 A and 8 µs respectively. The peak current value is much higher than value in real application and peak voltage subjected

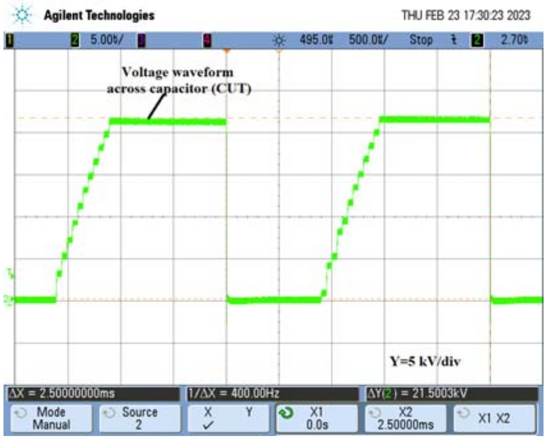

Fig.4 Waveform across capacitor (CUT) at 400 Hz PRR

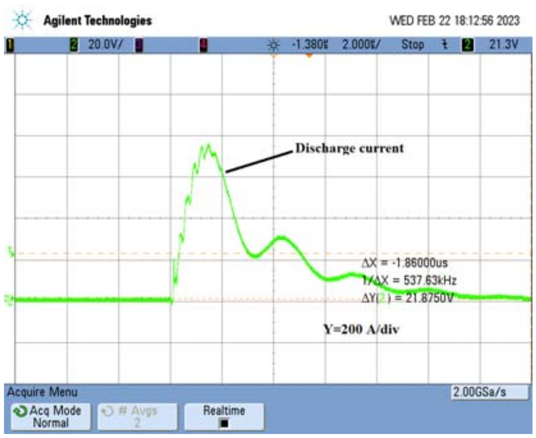

Fig.5 Waveform of capacitor discharge current

to CUT is kept at 21.5 kV. The temperature rise of the CUT has been monitored by Fluke make thermal imager after fixed hours of operation at 400 Hz.

CONCLUSION

A test stand has been designed and developed for the performance evaluation of high voltage PFN capacitors at parameters very close to real application parameters. The test stand operates at maximum charging voltage, peak current and repetition rate of 25 kV, ~800 A and 400 Hz, respectively. Several PFN capacitors have been tested using the developed test stand. The temperature rise data of CUT have been useful for the estimation of power loss within the capacitor as well as for design feedback.

REFERENCES

[1] P. Shrivastava, J.K. Mulchandani, Y. Wanmode, P. Mohania,“Performance of 6 MW peak, 25 kW average power microwave system for 10 MeV, 10 kW electron linac”, Asian Particle Accelerator Conference - 2007 , RRCAT, Indore , 2007, pp. 649-651.

[2] J. Mulchandani, P. Baboo, T. Reghu, M. Lad and P. Shrivastava, “IGBT switch based bouncer compensated pulse modulator for 10 mev electron linac applications”, InPAC – 2022

[3] T.Reghu, J.K. Mulchandani, V.Mandloi, Prem Baboo, Mahendra Lad and Purushottam Shrivastava Development of 6.0 MW, High Average Power S-Band Microwave System Test Stand”, InPAC – 2022.

DEVELOPMENT OF 8-WAY HIGH RF POWER COMBINER AT 75.6MHZ

A. Balkrishna†, S. Sumit, M. Aditya, S. Sudeshna, T. Swarnendu, G. Surajit, T. Shubham, S. Vikash, D. Abhishek , Variable Energy C yclotron Centre, 700064, Kolkata 700064, India

Abstract

In Variable Energy Cyclotron Centre (VECC), development of high RF power solid-state amplifiers and power combiners at 75.6 MHz is under progress for feeding LINAC Cavities of Rare Isotope Beam (RIB) facility. Efficient power combining is basic requirement for high power Solid State Power Amplifier (SSPA) design. The present work illustrates design and implementation of an equal split 8-way Radial RF power combiner/divider to generate combined 1KW RF output power at 75.6MHz. The combiner exhibits negligible insertion loss leading to no efficiency degradation and lesser heat dissipation. Measured performance of the power combiner is in excellent agreement with theoretical results at 75.6MHz with 1% desired bandwidth. A Gysel combiner type configuration has been incorporated with the 8-way combiner for achieving good peripheral port isolation. Finally, peripheral port isolation of better than 40dB has been achieved and the system was tested with 95% power combining efficiency.

INTRODUCTION

The improvements in modern solid-state devices over the last few decades have introduced transistors with very high breakdown voltage and high radiation tolerance. The present LDMOS based SSPAs can produce hundreds of watts of power. The way to Achieve RF Power in order of kWs is by combining RF Power From Multiple SSPAs. RF section in VECC is developing 10KW SSPA to excite the Linac cavities of the RIB facility. Figure 1, shows the 10kW RF power generation scheme by combining RF power from multiple medium power amplifier modules.

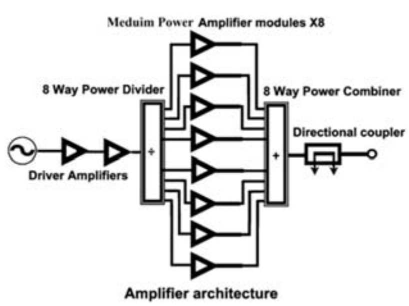

Figure 1: 10kw RF Solid State RF Power Generation Scheme

The present work illustrates design and implementation of an equal split 8-way Radial RF power combiner/divider to generate combined 1KW RF output power at 75.6MHz. This structure is to be used as a power divider to feed RF input of about 125W into 10 modules of 1KW amplifier to generate a combined 10KW RF power (by a similar structure made of copper with high power handling and cooling capacity) to feed the linac cavities of RIB facility in VECC.

COMBINER DESIGN

Among various RF power combiner topologies [1] single step N-way RF power combiners provide efficient way to sum up power from multiple SSPAs (N>4). At f=75.6MHz, λ = 3.97m, resonant cavity combiners and spatial combiners will occupy very large size, Therefore, Radial transmission line combiner with Central point Impedance matching using coaxial transmission line topology has been chosen. The present radial power combiner consists of three main sections. a) N way peripheral ports b) The radial strip line c) The launcher with coaxial impedance matching sections.

N way (N=8) 50Ω peripheral ports are located symmetrically in the radial direction. The combining path or radial strip line is a low-loss parallel plate transmission line which connects 8 peripheral 50Ω ports in a parallel fashion. A two stepped coaxial impedance matching section transforms the central point impedance of the radial line into 50Ω at the launcher or combined port.

Combining Radial Transmission Line Design

In the radial line, RF energy combines uniformly in the radial direction from the N-way Peripheral ports to central point with the dominant mode having an axial electric-field component. A. Fathy [2] gives a simple method to design a microstrip radial combiner. For the cyclotron applications, power combiners capable of handling higher power and operating at a lower frequency band (VHF to S-band) are required. Therefore, strip line-like rigid transmission slab line structures proposed by A. Jain [3] have been adopted. The main design challenge with radial lines is the variable characteristic impedance against radial distance. For a microstrip radial line with infinite radius (matched line), characteristic impedance at $r = r_0$ can be represented as[4]:

$$Z_0(r_0) = \frac{\zeta b}{2\pi r_o}$$

Where b is the substrate thickness and $\zeta = \sqrt{\frac{\mu}{\varepsilon}}$

Based on the strip line theory, an approximate but simple formula has been derived for real value of characteristic impedance of radial slab line at radius r by A. Jain [3] is given by:

$$Z_0(r) = \frac{\zeta(b-t)}{8\pi r} . \frac{120\pi}{\sqrt{\epsilon_r}}$$

Where b is the distance between ground plates of radial stripline, t is the thickness of the radial plate Figure 2(a).

Simulating the above stated model with 8 matched 50Ω peripheral ports and using b=46mm , t=20 mm, $Z_0(R) = \frac{50}{8}$ (parallel combination) we get R=64mm. With these initial design parameters, the impedance at the central point of the radial line combiner after the radial to coaxial line transition with inner and outer diameter of 16.5mm and 38mm is calculated using HFSS simulation software. And the input impedance is found as 9.5Ω. for optimising fabricated structure, parameter *b* can be varied by using metal disk of variable height at the bottom of the combiner.

Coaxial matching network initial design

The coaxial two step impedance matching section transforms the above calculated central point radial line impedance of 9.5Ω to50Ω impedance at the launcher port. Quarter wavelength matching section will occupy a lot of space. As the cavity needs to be excited at fixed frequency of 75.6MHz, the bandwidth requirement is less, hence Two-Section Series Impedance Transformer topology [5] has been adopted which provides feasible matching from central point impedance of Z_L=9.5Ωto Z_0=50Ω by using two coaxial sections of impedances Z_1=8.45Ω and Z_2=50Ω. Due to fabrication limitations at the site , it was difficult for us to make a structure with tapered line. Hence we used a simple two step impedance transformer design. The matching coaxial lines have uniform outer diameter of 38mm and unequal inner diameter of d_1=33mm and d_2=d_0=16.5mm. the lengths of these two section has been calculated using MATLAB *twosect* function and found as L_1=208mm and L_2=242mm.

Design optimisation and fabrication

With the calculated initial parameters, A 3D-model of complete structure is simulated in Ansoft HFSS.

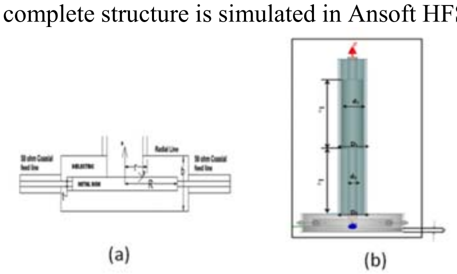

Figure 2: (a) Radial transmission line (b) completed HFSS 3D model

The Model is optimized for variable lengths and radii of coaxial line and radial line thickness to get minimum return loss of at least 20dB at the common port at 75.6MHz. Finally, the optimised parameters are used for fabrication. The Mechanical structure of

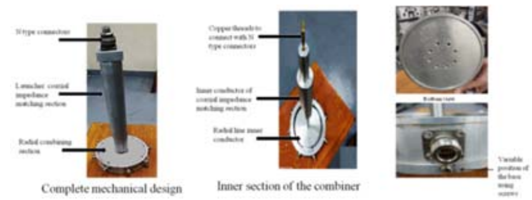

Figure 3: Mechanical Design of the Combiner

the combiner is shown in Figure 3. It is made up of Aluminium. We have used N-type connectors for both peripheral ports and combining ports. Copper threads are used to connect N-type connectors to the combiner. The position of the base of outer radial section can be altered using screws.

MEASURED PERFORMANCE

At low power, s-parameters of the combiner are measured using Rohde & Schwarz ZVB 4, vector network analyzer. The measurement results show that the common port return loss is better than 25dB from 72.3MHz to 78.6MHz meeting the desired requirement. The common port to peripheral port

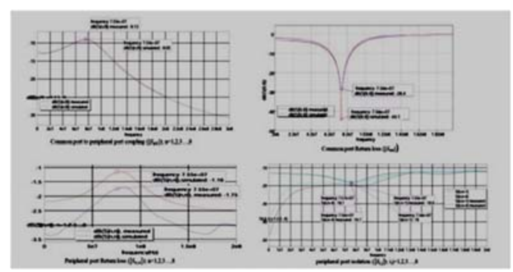

Figure 4 : S Parameter Measurements of the Combiner

coupling is obtained as 9.13dB implying the insertion loss of 0.13dB. Peripheral port isolation was measured to be around 18.5dB which is very close to the simulation results. These are shown in Figure 4.

GYSEL NETWORK WITH THE COMBINER

For high power testing of the combiner, power from eight amplifier modules of 250W SSPAs are added to generate RF power of 1.5KW at 75.6MHz.

For through characterisation of the combiner, 2 modules of 4-channel Direct Digital Synthesizer (DDS) have been used to generate 8 signals of 75.6MHz whose phase and amplitude can be adjusted by Linux-based epics software. These 8 signals can have a maximum of 4dBm RF power. These signals are boosted up by 8 modules of ZHL-32A+ mini-circuits pre-amplifiers of 30dBm output power. The

isolation between peripheral ports is necessary for the safety of high power RF amplifiers to avoid reflections during mismatch. It is not possible to directly connect isolation resistors of 100Ωs (like in Wilkinson combiner) between peripheral ports to dump the mismatched power. It has been observed many a times that RF 50ohm loads in high power applications often tend to damage in case of unwanted reflections at RF ports, hence we need a water cooled isolated high capacity loads. High power water cooled 50ohm RF loads has been fabricated in VECC. Which are safe to use. Hence, Gysel combiner topology[6] is used to dump the mismatched power in lumped loads and improve the isolation. The general Gysel power combiner topology deployed is shown in Figure 5(b).
r

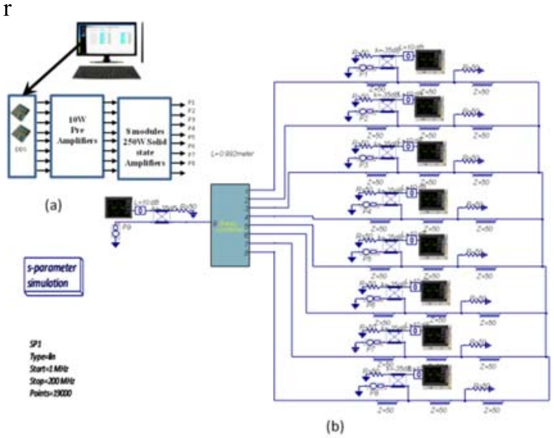

Although this Gysel combiner is bulky at 75.6MHz but it uses sections made of standard 50 ohm lines which are readily available. Hence there remains only one component to be properly tuned at are desired frequency that is the combiner section.

The output from SSPAs (P1 to P8) is fed into input section of the Gysel network through 8 directional couplers. Coupled power is then analyzed on oscilloscopes. To get the maximum efficiency, all input signals are adjusted to get same amplitude and phase.

HIGH POWER PERFORMANCE

An S-parameter simulation of the test setup was run from 1MHz to 200MHz. Figure 6 shows the simulation results.

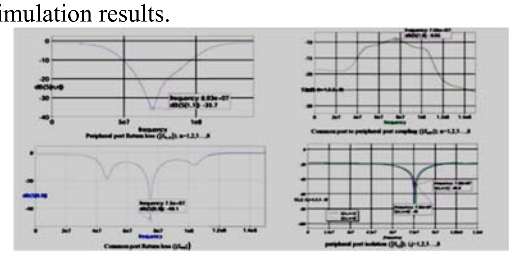

Figure 6: S parameter results with gysel combiner

We observed that coupling of 9.05dB and return loss of 48dB is still obtained. But the beauty of Gysel setup is seen in the improved peripheral port isolation of 45dB at 75.6MHz which was only 18dB without gysel configuration. Also the peripheral port return loss has also improved a lot with -26dB. which was very poor with around -1.15dB without gysel configuration.

A practical test setup (Figure 7) of the Gysel network was designed using RG-218 cables, and 1KW

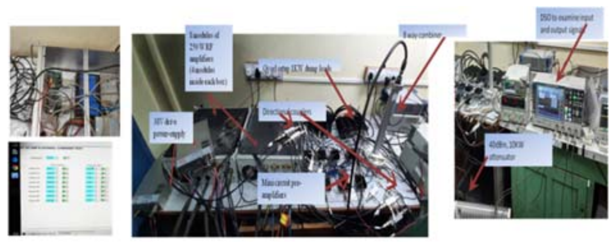

dump loads. The combined output was then measured in oscilloscope by 40dB, 10KW attenuator.

Table 1 gives the high power test results, more than 90% efficiency of the combiner along with the Gysel network was obtained for 1KW combined power.

Table 1: Power Combining Measurements and Calculation for 8-Way Combiner

Amplifier Module No.	1A	2A	3A	4A	1B	2B	3B	4B	*Total Input Power* ($\sum Pi$)	*Measured Combined Power* (Po)	*efficiency* $\eta = 100 \cdot \frac{P0}{\sum Pi}$
Attenuated Power (dBm)	3.99	4.04	4.31	3.93	3.70	3.84	3.70	3.91			
Actual Power (dBm)	49.29	49.34	49.61	49.23	49.00	49.14	49.00	49.21			
Actual Power (W); Pi	84.96	85.94	91.31	83.75	79.47	82.09	79.38	83.39	**670.28**	**631.102**	**94.15%**

(a)

Amplifier Module No.	1A	2A	3A	4A	1B	2B	3B	4B	*Total Input Power* ($\sum Pi$)	*Measured Combined Power* (Po)	*efficiency* $\eta = 100 \cdot \frac{P0}{\sum Pi}$
Attenuated Power (dBm)	4.98	5.06	4.90	5.05	4.66	4.69	4.78	4.71			
Actual Power(dBm)	50.28	50.3	50.20	50.35	49.96	49.99	50.08	50.01			
Actual Power(W); Pi	**106.73**	**108.57**	**104.76**	**108.44**	**99.13**	**99.84**	**101.79**	**100.25**	**829.51**	**780.369**	**94.07%**

(b)

Amplifier Module No.	1A	2A	3A	4A	1B	2B	3B	4B	*Total Input Power* ($\sum Pi$)	*Measured Combined Power* (Po)	*efficiency* $\eta = 100 \cdot \frac{P0}{\sum Pi}$
Attenuated Power (dBm)	6.00	5.95	5.99	6.01	5.87	5.97	5.98	5.81			
Actual Power (dBm)	51.30	51.25	51.29	51.31	51.17	51.27	51.28	51.11			
Actual Power (W); Pi	**134.93**	**133.20**	**134.52**	**135.11**	**130.89**	**134.00**	**134.15**	**129.18**	**1065.98**	**1022.82**	**95.95%**

(c)

CONCLUSIONS

An efficient and functional form of 8:1 radial transmission strip line-based 8-way RF power combiner/divider operating at 75.6MHz for accelerator applications in VECC has been successfully designed, simulated, fabricated, and tested. The structure is compact and consumes moderate space. The slab line design of the combiner makes it capable of handling high RF power which makes it appropriate for accelerator applications. The measured combined port return loss and insertion loss are better than 25dB and 0.2dB, respectively, at the operating frequency of 75.6MHz with 1% desired bandwidth.

With Gysel type combiner Network topology the 8-way combiner has peripheral port isolation of better than 40dB at 75.6MHz; the fabricated combiner has been tested to combine RF power of 125W from eight modules of RF amplifiers to generate 1KW combined RF power with 95% power combining efficiency.

In future it is planned to upgrade the combiner topology for summing higher RF powers up to 10s of KWs. Two similar combiners operating at 54MHz and 65MHz are under process in the VECC. Peripheral port isolation improvement by use of tuneable circulators is also further planned project in VECC.

ACKNOWLEDGEMENT

We sincerely acknowledge the efforts of all our team members for contributing their technical insight, practical experience and physical hard work in the development, simulation, assembly and detailed testing of the RF power combiner. We are thankful to RF Design groups in VECC for their valuable suggestions and for providing software for simulation. We also thank to all who have directly or indirectly contributed to the development work by their valuable comments and suggestions.

REFERENCES

[1] K. J. Russell, "Microwave Power Combining Techniques," IEEE Transactions on Microwave Theory and Techniques, vol. 27, pp. 472-478, May 1979.

[2] A. E. Fathy, D. Kalokitis and S.-W. Lee, "A simplified design approach for radial power combiners," IEEE Trans. Microwave. Theory Tech., Vols. vol. 54, no. 1, p. 247, 2006.

[3] A. Jain, A. K. Gupta, D. K. Sharma, P. R. Hannurkar and S. K. Pathak, "Design and analysis of a high-power radial multi-way combiner," International Journal of Microwave and Wireless Technologies, vol. 6, no. 1, p. 83–91, 2014.

[4] N.Marcuvitz Waveguide Handbook, MIT Rad. Lab.Series vol.10, vol.10, NewYork: McGraw-Hill,,1951

[5] F. Regier, "Impedance Matching with a Series Transmission Line Section," Proc. IEEE 59, 1133, 1971.

[6] U. H. Gysel, "A new N-way power divider/combiner suitable for high-power," in Proc. 1975 IEEE- MTT- S Int. Microwave Symp.,IEEE Cat. No. 75CH0955-5, p. 116, May 1975.

HORIZONTAL TEST STAND FOR THE TESTING OF SINGLE SPOKE RESONATOR SUPERCONDUCTING RF CAVITIES AT BARC *

Jitendra Kumar#, Mukesh Goyal, Anindya Chakravarty, Srinivas Krishnagopal, BARC, India
Thomas H Nicol, FNAL, U.S.A.

Abstract

Single spoke resonator (SSR) superconducting radiofrequency (SCRF) cavities are planned for the proposed Medium Energy High Intensity Particle Accelerator (MEHIPA) at BARC. The dressed SSR cavities, before assembly into a cryomodule, will be qualified in a purpose-built cryostat called horizontal test stand (HTS). The required tests, among others, include high power RF testing at 2 K, tuner, high power coupler and other auxiliary components. Tuner, high power coupler and other auxiliary components, required for testing, will be installed along with the jacketed SSR cavity for the testing in the HTS. The cryostat has three independently operable cryogenic fluid circuits. The liquid nitrogen (LN_2) circuit will serve to remove the heat load of the thermal shield maintained around 80 K. Helium incoming circuit, 4.5 K @ 1.2 bara, will be used to cool down the cavity. The third fluid circuit is of sub-atmospheric saturated 2-phase helium at 2 K. This sub-atmospheric circuit will cater to the 2 K refrigeration load of the cavity. The supply of cryogenic fluids will be regulated by an existing feed-box. The required liquid helium (LHe) and LN_2 will be supplied to the feed-box from respective Dewars. The facility is being planned to cater to a maximum isothermal heat load of 30 W at 2 K. Q_0 will be determined by experimental measurement of 2 K isothermal heat load. The performance of auxiliary components will also be investigated at cryogenic temperatures during testing. This work presents the description of the cryogenic process and cryostat design of the proposed HTS.

INTRODUCTION

Cryomodules consisting of SSR SCRF cavities are required for the proposed MEHIPA [1] at Vizag, India. The dressed SSR cavities, before assembly into cryomodule, need to be qualified for cryomodule worthiness. The proposed HTS cryostat will provide the same process conditions for testing, which will exist in the cryomodule, but for a single cavity. The supply of cryogenic fluid will be controlled by an existing feed-box. The feed-box was developed earlier by BARC. Long stem bellows sealed control valves and a JT heat exchanger along with cryogenic piping, dedicated thermal shield and check valves are the major components of the feed-box. The required LHe and LN_2 will be supplied to the feed-box from respective Dewars. The necessary supply of 4.5 K LHe will be provided by the independently developed helium liquefier LHP100 [2]. Along with HTS, the cavity testing facility will also house a vertical test stand (VTS) [3], fed by the same liquefier. Cavity quality factor (Q_0) will be determined by measurement of mass flow rate due to 2 K isothermal heat load. The performance of the tuner, piezo and high-power coupler will also be investigated at cryogenic temperatures during the cavity performance tests in HTS.

CRYOSTAT

The test cryostat consists of a horizontal vacuum vessel, room temperature magnetic shield, 80 K thermal shield, cryogenic fluid lines, pipe/ structural supports and instrumentation etc.

Cryostat Vacuum Vessel

This vessel provides vacuum insulation along with structural support to all the internal components. It also provides the required interfaces, such as connection for cryogenic fluid inlet/outlet and high-power RF coupler. The vessel is made of stainless steel (grade 304L) and is designed as per ASME boiler and pressure vessel code section VIII, division 1 [4]. The major dimensions of the cylindrical shell are given in Table 1.

Table 1: Dimensions of Vacuum Vessel

Parameter	Unit	Values
Length	mm	1430
Outer Diameter	mm	1372
Cylindrical shell thickness	mm	10
Thickness of formed heads	mm	8

The vessel has torispherical doors for the installation and removal of SCRF test cavities. A mitre bend opening at the top is provided for cryogenic interconnections. This bend is designed as per ASME process piping code B31.3 [5]. The vessel has an opening and interface for high power RF coupler, at 45 degrees from horizontal plane. The vessel also has ports for insulation vacuum, safety valve and instrumentation feedthroughs, etc.

Figure 1 shows the proposed layout of the HTS facility. In this figure the HTS is connected to the feed-box via a vacuum insulated transfer line. 4.5 K LHe and LN_2 will be supplied to the feed-box by Dewars using vacuum insulated flexible lines.

*Work supported by Bhabha Atomic Research Centre, Mumbai. A part of work was done at FNAL, Batavia, IL, USA.
#jitenk@barc.gov.in

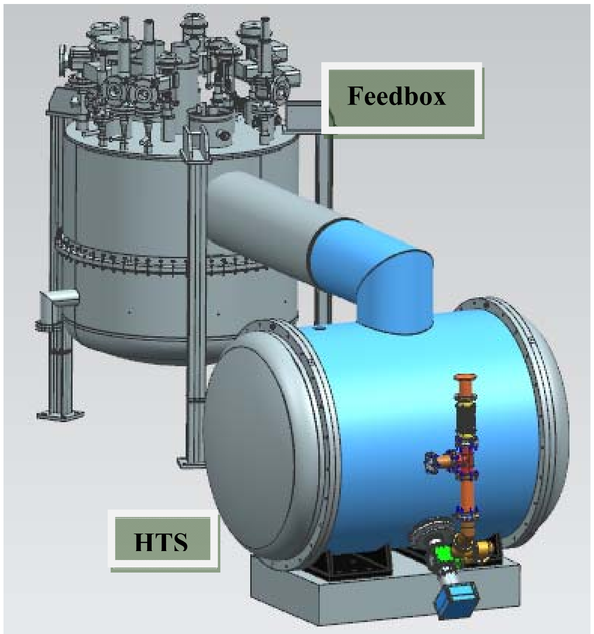

Figure 1: HTS with feed-box

Vacuum Break

The vacuum break serves two functions in the cryostat. It separates the insulation vacuum of the cryostat from that of the cryogenic transfer lines connected to the feedbox. It also provides structural support to cryogenic lines by transferring the forces to the vacuum vessel wall. The length of conduction path between the room temperature vacuum vessel and the low temperature cryogenic lines are increased using multi sleeve construction shown (Figure 2). It also has provisions for the 80 K thermal intercept. This intercept further reduces the conduction heat in-leak to the lines at 2 K. The estimated values of heat in-leak through vacuum break is listed in table 2.

Table 2: Conduction heat load due to vacuum break

Cryogenic Lines	**Nominal Temperature [K]**	**Heat Inleak [Watts]**
2 phase supply	2	1
Sub atmospheric return	2	1
Thermal shield	80	32

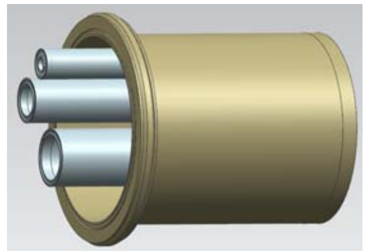

Figure 2: Vacuum break

Cavity Support

The cavity support is made of G10 tubes and aluminium and stainless steel rings (figure 3). It transfers the weight of cavity and thermal shield to the vacuum vessel. It is bolted to the welded support post of the vessel. The low conductivity of G10 helps in reducing the conduction heat in-leak to the cavity operating at 2 K. To reduce the heat in-leak, it is also provided with 80 K thermal intercept. The estimated values of heat in-leaks to the 2 K and 80 K temperature levels are listed in table 3.

Table 3: Conduction heat load due to cavity support

Cryogenic lines	**Nominal temperature [K]**	**Heat Inleak [Watts]**
SCRF test Cavity	2	0.9
Thermal shield	80	2.3

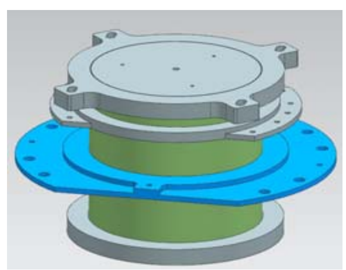

Figure 3: Cavity support (Designed by FNAL)

Thermal Shield

The test cryostat has an internal thermal shield (figure 4) which acts as the 80 K radiation shield for the component at 2 K and also function as thermal intercepts to mitigate conduction heat inleak. The shield is made of aluminium and will be actively cooled by LN_2 The shield is attached to the cavity support and is free to contract in the longitudinal as well as vertical directions during cool down. The mitre bend has its own thermal shield and is supported by the vacuum break. 30 layers of multilayer superinsulation will be wrapped on the copper shield to reduce the radiation heat in-leak from the vacuum vessel.

The heat load of the thermal shield is listed in table 4. Heat load is estimated by assuming 1.5 W/m^2 radiation heat in-leak from 300 K to 80 K shield and 0.5 W/m^2 radiation heat in-leak from 80 K to 2 K surface with 10 layers of superinsulation.

Table 4: Heat load to 80 K thermal shield

	Heat Inleak [Watts]
Radiation	8
Conduction	2.3

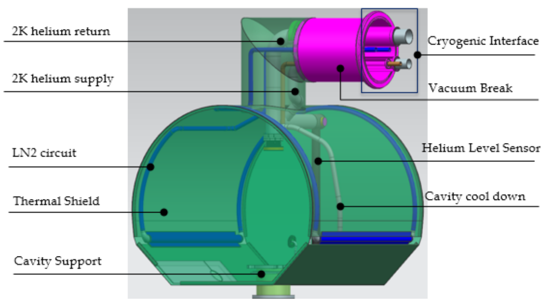

Figure 4: Thermal shield (in green) with cryogenic lines

Magnetic Shield

The cryostat has a room temperature magnetic shield made of 1.6 mm thick Mu-metal. The magnetic shield is intended to maintain less than 10 mGauss magnetic flux density near the surface of helium jacket. The weight of the magnetic shield will be supported directly by the vacuum vessel.

Cryogenic Lines

The HTS has three cryogenic circuits. The first circuit is 80 K LN_2 circuit. This circuit is anchored to the thermal shield and maintains the shield temperature around 80 K. The second cryogenic circuit is a cavity cooldown circuit. It is connected to the bottom of the helium jacket of the cavity. It will be used to cooldown the cavity from 300 K to 5 K. The third circuit is for sub-atmospheric helium supply and return. This circuit also contains a horizontal liquid helium header and a connected LHe level sensor pot. The horizontal header is also connected to the helium jacket of the cavity. Flow control valves of all the circuits are located inside the feed-box. Safety valves for these cryogenic circuits are provided in the feedbox. The flexibility and sustained load analysis of these piping are done as per ASME process piping code B31.3 [5].

HTS HEAT LOAD

The total estimated heat loads for the cryostat at its nominal operating conditions are listed in table 5. The dynamic and static components of the heat load of the cavity and input coupler are also given. Refrigeration capacity of 8.5 W at 2 K is required to operate the HTS cryostat with the cavity at nominal conditions. The proposed 30 Watts at 2 K cryogenic refrigeration capacity will provide the operational buffer during testing.

Table 5: Estimated heat loads for HTS

	Heat In leak [Watts]	
	80 K	**2 K**
Thermal shield	8	1.2
Cavity Support	2.3	0.9
Vacuum Break	32	2
Input Coupler (Static)	12.30	2
Input Coupler (Dynamic)	1.2	0.3
Cavity (Dynamic)	-	2.1
Total Static heat load	54.6	6.1
Total heat load including dynamic	55.8	8.5

CONCLUSION

A preliminary design and heat load estimation for the proposed HTS is described. An available feedbox will be used for the cryogenic supply and control for the cavity testing. Gross estimated heat load requirements, without applying any safety factor, are about 56 W at 80 K and 9 W at 2 K.

REFERENCES

[1] A. Pathak, S. Roy, S. Rao and S. Krishnagopal, "Design study for medium energy high intensity proton accelerator", Phy. Rev. Accel. Beams 23, 2020, pp. 090101 (1-29)

[2] M. Goyal, et al. "An update on indigenous helium liquefaction/ refrigeration systems at BARC" presented at ICC28 (2023).

[3] T. Rane, et al. "Design Methodology of a Vertical test cryostat in BARC for testing of superconducting cavities", being presented at Inpac2023.

[4] The American Society of Mechanical Engineers (ASME) Boiler and Pressure Vessel Code (BPVC) Section VIII- Rules for Construction of Pressure Vessels, Division 1 - 2021

[5] Process piping. ASME code for pressure piping B31.3- 2020.

DESIGN AND DEVELOPMENT OF PLC BASED RF CAVITY TUNER SYSTEM FOR 31.6 MHZ RF CAVITIES IN INDUS COMPLEX

Nitesh Mishra, Pritam S. Bagduwal, Nitesh Tiwari, Dheeraj Sharma, Pankaj Gothwal, Ekansh Mishra, M. Prasad and Mahendra Lad
Radio Frequency Systems Division, RRCAT, Indore (M.P.)-452013

Abstract

RF systems are indispensable part of particle accelerators. For faithful operation of machine and effective utilization of RF power, RF Cavity shall be kept tuned near to the RF generator frequency under all operating conditions. To keep the RF cavity automatically tuned, a Programmable Logic Controller (PLC) based RF cavity tuner system is designed and developed for Booster and Indus-1. Algorithm for appropriate movement of plunger for tuning of RF cavity has been successfully implemented in PLC. This development is an upgraded system of earlier system used in Indus complex that have extra features like “Auto/Manual” mode selection and limit switch interlock status in local, “Home” position during trip

In this paper, experience of design and development of “PLC Based RF Cavity Tuner System” and its lab testing will be presented.

INTRODUCTION

At RRCAT, Indus-1 and Indus-2 are two Synchrotron Radiation Sources (SRS), having stored electron energies of 450 MeV and 2.5 GeV respectively. Both these rings are filled using a common Booster synchrotron. Both Booster synchrotron and Indus-1 SRS are filled using a 31.6 MHz RF systems, which consist of RF signal generator, RF Amplifier, Circulator and RF Cavity along with Low-Level RF (LLRF) system. LLRF systems mainly have subsystems like Amplitude Control Loop (ACL)-Phase Control Loop (PCL), Power monitoring & Interlocks and RF Cavity Frequency Tuning loop (FTL). For faithful operation of machine and effective utilization of RF power, RF Cavity shall be kept tuned near to the RF generator frequency under all operating conditions. Since particle accelerator’s operating condition are changing in nature, Resonance frequency of RF Cavity may drift due to change in dynamic conditions like RF cavity water temperature, beam loading and ambient temperature etc. This refers to detuning which results in higher reflected power from the RF cavity. To keep the RF cavity automatically tuned, a Programmable Logic Controller (PLC) based RF cavity tuner system is designed and developed for Booster and Indus-1.

FLOW OF DESIGNED ALGORITHM

An algorithm to keep RF cavity tuned is designed and shown in figure 1. Logic controller checks the healthy status of accelerator machine and calculate detuning in RF cavity. Amount of RF cavity detuning from operating frequency is obtained by measuring the phase difference between forward RF power signal and RF cavity sense signal using RF phase detector. Based upon this detuning in RF cavity, PLC system moves the plungers via stepper motor driver following a stepper motor to keep RF cavity tuned throughout machine operation.

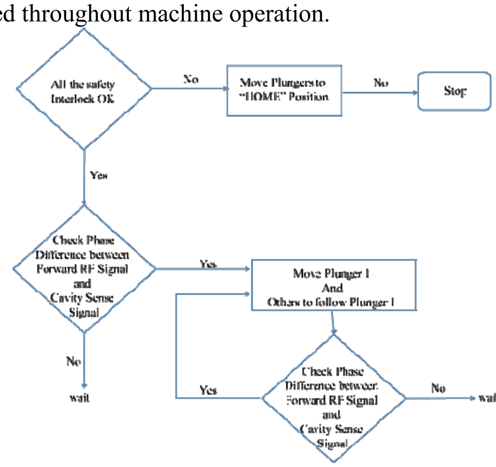

Figure 1: Flow Chart of Designed Algorithm

HARDWARE TESTING & CHARACTERIZATION

The designed algorithm is implemented in PLC with stepper motor and motor driver. Hardware testing and characterization has been done and explained as following

Stepper Motor and Motor Driver

To operate tuner system, Stepper Motor (PK296-01B) and Stepper Motor driver (CSD2145T) have been thoroughly tested with AFG (Arbitrary Function Generator) and block diagram of its Lab set-up is shown in figure 2. Stepper motor best work in 4.1 V peak –pulse amplitude, 100 to 1000 Hz rep-rate and 10 to 70% duty cycle.

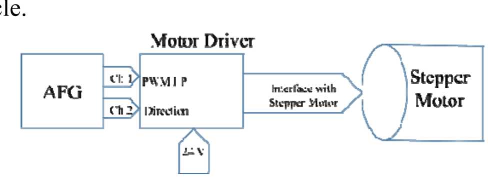

Figure 2: Block diagram of Stepper Motor interfacing via Motor Driver with AFG

A potential divider resistance of 5.5 kΩ is inserted to protect over-voltage from logic controller. The stepper motor via its driver is successfully interfaced with PLC and its block diagram is shown in figure 3. This stepper motor is operated from PLC at 1 kHz, 10% duty

*niteshm@rrcat.gov.in

cycle. This stepper motor with motor driver will be compatible to tune RF cavity in its full bandwidth. Its actual testing set-up in lab is shown in figure 4.

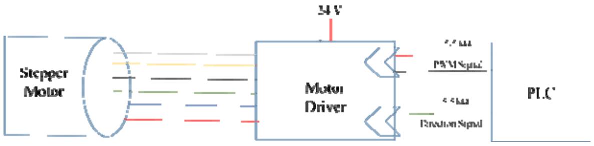

Figure 3: Block diagram of interfacing Stepper Motor via Motor Driver with PLC

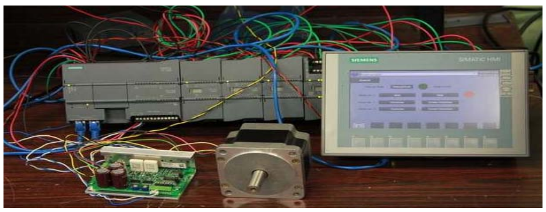

Figure 4: Actual Lab Test Set-Up for interfacing Stepper Motor via Motor Driver with PLC

RF Phase Detector Characterization

The detuning in RF cavity is measured via phase differences between RF cavity sense signal and RF forward powers. To measure phase difference, AD8302 phase detector is used. Its phase sensitivity is 10 mV/degree. A test set-up to characterize phase detector is made and its block diagram is shown in figure 5.

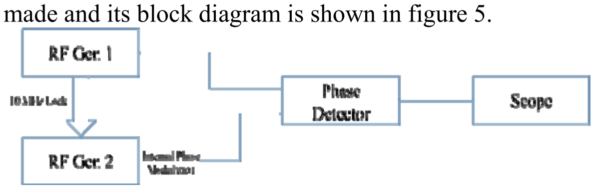

Figure 5: Lab Set-Up to Characterize RF Phase Detector

Two RF signals are fed to phase detectors via two RF Generators. These two generators are of same make and model and one (RF Gen 1) is (10 MHz) phase locked with other generator (RF Gen 2) as shown in figure 5.

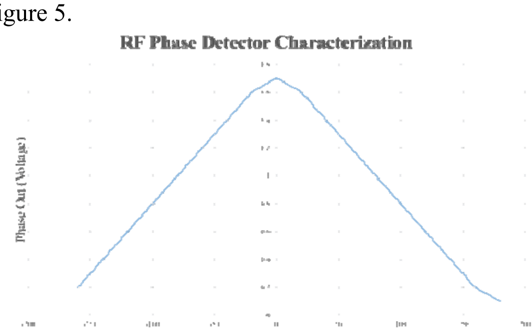

Figure 6: RF Phase Detector Characterization

RF Gen 2 is phase modulated and output of phase detector is observed on oscilloscope. The voltage output of phase detector is observed to be piecewise linear as shown in figure 6.

Human Machine Interface (HMI) Development

A human machine interface for FTL system has been developed. This HMI has a provision of tracking live status of safety Interlocks of FTL system, referred as "Limit-Switches" interlock. Their healthy status shows that FTL is in desired range. Live position of all the plungers are shown in HMI. During machine operation, to operate machine slightly differ from resonant frequency, a "Tuning-Compensation" feature is additionally implemented and live detuning can be observed. Developed Graphical User Interface (GUI) for HMI are shown in figure 7.

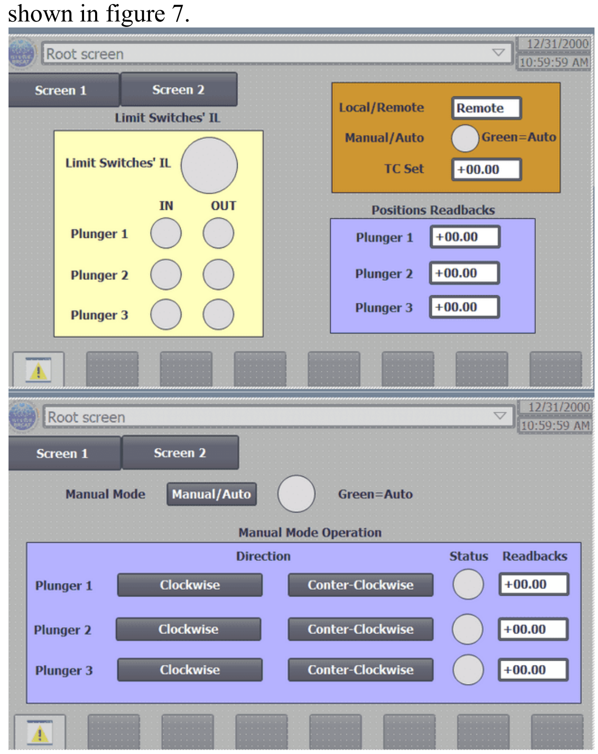

Figure 7: Developed HMI for FTL System

INSTALLATION & LAB TESTING

This complete lab set-up is installed in a rack as shown in figure 8. All the designed features are thoroughly tested in lab.

This designed algorithm has some advanced features from its earlier version like Soft-Limit, Home position. During machine operation or experiment, if safety interlocks becomes unhealthy, Tuner system will place Plungers into a predefined safe position called "Home" position. To keep this tuner system in safe operating range mode, a provision of "Soft-Limit" in software is done. These limits will not be crossed. However, additionally hard-wired "Limit-Switches" are implemented separately. These switches will stop going the tuner system beyond normal operating region and keep RF cavity safe. During machine experiment, Plungers are required to operate manually, considering this "Auto/Manual" mode selection option in local mode has been additionally implemented.

Lab Testing

All the plunger positions (voltages) are simulated using power supply voltages and Plunger-position “Read-back” are simulated. As RF signal is turned off, motor rotates until plunger read-back reaches predefined position (Voltage), hence “Home” position feature is simulated and tested. Actual “Limit switches” are implemented and installed in rack. As the limit switch is operated, Interlock fault is generated and tuner system is placed in Home position.

This entire system shall be used in Indus complex, so provision to operate in “Remote Mode” is added. This will be helpful in operating tuner system from Indus control room. This system will be installed in Indus complex in due course of time.

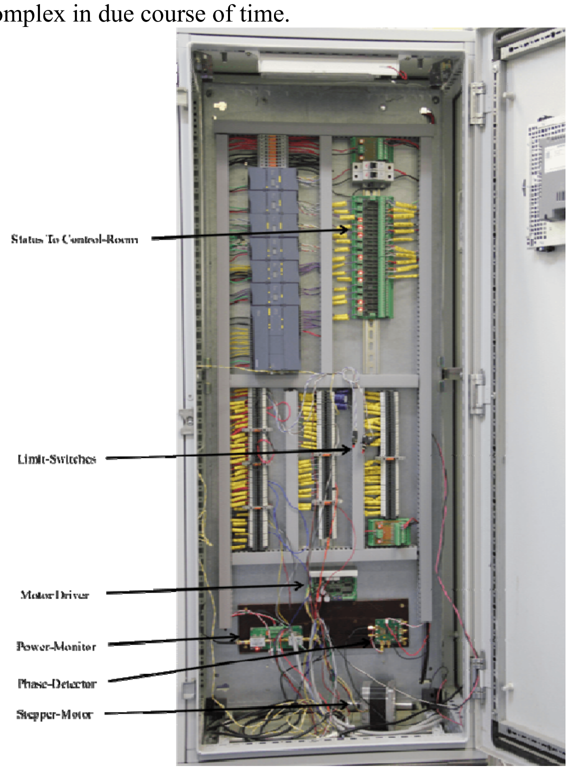

Figure 8: Actual FTL System Installed in a Rack

CONCLUSIONS & DISCUSSIONS

In this paper, Design and Development of PLC Based RF Cavity Tuner System for 31.6 MHz RF Cavities and its lab testing experience is presented. An additional feature of live Detuning (in KHz) will be implemented which shall be helpful in normal operation. In upcoming versions, additional features of data storage will be added that will be helpful in post mortem analysis and machine learning applications. This system is designed in such a manner that it shall be able to tune either Booster or Indus-1 RF cavity precisely in its entire bandwidth range. This system shall be installed in Indus-Complex in due course of time.

ACKNOWLEDGEMENT

The authors would like to thank our colleagues from the RF system division at RRCAT Indore, especially Sh. D. Suresh, Sh. Sudarsan Kishan and Sh. M. Manikandan.

REFERENCES

[1] N. Tiwari, P. S. Bagduwal, D. Sharma, N. Mishra, and M., Lad, “Development and Commissioning of Compact Digital LLLRF System for Indus-2 SRS”, InPAC 2019

[2] N. Mishra, P. S. Bagduwal, E. Mishra, D. Sharma, P. Gothwal, N. Tiwari and M. Lad, “Design, Development and Installation of PLC Based RF Power Monitoring and Protection System for Booster Synchrotron and Indus-1 SRS”, InPAC 2022.

DIGITALLY CONTROLLED PRECISION RF SIGNAL SYNTHESIS FOR LLRF APPLICATIONS

Dheeraj Sharma*, Pritam S. Bagduwal, Ekansh Mishra, Nitesh Mishra, Pankaj Gothwal, Nitesh Tiwari & Mahendra Lad
Raja Ramanna Centre for Advanced Technology (RRCAT), Indore, India

Abstract

Next generation particle accelerators using superconducting RF (SCRF) cavities demand high degree of control requirements for cavity RF field generation to be achieved by Low Level RF (LLRF) system. Using digital signal processing in Field Programmable Gate Array (FPGA) and digital I/Q modulation with high-speed DACs on modular, PCI eXtensions for Instrumentation (PXIe) platform along with indigenously developed RF up-converter PCB, a precisely controlled RF synthesizer has been implemented. This paper discusses the hardware, firmware, and measurement results of a stable and digitally controlled precision RF signal generation that can be used for superconducting cavity based accelerators.

INTRODUCTION

The RF field inside the SCRF cavities of next generation particle accelerators must be precisely generated and controlled, for maintaining the stability of the particle beam in an accelerator and also for cavity characterization at cavity test stands like Horizontal Test Stands (HTS). To cater to the stringent requirement due to very high quality-factor (Q) there is a need for highly stable and precise RF signal generation as well as advanced control algorithms that can quickly respond to changes in the cavity field. Characterization of superconducting cavities requires the cavity resonance frequency to be tracked and corresponding RF signal to be generated. The digital Low-Level RF (DLLRF) system plays a critical role in meeting these requirements by implementing the Direct Digital Synthesis (DDS) functionality using the digital & RF hardware. With advanced digital signal processing (DSP) & RF signal manipulation techniques a high-performance DLLRF system can be developed. Such digital LLRF system typically consists of FPGAs, high speed Digital-to-Analog (DAC) devices, RF filters and upconverters. Such a scheme has been implemented on a modular PXI platform along with an indigenously developed RF up-down converter PCB board and test results are presented.

ARCHITECTURE

The schematic of the digitally controlled precision RF synthesis is shown in Figure 1. On a PXIe chassis a controller and FPGA cards are installed. The controller communicates to the FPGA card for setting FPGA code parameters and also to acquire data from it. The FPGA card (Xilinx Virtex-7 NI-7962) implements the digital sine/cosine waves synthesis algorithm and its daughter card (NI-5781) containing DACs generate the IF frequency sine/cosine waves each as differential signals. These quadrature differential signals are then given to the RF up-converter board which contains the appropriate IF signal processing circuit and I/Q modulator. The clock for DACs and the LO signals both is generated from the RF signal generator to have the RF output signal quality comparable to the RF source itself. The I/Q modulator does the single sideband (SSB) up-conversion with the internal circuitry of RF mixers and produces the desired up-converted stable RF out signal which can be precisely controlled by FPGA.

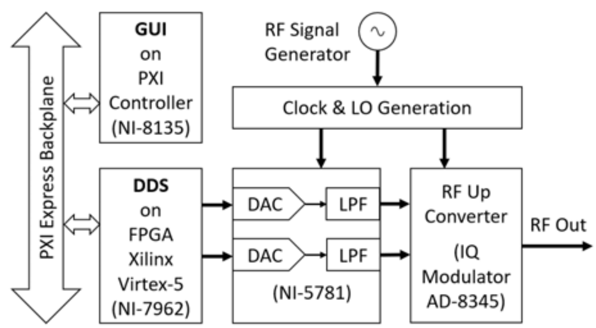

Figure 1: Architecture of Digitally Controlled Precision RF Synthesis

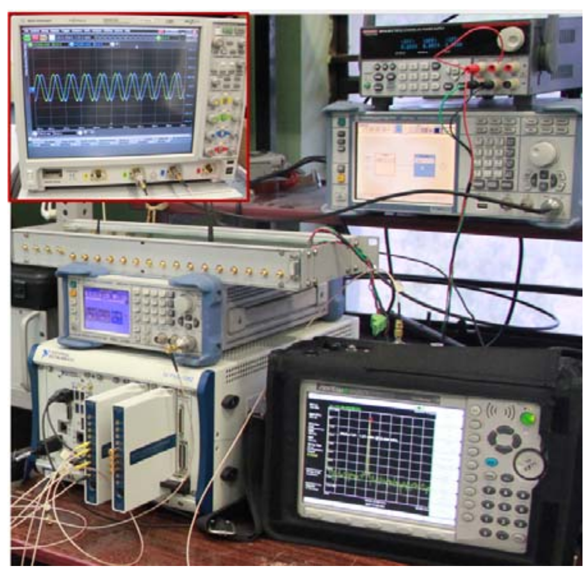

Figure 2: Lab Setup of Digitally Controlled Precision RF Synthesis

#dheerajsharma@rrcat.gov.in

HARDWARE

High Speed Digital Processing

For implementing the core functionality of generating quadrature sinusoidal signals (sine & cosine signals as I/Q) a modular PXIe-7962 FlexRIO card has been used. This card contains the Xilinx Virtex-5 SX50T as the FPGA. The card provides customizable I/O which can be programmed in LabVIEW FPGA module. The FPGA contains 8160 slices, 4752 kbit of Block RAM (BRAM), 288 DSP cores and other digital resources. These many resources are enough for DDS/NCO implementation as well as other feedback system functionalities of a DLLRF system.

Fast & High-Resolution DAC

The PXIe-7962 has been paired with FlexRIO adapter modules NI-5781 that offer high-performance analog and digital I/O. The NI-5781 serves as baseband transceiver which has been used as custom RF modulating signal generator. Together these two modules create a reconfigurable high-performance digital hardware which has been programmed for obtaining the IF frequency I/Q signals as sine & cosine waves with LabVIEW FPGA firmware discussed later. The DACs inside the adapter module is AD9777 which runs at maximum 100 MSPS sample rate (with x4 interpolation factor) with 16-bit resolution. Internally in NI-5781 module the clock is used as the reference to a PLL/clock distribution IC of Analog Devices AD9510 which generates the appropriate clock signals for individual DACs. DAC outputs are differential signals which are fed to Low Pass Filters (LPF) with cut-off frequency 40 MHz and serve as reconstruction filters. DACs are specified to produce a 5 MHz sine wave at (at 100 MS/s data rate) with the Spurious-Free Dynamic Range (SFDR) up to 64 dBc and Total Harmonic Distortion (THD) up to -64 dBc.

PXIe chassis & controller

The PXIe-1082 chassis has been used containing 8-slots with a high-bandwidth PXIe express backplane which provides hardware modularity and expansion with high-performance for various application needs e.g., driving multiple cavities in SCRF cavities cryomodule test stand. A PXIe-8135 controller operating with 2.7 GHz dual core processor has been used for GUI implementation in LabVIEW software for providing set parameters of FPGA firmware and data acquisition from it. The PXIe chassis and the controller are specified for extended operating temperature range and industry standards for robustness and 24x7 hours continuous reliable operation at the accelerator/test-stand site.

RF Up-converter PCB

In order to get the RF frequencies of the order of hundreds of MHz an analog RF up-converter is used. Considering the future requirements of large numbers of LLRF systems, 4-channel RF up-converter PCB has been indigenously designed & developed (Figure 3). Each up-converter channel contains a differential signal level shifter (AD8132) and I/Q modulator (AD8345) with input as split signal from a common LO source. Each channel has amplitude & phase control range of 35 dB & 360 degree respectively over the frequency range of 200 MHz to 1000 MHz with RF leakage less than -40 dBc and control I/Q signals bandwidth up to 80 MHz. Scheme of RF up conversion is shown in Figure 4.

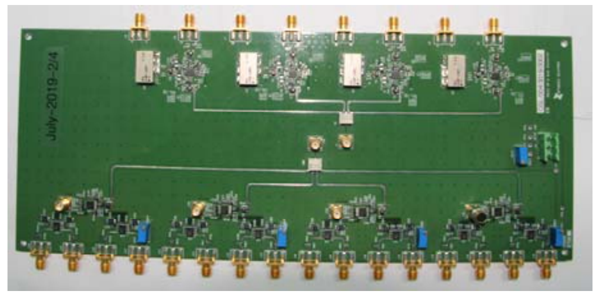

Figure 3: 4-Channel RF Upconverter PCB

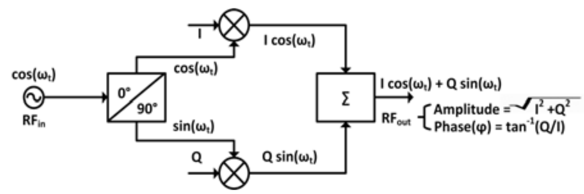

Figure 4: RF Up Conversion Scheme

FIRMWARE & GUI

A simplified diagram of the Direct Digital Synthesizer (DDS) firmware is shown in Figure 5 which makes up a Numerically Controlled Oscillator (NCO) generating sine/cosine waveforms[1]. The clock at 100 MHz has been derived from the LO source of up converter part, so that the spectrum quality & stability of the IF output from DACs become comparable to RF source itself. The 32-bit (N=32) phase accumulator register serves as address generator for sine/cosine LUTs and is able to achieve a frequency resolution of ~25 mHz which gives this scheme the capability of precise frequency change control at RF frequency after the up-conversion. By changing the value of the Frequency Tuning Word (M) the IF frequency from DACs can be set up to 50 MHz. Gain and phase adjustments are provided for minimizing undesired sideband during RF up conversion process.

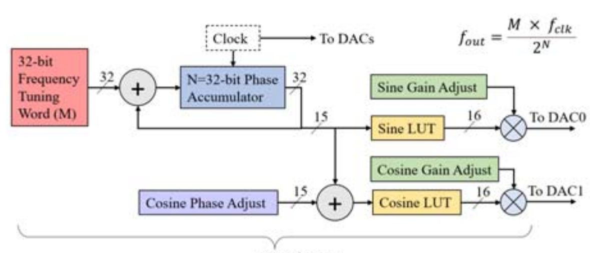

Figure 5: DDS/NCO Firmware Implemented in FPGA

The GUI for the application is shown in Figure 6.

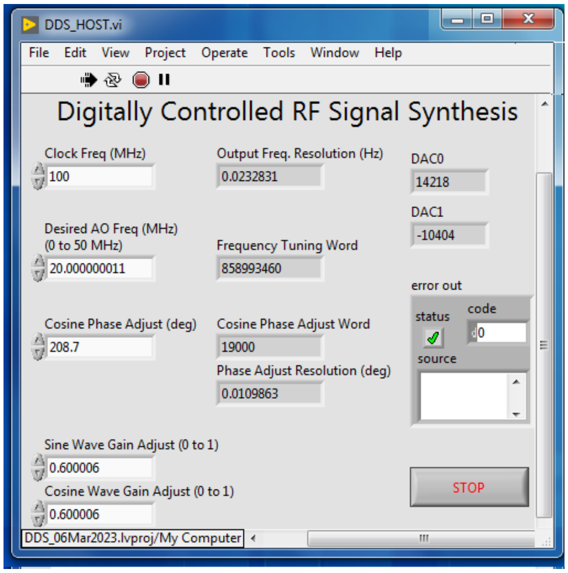

Figure 6: Host GUI for Digital RF Signal Synthesis

RESULTS

Figure 7 to Figure 10 shows the generated IF and RF signals phase noise & spectral measurements.

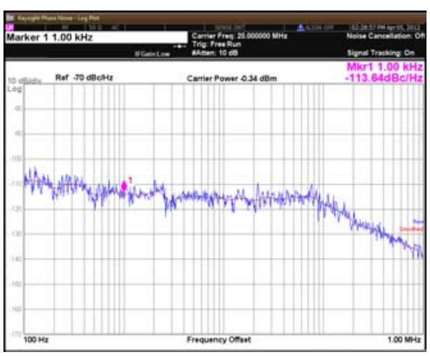

Figure 7: Phase Noise of IF @ 20 MHz at 1 kHz offset = -113.64 dBc/Hz

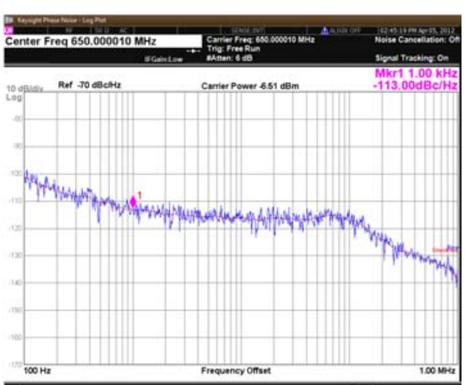

Figure 8: Phase Noise of RF @ 650 MHz at 1 kHz offset = -113.00 dBc/Hz

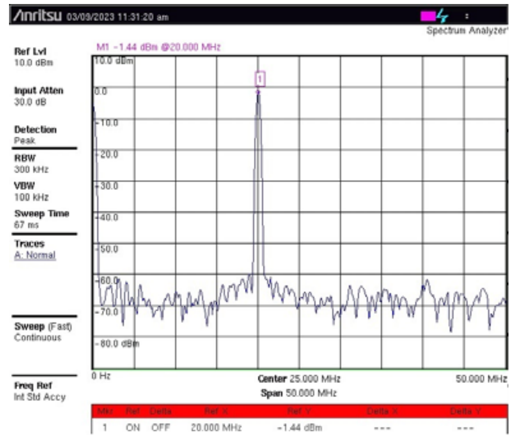

Figure 9: Spectrum of IF @ 20 MHz Signal

In the span 0-50 MHz the spurious free dynamic range of the generated IF signal at 20 MHz is ~58 dBc.

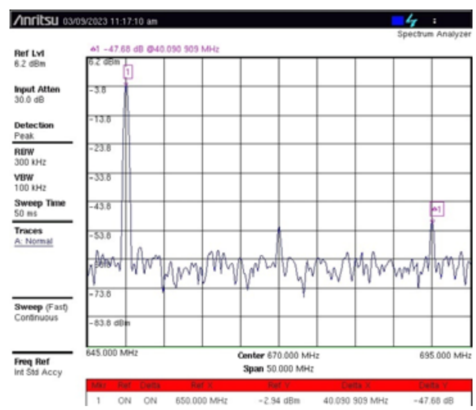

Figure 10: Up Converted SSB RF Signal @ 650 MHz

With optimum gain & phase settings for sine/cosine waves as I/Q signals the SSB RF signal at 650 MHz has been generated with ~45 dB down upper side band.

CONCLUSION

The presented scheme of digitally controlled RF synthesis using FPGA on a PXIe platform and RF up-converter has been developed and tested in laboratory which provides a versatile, scalable, and flexible architecture with highly stable and precisely controlled RF signal generation from 200 MHz to 1 GHz. This development can serve as an upgrade to our current DLLRF systems at RRCAT and satisfy the next generation superconducting accelerator LLRF applications.

REFERENCES

[1] Fundamentals of Direct Digital Synthesis (DDS), MT-085 Analog Devices.

MULTIPACTING ANALYSIS OF THE RADIO FREQUENCY CAVITY FOR COMPACT SUPERCONDUCTING MEDICAL CYCLOTRON (ID: F1-399)

Vikash Sahoo#, Sudeshna Seth, Surajit Ghosh , Shubham Tripathi, Balkrishna Arora, Aditya Mandal, Sumit Som, Variable Energy Cyclotron Centre

Abstract

VECC has planned to design and develop a 13MeV Compact Superconducting Medical Cyclotron (CSMC) [1]. CSMC will accelerate H- ions to an energy of 13 MeV with beam current of 50 µA. Radio frequency Cavity of the CSMC is one end short circuited quarter-wave (λ/4) coaxial transmission line [2], consisting of inner conductor called Dee stem, which is terminated by an accelerating electrode called Dee where accelerating Dee voltage at 54 MHz, will be produced. This paper presents the multipacting analysis of the RF cavity as it can produce vacuum degradation, localized heating etc. in the RF cavity. Multipacting is a phenomenon of resonant secondary electron emission from metal surfaces inside vacuum, which can lead to exponential growth of secondary electrons. The analysis of multipacting is carried out using 3D code CST-Particle Studio [3] and the results are discussed in the paper. Simulation results shows that when no DC magnetic field at the Dee region is present, multipacting exists at only lower input RF power while when the DC magnetic field is applied, multipacting is not observed at any input RF power.

INTRODUCTION

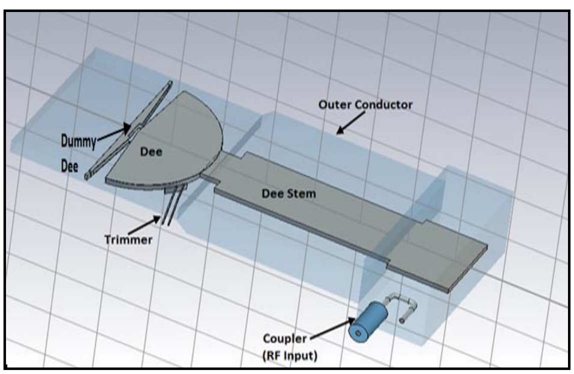

Figure 1:RF cavity for compact superconducting medical cyclotron

Figure 1 shows the Radio Frequency Cavity of the medical cyclotron is one end short circuited quarter-wave (λ/4) coaxial transmission line which consists of accelerating electrode called Dee and also consists of inner conductor called Dee Stem. At the Dee side, an accelerating Dee voltage at 54 MHz, will be produced to accelerate the Proton. Here the RF cavity operates in TEM mode. The cavity will be operated at 20kV Dee gap voltage. Multipacting Analysis has been done to find the regions at the cavity where multipacting exists. As multipacting does not exists at all input RF power levels, so through multipacting analysis the input RF power levels range where Multipacting occurs, can be found out. Multipacting reduction through geometry modification is also carried out in the paper. Multipacting has been simulated using 3D code CST-Particle Studio. In CST-Particle Studio, Furman model of secondary emission was used, which includes both backscattered electrons and rediffused electron with true secondary electrons.

MULTIPACTING SIMULATION

Multipacting has been analysed by application of particle source at different regions of the cavity like Dee region, Dee stem region etc. and then finding the particle growth from them respectively. Initially the electric field and magnetic fields are generated in CST-MWS. Then the electric and magnetic field are imported in CST-Particle studio. All the regions have been analysed with different scaling of imported electric and magnetic field values to find the voltage levels at which multipacting happens. The material used in the simulation is copper. All the below electron seed sources are simulated with equal no. of source density.

MULTIPACTING RESULTS

Multipacting is performed in CST particle studio in presence and absence of DC Magnetic Field of 3.5T at the Dee region. Different regions are selected as particular source and is simulated with different scaling of imported electric fields.

In absence of DC Magnetic Field

Source-Dee Region

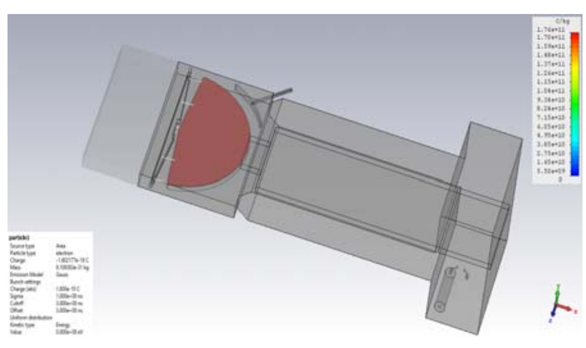

Figure 2: View of the RF cavity showing the red region (Dee) as particle source for Multipacting

#v.sahoo@vecc.gov.in

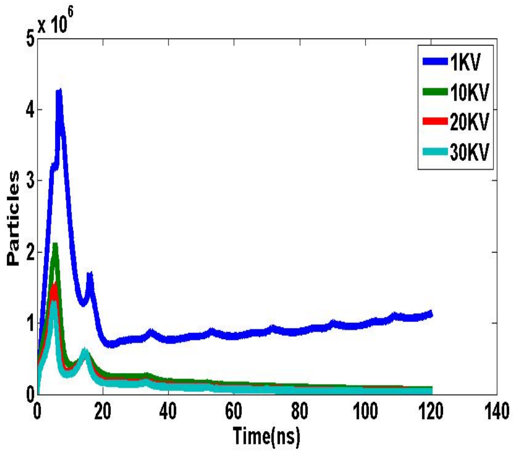

Figure 3: Plot of Particle number vs. time (ns) at different accelerating Dee voltages in the cavity, due to particle source at Dee. Particle growth is seen at Dee voltage of 1kV. No particle growth is seen at Dee voltages of 10kV, 20kV & 30kV

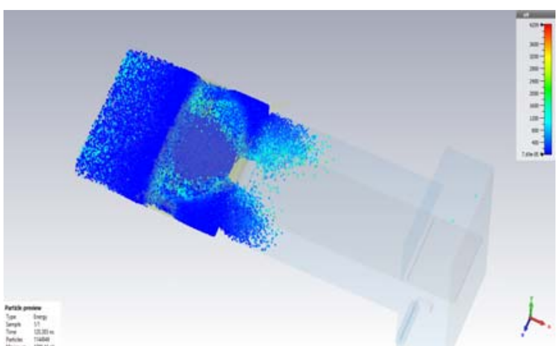

Figure 4: Particle growth at the Dee region of the cavity after 128 ns at Dee Voltage of 1 kV, due to particle source at Dee.

Source-Dee Stem Region

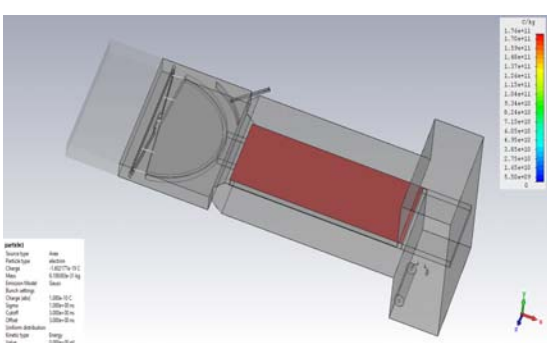

Figure 5: View of the RF cavity showing the red region (Dee stem) as particle source for Multipacting.

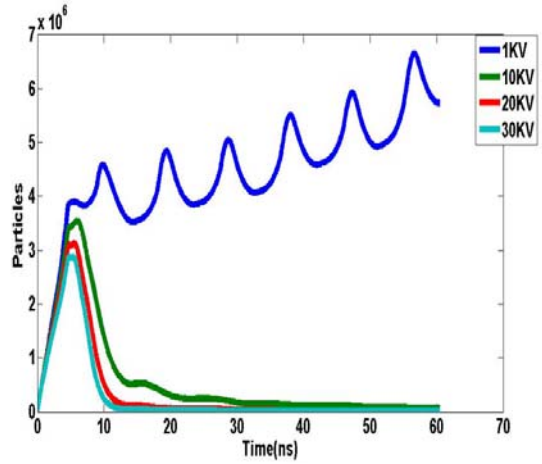

Figure 6: Figure showing Particle number vs. time (ns) at different accelerating Dee voltages in the cavity,due to dee stem as particle source. Particle growth is seen at Dee voltage of 1kV. No Particle growth is seen at 10kV, 20kV, 30kV.

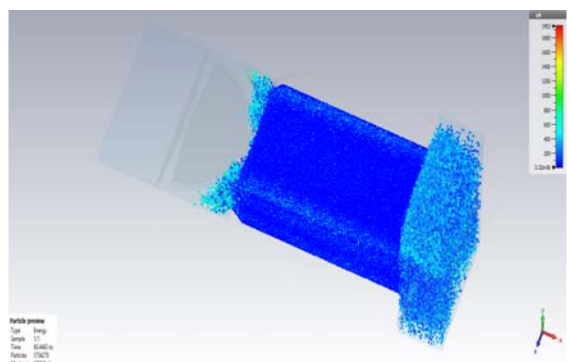

Figure 7: Figure showing Particle growth at the Dee stem of the cavity after 80 ns at Dee Voltage of 1 kV, due to particle source at Dee stem

It can be observed that in all the figures 3,7 that multipacting is observed at lower Dee voltages only.

In presence of DC Magnetic Field

We have to also study the multipacting effect in presence of an external magnetic field, as the cyclotron cavity will be operated in DC magnetic field near DC. In CST Particle Studio, there is a provision to include both the RF cavity imported electric and magnetic field and also DC magnetic field in a single simulation. So, in our simulation we have applied an external DC magnetic field of 3.5T at the Dee region.

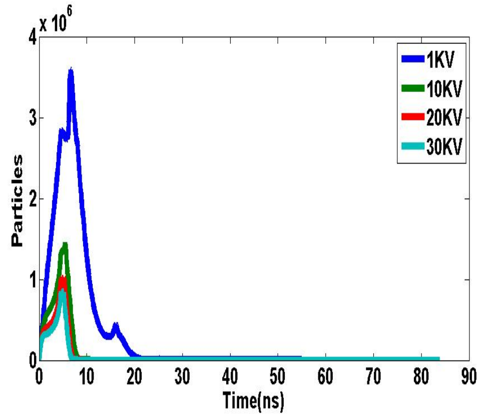

Figure 8: Figure showing Particle number vs. time (ns) at different accelerating Dee voltages in the cavity. No particle growth is seen at all Dee Voltages

Only Dee region has been analysed because the impact of the magnetic field will decide multipacting only in Dee region. Other regions will not get impacted. So, from figure 8 it can be concluded that on application of external DC magnetic field in the Dee region, multipacting discharges that was occurring at lower Dee voltages like 1kV does not occur.

MULTIPACTING REDUCTION BY GEOMETRIC MODIFICATION

While simulating the particle growth across different source regions around the Dee, we have seen that by bending of corners at the Dee side as shown in Figure 9 have reduced the particle growth, that was happening in absence of magnetic field. The particle reduction due to bending of corners is shown in Figure 10.

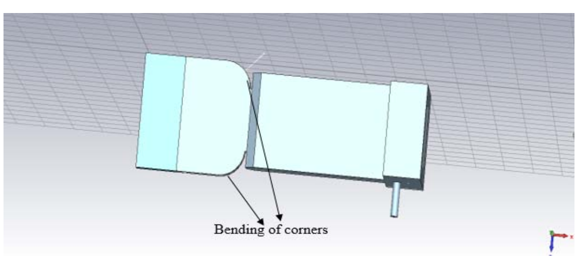

Figure 9: Rounding of the corners at the Dee outer conductor done to reduce multipacting occurring at 1kV at the Dee region

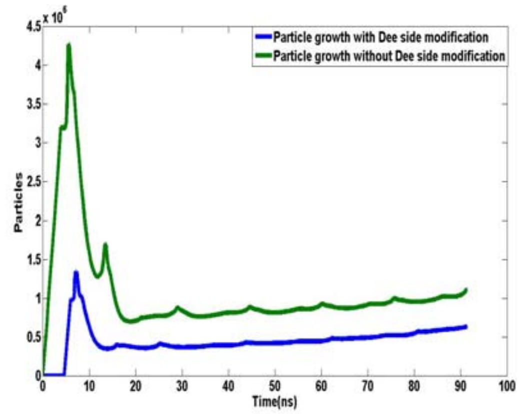

Figure 10: Plot of comparison of particle growth at 1kV Dee voltage between a RF cavity with Dee side modification and without Dee side modification. Cavity with Dee side modification has less particle growth compared to the one having no Dee side modification, that was happening in absence of magnetic field.

CONCLUSION

As observed from the results of the multipacting, in absence of the DC magnetic field. Multipacting is observed at lower Dee voltages like 1kV while at higher Dee voltages, it is not observed. In presence of external DC magnetic field, multipacting is not observed at any Dee voltages. Also, it was shown that by some geometrical modification at the Dee end, the multipacting that was earlier observed at lower Dee voltages in absence of magnetic field, is improved.

REFERENCES

[1] J. Pradhan et al., “Conceptual design of Compact Superconducting Medical Cyclotron for medical diagnostic application”, *InPAC* (2022).

[2] V.Sahoo et al., “Design Study Of Radio Frequency Cavity For Compact Superconducting Medical Cyclotron”, *InPAC* (2022).

[3] CST Studio Suite (2018) 3D EM simulation and analysis software(https://www.3ds.com)

DEVELOPMENT OF MULTI-CHANNEL PROGRAMMABLE TRIGGER GENERATOR FOR LINAC OF ELECTRON BEAM RADIATION PROCESSING FACILITY

Janardhan Musuku*, M Seema, Jatin.J, P Pawnarkar, T.V. Satheesan, and P Fatnani
Raja Ramanna Centre for Advanced Technology, Indore - 452013, INDIA

Abstract

A timing system for precisely time synchronization of subsystems is required for operation of Linac, measurements of various diagnostic parameters, irradiation process verification and process interrupt handling with several parameters & faults. Various delays are to be precisely adjusted in time domain with sub-system functions & measurements, with respect to the master reference trigger. To realize this, a multi-channel programmable trigger generator module is developed.

INTRODUCTION

The electron beam radiation processing facility (EBRPF) is being operated at Devi Ahilyabai Holkar fruit and vegetable mandi complex, Indore. The facility is based on in-house developed 10 MeV, 6kW electron linear accelerators (Linacs) by Raja Ramanna Centre for Advanced Technology (RRCAT), Department of Atomic Energy. The electron beam, which is in horizontal direction, is moved up & down in vertical direction to get radiation field in vertical plane. The products which are to be irradiated are transported in front of vertically scanning beam, with a roller conveyor in horizontal plane. This facility provides electron beam irradiation services for medical devices sterilization and irradiation of research samples for development of new crop varieties. The deliverable dose range is from few Gray (Gy) to several Kilo Gray (KGy) based on the product requirements.

PROGRAMMABLE TRIGGER GENERATOR

The multi-channel Programmable Trigger Generator (PTG) module for Linac comprises of in-house developed Field Programmable Gate Array (FPGA, Spartan 3, Xilinx) board and controller board with Optical Fiber transmitters and receivers. All the digital logic functions like Pulse Repetition Rate (PRR) generation, delay generation for all channels, keypad interface, LCD display interface and controller interface are implemented in FPGA using Very high-speed integrated circuit Hardware Description Language (VHDL). The block diagram is shown in figure-1 and snap shot of PTG module is shown in figure-2. The module is facilitated with front panel LCD display to indicate live status like PRR, operating mode, local/remote status, serial communication, to display set values of different delays and system interlock status. A 4 x 4 matrix key pad is interfaced for setting of PRR, delay time and trigger on/off like commands in local mode. There are two modes of operation, normal mode for regular operation and diagnostic mode for beam parameters measurement. In diagnostic mode the systems require 1 Hz PRR irrespective of PRR set value. The selectable communication ports RS232 / RS485 are given for remote operation from control room. The output trigger pulse generation is validated with the integrated healthy interlock of Linac system, so that in case of fault, the trigger pulse output stops.

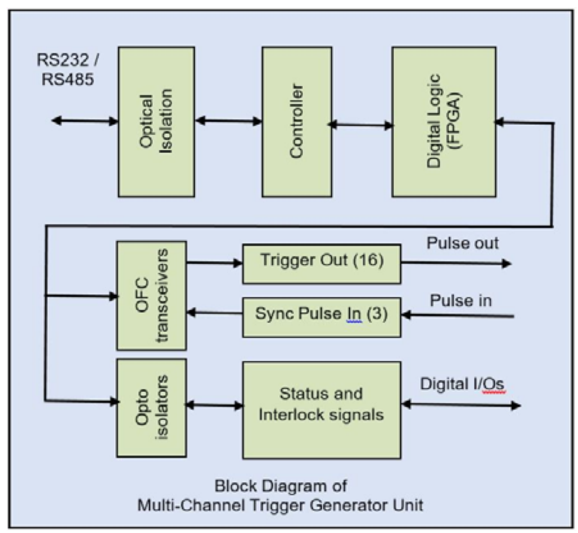

Figure 1. Block diagram of PTG

Sixteen trigger output channels are provided for different subsystems requirement and an input channel to synchronize with external sync pulse. These trigger pulses are provided for field device like RF modulator power supply, electron gun power supply, beam energy measurement system, beam pulse current measurement system, scan width measurement system, beam position indicator system, beam slit monitor system and beam profile monitor etc. The module is tested with the Linac system for proper operation.

*mjn@rrcat.gov.in

Figure 2. Programmable Trigger Generator Module.

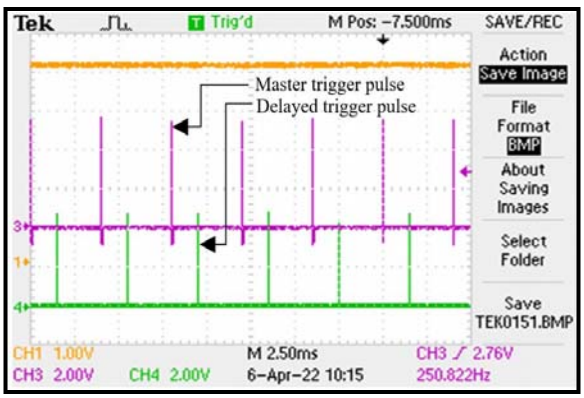

Figure 3. Trigger pulses without synchronization

In figure 3, the purple trace shows the master trigger pulse and green trace shows the delayed trigger pulse, without synchronization.

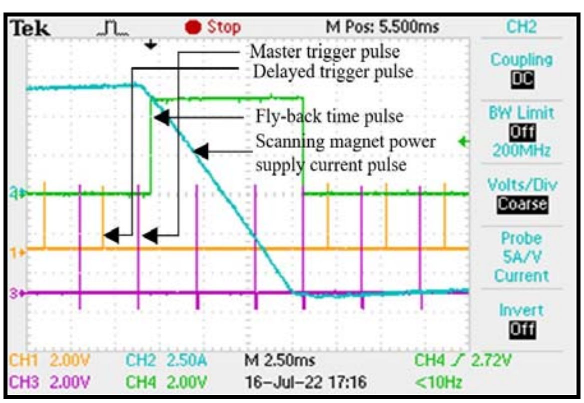

Figure 4. Trigger pulses with synchronization

In figure 4, the purple trace shows the master trigger pulse and yellow trace shows the delayed trigger pulse. Blue trace shows the scan magnet power supply current waveform and green trace shows the scan magnet current fly-back time pulse. With this fly-back time pulse negative edge, the master trigger pulse is synchronized same can be seen in fiure-4. By synchronising the master trigger pulse, the electron beam pulses will have the pre-determined locations of irradiation along the vertical axis. While fly-back time only master trigger and modulator related pulses are available, all other pulses are disabled during this time, so that during fly-back time electron beam pulses will be absent.

Main Features of the PTG

- Pulse Repetition Rate setting range 001 Hz – 500 Hz.
- Pulse width setting range from 5 µS – 10 µS.
- Adjustable delay range with respect to master trigger pulse 2 µS – 2000 µS.
- Provision to synchronize trigger output with external pulse input e.g. Scanning power supply current pulse.
- PRR limit set facility as per user requirement with authentication.
- Selectable mode free running / count mode. The count mode range is from 00001 – 30000 count pulses.
- Selectable Operation mode / Diagnostic mode. Diagnostic mode is to measure the beam parameters of Linac system
- Restoring last set values
- Set read back of delay settings values of all channels
- Read back value of PRR
- All the setting are available in Local mode as well as in remote mode

GRAPHICAL USER INTERFACE

A Graphical User Interface (GUI) for remote operation of PTG module of Linac is developed in LabVIEW. The GUI (figure 5) displays current status, set values of PRR, PRR limit & all delay triggers & read back of PRR. The software communicates with the PTG over serial link. All the parameters are continuously monitored and logged in the data base.

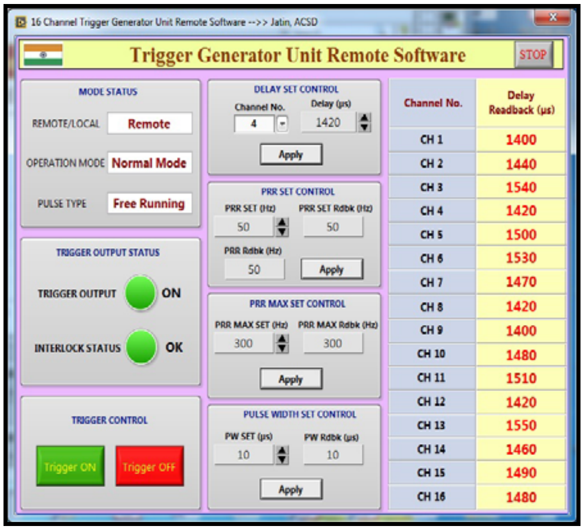

Figure 5. Graphical User Interface

CONCLUSION

The multi-channel Programmable Trigger Generator is developed using FPGA, micro-controller and associated optical electronics for transmitting pulses to the Linac sub systems. The module is tested with the Scan Magnet Power Supply during Linac operation at RRCAT. The re-configurable hardware of module allows easier enhancements and modifications of future requirements for Linac beam quality measurement & validation achievements.

ACKNOWLEDGEMENT

The authors would like to thank all our Accelerator Control Systems Division and Industrial Accelerators Division colleagues for their direct or indirect contribution in design, development, integration and testing of this module. Special thanks to Shri G H Ansari, APSD, RRCAT for his support in mechanical fitting.

REFERENCES

[1] Peter J Ashenden, "The VHDL Cook book," First edition 1990.
[2] Field Programmable Gate Array architecture by Xilinx

UPGRADATION OF LOW LEVEL RF SYSTEM FOR K500 SUPER CONDUCTING CYCLOTRON

#Swarnendu Thakurta*, Vikash Sahoo*, Abhishek Dutta*, Shubham Tripathi*, Surajit Ghosh*+, Aditya Mandal*, Sudeshna Seth*, Sumit Som*, *Variable Energy Cyclotron Centre, Kolkata
+Homi Bhaba National Institute.

Abstract

Variable Energy Cyclotron Centre has commissioned K500 superconducting cyclotron. There are three identical RF cavities for beam acceleration in SCC. RF cavity is formed with two one short circuited λ/4 transmission line section connected at central region operating in the frequency range 9 to 27MHz. The low level RF system (LLRF) has been designed with the stringent requirement of amplitude and phase stability of 100 ppm and ± 0.1^0, respectively. LLRF system broadly consist of Dee Voltage Regulator, Phase Regulator, Spark Detector, Fine Frequency (Trimmer) Control System, RF Tuning System and Interlock-protection System. This paper discusses detail insights into the various technical aspects of LLRF system for the K500 SCC at VECC, Kolkata.

RF SYSTEM OF K500 CYCLOTRON

The RF system of K500 cyclotron delivers RF power in the frequency range of 9MHz to 27MHz in the three identical RF cavities (Cavity-A, Cavity-B and Cavity-C) [1]. The block diagram of the RF system is shown in the Figure 1. The Direct Digital Synthesis (DDS) module [2] generates three RF signal which drives the solid state amplifiers and the power amplifiers that deliver power to the three RF cavities.

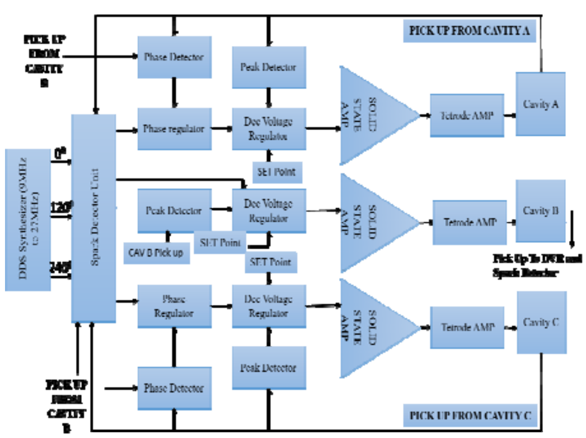

Figure 1: Block Diagram of RF System

The pickup signals from the cavities are used for amplitude and phase measurement which are later used in the Dee voltage regulator (DVR) and phase regulators to control the amplitude and the phase of the RF voltage.

LOW LEVEL RF CONTROL

The LLRF control system regulates the amplitude and phase of the RF cavity voltage using the feedback from the cavity. The spark detector unit uses the Dee pick up to detect the spark that may happen in the cavity during operation. Fine frequency tuning system maintains the resonance condition by adjusting a variable capacitive tuner called trimmer capacitor. LLRF system is operated from a remote computer using a GUI which communicates with the sub-systems.

Dee Voltage Regulator (DVR)

DVR maintains stable Dee voltage during RF operation. DVR unit consists of peak detector to detect the amplitude, AD834 based RF modulator card and a controller card. DVR can be operated in both open-loop condition (during RF conditioning & RF tuning) and in closed loop condition (during cyclotron operation). The output of peak detector is used as a feedback signal which is compared with the reference signal generated by ADAM-6024 analog output channel and generates an error signal. The error signal is sent to the PI controller. The final DC error output is used to modulate the RF signal using the AD834 IC based multiplier PCB. The system is tested using Amplitude modulation (10%) up to 10 kHz frequency range. It is observed in spectrum analyser that the sideband frequency is lowered very much with feedback loop in the DVR. The DVR block diagram is shown Figure 2. The modulator card and error detector card and the open/closed loop results shown in Figure 3 and Figure 4 respectively.

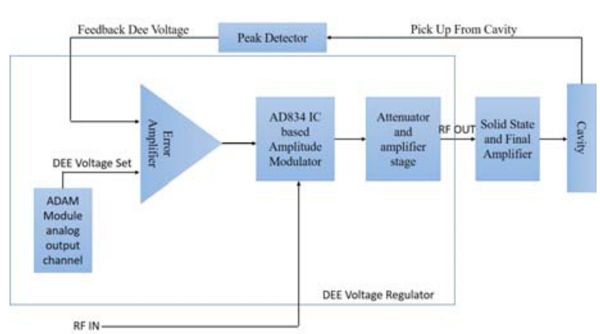

Figure 2: Dee voltage regulator

#swarnendu.thakurta@vecc.gov.in

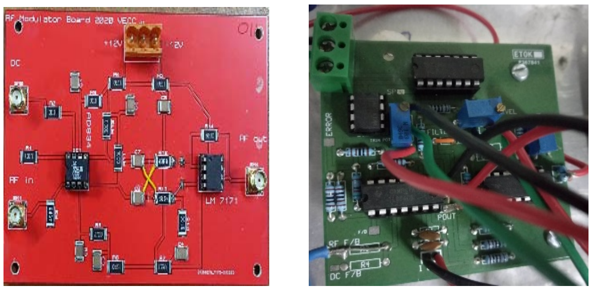

Figure 3: RF Modulator Board (left) and Error detector card (right)

.

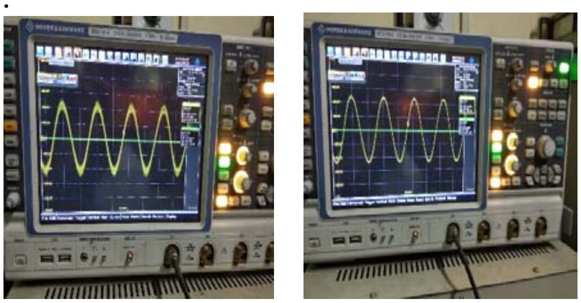

Figure 4:Regulator output under open loop (left) and closed loop (right) condition with 10% amplitude modulation

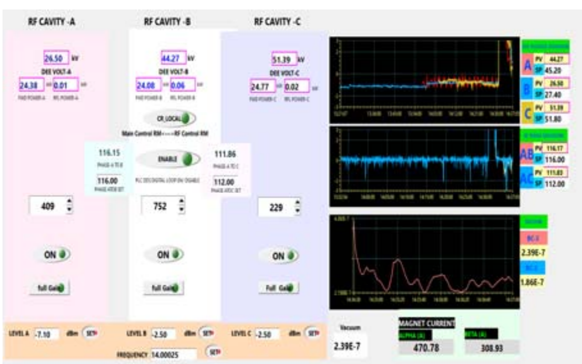

Figure 5: Remote Interface for RF System

An updated remote interface has been developed for user to set Dee voltage and phase during operation. Individual forward/reflected power, Dee voltage and phase between the cavity voltages are measured and displayed. We can set the Dee voltage set point and the phase set point through this GUI. The Dee voltage and the phase with respect to time is plotted in the fig 5. The user interface is developed using Control System Studio platform and EPICS based system.

Phase Regulator

The phase regulator, as shown in Figure 6, uses a DDS source as RF signal generator. A part of the signal is used for phase measurement and synchronization purposes. The signal passes through the LLRF loop containing a voltage controlled phase shifter which takes care of dynamic phase disturbances generated in the chain of LLRF components, amplifiers, and RF cavity. As we are interested only in maintaining relative phase shift between resonators, two instead of three phase loops have been used. Two phase detectors have been used to detect the relative phase shift between Cavity-A and Cavity-B (φ_{AB}) and between Cavity-B and Cavity-C (φ_{BC}). Voltage controlled phase shifters are installed in Cavity-A and Cavity-C which work on the error signal of φ_{AB} and φ_{BC}. The phase loop can correct phase shift in ±25-degree range. In case of larger phase shift occurred in the system DDS module generate additional phase shift to bring the phase regulator loop back to working range. The phase regulator consists of AD8302 IC based phase detector PCB, Error amplifier and PI controller and AD834 IC based IQ modulator card [3]. The phase stability is measured around ±0.1 degree. The block diagram is shown in Figure 6. The Scheme is shown for cavity A and the same is used in cavity C. The phase reference for the three RF system is 0^0, 120^0, 240^0 respectively for 1^{st} harmonic operation. The phase difference is measured by the phase detector board (AD8302IC Based) and compared with the set value generated by ADAM analog output channel and an error signal is generated. This error is sent to the PI controller. The final output is sent to the IQ modulator that control the phase of RF signal.

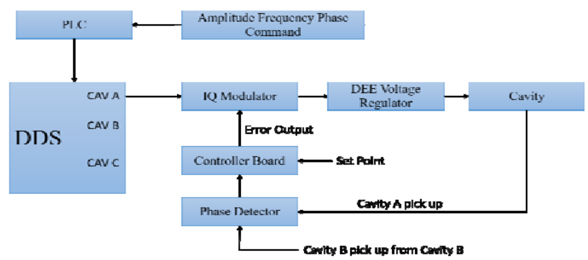

Figure 6: Phase Regulator diagram

Spark Detector

Spark detector circuit consists of a peak detector circuit with very low time constant (RC~ 1uS). Whenever spark occurs in the cavity and pickup suddenly falls, i.e. dv/dt ≥ 1V/us, differentiator produces a spike/pulse that is used to trigger a flip flop. The capacitor charging circuit is designed such a way that when the spark happens the output falls sharply to disable the RF input. After 0.5 ms that output will increase slowly so that the amplifier will not trip. The output of the spark detector is used in a voltage controlled attenuator which finally controls the RF input to the cavity. The block diagram is shown in Figure 7 and the output is shown in Figure 8.a and 8.b. It indicates that spark detected within 1us and the output gets off immediately (2.565 us) and increased slowly within 2ms.It is an upgradation of the existing LLRF system. It helps in stable operation of the system for longer duration without RF trip. The spark detector unit is very much useful specially during start up and cavity baking time when spark occurs more frequently.

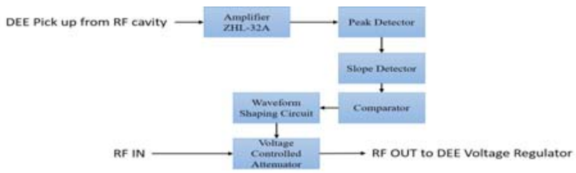

Figure 7: Spark Detector Unit

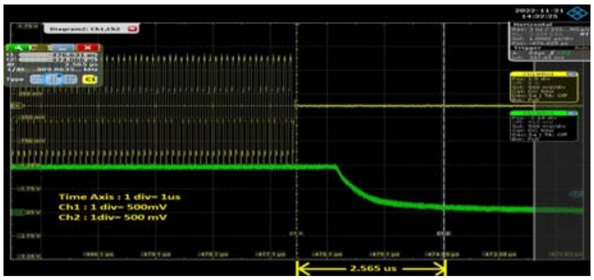

Figure 8.a.: Measurement of response time of spark detector

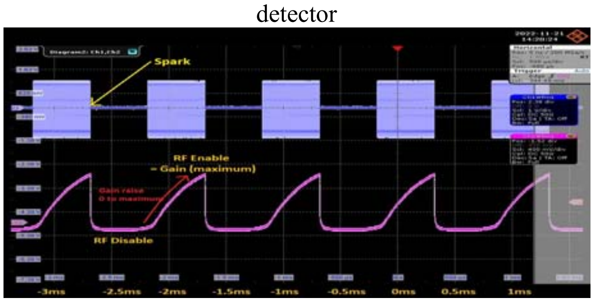

Figure 8.b.: Output of Spark detector circuit

Fine Frequency (Trimmer) Control System

During operation the cavity is detuned due to heating and other effect. There is a variable fine trimmer capacitor that is driven by hydraulic system that bring back the cavity to the tune frequency. The trimmer control system is a PLC based closed loop control system. The main components are Phase detector, PID controller (PLC based), Hydraulic drive for the trimmer. The phase difference between the Dee Pick up and the Dee in Pick up is 90^0 under tuned condition. But when the cavity is detuned this phase changes. This is measured by AD8302 IC based phase detector, which generates a DC voltage corresponding to the phase difference. This signal along with reflected power is used as error signal. The output of the PID controller drives the hydraulic drive system that drives the trimmer capacitor to tune the cavity. The frequency range of trimmer capacitor is up to 15 kHz. The interface for trimmer control is shown in Figure 9.

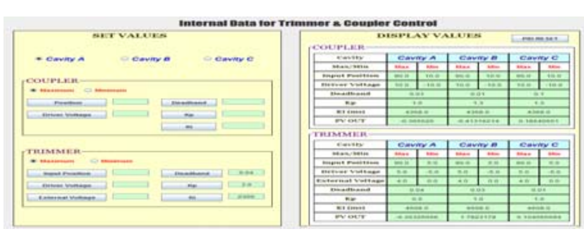

Figure 9: Trimmer and coupler control

Interlock protection system

For safe operation of the RF system PLC based interlock system is developed. For each electrode of the tetrode based power amplifier interlocks are developed when these interlocks are cleared then only that electrodes power supply will be on. For filament power supply water interlocks must be ok. Similarly, Screen power supply should be on when Anode is on. Interlocks are there so that sequentially the power supply will be on. Beside this forward/reflected power, vacuum, radiation safety and door interlocks are also there for safe operation. The forward and reflected power interlocks are used to turn off the driver amplifier. The user interface for different interlocks are shown in Figure 10.

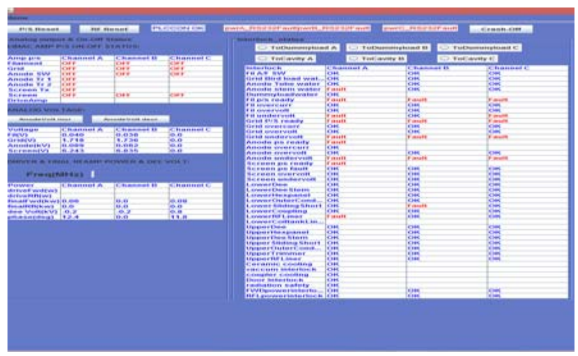

Figure 10: Interlock System for K500 RF system

SUMMARY

The LLRF system and the Remote control setup for RF parameters are represented. The Dee voltage regulator and the phase regulator developed is running round the clock in K500 cyclotron. Stable beam in first harmonic and second harmonic has been obtained at 14 MHz. Stable Dee voltage at different frequencies achieved and the upgraded system is found to be reliable.

REFERENCES

[1] "Commissioning experience of the RF system of K500 superconducting cyclotron at VECC", S. Som, Saikat Paul, Aditya Mandal, S. Seth, S. Saha, R.K. Bhandari, P. Gangopadhyay, P.R. Raj, *Proceedings of 19th International Conference on Cyclotron and their Applications (Cyclotrons-2010),* held at Institute of Modern Physics, Lanzhou, China, during September 6 –10, 2010 (*p.162*)

[2] Data Sheet for AD9959 4-Channel, 500 MSPS DDS with 10-Bit DACs A product of *Analog Devices*, Norwood, MA, USA;

[3] Precision phase control for the radio frequency system of K500 superconducting cyclotron at Variable Energy Cyclotron Centre, Kolkata Review of Scientific Instruments 84, 113303 (2013)

DEVELOPMENT OF A COMPUTER PROGRAM FOR LONGITUDINAL BEAM DYNAMICS STUDIES IN A TRAVELING WAVE CONSTANT IMPEDANCE ELECTRON LINAC

R. Dhingra#1, N.S. Kulkarni and V. Kumar[1], Proton Accelerator Group, RRCAT, Indore
[1]also at HBNI, Mumbai

Abstract

A computer program for longitudinal beam dynamics of electrons has been developed in Python [1]. The program employs the fourth order Runge-Kutta method to numerically solve first-order coupled differential equations in phase and energy. This program is capable of dealing with both CW as well as bunched beams. The effect of beam loading is explicitly considered through the calculation of accelerating field gradient profile in the linac, which is utilized during the dynamics calculations. The program can perform calculations for fixed, as well as, variable phase velocity structures. The in-house developed computer program has been validated by simulating the case of the 9.5 MeV, 10 kW Constant Impedance (CZ) traveling wave electron linac that has been designed and commissioned by RRCAT [2], and comparing the calculated output beam parameters with those obtained using commercial beam dynamics code. The accuracy of the program is further confirmed by benchmarking it against analytical calculations for a fixed phase velocity structure [3,4].

INTRODUCTION

Traveling Wave (TW) accelerating structures have a wide range of applications, and are used in industrial linacs, as well as in injector linacs of Synchrotron Radiation Sources and Free Electron Lasers. An indigenous computer program for study of longitudinal beam dynamics of electrons in TW linacs has been developed in Python. In this paper, we first present the details of the computer program, along with its specific features and capabilities. In the next section, we provide a description of the structure details of integrated bunching-cum-accelerating Constant Impedance (CZ) type accelerating structure, for which the longitudinal beam dynamics study has been performed. This is followed by the results of the beam dynamics calculations in this linac, and its benchmarking using the code PARMELA [5]. Subsequently, we evaluate the beam transmission efficiency, and threshold value of accelerating gradient for capture, for a fixed phase velocity structure, through analytical calculations. These values have been confirmed using the in-house developed computer program.

COMPUTER PROGRAM DETAILS

The computer program evaluates the profile of average accelerating gradient in the multi-sectional linac for "*no beam*", as well as for "*with beam*" case, considering a fixed input RF power. Different sections of the linac have different geometrical and RF characteristics. The electro-dynamical parameters of the cells are specified as the input in the program. The accelerating field gradient at the entry of first section is related to the input RF power $(P_{in,1})$[6] as $E_{entry,1} = \sqrt{2\alpha_{att,1} r_{sh,1} P_{in,1}}$, where $\alpha_{att,1}$ and $r_{sh,1}$ are the attenuation coefficient per unit length and the effective shunt impedance per unit length, respectively of the first section. In a CZ structure, the variation of accelerating field gradient in first section can be expressed as [6],

$$E_1(z) = E_{entry,1} e^{-\tau_1} - I_0 r_{sh,1}(1 - e^{-\tau_1}), \tag{1}$$

where τ_1 is the attenuation evaluated as $\tau_1(z) = \alpha_{att,1} z$, and I_0 is the macro pulse current. For calculating the input power in second section of linac $(P_{in,2})$ with different RF properties, one can use

$$\frac{P_{in,2}}{P_{in,1}} = \left(\frac{E_{exit,1}}{E_{entry,1}}\right)^2, \tag{2}$$

where $E_{entry,1}$ and $E_{exit,1}$ are the accelerating field gradient at entry and exit of first section respectively. Here, $E_{exit,1}$ is obtained by solving Eq. (1) at $z = L_1$, where L_1 is the length of first section. Having obtained the input RF power at entry of second section, the procedure followed for first section can be used to obtain the electric field profile in second section and so on. The program computes the fitting equations for the normalized accelerating gradient for each section, which go as its input. The normalized accelerating gradient is defined as $\alpha(z) = eE(z)\lambda/m_0c^2$, where e is the electronic charge, λ is the free space wavelength corresponding to operating frequency, m_0 is the rest mass of electron and c is the speed of light.

The computer program performs the longitudinal beam dynamics of electrons by solving the first order coupled differential equations in phase and energy [3], as given in Eq. (3) and Eq. (4). The numerical technique used is Runge-Kutta method of order four [7].

$$\frac{d\delta}{d\xi} = 2\pi\left(\frac{1}{\beta_w} - \frac{1}{\beta}\right), \tag{3}$$

$$\frac{d\gamma}{d\xi} = -\alpha(\xi) sin\delta. \tag{4}$$

Here, δ and γ are the electron phase and normalized energy of electron (with respect to its rest mass energy), respectively. The parameter ξ is the distance along the length of linac, normalized with respect to free space

#rinky@rrcat.gov.in

wavelength. The phase velocity and electron velocity (in unit of speed of light) are denoted by β_w and β, respectively.

Macroparticles are tracked through the electric fields in the bunching-cum-accelerating structure, with the given input energy distribution, and phase distribution. The program can generate different distributions in energy and phase, along with a provision to import the particle distributions from text files. The number of macro particles that can be tracked through the linac is limited by the available computer memory. A particle counter keeps count of survived and lost particles. The program considers a particle as lost, if either its velocity becomes zero, or its longitudinal phase exceeds the value specified in the computer program. The effect of space charge has not been considered in this program. The value of output energy and phase of each particle is exported for post-processing into a text file. The computer program generates the plots of energy and phase of each particle along the linac length. The program computes various output parameters like average beam energy, output beam power, average phase, rms energy spread, rms phase spread *etc*. Program also calculates the beam transmission based on longitudinal beam dynamics studies, and can be used to optimize the bunching section of the bunching-cum-accelerating structure. Figure 1 shows the flowchart depicting the sequence of the program.

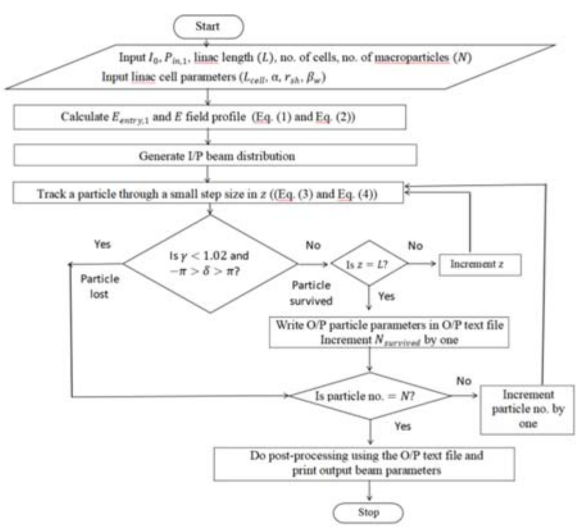

Figure 1: Flowchart of the computer program.

STRUCTURE DETAILS

The structure details of a 9.5 MeV, 10 kW Constant Impedance (CZ) electron linac at 2856 MHz are listed in Table 1. The macro pulse beam current (I_0) is 350 mA for a duty factor of 0.3% [2]. The structure parameters of the linac are listed in Table 1.

The profile of average accelerating gradient in the linac has been evaluated by the program, considering an input RF power of 5 MW, as shown in Fig. 2. The data points correspond to value of E_0 at cell output. The fitting equations obtained, using the 'Polyfit' function in the NumPy library of Python, for the normalized accelerating gradient are

$$\alpha = -0.1071\xi + 1.6688, 0 < \xi < 0.3733, \tag{5}$$

$$\alpha = -0.1135\xi + 2.0352, 0.3733 < \xi < 1.2733, \tag{6}$$

$$\alpha = 0.0010\xi^2 - 0.12071 + 2.1280, 1.2733 < \xi < 16.2584. \tag{7}$$

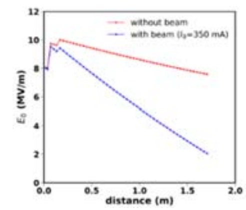

Figure 2: Average accelerating field gradient versus distance along the linac.

Table 1: Structure parameters [8]

Parameters	Buncher Type-I	Buncher Type-II	Regular
Number of cells	2	3	45
Phase velocity (β_w)	0.56	0.9	0.999
Attenuation coefficient (Np/m)	0.33	0.19	0.18
Effective shunt impedance (MΩ/m)	20	52	60
Length (mm)	19.594	31.490	34.955

BEAM DYNAMICS CALCULATIONS

For the beam dynamics calculations, 5000 macro particles have been tracked through the linac. A bunched beam is injected into the linac, and the input beam parameters considered are listed in Table 2. Uniform distribution in phase and random distribution in energy has been considered at input. Sufficiently small step size (~1 mm) has been used for calculations for higher accuracy. The beam loss criteria used in this program is $\gamma < 1.02$, and $-\pi > \delta > \pi$. The evolution of energy and phase of each particle in linac is shown in Fig. 3. We observe that the bunch is positioned near the peak of RF at linac exit. Table 3 lists the output beam parameters obtained using in-house developed computer program, and its comparison with the results obtained using PARMELA.

Analytical calculations

For a CW beam (with fixed input beam energy) injected into a structure with a constant phase velocity $\beta_w = 1$, the threshold value of accelerating gradient for capture (E_z) and transmission efficiency (F) are given by [3,4]

$$E_z = \frac{\pi m_0 c^2}{\lambda e}\left(\sqrt{p_0^2+1}-p_0\right), \qquad (8)$$

$$F = \frac{1}{\pi}cos^{-1}[-1+\frac{2\pi m_0 c^2}{\lambda e E_z}\left(\sqrt{p_0^2+1}-p_0\right)], \qquad (9)$$

where p_0 is the normalized momentum of the input beam, defined as $p_0 = \gamma_0\beta_0$ with $\beta_0 = v_0/c$ and $\gamma_0 = 1/\sqrt{1-\beta_0^2}$. Here, v_0 is the input velocity of electron beam. For input beam energy of 50 keV, E_z comes out to be 9.86 MV/m. The threshold value of accelerating gradient calculated by the in-house developed program is 9.71 MV/m, which is close to the analytical value. The RF parameters of the cells have been taken to be same as that of regular section of the CZ structure considered above. Figure 4 gives the comparison of transmission efficiency calculated analytically and using the in-house developed program, for different values of accelerating gradients. We see that there is a close match between the two values. In this study, electrons never acquire negative velocity, as accelerating gradient has been kept lower than E_{lim} given by [3,4]

$$E_{lim} = \frac{\pi m_0 c^2}{\lambda e}. \qquad (10)$$

Table 2: Input beam parameters

Parameters	Value
Average kinetic energy	50 keV
Current	350 mA
Input energy spread (tot)	±0.5 %
Input phase spread (tot)	±50^0 (bunched)

Table 3: Output beam parameters

Parameters	In-house program	PARMELA
Average energy	9.56 MeV	9.58 MeV
Peak power	3.35	3.35
Energy spread (rms)	2.1 %	1.9 %
Phase spread (rms)	4.8^0	5.1^0
Output average phase	-89.2^0	-89^0
Transmission	100 %	100 %

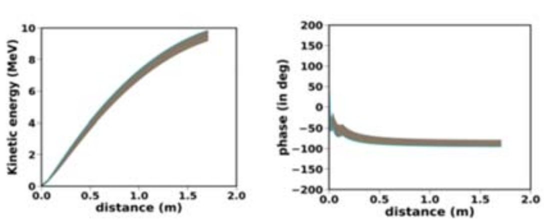

Figure 3: Evolution of energy (left) and phase (right) along linac length.

CONCLUSION

A computer program has been developed in Python for longitudinal beam dynamics of electrons. This computer program can be conveniently used for quick optimization of constant impedance TW structure geometries, as it does not require the 2D/3D field maps. After completing the quick optimization based on longitudinal dynamics, commercially available codes can be used for transverse beam dynamics and space charge calculations for further optimization, which will make the overall design optimization fast. The capabilities of the program can be extended to include a pre-buncher cavity before the bunching-cum-accelerating section, and also for other traveling wave structures like constant gradient structures *etc*.

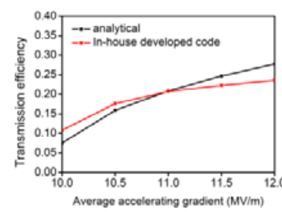

Figure 4: Transmission efficiency for different values of accelerating gradient.

ACKNOWLEDGEMENT

Author (RD) would like to thank Shri RamPrakash and Shri Sachin Raturi for extending help in facilitating a seamless transition from Matlab to Python.

REFERENCES

[1] www.python.org.

[2] P. Arora, P.K. Jana, N.S. Kulkarni and V. Kumar, "Electromagnetic design and beam dynamics studies of 9.5/7.0 MeV 10 kW industrial electron linac with pre-buncher" in Proc. of Indian Particle Accelerator Conference (InPAC 2018), RRCAT, Indore, Jan 2018.

[3] M. Chodorow et. al, "Stanford high energy linear electron accelerator (Mark-III)", Review of Scientific Instruments, 26, 134 (1955).

[4] G. Dome, "Electron bunching by uniform structures of disk loaded waveguide", Technical Report No. M-242-A, Stanford University.

[5] Lloyd M. Young, PARMELA-LA-UR-96-1835, LANL.

[6] B.V. Zverev and N.P. Sobenin, "Electrodynamic characteristics of accelerating cavities", Moscow Engineering Physics Institute University Press, 1999.

[7] E Balaguruswamy, "Numerical Methods", Tata McGRAW HILL, 2009.

[8] N.S. Kulkarni, R. Dhingra and V. Kumar, "Physics design of a 10 MeV, 6 kW traveling wave electron linac for industrial applications", Pramana-J.Phys., 87:74 (2016).

PHYSICS DESIGN OF MEHIPA LEBT FOR 30 KEV PROTON BEAM

Pallavi Priyadarshini[1,2], Jose V. Mathew[1], Rajni Pande[1], SVLS Rao[1]
[1]Ion Accelerator Development Division, BARC
Homi Bhabha National Institute, Mumbai

Abstract

The Low Energy Beam Transport (LEBT) channel for transporting and matching the 30 keV, 10 mA CW proton beam having transverse emittance 0.2 π.mm-mrad, from the ECR ion source to the RFQ has been designed and optimized. A provision for a 30-degree bending magnet has been proposed in the design. The optimized LEBT design comprises three solenoids and four drift sections interspersed between them. Achieving minimum transverse emittance during beam injection into the RFQ has been accomplished by optimizing the magnetic fields of the three solenoids and the drift spaces in between. The drift spaces have been optimized to enable the inclusion of beam steering magnets and beam diagnostics. The iterative method has been employed for the optimization of the LEBT design, beginning with tuning the magnetic field of the last two solenoids for minimum emittance with a fixed field in the first solenoid. The beam dynamics of the LEBT have been studied with a beam containing two species: H^+ and H_2^+. This paper will present the various simulation results of the MEHIPA LEBT design.

INTRODUCTION

The proposed Medium Energy High Intensity Proton Accelerator (MEHIPA) will be built at the BARC Facility in Vizag. MEHIPA will be a 40 MeV superconducting accelerator with a 10 MeV normal conducting front-end. The peak beam current will be 10 mA. To improve the beam quality, particularly in terms of beam emittance, the energy of the ECR ion source has been reduced from 50 keV to 30 keV, based on experimental observations [1, 2]. Consequently, the first accelerating structure, RFQ, has been redesigned to accommodate the 30 keV input beam energy.

The LEBT channel has been optimized for transporting and matching the 30 keV, 10 mA CW proton beam with a transverse emittance of 0.2 π.mm-mrad from the ECR ion source to the RFQ. The design includes a solenoid after the ion source, followed by a bending magnet and two solenoids with drift spaces in-between. The magnetic field of these three solenoids is tuned to achieve minimum emittance growth and ensure beam matching into the RFQ.

The proton fraction of the extracted beam is a crucial parameter for the proton ion source, as it should be maximized to prevent beam loss in the beam line due to other species such as H_2^+ and H_3^+. Moreover, a high proton fraction allows for direct injection into the accelerating structure without the use of selection devices. Despite the desirability of a high proton fraction, the reality is less favourable, with microwave ion sources currently achieving proton fractions in the range of 60-85% in the extracted beam [3]. The presence of a significant proportion of unwanted species can negatively affect the primary beam's dynamics during transport, leading to a degradation in beam quality, especially at high beam intensities. Therefore, proper design of the transport line is necessary to quickly reject unwanted species and in this LEBT design. Here, a 30-degree bending magnet is introduced to avoid injection of hybrid ions like H_2^+ and H_3^+ into the RFQ and beam dynamics studies are done with a beam consisting of 77% H^+ and 23% H_2^+. In addition, the introduction of bending magnet will maintain redundancy and improve reliability and availability by providing an option for two ion sources. The bending magnet in the LEBT introduces beam asymmetry, which is corrected by optimizing the two edge angles of the bending magnet.

LEBT DESIGN

A simplified layout of the LEBT design is illustrated in Figure 1. The first, second, and third solenoids are labelled as Sol 1, Sol 2, and Sol 3, respectively. BM is the 30-degrees bending magnet. The drift spaces from the ion source (IS) to Sol 1, from Sol 1 to Sol 2, and from Sol 2 to Sol 3 are identified as D1, D2, and D3, respectively. D1 is kept small to control the divergence of the beam from the IS. D2 is selected to accommodate a 30-degree bending magnet; the drift space before and after the bending magnet is referred as D2a and D2b respectively. The drift D3 is designated for housing all the beam diagnostics of the LEBT. D4 is chosen to accommodate the RFQ flange. In all simulations, solenoids with a physical length of 142 mm and field maps derived from magnet designs have been employed [4].

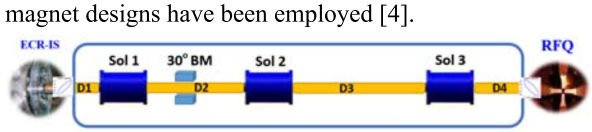

Figure 1. Layout of the LEBT of MEHIPA-1

LEBT OPTIMIZATION

After deciding on the layout of the Low Energy Beam Transport (LEBT), the Partran solver of TraceWin [5] is used to optimize it. The LEBT entrance is supplied with a mixture of uniformly distributed 10 mA, 30 keV proton beam and 3 mA, 30 keV H_2^+. This beam has a normalized RMS emittance of 0.2π mm-mrad.

Initially, the Sol 1 field is kept fixed, and the Sol 2 and Sol 3 fields are optimized to match the beam from the Ion Source (IS) to the Radio-Frequency Quadrupole (RFQ). This is done to minimize emittance growth at the LEBT exit. This process is repeated for different Sol 1 field values. Thus, all three solenoid fields are optimized to minimize overall emittance growth at the LEBT exit and to minimize beam loss throughout the channel. Furthermore, D1, D2, D3, and D4 are optimized by setting a minimum value for each drift space to contain all the components explained in the previous section.

After the first round of optimizing the solenoid fields and drift spaces, a 30º bending magnet is introduced between Sol 1 and Sol 2. This causes asymmetry in the transverse plane, as the bending magnet only bends the beam in the horizontal direction. To address this issue, the two edge angles of the bending magnet are optimized. The optimized LEBT lattice parameters and the bending magnet parameters are listed in Table 1 and Table 2, respectively.

Table 1: LEBT lattice parameters

Lattice Parameters	Optimised Value
D1	20 cm
D2a	26 cm
D2b	27 cm
D3	35.5 cm
D4	30 cm
Sol. effective length	15.2 cm
Sol. aperture radius	8.3 cm
Beam tube radius	6 cm
Total Length	2.73 m

Table 2: Bending magnet parameters

Magnet Parameters	Optimised Value
Pole face rot. angle	11 deg.
Curvature radius of bend	95.5 cm
Bend angle in the rot. Plane	30 deg.
Aperture	6 cm
Length	50 cm

BEAM DYNAMICS RESULT

In this section, the results of the beam dynamics studies conducted using a 77% H^+ and 23% H_2^+ beam with an optimized LEBT design are presented. The initial beam parameters at the entrance of the LEBT is listed in Table 3. Fig. 2 illustrates the proton beam envelope along the channel, accompanied by the optimized field maps of the three solenoids. The integrated magnetic field values for optimized Sol. 1, Sol. 2, and Sol. 3 are 0.291 T-m, 0.191 T-m, and 0.273 T-m, respectively. Fig. 3 displays the beam density profile along the LEBT channel, indicating that the H_2^+ beam is lost in the LEBT after the bending magnet, thereby not entering the RFQ. Fig. 3b further illustrates that the H_2^+ species are completely lost at approximately 1.7 m, with no proton beam loss observed in the LEBT. Fig. 4 demonstrates the beam profiles at the exit of the LEBT, both in phase space and coordinate space, with the maximum beam size at the LEBT exit being 3.4 mm and 3.6 mm in the x-axis and y-axis, respectively. Additionally, Fig. 5 exhibits the normalized root-mean-square (RMS) emittances of the beam in the transverse axes, with emittance values of 0.22 π.mm-mrad and 0.225 π.mm-mrad in the x-axis and y-axis, respectively. The transverse halo parameters is negligible and this is demonstrated in the Fig. 5b. Figure 6 illustrate the point-to-point focusing achieved by the edge optimisation of the bending magnet.

Table 3: Beam parameters at the LEBT input

Beam Parameters	Input Value	
Beam Species	H+	H2+
Beam Current	10 mA	3 mA
Beam Energy	30 keV	
Distribution	4D Uniform	
#particles	5e+5	2e+4
Emittance	0.2 π mm-mrad	

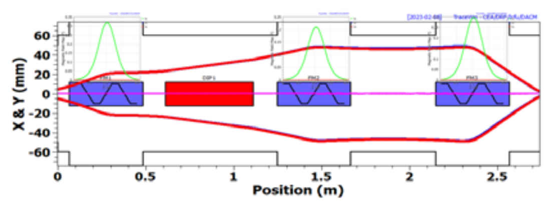

Figure 2. Proton beam envelope in the LEBT along with the solenoid field maps (in green).

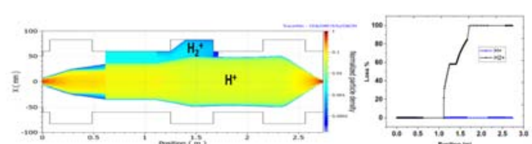
Figure 3. (a) Particle density profile along the LEBT, and (b) Loss % along the LEBT, for H^+ and H_2^+ beam species.

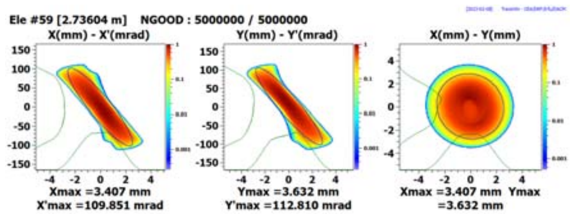

Figure 4. Beam phase-space profile at the LEBT exit.

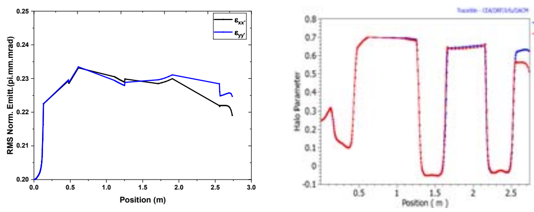

Figure 5. (a) Normalized RMS emittances, and (b) Halo parameter, along the LEBT.

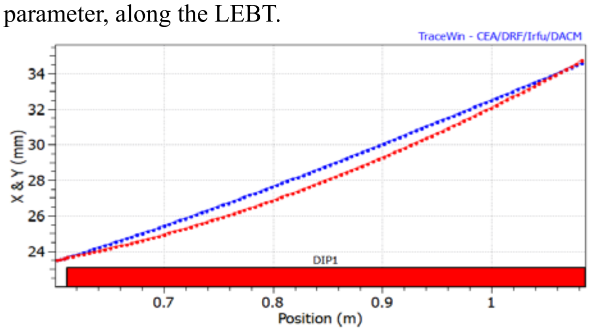

Figure 6. Correction of beam asymmetry in the bending magnet.

Table 4: Final beam parameters

Parameters	At LEBT exit (Weak focusing)
Transmission	100%
Transverse Emittance	0.22π mm-mrad
Halo Parameter	0.5 & 0.6
Sol. 1 mag. field	0.291 T
Sol. 2 mag. field	0.191 T
Sol. 3 mag. field	0.273 T

The final beam parameters obtained from the simulation is listed in table 4.

SUMMARY AND CONCLUSION

This paper presented the design and optimization of LEBT for MEHIPA-1 using a bending magnet, three solenoids, and drift spaces for beam diagnostics, aimed to achieve minimal emittance growth. The impact of introducing the bending magnet on the beam has been minimized by refining the edge angles of the BM. To simulate the LEBT scenario realistically, a proton (H^+) and H_2^+ mixed input beam has been considered. However, the simulation reveals that the H_2^+ component is lost entirely before it enters the RFQ.

Further, 1% RMS energy spread is introduced to the input distribution of LEBT and PIC simulation is done. It has been found that there is no loss along the LEBT and the asymmetry introduced is taken care by the bending magnet edges; emittance is found to increase to 0.27 π mm-mrad without any optimisation. For higher energy spread, we have noticed losses in the transport channel due to asymmetric beam.

REFERENCES

[1] Kewlani, H. M., J. V. Mathew, S. V. L. S. Rao, S. Gharat, S. Krishnagopal, BARC IADD, B. Dikshit, and B. A. R. C. L&PTD. "Beam Characterization of Five Electrode ECR Ion Source." (2021).

[2] Private communication with Hitesh Kewlani, IADD, BARC; journal paper is under process.

[3] S. Gammino, L. Celona, G. Ciavola, F. Maimone and D. Mascali, Review on high current 2.45 GHz electron cyclotron resonance sources, Rev. Sci. instrum. 81 (2010) 02B313.

[4] Field map of the solenoid magnet from magnet vendor (private communication).

[5] Uriot, D., and N. Pichoff. "TraceWin." CEA Saclay, June 596 (2014).

*Work supported by BARC, Mumbai and HBNI, Mumbai
#pallavip@barc.gov.in

ANALOGY OF PARTICLE-CORE MODEL WITH A VARIABLE-LENGTH PENDULUM

Pallavi Priyadarshini[1,2], Rajni Pande[1], Srinivas Krishnagopal[1]
[1]Ion Accelerator Development Division, BARC
[2]Homi Bhabha National Institute, Mumbai

Abstract

High intensity accelerators have variety of applications like in ADS, SNS, RIB and so on. For such accelerators, even a small percentage of the beam, when lost, can deposit significant amount of beam power, which can lead to activation/damage of the beamline. In order to allow hands-on maintenance of the accelerator, average beam loss in the linac, for beam energies above 100 MeV should not exceed 1 W/m. Therefore, it becomes crucial to understand the mechanism of beam halo formation, which is a major cause for beam losses in such accelerators. Beam halo is loosely defined as low-density distribution of particles with large oscillation amplitudes, which can reach the beam line aperture dimensions, thus creating uncontrolled beam loss. The particle-core model is a simple means to study the halo formation. In this model, a bunch of beam particles is treated as a "blob" of charge (beam core) with distinct boundaries, which then interacts with a single particle crossing the core. The focusing force and the oscillation of the beam core excite the single particle oscillation. In this paper, an analogy of the particle core model has been made with a variable-length pendulum. For this, the non-linear equation of the pendulum oscillation has been solved, considering a sinusoidal variation of the pendulum length with time. Sinusoidal oscillation of the length with time excites higher order resonances in the pendulum oscillations in theta with time. It has been observed that the amplitude oscillation becomes most significant for 2:1 resonance. This is very similar to the 2:1 parametric resonance, which is responsible for the halo formation in the particle-core model. Further, this simple variable-length pendulum is compared with the particle-core model analysis for a uniform focusing channel. Poincare map technique has been used to understand the resonance observed in both the cases. For the particle-core model studies, a mismatch has been introduced to excite the core oscillations, which further drives the single particle oscillation and if 2:1 parametric resonance gets excited, the single particle leads to the halo formation.

PARTICLE CORE MODEL

The particle-core model is a simplified approach used to study the effects of beam core oscillations on single particles. Here, it is applied to a round continuous beam that travels through a uniform beam transport system with azimuthal symmetry and linear radial focusing force. In this model, the transverse space charge force is approximated by assuming that the core is an infinitely long uniform cylinder of charge whose radius oscillates due to an initial mismatch. The influence of individual particles on the motion of the core is ignored.

The transverse equation of motion of the core-radius R is given as a function of axial coordinate z by [1]:

$$\frac{d^2R}{dz^2} + k_0^2 R - \frac{\epsilon^2}{R^3} - \frac{K}{R} = 0,$$

where, k_0 represents the phase advance per unit length of the transverse particle oscillations at zero current, K is the space charge term given by $qI/(2\pi\epsilon_0 mc^3\beta^3\gamma^3)$, and $\epsilon = 4\sqrt{\overline{x^2}\,\overline{x'^2} - \overline{xx'}^2}$, is the unnormalized emittance. The transverse equation of motion of a single particle moving radially in the field of the uniform core is:

$$\frac{d^2X}{dz^2} + k_0^2 X - F_{sc} = 0,$$

where X is the radial displacement and F_{sc} is the space charge term given for a uniform density by:

$$F_{sc} = \begin{cases} \frac{KX}{R^2}, & |X| < R \\ \frac{K}{X}, & |X| \geq R \end{cases}.$$

This model provides a useful framework for analysing the behaviour of single particles in the presence of beam core oscillations. Studies are done in line with the work explained in the reference [1].

VARIABLE- LENGTH PENDULUM

Consider a pendulum with a point mass m hanging from a string of length $l(t)$, which varies sinusoidally with time t, as illustrated in Fig. 1.

At any time t, the angle of deviation from the vertical position is denoted by $\theta(t)$, and g represents the acceleration due to gravity. The Lagrangian for the pendulum can be expressed as

$$L = T - U = m[\frac{l(t)^2\dot{\theta}^2}{2} + gl(t)\cos(\theta) + \frac{\dot{l(t)}^2}{2}]$$

The equation of motion for the pendulum with changing length, based on Lagrange's equation, results in a second-order non-linear equation in $\theta(t)$ and $l(t)$[2]:

$$\ddot{\theta(t)} + \frac{2\dot{\theta}\dot{l(t)}}{l(t)} + \frac{g\sin\theta(t)}{l(t)} = 0$$

If we consider the variation in the length of the pendulum to be sinusoidal as $l(t) = L + \boldsymbol{A}\cos\omega t$, where L represents the length of the pendulum at time $t = 0$ and ω

is the frequency of the oscillation of the variation in pendulum thread-length with time t. Then, there are two distinct oscillations in the pendulum. The first one is the variation of θ with time, while the second one is the variation of the length of the pendulum, $l(t)$, with time. Notably, the length oscillation is independent of $\theta(t)$. At $t=0$, when θ_0 is small and $l(t)=L$, the angular frequency of oscillation is $\omega_0=\sqrt{(g/L)}$. However, as the amplitude increases, the equation becomes non-linear.

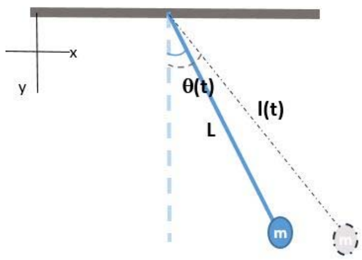

Figure 1. Schematic of a varying length pendulum.

In order to solve the second order differential equations presented in this section for the varying length pendulum and in the previous section for the Particle Core Model, program has been written in Jupyter Notebook of IPython [3]. Various numerical methods are available for solving ordinary differential equations (ODEs). In this case, we utilize one of the widely used approaches known as the Runge-Kutta method [4]. The simulation outcomes are elaborated in the subsequent section.

BEAM DYNAMICS RESULT

This section presents the results obtained by numerically solving the equations of the varying length pendulum using the RK4 method. Figure 2(a) and Figure 2(b) display the angle (θ) versus time t and the phase-space portrait ($\dot{\theta}$ vs θ), respectively. The plot in Figure 2(a) is a standard plot of the harmonic oscillation of a simple pendulum for $A = 0$, indicating no variation in the length of the pendulum. In this study, the frequency of oscillation of the length is varied such that it is an integral multiple of the natural frequency of oscillation of the pendulum, at $t=0$. Four different cases are considered: Case 1 is when the frequency of oscillation of the length is the same as the natural frequency of oscillation of the pendulum for small angles ($\omega\approx\omega_0$). Case 2 is when the frequency of oscillation of the length is twice the natural frequency of oscillation of the pendulum for small angles ($\omega\approx2\omega_0$). Case 3 is when the frequency of oscillation of the length is thrice the natural frequency of oscillation of the pendulum for small angles ($\omega\approx3\omega_0$). Finally, Case 4 is when the frequency of oscillation of the length is four times the natural frequency of oscillation of the pendulum for small angles ($\omega\approx4\omega_0$). In each of the aforementioned cases, two types of plots have been presented. The plot on the left-hand side (which is indicated as '(a)') shows the variation of the angle (θ) with respect to time t. On the other hand, the right-hand subplot (mentioned as '(b)') displays the continuous phase-space portrait (in grey) and stroboscopic plot (in red). The continuous portrait refers to the plot taken at each time steps whereas the red stroboscopic plot is generated by plotting $\dot{\theta}$ vs θ at times when there is minima of θ versus time t plot. The plots for Case 1, Case 2, Case 3, and Case 4 are displayed in Figure 3, 4, 5, and 6, respectively.

In Case 2, Figure 4(b) reveals two resonance islands, representing the 2:1 resonance islands. Similarly, Figure 5(b) and Figure 6(b) exhibit three and four islands, respectively, indicating the formation of third and fourth-order resonances. Additionally, it can be observed that the amplitude of oscillation is highest for the 2:1 resonance, with θ reaching as high as 1.5 radians. In contrast, for all other cases, even after a longer time compared to Case 2, θ does not exceed 0.5 radians. This helps to understand why accelerator physicists tend to focus more on the 2:1 parametric resonance, while the higher-order parametric resonances receive comparatively less attention.

Furthermore, we will attempt to understand these cases in the context of a simple uniform focusing channel, which presents a closer and simpler problem in accelerator physics.

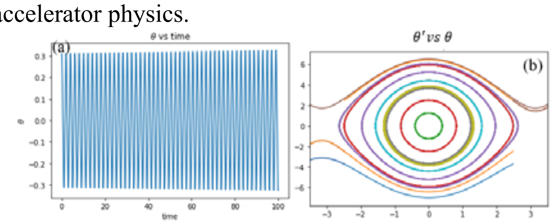

Figure 2. For $A=0$, (a) Phase-space portrait, and (b) Oscillation angle with time.

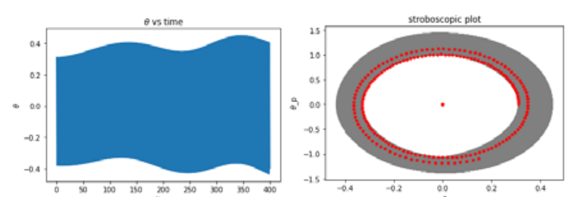

Figure 3. For Case 1 (a) plot of angle (θ) with time t, and (b) continuous phase-space portrait (in grey) and stroboscopic plot (in red).

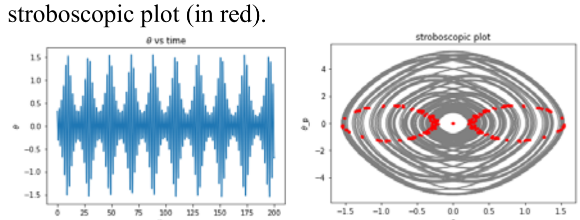

Figure 4. For Case 2 (a) plot of angle (θ) with time t, and (b) continuous phase-space portrait (in grey) and stroboscopic plot (in red).

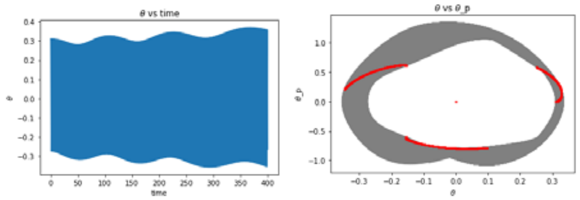

Figure 5. For Case 3 (a) plot of angle (θ) with time t, and (b) continuous phase-space portrait (in grey) and stroboscopic plot (in red).

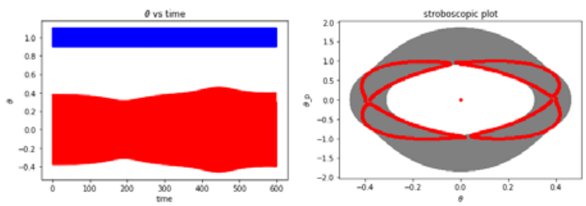

Figure 6. For Case 4 (a) plot of angle (θ) with time t, and (b) continuous phase-space portrait (in grey) and stroboscopic plot (in red).

To comprehend the analogy between the variable-length pendulum and the particle-core model, numerical analyses were conducted on a uniform channel, and the findings are presented below. The initial conditions (x_0 and x'_0) were changed to generate different cases for a core mismatch of 0.62 and a space charge factor of 0.5. Three scenarios, namely Case A, Case B, and Case C, were examined, akin to the variable length pendulum cases. Case A denotes when the particle's oscillation frequency ($\boldsymbol{\omega}_p$) is approximately twice the core's oscillation frequency ($\boldsymbol{\omega}_c$) (i.e., $\boldsymbol{\omega}_c \approx 2\boldsymbol{\omega}_p$), Case B corresponds to $\boldsymbol{\omega}_c \approx 3\boldsymbol{\omega}_p$, and Case C represents $\boldsymbol{\omega}_c \approx 4\boldsymbol{\omega}_p$.

In Figure 7(a), the oscillation of the core is depicted in blue, while the particle's oscillation is represented in red. A stroboscopic plot is generated by plotting the particle's position and divergence at the minima of the core oscillation. Similar plots for Case B and Case C have been shown in Figure 8 and Figure 9, respectively. For Case A, Case B, and Case C, we observe two, three, and four resonance islands, respectively, in the stroboscopic plot. Similar to the variable length pendulum, here also, the 2:1 resonance results in the maximum amplitude size.

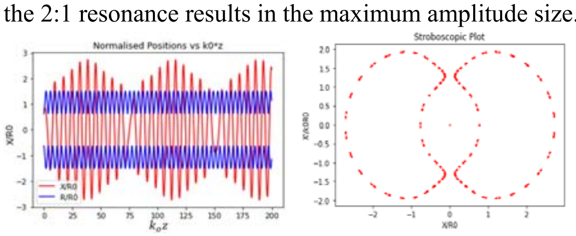

Figure 7. Case A of particle-core model, (a) Amplitude oscillation with time, and (b) Particle's stroboscopic plot (in red).

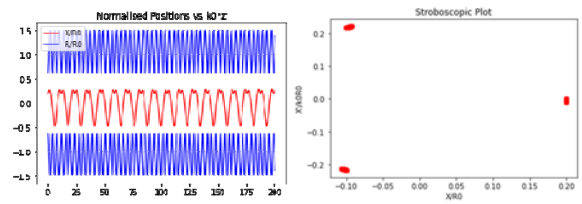

Figure 8. Case B of particle-core model, (a) Amplitude oscillation with time, and (b) Particle's stroboscopic plot (in red).

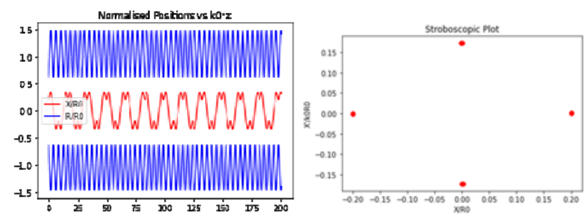

Figure 9. Case C of particle-core model, (a) Amplitude oscillation with time, and (b) Particle's stroboscopic plot (in red).

SUMMARY AND CONCLUSION

The Python simulations using the RK4 method for both the pendulum analysis and particle-core model have yielded important insights. Our study has assumed that the core oscillation in the particle-core model is independent of the particle oscillation, similar to the sinusoidal oscillation of the length of a pendulum. The particle oscillation, on the other hand, is driven by the core oscillation, similar to the angular oscillation of a varying length pendulum driven by its length oscillation. The resonance effect observed in both cases indicates that a 2:1 ratio results in the maximum increase in the oscillation amplitude. These studies provide valuable insights into parametric resonance and its comprehension in a simpler system.

REFERENCES

[1] Wangler, T. P., K. R. Crandall, R. Ryne, and T. S. Wang. "Particle-core model for transverse dynamics of beam halo." Physical review special topics-accelerators and beams 1, no. 8 (1998): 084201.

[2] Sahu, Subhayan, Shriya Pai, Naren Manjunath, and Janaki Balakrishnan. "The lengthening pendulum: Adiabatic invariance and bursting solutions." Physics Open 7 (2021): 100067.

[3] https://jupyter.org/

[4] Grewal, B.S. and Grewal. JS, 1996. Numerical methods in Engineering and Science. Khanna Publishers.

*Work supported by BARC, Mumbai and HBNI, Mumbai
#pallavip@barc.gov.in

TOMOGRAPHIC RECONSTRUCTION OF THE PHASE-SPACE DISTRIBUTION

Pallavi Priyadarshini[1,2], Jose V. Mathew[1], SVLS Rao[1]
[1]Ion Accelerator Development Division, BARC
[2]Homi Bhabha National Institute, Mumbai

Abstract

In particle accelerators, non-linear forces can enhance the higher-order moments of the beam distribution in phase space. In general, the technique by which n-dimensional image is reconstructed from various n-1 dimensional projections is referred to as computed tomography. The one-dimensional projection of a two-dimensional image as a function of viewing angle, $\boldsymbol{\theta}$, is described by the Radon transformation. The computed tomography is an attempt to achieve an inverse Radon transformation. In order to make an algorithm for the beam phase-space reconstruction, general Radon transformation equation is expressed in terms of transfer matrix. Here, beam profile at different viewing angle is basically the beam profile for different transfer matrix, which can be achieved by changing the focusing strength of the magnet. Varying transfer matrix will lead to the varying beam profiles in *x* or *x*' (number of particles vs *x* or *x*') which can be measured using a beam profile monitor. Further an algorithm has been written in Python, which can reconstruct a two-dimensional phase-space beam distribution (in *x-x'*) using several one-dimensional beam-profiles. This is referred as back-projection of the beam. Further, in order to generate a more accurate depiction of the actual beam, each projection is filtered before reconstruction. Various filtering techniques have been compared to understand which filter will lead to the reconstruction close to the actual initial distribution. After standardization of the code, we plan to extend the study to reconstruct the two-dimensional beam distribution from measured one-dimensional profiles.

TOMOGRAPHY

Tomographic reconstruction is a powerful technique used to reconstruct a higher n-dimensional space from projections at a lower (n-1) dimension. It involves the use of mathematical algorithms to reconstruct images from multiple projections obtained at different angles. In the field of medical imaging, tomographic reconstruction is widely used in computed tomography (CT) scans to create detailed 3D images of the human body. It is also an important tool in other fields such as materials science, biology, and physics. Tomographic reconstruction algorithms, such as the filtered back-projection (FBP) algorithm [1], are used to reconstruct 2D or 3D images from a series of one-dimensional projections. The accuracy and resolution of the reconstructed images depend on factors such as the number and quality of the projections, the imaging system used, and the reconstruction algorithm applied.

In accelerator physics, the tomography technique can become useful technique to reconstruct the phase-space distribution of a charged particle beam from various measured one dimensional beam profiles. This technique involves the measurement of beam profiles at different angles or different magnet strengths between 0 to π, followed by the application of the Filtered Back-Projection (FBP) algorithm. This paper will present a numerical discussion of the tomographic reconstruction technique in conjunction with the quadrupole scanning method.

TOMOGRAPHY IN ACCELERATOR

Let us assume a two dimensional distribution is given by f(x,y). The transverse projection of the distribution f(x,y), along the axis $\rho = x\cos\theta + y\sin\theta$, placed at an angle θ relative to the x-axis is given by g(ρ,θ). Such a projection is also known as the Radon transform of f(x,y) and is shown in Fig. 1.

$$g(\rho,\theta) = \iint dx\, dy\, f(x,y)\ \delta(x\cos\theta + y\sin\theta - \rho)$$

The two-dimensional Fourier transform, F(u,v), of a function f(x,y) can be used to express its inverse Fourier transform as

$$f(x,y) = \iint F(u,v)\, e^{j2\pi(ux+vy)}\, du\, dv$$

By replacing the rectangular coordinate system (u,v) in the frequency domain with a polar coordinate system (ω,θ), the above equation can be written as

$$f(x,y) = \int_0^{\pi}\!\!\int F(\omega,\theta)|\omega|\, e^{j2\pi\omega\rho}\, d\omega\, d\theta$$

Similarly, the Fourier transform of the Radon Transform can be expressed as

$$S(\omega,\theta) = \int g(\rho,\theta)\, e^{-j2\pi\omega\rho}\, d\rho$$

According to the Fourier Slice Theorem, $F(\omega,\theta) = S(\omega,\theta)$, and hence

$$f(x,y) = \int_0^{\pi}\!\!\int S(\omega,\theta)|\omega|\, e^{j2\pi\omega\rho}\, d\omega\, d\theta,$$

or simply f(x,y) can be expressed as

$$f(x,y) = \int_0^{\pi} Q(\rho,\theta)\, d\theta,$$

where, $Q(\rho,\theta)$ is given by

$$Q(\rho,\theta) = \int S(\omega,\theta)|\omega|\, e^{j2\pi\omega\rho}\, d\omega.$$

is known as the "filtered projection". Using these equations, a distribution can be reconstructed by back-projecting the filtered projections obtained at different angles (between 0 and π). Several studies have demonstrated a direct correlation between beam images and projections of the phase space distribution using a straightforward scaling equation [2, 3,4].

In order to apply filtered back projection (FBP) algorithm to beam phase-space distributions, analogy has to be made between the beam optics and the projections of an object at several different angles by modifying the beam projections. The transfer matrix, M, is used to represent the particle motion at two different positions and is given by $M = \begin{bmatrix} m_{11} & m_{12} \\ m_{21} & m_{22} \end{bmatrix}$, where $\begin{pmatrix} x_0 \\ x_0' \end{pmatrix}$ and $\begin{pmatrix} x_1 \\ x_1' \end{pmatrix}$ represent the position and angle of the beam at different locations. If we assume a linear system then the particle motion obeys $\begin{pmatrix} x_1 \\ x_1' \end{pmatrix} = M \begin{pmatrix} x_0 \\ x_0' \end{pmatrix}$. Suppose $\mu(x_1, x_1')$ is the two dimensional beam distribution at a location z_1, then the projection $\nu(x_1)$ can be obtained by integrating the two-dimensional beam distribution at z_1 as follows

$$\sigma(x_1) = \int \mu(x_1, x_1')dx_1'$$

Using the Dirac delta function, equivalent form can be written as $\sigma(x) = \iint \mu(x_1, x_1')\delta(x_1 - x)dx_1 dx_1'$ where x is a point within the beam distribution at z_1. Further, using the transfer matrix, the projection $\nu(x)$ can be modified as

$$\sigma(x) = \iint \mu(x_0, x_0')\delta(m_{11}x_0 + m_{12}x_0' - x)dx_0 dx_0',$$

which will be related to the Radon Transformation by defining a scaling factor s by $s = \sqrt{m_{11}^2 + m_{12}^2}$ and the phase space rotation angle θ, by $\tan\theta = \frac{m_{12}}{m_{11}}$. Using the scaling factor and the angle, the projections can be modified as

$$\sigma(x) = \frac{1}{s}\iint \mu(x_0, x_0')\delta(x_0\cos\theta + x_0'\sin\theta - \rho)dx_0 dx_0'$$

where $\rho = x/s$. Thus, the scaling factor and the angle provide a simple equation that relates the spatial beam projections to the Radon transform of the transverse phase space.

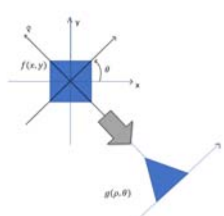

Figure 1. Illustration of the Radon Transform

NUMERICAL ANALYSIS

In this paper, we present the results of numerical analyses carried out to standardize the tomography technique for determining the beam phase-space distribution from measured one-dimensional beam profiles in accelerator physics. The procedure for numerical analysis involves considering a FODO channel with initial and final positions as z_0 and z_1, respectively. The numerical analyses procedure, similar to the procedure discussed in a conference [5], is as follows:

1. The first step in the process is to calculate the transport matrix, M, between two positions, z_0 and z_1.
2. The matrix M is then varied by adjusting the strength of the quadrupole magnet, which changes the rotation angle, θ, from 0 to π, as explained in the previous section.
3. For each value of the matrix M, the scaling factor, s, is calculated using the formula defined earlier.
4. At position z_1, the beam profiles are calculated and stored in a single array for different magnet strengths.
5. These profiles are then plotted as a Sinogram, which provides a visual representation of the beam profiles.
6. The beam profiles are scaled vertically by 's' and horizontally by '*x/s*', and the scaled Sinogram is plotted.
7. Using the filtered back projection technique with different filters, the beam phase-space distribution at z_0 is computed using "iradon" module of Python package "sci-kit image" in Jupyter notebook [6, 7]. The result is further compared with the actual beam phase-space distribution at z_0.
8. The final step involves comparing the computed phase-space distribution with the actual beam phase-space distribution for different filters and showing the errors between them.

SIMULATION RESULTS

Figure 2(a) illustrates the rotation angle resulting from varying the transfer matrix, while Figure 2(b) shows the corresponding scaling factor, s, with changing magetic fiel. The transfer matrix has been modified to obtain beam projections at several angles between 0 and π. At the exit of the FODO channel, beam profiles are obtained for different magnet strengths, as presented in Figure 3(a). These profiles are combined into a Sinogram, depicted in Figure 3(b), and referred to as an unscaled Sinogram.

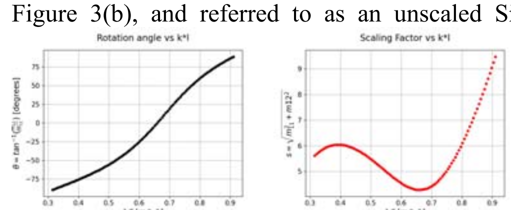

Figure 2. (a) Rotation angle, and (b) Scaling factor, for different quadrupole strengths.

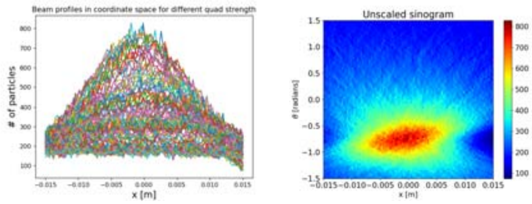

Figure 3. (a) 1D Beam profiles, and (b) unscaled Sinogram

The scaling factor, which is computed from the transfer matrix, is used to create a scaled Sinogram that is displayed in Figure 4(a). The reconstructed beam phase space using a Ramp filter is depicted in Figure 4(b). The RMS error for different filters in the "sci-kit image" module is calculated by subtracting the original phase-space distribution from the reconstructed beam distribution. The RMS error for different filters are shown in Figure 5. The red errors in Figure 5 indicate pixels that are missing from the reconstruction, while the blue errors represent artifacts that were introduced during the reconstruction process.

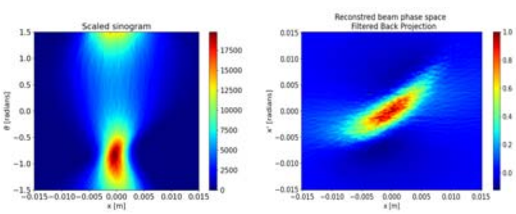

Figure 4. (a) Scaled Sinogram, and (b) the reconstruted beam phase-space distribution

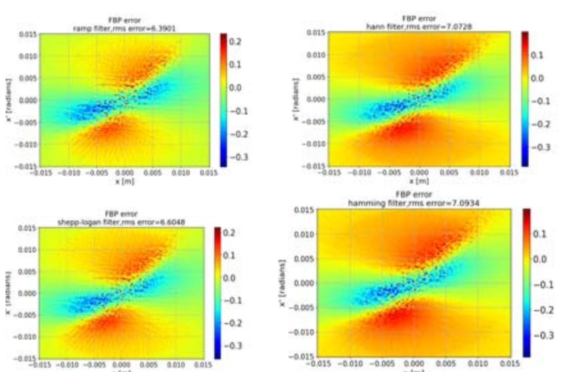

Figure 5. RMS error for (a) Ramp filter, (b)Hann filter, (c) Shepp-logan filter, and (d) Hamming filter.

SUMMARY AND CONCLUSION

In conclusion, the filtered back projection (FBP) algorithm was successfully applied to reconstruct the two-dimensional phase-space beam distribution at the entrance of a FODO lattice using various one-dimensional beam profiles at the exit of the channel at different orientation angles. The results indicate that the Ramp Filter has the lowest root mean square (RMS) error among the different filters simulated. This reconstruction technique can be applied to the measured beam in further studies. It is worth noting that the missing pixels in the reconstructed image are predominantly located away from the beam centroid. Overall, the findings suggest that this tomographic reconstruction approach can be a useful tool for characterizing the beam properties in accelerator physics.

REFERENCES

[1] A. C. Kak, and M. Slaney, “Principles of Computerized Tomographic Imaging,” New York, NY, IEEE Press, 1988.

[2] V. Yakimenko, M. Babzien, I. Ben-Zvi, R. Malone, and X. –J. Wang, “Electron beam phase-space measurement using a high precision tomography technique,” Phys. Rev. ST Accel. Beams 6, 122801 (2003).

[3] C. B. McKee, P. G. O’Shea, J. M. J. Madey, “Phase space tomography of relativistic beams,” Nucl. Instrum. Methods Phys. Res. A 358, 264 (1995).

[4] Stratakis, D., et al., "Tomography as a diagnostic tool for phase space mapping of intense particle beams" Physical Review Special Topics-Accelerators and Beams 9, no. 11 (2006): 112801.

[5] Watts, A., “Transverse Phase Space Tomography in Beamlines”, Tenth International Conference on Charged Particle Optics, 2018.

[6] https://scikit-image.org/

[7] Jupyter Notebook, Python

*Work supported by BARC, Mumbai and HBNI, Mumbai
#pallavip@barc.gov.in

COHERENT AND INCOHERENT SPACE CHARGE RESONANCES IN A DRIFT TUBE LINAC

Rajni Pande#,

Ion Accelerator Development Division, BARC, Mumbai 400 085

#rajnip@barc.gov.in

Abstract

High intensity proton accelerators for various applications are required to operate at high beam currents. At these currents, the non-linear space charge forces are very high and can lead to increase in beam emittance and formation of beam halo. The main design goal in high intensity accelerators in order to allow hands on maintenance is to minimize the beam loss by avoiding or minimizing contributions of various halo forming mechanisms. Among the various mechanisms for beam loss, there are two main mechanisms, which can cause significant halo formation: Incoherent and coherent effects due to the nonlinear space charge forces of the high intensity beam. These can lead to beam degradation causing increase in beam size, beam emittance and halo formation. We analyse these aspects for the case of a proton beam that is accelerated in a Drift Tube Linac from 3 MeV to 40.5 MeV.

INTRODUCTION

The coherent effects represent the collective behaviour of the beam as a whole. These are excited by beam mismatch and can lead to resonances and instabilities of the beam envelope. The envelope resonances are excited for $\boldsymbol{\sigma}_0$ > 180°/N, where $\boldsymbol{\sigma}_0$ is the zero current phase advance per period and N is an integer representing the order of the envelope resonance. The 2nd order envelope instability for N = 2 is a well-known collective effect of the beam as a whole and occurs for $\boldsymbol{\sigma}_0$ > 90°, and is responsible for accelerator designers keeping the zero current phase advance $\boldsymbol{\sigma}_0$ less than 90° [1]. For, $\boldsymbol{\sigma}_0$ > 90°, the envelope instability is excited for a range of σ values, where σ denotes the full current phase advance of the beam envelope. For N = 3, 4, 5… the corresponding envelope resonances are also excited in the beam in the presence of mismatch [2, 3].

The incoherent effects, on the other hand, represent the single particle behaviour of the beam and can be seen as single particle resonances. The single particle resonances are excited when the resonance condition mk_{xy} = 360° is satisfied. Here, m is the order of the single particle resonance and k_{xy} is the single particle phase advance per focusing lattice period in the presence of space charge. Here, m represents the number of lattice periods it takes for the particle to complete one full oscillation. The incoherent effects are excited even in the absence of beam mismatch.

Studies were done on a Drift Tube Linac (DTL) [4] that accelerates proton beam from 3 MeV to 40.5 MeV for a FODO focusing lattice. A single 24.31 m long DTL tank is assumed to accelerate the beam from 3 MeV to 40.5 MeV. This is done to minimize the introduction of mismatch between different tanks. In order to study the resonances in the DTL, the transverse phase advance per period in the DTL is varied from 60° to 130° for beam currents of 10 and 30 mA and the effect on beam emittance is seen. The results are shown in Figure 1. We see emittance growth at around 60°, 90° and 120°. It is also seen that the width of the resonance increases as the beam current increases. The increase in emittance at 90 degrees can be identified as the combined effect due to the 2nd order envelope instability and the fourth order resonance [5]. In the following sections, we analyse the emittance increase at the other peaks.

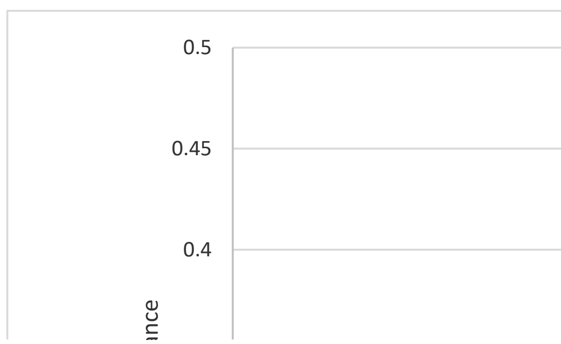

Figure 1. Variation of emittance with phase advance in the DTL.

SINGLE PARTICLE RESONANCES

It is seen that, for a well matched beam at the input of the DTL, the beam envelope from the envelope calculations remains stable throughout except in the envelope instability region around 90°. This indicates that the emittance increase in the other regions is due to single particle effects in the beam. The single particle resonances are the incoherent effects due to single particles. We analyse the beam phase space along the DTL for a matched beam at the input and try to identify the single particle resonance.

Third order single particle resonance

For σ_0 of 125° and a beam current of 30 mA, we see a 6-fold structure in x and y in phase space. If we see the particles on the 6-fold structure, they come back to the same position in phase space after 3 FODO periods. This can be seen in Figure 2 (Element 128-134. Two elements correspond to a FODO period). In other words, it takes 3 FODO lattice periods for the particles to complete one full oscillation. Hence, m = 3 and this corresponds to a 3rd order single particle resonance. The increase in beam emittance is shown in Figure 3.

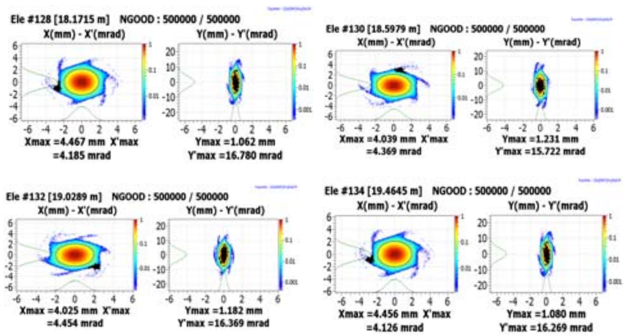

Figure 2. It takes the selected particles in beam phase space in X (shown in black) 3 FODO periods to come back to the same position in phase space indicating a 3rd order particle resonance.

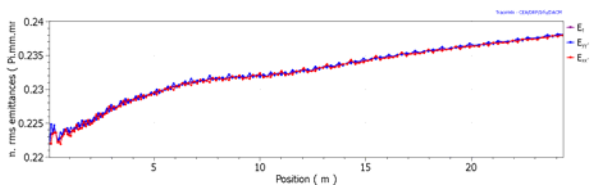

Figure 3. Increase in rms emittance for $\sigma_0 = 125°$.

Sixth order single particle resonance

For σ_0 of 65° and a beam current of 30 mA, we see a 6-fold structure in x and y in phase space. If we see the particles on the 6-fold structure, they come back to the same position in phase space after 6 FODO periods. This can be seen in Figure 4 (Element 142-154. Two elements correspond to a FODO period). In other words, it takes 6 FODO lattice periods for the particles to complete one full oscillation. Hence, m = 6 and this corresponds to a 6th order single particle resonance. The increase in beam emittance is shown in Figure 5.

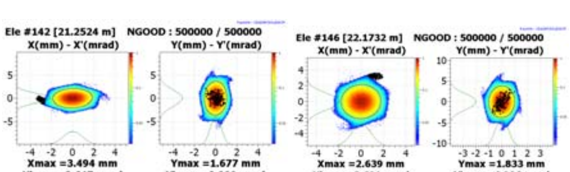

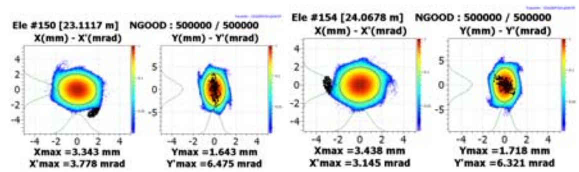

Figure 4. It takes the selected particles in beam phase space in X (shown in black) 6 FODO periods to come back to the same position in phase space indicating a 6th order particle resonance.

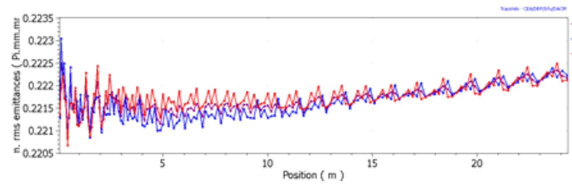

Figure 5. Increase in rms emittance for $\sigma_0 = 65°$.

It can be seen from Figure 6 that the emittance growth for the 3rd and 6th order resonances is more for the Gaussian distribution than the uniform distribution. The single particle effects are excited due to the non linearity of the space charge. A Gaussian beam is more non-linear than a uniform beam, hence the increase in emittance is more for a Gaussian beam. Note that the increase in emittance around 90° is both due to coherent and incoherent effects.

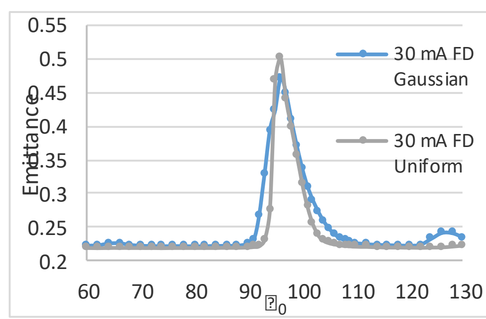

Figure 6. Variation of beam emittance with phase advance for uniform and Gaussian distribution.

ENVELOPE RESONANCES

The envelope resonances are a coherent effect of the beam envelope and are excited in the presence of beam mismatch.

For $\sigma_0 > 60$ degrees, Figure 7 (a) shows the beam envelopes in x and y without any mismatch. Figure 7 (b) shows the beam envelopes in x and y in the presence of 20 % mismatch. In the presence of mismatch, we see that an additional oscillation is superimposed on the betatron oscillations. For $\sigma_0 > 60$ degrees, we see that the periodicity of the additional oscillation corresponds to 3 betatron periods indicating a 3rd order envelope resonance. This can be seen clearly in Figure 7 (c) where the beam envelopes in x and y are plotted for the first few periods.

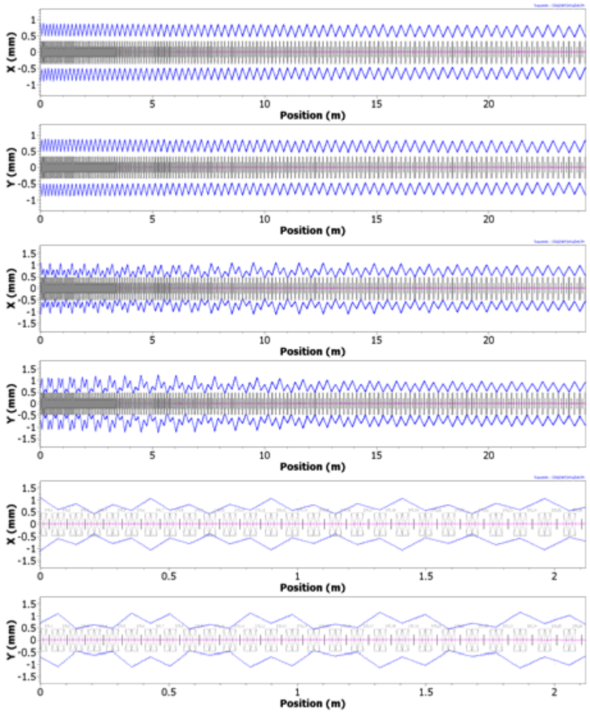

Figure 7 (a) The beam envelopes in x and y without any mismatch for σ_0 > 60 degrees, (b) the beam envelopes in x and y in the presence of 20 % mismatch, (c) the beam envelopes in x and y are plotted for the first few periods in the presence of 20 % mismatch.

In Figure 8 the beam envelopes in x and y are plotted for the first few periods for $\sigma_0 > 45°$. Here, we see that the periodicity of the additional oscillation corresponds to 4 betatron periods indicating a 4th order envelope resonance.

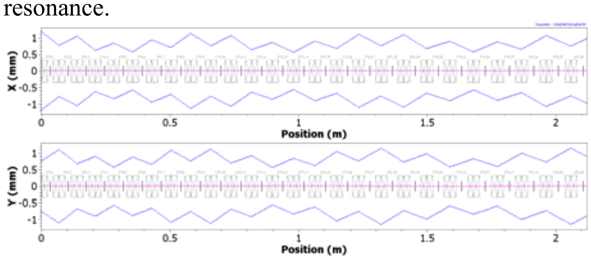

Figure 8. The beam envelopes in x and y for the first few periods for σ_0 > 45 degrees in the presence of 20 % mismatch.

SUMMARY AND CONCLUSIONS

We have studied the increase in beam emittance in a DTL due to coherent and incoherent effects due to beam space charge. It is seen that for a well matched beam at the entrance of the DTL, there is increase in beam emittance at a phase advance of around 60°, 90° and 120°. The increase in beam emittance at around 60° and 120° corresponds to single particle resonances that are incoherent effects. The envelope resonances that are coherent beam effects are excited only in the presence of beam mismatch except for the 2nd order parametric resonance that is an instability and can be excited even from an infinitesimal mismatch. The increase in beam emittance at around 90° is due to the envelope instability and 4th order single particle resonance [5].

REFERENCES

[1]. J. Struckmeier and M. Reiser, Part. Accel. 14, 227 (1984).

[2]. C. Chen and R. C. Davidson, Phys. Rev. Lett. 72, 2195 (1994).

[3]. Chen, Chiping, and Ronald C. Davidson, Physical Review E 49, no. 6 (1994): 5679.

[4] Rajni Pande, Shweta Roy, S.V.L. S Rao, P. Singh and S. Kailas, Pramana-J Phys., 78, 247 (2012).

[5]. Rajni Pande, Comparison studies of the 90° stopband in a DTL for different focusing lattices, Indian Particle Accelerator Conference, VECC, Kolkata, India, March 22-25 2022.

DEVELOPMENT OF PULSE AND EVENT SYNCHRONIZATION SYSTEM FOR LEHIPA

Deepak N. Mathad*, L. D. Tayade, P. R. Parate, A. Basu, S. K. Singh, IADD, BARC, Mumbai.

Abstract

A multi-channel digital pulse synchronization system is developed for LEHIPA Facility at BARC. This system provides the timing pulses for various sub-systems of the accelerator. The hardware is based on cPCI backplane and the basic pulse structure is generated by three programmable timer cards. In-house designed digital electronics board is used with each timer card to implement additional functionalities such as external / internal interlocks and external triggering, providing ease of reconfiguration. The EPICS driver for the timer cards is developed based on asynportdriver module. The EPICS IOC is hosted on a linux-based cPCI system controller. The system is successfully deployed in LEHIPA. Details of implementation of the system is discussed in this paper.

INTRODUCTION

The Low Energy High Intensity Proton Accelerator (LEHIPA) [1] is a 20 MeV, 10 mA proton accelerator being commissioned at BARC. It is operated in pulsed mode and hence various subsystems like high voltage power supplies, ion source, RF systems and data acquisition. The delay (relative to a master pulse) and pulse width of each timing pulse are independently configurable, however all pulses have a common repetition rate. The hardware used includes Adlink cPCI-8554 Timer/Counter cards that produce the synchronization pulses and in-house developed digital electronics for conditioning of pulses and interlocking. EPICS IOC [2] is developed based on asynportdriver and the GUI is developed on Qt-EPICS framework.

PULSE SYNCHRONIZATION SYTEM FOR LEHIPA

In LEHIPA, the subsystems that require pulse synchronization are ECR ion source, LLRF systems (for RFQ, buncher, DTL-1&2 and DTL-3&4), pulse modulator, RHVPS-2, RHVPS-3, beam diagnostics and data acquisition. The delay and pulse width requirements vary over different subsystems. The functional requirements of the pulse synchronization system for LEHIPA are as given in Table 1. The pulse related specifications of the system are summarized in Table 2 [3]. Compact PCI (cPCI) backplane based systems are used in various subsystems in LEHIPA and as a quick solution, the required system was developed with the cPCI-compatible hardware readily available with the facility.

* deepaknm@barc.gov.in

Table 1: Functional requirements of pulse synchronization system for LEHIPA

Parameter	Description
Repetition rate	Common for all subsystems
Pulse width	Independently settable
Delay (w.r.t master)	Independently settable
Interlock	All pulse outputs to be inhibited on interlock input signal going LOW.
Pulse output signal type	Electrical (TTL/LVTTL) Optical

Table 2: Summary of specifications (operational, at present) of pulse outputs for LEHIPA

Parameter	Description
Maximum repetition rate	2 Hz
Delay (w.r.t. master)	2 ms to 300 ms
Delay resolution	1 ms for RHVPS, 1 µs for other subsystems
Pulse width (ON time)	RHVPS : 10 ms to 300 ms Pulse modulator: 400 µs ECR IS: 1 ms to 5 ms LLRF (RFQ, buncher, DTLs): 20 µs to 5 ms Beam diagnostics: 25 µs to 5 ms
Pulse width resolution	1 ms for RHVPS, 1 µs for other subsystems
Interlock	External input signal (0 V ⇒ Fault, 5 V ⇒ No Fault). All pulse outputs have to be inhibited within 1 µs after occurrence of fault.

Structure of timing synchronization pulses

The common repetition rate is set by the master clock which is a square wave signal. Its rising edge is the reference for the delay parameter the pulse outputs. Once the delay time is elapsed, the pulse output will go high for the duration set by the pulse width / ON-Time parameter is elapsed (figure 1). This is applicable for all subsystems except RHVPS (2 & 3) where there are separate START and STOP pulses. The time duration between the rising edge of START and the falling edge of STOP is the actual ON time of the RHVPS (figure 2). The timing signals for RHVPS are in the form of optical pulses. The START pulse light goes ON for 5 ms after the delay is elapsed. The STOP pulse light goes OFF for 5 ms after the ON time is elapsed.

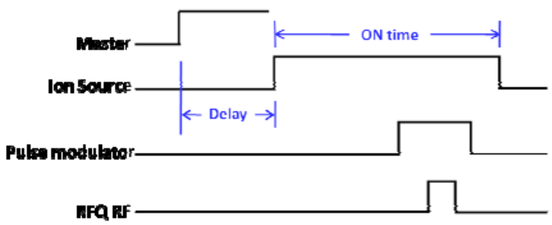

Figure 1: Pulse structure for subsystems (except RHVPS)

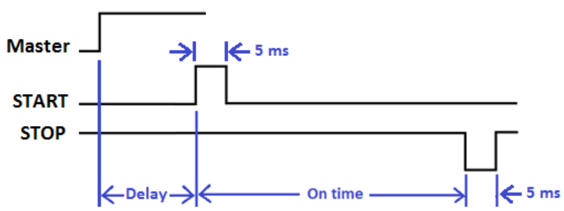

Figure 2: Pulse structure for RHVPS

Generation of basic timing signals

The basic timing pulses are generated using Adlink cPCI-8554 [4] timer/counter cards, that were available with LEHIPA facility. Each of these cards has twelve 16-bit counters (10 independent and 2 cascaded) and 8 MHz onboard clock for internal timebase. Using one counter with the timebase of 8 MHz, timing resolution of 125 ns and a maximum time duration of 8.2 ms can be achieved. For achieving longer time duration, multiple counters can be cascaded or lower frequency clock can be used for timebase. Timebase of 2 kHz is used for primary master clock (that sets the common repetition rate). With this, the minimum and maximum repetition rates achievable are 0.0305 Hz and 1 kHz, respectively. However at present, the operational maximum repetition rate is restricted to 2 Hz only. For timing greater than 8 ms and in the range of few tens of milliseconds to few hundreds of milliseconds, a timebase of 200 kHz is used. With this, minimum and maximum ON time / delay time of 10 µs and 327 ms, respectively can be achieved using one counter. Two counters are required for one pulse output – one for delay time (with respect to master) and another for ON time. These counters are used in 'ONE_SHOT' program mode wherein on every rising edge on its GATE input, the counter output goes LOW for the set duration and then goes HIGH.

The pulse-to-pulse jitter with respect to the rising edge of master (at GATE input) pulse can be minimized by increasing the frequency of timebase as its worst case value is one time period of the timebase. So, for pulse outputs that require delay in the range of few tens to hundreds of milliseconds (i.e., for subsystems except RHVPS), a secondary master pulse that is delayed with respect to the primary master clock is used as the reference at GATE input and the internal timebase of 8 MHz is used to generate additional delays as required up to 8 ms on individual pulse outputs. As the ON time of subsystems other than RHVPS require not more than 8 ms until near future, the same internal timebase of 8 MHz is used. With this setup, the pulse-to-pulse jitter is reduced to minimum possible of 125 ns, relatively among the pulse outputs. There is a maximum jitter of 5 µs due to 200 kHz timebase on the secondary master pulse, but as this is the common reference, there will be no additional effect on the jitter of pulse outputs for subsystems (except RHVPS), relative to each other. In case of RHVPS, the references for delay time and ON time are primary master clock and secondary master pulse, respectively. Hence, there is a worst case jitter of 5 µs + 125 ns = 5.125 µs between pulse outputs of RHVPS and other subsystems.

Custom designed electronics

Custom digital electronics (Timing System Electronics) is designed and fabricated for conditioning of the pulse outputs from the cPCI timer cards and to implement external/internal interlocks and inhibiting the pulse outputs. One board supports one cPCI timer card and can have maximum of 8 output pulses with corresponding 8 optical output channels. There is a 100-pin screw terminal block that gives full access to the timer card and the wiring is done according to the field requirement. So, the design is flexible and modular. There are jumper settings for individual channels to invert the raw pulse outputs and TTL / LVTTL output selection. All input and output signals are isolated.

There is an input port for external interlock signal which must be high for all pulse outputs to be enabled. If there is a fault in any of the subsystems, the interlock signal goes low and all the pulse outputs are inhibited (0 V), thereby stopping the operation of the accelerator. The interlock signal is latched using a PLC and can be reset manually. The response time to inhibit the pulse output after assertion of the external interlock signal is measured and is about 250 ns (figure 3).

Figure 3: Response time for pulse inhibition on interlock.

Distribution of timing signals

At present, three sets of timer cards and timing system electronics are used. The first set is used to generate the primary master clock, secondary master pulse and RHVPS pulse outputs. The other two generate the pulses for other subsystems as listed in table 1. TTL signal repeaters are used to fanout the timing pulses and distribute to various systems requiring the same timing signal. The delays (< 1 µs) due to cables used for distribution are not critical as of now in LEHIPA. Figure 4 depicts the components used for generation and distribution of timing signals in LEHIPA. As an additional protective measure, the AC power input to the timing system electronics and the repeaters is cut off through relays whenever there is a fault sensed by the external interlock signal.

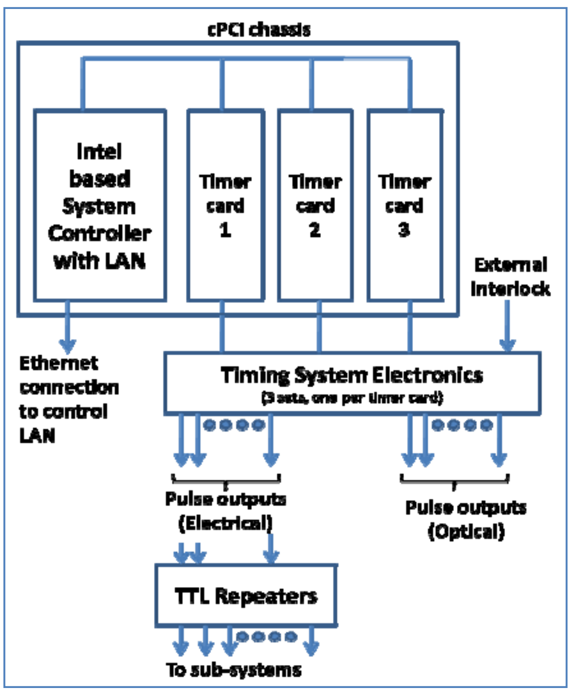

Figure 4: Distribution of timing signals

SOFTWARE DEVELOPMENT AND INTEGRATION

The application software is developed based on EPICS Asynportdriver module which also contains the code to program the timer cards. Modular approach is followed in coding and no changes in basic code are required to add more channels. The process variables (PVs) corresponding to the delay times and ON times have their limits configured in the EPICS database of the application. The system is configured such that the EPICS IOC automatically runs when the system controller boots. With EPICS compatibility, the timing system is directly integrated with the main control console of LEHIPA. The GUI (figure 5) is developed using Qt-EPICS framework. The system was deployed in LEHIPA after extensive testing in lab and is working satisfactorily.

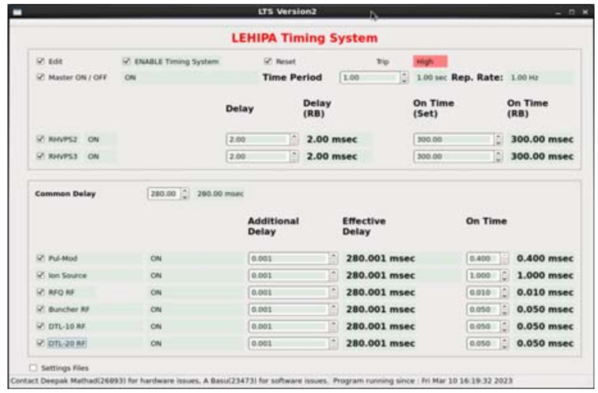

Figure 5: GUI for LEHIPA timing system.

CONCLUSIONS

The pulse synchronization system for LEHIPA is designed and developed based on cPCI platform. Custom digital electronics is designed for conditioning of the pulse outputs from the timer card and to implement interlocking with external fault signal. Primary master clock and secondary master pulse are used to get the best possible pulse-to-pulse jitter performance and optimization is done between the jitter performance and the requirement of longer timing durations. The application software is developed based on EPICS asynportdriver and the GUI is developed in Qt-EPICS framework. The system is tested , deployed in field and integrated with the main LEHIPA control system. The operational experience with this system is satisfactory.

ACKNOWLEDGEMENTS

We wish to gratefully acknowledge our colleagues at IADD, BARC for their inputs and feedback on the system developed. We also thank Dr. S. Krishnagopal, Head, IADD, BARC for his support to this work.

REFERENCES

[1] P. Singh et al, "Accelerator Development in India for ADS Programme", PRAMANA Journal of Physics, Vol. 68, No. 2, February 2007, pp. 331-342.

[2] Experimental Physics and Industrial Control System http://www.aps.anl.gov/epics.

[3] S. K. Singh, "Specifications for LEHIPA Timing System", Internal Document.

[4] User Manual – Adlink cPCI 8554 Timer/Counter card.

[5] A. Rhyder, "QE Framework – QEGui and User Interface Design", Australian Synchrotron.

COLD TEST AND RF TUNING OF THE FIRST SECTION OF 3 MeV, 325 MHz RFQ AT RRCAT

R. Gaur# [1,2], N. S. Kulkarni[1], V. Kumar[1,2], G. V. Kane[1], N. K. Sharma[1], A. Chaturvedi[1], V. Prasad[1], K. A. P. Singh[1], V. Rajput[1], D. Baxy[1], M. Lad[1] and P. Shrivastava[1]
[1]Proton Accelerator Group, Raja Ramanna Centre for Advanced Technology, Indore
[2]Homi Bhabha National Institute, Mumbai

Abstract

A 325 MHz, 3 MeV four-vane Radio Frequency Quadrupole (RFQ) linear accelerator has been designed, and is under fabrication at RRCAT, Indore for the envisaged Indian Facility for Spallation Research (IFSR). Total length of RFQ will be 3.49 m, and it will consists of three sections, which will be directly coupled to each other. Recently, the final machining and assembly of the 1.162 m long first section was completed, after which its low power characterization and RF tuning experiments have been performed. In this paper, we present the details about the methodology and results of cold test and RF tuning experiments for the first section of the RFQ.

INTRODUCTION

A 325 MHz Radio Frequency Quadrupole (RFQ) will be the pre-accelerator for the 1 GeV injector linac of envisaged Indian Facility for Spallation Research (IFSR) at RRCAT, which will be used for multidisciplinary research using high flux of pulsed neutrons [1]. The four-vane RFQ is designed to accelerate 50 keV H^- ion beam to 3 MeV in a total length of 3.49 m [1]. To facilitate machining and brazing, the RFQ cavity is divided in three sections along the longitudinal direction. Each section will consist of two major vanes and two minor vanes, each of about 1.16 m length. The three sections will be directly coupled to each other. Recently, the first section of RFQ has been assembled after final machining of the copper vanes. In the first section of RFQ, there are four tuners per quadrant to tune the cavity for desired frequency and field profile, one vacuum port per quadrant to achieve desired vacuum level in the cavity, and one sampling port per quadrant to sense the field for control purpose. To characterize the RF performance of the first section of RFQ, and to validate the in-house developed computer program for RF tuning of RFQ [2], the cold test and tuning exercises are performed. The first section has a provision of vane-end cutback at the entrance end; however, it does not terminate with a vane-end cutback at the exit end, which is necessary to satisfy the boundary condition of the operating TE_{210} mode, while testing it standalone. Therefore, a temporary end termination, which includes four unmodulated vanes with cutback, is designed, fabricated in aluminum, and used at the exit end of the first section for its standalone RF characterization. After machining and cleaning, individual segments of the RFQ section are mounted, assembled and aligned on the bead-pull test stand, which was developed earlier during characterization of the 3 MeV prototype RFQ [3].

DESIGN OF END TERMINATION

A 55 mm long temporary end termination, as described in the previous section, is designed using 3D EM code CST-MWS [4], to be attached at the exit end of the first section of RFQ. The geometrical parameters of vane-end cutback are optimized such that it resonates at the same frequency as that of the first section of RFQ with tuners at their nominal position, *i.e.*, 9.8 mm inside the cavity. A schematic of vane-end cutback with unmodulated vane is shown in Fig. 1, and the optimized geometrical parameters are listed in Table 1. The end termination piece is fabricated in-house by cutting a solid aluminum cylinder using EDM wire cut machine.

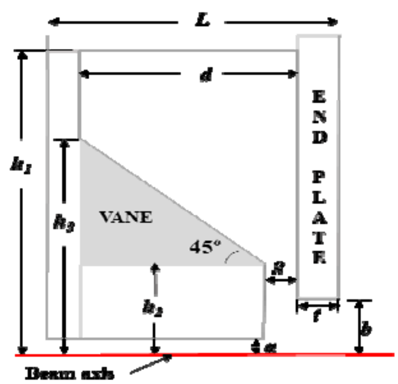

Fig. 1: Schematic of unmodulated vane with cutback.

Table 1: Geometrical parameters of vane-end cutback

Parameter	Value
g	5.00 mm
h_1	103.38 mm
h_2	30.00 mm
h_3	65.43 mm
d	40.43 mm
t	10.00 mm
b	20.00 mm
a	3.56 mm
L	55.00 mm

MEASUREMENT SET UP

To observe the EM field in an RFQ, bead-pull measurements [5] are performed, which is based on Slater

#rahul@rrcat.gov.in

perturbation theorem. As the bead enters the cavity, the resonant frequency as well as the phase of S_{21} parameter changes due to perturbation. Magnitude of electric field E in a quadrant of RFQ is related to S_{21} phase shift ($\Delta\phi$) as well as frequency shift ($\Delta\omega$) due to dielectric bead in that quadrant through the relation [5]

$$\tan(\Delta\phi)\Big|_{\omega_0} = 2Q_L\frac{\Delta\omega}{\omega_0} = -2Q_L\frac{3\Delta V}{4U}\frac{\epsilon_r - 1}{\epsilon_r + 2}\epsilon_0 E^2 \qquad (1)$$

where ω_0 is the unperturbed resonant frequency, Q_L is loaded quality factor, ΔV is volume of bead, U is stored energy in the field, ε_r is dielectric constant of the bead and ε_0 is the free space permittivity. Therefore, the field can be calculated by the measurement of either the square root of frequency shift or the square root of tan($\Delta\phi$).

The bead-pull set-up consists of various components - (1) Vector Network Analyzer (VNA) (Agilent E5071C), (2) pulley system (dielectric bead, nylon thread, and stepper motor), (3) test stand to hold the RFQ cavity and pulley system, and (4) LabVIEW program [6], which is developed in-house to control the pulley system and to collect the measurement data from VNA. The bead-pull set-up is shown in Fig. 2.

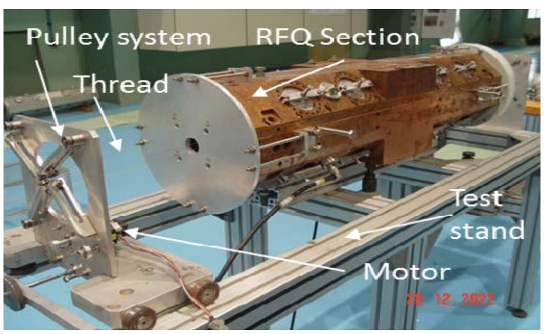

Fig. 2: Bead-pull set-up for first section of RFQ.

The set-up supports movement of pulley system, which helps in adjusting the tension of the nylon thread. An aluminum adapter is fabricated in-house, which consists of four slots in radial direction of quadrants to keep the bead at the bisector of the quadrants, and marking of circles of different radii to ensure the same radial location of bead at the bisector in each quadrant.

MEASUREMENTS AND RESULTS

For cold test of the RFQ section, four under-coupled loops are inserted in the four quadrants of the cavity through sampling ports, as shown in Fig. 3. At a time, one loop is used to feed a small RF power in the cavity, and another is used to pick up the signal. Measurements of S-parameters in reflection and transmission mode are performed, using a VNA to determine the resonant frequency of the electromagnetic modes in the cavity, as well as to identify these modes. All the tuners are set at their nominal position initially. In the relevant frequency span (315-330 MHz), the resonant modes are found at the frequency 320.8 MHz, 322.6 MHz and 325.1 MHz by observing the dips of S_{11} or the peaks of S_{21} parameter. The frequency spectrum of S_{21} for this RFQ section is shown in Fig. 4.

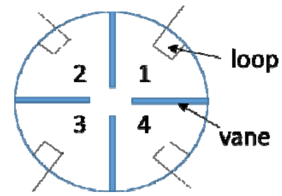

Fig. 3: Schematic of loops insertion in the four quadrants.

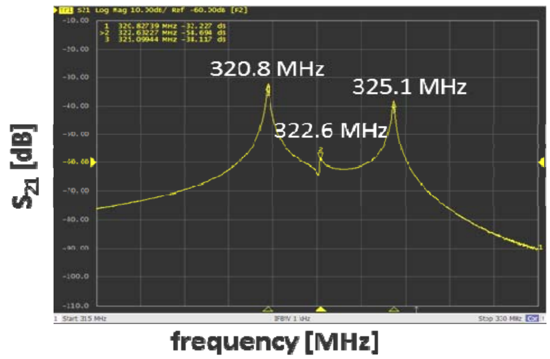

Fig. 4: Frequency spectrum of S_{21} for the RFQ section.

For identification of the modes as dipole or quadrupole modes, the phase measurement of S_{21} is performed. Phase of S_{21} is found to be almost same in all the four quadrants ($\Delta\phi \approx \pm 1^o$) for the mode at 325.1 MHz, which ensures that this is the quadrupole mode. On the other hand, the S_{21} phase difference is 173º and 166º between the diagonally opposite quadrants at frequencies 320.8 MHz and 322.6 MHz, respectively, which is ~180º, and therefore, ensures that these are dipole modes. Out of these dipole modes, the Dipole-1 mode at 320.8 MHz couples the quadrants 1 and 3, whereas the Dipole-2 mode at 322.6 MHz couples the quadrants 2 and 4. This is ensured by observing the S_{21} peaks, while keeping the feeder loop and pickup loop in the diagonally opposite quadrants. In case, the power is fed through the 1st quadrant and signal is picked up from the 3rd quadrant, the S_{21} peak at 320.8 MHz is dominant, which is shown in Fig. 4. Whereas, the S_{21} peak at 322.6 MHz is dominant in case the power is fed through the 2nd quadrant and signal is picked up from the 4th quadrant. Note that the unloaded quality factor Q_0 at 325.1 MHz frequency is found to be 4000 using VNA with under-coupled coupler having coupling coefficient 0.08. Theoretical value of Q_0, as obtained using CST-MWS simulation, is 9700. It is expected that Q_0 will increase further after brazing of the RFQ segments.

Further, the bead pull measurements are performed to determine the off-axis electric field profile in each quadrant of the RFQ section. During measurement, a spherical dielectric bead (diameter 6 mm) attached to a nylon thread is pulled inside the cavity in discrete steps using a stepper motor. In case of small perturbation, the phase shift measurement is more accurate than the frequency shift measurement; therefore, the phase shift of S_{21} due to perturbation is measured for the field calculation. The off-axis electric field profile in each quadrant of the RFQ section is shown in Fig. 4. Using these field profiles, the maximum value of fractional error due to dipole components is calculated to be 35% and 13%, corresponding to the mixing of Dipole-1 mode and Dipole-2 mode, respectively, which is shown in Fig. 5, using dotted curves. The Dipole-1 and Dipole-2 components of fractional field error are calculated using $(U_1-U_3)/(U_{q0}\times\mathrm{sqrt}(2))$ and $(U_2-U_4)/(U_{q0}\times\mathrm{sqrt}(2))$, respectively, where U_i is the value of intervane voltage (proportional to off-axis electric field) in the i^{th} quadrant (i = 1, 2, 3, and 4), and U_{q0} is the average value of $(U_1-U_2+U_3-U_4)/2$ over the length of RFQ section. A possible reason of the initial field error in the operating mode may be identified as a positional offset of the vanes, based on the case study of misalignment error discussed in Ref. [2]. Note that the quadrupole component of fractional field error $(((U_1-U_2+U_3-U_4)/2)-U_{q0})/U_{q0}$, corresponding to the mixing of higher quadrupole modes in the operating mode, is calculated to be less than 5%, which is acceptable from beam dynamics considerations [7].

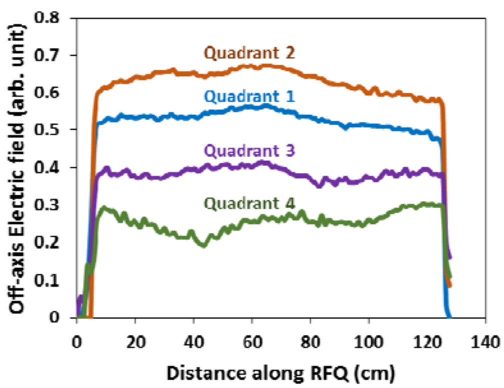

Fig. 4: Field profile in the RFQ quadrants before tuning.

The in-house developed computer program [2] for RF tuning based on transmission line model of RFQ is used to tune the RFQ at desired frequency and field profile by minimizing the fractional field error in the operating mode. After four iterations of the tuning program, the penetration depth of the four tuners are found to be 11.0 mm, 10.9 mm, 10.8 mm, and 10.7 mm in the 1st quadrant, 10.5 mm, 10.4 mm, 10.2 mm, and 10.1 mm in the 2nd quadrant, 13.0 mm, 12.9 mm, 12.7 mm, 12.6 mm in the 3rd quadrant, and 13.5 mm, 13.4 mm, 13.3 mm, and 13.2 mm in the 4th quadrant, inside the cavity. After setting the tuners at the calculated penetration depths, the dipole components of fractional field error are reduced to 4%, which is less than the maximum acceptable value of 5%, and is shown in Fig. 5 using solid curves. The field profile in each quadrant of the RFQ section after tuning is plotted in Fig. 6. Repeatability of the measurements is also checked by varying the radial location of the bead and the penetration depth of tuners. The measurements are found to be repeatable within ± 2%.

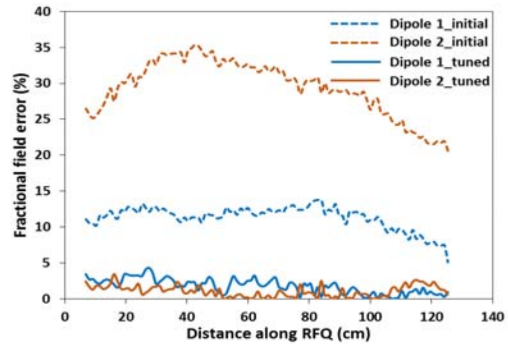

Fig. 5: Dipole components of fractional field error before tuning (dotted curves) and after tuning (solid curves).

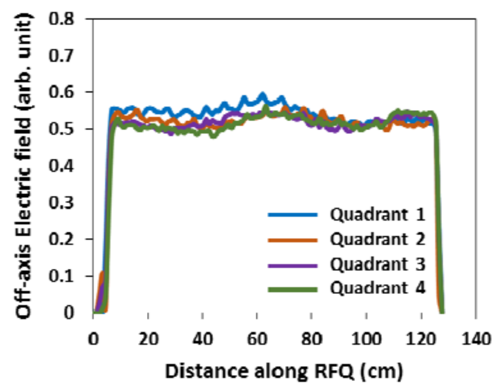

Fig. 6: Field profile in the RFQ quadrants after tuning.

CONCLUSION

Cold test and RF tuning of the first section of IFSR RFQ have been performed. The results are encouraging, which confirm the quality of machining of RFQ components, and also validate the tuning program. The next step will be to braze the segments of this section and to perform measurements with beam.

It is a pleasure to thank Dr. S. V. L. S. Rao for very useful discussions on RFQ characterization and tuning.

REFERENCES

[1] R. Gaur and V. Kumar, *European Physical Journal N*, **4**, 9 (2018), pp. 1-17.

[2] R. Gaur and V. Kumar, *Nuclear Instr. and Methods in Physics Research A*, 991 (2021) 165021, pp. 1-13.

[3] S. C. Joshi *et al*, in *Proc. LINAC2014*, Geneva, Switzerland, Aug-Sep 2014, MOPP124, pp. 345-347.

[4] CST Studio Suite 2014, www.cst.com.

[5] N. Akkurt *et al*, *AIP Conference Proceedings* **2042**, 020061 (2018).

[6] V. Rajput *et al*, in *Proc. InPAC-2018*, Indore, Jan 2018, ID-04.

[7] R. Gaur and V. Kumar, *Pramana – J. Phys.* (2022) 96:126, pp. 1-12.

INITIAL INVESTIGATIONS ON DISTRIBUTION OF ABSORBED DOSE IN WASTE WATER TREATMENT USING ELECTRON BEAM

Kapil Deo# and Umasankari Kannan, RPDD, BARC, Mumbai, India
Jyoti Sharma, A. S. Dhavale and Archana Sharma, APPD, BARC, Mumbai, India

Abstract

Irradiation of waste water using high energy electron beam has been found to be capable of removing various organic compounds, which are otherwise difficult to be removed using conventional treatment methods. An industrial demonstration system (EBWWT - Electron Beam Waste Water Treatment) using 1 MeV electron accelerator has been designed at BARC. Using the FLUKA monte carlo code, dose distribution in the waste water film irradiated by accelerated electron beam, was studied. The simulations generated valuable data for optimization of the EBWWT accelerator parameters. The results of these monte carlo simulations of EBWWT is discussed in this paper.

OVERVIEW OF EBWWT

BARC has developed an industrial demonstration system (EBWWT) for treatment of waste water containing non-biodegradable pollutants. Upon interaction with high energy electrons, different reactive radicals are formed in the waste water. These radicals then break down the pollutants [1]. A test facility using 1 MeV DC electron accelerator at EBC, Kharghar [2] has been developed for waste water treatment. A schematic of EBWWT set-up is shown in Fig. 1. The accelerated electron beam passes

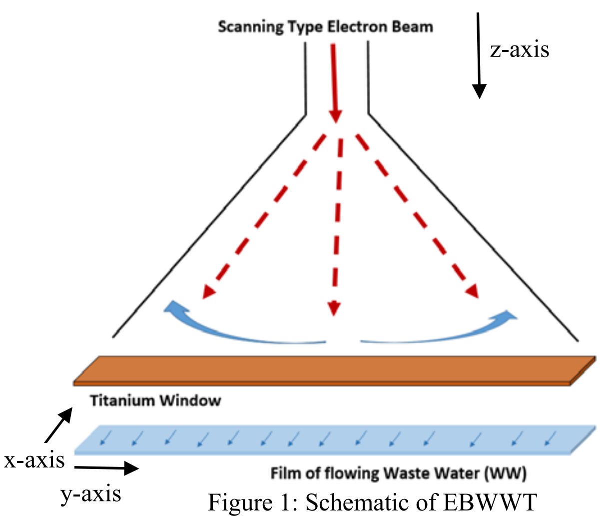

Figure 1: Schematic of EBWWT

through a thin Ti window and strikes the waste water flowing below in the form of a film. Monte Carlo simulations of the set-up was carried out using the FLUKA particle transport code [3, 4, 5] to study the distribution of absorbed dose distribution in the waste water film. Effect of various parameters om the flux distribution was also studied.

#: kapil@barc.gov.in

DESCRIPTION OF SIMULATION

The effectiveness of waste water treatment using electron beam, is dependent on the absorbed dose in the waste water. As mentioned earlier, for studying the distribution of this absorbed dose, monte carlo simulations were carried out using the FLUKA code. For initial investigations, the Ti foil and water film were modelled as a rectangular parallelepiped having cross-section 150 cm x 10 cm. The thickness of Ti foil was 50 µm and water film was assumed to be 4 mm thick. The centre of the Ti window and the waste water film lie on the z-axis. In actual set-up, the electron beam scans across the length and breadth of the Ti window. A series of static simulations were carried out to see dose profile corresponding to different positions of the electron beam. The point of interaction of the incident electron beam on the Ti window was varied across the length and breadth of the Ti foil.

Effect of variation of beam size on the absorbed dose was studied by changing the FWHM of beam size along x and y-axes. The electron beam was assumed to travel along positive z-axis and the beam shape was considered to be Gaussian in both the transverse direction. For optimisation of the distance between the Ti window and the waste water film, a separate set of simulations were carried out using beam size of 50 mm (FWHM). Finally, the variation of dose with depth of waste water was estimated.

All the simulations were carried out for 5 cycles with 10^6 particle histories in each cycle. The absorbed doses given in the subsequent sections are in the units of GeV/g/per primary particle.

RESULTS

Absorbed dose profile for 1 MeV electron beam

The first set of simulations were carried out to obtain the absorbed dose profile for the 1 MeV electron beam striking at the centre of the Ti window. The dose profile corresponding to this case is shown in Fig. 2. The distribution of electron and photon fluence for the case is shown in Fig. 3 and 4, respectively. Since, the electron beam scans across the length and breadth of the Ti foil, the point where the electron beam strikes the Ti foil was varied along both these directions. The locations of maximum absorbed dose in waste water for some of the incident locations of electron beam are shown in Table 1. The variation of dose profile for different position of beam along x-axis is shown in Fig. 5. As expected the dose profile is asymmetric for the case where the position of beam is near the edges.

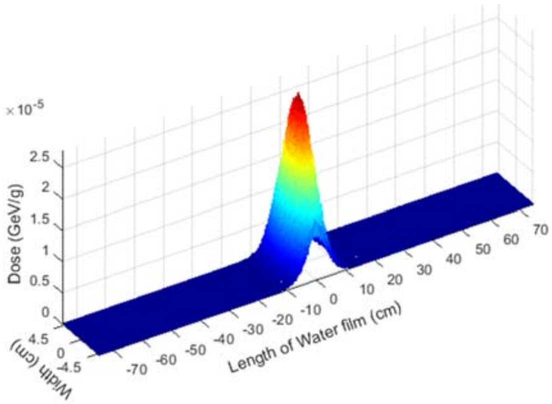

Figure 2: Absorbed dose variation for incident electron beam at the centre of Ti window

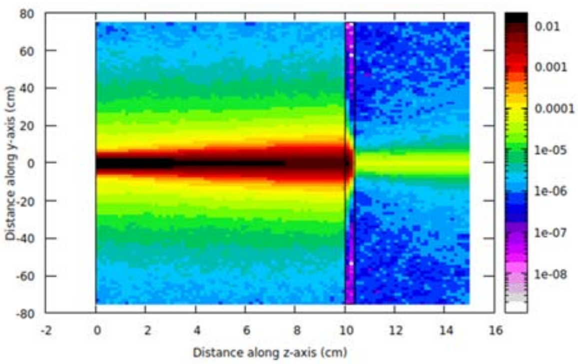

Figure 3: Electron fluence for EBWWT set-up (FWHM of beam = 50 mm)

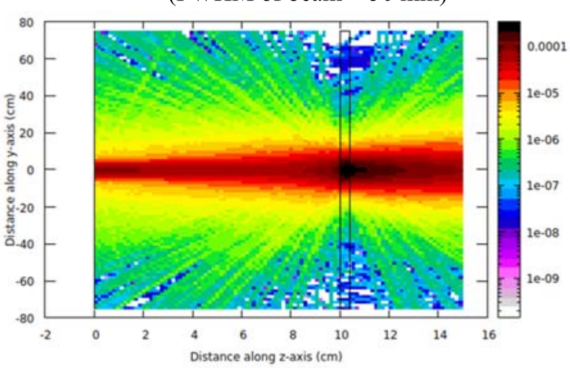

Figure 4: Photon fluence for EBWWT set-up (FWHM of beam = 50 mm)

Table 1: Location of maximum dose in waste water

Incident electron Beam		**Location of Maximum dose**	
X (cm)	Y (cm)	X (cm)	Y (cm)
0	0	-0.25	-0.08
0	-75	0.15	-74.78
0	75	0.15	74.78
-4.5	0	-4.85	-0.075
4.5	0	4.75	0.075

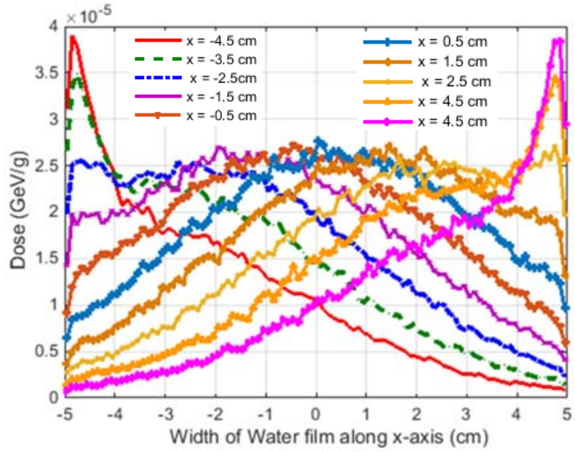

Figure 5: Dose profile for different x-position of beam

Effect of beam size variation

The beam size has a direct effect on the dose delivered to waste water. The dose profile in waste water was obtained by varying the FWHM of the beam from 10 mm to 50 mm along x and y-axes. For this study, the beam was assumed to be incident at the centre of Ti foil. The distance between Ti window and water film was kept as 10 cm. The variation of dose profile along-x-axis with different beam sizes is shown in Fig. 6. It can be clearly seen that for larger beam sizes, the dose is more uniformly distributed. However, the peak value of dose decreases as FWHM of beam is increased.

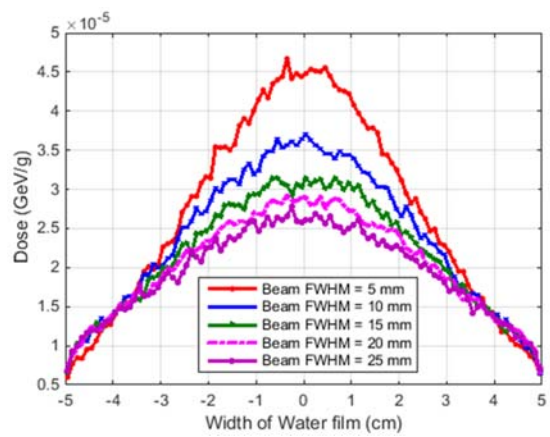

Figure 6: Variation of dose profile with beam size

Variation of absorbed dose with depth of film

The absorbed dose in the waste water is also dependent on the thickness of the film. In order to see the variation of absorbed dose with depth of film, the waste water film was divided into 1000 slices of equal thicknesses. The absorbed dose profile in each region was scored (see Fig. 7). The dose was found to be peaking at approximately 1 mm thickness.

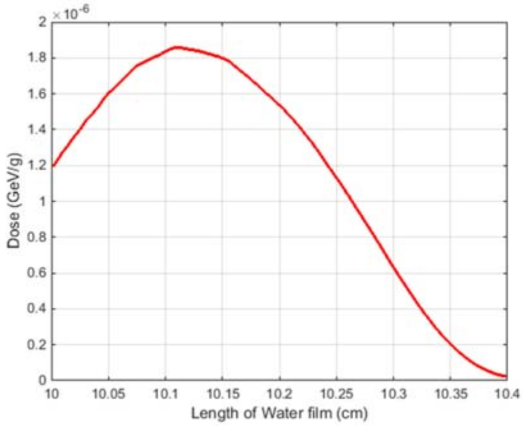

Figure 7: Variation of absorbed dose with depth of film

Effect of Ti window and Water Film separation

The uniformity of dose profile is also dependent on the distance between the Ti window and the waste water film. This distance should be optimised together with the beam size. For the present investigations, the effect of Ti window and waste water Film separation was studied for a beam size of 50 mm. For smaller separation between Ti foil and water film, the dose delivered is significantly higher. The peak dose corresponding to 1 mm separation is approximately 4 times that corresponding to 10 mm separation. The decrease can be attributed to the losses in air present in the intermediate region. As expected, the dose profile is becoming more uniform as the separation between the Ti window and waste water film is increased (see Fig. 8).

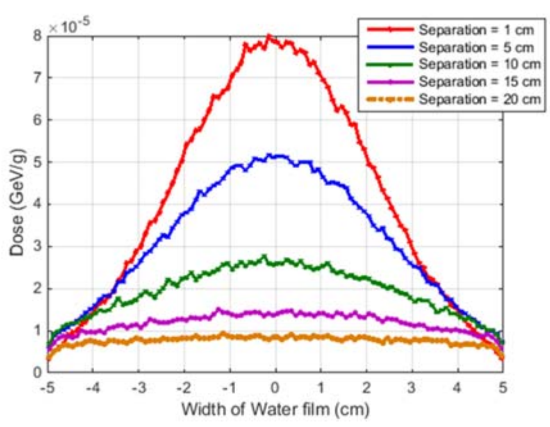

Figure 8: Dose profile for different Ti and waste water film separation

CONCLUSION

Monte carlo simulations of the EBWWT set-up was carried out to estimate the absorbed dose profile in waste water irradiated with 1 MeV electron beam. These simulations generated valuable data for optimization of the EBWWT accelerator parameters. The maximum dose delivered to waste water was found to be near the line of sight location of water film w.r.t. the incident location of electron beam on Ti foil. The peak value of absorbed dose per primary electron was approximately 2.5E-5 GeV/g for 50 mm FWHM electron beam incident at the center of the Ti window.

REFERENCES

[1] X. Li et. al., “Simulation studies on the interactions of electron beam with wastewater”, Proc. of IPAC21 held at Campinas, Brazil during 24–28 May, 2021.

[2] P. C. Saroj and DC Accelerator Team of EBC Kharghar, “Electron beam treatment of waste water”, pg. 57, BARC Newsletter, Vol. No. 381, March-April, 2022

[3] http://fluka.cern

[4] G. Battistoni, T. Boehlen, F. Cerutti, P.W. Chin, L.S. Esposito, A. Fassò, A. Ferrari, A. Lechner, A. Empl, A. Mairani, A. Mereghetti, P. Garcia Ortega, J. Ranft, S. Roesler, P.R. Sala, V. Vlachoudis, G. Smirnov, “Overview of the FLUKA code”, Annals of Nuclear Energy 82, 10-18 (2015).

[5] T.T. Bohlen, F. Cerutti, M.P.W. Chin, A. Fassò, A. Ferrari, P.G. Ortega, A. Mairani, P.R. Sala, G. Smirnov, and V. Vlachoudis, “The FLUKA Code: Developments and Challenges for High Energy and Medical Applications”, Nuclear Data Sheets 120, 211-214 (2014).

DESIGN AND TESTING OF COMPONENTS FOR HIGH POWER RF SYSTEMS FOR LEHIPA 20 MEV ACCELERATION*

B. V. Ramarao, Muthu S, J. K. Mishra, M. Pande, Gopal Joshi, and S. Krishnagopal

Bhabha Atomic Research Center, Mumbai-85

Abstract

The LEHIPA project is under development at BARC for acceleration of proton beam to an energy of 20 MeV. The three high power waveguide systems for RFQ and DTL-1 &2 is designed. The various waveguide components required in these systems like E/H plane bends, directional couplers, magic tees, phase shifters, windows, matched loads etc have been designed. These components have been characterised using VNA, and tested at high power. The waveguide systems for RFQ, and DTL-1 are commissioned for proton beam acceleration of 10.8 MeV, and for DTL-2 it is under installation.

INTRODUCTION

The LEHIPA RF system is shown in Fig.1.The LEHIPA basically consists of three accelerating cavities and one buncher cavity. The accelerating cavities are Radio Frequency Quadrupoles (RFQ), and two stages of Drift Tube Linacs (DTLs). Recently, proton beam acceleration up to 10.8 MeV has been commissioned through RFQ, buncher, and DTL-1. The three acceleration cavities RFQ, DTL-1, and DTL-2 are driven by a high-power RF klystron working at 352 MHz. The corresponding RF power required for these structures are 500 kW for RFQ, and 900 kW for each for DTL-1 &2. In between the high-power klystrons and the RF accelerating structures, there required a high-power waveguide transmission line at 352 MHz. These waveguide transmission systems have various high-power RF components in WR2300 waveguide like straight sections, E/H plane bends, directional couplers, magic tees, phase shifters, windows, loads etc. All these waveguide transmission line components have been indigenously designed, tested. The paper presents the analysis, design, implementation, and test results of the various waveguide components including the critical components like Waveguide matched load and RF window. The paper also presents the present status of commissioning of these waveguide systems.

DESIGN OF WAVEGUIDE SYSTEMS

The waveguide systems designed for RFQ, DTL-1, and DTL-2 are shown in Fig. 2 and 3. The RFQ has two coupling ports and its resonant mode is modified TE_{02} mode, the waveguides are coupled in horizontal or H-plane. Klystron RF output is divided into two equal and in-phase RF outputs and each arm is coupled through a directional coupler, window, RF coupler etc. The magic Tee & circulator ports are terminated into a matched waveguide load.

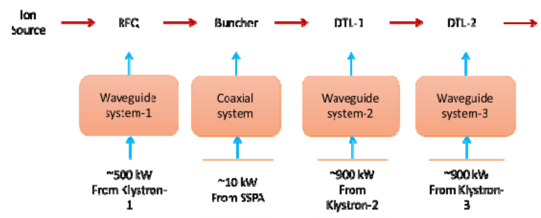

Figure 1: Block diagram of LEHIPA RF systems

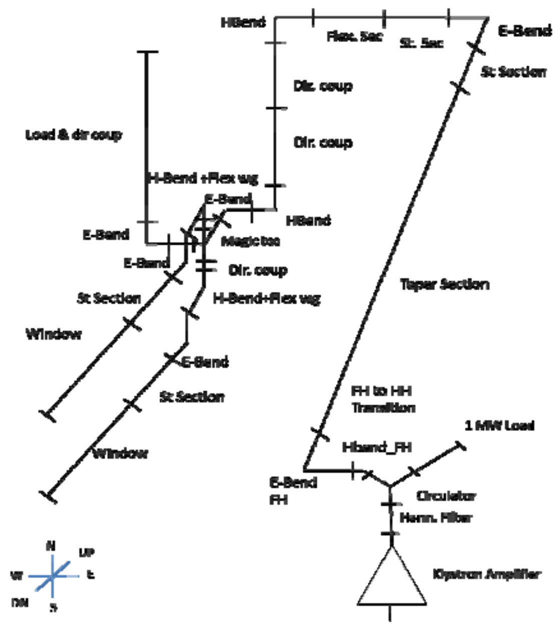

Figure 2 Waveguide layout of RFQ

DESIGN OF WAVEGUIDE COMPONENTS

The various high-power RF components in WR2300 half height waveguide like straight sections, E/H plane bends, directional couplers, magic tees, phase shifters, etc. have been designed, fabricated and tested for LEHIPA requirements. The design cycle of all these components is shown in Fig. 4. Initially, designed using simple equations then simulated and optimised RF parameters. The assembly and fabrication drawings are prepared. The fabricated prototypes are characterised using vector network analyser (VNA). After satisfactory results, the components are installed in LEHIPA. A waveguide matched load at 352 MHz is desired at various places in the waveguide distribution to terminate the un-balanced or reflected RF power in the system. The main locations of the RF waveguide loads are at the magic tee's balanced ports (4th port of the Magic Tee).

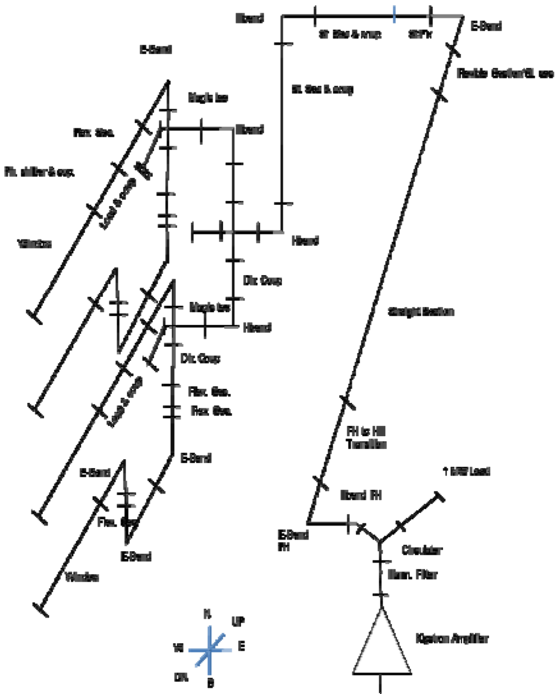

Figure 3: Waveguide layout of DTL-1

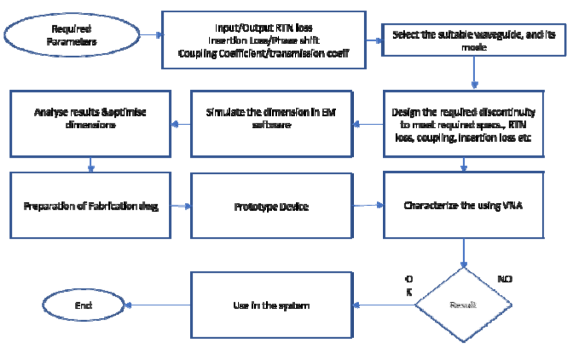

Figure 4: Design cycle of waveguide components

Fabricated waveguide components

The fabricated directional coupler, magic tee, E/H plane bends are shown in Fig. 5. The components have been fabricated in an alloy of Aluminium, Al 6061 T6. The rms surface roughness is less than 3 microns. The geometry tolerances are less than 1 mm. To protect the surfaces against environment, the inner surfaces are chromate converted and outer surfaces are powder coated with corrosion resistant epoxy paint. The flanges are EIA-2300 HH for main waveguide ports whereas for coupling and measuring signal ports N-type female connector. The surfaces have been tested against peel off, salt spray, contact resistance, scales, scratches etc.

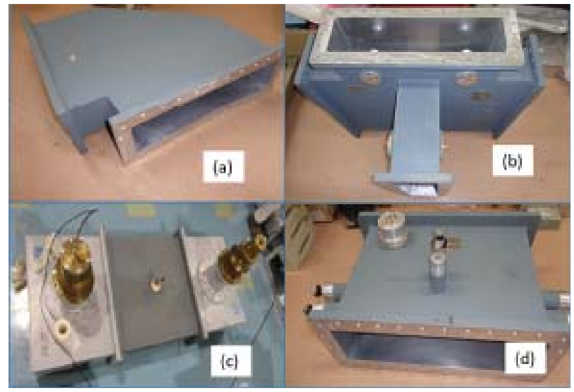

Figure 5: Fabricated WG components (a) H-plane bend, (b) magic tee, (c) dir. coupler, and (d) phase shifter

Measured results WG components

The typical measured results of $|S_{11}|$, $|S_{22}|$ and S_{21} of the bend and coupler is shown in Fig 6. The matching of the components is better than 25 dB and insertion loss are <0.1 dB. The measured S-parameters of the magic tee are shown in Fig 7.

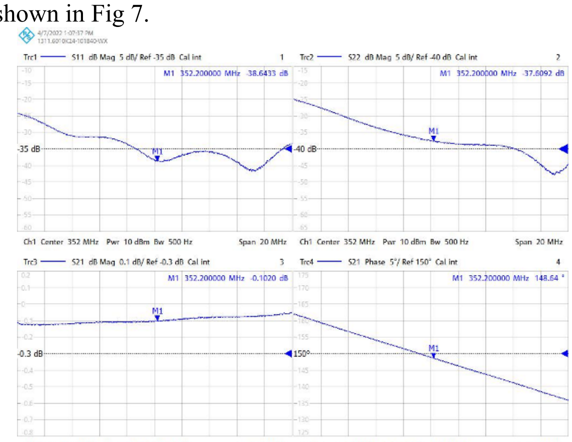

Figure 6: Measured $|S_{11}|$, $|S_{22}|$ and S_{21} of the bend and coupler at 352 MHz

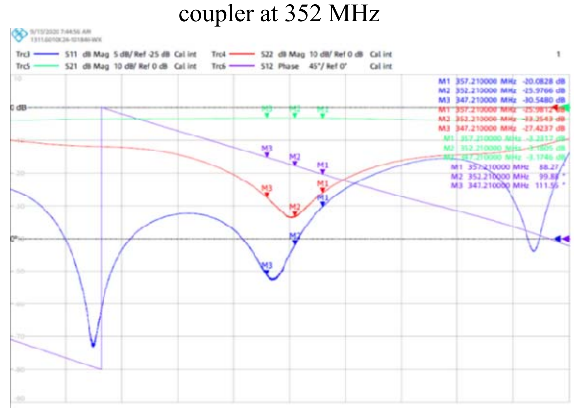

Figure 7: Measured $|S_{11}|$, $|S_{22}|$ and S_{21} of the magic-T

The critical wave guide components like windows and matched waveguide loads have been both fabricated, characterised using VNA, and tested at high power using klystron amplifier. The main locations of the RF waveguide loads are at the magic tee's balanced ports (4th port of the Magic Tee). A waveguide with salt columns is used as absorbent for a RF wave energy. The salt concertation has been varied to optimize the absorption coefficient. The length of the salt column, size, spacing of the columns have been designed for maximum absorption. The high-power test set-up of the window and load is shown in Fig. 8. The klystron output is routed through bends, straight section, directional couplers, and terminated in to a matched load through a developed RF window. It has been tested at >250 kW, 325 MHz in pulse mode.

Figure 8: High power testing of window and RF load

The measured RF performance parameters of waveguide components is shown in Table. 1. The WG have met the LEHIPA requirement specification. components

Table 1: Tested Specifications of WG components

Component	Parameter	Value
Dir. Coupler	Coup. Coeff/isolation	63 dB/ 90 dB
Load	RTN loss	25.3 dB
Window	RTN/Insertion loss	>16 dB/0.1 dB
Magic Tee	Mag./phase imbalance	0.1 dB/3 deg
Bend	RTN/Insertion loss	>28 dB/0.02 dB

WAVEGUIDE SYTEMS FOR RFQ & DTL

The waveguide systems for RFQ and DTL have been assembled, characterised, and high power tested for 10.8 MeV acceleration. The installed RFQ and DTL-1 system is shown in Fig. 9. The measured S_{11} result of DTL-1 is shown in Fig. 10. The WG system is close to critical match with the DTL-1 resonators at 352 MHz

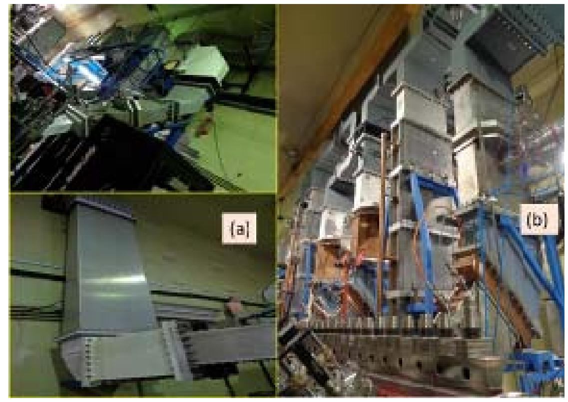

Figure 9: Photograph of commissioned (a) RFQ, and (b) DTL-1 waveguide systems.

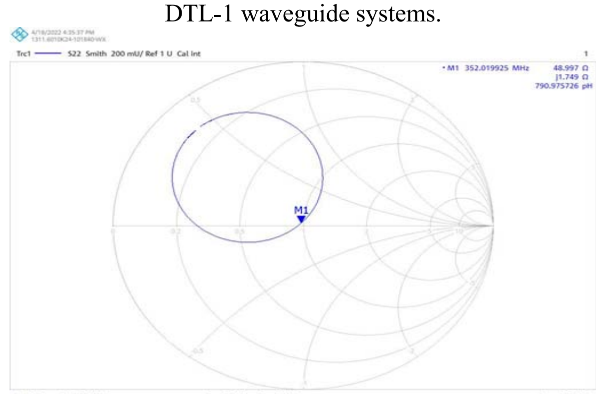

Figure 10: Measured S_{11} of DTL-1 WG at 352 MHz

CONCLUSIONS

The waveguide systems and its' for RFQ and DTL-1 have been successfully commissioned and beam acceleration up to 10.8 MeV has been achieved. The waveguide system and components for DTL-2 are characterized and ready for installation.

REFERENCES

[1] B. V. Ramarao, S. Muthu, J. K. Mishra, Manjiri Pande, Gopal Joshi, M. R. Mishra, V. M. Jose, S. V. L.S. Rao, Rajesh Kumar, and S. Krishna Gopal, "Coupling and Energising of 10 kW, 352 MHz Solid-State RF Power Amplifier for Buncher Cavity of Proton Accelerator", *Proc. InPAC-2019,*

[2] S V L S Rao, Jose V Mathew, S K Singh, M R Mishra, Rajesh Kumar, Mentes Jose, Hitesh Kewlani, Sandip Shrotriya, B V Rama Rao et. all "Commissioning Of The LEHIPA 3 Mev RFQ", Proc. of InPAC-2019, Nov-2019, IUAC,

PROTOTYPE DEVELOPMENT OF FOUR CHANNEL 2KV/5A POWER SUPPLY USING PULSE STEP MODULATION TECHNIQUE

Y. Kumar[1*], S. Srivastava[1,2], A K Kushwaha[1] and S.K.Thakur[1]
[1]Variable Energy Cyclotron Centre, Kolkata-700064, India.
[2]Homi Bhabha National Institute, Mumbai
email:- yashwant@vecc.gov.in.

Abstract

A 2kV/5A power supply is designed and tested utilizing Pulse Step Modulation (PSM) which comprises of 4 individual power supply modules (SPM) based on Pulse Width Modulation (PWM). A power supply with PSM techniques is used in the accelerator technology in order to avoid crowbar protection system. An analog phase shifted PWM signal is given to each SPM module. Output voltage of each SPM is added to obtain final output voltage. Each phase shifted PWM pulse is used to turn ON and OFF the IGBT connected in each module as a Buck converter mode which is fed from a 600 VDC source. Here, each SPM can produce 60V to 540V depending upon duty cycle of switching pulse. The final output is the summation of voltages of SPM modules connected in series resulting very less ripple at higher ripple frequency and thus the requirement of filter capacitor is very less. A free-wheeling diode connected at the output of the modules bypasses the current even it is in standby or non-function mode. There are various ways to obtained phase shifted PWM like using FPGA, DSP etc. In this paper, the phase shifted switching pulses are obtained by using analog IC LTC6994 which can produce a delay from 1µs to 33.6s. The use of analog IC, eases the complexity of design. Load regulation is obtained using PI controller fabricated on an externally SG3524 IC, which act as a master controller. The main advantages of PSM based high voltage power supply are smaller size, easy maintenance and low stored energy.

INTRODUCTION

PSM were first introduced by Brown Boveri [1]. The main advantage of PSM based power supplies are modular design, uniform power distribution, low EMI, high bandwidth, high efficiency, very low filter capacitor at output that leads to crowbar less protection system due to reduction in store energy [2-5]. PSM basically consist of a series connected switching modules known as SPM. Each module has an insulated DC power supply, a semiconductor switching element IGBT/MOSFET and a free-wheeling diode. Generally, in PSM phase shifted PWM pulses were used to ON/OFF the switching devices; this is generally achieved by FPGA and DSP board [6-7]. Synchronization is become tough task for obtaining phase shifted PWM signal when using more than two FPGA/DSP board. In order to overcome this problem a new approach is presented in this paper, which is based on using phase shifted analog IC LTC6994-2. LTC6994-2 can produce a delay of 1 µs to 33.6*s* based on the combination of resistor network as given in datasheet [8]. Using separate phase delay circuit leads to lesser programming complexity and then the concept of whole PSM can be achieved efficiently and systematically. In the present paper we have developed four channel 2kV/5A prototype power supply using PSM techniques which is the extension of our previous work [9].

WORKING PRINCIPLE

A 2kV/5A power supply based on PSM based is aim to design and developed in VECC. The principle of the PSM, the control system should switch all modules ON and OFF maintaining equal duty cycle, to ensure equal loading on all modules. This control method is called stage rotation [10]. This is achieved using First In First Out (FIFO) principle. Figure 1 shows the block diagram of the working principle of 2kV/5A power supply based on PSM. The PWM pulse is produce by a commonly available SG3524 IC. This PWM pulse is phase delay by $T_d = T/N$ using LTC 6994-2 IC. T is the time period of PWM and N is the number of SPM module used. The closed loop control circuit is implemented in SG3524. The output required very low value of filter capacitor due to N times increased in switching frequency at output.

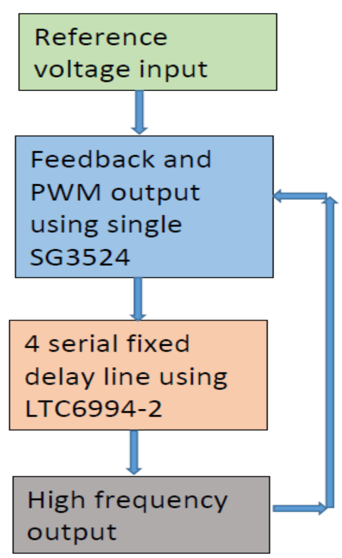

Figure 1: Block diagram of PSM based power supply.

*E- mail: yashwant@vecc.gov.in.

Obtaining fixed delay

For the design of 2kV/5A DC power supply, 4 SPM modules were used. Each module has a rating of 600V. Total 4 module where used to produce 2kV by varying duty cycle of PWM. The switching frequency of SG3524 where kept at 5 kHz, this leads to the requirement of 50 µs (*T*/*N*) fixed delay in order to obtain equal loading in each SPM module. Figure 2 shows the schematics of 50 µs delay time. In LTC 6994 resistor R_{SET} is used to programs an internal master oscillator frequency. The input-to-output delay is determined by this master oscillator and an internal clock divider, N_{DIV}, programmable to eight settings from 1 to 2^{21}. The output follows the input after delaying the rising and/or falling transitions of switching pulse. The time delay is calculated by:

$$t_d = \frac{N_{DIV} \times R_{SET}}{50k\Omega}\,\mu s \text{ , } N_{DIV} = 1,8,64,.....,2^{21} \qquad (1)$$

The N_{DIV} tells the combination of R2 and R3 that should be used in order to find the required delay. The LTC 6994 can produce delay either from 1-8µs, or in a combination of N_{DIV}*(1-8µs).

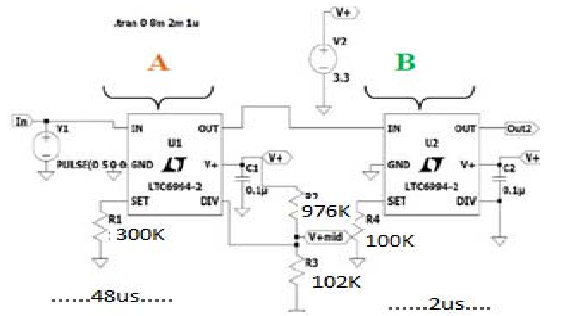

Figure 2: Schematic of delay Time (50 µs)

For example in order to produce 50 µs delay two LTC 6994-2 IC is used, first (as shown in Label A in Fig 2) produce 48µs delay and second (Label B in Fig 2) will produce 2µs delay. Proper choice of R1 (R_{SET}), R2 and R3 can produce a delay of 1µs to 33.6s. This schematic is built in LTSpice software which is freely available. The shifted PWM is then given to switching device (IGBT in present case) via optical fiber to turn ON/OFF the IGBT.

Figure 3 shows the schematics diagram of the 4 channel SPM module. Figure 4 shows the actual circuit setup. The pulse coming from each delay time (50 µs) is converted into optical light using HFBR-1521Z IC and

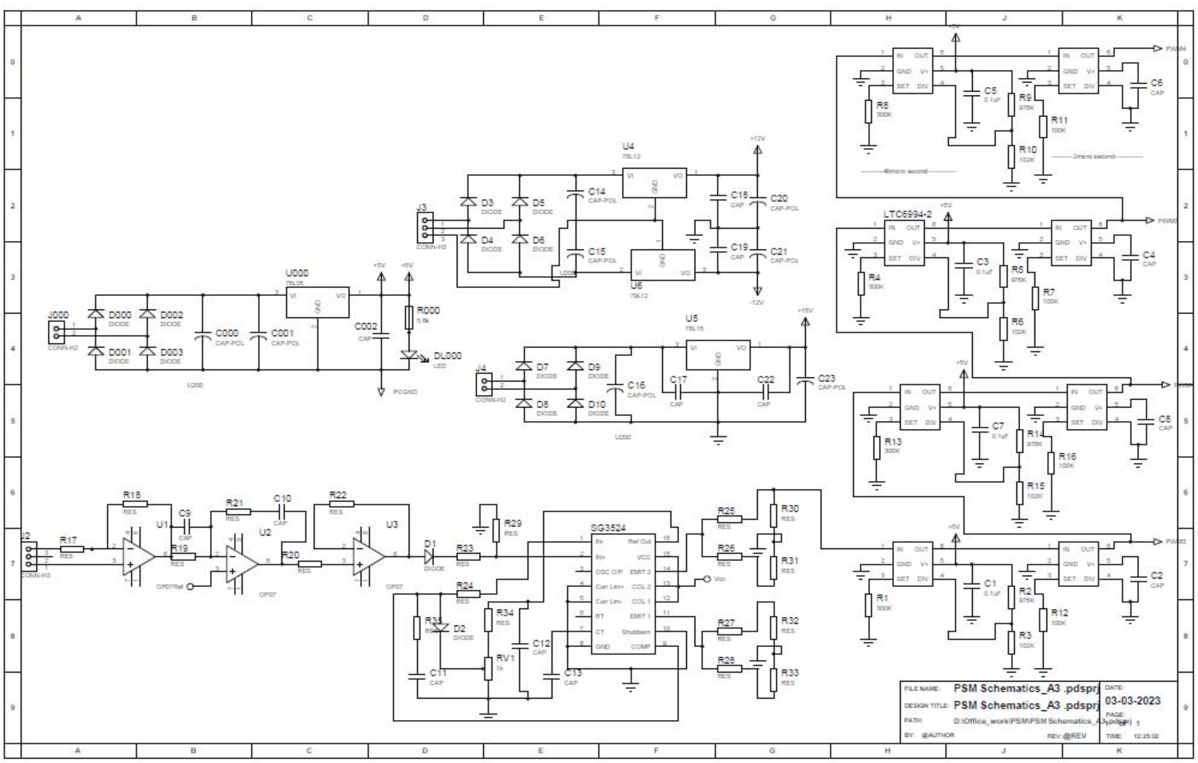

Figure 3: Schematics diagram

it is communicated to SPM module, where it is again converted to desired voltage using HFBR-2521Z. Figure 5 clearly shows that at the final stage the frequency is increased by 4 times, which reduce the value of filter capacitor. At large scale when the number of SPM module is more the output frequency will be much smaller and can leads to crowbar less operation. Table 1 shows the measured parameter of the power supply at present stage.

Figure 4: Actual setup

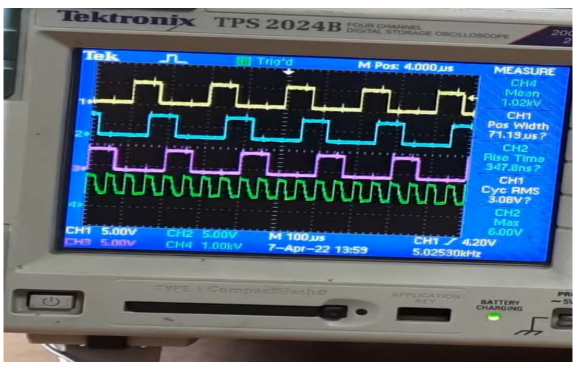

Figure 5: Final output

Table 1: Measured Parameters of power supply

S. No.	Parameter	Value
1	Output Voltage	2kV
2	Output Current	5A
3	Voltage Ripple	0.1%
4	Load Regulation	0.1%
5	Line Regulation	0.1%
6	Efficiency	60%
7	Stability	500 ppm/°C

CONCLUSION

A 2kV/5A power supply is designed, simulated and experimentally tested utilizing PSM technique which comprises of 4 SPM. The present scheme utilizes the analog LTC 6994-2 delay line IC for producing the fixed delay necessary to obtain phase shift. A single PWM controller IC SG3524 is used to drive PWM. The present designed is seems to be more rugged and easy to design when consider to its digital counterpart done previously.

ACKNOWLEDGEMENT

The authors would like to thank Dr. A. De, Mr. V. K. Khare, Mr. M. K. Ghosh, Mr. A. Kumar, Mr. A. Sadhukhan, technical staffs of PE and MCD section, VECC Kolkata for their sincere supports during the development and testing of power supply.

REFERENCES

[1] S. S W. Schminke, High-power Pulse-Step Modulator for500 kW Short-,Wave and 600 kW Medium-Wave Transmitter, Brown Boveri Rev. 73 (1985) (5) 235-240.

[2] S. M. Pan et al., "The Control System of The 100kV HVPS For NBI," 2011 IEEE/NPSS 24TH Symposium on Fusion Engineering.

[3] J. Alex and W. Schminke, "A high voltage power supply for negative ionNBI based on PSM technology," in Proc. 17th SOFE, San Diego, CA,1997, vol. 2, pp. 1063–1066.

[4] N. Tomljenovic, W. Schminke, "Solid state dc power supplies for gyrotron and NBI sources", Proc. of Symposium on Fusion Technology, 1992.

[5] Wolfgang Forster, J. Alex., "High voltage, high power, pulse-step modulators for the accurate supply of gyrotron and other heating devices" Conference Record of the Twenty-Fifth International Power Modulator Symposium, 30 June-3 July 2002, Page(s): 126 – 129.

[6] S.K.Thakur, S. K. Kumari and Y Kumar, "Design and performance analysis of a crowbar-less high voltage power supply based on PSM technique " Sådhanå (2018) 43:129.

[7] YAO Lieying et al., "A Fully Digital Controller of High- Voltage Power Supply for ECRH System on HL-2A," 2011 IEEE/NPSS 24TH Symposium on Fusion Engineering.

[8] Datasheet of LTC 6994. https://www.analog.com/media/en/technical-documentation/data-sheets/699412fb.pdf

[9] S. Srivastava et. al., "Simulation studies on 5kV/5A power supply using pulse step modulation technique". InPAC 2019.

[10] J. Alex and W. Schminke, "Fast switching, modular high-voltage DC/ACpower supplies for RF-amplifiers and other applications," in *Proc. 16th Symp. Fusion Eng.*, Champaign, IL, 1995.

DESIGN OF FPGA BASED RF INTERLOCK SYSTEM AND POWER MONITORING

Bhumeshwar Ponagani, Santhosh Chittimalla, Deepak N Mathad, S K Singh
Ion Accelerator Development Division, BARC, Mumbai-400085.

Abstract

The FPGA-based RF power monitoring and interlock system design was developed based on the results of the prototype microcontroller-based fast interlock system developed previously at LEHIPA [1]. In addition, studies were conducted to determine the time required to generate an RF interlock signal to prevent beam damage to the cavity [2]. The system's response time has been enhanced using fast comparators and the replacement of the microcontroller with an FPGA. The system also incorporates ADCs that are connected to the FPGA for RF power monitoring.

The system is composed of two units: an analog front-end unit and a digital unit. The analog front-end unit processes the RF signal from the forward and reflected ports of the directional coupler, converting it into a DC voltage proportional to power (in dBm). It also includes a low-pass filter to remove the peaks of the reflected path, which are responsible for generating false interlock signals. The resulting signal is then sent to a fast comparator for interlock signal generation. The digital unit, which includes the FPGA, receives all interlock signals from various RF signals and, based on user logic, generates the final interlock signal to turn off the RF switch. The threshold signal for comparators is produced using DACs connected to the FPGA. Additionally, ADCs connected to the FPGA are used to obtain the RF signal waveform, which is then displayed to the user in a GUI.

INTRODUCTION

Whenever the RF power in an accelerator system exceeds the rated power of devices such as couplers, windows, etc., there is a risk of generating arcs that can damage these components. Similarly, accelerator cavities must be protected when there is a possibility of the beam hitting the cavity walls due to any impedance mismatch that causes reflection in the RF power.

Previously, a prototype microcontroller-based RF interlock system [1] was developed with two channels, which can generate an interlock signal in less than 10 µs when the RF power exceeds the threshold power. Another study [2] was conducted to determine the response time required for generating an interlock signal to protect the cavity walls from beam damage caused by RF power reflections. The study calculated the required response times for interlock systems when beams of different energies hit copper or stainless steel cavity walls. The minimum response time required for a 3 MeV beam hitting the cavity was found to be less than 6 µs.

The response time of the on-board comparator used in the microcontroller-based system is approximately 4 µs to 8 µs, depending on the voltage difference between its two input terminals, making it very slow. Additionally, since the microcontroller executes instructions sequentially, there is an inherent delay of around 1.5 µs before the ISR is executed. This delay is due to the time required for current instruction execution before the ISR is triggered, and it further increases the response time of the system, exceeding the required value.

FPGA BASED INTERLOCK SYSTEM

The system was designed with the understanding that each cavity would have three RF signals: the forward power signal, the reflected power signal, and the cavity pickup signal. To accommodate these signals, the system was built with 9 channels considering 3 cavities. To address the limitations of the microcontroller-based system, fast comparators and FPGA were used in place of the on-board comparators and microcontroller.

Figure 1 displays the block diagram of the interlock system based on FPGA. The system is comprised of two units: Analog and Digital. Table 1 provides details of the individual components utilized in the system.

The Analog unit of the system is responsible for conditioning the incoming signals. The 9 RF input signals are first passed through an RF Bandpass filter with a center frequency of 350 MHz to remove any noise from other frequencies. A power detector, specifically the ZX47-40-S+ model with a slope of -25 mV/dB, is used to measure the power of the input RF signal in terms of DC voltage. The detector is calibrated for input RF power vs output DC voltage. Its output voltage range is from 0.5 V to 2.1 V, with 2.1 V when there is no RF signal and the voltage decreasing by 25 mV for every dB increase in power. A low pass filter is used to remove the peaks of the reflected power signal present at the start and end of the pulse. For other inputs, the low pass filter can be bypassed. The cut-off frequency of the low pass filter can be varied from 0.1 Hz to 50 kHz using a digital clock signal input to the LPF IC. The output of the LPF is then fed into the comparator located in the Digital unit to generate the trigger.

The Digital section of the system comprises of several components, including FPGA SoC, comparators, ADCs, and DACs. The output of the comparators are connected to the FPGA and another input terminal is linked to a DAC. The DAC provides the necessary threshold value for generating the interlock signal, and its output voltage is regulated by the FPGA SoC. In addition, the FPGA can directly receive digital input signals from external devices like BPMs and BLMs.

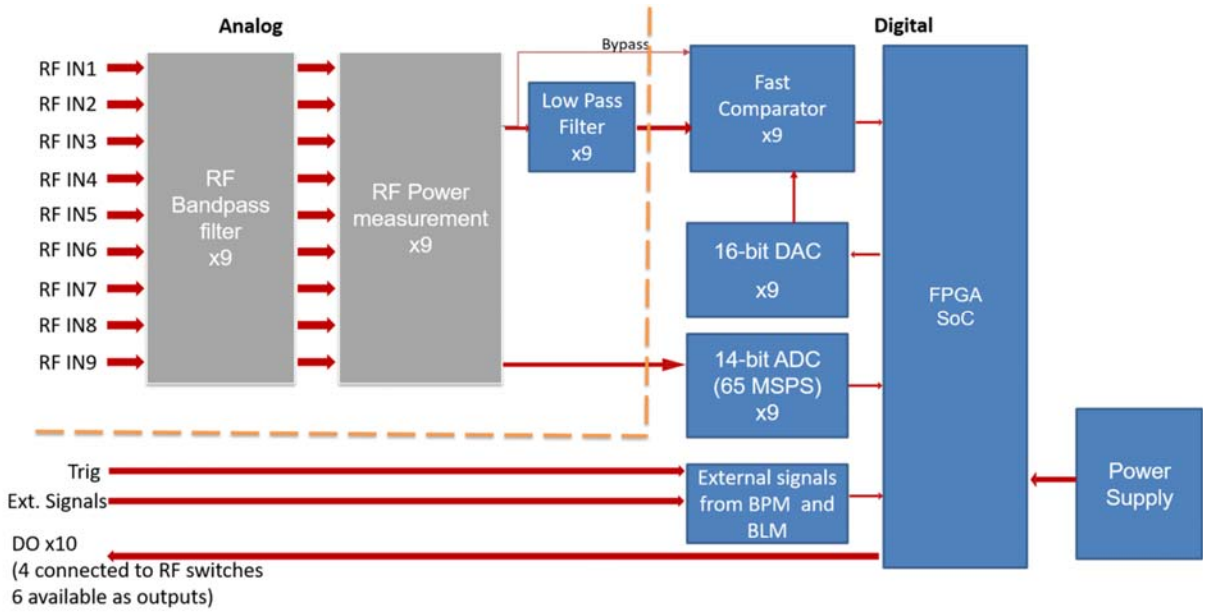

Figure 1: Block diagram of the FPGA based system

The FPGA will be utilized to produce the interlock signal for all 9 RF input channels as well as for the external digital input signals. Once generated, the interlock signal will be routed to 4 RF switches, which control the flow of RF signals to the cavities. Due to the fast clock period of the FPGA (5ns), and the elimination of comparator delay, the entire system's response time for generating the interlock will be in the range of hundreds of nanoseconds.

RF POWER MONITORING SYSTEM:

The SoC contains an ARM processor, which will be loaded with Linux and Experimental Physics and Industrial Control System (EPICS) IOC. As EPICS is the control system used in BARC's particle accelerator, it is essential to integrate every sub-system with EPICS and ensure compatibility with it. Therefore, the Interlock system and power monitoring system must be compatible with EPICS, which serves as the central control system for the accelerator.

The Digital unit also includes a 16-channel ADC with a sampling rate of 65 MSPS that receives the output of the power detector. The acquired data will be processed and the waveforms of each channel will be displayed on a graphical user interface (GUI) developed on EPICS Qt. The GUI will show the status of all interlocks and allow for enabling or disabling individual channels. Additionally, users will be able to bypass low pass filters for any specific channel using the GUI. The threshold for the DAC will also be adjustable through the GUI. The power waveform calibration will be included in the final displayed waveform.

Table 1: List of components used in the system and their features

Component	Model No.	Features
Bandpass Filter	SXBP-350+	Center Freq: 350 MHz Pass Band (<3 dB): 330-375 MHz
Power Detector	ZX47-40-S+	Slope: -25 mV/dB Output voltage range: 0.5-2.1 V
Low pass Filter	MAX-296	8th order Bessel LPF with clock Tunable corner frequency from 0.1 Hz-50 kHz
Fast Comparator	TLV3501	4.5 ns High speed comparator
ADC	AD9249	16-channel, 14-bit, 65 MSPS
DAC	DAC8568	16-bit, octal channel
FPGA	XC7Z045 FFG900	Xilinx SoC, 200 MHz clock
RF Switch	MSWA-2-20+	Very fast RF switch, 5ns typ.

CONCLUSION:

A conceptual design for a multi-channel RF power monitoring and interlock system has been proposed. The system will be integrated into the existing EPICS-based control architecture that is widely used in the accelerator community. The proposed system addresses the limitations of the current microcontroller-based interlock system and incorporates additional features. The development of the system is currently underway and it will be tested at LEHIPA.

REFERENCES

1. Prototype Microcontroller-based Instrumentation for Protection and Power Monitoring of RF Components in LEHIPA, Santhosh Chittimalla, P. Bhumeshwar, Deepak N Mathad, Laxman Tayade, S. K. Singh, InPAC-2022 Conference Proceedings
2. Study of thermal effects of proton beam interaction with accelerating structures to derive the response time of fast protection system, Santhosh Chittimalla, Deepak N Mathad, S. K. Singh, K. Rajesh, InPAC-2023 Conference.

Study of the effect of location of laser tracker on alignment uncertainty of components in circular particle accelerators

Vikas[1,2,*], R.K. Sahu[1], Rahul Shukla[2,3]

[1]Accelerator Alignment Lab., Indus Operation Division, Raja Ramanna Centre for Advanced Technology, Indore, India

[2]Homi Bhabha National Institute, Anushaktinagar, Mumbai, Maharashtra, India

[3]Accelerator Physics and Synchrotrons Utilization Division, Raja Ramanna Centre for Advanced Technology, Indore, India

Abstract

In particle accelerator machines, the alignment of components within specified alignment tolerances has always been of primary importance for their smooth operation. Imperfections in the position of components such as magnets, accelerating structures can perturb the motion of the beam of charged particles. These perturbations may limit the performance of these machines and in the extreme case of misalignment, the operation of the machines may fail. In these machines, specified alignment tolerances are of the order of ± 100 µm or less over the large dimensions ranging from few tens of meters to hundreds of meters to obtain a beam of extremely low emittance. Considering the large measurement volume of particle accelerator machines along with the very tight alignment tolerances, it is necessary to achieve the best possible performance using state-of-the-art instruments and best technique feasible for the given site conditions. Laser tracker, a 3D portable coordinate measurement machine is a common choice in particle accelerators for precision survey and alignment activities. In an accelerator machine, the location of a laser tracker station is generally fixed randomly or by considering the line-of-sight obstructions, sources of disturbance etc. Laser trackers have better measurement capabilities for distance as compared to the angles and the alignment tolerances for position-sensitive components of an accelerator are more stringent in the radial direction as compared to the circumferential direction. With this directionality in mind, the effect of location (w.r.t. the machine) of laser tracker stations on the measurement uncertainty in radial direction is studied for a nearly circular accelerator machine.

INTRODUCTION

The particle accelerators are the machines where a beam of charged particles is accelerated near to the speed of light while maintaining the charged particles on a well-defined orbit in vacuum envelope. These machines are extensively used in the fields of high-energy physics, material science, medical and biological sciences. The size of these machines varies from hundreds of meters to a few kilometres. Various position-sensitive components like accelerating structures, magnets, beam position monitors are placed in a sequence along the reference orbit. The key components of these machines are the magnets which are mainly responsible for keeping the charged particles on the designed orbit. Alignment of these magnets is a key requirement for stable beam of the charged particles and the synchrotron radiation emitted from them. Specified alignment tolerances for these machines, are of the order of ± 100 µm over the large dimensions from few tens of meters to hundreds of meters. The demand is still more stringent in the future generation particle accelerators to get a beam of extremely low emittance [1]. Due to the high measurement accuracy over the large dimensions along with the high speed data acquisition and ease in movability, Laser tracker is used for precision alignment activities in particle accelerators [2]. The laser tracker acts as a 3D portable coordinate measuring machine, which determines the coordinates of a point in the polar coordinate system, as shown in Fig. 1 and these coordinates are transformed to Cartesian coordinate system using the data processing software.

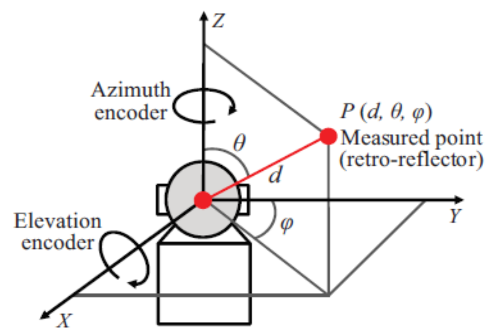

Figure 1: Schematic of a Laser tracker with its polar coordinate system

While performing measurements, the position of the laser tracker station in an accelerator machine is often fixed randomly or considering the visibility restrictions, sources of disturbances. Since the laser tracker has better measurement accuracy for distance than the angle, angular inaccuracies govern the uncertainty in coordinates of points measured by the laser tracker. Taking into account the directional dependency of alignment tolerances in an accelerator machine, where the radial direction requires more stringent alignment tolerance than the circumferential direction, a comprehensive study was conducted to evaluate the impact of laser tracker station locations (w.r.t. machine) on measurement uncertainty in the radial direction of a near-circular accelerator. A mathematical model based on the probability theory was developed and implemented in MATLAB to investigate the effects. A single laser tracker station can be used for aligning the multiple components which are in its measurement range with different combinations of distances and angles. Thereafter, the study will guide in limiting the working volume of a measurement station to the extent uncertainty is maintained within the specified alignment tolerances in the large low emittance accelerators. Synchrotron radiation (SR) source- Indus-2 at RRCAT was chosen as a case study to analyse the effects of the location of the laser tracker station.

MATHEMATICAL MODELLING

Using probability theory, a mathematical expression was derived to examine the impact of the location of the laser tracker station on the positional uncertainty of components, accounting for the inherent presence of random errors in distance and angle measurements, which conform to the normal distribution. The current study is limited to evaluating the uncertainty exclusively in the radial direction, whereby the random errors impinge upon the two variables obtained from the laser tracker measurements, specifically the horizontal distance (X_D) and azimuth angle (X_A). The coordinates of any point is a function of these two variables, so the joint distribution of these two random variables will be bivariate normal distribution. The shape of the uncertainty zone for the bivariate normal distribution will be an ellipse in which a given percentage of the data is expected to lie. The size of ellipse as well as its orientation will be different at different locations of the points. The major and minor axes of error ellipse represent the uncertainty in these two directions. The mathematical expressions were formulated and implemented in MATLAB to ascertain the level of uncertainty in the radial direction, under the diverse conditions such as the laser tracker station being situated both inside and outside the ring, highlighting the significance of the analytical approach applied in this study.

Laser tracker station outside the ring

The measurement setup depicted in Figure 2(a) illustrates the scenario where the laser tracker station is positioned outside the ring. In the figure 2(a), 'r' represents the radius of the ring, 'S' is the distance of laser tracker from the ring and 'L' denotes the laser tracker's measured horizontal distance from its station to the point of interest. Figure 2(b) further provides an enlarged representation of the error ellipse, elucidating the impact of the uncertainties in distance (U_D) and angular measurement (U_A).

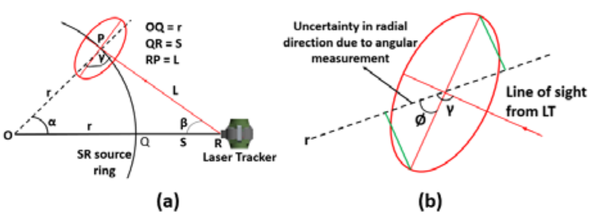

Figure 2: (a) Schematic of measurement setup where Laser tracker is placed outside the ring and (b) enlarged view of uncertainty ellipse

From figure 2, angle β and angle γ can be determined from eq. (1) and eq. (2), resp.

$$\angle\beta = \cos^{-1}\left(\frac{(r+S)^2 + L^2 - r^2}{2(r+S)L}\right) \quad (1)$$

$$\angle\gamma = 180^o - \angle\alpha - \angle\beta \quad (2)$$

To evaluate the effects of both angular and distance uncertainty in the radial direction, it is crucial to obtain angle Ø through eq. (3).

$$\angle\phi = \angle\gamma - 90^o \quad (3)$$

Uncertainty in radial direction at point P due angular uncertainty can be expressed as:

$$U_{R,A} = U_A \cos\phi \quad (4)$$

where, $U_{R,A}$ represents the contribution of angle measurement uncertainty (U_A) in radial direction.

Likewise, the contribution of distance measurement uncertainty (U_D) in radial direction ($U_{R,D}$) can also be determined using eq. (5).

$$U_{R,D} = U_D \sin\phi \quad (5)$$

Overall uncertainty in radial direction (U_T) can be estimated using eq. (6):

$$U_T = \sqrt{U_{R,D}^2 + U_{R,A}^2} \quad (6)$$

The workable area or the range of angle α up to which alignment of components can be done within specified alignment tolerance zone using single station of laser tracker can be estimated using the constrained eq. (7).

$$U_T \text{ is} \leq \text{ Specified alignment tolerance value} \quad (7)$$

Laser tracker station inside the ring

Using figure 3, we can also derive the mathematical expression for the uncertainty in radial direction when laser tracker station is fixed inside the ring. There will be slight change in equations 1 and 3 for this case and other equations will be similar to the case when instrument is placed outside the ring.

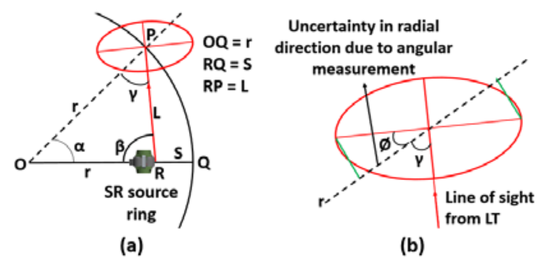

Figure 3: (a) Schematic of measurement setup where Laser tracker is placed inside the ring and (b) enlarged view of uncertainty ellipse

RESULTS AND DISCUSSION

Indus-2 is a synchrotron radiation source of energy 2.5 GeV and circumference 172.47 m, at RRCAT, is taken as a case study to analyse the effect of locations of laser tracker stations on the alignment uncertainty of components. The positioning requirement of magnets for this facility is ±100 µm for both the radial and vertical direction [3]. The parameters selected for the present study, are the position '*S*' of the laser tracker from the ring in both the inside and the outside, as well as the angle '*α*' which represents the extent of workable area (area of interest). Since the minimum measurement distance from laser tracker station should be greater than 0.8 m as specified by the manufacturers, S = 1 m was chosen as the lowest value of parameter S. The space available in accelerator complex imposes limit on maximum distance of laser tracker station from the ring. In the present case, it is 4 m. Based on Indus-2 geometry, range of angle α was chosen from 0 to 30˚ due to obstruction in line of sight from laser tracker beyond a certain angle. Table 1 shows the range of parameters along with the uncertainty specifications chosen for the present study. Figure 4 shows the effect of parameter '*S*' and angle '*α*' on alignment uncertainty for both the cases when laser tracker is placed outside and inside the ring.

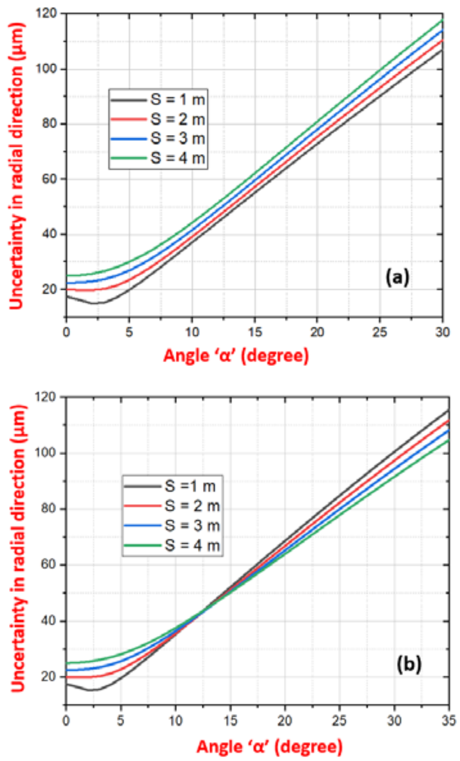

Figure 4: Effect of laser tracker station on alignment uncertainty: (a) outside and (b) inside the ring

Table 1: Range of chosen parameters and laser tracker's uncertainty specifications

Parameter	**Range**
Distance of laser tracker (LT) station from ring (S)	1 to 4 m
Workable area in form of angle (α)	0 to 30 ˚
1σ uncertainty in LT's distance measurement (U_D)	± (15 µm + 2 µm/m)
1σ uncertainty in LT's angle measurement (U_A)	±1.5 arc second

According to the data presented in Fig. 4, it is evident that the optimal workable area, in terms of angle *α*, is roughly ±27.5˚ or approximately 1/7th of a sector of the Indus-2 ring. This is the case when the alignment requirement is within ±100 µm, and the laser tracker is placed at a distance of 1 m outside of the ring. The workable area, in terms of angle α, is ~ ±34˚ when the instrument is placed 3 m inside of the ring. Similarly, when the alignment requirement is within ±50 µm and the laser tracker is located at a distance of 1 m outside and 3 m inside the ring, the maximum working area is about ±12.5˚and ±16˚, respectively, which is ~ 1/12th of a sector of the Indus-2 ring. When the laser tracker is placed outside and as it moves further away from the ring, the uncertainty in the radial direction increases. This is due to increase in distance between the laser tracker and the ring results in increase of horizontal distance (L). Due to increase in distance 'L', angle as well distance measurement uncertainty increases, however the impact of angular uncertainty on the radial direction reduces while the impact of distance uncertainty in the radial direction increases. The combined effect of these error sources results in a higher level of uncertainty in the radial direction. When the laser tracker is positioned inside the ring and as it moves away from the ring, upto certain position of components i.e. α ~ 12˚ uncertainty in radial direction is on the higher side while beyond this angle, uncertainty value reduces with the increase of distance of laser tracker station from the ring.

From figure 4, it can also be noticed that the location of laser tracker station inside the ring results in lesser uncertainty in measured coordinates of the points for the same component. This outcome can be attributed to curvature effect. Due to the curvature of particle accelerator ring, distance of the measured points from inside station is lesser which results in lower uncertainty in distance and angle measurements. In addition, it covers wider working volume while maintaining the required tolerances though the visible area which may be larger from outside of the ring.

CONCLUSIONS AND FUTURE WORK

In the present work, the effect of location of laser tracker stations on the measurement uncertainty in radial direction is studied for a nearly circular accelerator machine. Mathematical study was done by taking into account the effect of directional errors. The study indicates that positioning uncertainty in measured points decreases as the laser tracker gets closer to the ring. Moreover, placing the laser tracker station inside the machine reduces the uncertainty of measured coordinates of the points for the same component and allows for a wider working area to be covered while maintaining the required tolerances. However, it should be noted that the visible area from inside the machine may be lesser in this case. In the near future, laser tracker's performance will be evaluated for typical in-situ conditions, and these values will replace the manufacturer's provided values. Furthermore, simulations will be performed to estimate alignment accuracy and enhance our knowledge for the future particle accelerators where required alignment tolerance is ~ 50 µm.

REFERENCES

[1] R. J. Leao, C. R. Baldo, M. L. C. D. C. Reis, and J. L. A. Trabanco, "Engineering survey planning for the alignment of a particle accelerator: Part I. Proposition of an assessment method," *Meas. Sci. Technol.*, vol. 29, no. 3, pp. 1–7, 2018.

[2] Vikas and R. K. Sahu, "A review on application of laser tracker in precision positioning metrology of particle accelerators," *Precis. Eng.*, vol. 71, pp. 232–249, 2021.

[3] P. K. Nema, R. K. Sahu, and V. Prasad, "Review of alignment activities for Indus-1 & 2 at CAT," in *6th International Workshop On Accelerator Alignment*, ESRF, 1999.

STATUS OF DESIGN AND TESTING OF 20 KW SOLID-STATE RF POWER AMPLIFIER FOR BUNCHER CAVITY OF LEHIPA

B. V. Ramarao, Muthu S, Snigdha S, J. K. Mishra, Sandeep S., M. Pande, Gopal Joshi

Bhabha Atomic Research Center, Mumbai-85

Abstract

The LEHIPA project is under development at BARC for acceleration of proton beam to an energy of 20 MeV Recently, proton beam acceleration up to 10.8 MeV has been commissioned through RFQ, buncher, and DTL-1. To mitigate the requirement of increased beam parameters, a new solid-state power amplifier of power output of 20 kW at 352 MHz has been designed. It uses 24 RF power modules of each rated at 1 kW, which have been combined using a 24-way power combiner. The power combiner has an insertion loss of 0.1 dB, and amplitude and phase imbalances of among the input ports of ±0.3 dB and ±1° respectively. The RF power amplifier module has efficiency of 70% and power gain of 20 dB at 352 MHz. The modules are rated for both CW and pulse operation.

INTRODUCTION

The basic systems of LEHIPA are shown in Fig.1. LEHIPA, basically consists of three accelerating cavities and one buncher cavity. The accelerating cavities are Radio Frequency Quadrupoles (RFQ), and two stages of Drift Tube Linacs (DTL-1 & nDTL-2). Recently, proton beam acceleration up to 10.8 MeV has been commissioned through RFQ, buncher, and DTL-1. The three acceleration cavities RFQ, DTL-1, and DTL-2 are driven by a high-power RF klystron working at 352 MHz. The buncher cavity is driven by a solid-state RF power amplifier rated at 10 kW, 352 MHz. The RF power output of buncher is coupled through a coaxial waveguide transmission line, EIA -3-1/8".

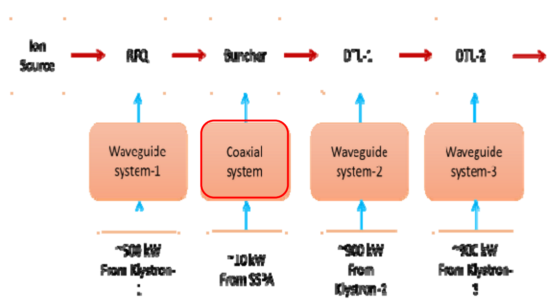

Figure 1: LEHIPA RF systems.

A new RF solid-state power amplifier of increased RF power output and with improved performance, which can also operate both in pulse and CW is planned and designed. As the present operating power amplifier is designed way back in 2014, and its operation and maintenance are costly and time consuming in future [1]. Many technologies of the RF devices have been changed over the years and availability of electronic parts are difficult. In order to avoid the down time of LEHIPA, in future it needs an innovatively designed SSPA. In view of these a 20 kW RF power amplifier design is taken up. It consists of 24 RF power amplifier modules which are combined using 24-way power combiner. Unlike two stage power combining used in earlier RF power amplifier, in this a single stage power combining technique is used. The following sections discuss about the design and status of testing of sub systems.

RF POWER MODULES

RF power modules have been designed using an RF LDMOS rated for a minimum RF power output of 1 kW at 352 MHz. Input and output matching networks have been designed for an optimum efficiency >66%. The deigned power amplifier has been fabricated using low loss (tan δ =0.01) substrate. The device has been soldered to a water-cooled cold plate to have minimum thermal resistance. The fabricated RF power amplifier module is shown in Fig. 2

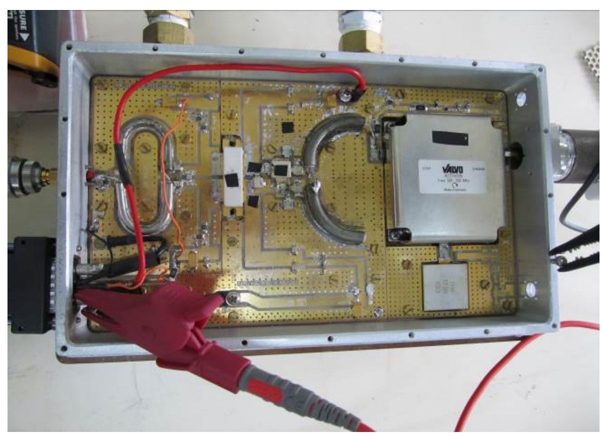

Figure 2: Photograph of fabricated RF power module

Test Results of PA module

The fabricated RF power module (RFPM) has been tested for its RF performance specification at 352 MHz both in CW and pulse operation. The CW power sweep measurements are shown in Fig. 3. The power amplifier has maximum power output of 1.035 kW at 352 MHz. It has 1 dB compression point at 975 W, with a power gain of 21.2 dB at 352 MHz. The RFPM has total phase variation of 32.2° over 20 dB dynamic range from 10 W to 1035 W. The measured RF performance specifications of the RF power module are summarised in Table. 1.

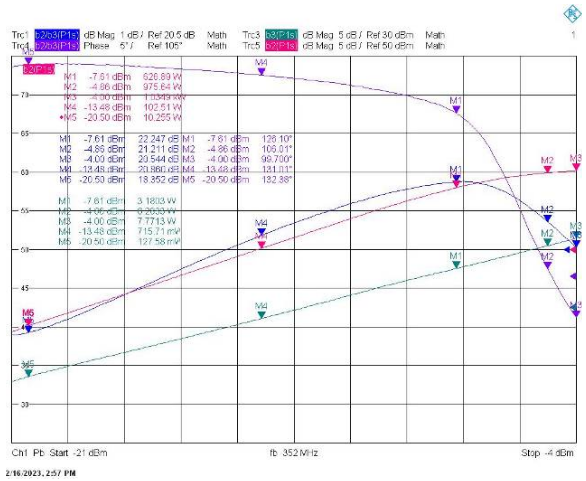

Figure 3: Measured RF input power vs power gain, P_o, phase at 352 MHz.

The measured frequency response of RFPM is shown in Fig. 4. The RFPM has 1 dB power bandwidth of 24.3 MHz.

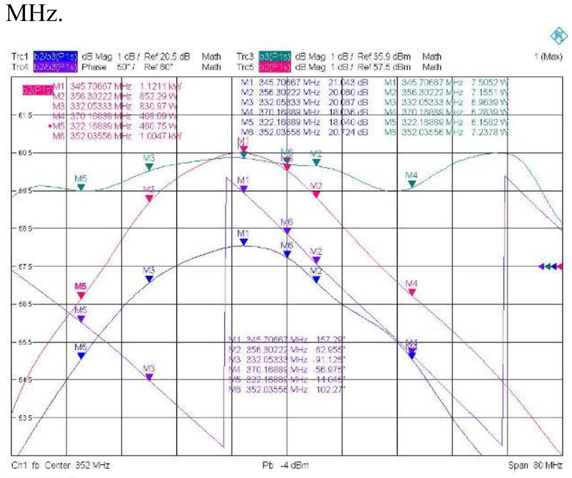

Figure 4: Measured frequency response of RFPM

Table 1: Measured CW, RF performance of RFPM

Parameter	**Value**
Max. power output (W)	1035
1-dB power output (W)	975
1-dB power gain (dB)	21.2
DC to RF efficiency (%) at 1 kW, 352 MHz	69.1
Phase variation (10 W- 1 kW) in deg.	32.6

The measured RF pulse performance parameters of RFPM at 1 kW, 352 MHz is shown in Fig. 5 (a). The test pulse has duration of 50 us with 50% duty cycle. The RFPM has risen time of 140 ns and fall time of 42 ns. The flat top of the pulse is > 25 us duration. Fig .5 (b) shows gain and phase variation with the coolant temperature variation. The gain is variation is 0.02 dB/deg and phase variation is 1 deg/deg.

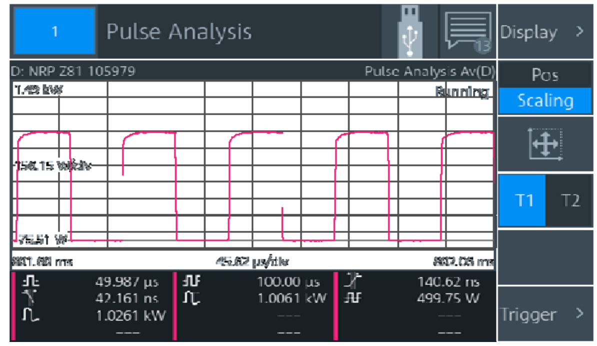

(a)

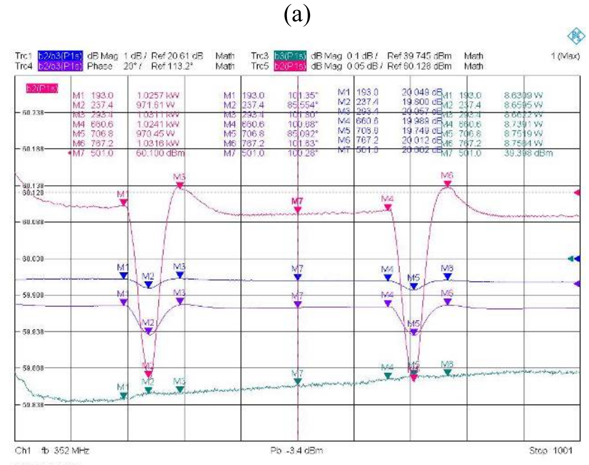

(b)

Figure 5: Measured (a) RF pulse parameters, and (b) Gain and phase variation with temperature of coolant of RFPM

The block diagram of the total RF power amplifier is shown Fig. 6. It basically consists of a 24 RF power module, a power divider, power combiner, directional couplers at frontend, input, and output locations. The DC power supplies rated at 50 V, 30 A, water flow lines, an RF switch, and an interlock and protection system.

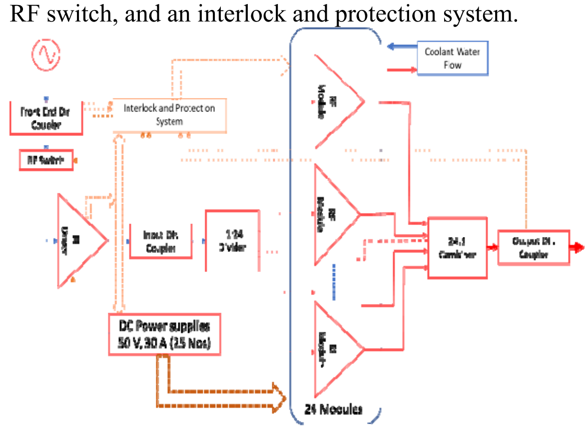

Figure 6: Block diagram of 20 kW RFPA for buncher.

RF POWER DIVIDER

A RF 24-way power divider has been designed using Wilkinson planer divider technique. The divider transmission coefficients and common port match have been optimised. The design has been implemented on a low loss (ε_r =2.2, tan δ =0.01) laminate. The fabricated RF power divider is shown in Fig. 7. Measured isolation parameters and output RTN loss are shown in Fig. 8.

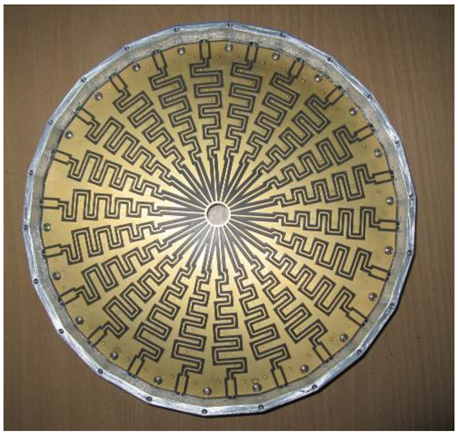

Figure 7: Fabricated power divider

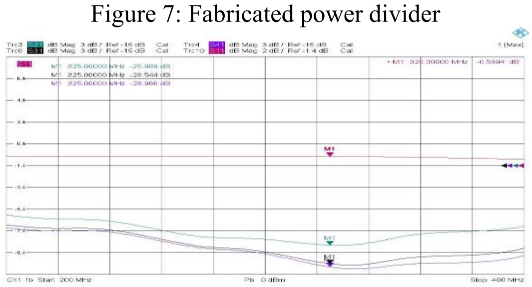

Figure 8: Measured RTN loss of output and isolation of divider

RF POWER COMBINER

A RF 24-way power combiner has been designed using Wilkinson coaxial combiner technique. The combiner has been optimised for its transmission coefficients and common port match. The design has been implemented in Al material outer conductor and Cu inner conductor. The fabricated RF power combiner is shown in Fig. 9. Measured result is shown in Fig. 10. It has |S21| of -13.9 dB at 352 MHz

Figure 9: Fabricated RF power combiner

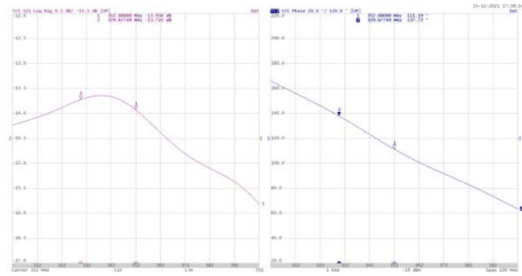

Figure 10: Measured S21 of combiner

The directional coupler has been designed coaxial transmission line and its simulated result is shown in Fig. 11. Loop and aperture dimensions have been optimised for coupling coefficient and directivity. The designed coupler has coupling coefficient and directivity of 51.3 dB and 28.7 dB respectively.

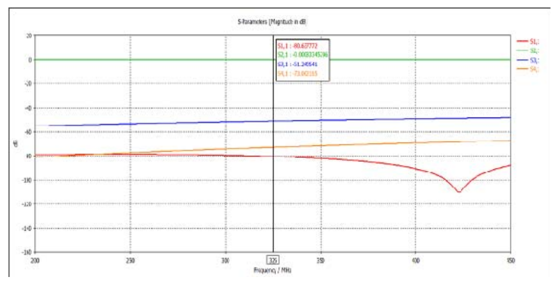

Figure 11: Simulated results of coupler

CONCLUSIONS

Design of RF power module, RF power divider, RF power combiner is done. The 12 Nos of modules tested and ready. The power divider and combiner, Interlock system are ready. The testing of remaining modules and integral testing is under progress.

REFERENCES

[1] B. V. Ramarao, et all, "Coupling and Energising of 10 kW, 352 MHz Solid-State RF Power Amplifier for Buncher Cavity of Proton Accelerator" in Proc. Indian Particle Accelerator Conference (InPAC-19)

[2] B. V. Ramarao, et. all "Development of 10 kW, 352 MHz Solid-state RF Power Amplifier for Buncher Cavity of Proton Accelerator", *in Proc. Of InPAC-2018*

INTEGRATION AND COMMISSIONING OF 150kV SOLID STATE PULSE MODULATOR FOR KLYSTRON

B M Barapatre[1*], B Maurya[1], G K Das[1], J S Pakhare[1],
V Yadav[2], Shiv Chandan[2], A R Tillu[2], U M Yerge[2]

Abstract

Solid State Pulse Modulator generates high voltage rectangular pulses at specified repetition rate. Traditionally in Klystron Modulators a Thyratron switch, Pulse Forming Network (PFN) and high-voltage pulse transformer [1] is used to convert High voltage DC into high voltage pulse to drive Klystron. Such designs are for fixed pulse-width and fixed frequency. Moreover, it requires frequent tuning. This configuration is bulky at the same time expensive. The switching side DC voltages are in the order of tens of kV in Thyratron based modulator.

Development of Solid State Pulse Modulator (SSPM) was taken up to demonstrate the feasibility to replace the Pulse Forming Network (PFN) type pulse modulator. In SSPM solid state semiconductor devices are used such as Thyristor [2], IGBT [3], MOSFET [4] and high voltage pulses are achieved while switching DC at comparatively very low voltage. SSPMs are more reliable.

A SSPM was indigenously developed using fast IGBT, fast diode, low inductance capacitor, fractional-turn pulse transformer and control & protection electronics with optical interface to provide higher HV isolation. In the event of any fault, control electronics inhibits the trigger pulses to the switching power devices. A self-integrating air core Rogowski coil was employed for current sensing and protection.

Keywords — Solid State Pulse Modulator, Pulse Transformer

INTRODUCTION

Pulse Modulator generates high-voltage rectangular pulses at specified repetition rate. Desired specification of Pulse Modulator is given in Table-1.

Table 1: Specifications of Pulse Modulator

Pulse voltage	150 kV
Pulse width	10 μsec
Pulse current	100 A
Pulse repetition frequency	200 Hz
Peak power	15 MW
Pulse rise and fall time	1μsec
Pulse droop	1%
Protection	Output short circuit, output over current, IGBTs over current and input DC over voltage

SSPM was indigenously developed to demonstrate the feasibility to replace the PFN type pulse modulator. Its peak pulse power is 15MW. The SSPM was integrated and commissioned with Klystron (TH2163) and water load at KTF, EBC Kharghar. Test trials were carried out. Various test results are presented in this paper.

SUBSYSTEM TESTING

To ensure the integrity of all the subsystems, in view of their transportation from laboratory to test facility, they were subjected to the testing at subsystem level prior to their final integration. SSPM consists of four major sub-systems namely DC source, control electronics, solid state switching power modules and HV pulse-transformer.

DC Source

This regulated DC Power supply has 100 – 1200VDC output voltage and 25A maximum output current. Power supply was tested separately for its functionality at lighter load before connecting it to the power part of SSPM. It is used to charge the energy storage capacitors placed inside the SPMs upto the pre-decided voltage level. Figure 1 shows the operation of Klystron modulator drawing 24.7A at 894V.

Figure 1: Regulated DC power supply

Control Electronics

It generates synchronized trigger pulses for each IGBT. Pulse width is adjustable from 3 to 10 μsec and frequency is variable from 1 to 250 Hz. Trigger pulses to all the IGBTs are blocked in case of any fault. Each signal between control electronics, SPMs and remote operation module are optically connected. It provides higher HV isolation, reduces transmission disturbance and better operational stability.

[1]Control Instrumentation Division, Bhabha Atomic Research Centre, Mumbai, India
[2]Accelerator & Pulse Power Division, Bhabha Atomic Research Centre, Mumbai, India
*bmb@barc.gov.in

Operating console has various switches for operating pulse modulator in local/ remote mode, indicators for monitoring health status and display for frequency.

Figure 2: Control Electronics

Switching Power Modules (SPM)

It consists of series connected energy storage capacitor, diode, IGBT switch with driver and a power board to facilitate the input and output connections. 16 nos. of modules are used in SSPM. These modules are connected to 16 primaries of the fractional turn transformer. Each SPM has a self integrating air-core Rogowski coil to sense the current through IGBT and a temperature sensor for sensing IGBT heat-sink temperature. Fault signal is generated in case of over-current and over-temperature. All SPMs were tested at site by charging them individually to 100VDC and discharging individually through 100 Ohm resistor.

Figure 3: Switching Power Module

HV Pulse Transformer

It is a special transformer called fractional turn transformer. It has half turn primary and 86 turns secondary. This has bucket shaped construction to have voltage isolation gradient and reduced circuit inductance resulting better rise time in the output pulse. Being unidirectional pulse at the output and to avoid transformer core saturation a reset winding is introduced to bias the flux in other direction. It's an oil cooled transformer assembled in a stainless steel tank which also houses Klystron and associated instrumentation. Transformer oil was tested for its breakdown before filling into the tank and ensured it to be higher than 12 kV/mm. Visual checks are must for the transformer before and after its wiring.

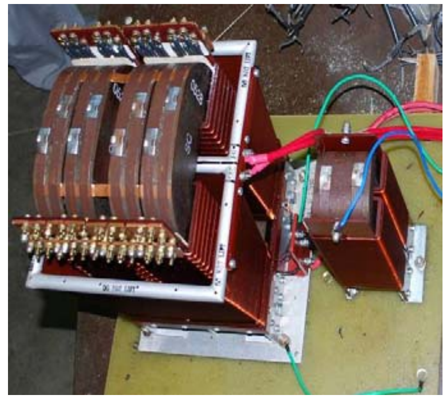

Figure 4: HV Pulse Transformer

SYSTEM COMMISSIONING

After testing all the subsystems, they were integrated in consideration to its commissioning with klystron.

Figure 5 shows Klystron Modulator after integration of subsystem. Figure 6 shows Klystron Modulator connected to Klystron (TH2163) on matched RF water load.

Figure 5: Solid State Pulse Modulator

Figure 6: Solid State Pulse Modulator connected to Klystron (TH2163) on matched water load

This solid state pulse modulator uses pulse transformer having low leakage reactance resulting better pulse rise time [5].

RESULTS

Indigenously developed SSPM was tested with Klystron (TH2163) on matched RF water load at 136kV, while Klystron current was 90A and pulse flat top was 7.5µsec. At this test condition, Klystron's peak output power was 5MW. Table 2a & 2b below shows input and output readings and Figure 7 shows the modulator output current waveform (90A). Table 3 shows recorded different pulse parameters.

Table 2a: Input and Output Readings

Input Volts (Vdc)	Input Current (A)	Input Power (kW)	Average Modulator Power (kW)
892	8.4	7.5	6.12
893	16.8	15.0	12.22
894	24.7	22.1	18.36

Table 2b: Input and Output Readings

Average Modulator Power (kW)	Average Modulator Power at flat top	PRF (Hz)	Klystron average O/P (kW)
6.12	4.59	50	1.875
12.22	9.18	100	3.75
18.36	13.77	150	5.625

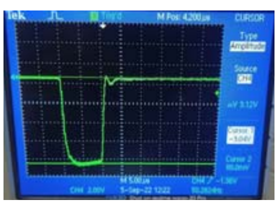

Figure 7 : Output Current Waveform(90A)

Average Modulator Power with Full Pulse width of 10 µsec: 136kV x 90A x 10µsec x 150Hz = 18.36kW
Klystron Average Power Output with Flat Pulse width of 7.5 µsec: 5MW x 7.5µsec x 150 Hz = 5.6 kW

Table 3: Recorded Pulse Parameters.

Pulse Parameter	Klystron
Pulse Rise Time	1.2 µs
Pulse Fall Time	1.0 µs
Pulse Droop	±1%
Pulse width	10 µs
Flat top	7.5 µs
PRF	150 Hz

Figure 8 shows the Klystron current pulse, RF spectrum & RF power pulse at 136kV, 90A and 4.5µsec flat top

Figure 8: Klystron Current, RF Spect & RF Power Pulse

CONCLUSION

In order to utilize this modulator for 10MeV/5kW (beam power) RF Linac with the operating parameter as given in Table 4, necessary up-gradation in the rating of a DC source is undertaken. Requirement for this application is mentioned in below Table 4

Table 4: Requirement of 10MeV Linac

S. No	Specification required	10MeV/5kW
1	Peak RF Pulse Power	4.5MW
2	Pulse width	7.5µsec flat top
3	PRF	300Hz
4	Modulator output voltage	133 kV
5	Modulator output current	86 A
6	Avg. Klystron Output power	10.1kW
7	Average Modulator Output power	25.7kW with 7.5µsec flat top

ACKNOWLEDGMENT

We would like to thank P C Saroj, Project Manager, EBC Kharghar and Awadhesh Kumar, Sushant S Bhange & Anand M Bankar, CnID, BARC for their timely support during commissioning of SSPM.

REFERENCES

[1] H. W. Lord, "Pulse transformers", IEEE Trans. Magnetics, Vol. 7, pp 17-28, 1971

[2] R. Hironaka, M. Watanabe, E. Hotta, A. Okino, M. Mayeama, K.- C. Ko, and N. Shimizu, "Performance of pulsed power generator using High Voltage Static Induction Thyristor", IEEE Trans. Plasma Sci., Vol. 28, pp. 1524- 1527, 2000

[3] Seung-Bok Ok, Hong-Je Ryoo, Sung-Roc Jang, Suk-Ho Ahn, and Gennadi Goussev, "Design of a High-Efficiency 40-kV, 150-A, 3-kHz Solid-State Pulsed Power Modulator" IEEE TRANSACTIONS ON PLASMA SCIENCE, VOL. 40, pp. 2569-2576, Oct 2012

[4] Y.-H. Chung, H.-J. Kim and C.-S. Yang, "MOSFET switched 20 kV, 500 A, 100ns pulse generator with series connected pulse transformers", Pulsed Power Plasma Science digest of technical papers, Vol. 2, pp. 1237-1240, 2002.

[5] J S Oh, M.H. Cho, W. Namkung, K.H. Chung", T. Shintake, H. Matsumoto, "Rise time analysis of pulsed klystron-modulator for efficiency improvement of linear colliders" Nuclear Instruments and Methods in Physics Research A 443 (2000) 223-230

DEVELOPMENT OF HELMHOLTZ COIL BASED MEASUREMENT SYSTEM FOR CHARACTERIZATION OF PERMANENT MAGNET BLOCKS

Ashok Kumar#, Kailash Ruwali, Sudhir Kumar, S.Das and S.N. Singh, Accelerator Magnet Technology Division
Raja Ramanna Centre for Advanced Technology, Indore .

Abstract

A majority of insertion devices used in synchrotron light source are undulators. Permanent magnet blocks made of Samarium Cobalt or Neodymium Iron Boron are used in undulators for getting spatially varying magnetic field. The quality of the magnetic field is related to the variation of magnetic properties of the individual permanent magnet blocks. Therefore, at the first step the magnetic properties of each block should be measured precisely to be able to sort them to minimize the field integrals and the phase error of the device [1]. This paper reports development of a Helmholtz Coil based measurement set up to characterize the permanent magnet blocks for the above purpose. The measurement setup consists of a Helmholtz coil, a suitable holder for the magnets, a mechanical system for rotating the magnet holder, a rotary encoder for measurement of angular position of the magnet, electronics for acquisition of the emf signal and its integration.

INTRODUCTION

In the Helmholtz coil setup, two identical circular coils are placed co-axially and separated by a distance equal to the radius of the coils. This pair of coils produces nearly uniform magnetic field in the central zone when same current is carried by the coils in the same direction. Therefore, if a magnetic dipole (magnet sample) is placed and rotated in the central zone of the coils, the information of its magnetic properties can be retrieved from the voltage induced in the coils due to change of flux. The flux w.r.t. the rotation angle can be found out by integrating the voltage signal over time. By fitting the signal with a sinusoidal function, the two components of the magnetic moment (e.g. m_x and m_z) of the sample in the plane (x-z plane) of rotation are found out. To find out the third component of the magnetic moment (m_y) , the magnet sample is rotated and the above procedure is repeated. In the present setup, the two identical circular coils of radius 400 mm have been developed and placed co-axially at a distance equal to the radius of the coils. The magnet holder made of Aluminium alloy is driven by DC motor. The voltage induced in the coils is sampled and integrated digitally to give information about the magnetic properties of the magnet being characterized.

The characterization of a permanent magnet block and description of development of measurement set-up along with measured results are discussed and presented in this paper.

MEASRURING SYSTEM

Theory of Measurement

A permanent magnet sample of size very small compared to the diameter of Helmholtz coil when rotated at the centre generates voltage (V) across the coil terminals due to the change of flux that interacts with the turns of the Helmholtz coils.

The voltage signal when integrated over the time gives magnetic flux (ϕ) [2,3] as

$$\emptyset = -\frac{1}{2N}\int_{t2}^{t1} V dt \qquad (1)$$

where N is the number of turns in each coil.

The amount of flux as a function of rotation angle θ generated by a rotating magnet sample of magnetic moment m placed at the centre that interacts with a single turn of one coil of the pair is given by [2]

$$\emptyset(\theta) = \frac{4\mu_o m(\theta)}{5\sqrt{5}\, r} \qquad (2)$$

where μ_o is the free space permeability and r is the radius of the coil.

Equating (1) and (2), the integrated voltage can be written as

$$\int_{t2}^{t1} V(\theta, t)dt = -\frac{m(\theta)}{\frac{5\sqrt{5}\, r}{8\mu_o N}} = -\frac{1}{k}(m_x cos\theta + m_z \sin\theta) + C \qquad (3)$$

where $k = 1.25^{3/2}\frac{r}{\mu_o N}$ *(A/T)* is the coil constant , m_x and m_z are the x and z components of the magnetic moments of the magnet sample respectively and the C is the offset. By fitting the voltage integral data with a sinusoidal function $a\, cos\theta + b\, sin\theta + d$ one can obtain the components of magnetic moment as $m_x = ka$ and $m_z = kb$.

A Helmholtz coil was designed using 2D POISSON code [4] and 3D TOSCA code [5]. While designing the Helmholtz coil, the radius of the coil was chosen as 400 mm so that a fairly uniform magnetic field (<1 %) is achieved at the centre for a test magnet sample of size up to 100 mm x 100 mm x 100 mm. The obtained field uniformity is found less than 1% in a distance of ±50 mm along X, Y and Z axes. Figure 1 and figure 2 show the magnetic flux lines and uniformity of magnetic field in a cylindrical and spherical volumes of radius 10 cm at the centre of the Helmholtz coils respectively.

The voltage induced in the pair of Helmholtz coils having 3000 turns in each coil separated by a distance of 400 mm equal to the radius of the coil is fed to digital voltage integrator (PDI-5025) to retrieve the flux information that have a resolution of 20 nVs. With this resolution and the

#ashokkumar@rrcat.gov.in

coil sensitivity of 6.7438 mT/A as obtained from designed value it can detect a minimum change in magnetic moment of approximately 3 μAm^2 while maximum magnetic moment can be measured up to ~5931 Am^2 (corresponding to the flux of 40 Vs) [6].

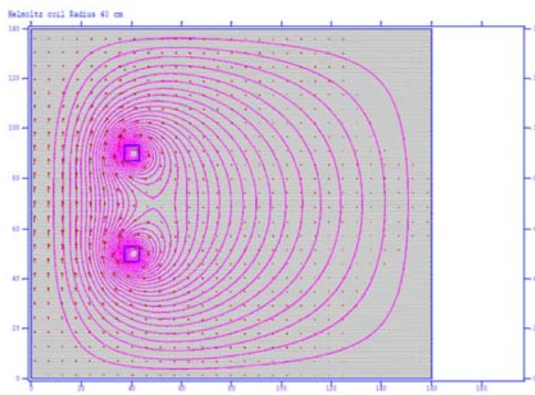

Figure.1: Flux lines as obtained using POISSON code.

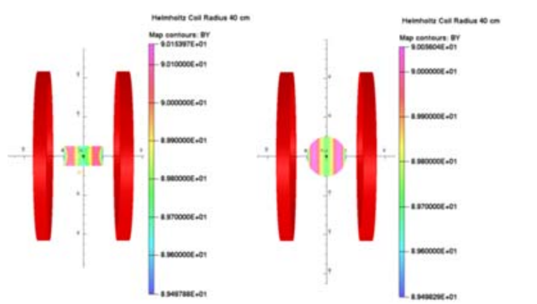

Figure.2: Magnetic field at the centre in a cylindrical space of radius 10 cm (left) and spherical space of radius 10 cm (right) of Helmholtz Coils.

Description of the Measurement Bench

The Helmholtz coil based measurement system as shown in figure 3 consists of a pair of circular coils of radius 400 mm and an aluminium magnet holder placed at the centre region between coils. The holder is coupled with planetary geared motion type DC motor and hollow shaft incremental rotary digital encoder through vertical aluminium shaft. It is ensured that the motor and encoder are mounted far below the coils to avoid the effect of their core material in the field uniformity of coils. The vertical aluminium shaft is supported by two Teflon bearings while other parts of structure are made of G-10 and Bakelite materials.

The voltage signal induced in the coils is sampled w.r.t rotation angle by digital voltage integrator. Resolution of encoder is 0.022 degree. There are 256 samples of data acquired in 360^0 and each sample-data comprises of 64 angular pulses that is time integrated. The coil ends are terminated in a box from where the output goes to the input of a Metrolab make digital integrator (PDI-5025) through specific low pass filters. The motor controller and digital integrator are interfaced with a PC. A GUI is developed for the data acquisition and control.

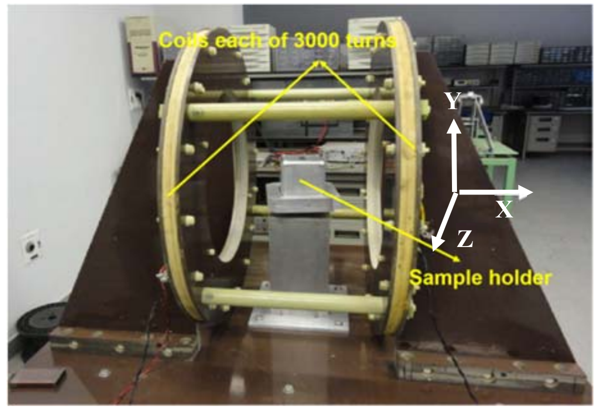

Figure.3: Helmholtz Coil set up for characterization of permanent magnets blocks.

Characterization of Magnet Block

Permanent magnet block to be characterized is firstly positioned in the magnet holder on the aluminium base plate and is rotated about y-axis (see figure 3). The index pulse of encoder is set in such a way that the angular position of the magnet block w.r.t x-axis decides the phase of the flux induced in the coils. So it is precisely matched with the initial position of magnet. By rotating the magnet, m_x and m_z components of the magnetic moment are found out. To correct the error in the initial position of the sample, it is rotated by 180^0 about y –axis and the measurement is repeated again as above. The m_y component is obtained by shifting magnet block by 90^0 and rotating the magnet block about its x-axis.

MEASUREMENT RESULTS

The Helmholtz coil constant i.e. the k value was measured using precision Keithley-6430 source meter and Mag-01 Bartington Fluxgate Magnetometer. The measured k value for the Helmholtz coils was obtained 149.58198 A/T.

To qualify the set up, a rectangular coil of average size of 13.117 mm(H) x 47.245 mm(W) x 89.03(L) mm with 8300 nos. of turns was made. The coil was excited using source meter at 6.003 mA. The value of the magnetic moment of the coil for the above parameters is 0.030877 Am^2. This sample was measured in the Helmholtz coil set up and the measured value of 0.029916 Am^2 was found which is in good agreement with the designed estimated value (absolute difference is 9.61x10^{-4} Am^2).

The GUI shown in figure 4 depicts the results obtained from measurement of an NdFeb magnet block. The information of flux integral in GUI shows the sinusoidal fitting along with raw data scan. A fully automatic measurement system has been developed that can acquire samples of the voltage signal, fit the signal with a sinusoidal function and then calculate the magnetic moments m_x, m_y and m_z of the sample. Figure 4 lists the components magnetic moments (x,y,z), their angular orientations, total strength of moments and its standard deviation at different set of data. The features that are added in the software are control of the speed of the DC motor, initial step count of the encoder to make low phase error, setting of the gain of integrator and saving of the raw

temperature because the setup would be used for sorting of permanent magnet blocks. The measurement of an NdFeB permanent magnet block was used to get repeatability of the setup. Data so collected reveal that the system provides

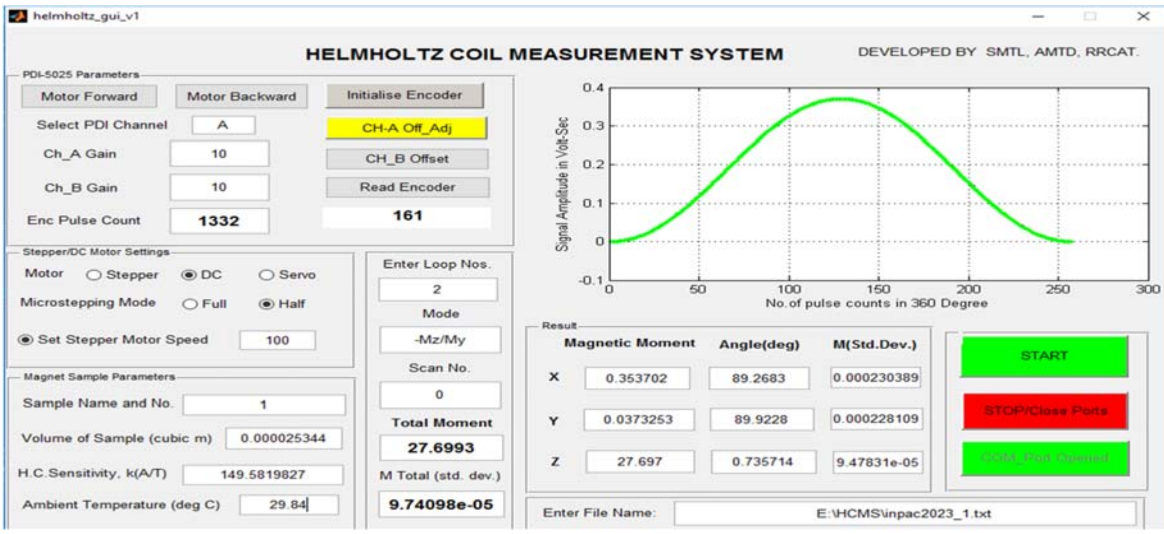

Figure.4: GUI of Helmholtz Coils measurement setup showing system controls and results.

data along with measured results in a file.

Figure.5: Magnetic moments vs temperature plot of NdFeB magnet block.

Measurement of an NdFeB magnet with size of 49mm x 49mm x 12mm was done at different temperatures. The data of the magnetic moments obtained at different temperatures is shown in figure 5. At each temperature measurement was repeated few times. We found the total magnetic moment ~27.70 Am^2 with angular orientation of 0.73^0 (with the z-axis) at 29.8 ^{0}C whereas the standard deviation of moment was found well below 0.05%.

Another magnet sample with volume of 28.812x10^{-6} m^3 was also measured repeatedly and found intrinsic induction (B) of ~1.2 T with standard deviation less than 0.05% of its magnetic moments.

CONCLUSIONS

The precision of the measurement setup in terms of repeatability should be very high at a particular

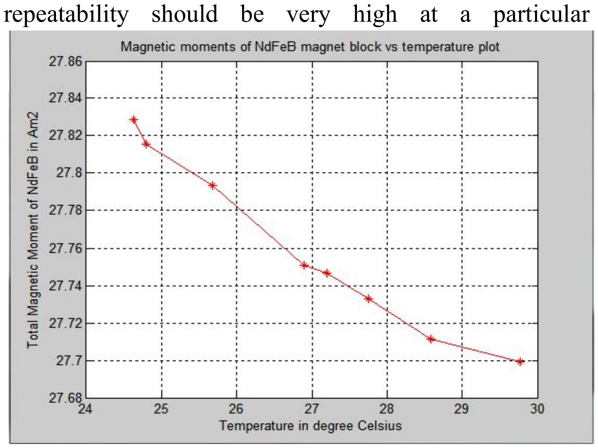

a repeatability of better than 0.1 % in total strength (27.82785 Am^2) and better than 0.1^0 in angular orientations of the components of magnetic moment w.r.t. the total moment.

REFERENCES

[1] J. Bahrdt , "Permanent magnets including undulators and wigglers", Magnets, CAS CERN Accelerator School, Bruges, Belgium 16 – 25 June 2009, CERN–2010–004, Proceedings 30 November 2010,pp 185-229, http://cdsweb.cern.ch/record/1158462/files/cern-2010-004.pdf.

[2] D.W. Carnegie and J. Timpf , "Characterizing permanent magnet blocks with Helmholtz coil", Nuclear Instruments and Methods in Physics Research A319 (1992) 97-99.

[3] Joseph Z. Xu and Isaac Vasserman, ANL, Argonne, IL 60439, U.S.A. , "A NEW HELMHOLTZ COIL PERMANENT MAGNET MEASUREMENT SYSTEM" Proceedings of ICALEPCS2011, Grenoble, France.

[4] POISSON group of codes, Los Alamos National Laboratory, Los Alamos, New Mexico 86545.

[5] Vector Field Ltd., Oxford, England.

[6] PDI5025 user manual, http://www.metrolab.com/uploads/Document/WEB_CHEMIN_118_1158928352.pdf.

DESIGN AND DEVELOPMENT OF FLOATING PULSE POWER SUPPLY FOR TRIODE ELECTRON GUN

A. Pandey*, A. Gupta, J. Mulchandani, Y. Wanmode, M. Lad, P. Shrivastava,
Radio Frequency Systems Division, Raja Ramanna Centre for Advanced Technology (RRCAT), India

Abstract
Triode type pulsed electron gun of 90 kV cathode voltage has been developed at RRCAT, Indore as a technology demonstration [1]. This electron gun source is proposed to be used for 10 MeV electron LINACs for irradiation of industrial and agricultural products. The control electrode (wehnelt) of the electron gun requires positive pulsed voltage up-to 2 kV floating at cathode voltage. Conventionally, a resistive voltage divider has been used to bias the wehnelt of the electron gun. A 0-2 kV floating pulse power supply has been developed to replace this divider based wehnelt biasing. This paper presents design, development and test results of this pulse power supply for triode type electron gun. The power supply has been tested and qualified on a resistive load of 10 kΩ up-to pulse repetition rate of 300 Hz. Also it is integrated with the electron gun test stand and tested at different wehnelt voltage values at -90 kV cathode voltage.

INTRODUCTION

Pulsed electron guns are a crucial source of electrons in RF linear accelerators. RRCAT has developed 50 kV and 90 kV triode type electron guns based on thermionic emission. The electrons emitted from cathode are accelerated inside the electron gun upto 50 keV or 90 keV energy before injecting into accelerating structure. The biasing pulse for these electron guns is derived from a solid state pulse modulator. A pulse modulator is a system which provides high voltage pulses at negative potential to the cathode of electron gun with anode at ground potential. A control electrode between cathode and anode of the electron gun is called wehnelt or grid. By varying the potential of the wehnelt, it is possible to control the gun current.

For the 90 kV triode type electron gun, the cathode is at -90 kV voltage and the wehnelt voltage is kept between 0 to 2 kV with respect to cathode voltage. Conventionally, wehnelt biasing is done by dividing the cathode voltage using resistive divider. However, this method suffers from disadvantages like,

- The wehnelt voltage cannot be varied online as the system needs to be turned off for changing the divider tapping.
- The wehnelt voltage can only be varied in steps depending on the number of resistors in the divider network.
- One point of the divider needs to be at ground potential for which electrical isolation has to be done from high voltage to avoid arcing.

To overcome above drawbacks, a 0-2 kV floating type pulse power supply has been developed for biasing of the wehnelt of the electron gun. This power supply floats at the cathode voltage of -90 kV.

SYSTEM DESCRIPTION

Fig 1 shows the developed scheme for wehnelt pulsing of 90 kV triode type electron gun. The power for filament heating of the cathode of electron gun is derived from a filament supply through a 100 kV epoxy potted isolation transformer of 1:1 turn ratio. A 230 V : 10 V filament transformer steps down the voltage as required by the filament (F) of the electron gun. 100 kV isolation transformer has been used for two purpose,

- It provides heating power to the filament of the cathode by isolating the input ac mains from cathode high voltage
- It provides ac power to the pulse power supply for wehnelt biasing

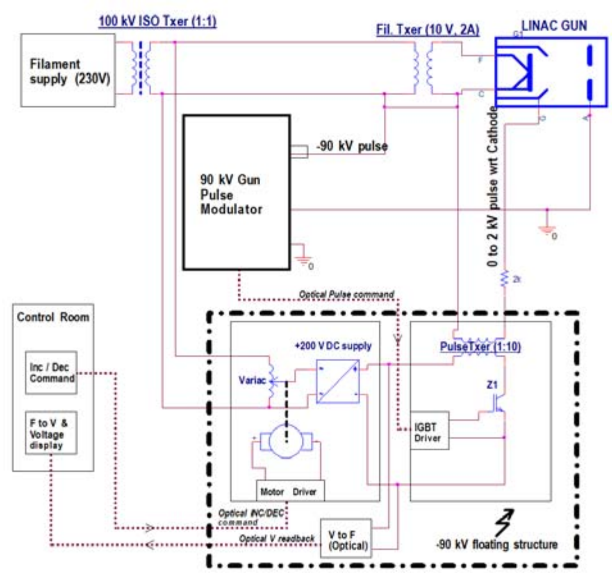

Figure 1: Overall scheme for wehnelt pulsing of electron gun

*ashwinp@rrcat.gov.in

Figure 2: 90 kV pulse modulator (front and rear views)

A 90 kV solid state hard-switched pulse modulator provides a -90 kV, 2 A, 16 µsec pulse between cathode (C) and anode (A) of the electron gun [2](Figure 2). A floating pulse power supply provides a 0-2 kV, 16 µsec between the wehnelt/grid (G) and cathode (C) of the electron gun in synchronism with the -90 kV pulse from the pulse modulator system. This power supply consists of a motorized variac which takes AC power input from the same isolation transformer used for filament supply. The output of the variac is converted into 0 - 200 V DC voltage which is switched through a 1:10 pulse transformer to provide 0 to 2 kV, 16 µsec pulse to the wehnelt with respect to the cathode. Since, complete power supply is floating at -90 kV cathode voltage, it is enclosed in a glass epoxy enclosure and mounted using epoxy bushes for isolation. The command for increase/decrease of wehnelt voltage is given to motor driver from control room and measurement/readback of wehnelt voltage is achieved using optical communication.

DEVELOPMENT

The developed pulse power supply consists of following main 3 systems;

0-2 kV pulse generator

A 0-2 kV pulse generator consists of motorised variac which is fed by an isolation transformer. The output of the variac is rectified, filtered and converted into DC voltage of 0 - 200 V. The value of DC voltage is controlled by adjusting the output voltage of motorised variac. This DC voltage is switched using an IGBT switch (IXYB82N120C3H1) through a 1:10 step up pulse transformer.

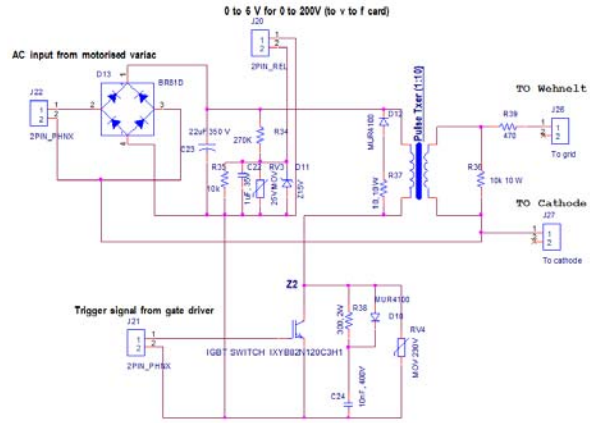

Figure 3: Schematic of 2 kV pulse generator

Figure 3 shows the schematic of 2 kV pulse generator circuit. The pulse transformer has been made from ferrite E cores. The primary winding (37 turns) and secondary winding (370 turns) are wound on the center limb of the E cores. A freewheeling circuit has been connected across the primary for dissipating the energy stored in magnetising inductance of pulse transformer. The output of the pulse transformer is connected between the wehnelt and cathode of the electron gun.

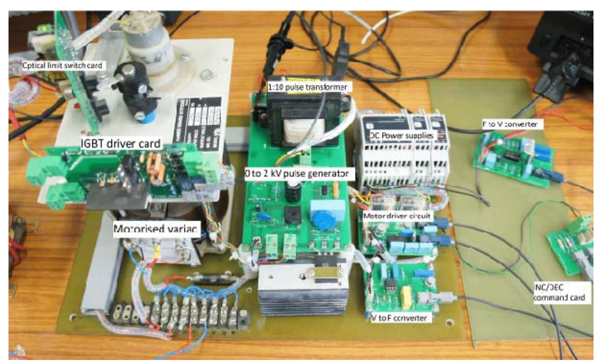

Figure 4: Assembly of circuits for the pulse power supply

Command and control circuit

It is required to pulse the wehnelt in synchronism with the main biasing pulse from the pulse modulator. The trigger signal to the IGBT switch of the pulse generator comes from the same trigger generator used for the pulse modulator switches. This optical trigger signal is converted into -8 V (low level) and +15 V (high level) pulse by the gate driver card before applying to the gate of the IGBT.

An optical command card enables the user to provide increase and decrease signals to the motorised variac for adjusting the output voltage of variac which in turn controls the amplitude of wehnelt to cathode pulse voltage. A motor driver circuit converts the optical signals from command unit to electrical signal for driving the DC motor of the variac. An optical limit switch circuit is used to set minimum and maximum limit of the variac output.

Measurement and readback circuit

The readback of the wehnelt voltage is done by sensing the DC voltage at the rectifier output using a voltage divider. A voltage to frequency converter circuit converts this voltage into proportional frequency signal. Since, the pulse power supply is floating at HV, this frequency signal transmitted optically. At the user end, a frequency to voltage converter circuit converts this frequency signal back into voltage signal. This voltage signal is calibrated in terms of wehnelt voltage and displayed on a digital meter.

All the above circuits has been designed and artworking has been done for fabrication of PCBs. The PCBs has been assembled and mounted as shown in Figure 4.

TESTING AND RESULTS

The developed pulse power supply was initially tested on 10 kΩ resistive load upto 300 Hz pulse repetition rate. Figure 5 shows the waveforms for wehnelt voltage at 500 V, 1 kV, 1.5 kV and 2 kV.

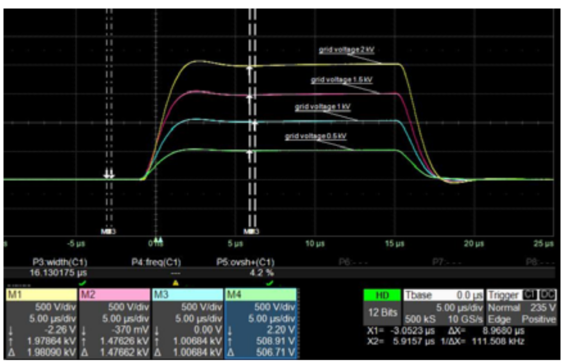

Figure 5: Waveforms for wehnelt voltage at 500 V (M4), 1 kV (M3), 1.5 kV (M2) and 2 kV (M1) on resistive load

After calibration and testing on resistive load, the pulse power supply was integrated with 90 kV electron gun test stand as shown in Figure 6.

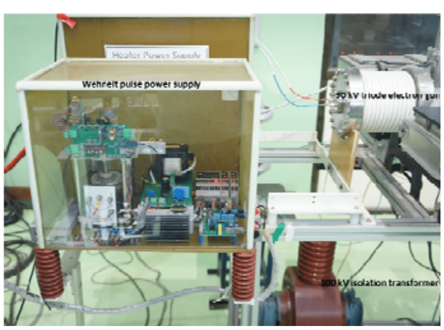

Figure 6: Wehnelt power supply integrated with 90 kV electron gun test stand

At 90 kV cathode voltage, the wehnelt voltage was varied and change in beam current of electron gun has been observed (Figure 7). At 500 V, 1000 V and 1500 V wehnelt voltage, beam current of 535 mA, 759 mA and 810 mA has been obtained respectively with cathode voltage -90 kV.

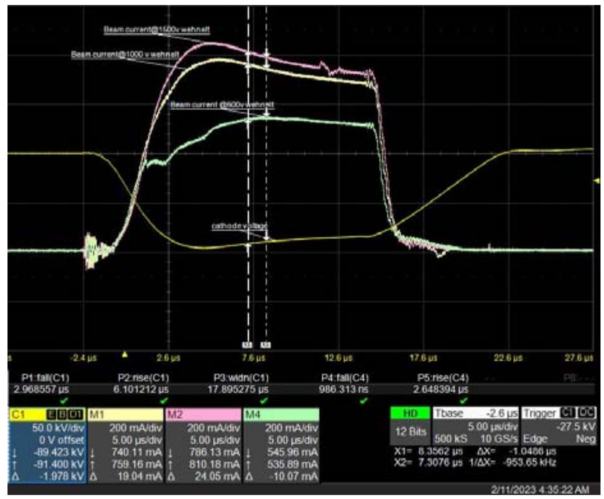

Figure 7: Waveforms of beam current at different wehnelt voltages at 90 kV cathode voltage

CONCLUSIONS

The paper presented design and development of 2 kV floating pulse power supply and its testing on resistive dummy load as well as with 90 kV triode electron gun test stand. The power supply has several advantages compared to conventional resistive divider based wehnelt control. It is shown that beam current from electron gun can be controlled using this power supply. This scheme will be finally implemented with LINAC test stand for beam current control.

REFERENCES

[1] Yashwant Wanmode , Ashwin Pandey , Ankit Gupta , Mahendra Lad , Purushottam Shrivastava, “Design and development of 90 kV triode electron gun”, *InPAC - 2022*

[2] A. Pandey et. Al. “Design and development of 90 kV, 2 A solid state hard switched modulator for electron gun” *InPAC 2022*

NUMERICAL STUDIES FOR EVOLVING MEASUREMENT METHODOLOGY FOR CHARACTERIZATION OF SINGLE CELL IN CONSTANT GRADIENT TRAVELING WAVE LINAC

Parul Arora[1, #], Prasanta Kumar Jana[1], Nita S. Kulkarni[1], and Vinit Kumar[1, 2]
[1]Proton Accelerator Group, Raja Ramanna Centre for Advanced Technology, Indore
[2]Homi Bhabha National Institute, Mumbai.

Abstract

Low power RF measurements are very crucial for the characterization of RF cavities/cells before installing or brazing them in a linac structure. These measurements are performed to estimate the resonant frequency, quality factor etc. of RF structures. For the identical cells of constant impedance traveling wave linac, the direct method using stack of similar cells in the multiple of three (*e. g.* "Half Cell-Full Cell-Full Cell-Half Cell"), is generally used for measuring the resonant frequency of desired (2π/3) operating mode. Whereas, in the case of non-identical cells of constant gradient linac, indirect methods are preferred. Single-cell measurement method is one of the methods, which is used to characterize the individual cells of a constant gradient linac structure, using a single measurement set-up. In this paper, we describe the details of single cell method for low power RF characterization of cells.

INTRODUCTION

A constant impedance (CZ) structure has identical geometrical parameters for all the cells designed for the same phase velocity. In the absence of beam loading, longitudinal electric field decays exponentially in these structures. Whereas, in a constant gradient (CG) structure, the aperture radius and cavity radius of each cell, even though designed for the same phase velocity, are suitably varied such that the group velocity varies linearly, to obtain constant electric field along the structure, without beam loading [1]. The CG structure has a higher RF to beam power conversion efficiency, compared to a CZ structure. We had earlier designed disk loaded, CZ type, traveling wave (TW) electron linacs, operating in 2π/3 mode at 2856 MHz [2, 3, 4]. Recently, design of a 9.5 MeV, disk loaded, CG type, TW electron linac structure has been done for industrial applications, which is presently being fabricated [5, 6]. In addition, we have also designed CG, TW accelerating structure for a 200 MeV electron linac for injector applications [7]. Low power RF measurements play a critical role in characterizing the cells prior to their installation or brazing in the linac structure. These measurements are utilized to determine important parameters such as resonant frequency and quality factor.

In the case of identical cells of a CZ structure, the resonant frequency of desired operating mode for a TW structure, i. e., 2π/3 mode, can be measured directly, using a single measurement set-up comprising of stack of identical cells in multiples of three. One of the configurations used for the characterization of cells of CZ structure is "Half Cell-Full Cell-Full Cell-Half Cell" configuration. In this configuration, the measurement set-up is fabricated in such a manner that one of the full cells, which is the test cell for which frequency is to be measured, is detachable. Different cells are positioned one by one at the place of test cell in the measurement set-up for characterization. Whereas in the case of CG structure, the direct method used in the CZ structure for measurement of the resonant frequency of the desired operating mode is not feasible due to variation in the geometrical dimensions of different cells. In a CG structure, all the cells are non-identical. Hence, indirect methods are preferred to estimate the frequency of 2π/3 mode for the cells of CG structure. Single-cell measurement method is one of the methods, which can be used to characterize the cells, using a single measurement set-up [8]. However, detailed explanation of the method and the measurement set-up are not readily available in the literature. In this paper, we describe the details of single cell method for low power RF characterization of cells.

MEASUREMENT METHODOLOGY

Single cell measurement method is an indirect method to estimate the resonant frequency of desired operating mode (2π/3 mode) for the cells in a CG TW structure, using a single measurement set-up. Fig. 1 shows the 2-D schematic of a disk loaded CG structure, which is cylindrically symmetric about the beam axis. Fig. 2 shows the 3-D schematic of a single cell in full cell view and cross-sectional view. The five important geometrical parameters are - cell length (*d*), cell radius (*b*), aperture radius (*a*), disk thickness (*t*) and disk edge radius (*r*).

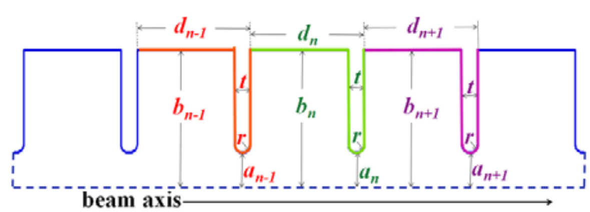

Figure 1: 2-D schematic of a disk loaded CG structure.

Fig. 3 shows the basic schematic of the measurement set-up with a test cell. The main components of the measurement set-up are lower plate, choke flange, test cell and measurement probes to pick up the sensing RF

[#]parul@rrcat.gov.in

signals. The test cell and the lower plate are connected by spring contacts, and form a cavity with a resonant frequency depending on the inner geometrical dimensions of the cell. The choke flange with a cutoff hole sits on the test cell and press the spring contacts between test cell and lower plate. It also acts as a beam pipe connected after the disc of test cell. Lower plate has two RF ports to connect the test cell with the Vector Network Analyzer to measure its resonant frequency and quality factor.

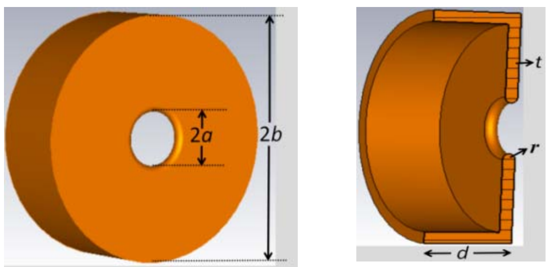

Figure 2: Three dimensional schematic of a single cell.

The test cell in the measurement set-up is equivalent to a single cell with a beam pipe, as shown in Fig. 3. Single cell measurement method gives the frequency of 0-like mode (f_0) of a single cell. The field distribution and resonant frequency (f_0) in the single cell test set-up is different as compared to the field and frequency of 2π/3 mode ($f_{2\pi/3}$) in the periodic structure of the same cell, and there is a systematic difference between these two frequencies for all cells. For finding this difference for n^{th} cell ($\Delta f_n = f_{2\pi/3,n} - f_{0,n}$) in a CG structure, we need to calculate f_0 for that cell with a beam pipe. The length of the beam pipe (choke flange with a cutoff hole) is selected such that it is sufficient enough to terminate the electric field lines. The diameter of the beam pipe is taken more than the aperture radius.

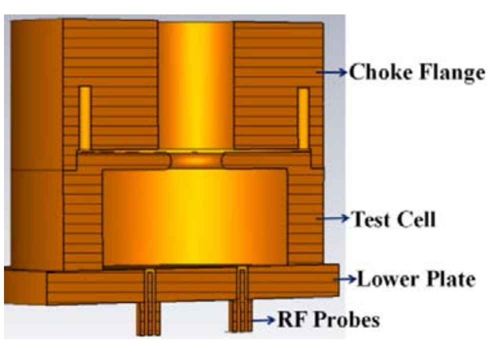

Figure 3: Basic schematic of the measurement set-up with a test cell.

RESULTS OF 2D ELECTROMAGNETIC SIMULATION STUDIES

In this paper, we are presenting a case study for a CG TW linac. We have performed 2D electromagnetic (EM) simulations using SUPERFISH [9]. The simulations were performed for six different cells in the CG structure, each having different value of β_g (group velocity in unit of speed of light), as per its aperture radius and cavity radius. Fig. 4 (a) shows the SUPERFISH simulation results for a test cell in the measurement set-up to find $f_{0,n}$. The frequency of 2π/3 mode ($f_{2\pi/3,n}$) for the same cell, is calculated by simulating 3-cells (Half Cell-Full Cell-Full Cell-Half Cell) configuration. Table 1 lists the simulated values of $f_{2\pi/3}$ and f_0 (sim) for six different cells in the CG linac structure. Fig. 4 (b) shows the variation of Δf with respect to β_g, and it is found to be linear.

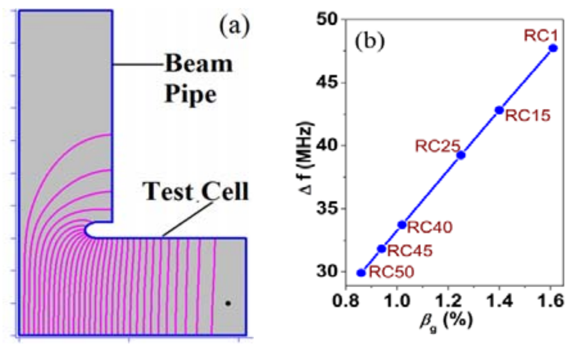

Figure 4: (a) SUPERFISH simulation result for a test cell. (b) Variation of Δf with respect to β_g.

Table 1: Values of $f_{2\pi/3}$, f_0(Sim) and f_0(Analytical).

Cell No.	β_g (%)	$f_{2\pi/3}$ (MHz)	f_0 (Sim) (MHz)	f_0 (Analytical) (MHz)
RC1	1.61	2856.02	2808.29	2810.75
RC15	1.40	2856.01	2813.19	2814.78
RC25	1.25	2856.02	2816.77	2817.77
RC40	1.02	2856.00	2822.26	2822.43
RC45	0.94	2856.03	2824.20	2824.11
RC50	0.86	2856.04	2826.13	2825.79

We have estimated the value of $f_{0,n}$ using analytical calculations as well. The single cell measurement setup, described here, is equivalent to a pill box cavity connected via one coupling slot to a beam pipe. The resonant frequency for the measurement set-up can be expressed by Eq. 1 as follows:

$$f_0 = \frac{2.405\ c}{2\pi b}\frac{\kappa}{4} \tag{1}$$

$$\kappa = \frac{4a^3}{3\pi\, J_1^2(2.405) b^2 (d-t)},$$

here, c is the speed of light, b is the cavity radius, a is aperture radius, d is cell length and t is disk thickness. The values of f_0 calculated using Eq. 1 are listed in Table 1, and are found to be in reasonable agreement with the simulated values. Hence, by calculating Δf for the test cell using simulations, and measuring the value of f_0 for the test cell in measurement set-up, we can estimate the resonant frequency of 2π/3 mode for that cell. Along with this indirect method to measure the frequency of 2π/3 mode, the resonant frequency of 2π/3 mode should be measured using the direct method, for example-"Half Cell-Full Cell-Full Cell-Half Cell" configuration, for few of the selected cells. Comparison of these measured values with those obtained using single cell measurement method, will help in establishing the correlation between the measured value of $f_{2\pi/3}$ and f_0, and therefore setting reference values using measured data. Apart from this, brazing of structure may lead to changes in RF parameters. Tuning could be done post brazing for optimization [8].

RESULTS OF 3D ELECTROMAGNETIC SIMULATION STUDIES

We have also performed the 3D electromagnetic simulation studies for the single cells in measurement set-up using CST-MWS [10]. As shown in Fig. 3, the 3D EM design studies were performed by incorporating the main components of the measurement set-up like lower plate, choke flange and measurement probes with the test cell, in the simulations. The values of f_0, calculated using CST-MWS for the single cells in measurement set-up, were found to be in good agreement with those obtained using equivalent 2D EM simulations in SUPERFISH.

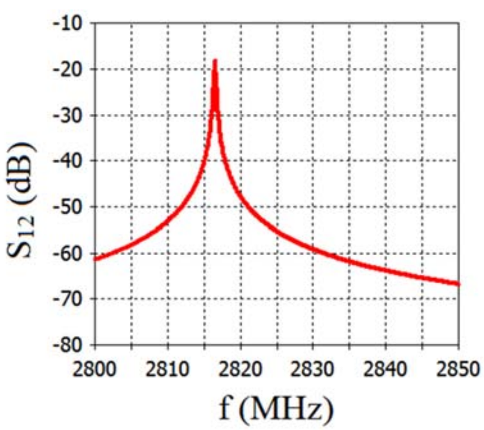

Figure 5: Variation in S12 with respect to frequency for the test cell (RC25).

The 3D EM simulations were also performed to find the effect of dimensions of choke flange, on the resonant frequency of the 0-like mode of the single cell. The initial studies were performed by using the geometrical dimensions of the standard choke flange. It was found that the vertical length of choke flange has no effect on the f_0 value after a certain length, where the electric field lines are terminated. Whereas, the gap between the disk of test cell and lower surface of choke flange (shown in Fig. 3) considerably effects the f_0 value. It was found that the gap in standard choke flange is suitable.

Studies were also performed to optimize the position of RF measurement probes to pick up the sensing RF signals, without perturbing the cavity frequency. It was found that placing the RF probes just near the cell surface is suitable. A lower depth was giving weak signals, and more depth was effecting the resonant frequency. Fig. 5 shows the plot of S_{12} with respect to frequency for a test cell (RC25) in measurement set-up.

CONCLUSION

We have performed detailed 2D and 3D EM simulation studies for evolving the measurement methodology to characterize the single cells of constant gradient, disk loaded TW linac. This method will be used to perform low power RF measurements and characterize the non-identical cells of a constant gradient linac structure, using single measurement set-up. It is an indirect method to estimate the resonant frequency of 2π/3 mode, by measuring the resonant frequency of 0-like mode of single cell in measurement set-up. Simulations have been performed to estimate the dimensions and effects of crucial components like choke flange and position of measurement probes to pick up the sensing RF signals, without perturbing the cavity frequency.

REFERENCES

[1] T. P. Wangler, "Principles of RF Linear Accelerators", Wiley, 2008.

[2] N. S. Kulkarni et al., "Physics Design of a 10 MeV, 6 kW traveling wave electron linac for industrial applications", Pramana-J. Phys., Vol. 87, pp. 74, (2016).

[3] P. Arora et al., "Electromagnetic Design and Beam Dynamics Studies of 9.5/7.0 MeV 10 kW Industrial Electron Linac with Pre-Buncher", InPAC-2018, RRCAT, Indore, Jan 9-12, 2018.

[4] R. S. Sandha et al., "Commissioning and performance optimization of 9.5 MeV, 10 kW food irradiation linac", InPAC-2022, VECC, Kolkata, March 22-25, 2022.

[5] P. Arora et al., "Physics Design of a 9.5 MeV Constant Gradient Electron Linac for Societal Applications", RRCAT Internal Report No.-RRCAT/2021-05.

[6] P. Arora et al., "Design Optimization Studies for a 9.5 MeV Constant Gradient Electron Linac for Societal Applications", InPAC-2022, VECC, Kolkata, March 22-25, 2022.

[7] P. Arora et al., "Physics Design Studies for Accelerating Section of 200 MeV Injector Linac for High Brilliance Synchrotron Radiation Source", InPAC-2019, IUAC, New Delhi, Nov 18-21, 2019.

[8] T. Khabiboulline et al., "S-band Single Cell Diagnostic", Internal Report-DESY M 96-03, Feb 1996.

[9] J. H. Billen, and L. M. Young, "POISSION/SUPERFISH", LA-UR-96-1834.

[10] CST STUDIO SUITE 2014, Publisher: CST Computer Simulation Technology AG, Version 2014.01.

Design, Fabrication and Characterization of HOM Damped RF Cavity

M Prasad*[1], Nitesh Mishra[1], Pritam S Bagduwal[1], Nitesh Tiwari[1], Brahmanand Sisodia[2], T Veerbhadraiah[2], Rajesh Kumar Prasad[2], Utpal Chaterji[2], Sanjay Sharma[2], Sanjay Chouksey[3], G Mundra[4] & Mahendra Lad[1]

[1]*RF Systems Division, RRCAT, Indore*

[2] *Design & Manufacturing Technology Division, RRCAT, Indore*

[3] *Superconducting Cavities Development Division, RRCAT, Indore*

[4]Technology Development and Support Group, *RRCAT, Indore*

* *mprasad@rrcat.gov.in*

Abstract

The performance of synchrotron radiation source at higher current is degraded due to one of the main problems of the Higher Order Modes (HOM) of RF cavities. A single cell HOM damped RF cavities are suitable to reduce the HOM related issues in low emittance machine synchrotron radiation machine.

A prototype pillbox type 500 MHz HOM damped RF cavity [1] with nose cones has been designed towards capacity building for High Brilliance Synchrotron Radiation Source (HBSRS). Preliminary parameters HBSRS are given in Table-1. For ease of fabrication development of HOM damped RF cavity is done in three parts, namely hexagonal body, end plates and three HOM dampers. HOM damper is ridged circular waveguide to coaxial transition (CWCT) [2] consisting of a tapered circular double-ridged waveguide, mode transformer section and 7/8" coaxial line of 50Ω impedance. This damper will ensure the propagation of HOMs out from main cavity. To build up confidence in fabrication of complex RF accelerating structure this prototype HOM damped RF cavity and all the parts have been fabricated in aluminium alloy. Before assembly in the RF cavity, characterization of HOM dampers was carried out. This paper describes RF design, challenges faced in the fabrication and assembly of RF cavity with three HOM dampers along with test results of important RF cavity parameters.

INTRODUCTION

Synchrotron storage ring has many beam based longitudinal modes depending upon the RF frequency and ring parameters. The beam harmonics in the storage ring are separated by the orbital frequency and the HOM frequencies are as such unrelated to this frequency but may accidentally fall close to them. For a non-uniform filled beam, the beam spectra will contain components:

$$f_{\mu,n}^{\pm} = nBf_{rev} \pm (\mu f_{rev} + f_s)$$

Where, n is zero or a positive integer, B is the bunch number, μ is a mode number of the coupled bunch oscillation, and f_s is synchrotron frequency (Hz).

One of the main cause of these instabilities is when any of beam harmonic mode coincides with HOM of the RF cavities. Significant growth in any of these mode can cause beam instabilities and in turn increase in the beam emittance. These instabilities can be reduced in many ways, shifting the HOM frequencies of the RF cavity away from the beam harmonic frequency is one of them. In SRS Indus-2, HOM frequency shift is being achieved by precisely changing the RF cavity temperature and moving the HOM frequency shifter plungers of cavity. Difficulty with these schemes is that, if we tune away one HOM in RF cavity, other HOM may come closer to beam harmonics and can still drive the instabilities. This will be tedious task if there are large number of cavities and HOMs, like in the case of low emittance machines. It also becomes a very serious issue in large diameter storage rings where the orbital frequency is small or comparable to the bandwidth of the modes. For trouble free operation at higher currents single cell HOM damped cavity is preferred. In this cavity HOMs are damped by only ridged waveguide dampers followed by 50 Ω coaxial transition. This cylindrical cavity is nose cone in its shape and is equipped with three HOM dampers. These dampers are in the form of ridged Circular Waveguide to Coaxial Transition (CWCT).

Table-1: Preliminary parameters of HBSRS

Electron beam energy	6	GeV
Beam current	200	mA
Circumference	1069	m
Energy radiated/turn	2.457	MeV
Accelerating voltage	7	MV
Beam Power (Bending M.)	491	kW
Beam Power (Insertion D)	100	kW
Total Beam Power	591	kW
Harmonic number	1536	
Synchrotron frequency	1.59	kHz
RF Frequency	500	MHz
Total RF Cavity	20	Nos.
Voltage across each cavity	350	kV
Power loss/cavity	20	kW

Total power loss in cavities	400	kW
Total required RF power	991	kW
Required RF power/cavity	50	kW

RIDGED WAVEGUIDE HOM DAMPERS AND DESIGN OF RF COUPLERS

The design of HOM dampers is challenging because it has to couple HOMs without affecting the fundamental. In a CWCT, the TM modes (except the fundamental mode) of RF cavity propagate in the tapered waveguide as TE-like modes, which finally transformed to the TEM-mode of the 50Ω, 7/8" coaxial line by means of a transformer section. Optimization of a CWCT of ridged waveguide has been carried out. The HOM damper is designed by varying the dimensions of W, G, ΦD and Φd. It works in the frequency range from 0.7 GHz to 2.6 GHz. The power of HOMs field remove from the 50 Ω coaxial load. Figure 2 shows the geometrical parameters of the CWCT.

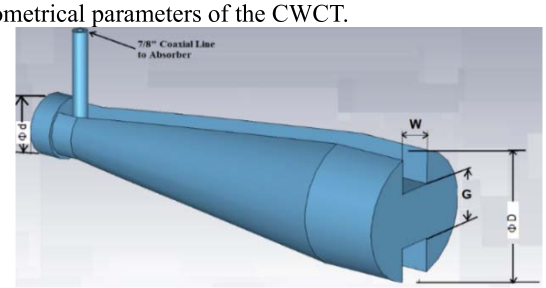

Figure 1: Geometrical parameters of CWCT

Simulated electric field plot and S_{11} parameter at port 1 of the HOM damper are shown in Figure 2.

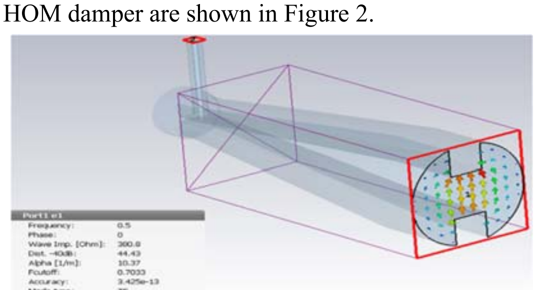

Figure 2: Simulated electric field plot at port 1 in HOM damper

Two coaxial transmission line type of RF couplers of $3^1/8$" and 7/8" have also been designed and fabricated for this RF cavity. A $3^1/8$" coupler is used to feed RF power into the RF cavity. Three 7/8" couplers are mounted on the CWCT dampers to extract HOM power from RF cavity. Another sensor is used to sense the RF power from the RF cavity. The sketch of $3^1/8$" coupler is shown in Figure 3.

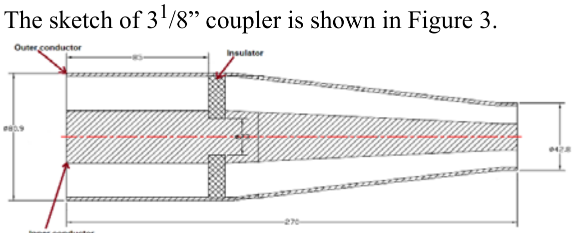

Figure 3: 2D cross-sectional of $3^1/8$" coupler.

DESIGN AND ELECTROMAGNETIC SIMULATION OF RF CAVITY

The RF cavity is designed a pillbox with nose cone type. After mounting three HOM dampers the shunt impedance of RF cavity will be reduced. For higher shunt impedance, nose cone is provided in the end plates [2]. The RF cavity is simulated with electromagnetic computer code 3D CST Studio Suite[3]. The frequency, quality factor, shunt impedance and R/Q for fundamental as well as HOMs are simulated & compared for both structures. The R/Q parameter of HOMs are reduced. Figure 4 shows the simulated 2-D electric field in the RF cavity with dampers at 500 MHz. Simulated parameters of HOM damped RF cavity are given in Table-2. Simulated damping mechanism of modes for first longitudinal & dipole modes are shown in Figure 5.

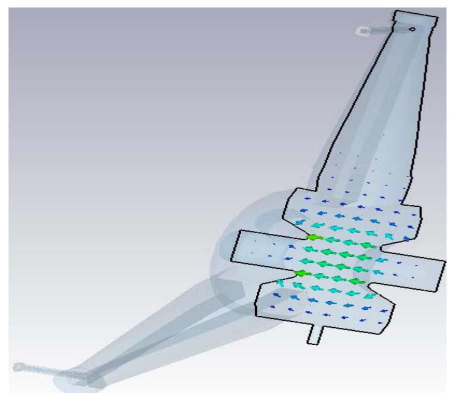

Figure 4: Electric field plot for fundamental mode.

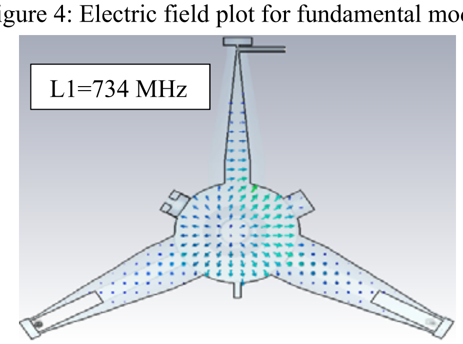

Figure 5: longitudinal mode field coupled to dampers.

Table 2: Simulated parameters of HOM Damped RF cavity

Operating frequency	500	MHz
Shunt Impedance (Rsh)	7.0	MΩ
Quality factor (Q_0)	28000	
R/Q	250	Ω
Max. accelerating voltage	350	kV
Power loss	20	kW
Frequency of First HOM	734	MHz
Cavity Diameter	370	mm
Cavity length (Flange to Flange)	400	mm

FABRICATION AND RF CHAEACTERIZATION OF HOM DAMPED RF CAVITY

Fabrication of RF Cavity

Each components of RF cavity have been machined with aluminium alloy of 6061. The machining of RF cavity was carried out on the precision NC and CNC machines. The cylindrical shaped dampers were sliced on the NC controlled vertical band saw machine. The surface profile machining was done on vertical and horizontal machining centers maintaining the profile accuracies in the order of 0.02 mm. In order to achieve the desired surface finish, tailored made polished carbide lollipop cutter of diameter 6 mm was used. The surface finish achieved during manufacturing of the cavity components was better than 0.4 micron. CNC programming was done using CAM software for machining of 3D complex geometries. Photographs of machined parts are shown in figure 6.

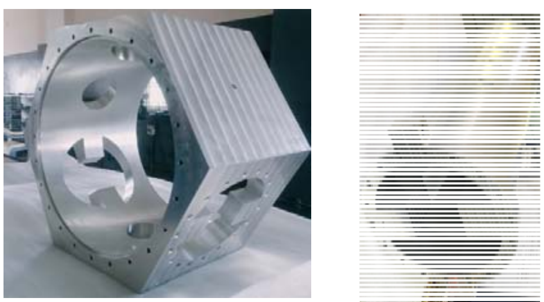

Figure 4: Photos of components of RF cavity.

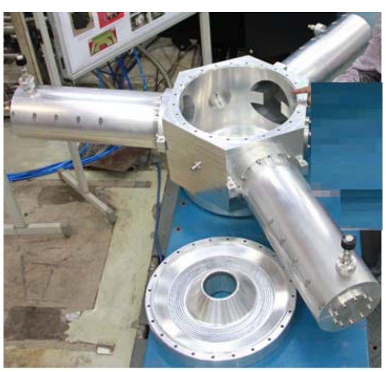

Figure 4: Photo of HOM damped RF cavity.

RF Characterization of Dampers and RF Cavity

RF characterizations of HOM dampers and RF cavity have been carried out in transmission as well as reflection mode [4]. Simulated and measured S parameters of HOM dampers are shown in figure 5. The resonant frequency and quality factor have been measured for cavity with and without three dampers. HOMs have been identified using bead perturbation techniques. A ceramic bead of diameter Φ10 mm is used. The resonant frequency of RF cavity with three dampers is 515 MHz as shown in Figure 6.

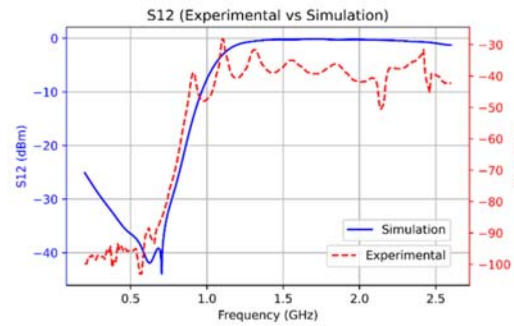

Figure 5: Simulated & measured S_{12} parameter of damper.

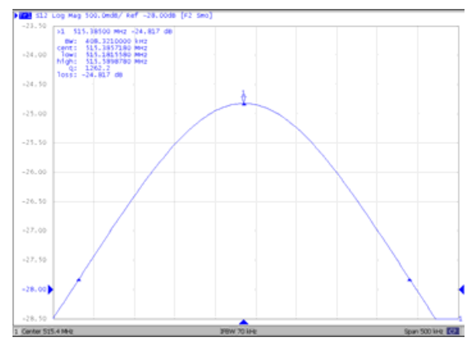

Figure 6: Measured amplitude vs resonance frequency.

CONCLUSION

The design, fabrication and RF characterization of the HOM damped RF cavity have been carried out. RF characterization of HOM dampers have been done. The resonant frequency and quality factor of RF cavity with three HOM dampers have been measured.

ACKNOWLEDGMENT

Authors would like to thank DMTD of RRCAT for machining of HOM Damped RF cavity and its components. Also thanks to Mr D Suresh, Sudarsan Kishan & Manikandan M for the characterization of RF cavity and its components.

REFERENCES

[1] M. Prasad, N. Tiwari, P. S. Bagduwal and M. Lad, "Design and Electromagnetic Simulation of HOM Damped RF Cavity for Low Emittance Storage Ring", Proc. of InPAC-2018, RRCAT, Indore

[2] F. Marhauser et.al, "Numerical Simulations of a HOM Damped Cavity", Proc. Of EPAC 2003, Vienna, Austria, pp. 1972-1974.

[3] CST- MW Studio, Version 2017, CST, Darmstadt, Germany.

[4] E. Weihreter et.al, "Optimization and Experimental Characterization of a Broadband Circular Waveguide to Coaxial Transition", Proc. of EPAC 1998, pp. 1826-1828.

Design, Development and RF Characterization of Tunable RF Cavity for LLRF Control Systems

M Prasad*, Pritam S Bagduwal, Nitesh Mishra, Ekansh Mishra, Dheeraj Sharma, Pankaj Gothwal, Nitesh Tiwari & Mahendra Lad

Raja Ramanna Centre for Advanced Technology, Indore-452013, INDIA

Abstract

A wide band capacitive loaded tunable aluminium RF cavity in the range of 320 MHz to 725 MHz, has been designed and developed for testing of LLRF systems in lab. This cavity can be tuned to any frequency in its tunable range for LLRF system testing. Electromagnetic simulations for this cavity have been performed with the help of SUPERFISH and 3D-CST Studio Suite. Simulated unloaded quality factors at resonant frequencies of 325 MHz, 505 MHz and 650 MHz are 9100, 10600 and 12900 respectively. Change in fundamental frequency and unloaded quality factor with change in penetration length of plunger have been computed. Low power RF characterization of cavity has been carried out over a frequency range of 320 MHz to 725 MHz. By tuning this cavity to 325 MHz, Digital LLRF system at 325 MHz for RFQ has been tested and optimization of LLRF parameters was done. By tuning this cavity at 476 MHz, adaptive feed forward based pulsed Digital LLRF system for IRFEL was optimized before installation in IRFEL. This cavity is being used in Lab for the characterization and optimization of LLRF systems at different frequencies and applications [1]. This paper describes the design, electromagnetic simulations, development and RF characterization results of the tunable RF cavity. Optimization of PI parameters carried out in Lab for different LLRF systems using this cavity along with results will also be presented in this paper.

INTRODUCTION

RF Cavities are one of the most important components of any particle accelerator. It not only imparts the energy to the charge particles but also the overall response of the RF system is strongly governed by the RF cavity due to its high Quality factor. These RF cavities are not readily available for testing and optimization of Low Level RF control (LLRF) systems. Different accelerators operate at different RF frequencies; accordingly, their LLRF systems are designed. Tuning of the RF cavity to required frequency is achieved by varying the length of tuning plunger inside the RF cavity. Five ports are provided on the cavity which can be used as feed and sensing ports. Also by terminating these ports appropriately, the loaded quality factor at desired operating frequency can be controlled. This provides flexibility in characterization of LLRF system for a wide range of response time. In order to reduce the installation time of LLRF systems, their characterization and optimization has to be done. Availability of RF cavity helps in optimization of PI parameters in close loop operation[2].

TUNABLE RF CAVITY

Cylindrical type capacitive loaded tunable RF cavity is designed. The capacitance of the cavity is given below

$$C = \frac{\varepsilon A}{d}$$

Where ε , A and d are dielectric constant in RF cavity, cross-sectional area of disc and distance between plunger and disc respectively.

Resonant frequency (f) of RF cavity is related to inductance (L) and capacitance (C) is as follows.

$$f = \frac{1}{\sqrt{LC}}$$

For a fixed diameter of the RF cavity, the inductance and capacitance of the cavity are changing by varying the position of tuning plunger. The resonant frequency of the RF cavity is controlled only by the position of tuning plunger. The required RF parameters of tunable RF cavity are given in Table-1.

Table -1: Required RF Parameters for Tunable RF Cavity

Operating frequency range	320-725 MHz
Max. RF Power	10 dBm
Operating Voltage	1 V
Quality factor (Q_0)	Upto 13000

DESIGN OF RF CAVITY

This RF cavity operates at very low voltage over a wide frequency range; cooling and fine tuning provision is not required. Multipacting, RF arcing, and other RF-related issues need not be taken care of in the design phase. Optimization of higher RF parameters such as shunt impedance, transit time factor and quality factor are not taken into account. The design of the RF cavity is not complicated. The diameter and the length of RF cavity are chosen for ease of fabrication and handling.

For the design of the RF cavity, the cylindrical body is chosen to accommodate the full plunger range in the RF cavity for tuning the wide frequency range. Four ports are provided on one end plate and one port is provided on the other end plate. The input coupler is designed in such a way that it acts as a coupler as well as a capacitive disk. The coupler couples the electric field to feed RF power into the RF cavity. The other four RF sensing couplers are designed as inductive coupler to sense RF power from RF cavity. This tunable RF cavity is designed for wide resonant frequency range of 320 MHz to 725 MHz. The optimized diameter and length of RF cavity are Φ233 mm and 409 mm respectively. The diameter of capacitive disk is Φ35 mm. The minimum gap (x) between the tuning plunger and the capacitive disk is optimised for a resonant frequency of 320 MHz.

The 2D-cross-sectional view of the optimized RF cavity and its details are shown in figure 1. This cavity is designed with a tuning plunger to tune the fundamental mode to a wide band width [3]. The diameter of the input coupler port and four sensing ports have been kept the same.

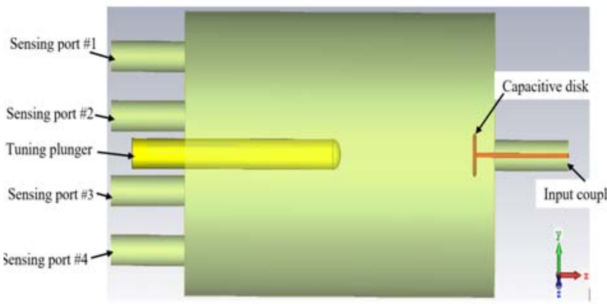

Figure 1: 2D cross-sectional view of tunable RF Cavity

ELECTROMAGNETIC SIMULATION OF TUNABLE RF CAVITY

RF Cavity Simulation

The RF cavity is simulated with the electromagnetic computer code 3D CST Studio Suite. The RF cavity is modeled with an input coupler, four sensing coupler ports along with tuning plunger [4]. Resonant frequencies and quality factors at different tuning plunger locations have been computed. Figure 2 shows the simulated 2-D electric field in the RF cavity at 325 MHz. Design parameters of tunable RF cavity are given in Table-2.

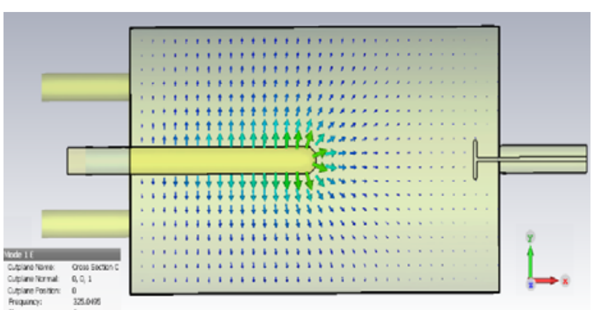

Figure 2: 2-D Electric field plot @ 325 MHz.

Table-2. Design parameters of tunable RF cavity

Operating frequency range	320 - 700 MHz
Quality factor (Q_0)	9000 - 13000
Max. Input RF Power	10 dBm
Operating voltage	1 V
Tuning stroke	200 mm
Tuning range	400 MHz

Tuner Optimization

The tuner is located in the centre of the end plate of the cavity. Tuner diameter and tuning stroke are optimised to obtain the desired resonant frequency and quality factor. The tuning plunger is moved from the cavity gap to one of the end plate. Resonant frequency and quality factor have been computed at different plunger positions. The variation of tuning plunger movements vs resonant frequency for the tuning plunger is shown in figure 3. Similar variation of tuning plunger movements vs unloaded quality factor is also shown in figure 4.

Figure 3: Variation of resonant frequency vs tuning plunger movements.

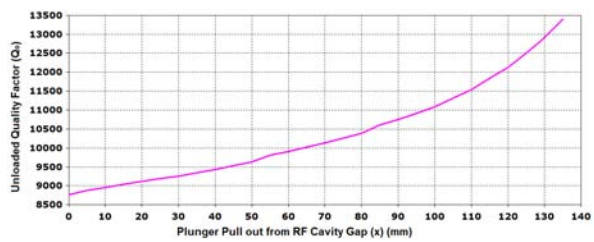

Figure 4: Variation of unloaded quality factor (Q_0) vs tuning plunger movements.

DEVELOPMENT AND RF CHAEACTERIZATION OF TUNABLE RF CAVITY

Development of RF Cavity

The RF cavity is machined with a cylinder of outer diameter Φ245 mm and of length 410 mm. End plates of 20 mm thickness are machined with suitable lip. An input coupler port of length 100 mm brazed to the center of an end plate. Four sensing ports; each of length 100 mm and 150 mm PCD have been brazed at second end plate. The material of this RF cavity is aluminium alloy 6061. This RF cavity is design to operate in air only.

RF Characterization of RF Cavity

The RF characterizations of the RF cavity has been carried out in transmission as well as reflection mode. In transmission method the RF power feeds into the RF cavity through one coupler and is detected by the other coupler vice versa. S-parameters likes S_{11}, S_{21} and S_{12} also are measured in transmission as well as in reflection mode. Resonant frequency and quality factor have been observed at different plunger position. Figure 5 shows the measured amplitude vs resonance frequency at 325 MHz. Measured resonant frequency and loaded quality factor are 325 MHz and 1300 respectively.

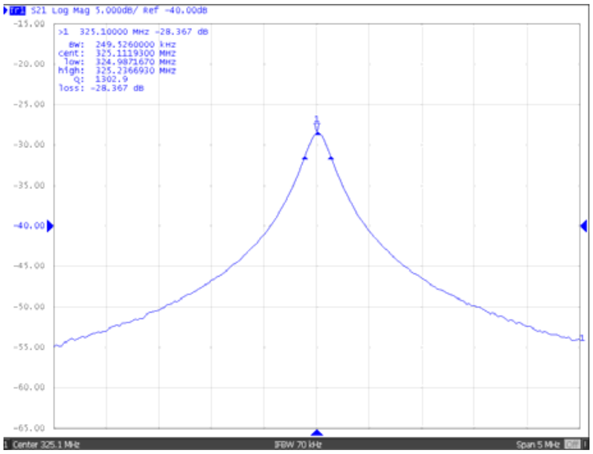

Figure 5: Measured amplitude vs resonance frequency at 325 MHz

RF Characterization of LLRF Systems

A tunable RF cavity with four feed ports and a sense port was tuned at 325 MHz to simulate RFQ for LLRF system testing. RF system simulator at 325 MHz having attenuator and phase shifters along with 10 watt RF amplifier was used to simulate RF system. A data acquisition system was developed to fetch and analyse data from RF instruments. A photograph showing digital LLRF system during testing in Lab along with other sub systems is shown in figure 6. Waveform of RF signal of LLRF system with RF cavity is shown in figure 7.

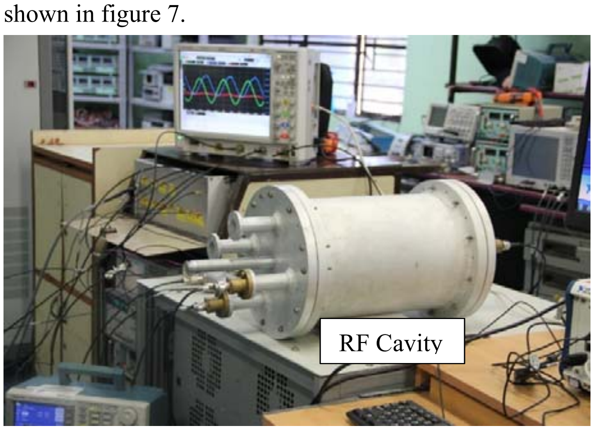

Figure 6: Photograph of digital LLRF system along with other sub systems.

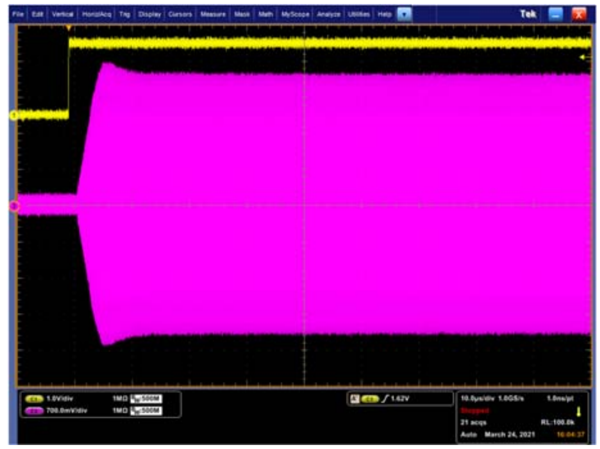

Figure 7: Waveform of RF signal of LLRF system with RF cavity.

CONCLUSION

The design, electromagnetic simulations, development and RF characterization of the tunable RF cavity have been carried out. Resonant frequency and quality factor at different plunger position have been measured. Optimization of PI parameters carried out in Lab for different LLRF systems using this cavity along with results.

ACKNOWLEDGMENT

Authors would like to thank to Mr D Suresh, Sudarsan Kishan & Manikandan M. for the characterization of RF cavity and LLRF systems.

REFERENCES

[1] N. Tiwari, P. S. Bagduwal, D. Sharma, N. Mishra and M. Lad "Development and Commissioning of Compact Digital LLRF System for Indus-2 SRS", in Proc. Vol 1, InPAC, IUAC, New-Delhi, India, 2019, pp. 22.

[2] N. Tiwari, P. S. Bagduwal, D. Sharma, E. Mishra, N. Mishra, P. Gothwal, M. Prasad and M. Lad, "Design and Development of Digital Low level RF System for RFQ at RRCAT", InPAC, VECC, Kolkata, India, 2022

[3] M. Prasad, et al., "Design, Electromagnetic Simulation and RF Characterization of Broadband Kicker RF cavity for longitudinal multi bunch feedback system for Indus-2", InPAC-2018, RRCAT, Indore, Jan., 9-12, 2018.

[4] M. Prasad, et al., "Design and Electromagnetic Simulation of HOM Damped RF Cavity for Low Emittance Storage ring", InPAC-2018, RRCAT, Indore, Jan., 9-12, 2018.

DESIGN, DEVELOPMENT AND DEPLOYMENT OF 2KW S-BAND SOLID STATE PULSE POWER RF AMPLIFIERS FOR LINEAR ACCELERATOR FACILITIES AT RRCAT

Ashish Mahawar*, Praveen Mohania, Raj Kumar Namdeo, Deodatta Baxy and Mahendra Lad
MICTL, Radio Frequency System Division,
Raja Rammana Centre For Advanced Technology,Indore – 452013

Abstract

RRCAT Indore has developed 10 MeV,10 kW Electron LINAC named KIRTI-1010, for electron beam radiation processing. The LINAC will be installed at M/s. Microtrol Sterilisation Services Pvt. Ltd. Bangalore under incubation agreement. A 2856 MHz, 2 kW pulse amplifier has been designed and developed to energize S-Band pre-buncher of the LINAC. The amplifier will be incorporated in the LLRF system of the LINAC, the details of which are presented in [2]. The amplifier is developed by combining two 1 kW amplifier modules previously fabricated using a LIM-EOM based planar RF combiners, the details of which were presented in [1]. The amplifiers supersede our earlier 2 kW amplifier design presented in [3]. The earlier design utilizes 8 LDMOS devices combined via 3 stage 8:1 Wilkinson combiner while the new design requires only 6 LDMOS devices.

The S-Band amplifier provides a peak power of more than 2 kW, at an operating pulse width of 16 µs and a pulse repetition rate in excess of 300 Hz. The amplifier provides a gain greater than 57 dB, 0.1 dB bandwidth of 2856 MHz ± 5 MHz and operates in class AB mode. The amplifier has 4- stages of amplification starting with a Low Noise Amplifier (LNA) followed by a pre-driver, a driver stage and finally the high-power stage consisting of two 1 kW modules combined via hybrid combiner. A dual directional coupler is incorporated in the high-power combiner eliminating the need for a separate coupler. The output of each 1 kW amplifier module is protected by a co-axial circulator against reflection from pre-buncher. An RF switch is used before the LNA to provide pulse width modulation, synchronization with trigger signal using trigger circuit. Two such amplifiers have been installed in the S-Band RF system for the KIRTI-1010, with one functioning as a spare for quick replacement. Both the amplifiers have been extensively tested during the LINAC operation at RRCAT. The amplifiers have performed satisfactorily during the trial operation with no failure during nearly two months (equivalent to ~ 200 hrs) of operation. Development of more amplifiers of same design is also being carried out to meet future requirements of upgrades and spares at other accelerator facilities at RRCAT.

The present paper describes the design details and test results of the amplifiers.

INTRODUCTION

RRCAT Indore has linear accelerator facilities of 6-10 MeV & 15-25 MeV which are used in different application such as radiation processing of agricultural material, medical sterilization and infra red free electron laser. A pre-buncher cavity is used for bunching the electrons emitted from electron gun. To increase the bunching a 2 kW pulsed RF power solid state power amplifier is designed, developed and installed in LLRF system of LINAC to energize the pre buncher cavity. In this paper we present the design, development, testing and qualification of RF amplifier.

AMPLIFIER CONFIGURATION AND DESIGN DESCRIPTION

For development of 2 kW pulsed amplifier at 2856 MHz using solid state devices, the main concern arises due to non availability of high power devices(in kW regime) such as LDMOS; as maximum power available in solid state device is ~400 W at the time of initialization of development. Hence it becomes necessary to use multiple devices to achieve high power.

Planar combiner/divider has been used in this design as it is suitable at the frequency of operation and it is easy to realize them on planar circuit. Instead of utilizing standard conventional planar combiner/divider we have opted Lim-Eom divider/ combiner due to its suitability to combine 3 RF devices easily [1] and [4]. For practical utility of Lim-Eom combiner/divider is to minimize its phase imbalance by adding a precise delay line. The purpose of selection a 3 way combiner is to combining the power of 3 LDMOS RF amplifier pallets operating in class AB mode of operation.

Fig.1 shows the scheme of the amplifier. It is developed as three stage amplifier; first stage A1 is pre-driver amplifier. Driver stage is also a two stage amplifier denoted as B1 & B2 and developed in single module with a hybrid divider. It is a 100 W amplifier module developed using LDMOS transistor operating in class AB mode.

* amahawar@rrcat.gov.in

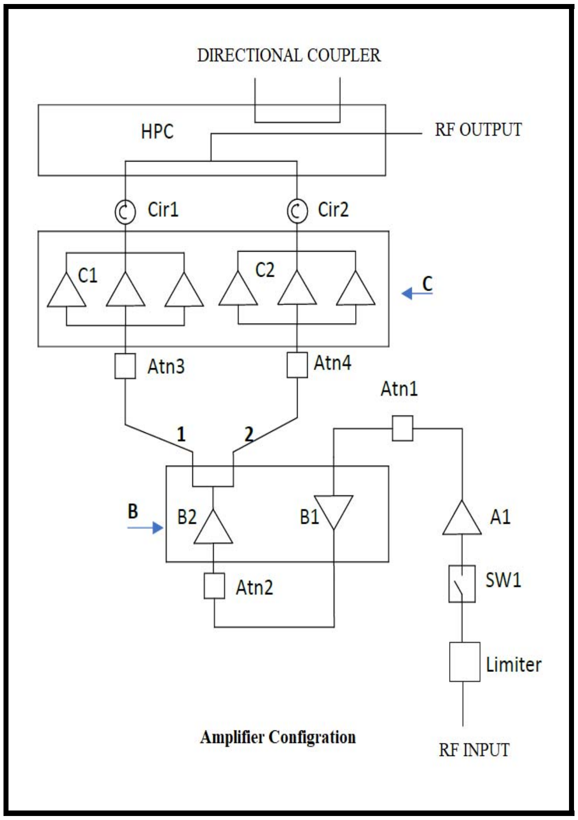

Figure 1: Amplifier configuration

High power stage is developed using two amplifier (C1 & C2) modules. Each module can deliver more than 1 kW pulsed power at the output. One stage 2:1 hybrid combiner is used to achieve 2 kW output power.

Figure 2: Driver amplifier

One stage 1:3 Lim-Eom divider is used to divide input power into three parts for each module as shown in Fig. 3. The power is then amplified by three individual LDMOS transistors in each of the modules using ~400 W RF device and combined together using single stage 3:1 Lim-Eom combiner to achieve >1 kW RF output power. The matching circuits of each module are fabricated using high dielectric constant (9.7), 50 mils thick RF laminates to reduce the size.

To ensure phase match between the three ports in each module, the combiner/divider circuits have been fabricated using 2.2 dielectric constant and 60 mils thick RF substrate. It allows higher dimensional tolerance.

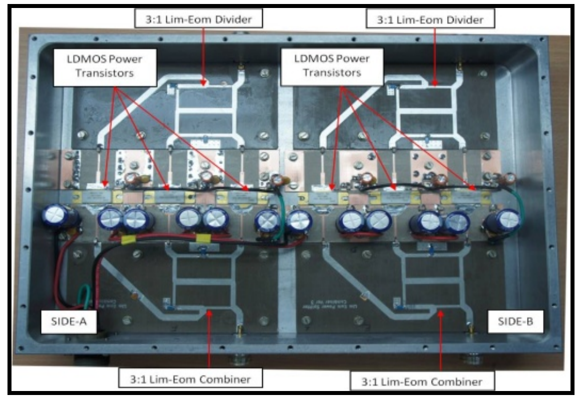

Figure 3: 2 kW SSPA configuration with matching circuits and Lim-Eom divider and combiner

Owing to high reflections in accelerator applications the output each 1 kW module is protected by using circulators at the end as shown in Fig. 4. The overall gain is 15 dB of each amplifier module inclusive of losses due to combiners and circulators.

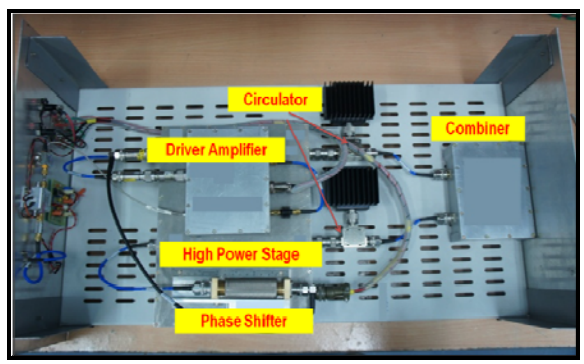

Figure 4: Developed 2 kW amplifier module with driver, phase shifter, circulators, RF switch and trigger card

One of the two outputs of driver amplifier is connected to the input of 1 kW amplifier using a manual phase shifter and the other one is connected without a phase shifter for optimizing the phase for maximum output.

Output power of both 1 kW RF amplifiers is combined using a 2:1 hybrid combiner which has a dual directional coupler in the output as an additional feature for measurement of forward and reflected RF power and circulators were used for protection of amplifier as shown in Fig. 1 & Fig. 5.

The amplifier developed is air cooled. Each amplifier module and divider/combiner is completely shielded and enclosed using aluminum enclosure after calculating skin depth at operating frequency, so that it may not cause any oscillations during operation.

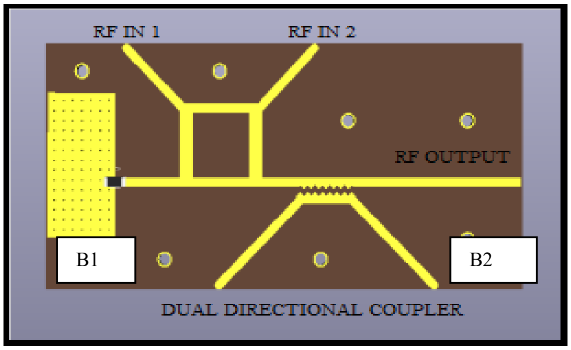

Figure 5: Hybrid combiner with directional coupler used at output

TEST RESULTS

The developed RF amplifiers were thoroughly tested and qualified for their performance at 2 kW pulsed output with operating frequency of 2856 MHz & 0.1 dB bandwidth of ±5 MHz, 300 Hz pulse repetition rate (PRR) and 20µs pulse width. Tests were carried out on the amplifier for gain response and pulse shape using complete test setup.

Again every individual stage of amplifier was subjected to thorough testing for its performance and reliability. It has also undergone for one man week long tests for its stability and thermal performance. No significant temperature rise was observed; further any significant variation in power and pulse shape was also not observed.

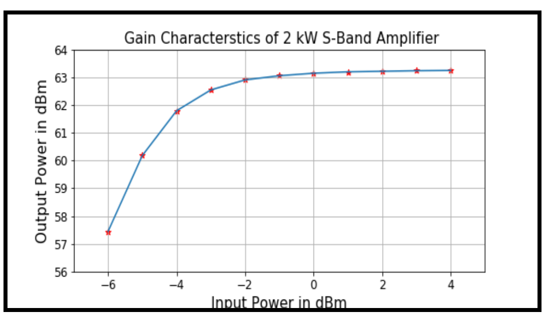

Figure 6: Gain characteristics of 2 kW amplifier modules

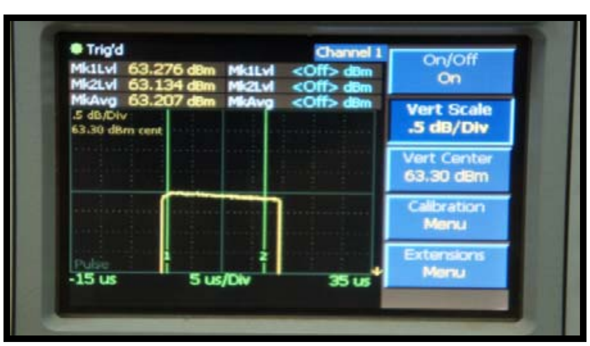

Figure 7: Pulsed output of 2 kW amplifier modules measured on peak power meter in lab

CONCLUSION

Power amplifiers have been designed and developed for the project for RF system of Linear Accelerator Facilities at RRCAT. Out of which one will serve as readily available spare. Both the amplifiers have been installed as part of S-Band LLRF system; the details of which are presented in [2].

These amplifiers with S-Band LLRF system have been thoroughly tested for their performance during the LINAC operations for ~1 month during Dec '22 to Jan'23 at RRCAT. Later in Feb 2023 S-Band LLRF system have been shipped to Microtrol Sterilisation Pvt. Ltd., Bangalore; where installation of LINAC is under progress under incubation.

ACKNOWLEGDEMENT

The authors are thankful to Shri Jitendra Parate, Shri Akhilesh Rajak and Shri Amar Kuldeep Lakra for their support in mechanical assembly work of amplifiers and Shri Arun Pratap Singh for the assembly of RF components, RF cable and wiring of amplifier. Their efforts were essential for the completion of this development.

REFERENCES

[1] Mahawar A., Mohania P., Namdeo R.K., Lad M., "Development of a 1 kW S-Band amplifier module based on planar Lim-Eom combiner", Indian Particle Accelerator Conference (InPAC-2022), VECC Kolkata, Mar., 22-25, 2022

[2] Praveen Mohania et al., "Design and Development of S-Band Low Level RF System for 10 MeV, 10 kW Electron Linear Accelerator KIRTI-1010", this conference.

[3] Mahawar A., Mohania P., Singh K.A.P., Namdeo R.K., "Design and development of S-Band, 2 kW pulsed solid state amplifier for energizing pre-buncher cavity of IRFEL injector" Proc. of InPAC-2018, RRCAT, Indore, Jan 9-12,2018, pp.1040-1042.

[4] J. Lim and Soon-Young Eom, "A new 3-way power divider with various output power ratios", *IEEE MTT-S International Microwave Symposium Digest 2 (1996): 785-788 vol.2.*

INSTALLATION AND COMMISSIONING OF HIGH VOLTAGE DC POWER SUPPLY WITH ELECTRON GUN FOR POWER TESTING OF PHOTON ABSORBERS

Sachin Rathi†, Rajeev Kumar Tyagi, Akhilesh Tripathi, Rinki Upadhyay, M. K. Badapanda and Mahendra Lad
Raja Ramanna Centre for Advanced Technology, Indore, MP, India- 452013

Abstract

AC regulator based -25 kV, 5 A high voltage DC power supply has been installed, commissioned and integrated with electron gun for testing of photon absorbers in 2.5 GeV Indus-2 synchrotron radiation source. The control of power supply has been implemented though silicon controlled rectifiers in AC regulator configuration. In this power supply, over voltage, under voltage, over current, thermal overload, transformer oil over temperature and phase failure protection have been incorporated. For smooth operation of power supply, its preventive maintenance is carried out at regular intervals. This includes multiple checks such as testing dielectric breakdown voltage of transformer oil, checking integrity of power circuit connections and dust cleaning of high voltage components of power supply. This power supply has been operating satisfactorily with 20 keV strip type DC electron gun for testing of photon absorbers. The details of installation, commissioning and integration of -25 kV, 5 A DC power supply with electron gun are presented in this paper. During testing with electron gun, this power supply is operated at -20 kV, 100 mA operating point and output voltage ripple ≤ 0.5% and output voltage stability ≤ 0.5% have been observed. These experimental results are also presented in this paper.

INTRODUCTION

In the electron storage ring of synchrotron radiation source (SRS), emitted non-experimental synchrotron radiation is generally stopped by high power density photon absorbers. The qualification testing of these photon absorbers is therefore, a crucial aspect and generally carried out using a DC electron gun which is biased by a DC power supply [1].

A high voltage DC (HVDC) power supply based on AC voltage regulator scheme has been employed as bias power supply for strip type DC electron gun used for power testing of photon absorbers in 2.5 GeV Indus-2 synchrotron radiation source. The system layout including DC electron gun and auxiliary power supplies has been shown in Fig. 1. In this system, HVDC power supply is used for acceleration of electron from cathode to photon absorber. Filament power supply is used for heating filament located in electron gun and it is floated on -20 kV with help of HVDC power supply. For HVDC power supply, AC regulator scheme has been chosen as primary control through SCRs as AC regulator configuration is simple, cost effective and proven topology for controlled HVDC power supplies. The operating point of this HVDC power supply is kept at -20 kV, 100 mA as per load requirements such as to simulate similar power density as experienced by photon absorber in Indus-2 SRS.

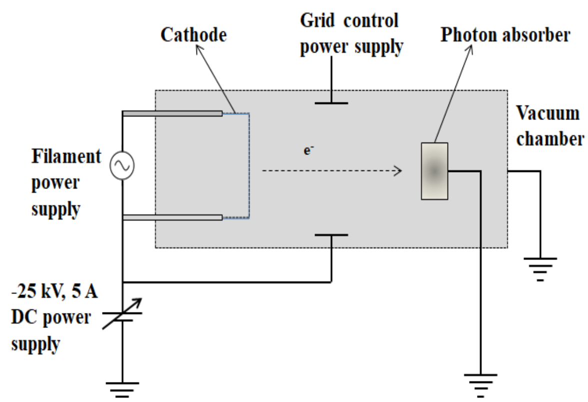

Figure 1: Schematic of test setup of 20 keV DC electron gun with -25 kV, 5 A DC power supply.

This paper describes the detailed scheme of -25 kV, 5 A AC regulator based primary controlled HVDC power supply. The details of installation, commissioning and integration of this HVDC power supply with DC electron gun have been presented in this paper. The complete system has been operating satisfactory and its operational experiences have been presented in this paper.

SCHEME

In -25 kV, 5 A DC power supply, primary control through silicon controlled rectifiers (SCRs) in the AC regulator configuration has been employed using which output voltage can be regulated to required voltage level [2]. This also takes care of possible input and output variations due to external factors. AC regulator based primary controlled HVDC power supply has been designed to operate from -10 % to +10 % variations in 3-phase input voltage. The detailed schematic of -25 kV, 5 A HVDC power supply along with values of major components is shown in Fig. 2. The firing angles at different operating points are predicted which in turn increases or decreases ON time of SCRs and hence output voltage. The controlled AC regulator output is fed to the main transformer, which is then rectified and suitably filtered to provide the required regulated DC output voltage.

†srathi@rrcat.gov.in

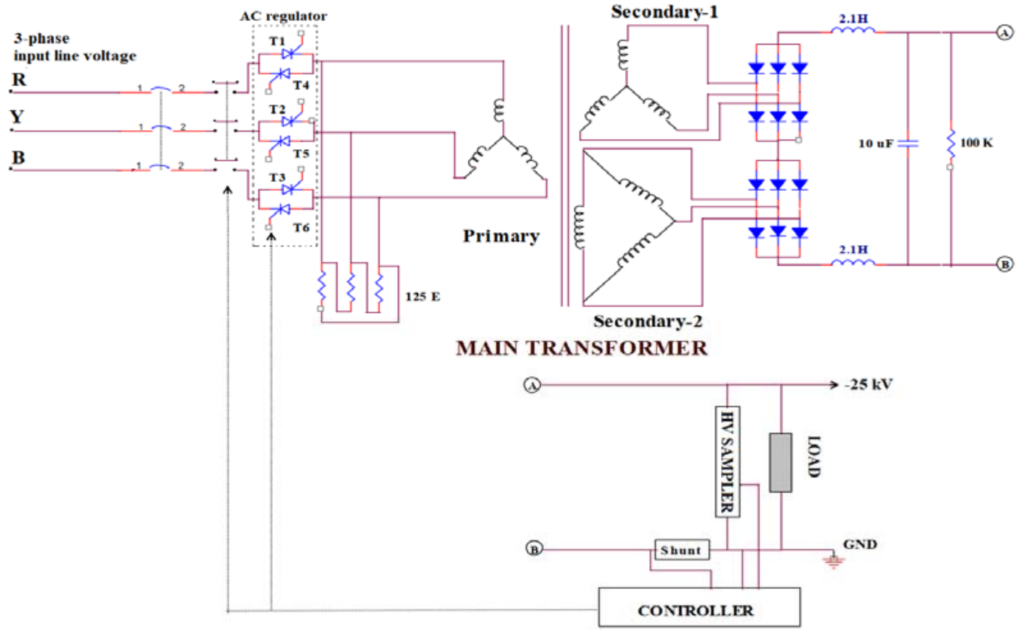

Figure 2: Schematic of –25 kV, 5 A HVDC power supply.

Siemen's make phase control integrated circuit (IC) TCA-785 has been employed for firing SCRs at desired instant. Automatic feedback control is made feasible with help of this phase control IC. When the output voltage is more than the desired voltage, more control voltage goes to these phase control ICs, which is crossed by internally generated ramp voltage (synchronized with the input line voltage) at a later instant, decreasing the voltage input into the main transformer, thereby reducing the output voltage and vice versa. The controlled voltage output of SCRs is given to the primary winding of STAR connected 3-phase step-up transformer. The secondary winding of this transformer has been split into two windings, one connected in STAR and other in DELTA configuration. These secondary windings are feeding to corresponding 3-phase diode rectifier bridge. This rectified output is filtered to obtain -25 kV, 5 A high voltage DC output. This ripple filter has been employed in LC configuration consisting of 4.2 H inductance and 10 µF capacitance to limit output voltage ripple. This 10 µF capacitance in LC filter has been realized with help of four nos. of 2.5 µF capacitances connected in parallel configuration. The peak current carrying capability of individual 2.5 µF capacitance is 2.5 kA. This HVDC power supply also consists of series limiting inductor at the output of AC regulator, which limits input fault current during any unfavourable condition. After introduction of series limiting inductor, input fault current under worst case secondary short circuit condition is limited to three times rated current. The SCRs along with input switch gear and various control cards are housed in AC voltage regulator (ACVR) panel of this power supply. The transformer, rectifier and filter inductor of this power supply are kept in an oil filled tank.

In order to maintain output DC voltage stability within limit, highly stable reference voltage as well as stable output feedback components and precision ICs for comparing the reference signal with the feedback signal have been used in this power supply. Further, to ensure smooth operation, various safety and protection features have been implemented in this power supply by using protection cards. These include cards for over voltage protection, over current protection, under voltage protection, di/dt protection, phase failure protection, thermal overload protection and transformer oil over temperature protection.

INSTALLATION AND COMMISSIONING

Before installation of HVDC power supply with electron gun, functioning of various control cards was checked and voltage levels at various test points were monitored. Functioning of SCRs and other components was also checked. During installation, the health status of high voltage transformer was checked through megger. Afterwards, the output of ACVR panel was connected with transformer-rectifier unit and filter capacitors and power supply were energized. A 100 kΩ bleeder resistor was connected across the output terminals of this HVDC power supply and its performance parameters were checked. All exposed metallic portions of various parts of this power supply were grounded as a part of equipment grounding for ensuring personnel safety. In this power supply, feature of maintenance grounding has also been incorporated, wherein under power supply OFF condition, all HV points are made shorted and connected to ground, before carrying out any maintenance work. This practice ensures discharge of stored energy, if any, before allowing entry of any personnel into the high voltage barricade.

After installation and commissioning of HVDC power supply with electron gun, integrated system has been shown in Fig. 3. Its 3-phase step-up transformer and 100 kΩ bleeder resistor have been shown in Fig. 4. In order to ensure smooth operation of this HVDC power supply, preventive maintenance of various subsystems is carried out at regular intervals. This includes multiple checks such as testing dielectric breakdown voltage of transformer oil, checking moisture content of silica gel in transformer breather, checking integrity of power circuit connections and dust cleaning of various components of power supply. Functioning of various protection cards used in power supply, is checked along with the calibration of multiple meters. During operation of power supply, several performance parameters such as output voltage, output current etc. along with voltage levels of multiple signals in interlock cards are monitored. This power supply has been operating satisfactorily with 20 keV strip type DC electron gun for qualification testing of photon absorbers.

Figure 3: Installed -25 kV, 5 A DC power supply with voltage sampler.

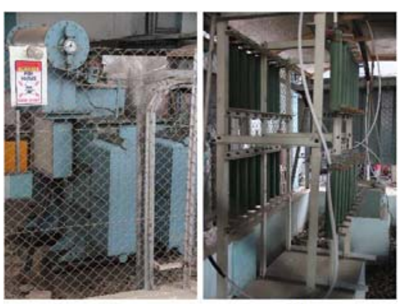

(a) (b)

Figure 4: (a) 3-phase step-up transformer for -25 kV, 5 A DC power supply, (b) 100 kΩ bleeder resistor and capacitor.

TESTING AND EXPERIMENTAL RESULTS

The -25 kV, 5 A DC power supply has been tested with 20 keV strip type DC electron gun and its performance parameters are shown in Table 1. Output voltage ripple ≤ 0.5% has been achieved and shown in Fig. 5.

Table 1: Performance parameters achieved

Performance parameter	Achieved result
Output voltage	-20 kV DC
Output current	100 mA
Output voltage stability	≤ 0.5%
Output ripple	≤ 0.5%
Voltage THD	≤ 5%
Input supply variation	3 Phase, 415 V (+10%, -10%)

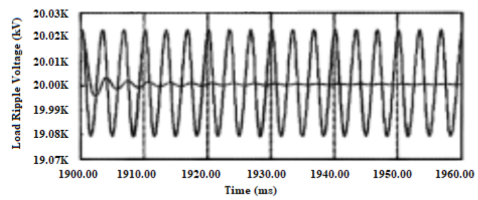

Figure 5: Output voltage ripple at full load.

CONCLUSION

AC regulator based -25 kV, 5 A high voltage DC power supply has been installed, commissioned and integrated with electron gun for power testing of photon absorbers in 2.5 GeV Indus-2 synchrotron radiation source. In this power supply, over voltage, under voltage, over current, thermal overload, transformer oil over temperature and phase failure protection have been incorporated. The preventive maintenance of this power supply and its various sub-systems is carried out at regular intervals. During testing with electron gun, this power supply is operated at -20 kV, 100 mA operating point and output voltage ripple ≤ 0.5% and output voltage stability ≤ 0.5% have been observed.

ACKNOWLEDGEMENT

Authors would like to acknowledge the contribution made by Mr. Santosh Tambe, Sr. Tech./H and other members of RF Systems Division for regular maintenance of this power supply and its successful operation.

REFERENCES

[1] M. Rana, P. Radheshyam., A. D. Ghodke, B. Sindal, S. Joshi, D.P. Yadav, “Simulation of 20 keV/100 mA strip electron gun for testing photon absorbers”, Indian Particle Accelerator Conference, VECC, Kolkata, Mar., 22-25, 2022.

[2] M.K. Badapanda., P.R. Hannurkar, “Klystron Bias Power Supplies for Indus-2 Synchrotron Radiation Source”, IETE Journal of Research, Vol. 54, no. 6, p. 403-412, Nov. 2008.

DESIGN AND CHARACTERISATION OF ANODISED ALUMINIUM STRIP SOLENOIDS

Gautam Sinha#, Ritesh Malik, K. Sreeramulu, B. Srinivasan, Kushraj Singh, Anil Mishra, Bhim Singh, Preveen Kumar, Rajesh L. Prasad Shah, Navin Awale, and Kailash Ruwali

Accelerator Magnet Technology Division, Raja Ramanna Centre for Advanced Technology, Indore

Abstract

RRCAT has developed 9.5 MeV, 10kW electron Linac for industrial applications. Solenoids are used to focus charged particle beams and increase the transmission in the Linac. Earlier the solenoids were made using hollow OFHC copper which were imported. Now solenoids are made, as an import substitution, using anodised aluminium strip which are available in the country. Solenoids are designed, fabricated and characterised to meet the requirement of the Linac. Details of magnetic field design and measurements are presented in this report. Comparison between design and measured data are reported. Various important parameters of the solenoid like coefficient of spherical aberration, effective length, peak field are calculated. Demountable iron disks on the outer jacket are used and advantages of such arrangements are explained.

THEORY AND DESCRIPTION

Field produced by a circular current loop can be analytically expressed in terms of elliptic integrals. The ideal solenoid can be treated as a stack of such current loops and its magnetic field can be obtained by performing the integration [1]. Alternatively, the field may be derived by solving a boundary value problem with cylindrical symmetry using FEM code [2,3].

The magnetic field produced by an infinitely thin circular current loop of radius R_i located at position Z_i with current I_i can be expressed as [3]

$$B_z^i(r,z) = \frac{\mu_0 I_i}{2R_i}\left[\frac{1}{\pi\sqrt{q}}\right]\left[E(k)\frac{1-A^2-B^2}{q-4A}+K(k)\right]$$

$$B_r^i(r,z) = \frac{\mu_0 I_i}{2R_i}\left[\frac{g}{\pi\sqrt{q}}\right]\left[E(k)\frac{1+A^2+B^2}{q-4A}-K(k)\right]$$

$$where\ A=\frac{r}{R_i}, B=\frac{(z-Z_i)}{R_i}, g=\frac{(z-Z_i)}{r},$$

$$q=[(1+A)^2+B^2], k=\sqrt{\frac{4A}{q}}$$

K(k) and E(k) are the complete elliptical integral function of first and second kind. Central magnetic field is

$$\frac{\mu_0 I_i}{2R_i}$$

On the axis field at any point p(z) can be expressed as

$$B(0,z)=\frac{\mu_o J}{2}\left[\left(\frac{L}{2}+z\right)\ln\left(\frac{a_2+\sqrt{a_2^2+\left(\frac{L}{2}+z\right)^2}}{a_1+\sqrt{a_1^2+\left(\frac{L}{2}+z\right)^2}}\right)+\left(\frac{L}{2}-z\right)\ln\left(\frac{a_2+\sqrt{a_2^2+\left(\frac{L}{2}-z\right)^2}}{a_1+\sqrt{a_1^2+\left(\frac{L}{2}-z\right)^2}}\right)\right]$$

Where a_1, a_2 and L are the inner radius, outer radius and length of the solenoid and J is the current density [1].

Two anodised aluminium strips of suitable dimension as available in the market are used for fabricating the solenoid coils which are placed inside a thick iron jacket. Demountable iron disk of suitable diameter is assembled at both the ends to make the ID of the solenoid variable as per the need of the field requirement. Resistance and Inductance of the magnet are 0.46 Ω and 63.28 mH at 12 Hz, respectively. Current density in water cooled OFHC solenoid can be 6 to 7 A/mm^2 whereas for aluminium strip is limited to maximum 1.8 A/mm^2. Therefore, the dimensions of the new magnets are quite different and needs proper optimisation to achieve the require magnetic field profile.

MEASUREMENT AND ANALYSIS

This is a water-cooled magnet and cooling arrangement is made at both the ends. The magnet is energised with different currents varying from 47.5A to 80A and allows for stabilizing for 45 minutes before measurement. The magnetic field is measured along the length in a grid. Horizontal, vertical and the length along the axis of the magnet is defined as X, Y and Z axis. On axis field means the magnetic field is measured from -Z to +Z for X and Y both zero. Magnetic field is measured using a 3-axis motion system and SENIS make 3-D Hall sensor and digital tesla meter. Magnetic field sensitive volume of the sensor is (0.15x0.01x0.15) mm^3. External dimension of the probe is (4.0x0.9x8.0) mm^3. Magnetic field measurement accuracy is of the order of 400 ppm.

Figure 1: Photograph of the solenoid (FC1).

gautam@rrcat.gov.in

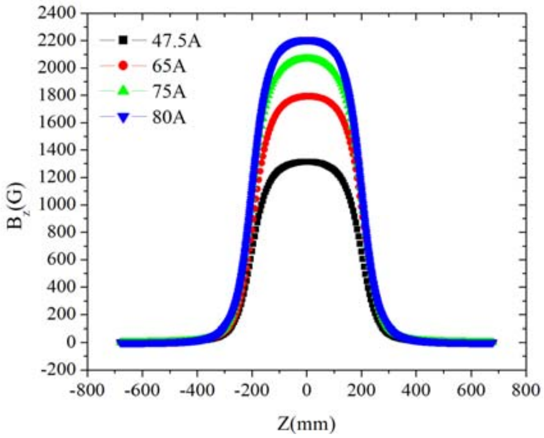

Figure 2: On-axis field profile for different currents, I=47.5A, 65A, 75A, and 80A for the solenoid having ID 149mm.

Total 6 solenoids are planned for the present Linac [4]. Two smaller solenoids are placed in the LEBT section and rest 4 in the Linac section. Out of these 4 solenoids three are of FC1 type as shown in Figure 1 and another one is FC4.

To satisfy the desire field requirement, the peak field of the FC1 may vary from 1200G to 2200 G. It is experimentally found that these field values are achieved by varying the current from 47.5 A to 80A as shown in Fig. 2. Theoretical estimation of the field is closely resemblance with the measured field values as shown in Fig. 3. By placing the three FC1 at their desired positions the required field profile shall be obtained. The de-mountable disks will provide flexibility which will be useful during installation.

During operation, the current of the magnets shall be set as per the requirement. Therefore, the variation of the peak field with current is measured and shown in the Figure 4.

Demountable disks of different diameters are provided

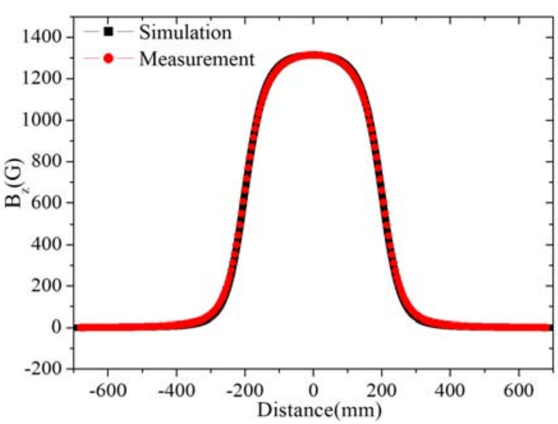

Figure 3: Comparison of measured field with the simulation. Current is normalised to match the peak field.

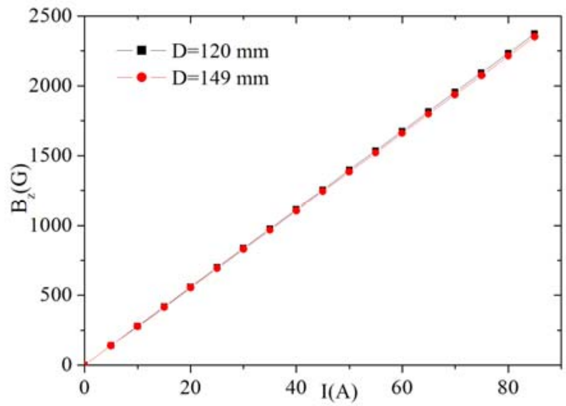

Figure 4: On-axis peak field at the centre for different currents.

to generate different peak field and field profile using the same coil system. However, field integrals $\int B_Z.dz$ remain same for both the cases. Peak field is more and field spread is less for lower diameter disk in comparison with the larger disk diameter as shown in the measured field data in Fig. 5. Qualitative estimation of the coefficient of spherical aberration can be done from the field profile.

Coefficient of spherical aberration is defined as

$$C = \frac{\int \left(\frac{dB_z}{dz}\right)^2 .dz}{2.\int B_Z^2 .dz} \text{ and } L_{effective} = \frac{\int B_Z.dz}{B_z(Peak)}$$

$$\frac{1}{f} = \left(\frac{q}{2\gamma m v_z}\right)^2 \int_{-\infty}^{\infty} B_Z^2 dz \quad \text{and } \gamma = \frac{1}{\sqrt{1-\frac{v^2}{c^2}}}$$

In any ideal solenoid B_z on the axis is only present and B_x and B_y both are zero. However, in any practical magnet small amount of B_x and B_y remain present due to fabrication in accuracies. Therefore, magnetic field is measured in a grid using three-axis Hall sensor. Based on the magnetic field measurement data a practical magnetic axis is determined and the reference is transferred to the fiducial posts on the top of the magnet.

Table 1: Various important parameters of the FC1 solenoid at I=47.5A.

Parameter	Value
$\int B_z^2.dz$ ($T^2.m$)	0.00580
$\int (dBz/dz)^2.dz$	0.18493
C($1/m^2$)	15.92868
$\int B.dz$ (T.m)	0.05289
B peak (T)	0.13134
$L_{effective}$(m)	0.40273
f (m) for 10 MeV	0.85

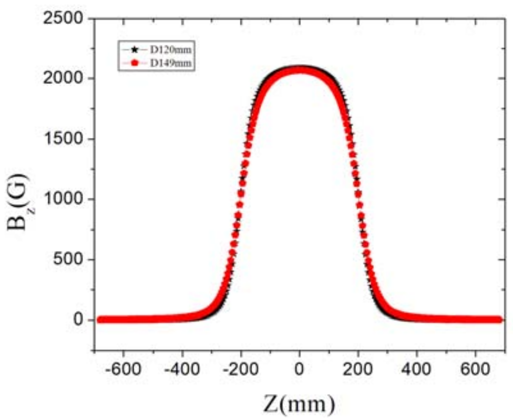

Figure 5: Measured on-axis magnetic field profile at 75 A for different disk diameters of the end disk.

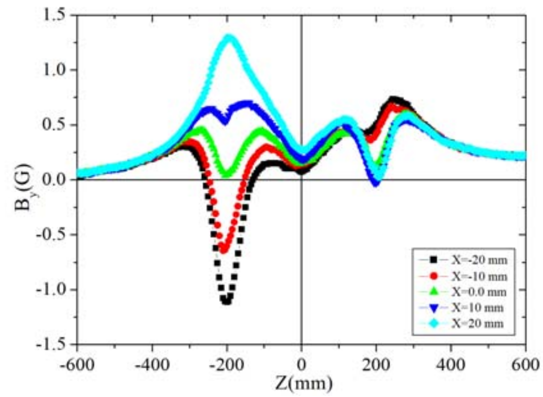

Figure 7: Variation of vertical field, By along the axis for various horizontal distances for I= 47.5A.

On the axis error field is within ± 1.5G which is clearly evident both from the Fig. 6 and Fig. 7. This is including the fabrication and measurement error and these values are well within the acceptable limits. Also, from the Fig. 6 the zero-crossing point indicate the center of the solenoid. Placement of the solenoids in the machine is done with respect to the mid-point.

In any solenoid, B_z is maximum at the center of the magnet and decreases towards the end as evident from Fig. 2 and 5. However, the off-axis radial magnetic field is the maximum at the end as evident from Fig. 6 and this radial field is responsible for focusing action of the solenoid magnet.

The current and resistance of the solenoid using hollow OFHC copper to generate 1500G central magnetic field are 180A (N=300) and 0.159 Ω. However, to generate the same field using the aluminium strips solenoid, FC1, the required current and resistance are 54.27 A (N= 916) and 0.46 Ω. Therefore, the power loss in copper and aluminium solenoids are 5.15 kW and 1.35 kW, respectively. Lower current density used in aluminium solenoids resulted in low power loss.

.

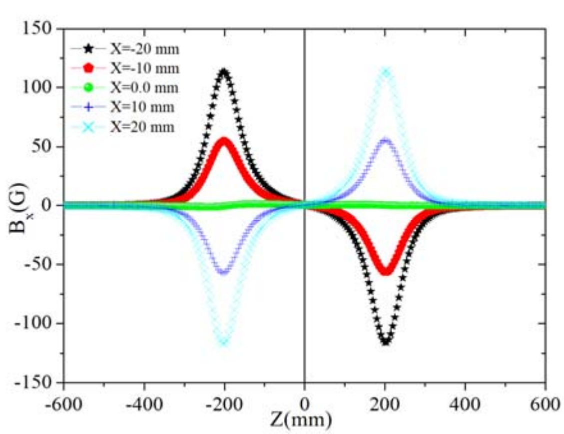

Figure 6: Variation of horizontal field, Bx along the axis for various horizontal distances for I=47.5A.

Total NI required to generate 1500 G central magnetic field in air core solenoid using hollow OFHC copper is 54000 which is around 8% more than that of Aluminium strip solenoid. The cost of the material and fabrication of aluminium strip solenoid (FC1) is around 50 % lower than the OFHC solenoid.

STEERING COILS

A set of horizontal and vertical steering coils will be placed inside each solenoid for beam steering, if required as shown in Fig. 8. These coils can generate 180 G-cm

Figure 8: Steering coils for producing both Bx and By.

integrated field in each direction. These are made in such a way that it can be removed if not required without disturbing the set up.

MEASUREMENT OF FC4 SOLENOID

FC4 solenoid is of smaller in length and having different numbers turn compare to FC1 but will produce stronger peak magnetic field. This will be used to focus the beam so that the converging beam can enter the energy filtering magnet. Figure 9 shows the photograph of the solenoid FC4.

Figure 10 shows the field variation of FC4 magnet for different currents varying from 50 A to 106 A. The peak magnetic field for 90A current is 0.237 T and the focal length for 10MeV electron is 0.47m. Though the length of the FC4 is smaller but the focusing power is stronger compare to FC1. Further studies shall be carried out for FC4 solenoid.

Figure 9: FC4 solenoid is placed on the field measurement bench for field characterisation.

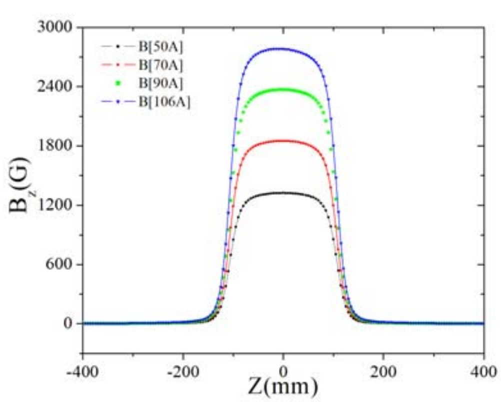

Figure 10: On-axis field profile for different excitation currents of the FC4 solenoid.

CONCLUSION

A Set of solenoids are designed, fabricated using anodised aluminium strip and characterised. Measured field profile of the solenoids is in good agreement with the design values and satisfies the field requirement. This is not only the import substitution but reduces the power loss and price considerably. The power loss in copper and aluminium solenoids (FC1) for 1500 G central field are 5.15 kW and 1.35 kW, respectively. The cost of the material and fabrication of aluminium strip solenoid (FC1) is around 50% lower than that of the OFHC solenoid. A separate report shall be published highlighting the fabrication details which are beyond the scope of the present report.

REFERENCES

[1] Gautam Sinha, Ravishankar Sundararaman, and Gurnam Singh, “Design Concepts of Optimized MRI Magnet”, IEEE transactions on magnetics, vol. 44, no. 10, page 2351, October 2008.

[2] POISSON Group of Codes, Los Alamos National Laboratory, New Mexico, 86545.

[3] Vector Fields Limited, 24 Bankside Oxford, OX5 1JE. Kidlington, England.

[4] Development of 9.5MeV, 10kW Linac meeting energy regulations on food irradiation” by RS Sandha et al. InPAC 2022.

DEVELOPMENT OF PROTOCOL CONVERTER FOR C BASED APPLICATION DEVELOPMENT PLATFORM AND EPICS

Joshi Namrata[1,2*], Ponagani Bhumeshwar[1] and Singh S K[1]

[1]Ion Accelerator Development Division, Bhabha Atomic Research Center, Trombay, India [400088]

[2]Homi Bhabha National Institute, Anushaktinagar, Mumbai, India

Abstract

A C based application development platform software typically used for development environment which provides a comprehensive set of programming tools for creating test and measurement applications for the Microsoft Windows platform. EPICS is Experimental Physics and Industrial Control sys-tem. It is an open-source distributed SCADA framework which can run on various operating system for soft real time control system for scientific instruments. EPICS tools and libraries are developed using C++ language which enables OOP concept for programming. A TCP/IP based protocol is developed for the C based application development platform to convert the commands and data coming from that application into EPICS, to get EPICS interface onto that C based application.

INTRODUCTION

The C based application platform programming environment is used to create test and measurement applications. It provides an easy interface and tools to create projects, edit and debug source code, build a user interface, and test code output and performance in one streamlined, tabbed workspace. The software also makes it able to acquire data from GPIB, USB, serial, Ethernet, PXI, VXI, and FPGA instruments using the built-in instrument I/O libraries and built-in instrument drivers.

EPICS is Experimental Physics and Industrial Control system. It is a set of Open Source software tools, libraries, and applications developed collaboratively and used world-wide to create distributed soft real-time control systems for scientific instruments such as particle accelerators, tele-scopes, and other large scientific experiments. EPICS uses Client/Server and Publish/Subscribe techniques to communicate between the various computers. Most servers (called Input/output Controllers or IOCs) perform real-world I/O and local control tasks and publish this information to clients using the Channel Access (CA) network protocol, which uses Ethernet protocol.

*namrata@barc.gov.in

LEHIPA control system is a distributed control system, in which the majority of the systems are now EPICS-based IOC but there are still a few systems that are working on C based application software. Above all the advantages the software provides the major drawback of using a C language-based application for a huge distributed system like the LEHIPA control system which is lack of Object Oriented Programming model, which implements abstract classes and inheritance. Implementation of classes makes it easier to implement SOLID design principles. SOLID design principles are intended to make object-oriented designs more understandable, flexible, and maintainable. The principle implemented in the new design is Open Closed Principle(OCP), which states that the module should be Open for extension but Closed for modification. As C language does not provide Object Oriented Programming support, implementation of OCP becomes difficult with structures and global variables. As a consequence, an EPICS, C++ based module was required in order to implement OCP. And in order to convert the C application into EPICS a TCP/IP routine is required to be developed.

PROTOCOL

The protocol implements a data transfer routine from the C application. Any type of data can be sent along with a protocol bit specifying the field from which the data has been received in order to map it into QT-based EPICS application. The type of data can be integer, float or double or an array according to the kind of field input received from the application. The protocol field is a fixed one-byte data that contains a number uniquely identifying every input and output widget to the corresponding widget of the other application.

Augmentation on the C Application

An additional routine is added to the C application which establishes a new connection to a remote server. Whatever data is received from the field, is sent over the communication channel established between the remote server and the application. This data can be of any type, integer, float, or double. Data sent from the C application is encapsulated in the form of a structure and sent along with a protocol number which helps in uniquely mapping the field to the EPICS application. Reason for choosing structure as the appropriate type of datatype, instead of sending 2 data fields separately a single combined packet is sent. Also, implementation of the class would be an ideal choice but the C does not support the object-oriented programming methodology.

TCP/IP Routine

In order to actual transmit the data onto the channel the type of datatype chosen is heterogeneous datatype, structure. Structure contains two fields one is protocol which is of Enum type which specifies the field for appropriate mapping from C application to EPICS based GUI developed on QT. Second field specifying fieldData which is a Union type data. The reason for choosing union is to store different data types in the same memory location. This way implementation of various type of data like integer, float, double can be executed. This structure is sent over the TCP/IP channel and similar structure is added onto the EPICS side to receive the data from the C application.

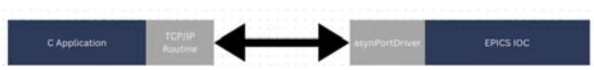

Figure 1: Architecture of the protocol.

asynPortDriver Class

An independent server is developed using asynPortDriver class which implements a routine that accepts connection from the the C application and establishes a connection. AsynPortDriver is a C++ base class that is extended from the asynDriver interface that is used for interfacing device-specific code to low-level drivers. asynDriver allows non-blocking device support that works with both blocking and non-blocking drivers. asynPortDriver simplifies the job of writing an asynPortDriver tasks like registering the port, registering the interfaces, and calling interrupts clients. Extending all the functions from the base class as that function performs operations like accepting new values from the device, changing the value of parameters, setting a flag bit for every parameter noting the change, and calling a call-back for changed parameters. In addition to extended functions, a new function for actual simulation which runs in a separate thread is created in the constructor. This new function will be always in listening mode in order to receive data from the client.

TCP/IP Protocol

In order to actually transmit the data onto the channel the type of datatype chosen is heterogeneous datatype, structure. Structure contains two fields one is protocol which is of Enum type, specifying the field for appropriate mapping from the C application to EPICS based GUI developed on QT. Second field is fieldData which is union datatype. The reason for choosing union is to store variety of datatypes like integer, float, double. This structure is sent over the Ethernet and the similar structure is used for receiving on the other side.

```
struct TransmittedData{
  enum protocol;
  union fieldData;
};
```

Figure 2: Structure used to send and receive data

The OCP is implemented such that in order to connect to the C application an abstract class, asynPort_base is created. Through inheritance from the abstract base class, derived class is formed that implements the function from the abstract class and defines the protocol and getter setter functions for the parameters in the C application. In this way if some new functionality was supposed to be add into the EPICS program this interface is independent of functionalities added into the class. Likewise, if some new IOC was supposed to be connected to the C application it can directly extends the interface and start implementation.

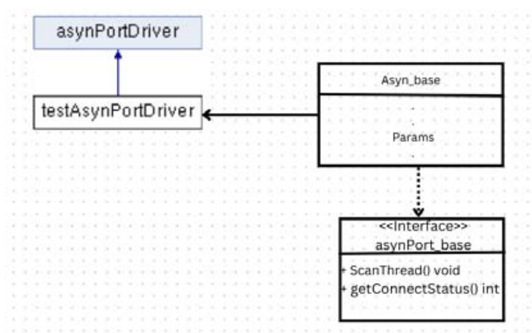

Figure 3: Class diagram for the EPICS IOC developed

CONCLUSION

Development of this protocol converter for C application and EPICS compatibility includes Object Oriented Programming approach which promotes implementation of SOLID principle. This protocol is open for extensions as classes are extensible and closed for modification as it can only be re-factored no modification to the behaviour of the module is tolerated. During transmission structure is used which eliminates lots of dependencies while dealing with mapping data to the source.

REFERENCES

[1] EPICS-Experimental Physics and Industrial Control System, https://epics.anl.gov/

[2] asynPortDriver, https://epics.anl.gov/modules/soft/asyn/R4-29/asynPortDriver.html/

PROCESSING AND CLEANROOM PREPARATION OF SCRF CAVITIES FOR PERFORMANCE TESTING IN VTS CRYOSTAT

S Suhane#, A Bose, S K Chauhan, K K Das, S V Kokil, Amar Singh, D S Rajput, Md A Hussain, K Prasad, S Raghavendra, Purushottam Shrivastava

Proton Accelerator Group
Raja Ramanna Centre for Advanced Technology, Indore (MP) India

Abstract

RRCAT is pursuing research and development activities related to high-β 650 superconducting radio frequency cavities which shall be major component for future high intensity superconducting proton linac for Indian Facility for Spallation Research (IFSR). Under the program, development of infrastructure facilities for processing & testing of superconducting RF (SCRF) cavities are taken up. After fabrication, superconducting RF cavities are processed, assembled and prepared for performance test at 2K in Vertical Test Cryostat. Cavities need to be processed and assembled under controlled environmental conditions. Any particulate impurity on the superconducting cavity surface can influence its maximum achievable accelerating gradient and limiting its performance, hence contamination by particulates has to be avoided. High Pressure rinsing is the final cleaning procedure before vertical test. The rinsing and assembly procedures have been modified and upgraded to improve the process and cavity performance. The paper describes various facilities developed and processed involved in preparing the cavities for testing in VTS Cryostat.

INTRODUCTION

RRCAT is pursuing research and development activities related to high beta 650 MHz superconducting radio frequency (SCRF) cavities which shall be major component in high intensity superconducting proton linac for future Indian Facility for Spallation Research (IFSR). Niobium SCRF cavities are major building block of the LINAC. Under this program, development and setting up of infrastructure facilities for fabrication, processing & testing of SCRF cavities are taken up, which is also useful for Indian Institution Fermilab collaboration (IIFC) for PIP-II (Proton Improvement Plan)[1]. After fabrication the elliptical shaped Nb SCRF cavities need to pass through a series of processing steps like elctropolishing, centrifugal barrel polishing, high pressure rinsing etc to remove any surface defect, the damaged surface layer, impurities, and improve the surface finish. HPR with ultrapure water is the final cleaning step performed on the cavity. HPR, preparation of components and final assembly is carried out in class 10 clean cleanroom. Cavity is further assembled with instrumentation and prepared for testing in VTS cryostat. Details of upgraded facilities and processes involved in preparing the cavities for testing at 2K in VTS Cryostat are presented in the paper.

PROCESSING OF Nb SCRF CAVITY

Facilities have been indigenously developed and established at RRCAT to process the niobium SCRF cavities. Various processing steps for a Nb SCRF cavity includes: Ultrasonic degreasing, bulk electropolishing(~120-150 μm), high pressure rinsing, thermal processing, light elctropolishing (~5-20 μm), HPR, Drying in cleanroom, final assembly, evacuation and preparation for low power RF test in VTS cryostat.

Ultrasonic (US) Cleaning of cavity

Ultrasonic cleaning of cavity is carried out to remove any ,oil, dirt or contaminant from cavity surface. Ultrasonic rinsing is carried out before and after electropolishing in a solution of ultra-pure water and detergent Micro-90 (2%) at 48°C for one hour. Before ultrasonic rinsing, the US tank is dried and wiped with propanol to eliminate any bacterial contamination.

High Pressure Rinsing (HPR)

In HPR cavity RF surface is sprayed with high pressure jets (80-100 bar) of ultrapure water for a prolonged duration in class 10 cleanroom to dislodge micron size particulate contaminants which otherwise causes “Field emission” limiting the maximum achievable accelerating gradient of the cavity. HPR of cavity is a critical process and carried out several times e.g. after electropolishing, after VTS testing (to mitigate field emission, if present) or if any vacuum leak is detected in the cavity during low temperature test. External surface of cavity is also rinsed to prevent cross contamination with particles during cavity assembly, as shown in figure 1.

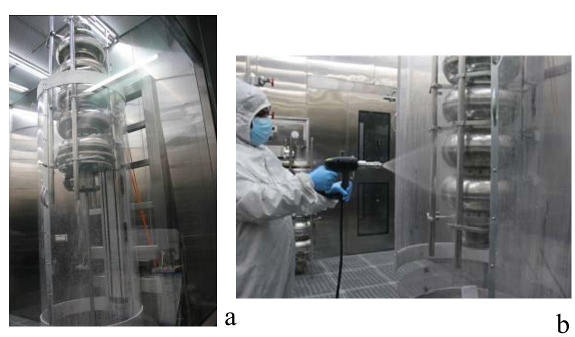

a b

Figure 1: (a) HPR (b) External rinsing of cavity

suhane@rrcat.gov.in

The existing HPR set up has been upgraded to accommodate both bare as well as jacketed 650 Mz 5-cell Nb cavity. It comprises of a rotating wand with nozzles at its top with cavity traversing linearly around it via a motorized actuator. The nozzle head has been modified to incorporate three fan jet nozzle tips, in order to have higher throughput of water and improved particle removal on curved surfaces. Two nozzle tips (40º fanjet) are at zero degree inclination for cleaning of equator and iris and third nozzle is at an inclination to clean the wall between iris and equator. In the modified set up the removable water splash guard facilitates easy loading and unloading of cavity on the HPR tool.

Special precautions in HPR process include – replacing the sub-micron filter after swivel joint every year, flushing the water through nozzles uninterruptedly to avoid bacteria growth, collecting rinse water sample at regular interval for bacteria analysis.

In the improved process, number of cavity passes have been increased from 3 to 5 and at reduced speed of <10 mm/min. before final assembly of cavity, leading to total duration of >15 hours for final round of HPR, consuming around 15000 litres of ultrapure water. To meet the higher demand of UPW, the raw water storage capacity of UPW generation plant has been augmented with additional tanks of 20000 litres as shown in figure 2.

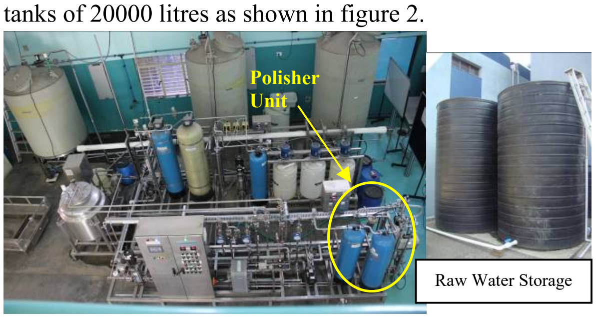

Figure 2: Ultrapure water generation system

Ultrapure water distribution system

The ultrapure water having Resistivity ≥ 18 M ohm-cm, TOC <10 ppb and Bacteria count < 1 cfu/1 ml is susceptible to degradation upon storage, hence the stored water is continuously re-circulated through the polisher unit of the plant. Sanitization of storage tank and UPW distribution loop upto HPR nozzles is carried out one in a year using cold sterilant disinfectant.

CLEANROOM PREPARATION OF CAVITY

For achieving the desired performance of cavities in terms of high accelerating gradient and quality factor, it is required to work under clean and controlled conditions. Any particulate impurity on the superconducting cavity surface can influence it's performance hence contamination by particulates has to be avoided. Final preparation of the Niobium cavity and associated components is carried out inside a cleanroom of ISO class 4 (FED STD 209 E equivalent class 10) having < 10 particles of ≥0.5 micron size in a cubic foot of clean air.

Cleanroom Infrastructure

The cleanroom facility at RRCAT is located in front of EP enclosure shown in figure 3. It has ante-rooms of class 1000 for hardware preparation and gowning and class 10 room for HPR and final assembly of cavity. Entry to class 10 area is thru air shower. Dynamic pass box is used for transfer of small components from class 1000 to class 10 room. For consistent performance of cleanrooms AHU filters and cleanroom walls are cleaned on a regular basis using suitable cleaning agents. Components blowing area is away from final assembly station. UPW distribution line of PFA material has been installed in ante-room for rinsing of components.

Figure 3: Cleanroom at RRCAT

Upgradation of Nitrogen Purge Line

The nitrogen gas line in the cleanrooms for venting SRF cavity and component flushing prior to its assembly on cavity has been upgraded. Electropolished SS316 tubing was fitted to the boil off nitrogen gas outlet of liquid nitrogen Dewar. Pressure regulator and gas control valves were attached to control flow rate of nitrogen. The cavity purging line was attached to the slow pumping section to purge the cavity. The component flushing line was extended to Class 10 as well as Class 1000 clean room via SS tubing and fitting. Control panel of nitrogen purge line is shown in figure 4.

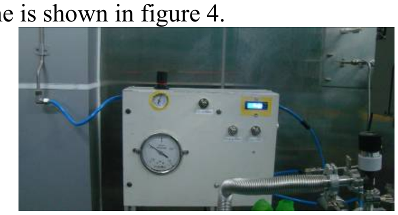

Figure 4 : Control panel for nitrogen supply line

Component Preparation in cleanroom

All the hardware and flanges reaquied for cavity assembly are first cleaned in class 1000 room using ultrasonic cleaning followed by hand HPR. Ultrasonic cleaning is carried out at 50C for 1 hours in solution of Citrenox mixed with ultrapure water. After rinsing with plain UPW the components are blown off with ionized nitrogen. Special lint ftree cloths are used for wiping of components. In the class 10 cleanroom, the hardware and flanges are blown off with ionized nitrogen monitoring the particles generated. Blowing is continued until zero particle count is observed. Cleanroom preparation of components is shown in figure 5 .

Figure 5: (a) and (b) Component preparation in class 1000 cleanroom. (c) and (d) Component preparation in class 10 cleanroom

Cavity Assembly in Cleanroom

After first round of HPR and drying of cavity, assembly of end flange and RF coupler flanges is carried out. It is followed by second round of 5 pass HPR and after 24 hour drying, final assembly of closing flange with burst disk and angle valve. Torque wrench is used for tightening of bolts to the preset torque values. During component preparation and assembly the training and skill of technician plays a critical role. All the movements and actions are carried out slowly and smoothly to avoid turbulence in the air. Generation of particles during assembly is continuously monitored using the particle counter shown in figure 6(a).

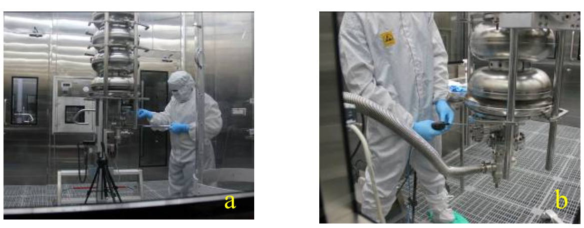

Figure 6 (a) Cavity Assembly ; (b) Vacuum Leak testing

Cavity Evacuation

After final assembly, evacuation of cavity is carried out using dry scroll pump and TMP. The vacuum pumping line and station has been modified. All the vacuum fittings have been electropolished and reassembled. For slow evacuation of cavity a fine leak valve with précised control has been used. PI diagram of modified pumping station is shown in figure 7. After leak testing using MSLD the cavity is sealed at < 7E-7 mbar pressure.

CAVITY PREPARATION FOR VTS TEST

The vacuum sealed cavity is rolled out of cleanroom and moved to VTS insert assembly area on a cart.

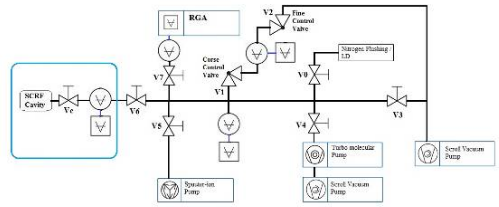

Figure 7 : PI diagram of upgraded cavity pumping line

Diagnostic instruments like temperature sensors, second sound sensors are mounted on the cavity as shown in figure 8(b). Assembly is carried out in a clean enclosure fitted with HEPA filters. Cavity is then lowered in VTS cryostat for low power RF test. One 5-cell HB650 cavity # 505 processed twice in class 10 cleanroom and tested in RRCAT VTS achieved max. accelerating gradient of 18.9MV/m limited by field emission. The cavity is now being prepared again in cleanroom for re-test in VTS.

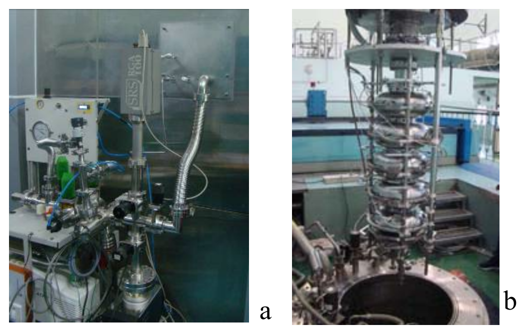

Figure 8 (a) Pumping station (b) Cavity on VTS insert

CONCLUSION

Infrastructure and required procedures for processing and cleanroom preparation of SCRF cavities for VTS test have been upgraded. Few cavity processing and testing cycle have been completed. With the experience gained in processing of SCRF cavities in class 10 cleanroom, the specified accelerating gradient and quality factor will be achieved in minimum number of reprocessing cycles.

ACKNOWLEDGEMENTS

Authors are thankful to the Fermilab colleagues particularly Mr. Genfa Wu, Mr. Fumio Furuta and Mr. Brent Stone for their support during facility development and processing of SCRF cavities at RRCAT. We also acknowledge the support of CSD team at RRCAT in establishing the cleanroom facility.

REFERENCES

[1] Purushottam Shrivastava, et. al., “Progress of Recent Superconducting RF activities in India”, International Conference on RF Superconductivity, SRF 2021, MSU.

Development of Titanium gr-2 Bellows for HB 650 MHz 5-cell SCRF cavities

V K Srivastava*[1], T Maurya[1], Sanjay Chouksey[1], P. Shrivastava[1]
Raja Ramanna Centre for Advanced Technology, Indore - 452013, India [1]

Abstract

R & D activities are going on at RRCAT for development of high energy regime (HB) 0.92, 650 MHz, five-cell superconducting radio frequency (SCRF) cavities required for proposed high energy superconducting proton accelerator. In addition, these cavities will be a part of deliverables from RRCAT to Fermilab under Indian Institutes Fermilab Collaboration (IIFC) **[1]**. *Each SCRF cavity is enclosed within titanium vessel containing liquid helium.*

Titanium bellows joins helium vessel with cavity at field probe (FP) end. Titanium was chosen for its low temperature toughness, weldability and closeness of linear coefficient of thermal expansion with high RRR niobium. The bellows ~~has~~ to compensate for axial displacement and differential expansion/contraction between cavity and vessel. Also, the bellows must be stiff enough to withstand liquid helium pressure (0.2 MPa) and flexible enough to facilitate axial displacement. U-shaped titanium bellows development involves design using EJMA-7 and challenges of thin (0.4mm) sheet forming, titanium welding and qualifications for rated parameters. Welding was carried out by micro-TIG welding process using ERTi-2 filler as per AWS G2.4M, to ensure sufficient toughness/ductility of welds at 2K temperature. Three cavities, dressed utilizing theses bellows have been qualified for HTS test parameters at Fermilab and have been assembled in cryomodule significantly helping DAE/India to meet their deliverables to Fermilab in the R&D phase of IIFC. The experience thus gained is very helpful for their indigenous development.

INTRODUCTION

Titanium U-shaped bellows serves as a flexible member between cavity and vessel to facilitate cavity tuning (both offline and online) and to compensate differential expansion/contraction during warm up and cooling. The bellows is welded between Field probe (FP) transition ring and adaptor ring. Bellows is designed for MAWP of 2bar (30 Psi) using EJMA-7. During cavity cool down, the inner space of bellows surface bears the liquid helium at 2 bar pressure while outer surface is exposed to vacuum.

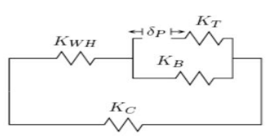

Figure-1: Equivalent spring diagram for cavity assembly

Figure-1 explains the equivalent stiffness diagram of dressed cavity. K_{WH}, K_T, K_B, K_C are stiffness of helium vessel, off-line tuner, bellows and cavity respectively. Titanium gr-2 was chosen for its low temperature toughness, weldability and closeness of linear coefficient of thermal expansion with high RRR niobium.

Figure-2: HB 650 MHz five-cell dressed cavity

DESIGN OPTIMIZATION

The U-shaped Ti gr-2 bellows is designed as per EJMA7 guidelines [6]. The U-shape facilitates higher deflection at lower pressure requirements. Bellows are intended to work with deflection stresses beyond yield strength. This may lead to permanent set after rated cycles, therefore, design for fatigue is essential.

Design Requirements

- MAWP: 2 bar (30 Psi)
- Inside Diameter: 234 ± 0.3mm
- Outside Diameter: 252.6 ± 1.0 mm
- Material: Ti gr-2 as per ASTM B265
- Leak Rate qualification: ≤ 2E-10 mbar-l/s
- Free Length: 33.6 mm
- Axial movement: ± 2 mm
- No of Cycles: 200 (cavity's cool down, in life)

Design Assumptions

- Uniform ply thickness
- Homogeneous & isotropic material
- Perfectly elastic behaviour

Design Inputs

- Inside Diameter: 234mm
- Thickness: 0.4 mm (iterative)
- Pitch: 7.2 mm
- Height: 7.4 mm
- No. of convolution: 2.5
- No. of plies: 1
- Material: Ti gr-2 as per ASTM B265
- Manufacturing Method: Mechanical Forming

*vks@rrcat.gov.in

Excel based design template as per EJMA7 was used to design the bellows. The bellows has been designed to qualify for various stresses due to internal pressure and deflection, instability (squirm), fatigue life and theoretical spring force. Iterative design method was used by opting different ply (sheet) thickness.

- Theoretical Stiffness: 920 N/mm
- No of Cycles: 5,25,704

FABRICATION

Prototyping and series production (for 6 No.) of Ti gr-2 bellows were carried out at USA based industry.

Mechanical Forming

For convolutions forming, a blank was cut from 0.4 mm thick sheet and seam welded to make a cylinder shape. By mechanical forming followed by precision rolling using fixtures and radius templates the convolutions were formed to make the bellows. Finally the ends were trimmed to free length.

Machining

The blanks were cut and using suitable machining fixtures either side rings were machined to possess circumferential lip, for welding with convolution.

Cleaning

The bellows and machined rings were chemically cleaned as per AWS G2.4M guidelines and packed with nitrogen gas individually.

Welding

Before welding WPS, WPQ and PQR were carried out for either side rings. Welding coupons/specimens ~3mm thickness was made to qualify for discoloration, weld radiography, tensile test, root and face bend tests. Radiography was done using X-ray source with IQI sensitivity 2T seen. ASME section VIII division 1 mandatory appendix 4 was applied for acceptable porosity limit of radiograph. The acceptance criterion for discoloration was as per AWS G2.4M and for tensile test was conforming to ASME IX, QW-153 and table QW-422 (tensile strength ≥ 345 MPa).

Later, machined end rings were welded at either ends of bellows. Welding was carried out by micro-TIG Welding process using ERTi-2 filler wire. Trail shielding and back purging was maintained till the weld bead cool down below 200 °C. After welding end ring's faces were buffed to restore flatness, using fixtures.

Figure-3: Bellows with end rings

INSPECTION and QUALIFICATION

Ti gr-2 bellows were cleaned as per AWS G 2.4M guidelines. Visual and dimensional inspections were carried out. Later, actual stiffness measurement, vacuum leak rate measurement and pressure test were carried out for each bellows and recorded.

- Dimensions: as per drawing
- Actual Stiffness: 550 – 700 N/mm
- Leak Rate qualified: ~ 2E-10 mbar-l/s
- Hydro test qualified: ~ 3 bar for 1 minute

Figure-4: Leak rate measurement ofTi gr-2 bellows

CONCLUSIONS

Ti gr-2 bellows were developed successfully meeting all design and functional parameters. Three cavities, dressed utilizing theses bellows have been qualified for HTS test parameters at Fermilab and have been assembled in cryomodule significantly helping DAE/India to meet their deliverables to Fermilab in the R&D phase of IIFC.

FURTHER STUDIES

Refer EJMA-7, para 4.12.1.7, for stainless steel bellows ~ 30% variation is permitted/ observed in industries and even more in inconel, titanium and other alloy bellows. Ti gr-2 bellows were observed to possess large variations in theoretical and actual stiffness .This difference need to be investigated. Further, bellows welding using electron beam welding need to be explored.

REFERENCES

[1] S. C. Joshi et al., "Development of infrastructure facilities for superconducting RF cavity fabrication, processing and 2K characterization at RRCAT", 2017 IOP Conference series, Material science and engineering.

[2] Tadayuki Otani, "Ti welding technology, Nippon steel technical report" No.95 January 2007.

[3] Tim Pasang et al., "Welding of Ti alloys", ICPMMT 2017.

[4] Technical specification for welding Ti helium vessels at Fermilab, 5500-ES-371040, 13th August 2007.

[5] A. K. Dureja et al., "Design analysis and shape optimization of metallic bellows for nuclear valve applications", SMiRT 21, 6-11 November, 2011, New Delhi, India.

[6] Joseph D. Beal et al., "Forming of Ti and Ti alloys", page 656-669, ASM Handbook, volume 14B.

CRYOGENIC TRANSFER LINE FOR CRYOMODULE OF E-LINAC AT VECC [ID:E3-505]

Abhishek Mitra, Manas Mondal, Sandip Pal, Vaishali Naik, VECC, Kolkata, India

Abstract

It is planned to generate Rare Isotope Beam (RIB) using the photo-fission route at Variable Energy Cyclotron Centre (VECC), Kolkata. To achieve this, VECC is constructing an electron linear accelerator (e-LINAC) facility comprising of a number of cryomodules having superconducting cavities inside. The proposed Cryogenic Transfer Lines (CTL) will cater liquid helium (LHe) to cryomodules from Dewar of helium liquefaction plant. 4.5K LHe from Linde 280 LHe plant will be fed to the Cryomodule via LN2 cooled and Multi-Layer Insulation (MLI) shielded cryogenic transfer lines (CTL). The CTL is divided into multiple transportable segments. These segments are connected to each other by means of vacuum insulated field joint. The heat in-leak calculation has been carried out for a typical pipeline segment as well as field joint separately. The control system for cryogenic distribution is SCADA based. The Central Control Room will be remotely located. The SCADA will supervise and control the overall system through the LAN network. The PLC will continuously monitor values of all the cryogen delivery system process parameters and primarily use these signals to control the cryogen delivery system. All the spools/segments of CTL have been fabricated and tested at factory. The installation and commissioning of the CTL will be carried out at the RIB facility at VECC, Kolkata.

INTRODUCTION

Photo-fission route will be used to generate Rare Isotope Beam (RIB) in the ANURIB project planned at VECC's Rajarhat campus [1]. For this purpose, VECC is constructing a 50 MeV, 100 kW superconducting electron linear accelerator (e-LINAC) comprising a number of cryomodules having five superconducting cavities inside. In the first phase, an injector cryomodule (ICM) housing one 9-cell, β=1 niobium accelerating cavity has been developed jointly with TRIUMF Canada and installed at VECC. The thermal shield in the ICM is liquid nitrogen (LN2) cooled and the niobium accelerating cavity is cooled to 2K using liquid helium (LHe). A Linde 280 LHe plant has been commissioned for the purpose. Inside the cryo-module, 4.5K helium is brought into a reservoir and 4.5K to 2K cool-down is done internally. 2K LHe is distributed to the niobium cavity via a distribution pipe connected to annular shell of the cavity. This pipe is evacuated using sub-atmospheric helium vacuum pumps via vacuum-jacketed sub-atmospheric (SA) line, to maintain an internal pressure of around 30 mbar thereby maintaining the LHe at 2K.

OBJECTIVE

4.5K LHe from Linde 280 LHe plant will be fed to the Cryomodule via LN2 cooled and Multi-Layer Insulation (MLI) shielded cryogenic transfer lines (CTL). Vacuum-jacketed LN2 CTL provides LN2 to the actively cooled shield of the LHe line as well as to the thermal radiation shield of the cryomodule. Thus, the Cryogenic Transfer Lines (CTL) comprise three different types of lines (i) 60 m long vacuum jacketed, LN2 cooled helium lines that will transport 4.5K liquid helium from the LHe plant to the ICM and a cryomodule test area and transport back the GHe at 4.5K; (ii) about 200 m long vacuum-jacketed LN2 CTL and (iii) 35 m long vacuum-jacketed sub-atmospheric line connected to the 2K return line of the ICM. The CTL is divided into multiple transportable segments. These segments are connected to each other by means of vacuum insulated field joints. The objective of the present work is design, fabrication, testing, installation and commissioning of the cryogenic transfer line for ICM.

DESCRIPTION

The LHe Dewar is located on first floor whereas ICM & cryomodule test area are located on the ground floor – ICM just below the LHe plant in the same building and cryomodule test area in adjacent RIB annex building around 10 m away (Fig. 1).

The LHe supply line is DN 15, Sch 5 and the corresponding vacuum jacket is DN 150, Sch 10. The GHe return line is DN 40, Sch 5 and the corresponding vacuum jacket is DN 200, Sch 10. Cryogenic control valves have been used in the LHe supply and GHe return transfer lines as well as in the cryomodule supply and return lines. Cryogenic ON/OFF valves have been used in the LN2 transfer lines. The cryogenic transfer lines also employ several instrumentation viz., Si diode temperature sensor, thermocouple, RTD, pressure transmitter, pressure relief valve etc.

There are two LN2 phase separators (each of 200 litre capacity) for separating gas from liquid nitrogen so that bubble free LN2 is supplied to the cryo-modules and LHe transfer lines. Vacuum jacketed LN2 transfer lines transport LN2 from storage tank to the phase separators which in turn provide single phase LN2 to the cryomodule as well as to the LN2 shield of the LHe transfer lines. Six ambient vaporisers (each of capacity 50 m^3/h) have been employed in the nitrogen circuit. Finned aluminium tube vaporizers with natural convective air cooling are used for this purpose.

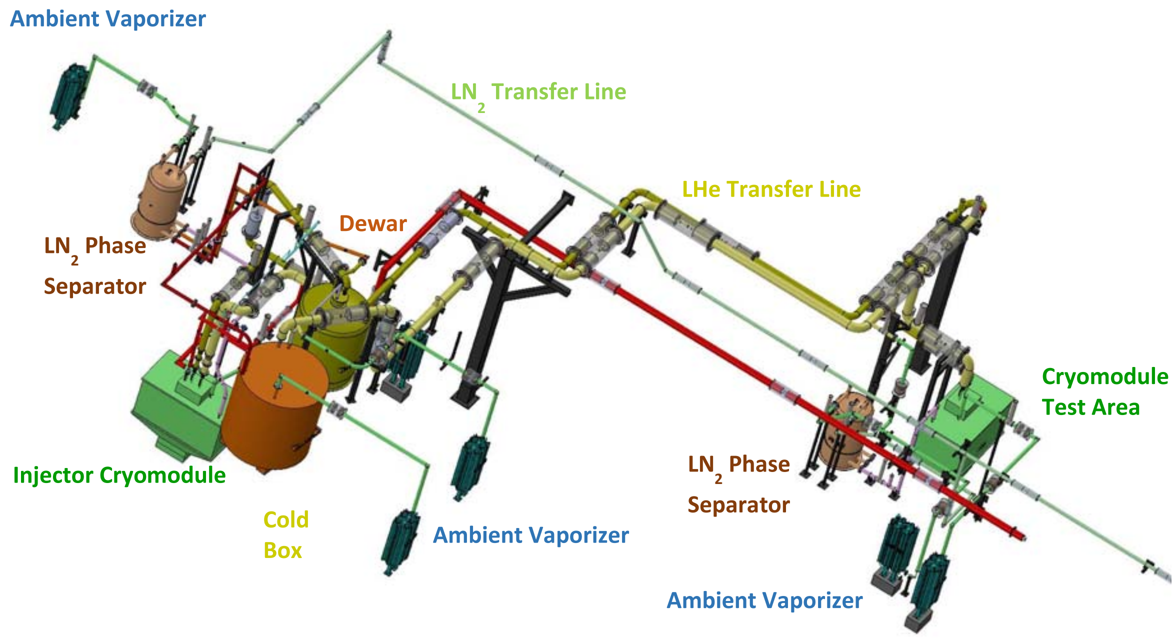

Figure 1: Layout of Cryogenic Transfer Line.

DESIGN

Thermal Insulation Design

The LHe transfer line is insulated using a combination of Multi-Layer Insulation (MLI), an actively cooled thermal radiation shield and a vacuum jacket. The inner pipe conveying LHe is wrapped with 10 layers of MLI. The thermal radiation shield is comprised of 500 µm thick copper foil which encloses the inner pipe. This copper foil is interwoven with a helical stainless steel tube. LN2 flowing through the helical tube keeps the copper foil at LN2 temperature and thus it acts as a thermal radiation shield. 30 layers of MLI are wrapped over the copper foil to reduce the heat flux on the thermal radiation shield. The inner pipe along with the thermal radiation shield is vacuum jacketed and the annular space evacuated to a vacuum of the order of 1×10^{-2} mbar. (In case of the LN2 transfer line, thermal insulation is achieved using MLI and vacuum jacket).

To preserve the insulation vacuum, the inner pipe and the outer jacket are connected at the end of each segment (spool). To reduce heat in-leak due to this conduction path, convolutions have been provided in the outer jacket at the end, increasing the length of the conduction path. Furthermore, the convolutions are cooled using LN2 to reduce the temperature gradient of the conduction path (Fig. 2). The possibility of icing/condensation on the convolutions is ruled out since they are enclosed by an evacuated 'vacuum joint box', as detailed below.

Joint Design

As mentioned in the Section 'Objective', the cryogenic transfer line is comprised of multiple segments which are prefabricated at factory. Length of each segment is limited to 5 m. The adjacent segments are connected to each other by field joint at site. An MLI insulated junction (joint) box serves to maintain the vacuum at the interface of the two adjacent segments (Fig. 2). The inner pipe (LHe line) of adjacent segments is joined at site using VCR fitting. The portions of joint box of adjacent segments are joined at site using ISO-F flanges. The inner pipe as well as the joint box have bellows to accommodate differential thermal expansion/contraction and for facilitating installation at site.

Support for Outer Jacket and Inner Pipe

The outer jacket pipe is suitably supported with the building wall / metal structures by supports to absorb loads on the pipe at design and working conditions. LHe transfer lines are designed so that their outer jacket surfaces remain within 5°C of the ambient temperature. Therefore, supports for inner pipe are designed to minimize heat in-leak (by conduction) to LHe at 4.5 K. A 4 mm thick support spacer of G10 material has been used (Fig. 3).

Estimation of Heat In-Leak

Heat in-leak value has been estimated for the LHe line considering thermal radiation, conduction through the spacers (support for inner pipe) and conduction through the junction between outer jacket and inner pipe at the end of a segment (spool). Thermal radiation has been taken into account considering the heat flux value mentioned in the MLI manufacturer's catalogue. Heat in-leak due to conduction has been calculated using the thermal resistance circuit analogy. The estimated heat in-leak values for the LHe supply and GHe return lines are 0.07 W/m and 0.077 W/m respectively. These values are less than that reported for LHC (0.2 W/m) and HERA (0.17 W/m) [2,3]; thus ample margin is available to account for uncertainties. Similarly, the heat in-leak at the field joint of the LHe supply and return lines have been estimated to be 0.76 W and 1.09 W respectively.

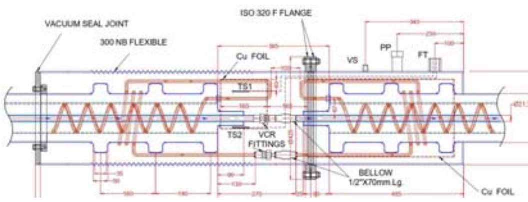

Figure 2: Field Joint between two adjacent segments of CTL.

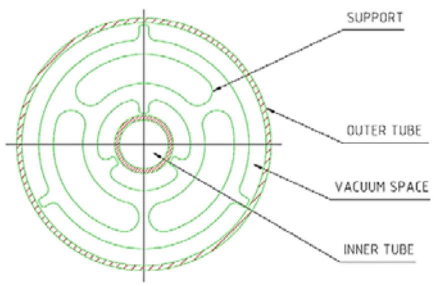

Figure 3: Typical cross-section of vacuum jacketed Cryogenic Transfer Line.

CONTROL

The cryogenic transfer line is equipped with different sensors for monitoring the operation, viz., Si diode temperature sensor, thermocouple, RTD, pressure transmitter etc. Cryogenic Control and ON/OFF valves have also been used in the cryogenic transfer line. The control system is SCADA based for facilitating supervision and control through LAN from a remotely located Central Control Room (SCADA software: WinCC system software V7.5 SP2). The PLC will continuously monitor values of all the cryogen delivery system process parameters and primarily use these signals to control the cryogen delivery system (PLC software: SIMATIC S7, STEP 7 V5.6 SP2). The PLC requires the following I/Os - Digital Input: 48; Digital Output: 12; Analog Input: 12; Analog Output: 16; RTD input: 7.

PRESENT STATUS

The fabrication of the cryogenic transfer line has been completed at the works of M/s Shell-N-Tube, Pune. Pre-dispatch inspection has also been carried out. The CTL segments/spools have been subjected to the following factory acceptance tests:-

- It has been checked that the annular space of the spool is able to maintain a vacuum level of $1x10^{-2}$ mbar or better, after isolating the vacuum pumps, at room temperature.
- The spools have been subjected to thermal cycling and tested at both warm condition and cold condition. Thermal cycling was done by allowing LN2 to flow through the lines. Thermal cycling was carried out thrice.
- All the spools have been leak tested using helium mass spectrometer leak detector (MSLD). Leaks higher than $1.0x10^{-8}$ mbar.l/s are unacceptable. The process line (inner tube) was pressurized, with a mixture of 90% dry nitrogen and 10% helium gas, upto 3 bar. MSLD was connected with the annulus vacuum to check helium leak integrity of the welds in the process line. Leak test was also carried out by spraying helium gas on the welds in outer jacket.

Out of the total number of 40 spools, five spools of the cryogenic transfer line failed in the leak tests during PDI. These were rectified and re-tested. The spools (along with the associated equipment and instrumentation) have now been delivered to VECC, Kolkata. Installation and commissioning will start very soon at the designated site in VECC, Kolkata. In order to check the feasibility, a mock-up layout of cryogenic transfer line has been carried out at the site in VECC, using PVC pipes.

A photograph of CTL fabrication is shown in Fig. 4.

Figure 4: Photograph of CTL spools at the manufacturer's works.

REFERENCES

[1] A. Bandyopadhyay *et al.* , "ANURIB – Advanced National facility for Unstable and Rare Ion Beams", PRAMANA – Journal of Physics, Vol. 85, No. 3, pp. 505-515.

[2] L. Serio *et al*., "Validation and performance of the LHC cryogenic system through commissioning of the first sector", AIP Conference Proceedings 985, 1411–1418 (2008).

[3] W. Eschricht *et al*., "Cryogenic Test of Helium Transfer Line Modules for HERA", Proceedings of the 12th International Cryogenic Engineering Conference Southampton, UK, 12–15 July 1988.

EB welding of Helium Vessel Assembly for 650 MHz SCRF Dressed Cavities

Vijayakumar V *[1], Ashish Singh[1],Syed Moulali[1] ,Tilak Maurya[1], Ajay Yedle[1], V.K.Srivastava[1], Manish Bagre[1],
Vikas Kumar Jain[1], Sanjay Chouksey[1],
Purushottam Shrivastava[2]
[1]Superconducting Cavity Development Division
[2]Proton Accelerator Group
Raja Ramanna Centre for Advanced Technology, Indore - 452013, India

Abstract

The Proton Improvement Plan-II (PIP-II) project at Fermi National Accelerator Laboratory (Fermilab), USA, requires the development of 650 MHz β=0.92 dressed Super conducting Radio Frequency (SCRF) cavities under the Indian Institutions Fermilab Collaboration (IIFC). These cavities have to be delivered by RRCAT. Similar SCRF cavities will be required for the research and development of future high energy (1GeV) superconducting proton linear accelerator at RRCAT. In-house infrastructure and expertise have been developed by RRCAT, primarily for the manufacturing, processing, and qualification of SCRF cavities. After initial testing of the 'bare' SCRF cavity in a vertical test stand (VTS) the cavity is required to be jacketed or dressed with helium vessel, end caps, bellow, tuner and power coupler. Helium vessels made of titanium are used for dressing these cavities due to its compatibility of thermal expansion coefficient with Niobium. Fabrication of the vessel is challenging as it has pressure boundary joints working at 2K temperature. Conventionally, the vessel is fabricated by welding components in the controlled atmosphere glove box using Tungsten Inert Gas (TIG) welding. This paper elaborates fabrication of the helium vessel using an EB welding (EBW) machine. This technique is being used for the first time with added advantages over the conventional method. All the joints have been designed to make it suitable to be welded by in house EBW machine. This paper also discusses the advantages of welding various vessel component of the 650 MHz β=0.92 five cell SCRF cavities by EB welding with steps and precautions followed, the difficulty faced and their remedies performed. The advantages of the EB welding method over TIG welding in glove box facility is also discussed in this paper.

Keywords: SCRF cavity, Dressing, Linac, Helium Vessel, Niobium, Titanium, EBW, Weld Joint Qualification.

Introduction

Conventionally, a titanium helium vessel is welded by the controlled atmosphere glove box using TIG [1]. Titanium is a highly reactive material and needs to be welded in a controlled atmosphere with pressure boundary joints operating at 2K temperature, thus fabrication of Ti vessels becomes more crucial. During welding the oxygen level is required to be maintained below 20 ppm to avoid oxidation of titanium [2] which is time-consuming, labourius and tedious. Welding in the Glove box is a very skillful job and takes more time. The rate of production of dressed helium vessels is quite low. To overcome such challenges,electron beam welding (EBW) seems to be a solution for the problems increasing production rate with high weld quality and defect-free weld joints for Ti made dressed helium vessel. The EB welding route offers a faster, repeatable and automated process with the possibility of making several joints in one setting. Also it produces low distortion during welding which is very essential, as cavity support brackets are used as a reference for precision alignment of the dressed cavities in the cryomodule. Fig.1 shows the typical CAD Model diagram of a helium vessel equipped with components and weld joints.[2]

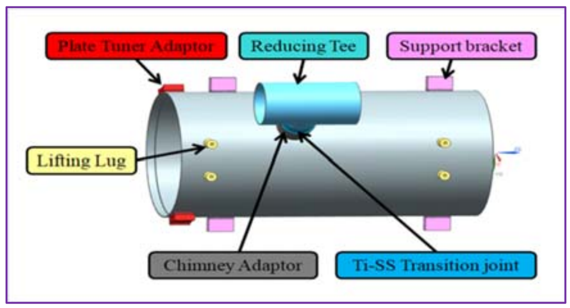

Fig 1: Model of Helium Vessel & Its Components

Electron Beam Welding

Electron beam welding is a fusion welding process that produces the joining of material with heat generated by impinging a beam of high-energy electrons onto the joint to be welded by conversion of kinetic energy (mechanical energy) into heat energy. EBW produces comparatively high depth to width ratio welds in single pass, low thermal distortion, minimum weld shrinkage and smaller Heat Affected Zone(HAZ), high speed, high power density, high reliability welds[3].

Fig 2: In-house EB Welding facility at RRCAT

vijayakumar@rrcat.gov.in

The seven axis 15 kW EB welding facility at RRCAT is shown in Fig.2. The vacuum chamber size of 3800×1500×1950mm is capable to weld low beta as well as high beta 650 MHz 5-Cell SCRF cavities. The components of the vessel like the lifting lug, tuner mounting pad, rolling pad and chimney adaptor were welded by the developed EB weld parameters using EB welding. Welding of all the joints of the vessel assembly is performed by EB welding under high vacuum < 5×10^{-6} mbar and achieved the required depth of penetration.

Weld Parameter optimisation

Weld parameters like beam current, accelerating voltage, beam focus, beam oscillation, weld speed, gun to work distance plays an important role to achieve sound weld joints. These parameters were optimized on linear and circular test coupon / samples. Linear test coupons are used to test micrograph of weld cross-section and mechanical strength. Circular coupons are used to examine the micrograph of the weld cross-section. Weld parameters were adjusted to get full penetration based on micrograph feedback. A quality control plan was prepared to check the dimensions, like parallelism and weld shrinkage after welding. Further, the welding of actual titanium vessel joints was done by the optimized parameters.

EB Welding Sequence of Helium Vessel

After the development of the Weld Parameter the following sequence was followed for EB Welding of the helium vessel :

1. Machining for edge preparations, marking and de-burring.

2. All the components were ultrasonically cleaned, and then chemical cleaned with HF+ HNO_3 solution.

3. Chimney adaptor to the Ti-SS transition pipe is welded as shown in Fig.3 Chimney Adaptor is crucial as it is a full penetration weld with 3D geometry. Also EB welding is useful due to low heat input to protect possible damage to bi-metallic Ti-SS transition pipe in close vicinity.

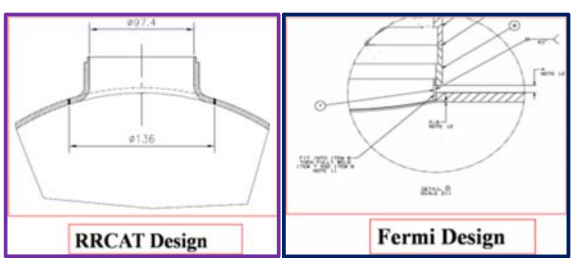

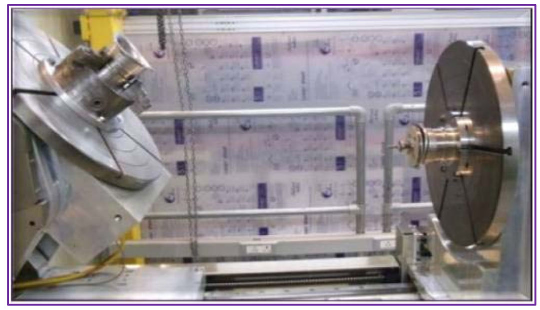

Fig3: Chimney Adaptor Ti–SS Transition EB Welding Inside & Outside

4. Marking and positioning of all the components on the helium vessel followed by assembling it for the horizontal and circular welding as shown in Fig. 4.

Fig 4: Horizontal Position

5. The support bracket, lifting lugs, chimney adaptor assembly and tuner mounting bracket are located on the proper marking and tacked by local argon purging using (TIG) tungsten inert gas welding.

6. EB welding of the tacked parts is then done with the vessel in the horizontal position. In this cycle all circular welds and the linear welds was completed except support bracket and tuner mounting bracket joint due to non accessibility of the joint Fig. 5. All circular and linear joints of the vessel assembly were EB Welded.

Fig 5: All circular and linear EB welded vessel Assembly.

vijayakumar@rrcat.gov.in

7. At the end, the position of the assembly is changed from horizontal to vertical and the support brackets and tuner mounting bracket were welded and the remaining linear welding in the vertical position was completed as shown in fig. 6.

Fig 6: Vertical Position

Electron Beam Welding Vs Glove Box Technique

The EB welding method offers several advantages including a faster and automated process. In EB welding technique, weld speeds are faster, resulting in narrow weld bead with low heat input for a comparable depth of TIG weld joint. The energy conversion efficiency of electron beam welding is very high minimizing shrinkage, heat input and heat effected zone. This is very helpful as cavity support bracket are used as reference for the precision alignment of the dressed cavity in the Cryo-module. In addition, it is possible to make several welds in one setting. The comparison is tabulated in table no. 1.

Table 1: Comparison between EBW Vs Glove Box TIG Welding Technique

Sr. No.	Descriptions	Glove Box TIG Welding	EBW
1.	Weld Bead	Non Uniform	Uniform
2.	Distortion	High	Low
3.	Heat Affected Zone	Large	Small
4.	Welding Time	More	Less
5.	Repeatability	Compatibility	Reproducible
6.	Accessibility	Difficult	Easier
7.	Lead Time	Very High	Low
8.	Production rate	Low	High
9.	Weld Quality	Good	Better
10.	Weld strength	Compatible	Compatible

Weld bead quality comparison between EB welding Fig.7 and TIG welding Fig.8.

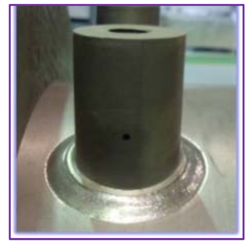

Fig 7: EB welding bead

Fig 8: TIG welding bead

Testing /Qualification

The vessel assembly has been dimensionally inspected and found to be satisfactory. It was also successfully leak tested at the leak test for vacuum leak rate of 1E-10 mbar l/s at room Temperature .

Summary

The electron beam welding of helium vessel is an efficient alternative to the conventonal process in the fabrication of dressed SCRF cavity. The desired geometrical tolerance, weld shrinkage and weld quality is achieved with advantages of lesser weld time, lower distortion, minimum weld shrinkage, lesser heat input and heat effected zone. RRCAT has successfully fabricated five numbers of 650MHz β=0.92 Titanium vessel assembly for SCRF cavity dressing. Three 650MHz β=0.92 Titanium Helium vessel with ID 502,503 and 504 were fabricated at RRCAT and dressed at Fermilab and qualified for prototype cryomodule (PCM) string assembly of PIP-II Project.

Acknowledgment

We would like to express our sincere thanks to P Ganesh, P Ramshankar and team, Mr. Rajendra Adbol, Mr. Umakant Shrivastava, Mr. Shailesh Maratha and Mr.Anuj Kumar Saiyam (RRCAT) for their technical support.

References

1. Syed Moulali, Vijayakumar V, et.al. “Dressing Joint Qualification of High Beta 650 MHz Five-Cell SCRF Cavity” Proceedings of the Indian particle accelerator conference 2022.
2. Vikas Jain, M. Bagre, S. Moulali “Progress on HB 650 MHz superconducting cavity dressing and its infrastructure” In PAC 2019.
3. Schultz, H., “Electron beam welding”, Wood head publishing, book 1993 ISBN 3-87155-111-2.

vijayakumar@rrcat.gov.in

PROTOTYPING OF FPGA BASED TIMING AND INTERLOCK SYSTEM FOR ECR ION SOURCE

Sweta Agarwal[1,2,*], Hitesh Kewlani[1,2]

[1]Ion Accelerator Development Division, BARC, Mumbai

[2]Homi Bhabha National Institute , Mumbai

*swetaag@barc.gov.in

Abstract

For pulsed operation and characterization of Electron Cyclotron Resonance (ECR) ion source, a timing and interlock system has been designed and developed. The timing system generates user programmable synchronizing pulses which are used to trigger various subsystems such as magnetron, high voltage pulse, diagnostics and data acquisition system in the correct sequence. The fast interlock system is designed for quick shutdown of the ion source within ~50 µs.
Xilinx make zynq 7010 SOC has been used along with a graphical programming language. The graphical program gets translated to HDL code and finally to a binary file that can be downloaded on the FPGA. The code is optimized such that the processing of the inputs and the generation of corresponding output completes in the clock period of 25 ns.

The five-channel timing system generates pulses with duration ranging from 1 µs to 200 ms at frequency of 1-10 Hz. A GUI is developed with control of individual channel on-off, master on-off, pulse width and its delay input from user. The interface has been designed with inbuilt range limit, thereby assuring the system safety. The five input channel interlock module generates an active low interlock with a response time of 25 ns. The GUI for interlock system has indicators for individual channel showing if interlock is generated on any of the channels. The timing system has been tested for varied values of pulse width, delay and frequency. The FPGA output pins are by default pulled to ground which ensure in case of any power failure the outputs are automatically pulled to ground and fail safe condition is ascertained

INTRODUCTION

Timing system is used to generate pulses to synchronize various subsystems of a system. These pulses ensure that components are triggered at the right time and in the right sequence so that the desired results are achieved [1]. In this paper a timing system is designed and developed for the ECR Ion Source.

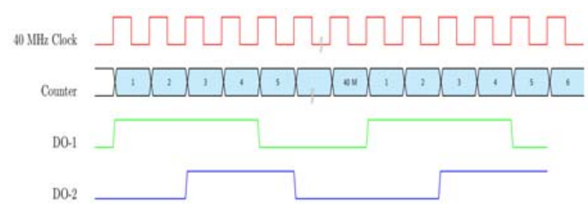

Figure 1: Pulses at the output channels of a timing system

There are 5 output channels in this system, numbered from 0 to 4 out of which the channel 0 is considered to be the master channel. The individual channel pulse width and the delay between the pulses is user specified in the system designed. The delay is to be specified with respect to the master channel. The Figure 1 illustrates the pulses at the output of a timing system. These are generated with reference to a system clock. DO-1 and D0-2 indicate the signals at the digital output pins 1 and 2 respectively. A pulse of desired width is generated by raising the output pin high for an integral number of clock periods. For example, consider the D0-1 signal which has a pulse width which is equivalent to 4 clock cycles. Similarly the D0-2 signal has a pulse width which is equivalent to 3 cycles of the reference clock. If DO-1 is considered to be the master channel then the delay for D0-2 is specified as 2 cycles of the reference clock such that when D0-1 goes high the DO-2 will go high after two clock cycles have expired. The above explains the logic behind the system design.

Interlocks are a way of preventing the system from operating under undesired conditions for the safety of the system and the operator. Depending on the speed of response required, the interlock can be either slow interlock or fast interlock [2]. The figure 2 illustrates the input and the output signals of an active low interlock system. DI-1 and DI-2 are the inputs to the system. The high on the inputs indicate that all systems are working under desired conditions so the corresponding Interlock signal is also high indicating a normal operating condition.

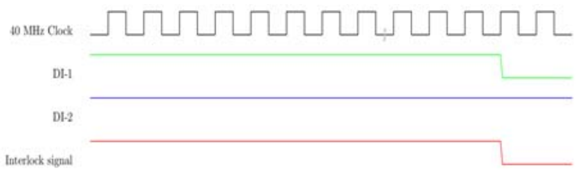

Figure 2: Inputs and Output of Interlock system

At a later time the input DI-1 goes low indicating error condition and thereby the active low interlock signal also goes low and stops the system from operating further. The status of the input signals is continuously monitored and interlock is generated when such erroneous situations arise. After the issue is resolved, the interlock is reset.

FPGA SELECTION

The FPGA is selected based on the FPGA resource requirement which in turn depends on the design, I/O pin requirement, operating frequency needed and several other factors like cost.

EXPERIMENTAL SETUP

Figure 3. Experimental setup

The figure 3 illustrates the experimental setup. Xilinx make zynq 7010 SOC [3] has been used along with a graphical programming language. The graphical code is translated into an HDL code and then a bit-file which gets loaded onto the FPGA. The communication between the FPGA and the PC is done over USB. A digital oscilloscope is used for viewing the signals at the output pins of the target device.

ALGORITHM

The figure 4 illustrates the algorithm of the timing system designed. The frequency of the pulses at the channel outputs is user specified. The pulse width and delay of each pulse with respect to the master channel 0 can be specified using the graphical user interface. In this paper the system clock is of 40 MHz implying a clock period of 25 ns. The logic explained previously has been used where the output is pulled high for an integral number of clock periods to achieve the desired width and delay is inserted by pulling the output high after a integral number of clock periods of the master channel output going high.

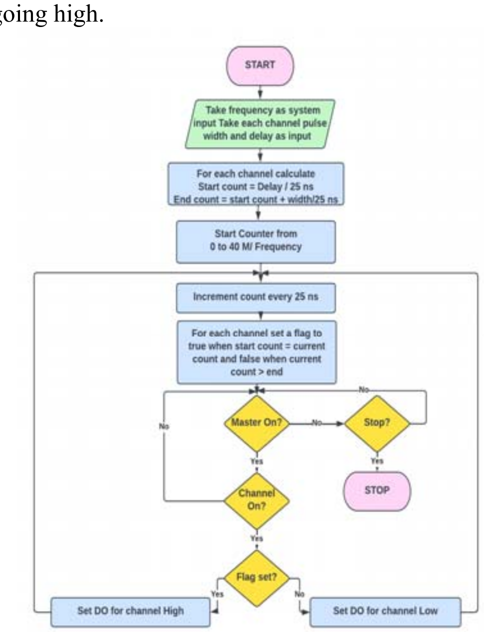

Figure 4: Algorithm of Timing system developed

The figure 5 shows the GUI of the Timing system. Master On push button is for the entire system whereas channel On push button is for individual channels.

Figure 5: GUI of Timing system

The algorithm of the Interlock system is illustrated in Figure 6.

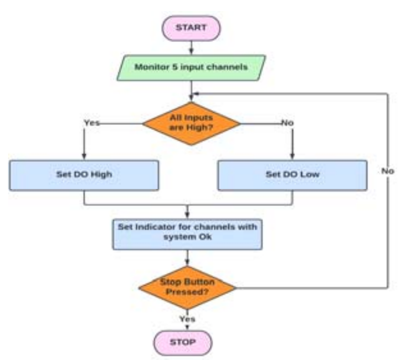

Figure 6: Algorithm of Interlock system

Each channel is monitored for any interlock condition and on detection of it, the active low interlock signal is generated.

Figure 7 shows the graphical user interface of the interlock system. The indicators go green when channel is healthy. The system ok indicator is green when all the input channels are healthy else interlock is generated.

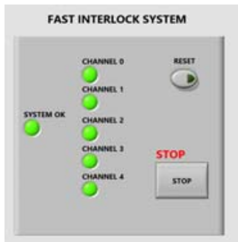

Figure 7: GUI of Interlock system

RESOURCE UTILIZATION

The FPGA resources available and the quantity used in each deisgn in shown in the table below

Resources	Available	Used In Timing System	Used In Interlock System
Flip Flops	35200	12713	8233
LUTs	17600	12767	8437

Table 1. FPGA resources available and used

RESULTS AND DISCUSSION

The figure 8 shows of the output of the timing system. Channel 0 is the master channel. The pulse width for each channel is set at 1 μs and the delay values are set to 1 μs, 2 μs and 3 μs for channel 1,2 and 3 respectively.

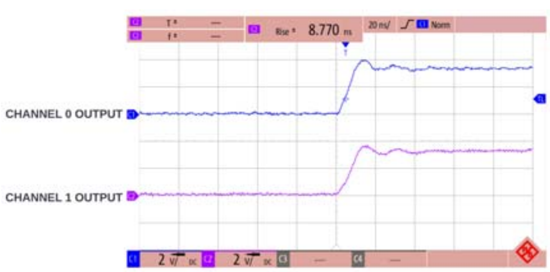

Figure 9: Timing system output pulses with rise time of 8.77 ns

The clock period being of 25 ns allows to generate pulse width with an accuracy of $\pm$ 25 ns. The Figure 9 shows the rise time of the output pulses indicating the fast response time of system.

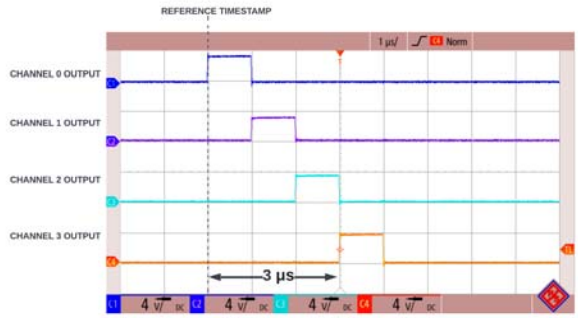

Figure 8: Output of Timing system with each channel pulse width set to 1 μs.

The inputs and the output of the interlock system is shows in Figure 9. The clock period being of 25 ns, we have achieved a response time of 25 ns. The response time is evident from the figure. When one of the of the inputs i.e. channel 0 input goes low then the system ok output also goes low which implies that the active low interlock signal is generated and the further operation of the system in turn is prevented. One such situation could be when the vacuum in the ion source goes poor then the system operation is stopped by the interlock generated.

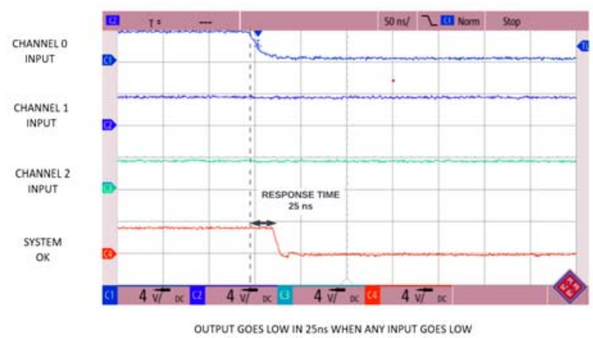

Figure 9: Response time of Interlock system

Thus the desired outputs are achieved from both the system. The systems are also tested for reliability and repeatability. Also when power is disconnected the output pins are pulled to ground and ensure fail-safe condition.

REFERENCES

[1] R. Steinbrück et al., “Trigger generator for the superconducting linear accelerator elbe,” IBIC, 2015

[2] D. Piso et al., “Ess bilbao interlock system approach,” in Proceedings of ICALEPCS2013, San Francisco, CA, USA, 2014

[3] Xilinx, Zynq-7000 soc data sheet, version 1.11.1, Xilinx, Jul.

DEVELOPMENT AND PRELIMINARY EVALUATION RESULTS OF PROTOTYPE 100 NM SPATIAL RESOLUTION DIGITAL BEAM POSITION MONITOR ENVISAGED FOR HIGH BRILLIANCE SYNCHROTRON RADIATION SOURCE

B. B. Shrivastava*[1], Surendra Yadav[1], Anil Holikatti[1], Avanish Ojha[1], Rahul Jain[1], L.K. Babbar[1], Ankita Kumari[1], Raja Khan[1], Abhisek Nayak[2], Bhavna N. Merh[2], T.A. Puntambekar[3]
[1]Beam Diagnostics & Coolant Systems Division
[2]Accelerator Control Systems Division
[3]Electron Accelerator Group
Raja Ramanna Centre for Advanced Technology, Indore, 452013, India

Abstract

Envisaged Indian High Brilliance Synchrotron Radiation Source (HBSRS) is expected to be a key enabler for the scientific and technical community to carry out advanced scientific and technological investigations in India. FPGA based Digital Beam Position Monitoring (DBPM) electronics has been indigenously developed for the HBSRS. This processing electronics determines the position of electron beam using four-electrode capacitive pick-up device. The processing electronics consists of RF Front End (RFFE) electronics and FPGA based digital processing electronics. The rms positional uncertainty in the beam position has been measured for different power levels of simulated beam conditions in the laboratory. Measured positional uncertainty is less than 100 nm for signal power level of -48 dBm and higher at the input of processing electronics for SA data. The paper describes the development and preliminary test results of the processing electronics.

Introduction

Modern day particle accelerators are extremely complex machines, where elementary particles, mainly electrons or protons, move in a predefined path with extremely high positional accuracy. Accelerators are in use today in several areas of basic and applied research, industries, medical sciences, etc. Besides, the several parameters that define a high-quality particle accelerator like the beam energy, energy spread of the beam, beam current stability etc, a key parameter that defines the quality of the beam in the accelerator is the positional accuracy of the particle beam. A combination of a large number of magnets are arranged to ensure high current and intense particle beam moves along the pre-determined path. Beam position monitors play a crucial role in ensuring the above and thus their development and deployment is key to the successful operation of any particle accelerator.

Raja Ramanna Centre for Advanced Technology, a unit of Department of Atomic Energy, Government of India houses two synchrotron radiation sources namely, Indus-1 and Indus-2 which are national facilities. A strong need for High Brilliance Synchrotron Radiation Source (HBSRS), having very low electron beam emittance, is felt by the Indian scientific community. In view of this, there is a proposal for HBSRS which is expected to be a key enabler for the scientific and technical community to carry out advanced scientific and technological investigations in India. Among all the accelerators of interest at RRCAT, possibly the most stringent requirement for monitoring the beam position is in HBSRS, where the dimension of the electron beam size in the storage ring is ~ 3 microns. To accurately determine this position within 10% of its dimension, the typical resolution of the BPM required is better than ~ 30 nm. The work reported here is a step towards the same.

.

Design and development of processing electronics

A 16-layer PCB for FPGA based digital processing electronics and 6-layer RF front end electronics was designed and developed. The 3D model of these processing electronics are shown in Fig. 1 and Fig. 2

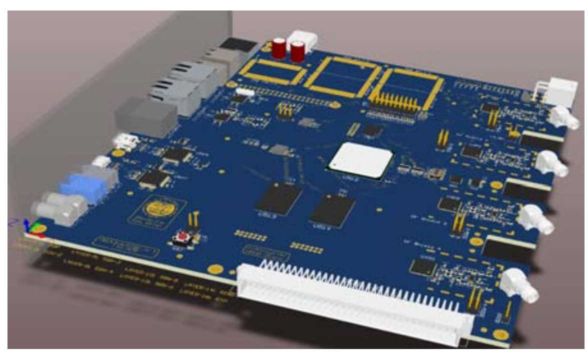

Fig.1. 3D model of 16-layer PCB layout developed for FPGA based digital processing electronics.

FPGA based digital processing electronics houses four high speed ADCs, ultra-low jitter PLL based reconfigurable sampling clock generator, dual Gigabit Ethernet controller, dual USB controller, Gigabit optical fiber link, 144 Mb FIFO, 512 Mb SRAM, EEPROM, on board temperature sensor etc. The Gigabit optical fiber link will be used for grouping of fast acquisition (FA) data at 10 kHz for fast orbit correction. The processing electronics provides Turn-by-Turn (TBT), post-mortem data, Fast Acquisition (FA) data, Slow Acquisition (SA) data at 10 Hz and 1 Hz. It also provides configurable interlock facility (trigger out) for machine protection in case the measured beam position is out of the stable zone.

*Corresponding author: bhushri@rrcat.gov.in

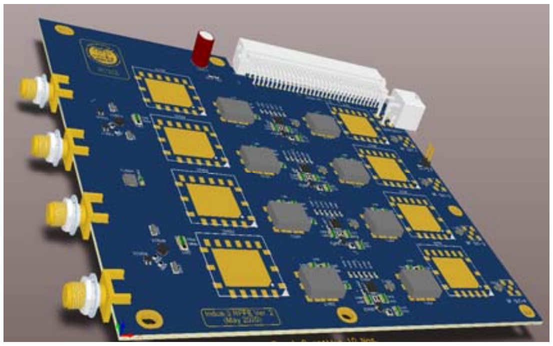

Fig.2. 3D model of 6-layer PCB layout developed for RFFE processing electronics.

The RF processing electronics has been designed and developed for simultaneous signal conditioning of all the four pickups at 505.8 MHz. It mainly consists RF cross-bar DPDT switch, ceramic band pass filter, RF amplifier and digital step attenuators.

The processing electronics shown in Fig. 3 has been developed in 1U size 19” sub-rack

Fig.3. Photograph of prototype DBPM processing electronics.

Laboratory testing

For laboratory testing of the processing electronics, a test setup was made. RF signal at 505.8 MHz was generated and was split into 4 parts using zero degree 4-way power splitter. The output of power splitter was fed to the processing electronics. The frequency responses of RF front end (RFFE) electronics is shown in the Fig.4.The measurement has been carried out upto 6 GHz. Only pass band signals are present in the spectrum. The noise floor of measurement is below -80 dBm for the entire range (DC-6 GHz). The 3dB bandwidth and full power bandwidth is 7.6 MHz and 33 MHz respectively. The cross-talk isolation of processing electronics is better than 49 dB for all the four channels. The temperature dependency is less than 0.2 µm/ °C. Measured sensitivity of the processing electronics is -90 dBm

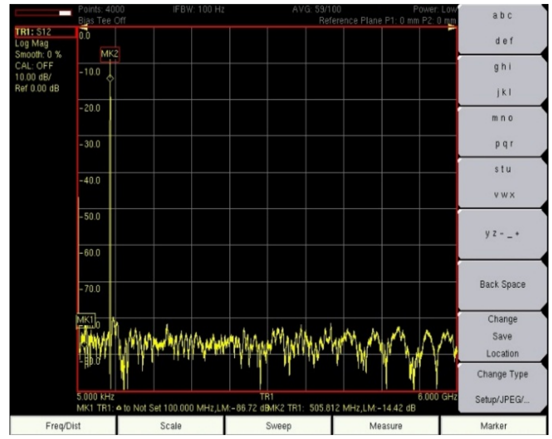

Fig.4. Wide band frequency response RFFE

RMS noise in beam position measurement with respect to RF signal power is shown in Fig. 5. The RMS noise is ~3µm for the simulated beam current of 0.1 mA. For simulated beam current of 2 mA noise is less than 100 nm. The RMS noise is less than 50 nm for the simulated beam current of 5 mA or higher.

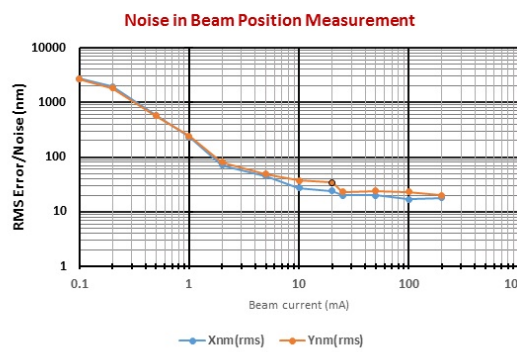

Fig.5. RMS noise in beam position with beam current

Variation in beam position with input signal power is shown in Fig.6. The beam current dependency for positional measurement is within ±1 µm for the signal power level of -41 dBm (1mA) and higher.

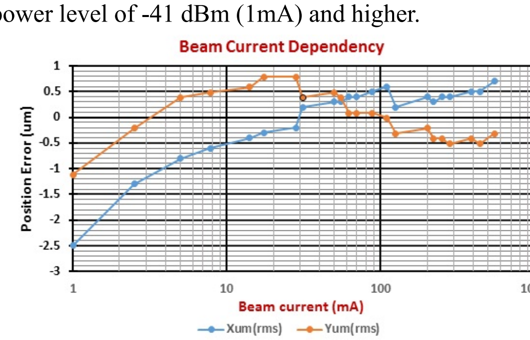

Fig.6 beam current dependency in beam position measurement

.Field testing

Field testing of processing has been carried out on Indus-2 accelerator. For this developed processing electronics was interfaced with one set of electrode whereas commercial DBPM electronics [1] was connected with another set of electrodes of TWIN BPI device [2]. For the performance comparison, Indus-2 beam was steering using steering coils. The response curve for 2.5 µm step size for indigenously developed DBPM and commercial system is shown in Fig. 7 and Fig. 8 respectively

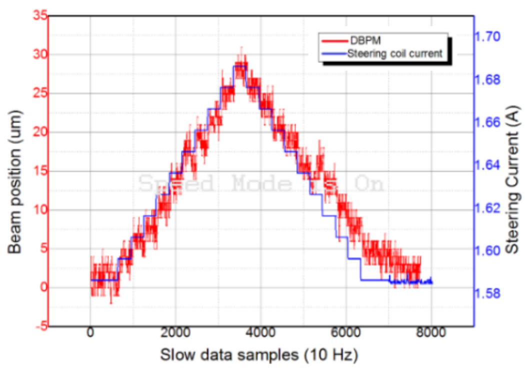

Fig.7 Beam position variation captured by developed DBPM

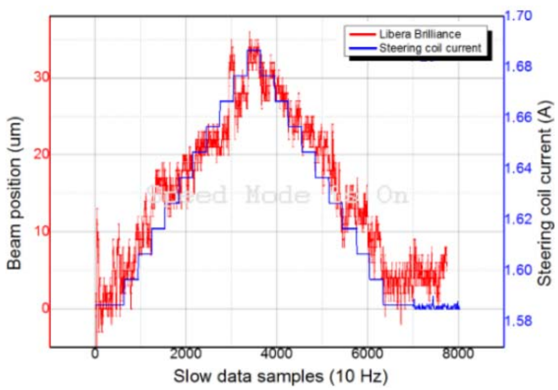

Fig.8 Beam position variation captured by Libera Brilliance + size for the same event

As evident from Fig.7 and Fig. 8, the position captured by developed DBPM has less fluctuations. To verify the same positional data at steady state (Shown in Fig. 9) was analysed.

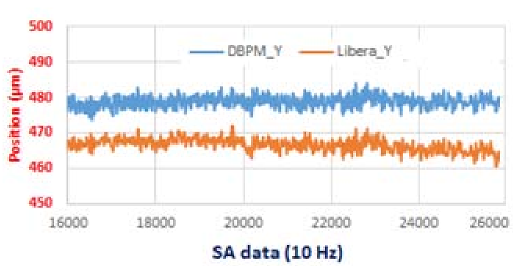

Fig.9 Beam position variation at steady state of the beam

The analysis reflects that the rms variation is position (standard deviation) of the developed DBPM is 1.337 µm whereas 1.378 µm was observed for Libera Brilliance+ for the same event. Turn-by-turn (TBT) data (1.738 MHz) and fast acquisition (FA) data (10 kHz) were also capture at study state. Spectrum of TBT data is shown in Fig. 10. Fourier transform of horizontal TBT data of both the electronics shows first peak at ~25 kHz (Synchrotron frequency). Indigenously developed electronics also shows peak at 525 kHz (Betatron freq.).

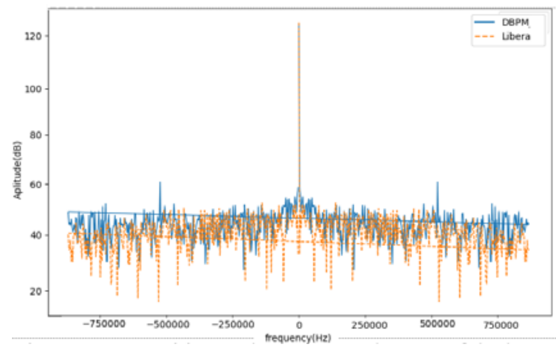

Fig.10 Fast Fourier Transform (FFT) of TBT data

Fourier transform of horizontal FA data of both the electronics shows first peak at ~600 Hz. Indigenously developed electronics also shows peak at 3.6 kHz and 4.2 kHz. These signals are not present in Libera Brilliance +.

Conclusion

Digital Beam Position Monitor Processing electronics has been designed and developed for storage ring of envisaged HBSRS. The performance of DBPM has been studied in laboratory and in the field on Indus-2 storage ring. Initial results are highly encouraging and response of developed DBPM and commercial DBPM are in close agreement.

Measured uncertainty in position is less than 100 nm for signal power level of -48 dBm and higher at the input of processing electronics for SA data. The beam current dependency for positional measurement is within ±1 µm for the signal power level of -41 dBm to 0 dBm and the temperature dependency is ≤ 0.2 µm/ °C. Measured sensitivity of the processing electronics is -90 dBm. The detailed studies under different operating conditions of the machine are in progress.

REFERENCES

[1] https://www.i-tech.si/products/libera-brilliance-3/

[2] Babbar L. K., Kumar Mukesh, Upadhyaya B. N., Bhatnagar V. K., Yadav D. P., Sisodia Brahmanand, Tiwari S. K., Holikatti A. C., Yadav Surendra, Vaishnav Deepjwalit, Soni Ajay Kumar, Sheth Yogendra M. and Puntambekar T. A. "Design, Development and Installation of Twin Beam Position Indicator in Indus-2 Synchrotron Radiation Source", DAE-BRNS 10th Indian Particle Accelerator Conference (InPAC-2022), VECC, Mar. 22-25, 2022

IMPROVEMENT IN INDUS-2 COOLANT TEMPERATURE STABILITY DURING BEAM ENERGY RAMP UP WITH FLOODED EVAPORATOR TYPE CHILLER SYSTEM

M. K. Singh, R. M. Pandey, Rakesh Kumar, Yogesh Kumar, Ravi Parkash, Jimmy James, T. A. Puntambekar,

Raja Rammanna Centre for Advanced Technology, Indore

Abstract

The process heat of machine components in the Indus-2 Synchrotron Radiation Source (SRS) is transferred to secondary cooling loop by circulating the low conductivity process water through plate heat exchanger (PHE) units. The electric current in SR magnets - such as dipole, quadrupole, sextupole etc., is required to be increased in a short duration of time, typically of the order of 10 minutes, during beam energy ramp-up from ~ 550 MeV to 2.5 GeV which causes the surge in the demand for cooling. The existing air-cooled chiller of 1 MW cooling capacity with dry expansion (DX) type evaporator was not able to match the requirement of fast cooling demand in Indus-2 during beam energy ramp-up. This response lag was causing the increase in chiller tank temperature by nearly 5 °C. Hence, an improved chiller unit with flooded evaporator was installed and connected to existing cooling loop. The flooded type evaporator unit provides more uniform temperature profile in heat transfer [1]. The new chiller evaporator contains refrigerant in sub-cooled liquid form and it is capable of handling the higher cooling rate demand during beam energy ramp-up condition [2,3], even when the chiller starts during the subsequent load cycle, the sub-cooled liquid refrigerant present in the evaporator starts absorbing the heat load immediately. This characteristic has been suitably utilized for getting the improved chilled water temperature stability during thermal transient condition.

This paper reports the developments carried out for the improvement in supply water temperature stability better than ±0.5 °C compared to the previous stability of more than ±1 °C during beam energy ramp-up. The upgradation has also improved the supply water temperature stability to better than ± 0.2 °C during stored beam condition at 2.5 GeV energy which was earlier around ±0.5 °C.

Key words: Cooling, Chiller System, Accelerator.

Indus-2 SR Ring Cooling Scheme & it's Limitations

The cooling scheme of Indus-2 SR ring magnets was designed to supply coolant at temperature of 26 °C. The control system was maintaining temperature stability of ± 0.5 °C. This temperature stability was achieved by cascading of three closed cooling loops, as shown in Figure 1.

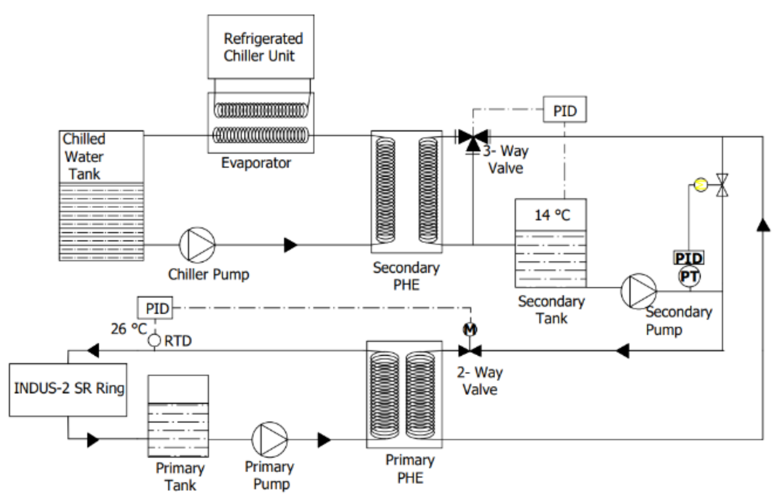

Figure 1: Indus-2 SR cooling system showing the process loop, secondary loop, and chilled water loop.

The first loop is primary process cooling loop which supplies low conductivity water (LCW) to SR magnets at 26 °C, the return water temperature goes up to 33 °C when the electron beam is at energy level of 2.5 GeV. This return heated water is circulated through the primary plate heat exchangers (PPHE) where it gets cooled down using the secondary soft water. The secondary water is entering the PPHE at 14 °C. A PID controlled valve installed across the secondary cooling loop maintains the process water temperature at 26 ± 0.5 °C.

The secondary water temperature is maintained at 14 °C with the help of secondary plate heat exchanger (SPHE) by circulating chilled water through other side of the chiller SPHE. The chilled water enters the SPHE at 8 °C which maintains the secondary water temperature at 14 °C with the help of PID controlled three-way valve. The controller regulates secondary flow in SPHE to maintain secondary temperature of 14 °C which cools the process water inside PPHE and maintain it at 26 ± 0.5 °C.

In the chilled water-cooling loop, the temperature is maintained at 8 °C by circulating it through dry expansion (DX) type evaporator of 1 MW capacity air cooled chiller. The chilled water circulates in SPHE and cools secondary water to 14 °C.

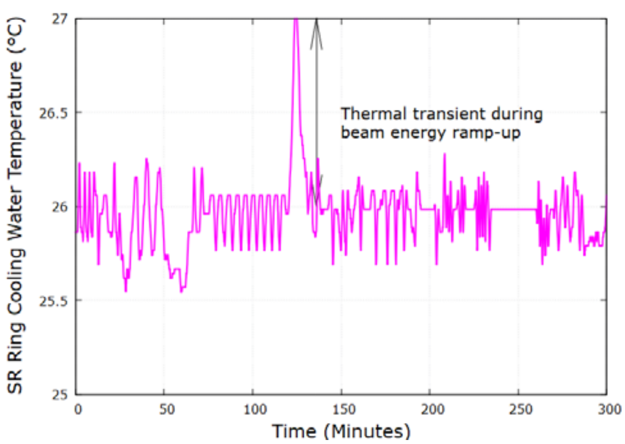

Figure 2: Variation of temperature with time during beam energy ramp up in Indus-2

The real time temperature trend of the SR ring supply water (refer Figure 2) was recorded during beam energy ramp-up of Indus-2 accelerator machine. At full load, the maximum cooling requirement for SR ring is nearly 900 kW. The air-cooled chiller of the cooling capacity of 1 MW seems to be sufficient to serve the purpose with beam filled condition. It should be noted that it is valid only during steady state operating condition of the accelerator machine. When Indus-2 beam energy is ramped-up from 550 MeV to 2.5 GeV in roughly 10 minutes, the current to the SR ring magnets is also increased proportionally [2,3]. Due to the limitation in the cooling performance of DX type evaporator, the secondary water temperature is increased by nearly 5 °C after this thermal transient condition. As shown in Figure 2, the collateral effect of this heat transfer crisis can be seen in the form of temperature rise from 26 °C to 27 °C at around 125 minutes in the primary process cooling loop.

Up-gradations in cooling Scheme

The issue of temperature rise in the secondary water loop during beam energy ramp up is investigated and necessary upgradations are introduced. To cater the requirement of fast cooling during thermal transient condition a new water-cooled chiller with flooded type evaporator has been introduced in the chiller cooling circuit. The time to reach the full load condition for the chiller with DX type evaporator and flooded type evaporator are shown in Figure 3 (a) and (b), respectively. The time required by the chiller with the flooded type of evaporator to achieve the full load condition is nearly 12 minutes which is significantly lower (>2 times) as compared to the time needed for air cooled chiller to achieve the full load condition. The quicker response to the sudden increase in the cooling demand is due to the fact that the refringent in the flooded type of evaporator is

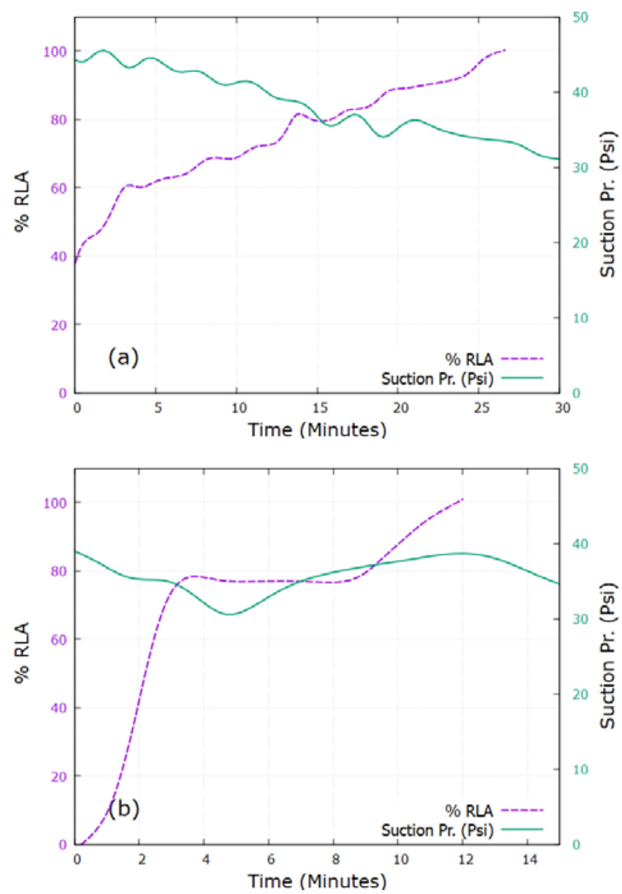

Figure 3: Rated load amperes (RLA) % and Suction pressure with respect to time for (a) DX type Evaporator and (b) Flooded type Evaporator

available in liquid state whereas in DX type it is in wet state [1]. Furthermore, the thermal conductivity of the refrigerant in liquid state is nearly 10 times more than the refrigerant at vapor state [2,3]. At evaporator, the operating temperature is 8 °C. Hence, the availability of refrigerant in the liquid state significantly enhances the capacity to handle the transient heat load with lower response time.

A secondary PHE of higher capacity was installed to ensure the availability of higher heat transfer area and better utilization of temperature gradient. The chilled water tank capacity was increased to provide more thermal inertia for cushioning of the thermal transient.

Results and Discussion

The outcome of the upgradation introduced is represented in Figure 4, showing the SR ring supply water temperature with time. The upgradation has helped in maintaining the SR ring supply water temperature within 26 ± 0.5 °C during beam energy ramp-up condition and 26 ± 0.2°C with stored beam energy at 2.5 GeV. Figure 4 also shows the variation in the secondary water temperature at inlet of secondary PHE with respect to time. The flooded type of water-cooled chiller unit along with the upgraded cooling system kept the secondary water temperature below 14 °C for satisfactory operating conditions of the system.

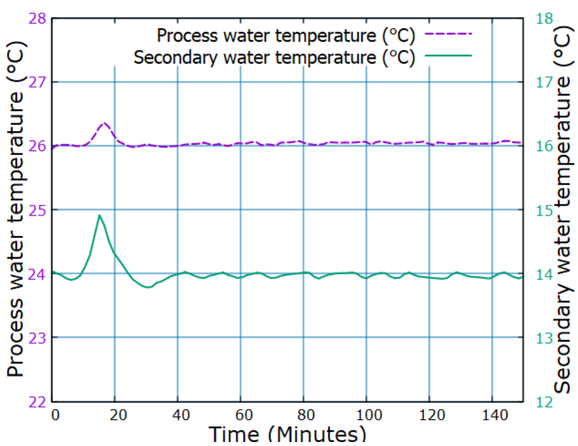

Figure 4: Variation of temperature with time during beam energy ramp up & at 2.5 GeV stored condition

Conclusions and future work

The Indus-2 SR ring cooling system has been upgraded with the installation of water-cooled chiller, higher capacity chilled water tank and heat exchanger. The replacement of the existing air-cooled chiller with DX type evaporator to a water-cooled chiller with the flooded type evaporator has improved the coolant supply temperature stability from ± 1 °C to ± 0.5 °C during beam energy ramp-up (from 550 Mev to 2.5 GeV) and from ± 0.5 °C to ± 0.2 °C during stored beam condition at beam energy 2.5 GeV energy.

The response of the cooling system using pre-cooling with the evaporative cooling system followed by cooling with the chiller unit having flooded type evaporator in similar thermal transient condition will be carried out in the near furture. Furthermore, the experience gained in this development will also be useful in design of cooling system for proposed High Brilliance Synchrotron Radiation Source.

REFERENCES

[1] J.F. Silva Gomes and S.A. Meguid, Flooded Evaporators Versus Dry Evaporators: In Which Conditions", Proceedings of the 7th International Conference on Mechanics and Materials in Design, Albufeira/Portugal 11-15 June 2017.

[2] https://www.mechanicaleducation.com/difference-between-flooded-dry-type-evaporator/

[3] https://www.swep.net/refrigerant-handbook/6.-evaporators/asas2/

A DIGITAL BEAM POSITION INDICATOR DESIGN AND DEVELOPMENT ON VME PLATFORM FOR ORBIT CONTROL APPLICATIONS IN INDUS-2

Rishi Pal Yadav, B.B.Shrivastava, Avanish Ojha, Amit Chauhan, Surendra Yadav, Anil C. Holikatti, Riyasat Husain, Rahul Rana, Rahul Jain, Puneet Maheshwari, Pravin Fatnani, T. A. Puntambekar
Raja Ramanna Centre for Advanced Technology, Indore, 452013, India

Abstract

The Beam Position Indicators (BPI) are used for measuring the beam position in particle accelerators. The digital BPI in Synchrotron Radiation Source (SRS) uses the high-speed, high-resolution analog to digital converters to directly under-sample the radio-frequency (RF) signal between 300 MHz to 600 MHz in two orthogonal streams (In-phase and Quadrature-phase) by precisely adjusting the sampling clock frequency. This simplifies the analog and digital processing circuit development and testing by performing the downconversion directly in digital domain. The orbit control applications in modern SRS are divided in two systems viz. Slow Orbit Feed Back (SOFB) control system that works with loop rate up to 10 Hz and Fast Orbit Feed Back (FOFB) control system that operate upto 10 kHz. Both the systems work together to suppress the disturbances covering frequency spectrum from milli Hertz to few hundred Hertz. A Digital BPI (DBPI) has been developed for use in Indus-2, a 2.5GeV SRS machine. This DBPI has been designed to generate Slow Acquisition (SA) data at 10Hz update rate, Fast Acquisition (FA) data at 10 kHz update rate. The Turn-by-Turn (TbT) data sampled at the bunch revolution frequency (~ 1.73 MHz) and raw ADC data sampled at sampling frequency (~ 120 MHz) have been made available on demand. VME platform has been chosen for the digital BPI development so that the slow and fast orbit feedback control algorithms can be developed with minimum latency and can run on the Digital BPI CPU with RTOS thus simplifying their overall implementation. The development is aimed towards integration of multiple BPIs in one VME crate so as to save space through system integration comparable to the commercially available digital BPI platforms. The digital domain signal processing for all the four channels has been implemented in one FPGA chip with configurable digital filters and sampling clock modules. The sampling clock PLL has been synchronized to accelerator RF using the standard 10 MHz clock method as employed in commercial DBPIs. The channel to channel gain and phase equalization method has been used for improved long term stability. Automatic gain control and piece-wise linearization methods have been provided to get the improved accuracy over large dynamic range of input signal.

For testing in Indus-2, the developed DBPI electronics was connected to Undulator-3 exit BPI (BPI-31) electrode cables. It was then interfaced with Indus-2 Digital BPI server application and Indus-2 SOFB control system. The test results showed very good beam position control ability at the Undulator location with this DBPI as part of the SOFB correction loop. Also the integrated operation of SOFB with this DBPI, passes the beam position interlock requirements for normal Undulator operation. This paper discusses the overall digital BPI design, test and characterization results and the Indus-2 machine performance with developed BPI included in SOFB operation under different operating conditions.

INTRODUCTION

In Indus-2 there are 56 BPIs for beam position measurement. Out these 16 are Digital BPIs and rest are of analog type. To steer the electron beam at the desired user orbit and to maintain the beam position at user orbit against the undesired beam movement occurring due to dipole field errors, magnet alignment errors, slow power supply drifts, thermal position dependence, insertion device open/close operations, etc, there are two orbit feedback control systems used in Indus-2 viz. SOFB control system [1] and FOFB control systems. Both of these systems use the beam position data acquired from BPI's installed in Indus-2 at different data rates (10Hz rate and 10kHz rate). To replace the analog type BPI in Indus-2 with the indigenous developed digital BPIs, the new digital BPI is being developed in VME form factor.

BPI DESIGN

The initial envisioned Digital BPI system in VME form factor comprised of three types of VME32 boards 1) Analog Front End (AFE) board, 2) digitization and digital signal conditioning (DSC) board[2], 3) Time synchronization and data grouping (TSDG) board.

The required functionality has been achieved through division of features at FPGA and VME CPU [3] level aiming towards the easy implementation of SOFB and FOFB applications through sharing of the VME crate for modular and overall distributed system implementation.

Figure 1 shows the developed BPI system under testing in Lab. Figure 2 shows the logical block diagram for the designed BPI system.

Analog Front End

The RF signals coming from the BPI button electrodes are first passed through the low pass filters to limit the signal bandwidth up to 550MHz. It is then provided to analog crossbar switch. The Analog crossbar switch can redirect any of the 4 input button electrode signals to any of the 4 analog RF channels. There are 4 identical analog RF channels that band limit the input signal to 10MHz range around the central frequency of 505MHz and can provide up to +40dB gain in steps of 0.25dB.

Digitization and digital signal conditioning

The pickup signal from four button electrodes after processing by the AFE is passed to the DSC board. In the DSC, the signal is digitized by high speed ADC to 16bit code values at a sampling frequency lower than the accelerator RF frequency and given by Eq.1 with $n = 4$.

$$f_s = \frac{4}{4n+1} f_{acc} \quad \text{where } n = 1, 2, 3, \ldots, n . \qquad (1)$$

The raw ADC data coming from each RF channel is offset and gain compensated. It is then passed through the digital crossbar block to mark the switching boundaries. The digital crossbar switching method minimizes the effect of channel to channel mismatch of individual RF channels thus improves the long term stability. This method of crossbar switching adds the switching glitch to the data. The effect of this glitch is more on the wide-band data as compared to the narrow-band data. To minimize the effect of the glitch, the channel to channel gain and phase equalization loops are implemented that runs at 0.1Hz rate. The data is then mixed with the fs/4 frequency to generate the I and Q signal streams. The I/Q data streams are then digitally down converted to 1/68 of sampling frequency A 16 bit CORDIC engine is implemented in FPGA to convert the I/Q data to amplitude and phase data streams. The amplitude data is further digitally down converted to about 10kHz rate and 10Hz rate in different steps using the CIC decimation stages and polyphase FIR filter as the gain compensation filter. The amplitude data streams at 10kHz rate and 10 Hz rate writes the data in the FPGA registers that are directly accessed by the VME BUS as 32 bit registers. The TbT data and the ADC data is read from the corresponding buffers in asynchronous mode through VME bus.

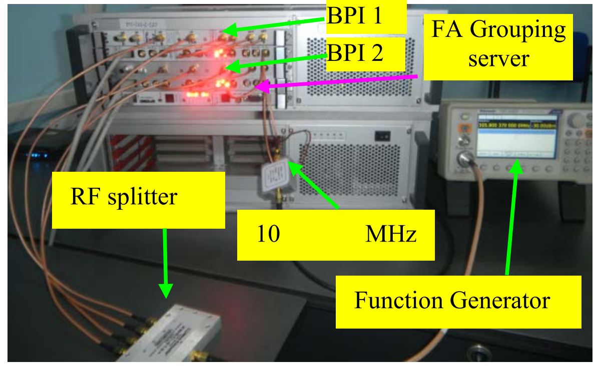

Fig 1: DBPI under testing.

Time synchronization and data grouping

The FA data at 10kHz rate is updated in the registers that are read by the VME CPU. The FA data packet as per the grouping protocol is formulated and transmitted on the network. The inter BPI timings have been synchronized using dedicated trigger lines on user I/O lines of VME P2 connector. The sampling clocks of different BPIs are synchronized using PLL of 10MHz reference clock connected through front fascia connector.

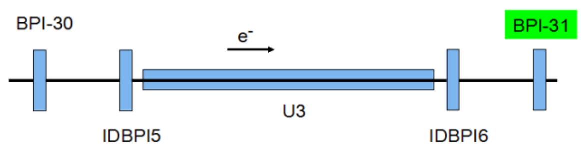

Fig 3: DBPI installed at Undulator U3 exit location.

INTERFACING OF THE BPI WITH INDUS-2 CONTROL SYSTEM

The developed BPI electronics was installed in Indus-2

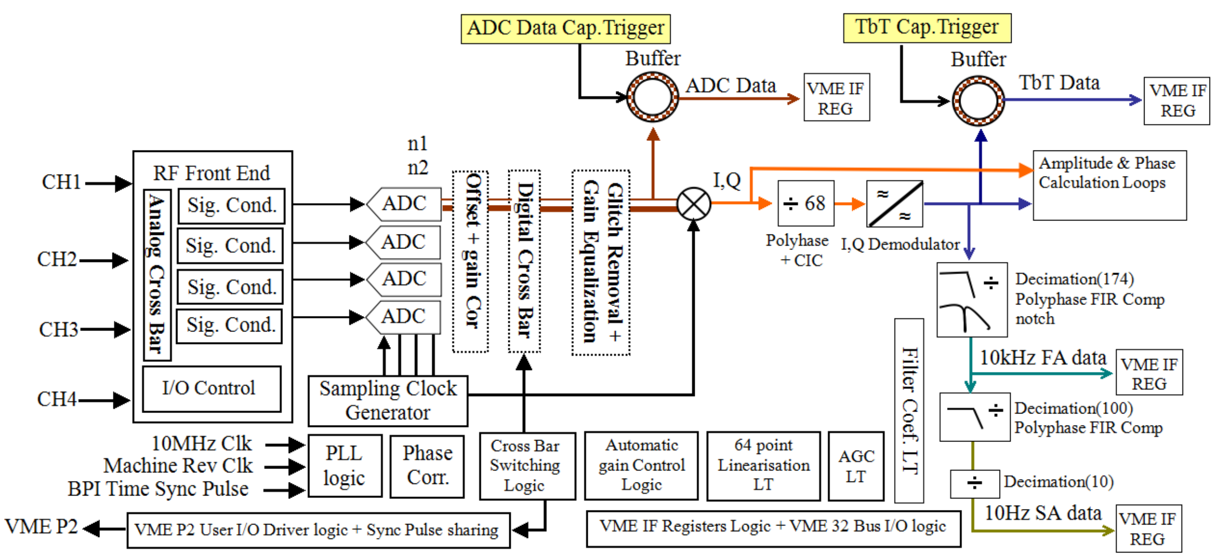

Figure 2: Logical Block Diagram of the developed digital BPI (only one channel is shown) .

at Undulator U3 exit BPI location (BPI-31) and included in Indus-2 "Digital BPI server" as NAYAN01 unit in place of commercial unit as shown in Fig 3.

The present system level has been reached through the combined contribution of different development activities in incremental manner. Fig 4 shows photographs of different modules and cards developed by the contributing working group members during the development stage.

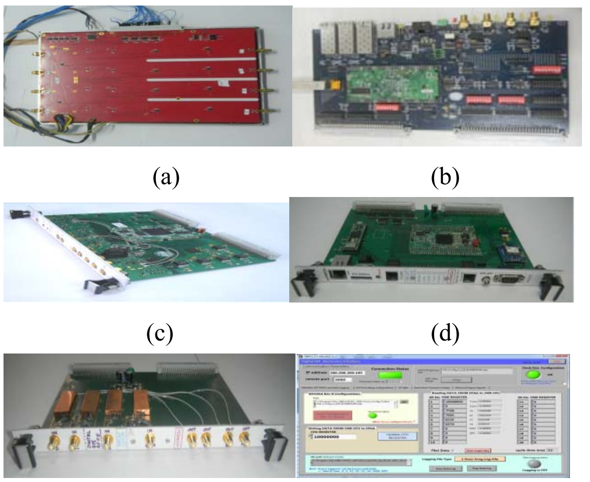

Fig 4:DBPI related developments (a) RFFE v1[4] (b)TSDG board (b) DSC Board (d) VME CPU (e) RFFEv2(f) software

TEST RESULTS

Figure 5 Shows the effect of AGC switching on the beam position measured by the developed BPI when beam current is made to decay from 90mA to 5mA and shows that the AGC glich is < 30µm. Figure 6 shows the difference in beam position measured with the new developed BPI and the commercial BPI during Energy Ramping stage and shows that the error is < 200µm. Table 1 lists the important test results for the developed BPI.

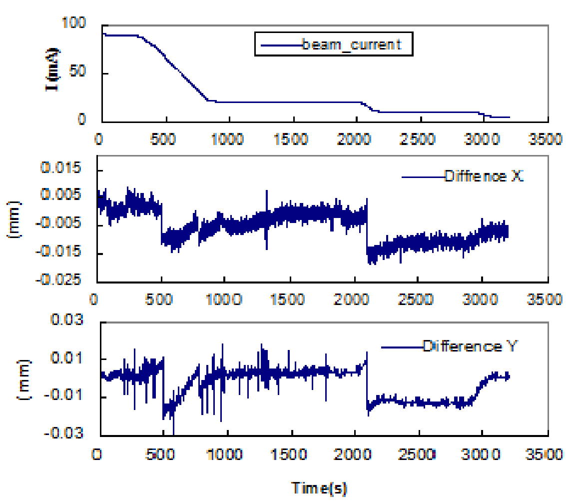

Fig 5: position dependence with AGC switching.

CONCLUSION AND FUTURE WORK

A new digital BPI has been developed for use in Indus-2. This BPI has been interfaced with the Indus-2 control system. The test results show very good beam position control ability at the Undulator location with this BPI in SOFB. Also the integrated operation of SOFB with this DBPI passes the beam position interlock requirements for normal Undulator operation. The second unit of the BPI has been developed along with the timing synchronization and Grouping features. The unit has been tested in lab. In the stage-2 testing the unit will be tested now for Local FOFB operation at U3 site with four correctors and two BPIs in Local FOFB loop.

Table 1: Important test results

Parameter	Value
Resolution (lab test at -10dBm)	~75nm (S_x =S_y = 0.060)
AGC glitch (on Indus-2)	< 30µm(I_{beam} 90mA to 5mA)
Data Correlation with commercial DBPI (10Hz) rate (on Indus-2)	σ_x = ~1.2µm , σ_y = ~740nm
Beam Control ability at U3 site with new BPI in SOFB loop	Better than 30µm

REFERENCES

[1]. R. Rana , R. P. Yadav , P. Fatnani , S. Yadav , R. Husain, SOFB operation and performance assessment towards orbit stability in Indus-2 SRS, Proceedings of InPAC-2022, VECC, Kolkata, India, Mar., 22-25, 2022.

[2]. R.P. Yadav, R. Rana and P. Fatnani, 120 MSPS VME Based ADC Card For Digital BPI, Proceedings of InPAC-2019 , IUAC, New Delhi, India, Nov., 18-21, 2019.

[3]. R.P. Yadav, R. Rana, A. Kumar and P. Fatnani, “Design of MicroBlaze SoC based VME CPU mVME2C for Accelerator Control Applications”, Proceedings of InPAC-2022, VECC, Kolkata, India, Mar., 22-25, 2022.

[4]. B.B.Shrivastava etal,Development of prototype RF front end electronics for digital beam position monitor of Indus-2, Proceedings of InPAC-2018, pp 559-561

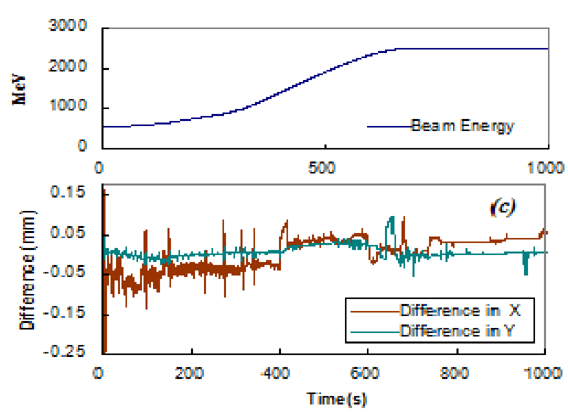

Fig 6: Position variation during beam EnergyRramping.

Design and Development of NiAlCo Ferrites for High Power Circulator at S-Band

Lakshmikanta Aditya*, Manjeet Ahlawat, Ramkesh Meena, Prashant Pareek and Shesh Nath Singh
Accelerator Magnet Technology Division, RRCAT, Indore

Abstract

NiAlCo spinel ferrites are promising materials as non-reciprocal ferrite phase-shifter owing to their high-power handling capability with tailorable magnetization and high Curie temperature. We have designed and developed a range of NiAlCo spinel ferrites of optimum room temperature saturation magnetizations ($4\pi M_S$: 260-475 Gauss), high Curie temperatures (T_C : 300-360°C) and reasonable FMR linewidths (Δ_H) by selective doping of aluminium in the nickel ferrite lattice using solid state ceramic process techniques. This paper presents the dependence of $4\pi M_S$, T_C and Δ_H of the developed spinel at various Al concentrations. Electromagnetic simulation of S-band waveguide phase shifter using the ferrite properties shows non-reciprocal differential phase shift of scattering parameters S_{12} and S_{21} at 2856 MHz.

INTRODUCTION

The discovery of magnetic spinels in the late 1940's permitted the birth of the now flourishing microwave ferrite devices that manipulate, receive and send electromagnetic signals at radio-frequency, microwave and millimeter-wave frequencies. These spinels (MFe_2O_4) were the first and the simplest range of magnetic mixed oxides known as ferrites [1-3]. In the microwave regime, aluminium and cobalt substituted nickel ferrites are promising materials for pulsed microwave power applications owing to their high-power handling capability [4] coupled with tailorable magnetization, high Curie temperature, high permeability, high resistivity, moderate to high permittivity and low-losses at microwave frequencies. This paper presents thermo-magnetic, microwave-magnetic and microstructural properties of Al and Co substituted nickel ferrites developed by us in relation to S-band circulators.

DESIGN OF COMPOSITION

The crystal structure of nickel ferrite ($NiFe_2O_4$) is cubic spinel (space group Fd3m) with oxygen anions in the face centre cubic arrangement. Cations have either four-fold or six-fold coordination forming tetrahedral and octahedral sub-lattices. Magnetism in nickel ferrite arises from superexchange interaction resulting antiparallel cation spin alignment [5,6]. The saturation magnetization and Curie temperature of $NiFe_2O_4$ is 3000 Gauss and 587°C respectively [7]. Since such a high value of magnetization is undesirable at high power microwave application, we have incorporated non-magnetic aluminium in the basic Ni-ferrite lattice to reduce the magnetization [8,9]. Introduction of 0.03 Co^{2+}/f.u. leads to indirect spin–orbit coupling which raises the power handling capability by raising the peak-power threshold [4, 10, 11]. With the aim of S-band application, we have designed a range of NiAlCo inverse-spinel ferrites of compositions $Ni_{0.94}Co_{0.03}Mn_{0.03}Cu_{0.03}Al_zFe_{1.97-z}O_4$ (z: 0.85, 0.90, 0.93 and 0.96).

FABRICATION & CHARACTERIZATION

NiAlCo spinel ferrites with the above designed compositions have been developed using conventional ceramic techniques with the following process flow diagram:

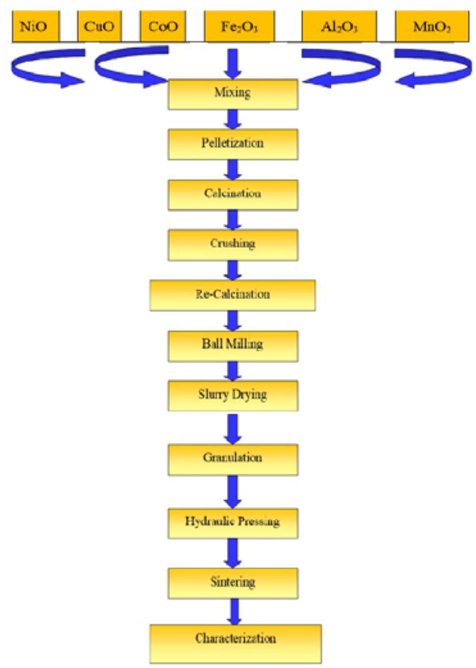

High purity (≥ 99.5%) micronized powder of NiO, Fe_2O_3, Co_3O_4, MnO_2 and CuO have been used as the starting raw material. The mixed batch have been pelletized, calcined, crushed, wet ball-milled (APS~ 1 µm), granulated with binder, compacted to discs and coaxial cylinders and finally sintered at 1250°C in air atmosphere to achieve >95% theoretical density.

Structural studies of the sintered samples have been conducted by X-ray diffraction (XRD). Thermo-magnetic measurements of ϕ8 x 8 mm disc samples have been conducted using a pulse magnetometer. The electromagnetic measurements have been conducted in the broadband (1-9 GHz) on co-axial cylindrical samples (ϕ3 x ϕ7 x 5 mm) using Keysight Technologies N9915A vector network analyser. Microstructural studies of the gold coated fractured surfaces of sintered samples have been performed using a ZEISS field emission Scanning Electron Microscope (SEM) equipped with Energy Dispersive X-Ray Analyser (EDX).

*corresponding author: aditya@rrcat.gov.in

RESULTS AND DISCUSSION

Single phase polycrystalline cubic spinel structure of the sintered samples have been confirmed by XRD. Fig. 1. shows temperature dependence of saturation magnetization of the studied samples with different Al concentrations. Monotonous drop of room temperature $4\pi M_S$ (475 to 260 Gauss) and T_C (360 to 300) with increasing Al concentrations (0.85 to 0.96/f.u.) have been observed.

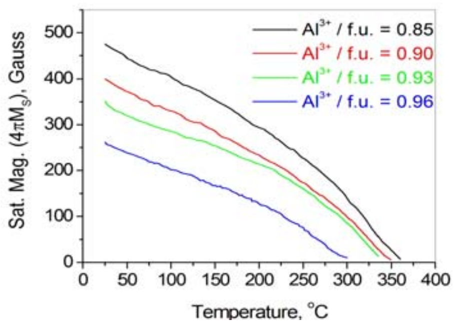

Figure 1: Saturation magnetization as a function of temperature for different Al concentrations

Fig. 2 shows normalized impedance (ZL) vs frequency plots in the 1 to 9 GHz region. The real ZL and imaginary ZL spectrum have been computed from the electromagnetic measurements. The 3-dB ΔH values (320-600 Oe) have been determined from the ZL real spectrum. Significant reduction of ΔH value (320 Oe) is observed at the Al concentration of 0.96 /f.u.

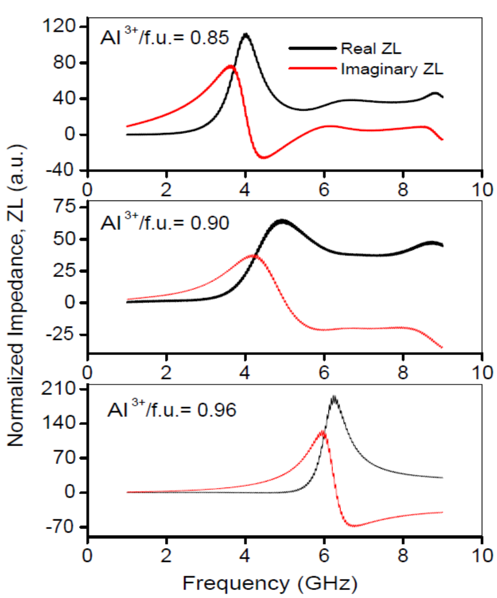

Figure 2: Impedance vs frequency plots for different Al concentrations

Microstructural studies using SEM-EDX show granular microstructure with grain size 7 – 10 µm with presence of major constituent elements, as shown in Fig. 3.

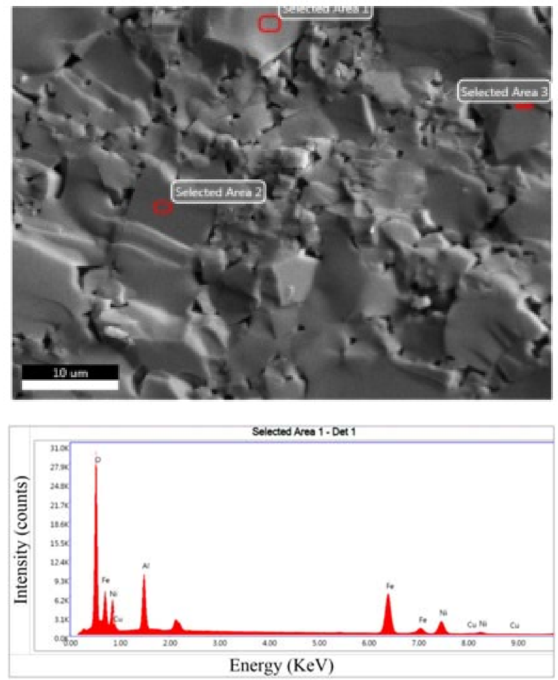

Figure 3: SEM image (top) and the corresponding EDX spectra (bottom) of fractured surface of NiAlCo ferrite with Al^{3+}/f.u. = 0.93

The measured properties of the ferrites are shown in Table 1. We achieved higher density with higher T_C in compared to the literature reported values for the similar compositions [4,8]. Our NiAlCo ferrites have excellent temperature stability of magnetization characterized by very low negative temperature coefficient of saturation magnetization (α_M :-0.15 to -0.23 %/ °C), as shown in the table. Introduction of 0.03 Co^{2+}/f.u. in the designed composition corresponds to enhanced spin wave line-widths (12-15 Oe) [4]. This combined with observed thermo-magnetic and microwave properties in our NiAlCo ferrites are very promising for high power circulators

Table 1: Properties of our NiAlCo spinel ferrite

Al^{3+}/f.u. →	0.85	0.90	0.93	0.96
$4\pi M_S$ (Gauss)	475	400	350	260
T_C (°C)	360	350	335	300
α_M (% / °C)	- 0.15	- 0.17	- 0.19	- 0.23
ρ (gm/cc)	4.78	4.77	4.75	4.71
ΔH (Oe)	350	550	600	320

Using these ferrite properties, electromagnetic simulation of S-band rectangular waveguide phase shifter has been carried out using CST microwave studio for stable operation at 2856 MHz. Simulated scattering parameters are shown in Fig. 4. Clear phase difference between scattering parameters S_{12} and S_{21} can be seen in the figure. This implies that the amount of phase difference observed is not reciprocal i.e. phase change is different depending on direction of propagation of microwave power. The non-reciprocal differential phase shift between scattering parameters S_{12} and S_{21} at S-band indicates usefulness of the material for S-band application. The results can be implemented in the development of 4-port differential phase shift circulator at S-band using two magic tees and a ferrite phase shifter.

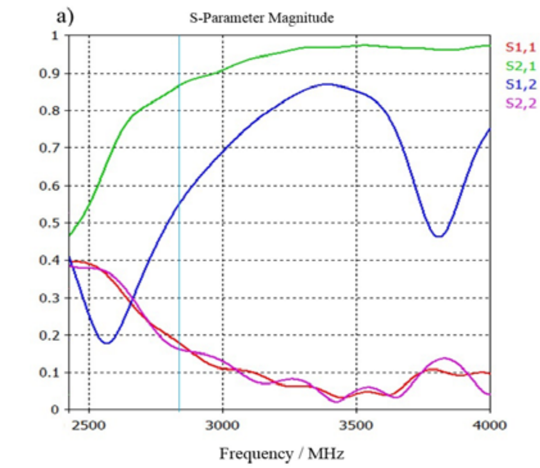

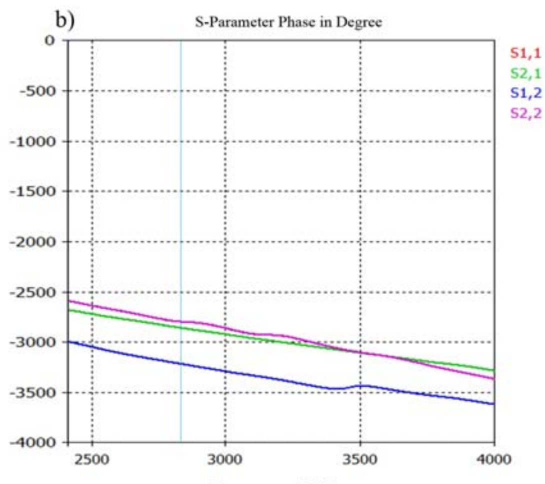

Figure 4: Simulated scattering parameters of the S-band phase shifter in a) magnitude, and b) degrees (unwrapped phase difference)

CONCLUSIONS

NiAlCo spinel ferrites have been successfully developed with optimum saturation magnetizations (260-475 Gauss), high Curie temperatures (300-360°C), reasonable FMR linewidths (320-600 Oe) and excellent temperature stability of saturation magnetizations (-0.15 to -0.23 % / °C). Non-reciprocal differential phase shift between S_{12} and S_{21}, as observed in electromagnetic simulation, indicates usefulness of the developed ferrites as phasor-cell for s-band phase-shift circulators.

ACKNOWLEDGEMENTS

The authors sincerely acknowledge Shri T. A. Puntambekar, Director- EAG for scientific discussion and evaluation. The acknowledgements are also due to the colleagues from AMTD (Shri R. R. Yadav, K. Singh, and L. Ghongde), and MSG (Dr. P. Ganesh) for extending co-operation during experiments.

REFERENCES

[1] J. L. Snoek, “Non-metallic magnetic material for high frequencies,” Philips Tech. Rev., vol. 8, p. 353 (1946).
[2] J. L. Snoek, “Magnetic and electrical properties of the binary system MOFeO,” Physica, vol. 3, p. 463 (1936).
[3] A. S. Hudson, “Molecular engineering in the design of microwave ferrimagnetic garnets”, J. Phys. D: Appl. Phys. 3, 251 (1970).
[4] N. S. Bhattacharya and G.P. Srivastava, “On the instability threshold of cobalt substituted Ni–Al ferrite at high-microwave-power levels”, J. Magn. Magn. Mater. 262 pp.212–217 (2003).
[5] J. Smit and H. P. J. Wijn, “Ferrites”, Wiley, New York, p. 157 (1959).
[6] P. W. Anderson, “Antiferromagnetism. Theory of superexchange interaction,” Phys. Rev., vol. 79, no. 2, pp. 350–356 (1950).
[7] V. G. Harris, Modern Microwave Ferrites, IEEE Transactions on Magnetics, Vol.48, No. 3 (2012).
[8] N. Saxena, B. K. Kuanr, Z. H. Zaidi, G. P. Srivastava, “Effect of aluminium substitution on electric, magnetic and microwave properties of LiTi ferrite” Phys. Stat. Sol. A127, 231 (1991).
[9] A. Lassoued, M. S. Lassoueda, B. Dkhilb, S. Ammara, A. Gadria, “Substituted effect of Al^{3+} on structural, optical, magnetic and photocatalytic activity of Ni ferrites”, J. Magn. Magn. Mater. 476, 124–133 (2019).
[10] R.L. White, “Ferrimagnetic resonance line widths and g-factors in ferrites” Phys. Rev. Lett., 465 (1959).
[11] J. B. Goodenough, “Magnetism and Chemical Bond”, Wiley, New York (1963).

DESIGN OF THREE ELECTRODE BEAM EXTRACTION SYSTEM FOR ECR ION SOURCE USING IBSimu CODE*

Alok Kumar Ghosh[1,2], Monika[1], Jose V. Mathew[1], SVLS Rao[1]
[1]*Ion Accelerator Development Division, BARC, Mumbai-400085*
[2]*HBNI, Mumbai-400085*

Abstract

Three-electrode extraction system has been simulated using IBSimu ion optical code for ECR Ion Source (IS). The MEHIPA linac has been designed for 30keV, 10mA proton beam. Moreover, the experimentally measured values of beam emittance in our ECR Ion Source are found to be higher in compared to its estimated values from simulation. To understand the discrepancies between simulation and experimentally measured values of emittance, a simulation study of the beam extraction is necessary. Here, we present the preliminary simulation results of the ion beam extraction, which was performed using the ion optical code IBSimu. The shape of the electrodes has been kept same as that of the existing LEHIPA IS. Beam emittance and Twiss parameters of the rms ellipse are calculated at various locations. Different parameters of the extraction system such as extraction gap (distance between plasma and extraction electrode), suppressor voltage, extraction voltage has been optimized to get minimum rms emittance at 200 mm distance from the exit hole of the plasma electrode.

INTRODUCTION

The Electron Cyclotron Resonance Ion Source (ECR IS) is nowadays most powerful plasma device to feed high energy accelerators with intense ion beams. Its reliability and reproducibility have made itself best tool for various applications concerning ion beam. An ECR IS is basically a plasma trap system, which needs an extraction electrode assembly for producing a well-behaved ion beam. Design and development of this extraction electrode is a tricky task, as the extracted beam current and quality depend on the electrode geometry.

Schematic of an ECR IS set up with triode extraction electrode has been shown in figure-1. The beam energy of our operating ion source for LEHIPA is 50 keV. But, as various experimental studies have suggested that the emittance of the extracted beam is minimum when the extraction voltage is around 30 kV, the MEHIPA linac has been designed for 30keV proton beam energy, with 10 mA current. It requires a preliminary design study. On the other hand, the experimentally measured values of beam emittance in our ECR Ion Source are found to be higher in compared to its estimated values from simulation. So, a simulation of beam extraction is needed to understand the discrepancies between experimentally measured values with simulation results. For these reasons, a preliminary simulation of a proton beam extraction has been performed using the ion optical code IBSimu [1]. The shape of the electrodes has been kept same as that of the existing LEHIPA IS. For simulation the best values of mesh sizes and iteration number have been obtained. Simulation has been done up to 250mm distance from the exit hole of the plasma electrode. Beam emittance and Twiss parameters of the rms ellipse are calculated at various locations. Different parameters of the extraction system such as extraction gap (distance between plasma and extraction electrode), suppressor voltage, extraction voltage has been optimized to get minimum rms emittance at 200 mm distance from the exit hole of the plasma electrode. The extraction gap has been changed in the range of 16-30 mm. The extraction voltage is varied from 20 kV to 50 kV. The dependence of emitted beam on the suppressor voltage has also been tested.

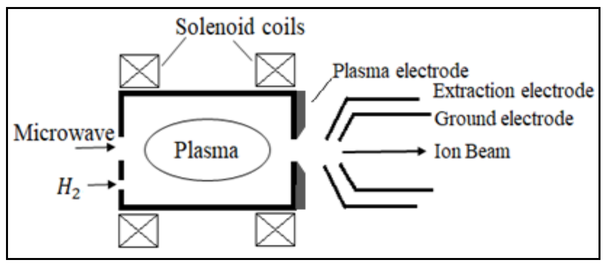

Figure 1: Schematic of ECR IS set up with extraction system.

SIMULATION OVERVIEW

IBSimu is a general-purpose ion-optical code for charged particle optics. Flow diagram for the calculation of particle trajectories and related electrostatic fields is shown in figure-2. The calculation of electrostatic potential is based on solving Poisson's equation using finite difference method (FDM), by discretizing the simulation domain with rectangular meshes of fixed step size.

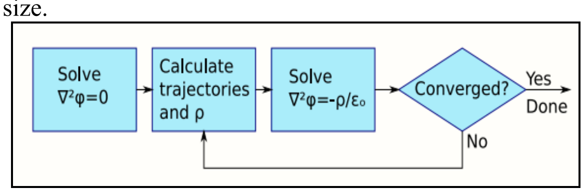

Figure 2: Flow diagram of calculating extracted particle trajectories.

A generally accepted non-linear plasma model is used for positive ion extraction. The thermal background electrons of the plasma are taken into account analytically in Poisson's equation,

$$\nabla^2 \phi = -\rho/\epsilon_0 \tag{1}$$

Where, $\rho = \rho_{ion} - \rho_{e0}\exp[e(\phi - \phi_p)/(kT_e)]$. Ion charge density ρ_{ion} is calculated from required beam current density, and ρ_{e0} is set to ρ_{ion} at plasma potential. The model parameters are plasma potential ϕ_p and electron temperature T_e.

RESULTS AND DISCUSSIONS

The simulation is done for 10 mA proton beam current. The geometry of the three electrodes can be viewed in figure-4, which is cylindrically symmetric. As in our system the diameter of plasma electrode (PE) aperture is 8 mm, the current density comes around 200 A/m^2. The input values of two model parameters, plasma potential and electron temperature are taken to be 25 V and 10 eV, which are experimentally measured. And ion temperature is 1 eV. The bias voltage imposed on the extraction electrode (EE) is -4 kV (also known as suppressor voltage), for reducing the emission of secondary electrons from plasma electrode (PE) due to back-steaming electrons.

Here, simulation results are mentioned to observe the effect of extraction gap and extraction voltage on the beam characteristics.

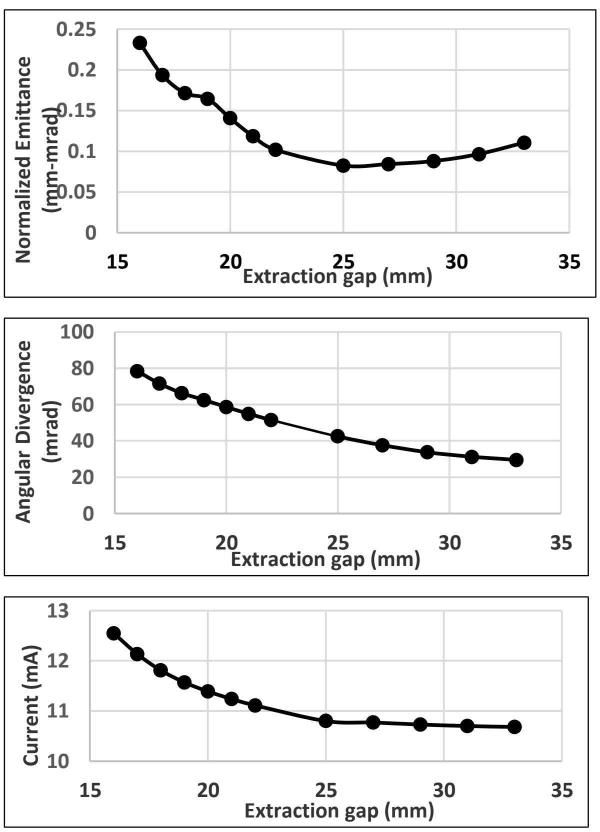

Figure 3: Variation of beam emittance, angular divergence & beam current (at 200 mm distance from PE) versus extraction gap.

Optimization of extraction gap

The dependence of beam emittance, angular divergence and beam current on the extraction gap has been shown in figure-3. The imposed extraction voltage has been considered to be 30 kV. It is seen that the emittance is minimum at 25 mm extraction gap. The variation of emittance with extraction gap can be attributed to the shape of the plasma meniscus at the plasma electrode aperture. For 200 A/m^2 beam intensity and 25 mm gap the plasma meniscus is slightly concave, and hence emittance is minimum. For larger gap meniscus becomes convex and for smaller gap it is concave, leading to defocussed or over-focussed beam respectively and hence larger output emittance. The angular divergence, on the other hand, decreases with extraction gap, which can be seen both from figure-3&4. The reason is that, with larger gap and convex meniscus the beam waist location shifts towards away from the exit aperture, but it is measured at 200 mm fixed distance. Extracted beam current increases slightly with decreasing the gap (figure-3), due to the increase of electric field around plasma electrode aperture.

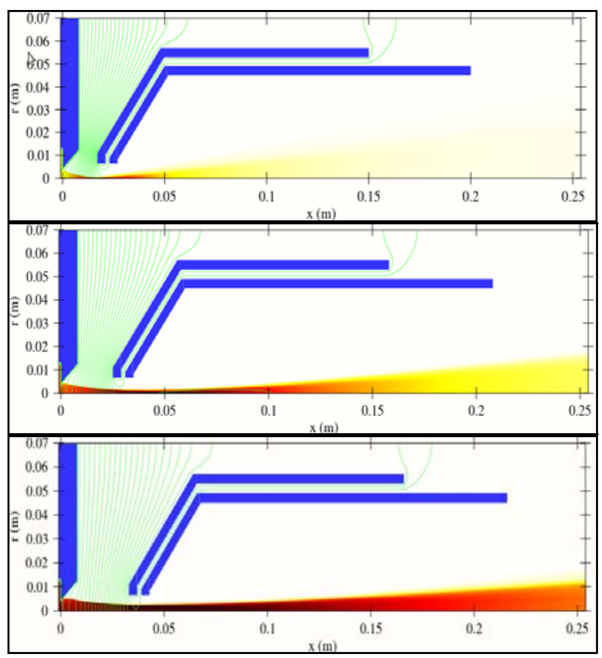

Figure 4: 2-D (cylindrical symmetry) simulation of beam extraction for (a) 17 mm, (b) 25 mm, & (c) 30mm extraction gap.

Phase space ellipse of the extracted proton beam for 30 keV extraction energy and 25 mm gap, is shown in figure-5. The calculated Twiss parameters at 200 mm distance from PE are α = -21.97, β = 2.77 *mm/mrad*, γ = 174.3 *mrad/mm* and emittance ε is 10.3 π*-mm-mrad*.

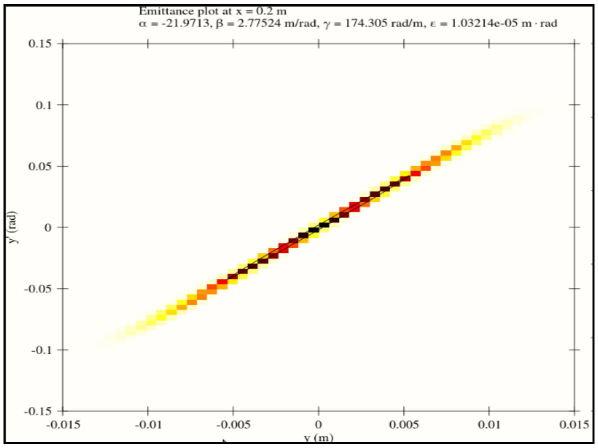

Figure 5: Typical emittance plot at 200 mm distance from PE, for 30 kV extraction voltage and 25 mm gap.

Optimization of extraction voltage

The variation of beam emittance versus imposed voltage to plasma electrode is shown in figure-6. Minimum emittance is found at 30 kV of extraction voltage, which is in compliance with various experimental results.

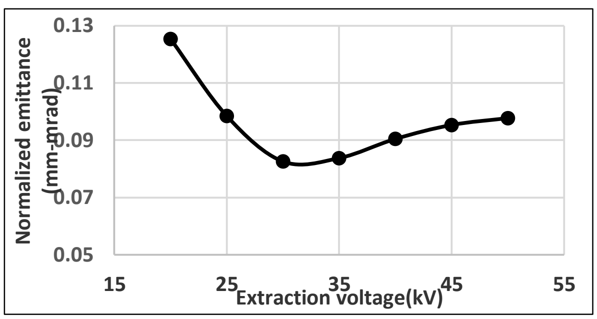

Figure 6: Variation of beam emittance with extraction voltage.

Imposing more potential to PE increases electric fields in the beam acceleration region, which makes the plasma meniscus concave. So, the beam is overfocussed. For very low extraction voltage, meniscus is convex and beam is defocussed. For optimized extraction potential, meniscus is slightly concave or flat, in which case emittance is minimum. The extracted current increases with increasing extraction voltage.

Variation of suppressor voltage

The variation of beam emittance and angular divergence verses suppressor voltage is shown in figure-7. It is found that, though the emittance has almost no dependence on suppressor voltage, the angular divergence increases slightly as the voltage is varied from 2 to 4 kV.

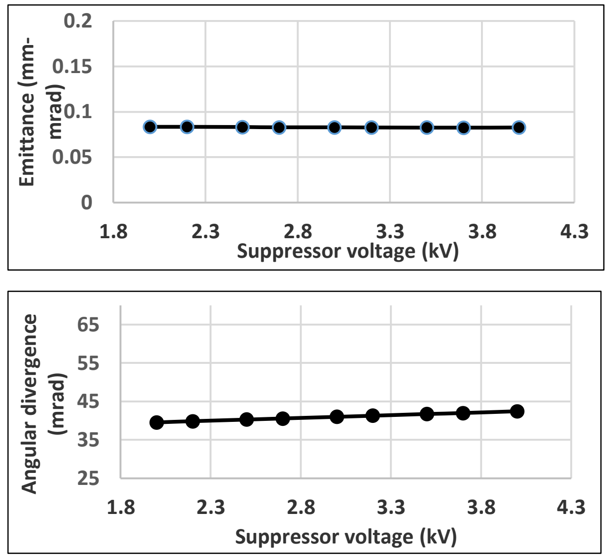

Figure 7: Variation of emittance and angular divergence with suppressor voltage.

CONCLUSIONS

The quality of the beam is related to various factors of the ECR ion source. Here, dependence of beam emittance and intensity on various parameters, especially the extraction gap and extraction voltage has been studied. At first the emittance decreases with extraction gap, but later it starts increasing with larger distances. The optimum distance between plasma electrode and the suppressor electrode has been found to be around 25mm. The variation of beam emittance with extraction voltage has also been shown. The beam emittance is minimum when extraction voltage is 30kV. The suppressor electrode is biased in negative potential, for reducing the emission of secondary electrons from plasma electrode and also to maintain adequate gradient in the acceleration region. It is seen that, the beam emittance and angular divergence are quite insensitive to the suppressor voltage.

REFERENCES

[1] Kalvas, T., Tarvainen, O., Ropponen, T., Steczkiewicz, O., Ärje, J., & Clark, H. (2010). IBSIMU: A three-dimensional simulation software for charged particle optics. Review of Scientific Instruments, 81(2), 02B703.

[2] Khoshhal, M., Habibi, M., & Boswell, R. W. (2018). Development of a new high-current triode extraction system for helicon ion source: design and simulation. Laser and Particle Beams, 36(4), 477-486.

[3] Ren, H. T., Peng, S. X., Lu, P. N., Zhang, M., Zhou, Q. F., Yuan, Z. X., ... & Chen, J. E. (2011). Methods to obtain high intensity proton ion beams with low emittance from ECR ion source at Peking University. Proceedings of IPAC, 3463-3465.

DESIGN, DEVELOPMENT AND TESTING OF 200V, 1A POWER SUPPLY FOR GRID ELECTRODE OF RF AMPLIFIER TUBE OF MC18 CYCLOTRON

Y. Kumar[1*], A. Bera, S. Srivastava[1,2], and S.K.Thakur[1]
[1]Variable Energy Cyclotron Centre, Kolkata-700064, India.
[2]Homi Bhabha National Institute, Mumbai

Abstract

Medical Cyclotron 18MeV (MC18) is under development in VECC, Kolkata. Radio frequency (RF) system is most vital part of cyclotron which is also under development. The grid biasing plays most critical role in triode power amplifiers. A linear regulated power supply rated -200V/ 1A dc is designed, developed and tested with resistive load for biasing grid electrode of RF amplifier tube. This power supply is developed by incorporating single phase step down transformer, single phase full bridge rectifiers, LC filters and a bipolar transistor as a shunt regulating element. The output voltage is controlled and regulated by feedback technique. This is achieved by first sampling output voltage and compared it with a reference voltage to generate an error signal. This error signal is given to an analog proportional and integral (PI) controller that controls the base current of transistor to put the output voltage within desired limit. The power supply has features of over voltage, over current and over temperature protection with one external interlock. Simple control circuit, no EMI and high reliability are main advantage of liner regulated power supplies. Also, short circuit proof is added advantage of shunt regulated linear power supplies due to use of series resistance. The simulation of the designed is performed in PSIM to analyses the circuit performance. In this paper, circuit topology, function of system components, simulated and experimental result of power supply are discussed.

INTRODUCTION

Medical Cyclotron 18MeV (MC18) is under development in VECC, Kolkata. Triode tube 3CW40000A7, will be used as a RF amplifier, is a part of RF system of MC18 cyclotron [1, 2]. All three electrodes such as anode, grid and filament are biased by 10kV/ 7A DC, -200V/1A DC and 10V/110A AC power supplies respectively. The grid biasing plays most critical role in triode power amplifiers is designed and developed by using shunt pass linear regulated topology and tested.

A linear regulated power supply regulates the output voltage by dropping excess voltage in a series dissipative component [3, 4, 5]. Linear regulators are known for their poor efficiency and large size. Linear regulators have a very low output voltage ripple and high bandwidth. This makes them ideal for any noise-sensitive applications including communication and radio devices.

The shunt-pass regulator is the simplest and most frequently used but is least efficient regulation technique. Also, short circuit proof is added advantage of shunt regulated linear power supplies due to use of additional series resistance.

OPERATING PRINCIPLE

The concept of basic shunt pass regulator is shown in Fig. 1. Here transistor is a linear regulating element work as a variable resistance. The output of the power supply is kept constant by changing the resistance of shunt-pass element consisting of one or more parallel/ series transistors. As the input voltage rises or falls, the effective resistance of the shunt element decreases or increases respectively to mitigate the change in the input voltage. This way the output voltage remains within specified limit. The shunt element is controlled to give a constant output voltage by the negative feedback loop. Feedback loop composed of the resistor chain, the differential amplifier and voltage amplifier-level shifter element.

A fraction of the output voltage V_f, V_f = [R2/ (R1+R2)] Vo is compared with a constant reference voltage V_{ref}. Differential amplifier yields a voltage proportional to the difference between V_{ref} and output sample V_f. The amplified difference voltage is further amplified, and the DC level shifted to derive the base terminal of the shunt pass element. Voltage polarities should be such that a small increase or decrease in output voltage due to the line or load voltage changes can correct by increasing or decreasing shunt element impedance. The output voltage adjusted such that the sampled fraction [R2/ (R1+R2)] Vo, is closely equal to the reference voltage.

At steady state

$$V_{\text{ref}} = V_{\text{f}} \tag{1}$$

and
$$V_{\text{f}} = V_0 \times \frac{R_1}{R_1 + R_2} \tag{2}$$

i.e.
$$V_0 = V_{\text{ref}}\left(1 + \frac{R_2}{R_1}\right) \tag{3}$$

Equation (3) shows that output voltage follows the reference voltage (V_{ref}).

*yashwant@vecc.gov.in

DESIGN TOPOLOGY

Figure 1 shows the schematic diagram of grid power supply. These are voltage control shunt pass linear regulated power supplies. In order to obtain the regulated DC output voltage initially 230V single phase AC is first rectified with single phase full wave bridge rectifier, then filtered with low pass LC filter to obtain unregulated 325V DC bus. BJT is used as a shunt pass linear regulating element.

The developed power supply is built to work as a constant voltage source (CV mode) for the given application. This is achieved by sensing output voltage via voltage divider circuit to get a corresponding feedback voltage, which is compared with reference to generate a error signal. This error signal is given to an analog proportional and integral (PI) controller that controls the base current of transistor to put the output voltage within desired limit.

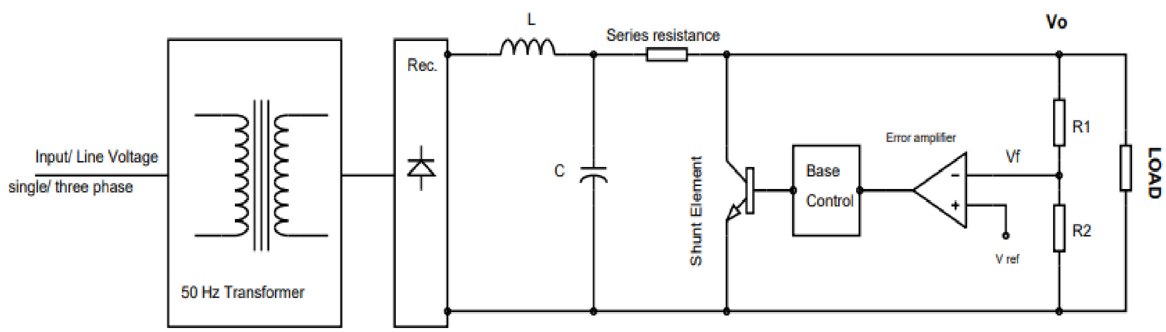

Figure1: Schematic diagram of power supply

EXPERIMENTAL TEST RESULT

The actual photographs/setup of -200V/1A shunt regulated power supply are shown in Figure 2. Some important components are labelled for better understanding.

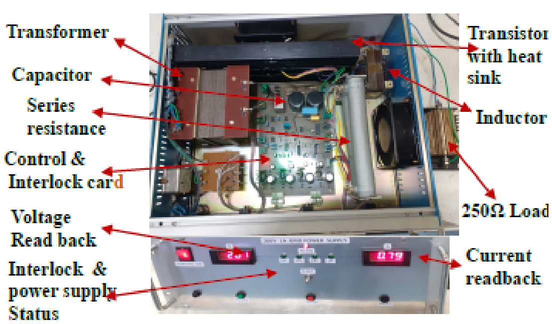

Figure 2: Photographs/ setup of power supply (Top view).

Figure 3 shows ripple waveforms of the power supply with resistive load. Channel 1 shows ripple across capacitor, channel 2 have voltage ripple across load and channel 3 indicates ripple current across load. Reductions of voltage ripple 10V (across capacitor) to 100mV (across load) due to the closed loop gain of controller circuit. Figure 4 shows transient response of controller with 50% change in load. Figure 5 shows the zoom view of Figure 4 which shows that settling time of controller is about 5ms.

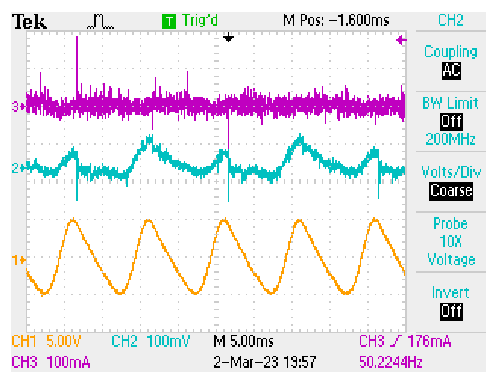

Figure 3: Ripple waveforms of the power supply

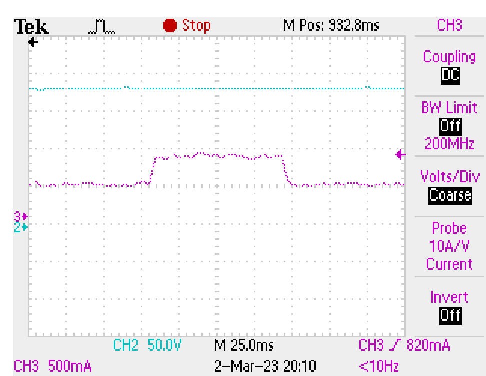

Figure 4: Transient response of the power supply

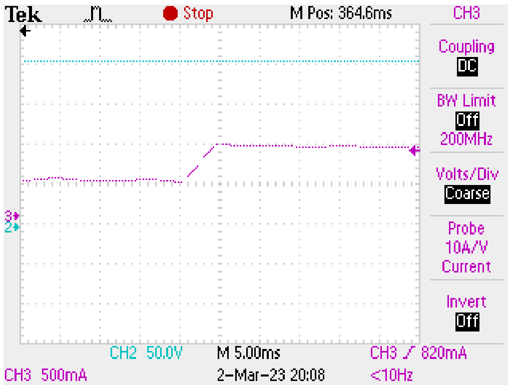

Figure 5: Transient response of the power supply (Zoom view of Figure 4)

Table 1 consist of important measured parameters of the power supply with resistive load.

Table 1: Measured Parameters of power supply

S. No.	Parameter	Value
1	Output Voltage	-200V
2	Output Current	0.8A
3	Voltage Ripple	85mV rms
4	Load Regulation	0.04 %
5	Line Regulation	0.02%
6	Efficiency	70%
7	Stability	200 ppm/°C

CONCLUSION

In the present paper shunt pass linear regulation topology is used for development of power supply. The power supply has features of over voltage, over current and over temperature protection with one external interlock. Power has been tested with resistive load (250Ω) up to -200V and 0.8A current. The power supply has features of over voltage, over current and over temperature protection with one external interlock. We have achieved ≈ 0.04% load regulation and 0.02% line regulation. The stability of the power supply is found to be around 200ppm/°c, which is quite satisfactory for the present application. This stability is measured by monitoring the output voltage, input AC voltage and temperature of the heat sink on data logger for 7 hours. Power supply is ready to test on actual load in near future.

ACKNOWLEDGEMENT

The authors would like to thank Mr. V. K. Khare, Mr. M. K. Gosh, Mr. A. Kumar, Mr. A. Patra and Mr. V. K. Meshram, technical staffs of PE & MCD Section, VECC Kolkata for their sincere supports during the development and testing of power supplies successfully.

REFERENCES

[1] Yashwant Kumar, "Study, design and development of 55V/150A DC, regulated Switch Mode Power Supply (SMPS) for high power solid state Radio Frequency (RF) amplifier", a dissertation Submitted to the Board of Studies in Engineering Sciences in partial fulfilment of the requirements for the degree of master of technology of Homi Bhabha National Institute, October, 2017.

[2] Yashwant Kumar et al., "Design & development of switch mode power supply for 3.0 kw solid state rf amplifier," InPAC-2015, BARC, Mumbai, Dec. 21-24, 2015, p. 543-545.

[3] Yashwant Kumar , Sabyasachi Pathak, M.K. Ghosh, Mousumi Garai, Anirban De, S.K. Thakur, "Aayan beem prerit electron utsarjen kriya ka adhayan aur upyog ke liye 300V, 50mA DC viniyamit vidyut aapurti upkaran ki rachana avam nirman" Vaigyanik Sangoshthi (Samaveshika) 1, 2018, 49-52.

[4] R. W. Erickson and D. Maksimovic, *Fundamental of Power Electronics: Regulator design*. (Springer, 2005)

[5] N. Mohan et al., *Power Electronics: Convereter application and Design*,(John willey & Sons Inc, 2002).

Simulation of feedback control of beam position and an implementation of algorithm for beam focusing in BARC-TIFR Pelletron accelerator

G. Agrawal, R.R. Sahu, S. Goel, M.L. Yadav, R. N. Lokare, S. Mohapatra, P.V. Gudekar, J. A. Gore and A. K. Gupta

Nuclear Physics Division, Bhabha Atomic Research Center, Trombay, Mumbai

gaurang.agrawal@tifr.res.in

Abstract

The 14UD Pelletron Accelerator is an electrostatic tandem accelerator operating round-the-clock since 1988. Various ions of specific mass, energy and current can be accelerated by employing several electromagnetic quadrupoles and steerers located across the accelerator. A well-focused and non-steering beam of a particular energy and current is delivered as per the user requirements for carrying out experiments pertaining to nuclear physics and allied areas.

At present, the beam focusing and steering is performed manually. For beam tuning, the beam position and focusing information is obtained from a rotating wire Beam Profile Monitors (BPM). The working of the BPM, a non-intrusive diagnostic element employed to estimate the position and intensity distribution of the beam, is briefly described. It is proposed to implement a basic linear feedback system to control the beam position along with the algorithm for focusing in one section of Pelletron accelerator. The feedback system for beam position control will generate the output position according to the reference or set point position. The algorithm for focusing will set the current values to quadrupoles at the point of maximum focus. The knowledge of plant that is to be controlled with closed loop feedback is estimated through recorded input-output data in the form of transfer function model. The controller transfer function is obtained from linear design techniques like Root locus and frequency response methods.

This paper describes the identification of plant transfer function (in the forward path) model through the obtained time domain input-output data. Data for estimating the transfer function is obtained by varying the steerer power supplies and measuring the corresponding position through BPM. The time domain input-output data is utilized in estimating plant transfer function. The data-driven modelling of plant is carried out utilizing MATLAB routines. The obtained plant transfer function is utilized to estimate the controller transfer function for position control in beamline. The closed loop feedback system is simulated in SIMULINK. The LABVIEW routines employed for automating the process of focusing the beam are also described. The results of simulation for position control and the routines for focusing the beam of one section of the quadrupole-steerer section shall be presented.

Introduction

Beam positioning can be achieved by either remotely changing the spatial position of the target or by means of beam deflection. The beam deflection is achieved through NEC magnetic steerers in high energy section of Pelletron accelerator. The control of beam position is done in general manually by changing the current through steerers from potentiometers knobs. In order to get deflection through electronic control means where we have to set the deflection amount in distance units like cm’s or mm’s, it is required to implement a feedback control system. The controller in a basic feedback loop structure gives the necessary actuating signal to steerer’s power supply so that the desired deflection is achieved. The implementation of beam position control via feedback is shown in the figure 1. The steerer and its power supply along with the BPM that is placed ahead in the beamline section are part of the system to be controlled by a feedback control. The feedback system marks a step towards automation of accelerator beam tuning of one section of the beamline. The knowledge of plant model needed for controller design is obtained through data-driven modelling approach. The transfer function describing the ratio of output to input in Laplace domain of suitable structure is assumed and the coefficients are estimated using the recorded data set by Least squares estimation method.

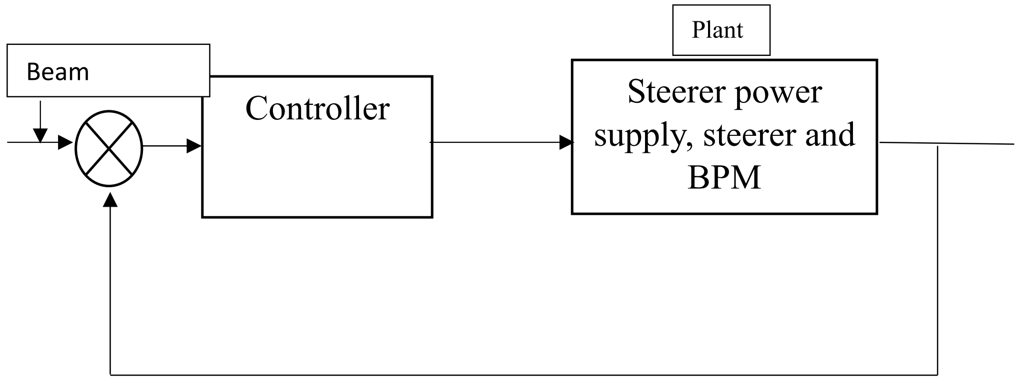

Figure 1: Schematic of feedback control

Steering system modelling

The cascaded system considered for modelling is described in the following block diagram:

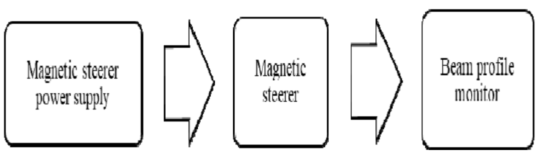

Figure 2: Cascaded system for modelling

The magnetic ion beam steerer has a pair of steerer coils that generate the magnetic field along the transverse directions. The current in an individual coils is supplied with power supplies. The steerer power supply's output current can be controlled by an analog control voltage of 0-5V, for 0 to 10 Amperes. Beam profile monitors provide a continuous display of shape and position of the beam cross-section in both X and Y co-ordinates. It has a rotating wire which sweeps across the beam in transverse palnes in one revolution genearting two X and Y profile peaks.

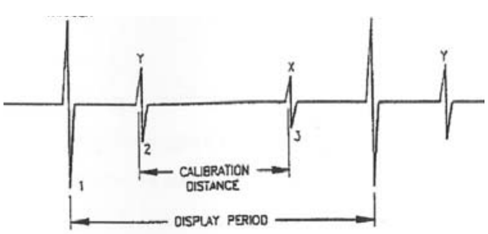

Figure 3: Fiducial markers during rotation of the wire

The system considered for modelling is linear in the normal operating range i.e., 0 to 2 Amperes. It can also be checked by applying superposition property. The results are showed in the below table using Oxygen beam,

Control voltage, Volts	Deflection, mm
0.1V	0.7
0.3V	1.9
0.4V	2.6

The input excitation, control voltage of 0.5 Volts, applied to the system is as follows:

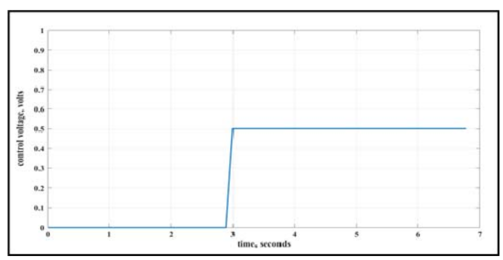

Figure 4: Input excitation to the system

The beam deflection output from BPM in mm to step input is shown below:

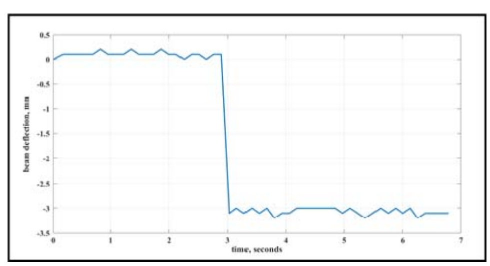

Figure 4: Output deflection in millimetres

The input signal is applied via analog output pin of NI card and the corresponding beam deflection is observed by digitizing BPM output using AI pin. The sampling rate is chosen to be 10kHz as per the rise time of the BPM profile.

The time-domain input and output data are saved in Excel file. The data file is loaded into MATLAB workspace. The time-domain data is stored in 'iddata' object. From the measured data, transfer function is estimated with 2 poles and no zero-structure using, 'tfest'

$$G(s) = \frac{-3794}{s^2 + 35.21s + 618.6}$$

The estimated transfer function is validated by comparing the simulated model output with the actual measured data.

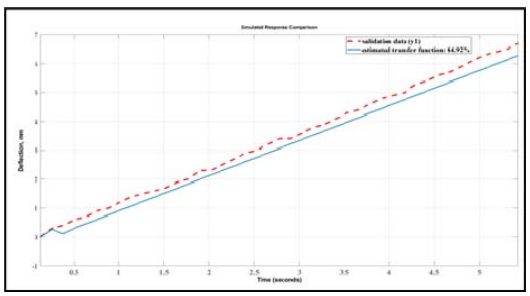

Figure 5: Comparison of simulated output with the measured data

Controller design.

PI controller is added in series with the estimated plant transfer function. The zero zc is located close to origin such that the pole at origin and zero forms a stable dipole. The transient response parameters with the PI controller are almost the same as those for the original system, but the steady state error is drastically improved due to the fact that the feedback control system type is increased by one. Using PI controller with the zero location at -0.01. -0.1 and -0.5. In each case the steady-state error is zero i.e., ess=0. The step responses of the compensated system, now given by

$$G_C(s)G(s) = \frac{3794(s + z_c)}{s^3 + 35.21s^2 + 618.6s}$$

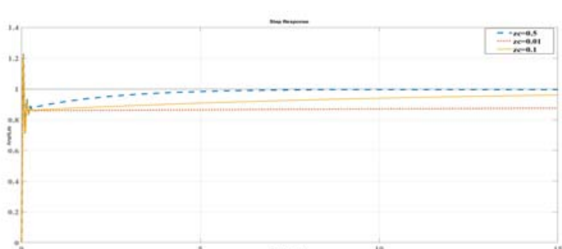

It is seen from above figure that the settling time is lowest when the zero is located at -0.5 i.e., zc=0.5. This is due to reason that as the zero zc moves away from the origin, the closed-loop real pole shifts towards right of the imaginary axis making the response faster.

Hence, the open-loop transfer function of the compensated system for gain K is shown below,

$$G_c(s)G(s) = \frac{3794(s + 0.5)K}{s^3 + 35.21s^2 + 618.6s}$$

Simulation Results

The controllers $G_C(s)$ is simulated in MATLAB SIMULINK with the data-driven based identified plant transfer function $G_P(s)$ in a negative unity-feedback control system. The block diagram of closed-loop control in SIMULINK are presented below

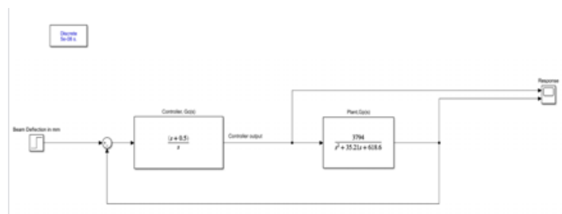

The simulation result is shown in below figure. Both the controller output and the closed-loop system output are shown.

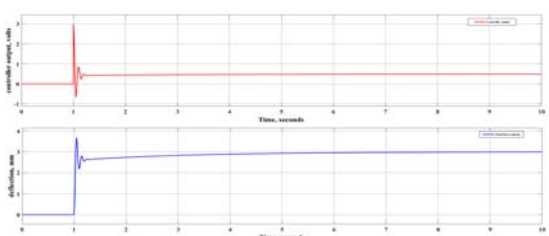

Conclusion

The system comprising steerer, its power supply and BPM is modelled as empirical transfer function. The controller transfer function is obtained through Root locus technique. The implementation of an algorithm for beam focusing is still in progress due to an unavailability of accelerator beam time. The machine has been running continuously so it was unable to test the program written in LABVIEW for beam focusing.

HIGH POWER (30 KW) TESTING OF RESONANT RING IN TRAVELING-WAVE MODE

***Sonal Sharma, Gireesh N Singh, Mentes Jose and Rajesh Kumar**

Ion Accelerator Development Division, Bhabha Atomic Research Centre, Mumbai - 400085, India

*sonal@barc.gov.in

Abstract

Under IIFC collaboration, coaxial RF couplers at 325 MHz and 650 MHz are being developed at IADD, BARC. Presently, fabrication of 325 MHz couplers is in prgress. For high power testing of these couplers, RF power of about 40-50 kW is required. So, design and development of high power RF test facility has been initiated at IADD, BARC. The test facility is based on a travelling wave resonating ring structure[1] consisting of low loss waveguide components. The simulation of the resonant ring has been done in CST microwave studio. All the components of this resonant ring have been designed, fabricated and installed. RF characterization of the ring is being carried using a Vector Network Analyzer (VNA). The ring has been tuned to the desired frequency of 325 MHz. Tuners are also used to optimize the resonance frequency and gain of the ring. Power gain of more than 10 dB has been measured. This paper presents the results of design optimization and RF measurements on the resonant ring.

INTRODUCTION

A resonant ring, is a test setup in which high power builds up in the ring under certain operating condition at resonant frequency [1]. In this set up power is fed to the ring via a directional coupler continuously leading to development of high circulating power in the ring when the length of the ring is a whole number of wavelengths at the desired frequency.

Resonant ring has advantage of providing high power by using passive low cost RF components. It is cost effective, simple in design and doesn't require very high voltage for operation. Such type of facility is being used in many reputed labs across the world such as ELBE-Germany, Cornell, Peking University (China), LANL, IHEP, NASA etc. for testing the performance of RF and microwave components at high RF power. Under Indian Institutes and Fermilab (IIFC) collaboration, a number of coaxial RF couplers at frequency of 325 MHz are being fabricated in BARC. To check high power performance of these couplers, RF power of about 30 kW is required. Such type couplers will also be used for future DAE projects. So, design and development of 30 kW resonant ring high power RF test facility has been taken up in BARC.

GAIN OF THE RING AND POWER BUILDUP

General theory

A Resonant ring consists of primary line and a secondary loop or ring [1]. A part of the power generated from the RF source in primary line is coupled to the secondary loop/ring with the help of a directional coupler. If the ring length is an integral multiple of the wavelength at the required frequency (L=nλ), resonance condition is achieved and an optimum gain in RF power can be obtained [1]. The component to be tested has to be part of the ring. It is planned to place two RF couplers back to back (with a cavity in between) as a part of this ring. In this way two couplers can be tested simultaneously for high power.

Power build-up in the ring

The way in which power build- up takes place in the resonant ring is shown in fig 1.

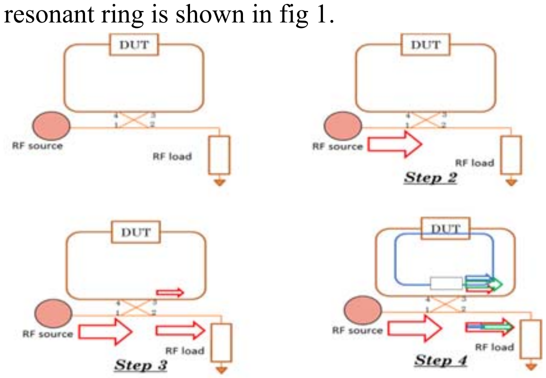

Figure 1: Power build-up in the ring

Gain of the ring

Under resonance, assuming no return loss in the ring, the formula for the power gain in the resonant ring [1][2] is given as

$$G = C^2/ (1-T\sqrt{1-C^2})^2 \qquad \text{------ (1)}$$

Where, C= voltage coupling coefficient of the directional coupler which couples power from main line to the ring, T= Transmission in the ring and accounts for attenuation in the ring

Fig 2 illustrates the behaviour of the gain for different coupling coefficients.

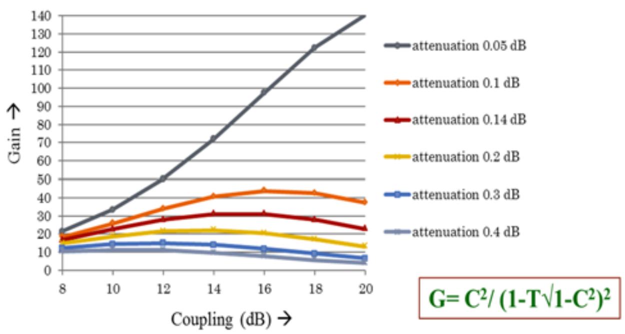

Figure 2: Gain vs coupling coefficient

DESIGN OF THE RING

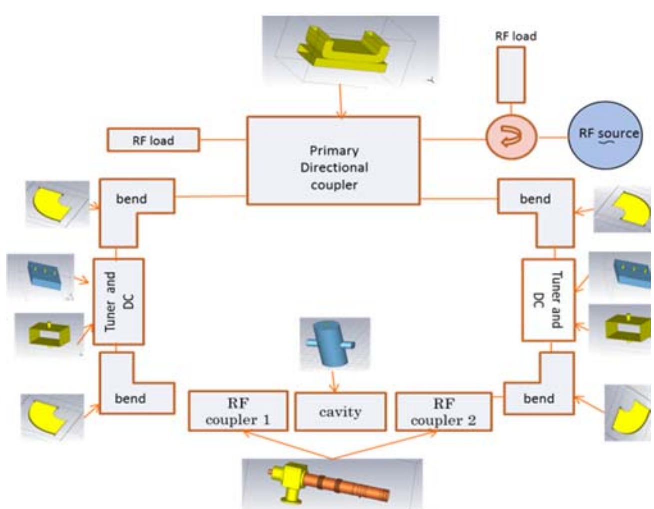

Figure 3: layout of the ring with all components

Fig 3 shows the layout of the ring. Design of resonant ring starts with the operating frequency and power required. Main components required for the rings are primary directional coupler, secondary directional coupler, bends, tuners etc. The estimated total attenuation of all the waveguide components in our 30 kW design came out to be 0.05 dB without couplers. Practically there will be more losses due to surface roughness and losses in the joints. When coupler comes into picture the losses in the ring is estimated to be increased to 0.4 dB. An optimized coupling value of 13 dB was chosen for the primary directional coupler for the design.

SIMULATION OF THE RING

The ring has been simulated in CST microwave studio using the CST models of individual components. The S_{21} parameter with port 1 at input of primary directional coupler and port 2 at secondary directional coupler gives the information about the gain of the ring. CST model is shown in fig 4 and S_{21} is shown in fig 5. S_{21} is 33.1 dB.

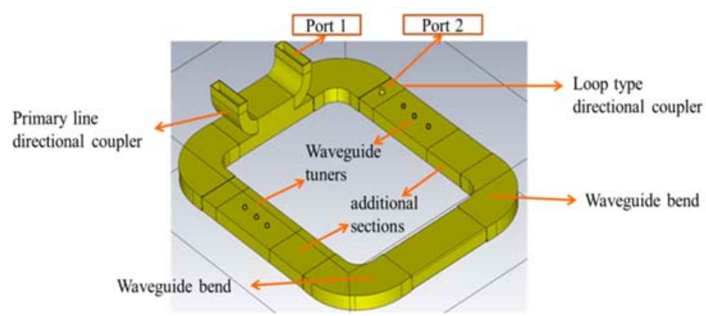

Figure 4: CST model of the ring

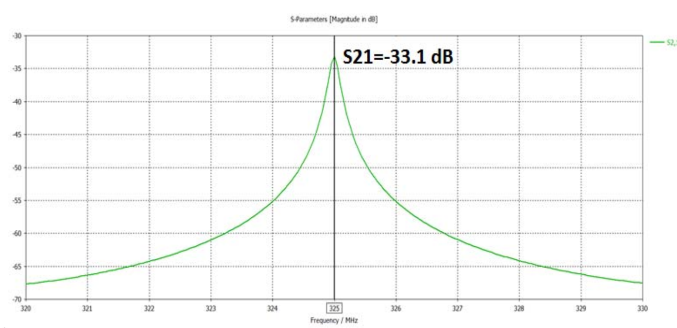

Figure 5: S_{21} of the ring

Gain (G) = 51.4-33.1= 18.3 dB

LOW POWER TESTING OF THE RING

Low level test setup [2] of the resonant ring is shown in Fig 6. Low power characterization of the ring was done using VNA. Power gain has been calculated from the measured s parameter (S_{21}) which is shown in Fig 7.

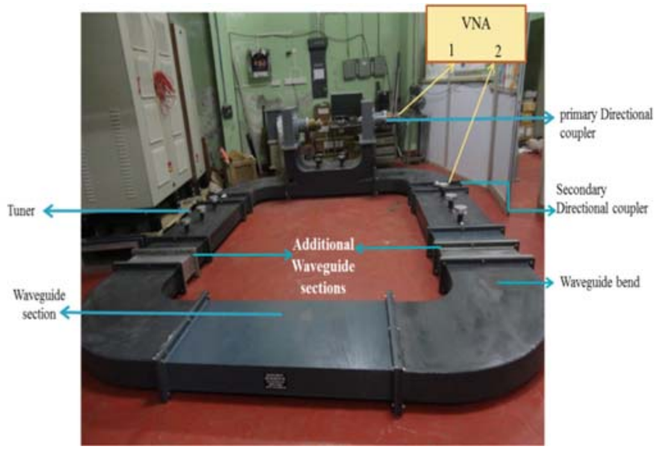

Figure 6: Low level testing of Resonant ring

The value of S_{21} at 325MHz is -36.4 dB. So the actual gain of the ring is,

Gain = 50.5-36.4= 14.1 dB

Earlier this gain was about 11 dB as described in earlier papers [2]. It has been optimized now to about 14.1 dB with the new directional coupler installed in the ring.

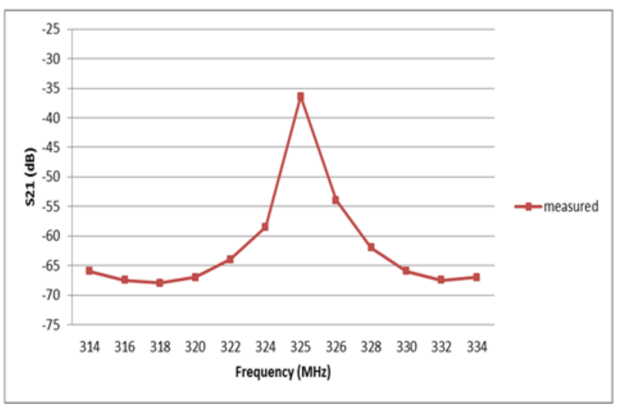

Figure 7: S21of the ring tuned at 325 MHz

HIGH POWER TESTING OF THE RING

After low power testing RF source/amplifier has been connected at the input via transmission lines. High power testing was done by increasing power of the amplifier. The setup for high power testing is shown in fig 8. After integration of all the components the input amplifier power was slowly increased and the output power was observed. The input and output power are shown in fig 7.

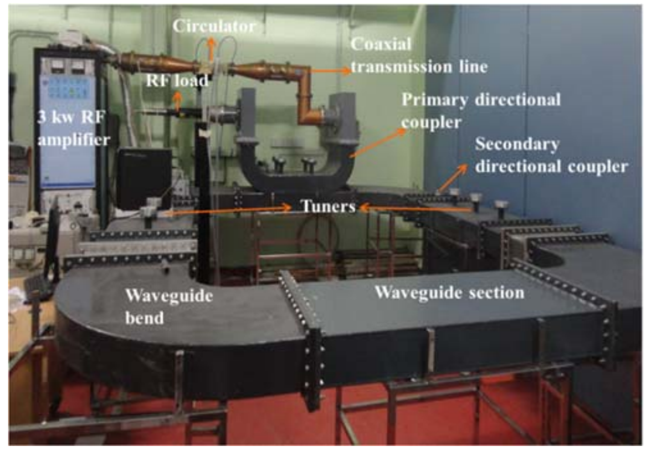

Figure 6: high power test set-up

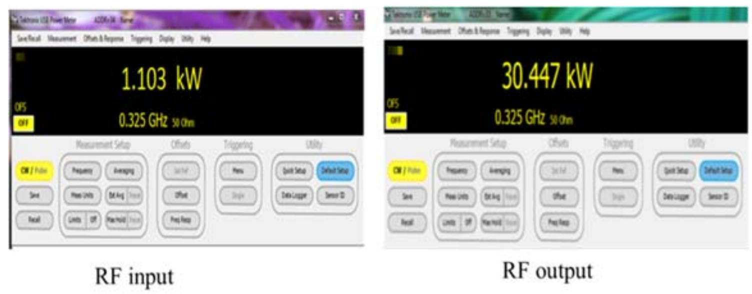

Figure 7: high power test set-up

CONCLUSION

The resonant ring has been tested at output power of 30 kW with input power of 1.1 kW. Gain is 14.4 dB. The ring testing has been done for 100 hours. Presently two RF couplers are under fabrication in BARC. After fabrication these couplers will be installed in the ring and will be tested at high power.

ACKNOWLEDGEMENT

The author would like to thank Group Director (N), MRG and Shri Arun Agrawal, IADD, BARC for their support in this development. Also we are thankful to Mr. Chougale, Mr D'souza, Mr Kawale, Mr Prashant and Mr Koli of IADD for their help in the project.

REFERENCES

[1] V. Veshcherevich, http:// www.lns.cornell. edu/public/ERL/2003/ERL03-15/ERL03-152.pdf

[2] .Sonal Sharma, Mentes Jose, G.N. Singh, Rajesh Kumar and P.V Bhagwat, "Design, development and low level RF characterization of resonant ring for eighth DAE-BRNS Indian particle accelerator conference (InPAC 2018), Indore, M.P. India, Jan 2018.

STUDY OF THERMAL EFFECTS OF PROTON BEAM INTERACTION WITH ACCELERATING STRUCTURES TO DERIVE THE RESPONSE TIME OF FAST PROTECTION SYSTEM

Santhosh Chittimalla[1,2], Deepak N Mathad[1], S K Singh[1], K. Rajesh[1,2]

[1]Ion Accelerator Development Division, BARC, Mumbai 400085
[2]Homi Bhabha National Institute, Anushaktinagar, Mumbai 400094

Abstract

Beam loss monitor's output signal is used as one of input for fast protection system to generate beam stop signal when beam loss exceeds acceptable range. The maximum allowable response time of fast protection system is determined by time taken by full beam to start melting of accelerating structure. Fast protection system should be able to protect equipment even when full beam loss occurs, for this response time of protection system should be lesser than the time taken by full beam to melt the structure. The time to start melting a structure depends upon different parameters like beam energy, beam current, beam size and type of material. When a proton beam hits any material, it deposits energy in it. Depending on energy and properties of material it will travel some distance before losing all its energy. The amount of energy deposited in the material depends upon dE/dx known as stopping power of material. For lower beam energies, the average energy transfer dE/dx is larger and it is even higher at the end of the proton range. In any accelerator most of the components are made of steel and copper. Here we assumed that the beam deposits energy in steel/copper accelerator components instantaneously and estimated the FPS time response required to prevent start of melting the steel/copper for energies 10 keV - 200 MeV.

CALCULATION MODEL

When a proton beam hits the block of steel/copper it deposits its energy in it and heats it up. Due to energy deposition the temperature of the material increases, the temperature change can be given by equation (1). The following calculations are done for worst case i.e assuming there is no cooling provided to the structure under consideration.

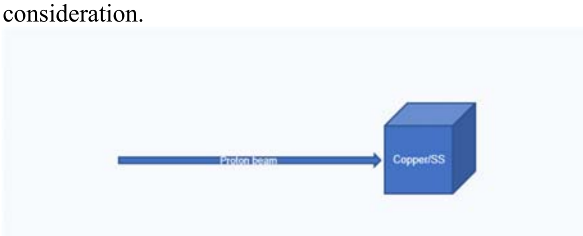

Figure 1: Proton beam hitting accelerator structure.

$$cm\Delta T = E_{dep} \tag{1}$$

Where c = Heat capacitance of material
m = Mass of material
ΔT = change in temperature
E_{dep}= Energy deposited by proton beam If we assume that the beam shape is circular with radius r then

$$\int_0^R c\,\rho\pi r^2\,\Delta T\,dx = \int_0^R \frac{dE}{dx}\,N\,dx \tag{2}$$

$\frac{dE}{dx}$ = Stopping power at the entrance of the material (For simpler calculations stopping power at entrance has taken effect of bragg peak is added later)
R = Range of proton in material
$\frac{dE}{dx}\,dx$ = Energy deposited in the infinitesimal length dx of material by one proton. Now we will calculate number of protons required to change the temperature of the material from T_i to T_{melt}.

$$N = \frac{c\,\rho\pi r^2\,(T_{melt} - T_i)}{\frac{dE}{dx}} \tag{3}$$

r = Radius of beam
T_i= Initial temperature of material
T_{melt} = Melting temperature of material
N = Total number of protons required to melt material

Stopping power of a material changes with depth inside the material and it is maximum at range of proton. Here we are considering only stopping power of material at the entrance of interaction for time response calculation. SRIM software has been used to generate stopping power for different energies. Stopping power is function of energy of beam, properties of material and depth in material. In SRIM software we can generate stopping power for different material as function proton energy. In Figure 2 stopping power has been plotted for copper and steel for energies from 10 keV to 200 MeV. We can observe from graph as the beam energy increases the stopping power of material decreasing.

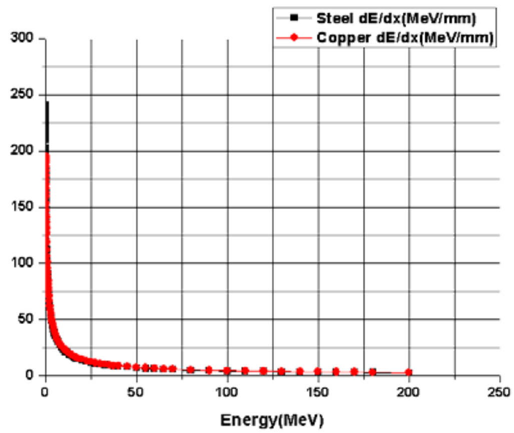

Figure 2: Stopping power of proton at entrance of steel and copper as a function of energy.

In the Figure 3 range of protons for different energies calculated using SRIM/TRIM software. The graph is plotted for steel and copper for different energies from 10 keV to 200 MeV. From graph it can be observed that as the energy increases the range of proton in the material increases, it means proton penetrate more into the material. For a given proton energy steel has higher range as compared to copper.

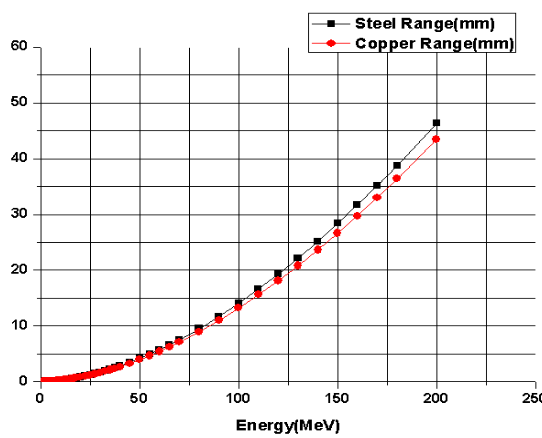

Figure 3: Range of proton in steel and copper as a function of proton energy.

In Figure 4, the time required to melt steel/copper by 10 mA proton beam plotted for different beam radius as function of beam energy. It can be observed that as the beam energy increases the time required melting steel/copper increasing for particular beam radius. As the beam size decreases the time required to melt the material is decreasing because beam is more focused.

In the above calculations the effect of Bragg peak has not taken into account and the stopping power of material at the entrance only considered for calculating the number of protons required for melting structure. In reality, energy deposition per unit length by proton changes as it penetrates into the material, and it is maximum at the range of proton called Bragg peak.

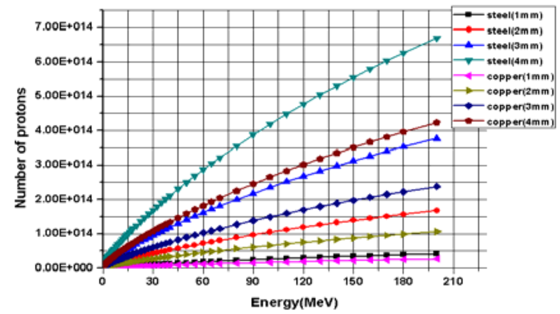

Figure 4: Number of protons which would melt steel/copper with different beam radius as a function of energy.

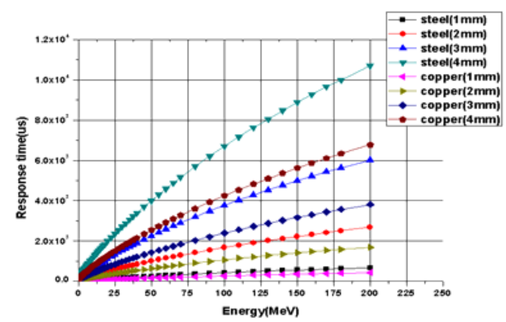

Figure 5: Response time for steel and copper for different beam radius as function of energy.

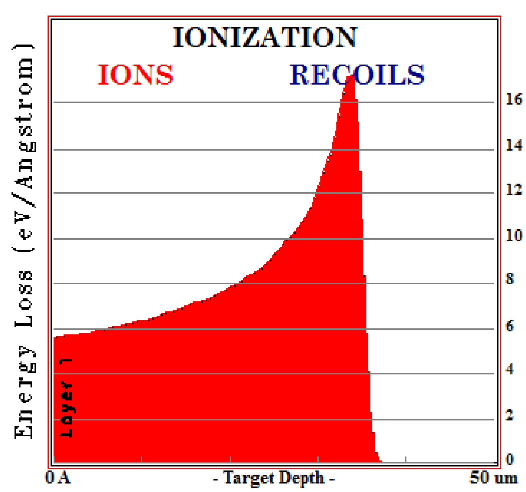

Figure 6: Bragg peak of 3 MeV proton in copper.

Proton Energy (MeV)	Bragg ratio for Copper	Bragg ratio for Steel
3	3.14	3.50
10	4.32	4.71
40	5.43	5.82
100	5.84	5.83
200	5.95	6.04

Table 1: Bragg ratio for copper and steel at different energies of proton.

Energy (MeV)	Response time for Copper (μs)		Response time for Steel (μs)	
	Without Bragg peak	With Bragg peak	Without Bragg peak	With Bragg peak
3	20.71	6.59	31.64	9.04
10	47.47	10.98	73.75	15.65
40	134.39	24.75	211.10	36.27
100	265.34	45.43	418.84	71.84
200	423.59	71.19	670.35	110.98

Table 2: Response time for copper/steel corrected for Bragg peak.

CONCLUSION

From above studies it is understood that full beam with 3 MeV energy and 10 mA current can melt copper and stainless steel in about 6 μs and 9 μs time respectively. However, 200 MeV, 10 mA beam will take 71 μs to melt copper and 110 μs to melt stainless steel. Because at higher energies proton deposits less amount energy per length and penetrate more deeper into the material. Which we can understand from stopping power and range variation as a function of energy. Fast protection system should be able to protect the accelerating structures in case of full beam loss, so response time of protection system should be less than 6 μs. Here the response time calculations are done for copper and steel, however after 10 MeV beam will be accelerated using superconducting cavities which are made of niobium. These studies need to be carried out for niobium cavities in future. In above study it is assumed that energy is instantaneously deposited and increased the temperature of the material. Here conduction and radiation of heat energy not considered for calculations.

REFERENCES

[1] Lali TchelidzeIn, A technical report on the, How Long the ESS Beam Pulse Would Start Melting Steel/Copper Accelerating Components-2012.

RF CHARACTERISATION AND TUNING OF DTL TANKS-3 & 4 OF LEHIPA

Elina Mishra[1*], Monika[2], Alok K. Ghosh[2], Sumit Meshram[1], Prashant Kumar[1], Manas Mishra[2], Vikas Teotia[1], S.V.L.S Rao[2], Sanjay Malhotra[1], S. Krishnagopal[2]

[1]Electromagnetic Application & Instrumentation Division,
[2]Ion Accelerator Development Division
Bhabha Atomic Research Centre, Trombay

**Email ID of the corresponding author: elinam@barc.gov.in*

Abstract

A 20 MeV Low Energy High Intensity Proton Accelerator (LEHIPA) is being developed at BARC, Mumbai. Recently, it was commissioned up to 11 MeV. Each Drift Tube Linac of LEHIPA consists of several drift tubes housing Permanent Magnet Quadrupoles, Tuners, Post Couplers, RF ports and vacuum ports amongst others. RF qualification, characterization and tuning of DTL cavity is paramount for determining & tuning the key performance indices of DTL. These include resonant frequency of the cavity, achieving the electric field flatness and tilt sensitivity in each RF gap within the required specifications, loaded & unloaded quality factor, and spectrum of all the post coupled modes. This paper describes complete RF characterization and tuning methodology to achieve above key performance indices within required specifications.

INTRODUCTION

Bhabha Atomic Research Centre is developing a 20 MeV Low Energy High Intensity Proton Accelerator [1]. It consists of a 50 keV ion source, Low Energy Beam Transport line, 4 MeV RFQ, Medium Energy Beam Transport line and 4-20 MeV DTL cavities fabricated in 4 parts [2,3]. Using RFQ and first two DTL cavities, 11 MeV proton beam has been accelerated. 11-20 MeV DTL cavities have been aligned, vacuum tested and RF characterised. They have been installed in the beamline. 11-20 MeV DTLs are made in two parts. DTL operates in TM_{010} mode, where E-field is in axial direction and magnetic field is in azimuthal direction. Figure 1 shows the E-field distribution in the DT gaps of the cavity.

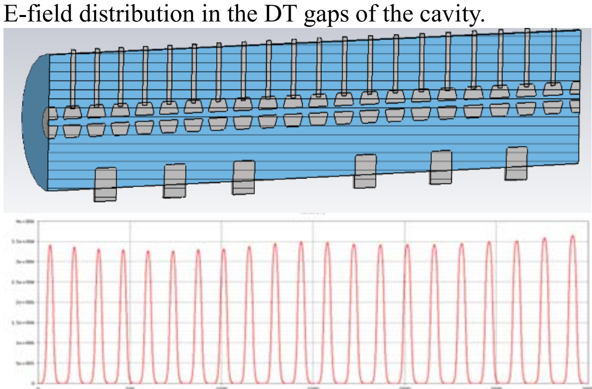

Fig 1(a): Model of 11-15 MeV DTL; (b) E-field distribution in DT gaps

Figure 2 shows the assembled DTL cavities. After complete assembly of the DTL cavity, extensive low power RF characterisation and tuning needs to be carried out to maintain the required resonant frequency, E-field flatness, tilt sensitivity etc.

Fig 2: Developed 11-20 MeV DTL cavity for LEHIPA

This paper gives a detailed report on the RF characterisation and tuning of 11-20 MeV DTL cavities to the desired specifications.

RF CHARACTERISATION OF DTL

Due to fabrication errors, assembly errors, thermal detuning, resonance frequency and axial electric fields may vary from the design values. These variations can cause deterioration in beam quality and beam transmission. RF characterisation of DTL involves optimisation of the following key performance indicators [4] to the specified values:

Determination of resonant frequency: 352.12 MHz
Tuning of resonant frequency
Maintaining electric field flatness: ~ ± 2 %
Reducing tilt sensitivity: ~ ± 20 %/MHz

Bead-pull setup for RF characterisation

Fig 3 shows the schematic arrangement of a typical bead-pull setup used for RF characterisation of DTL.

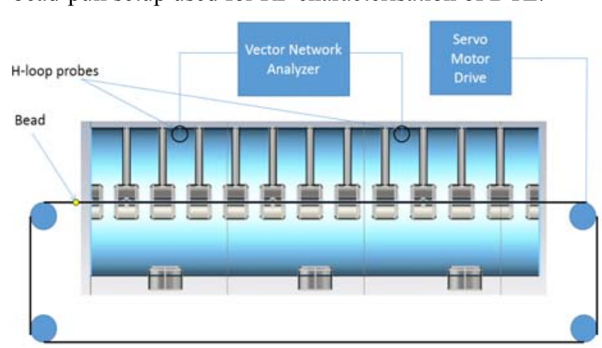

Fig 3: Schematic arrangement of bead-pull setup

It consists of a braided insulating wire that runs through axis of the cavity through beam aperture of concentrically aligned DTs. An 8 mm diameter runs through the DTL axis and patterns the electric field in the DT gaps. As the bead traverses, the resonant frequency changes (δϖ) according to Slater Perturbation theorem as given in equation 1.

$$\frac{\Delta\varpi}{\varpi_0} = \frac{\int(\mu H^2 - \varepsilon E^2)dV}{4U} \qquad (1)$$

Where E and H are electric & magnetic fields of unperturbed cavity modes and U is the total internal energy stored. When a metallic bead is travelled in TM_{010} mode, equation 1 can be re-written as

$$\frac{\Delta\varpi}{\varpi_0} = -\frac{3\Delta V \varepsilon_0}{4U}|E_o| \qquad (2)$$

This change in frequency can also be expressed as a change in phase Δϕ as given in equation 3

$$\Delta\phi \approx -2\, Q_L \frac{\Delta\varpi}{\varpi_0} \qquad (3)$$

Where Q_L is the loaded quality factor. A VNA is used to determine the scattering parameters to evaluate resonant frequency and electric field pattern in the DT gaps.

LOW POWER RF MEASUREMENTS

Initially, before tuning, the untuned resonant frequency of 11-15 MeV cavity was 351.28 MHz. Figure 4 shows the resonant frequency plot of the 11-15 MeV DTL.

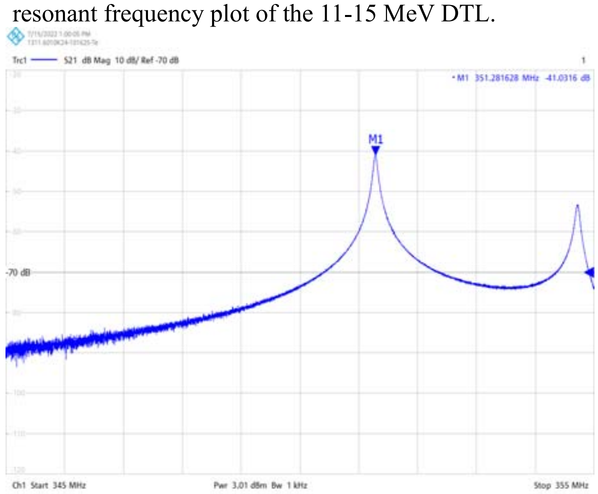

Fig 4: Resonant frequency of untuned 11-15 MeV DTL

When tuners were adjusted up to 53.5 mm, resonant frequency was tuned to 352.03 MHz. Considering an increase of 90-100 kHz in resonant frequency during vacuum conditions, during bead-pull a frequency of around 352.02 MHz was aimed for. Figure 5 shows the resonant frequency after tuning. The unloaded quality factor of the cavity is >30000. Figure 6 shows the change in phase of the received signal as the bead passes through 21 DT gaps in 11-15 MeV. From the figure 5 below, electric field in the DT gaps can be calculated.

TILT SENSITIVITY USING PCs

In TM_{010} mode, electric field distribution is very sensitive to frequency perturbations of the cells, power losses and beam loading [4]. PCs form a resonant coupling mode with the TM_{010} mode which improves field stabilisation by increasing the slope of dispersion curve; increasing the mode separation. This mode increases the group velocity and helps in the power flow across the structure.

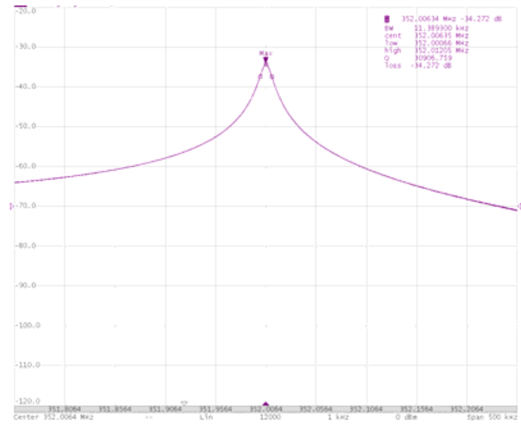

Fig 5: Resonant frequency of tuned 11-15 MeV DTL

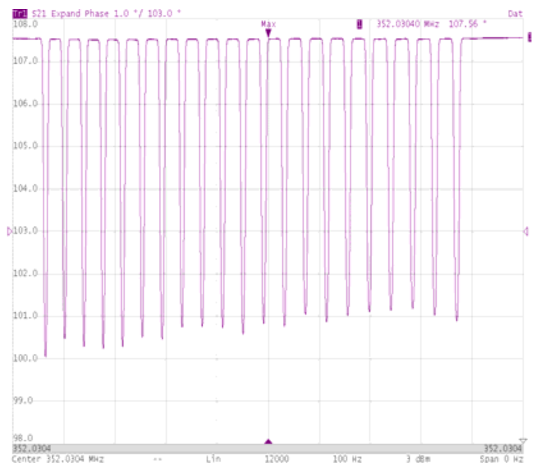

Fig 6: E-field distribution in 11-15 MeV DTL

For LEHIPA, the TS is aimed to be maintained within ± 20 %/MHz. Local perturbations were introduced from both sides of the DTL axis using metallic rods inserted in the 1st and last DT gaps. Lengths of the PCs were adjusted individually and bead pull measurements were carried out iteratively to bring TS below ± 20 %. Equation 4 gives the tilt sensitivity in individual cell.

$$TS_n\ (\%/MHz) = \frac{(E_{0n}^{le} - E_{0n}^{he})}{\Delta f} \qquad (4)$$

Where E_{0n}^{le} is low energy perturbed E-field and E_{0n}^{he} is the high energy perturbed E-field distributions and Δf is the change in resonant frequency introduced.

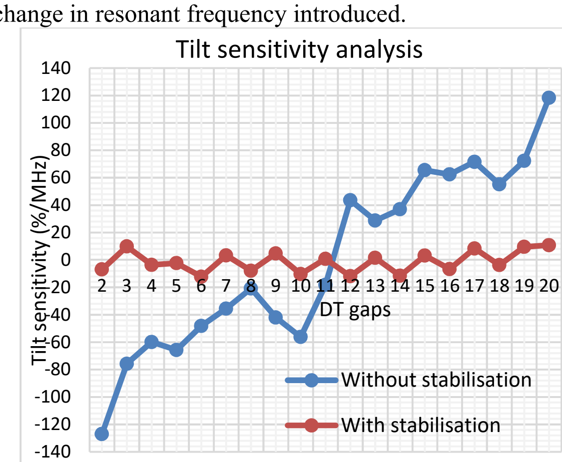

Fig 7(a): Tilt sensitivity analysis in 11-15 MeV DTL

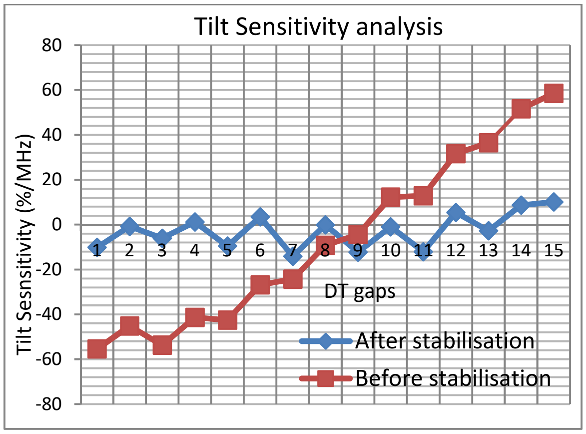

Fig 7(b): Tilt sensitivity analysis in 15-20 MeV DTL

Figure 7 shows the tilt sensitivity studies for 11-15 MeV and 15-20 MeV DTL. After tuning, TS reduced from ± 120 %/MHz to ± 20 %/MHz.

FIELD FLATNESS USING TUNERS

After optimising TS, E-field distribution in the DT gaps was adjusted using tuners to maintain field flatness within ± 2 %. using slug tuners, which when inserted inside the cavity, change the resonant frequency [5]. E-field flatness can be given in equation 5 below

$$E = \frac{(Emax - Emin)}{Emean} X\ 100\ \% \qquad (5)$$

Figure 8 shows E-field flatness achieved for both the DTL before and after optimisation. Complete frequency spectrum including all the post coupler modes are plotted for both the DTLs. 11-15 MeV DTL has 10 post coupled modes and 15-20 MeV DTL has 8 post coupled modes. Figure 9 shows the spectrum for both DTLs.

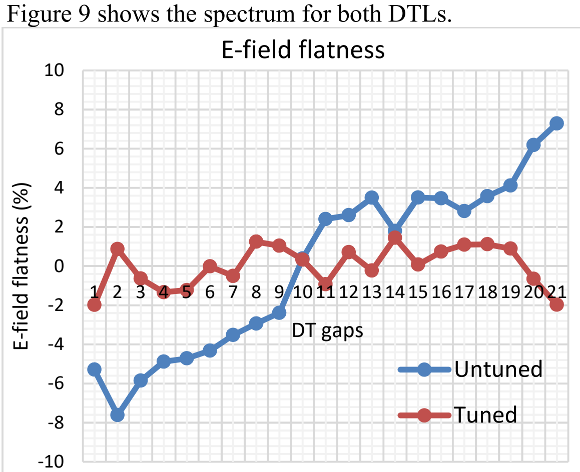

Fig 8(a): E-field flatness in 11-15 MeV DTL

CONCLUSION

RF characterisation and tuning of 11-20 MeV DTL were carried out. Resonant frequency of the cavities was tuned to 352.12 MHz. Electric field flatness of the cavities was maintained within ± 2.5% in the final stage of tuning and tilt sensitivity was maintained within ± 25 % using PCs. 11-20 MeV cavities are installed in beamline, ready for beam commissioning.

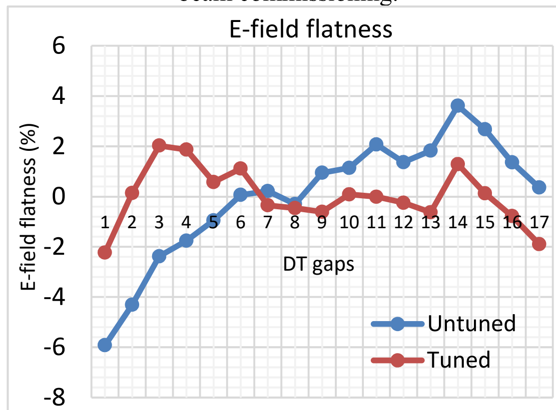

Fig 8(b): E-field flatness in 15-20 MeV DTL

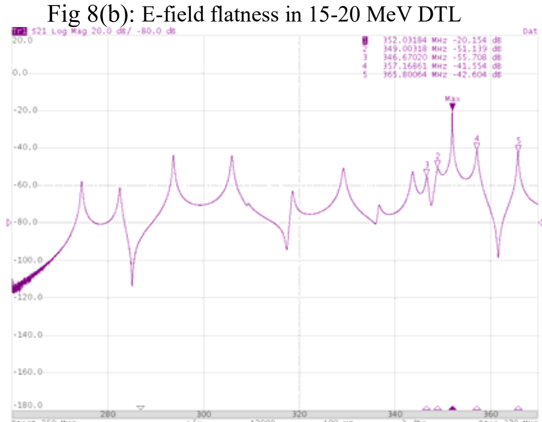

Fig 9 (a): Frequency spectrum in 11-15 MeV DTL

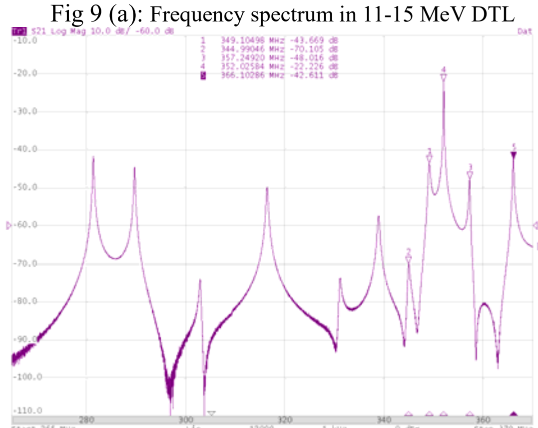

Fig 9 (b): Frequency spectrum in 15-20 MeV DTL

REFERENCES

1. SS Kapoor, "Accelerator-driven sub-critical reactor system (ADS) for nuclear energy generation", PRAMANA Journal of Physics, Vol. 59, No. 6, page 941–950, December 2002
2. P. Singh et al., "Accelerator Development in INDIA for ADS programme, PRAMANA Journal of Physics, Volume 68, No.2, February 2007.
3. S. Roy et al, "Electromagnetic and Beam dynamics studies of a high current drift tube Linac for LEHIPA", Journal of Instrumentation, Volume 9, June 2014.
4. Mohammad Reza Khalvati, Suitbert Ramberger, "Straightforward and accurate technique for post-coupler stabilization in Drift Tube Linac structures", in Physical Review Accelerators and Beams 19, 2016 pp. 042001-1-042001-12
5. H.C. Liu, A.H. Li, J. Peng, M.X. Fan, P.H. Qu, et al, "Low Power RF Tuning of the CSNS DTL", in Proc. of IPAC2016, Busan, Korea, 2016, pp. 913-915.

DEVELOPMENT AND COMMISSIONING OF A THERMAL PROFILE DATA LOGGING AND PROTECTION SUBSYSTEM FOR INDUS-2 RF CAVITY

Narendra Kumar*, Deeksha Vyas, Akhilesh Jain, Ramesh Kumar, and Mahendra Lad
Raja Ramanna Centre for Advanced Technology, Indore, India

**narendra@rrcat.gov.in*

Abstract

Indus-2 RF system at Raja Ramanna Centre for Advanced Technology (RRCAT) Indore, is equipped with six 60 kW, 505.8 MHz, CW RF power stations [1] feeding to normal conducting elliptical RF cavities generating over 1.5 MV of gap voltage. Among these, the RF cavity installed in RF station #5 is developed inhouse by RFSD, RRCAT indigenously. In a synchrotron radiation source, it is essential to keep the resonant frequency of the RF cavity constant. Hence for the proper filling of electron beam current and smooth energy ramping to 2.5 GeV level, a precision chiller unit for each RF cavity is used which keeps the thermal profile of RF cavity precisely stable during full operation. A 'Thermal Profile Data Logging and Protection Subsystem' for Indus-2 RF cavities, was installed and commissioned in the Indus-2 RF system to display and log the thermal profile data, as well as to provide thermal protection to the RF cavities. This protection is against any incidental excessive rise in RF cavity surface temperature during the round 'O' clock operation of Indus-2 synchrotron Radiation Source.

The system uses a Hioki make 60 universal channel data logger, K type and T type thermocouples suitably customised for proper mounting upon the surface of the RF cavity, interface cables and connectors compatible for the used thermocouples. As the mechanical mounting of the thermocouples upon the surface of RF cavity is not recommended due to various reasons, customised thermocouples having flat square shaped copper strip brazed on the junction tip were mounted, using thermally conductive epoxy adhesive paste which can withstand high temperature of the surface without losing its properties. Around 7 numbers of K-type thermocouples are fixed at suitable places upon the surface of the RF cavity, so that a comprehensive data of the RF cavity thermal profile may be obtained. As the cavity is installed in the extremely high radiation area (zone # 3), K type thermocouples are used due to their high relative radiation hardness. Connectors (for K type, Omega make thermocouple terminal barrier strip model # BS16A and for T type, Omega make low noise miniature M-F connector pair model GMP-T) and cables used to interface the thermocouples with the data logger placed in RF equipment hall area are also made up of the compatible material (for K type: Chromel & Alumel and for T type: Copper & Constantan, both with PVC insulation as per IS5831:84) to maintain the compatibility. In total, approximately 200 m of shielded cable (~60 cables of 3.33 m length each) is routed through the trench to provide the interface between the 60 sensors and the datalogger. Shield jackets of all the cables have been grounded to check the noise and interference related issues. A T-type thermocouple (T_{Ref}) is also mounted in the same location as K5, but on the opposite surface of the cavity to cross check the 2 read values. This has been used for the reference purpose due to better accuracy.

The 60 universal channel datalogger has been programmed with OR logic to generate a potential free contact to trip the interlock unit [2] of the respective RF station in case the temperature of any thermocouple exceeds the safe limit. The system was tested okay after installation and has been working properly since it's commissioning in 2017.

This paper presents the scheme, technical considerations and issues related to maintenance of the subsystem.

INTRODUCTION

200 mA, 2.5 GeV synchrotron light source Indus-2 is a national facility which run 24X7 in user mode at RRCAT, Indore. Electron beam current is energised till 2.5 GeV by generating over 1.5 MV RF gap voltage at 505.8 MHz in six normal conducting RF cavities installed in series. In order to keep the resonance frequency constant, it's important to maintain the surface temperature of these cavities precisely stable at the stipulated value. This objective is achieved by circulating the low conductivity coolant water through the cooling channels of the RF cavity. To maintain the temperature of the RF cavities precisely at stipulated level, dedicated precision chillers are used with temperature stability of ± 0.1 ^{0}C for each cavity and proper flow rate and pressure is maintained throughout the operation at the stipulated required level down into the line.

Figure 1: RF cavities installed in Indus-2 ring

#narendra@rrcat.gov.in, **ID:F11-575**

DEVELOPMENT AND DESIGN SCHEME LAYOUT

The development scheme of the system is shown below-

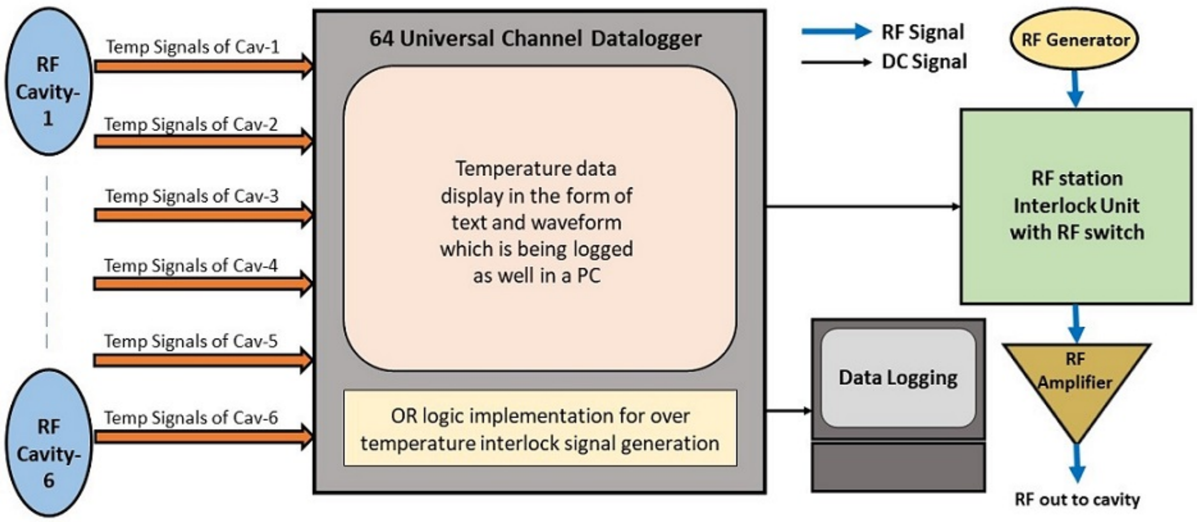

Figure 2: Schematic lay out of the setup

Used Various Types of Thermal Sensors

On the imported ones, as well as indigenously inhouse developed RF cavity, around 60 numbers of various types of thermal sensors (total 10 on each cavity) are used suitably to sense the temperature at various locations on the surface and RF coupler window of the cavity. A brief description about these is given below-

Customised K Type Thermocouple

Seven numbers of K type thermocouples suitably customized for proper mounting have been mounted upon suitable locations upon the surface of each RF cavity. To make mounting easy flat square shaped copper strip is brazed on the junction tip of these thermocouples as shown in the following figure #3.

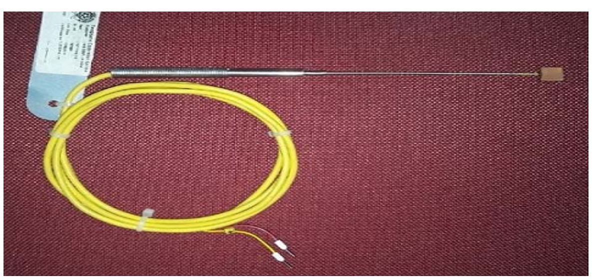

Figure 3: Customized K type thermocouple

Customised T Type Thermocouple

A customized T type thermocouple is used for cavity reference temperature measurement purpose.

Figure 4: Customized T type thermocouple

Customised RTD Sensor (PT100)

Two numbers of customized RTD sensor PT 100 are used for cavity window air inlet and outlet temperature measurement purpose.

Figure 5: Customized RTD sensor PT100

Above thermal sensors are mounted on suitable locations on the surface of cavity and RF coupler window as shown in figure below-

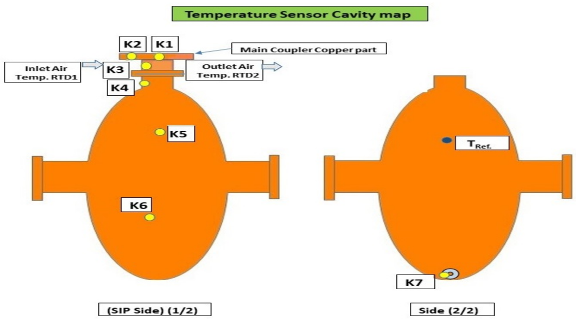

Figure 6: Thermal Sensors Locations on the Cavity

There are six RF stations in Indus-2 RF system. Five stations run with the imported RF cavities while the sixth one uses an indigenously in-house developed cavity. Thermal data sensed by all these 60 sensors (10/cavity) is logged and monitored by a Hioki make, data logger which can process the 60 universal inputs parallelly. It continuously compares the process values with the set values and generates a trip fault and sounds the alarm buzzer, in case any of these exceeds the set safe limit.

Figure 7: 60 universal channel data logger unit

The fault signal trips off the RF being fed to the cavity with the help of an in-house developed high speed CMOS logic gate based hardwired interlock unit [3] of the respective RF station. The fault is latched and disappears only on giving Reset command after turning it healthy.

Figure 8: 36-channel RF interlock unit

RESULTS

Cavity thermal profile data is being displayed locally on the TFT screen and logged into the hard disk of a PC at every second time interval. If required, the data can be refreshed and logged at an even faster rate, i.e., every 10 ms time interval, but then storage space will be consumed faster.

After arrival of a fault, the response time to trip off the RF of respective cavity had been measured and found to be of the order of around 30 µs, which is well within the stipulated safe time limit.

Figure 9: Interlock unit response time measured on DSO

CONCLUSIONS

The thermal profile data of all six RF cavities received through 60 various kind of sensors is being monitored and logged continuously into the hard disk of a PC with the help of a Hioki make 60 universal channel data logger unit. This data is important from the point of view of thermal fault diagnosis and other related issues.

Temperature overload interlock is also very important to ensure the safety of RF cavities, as these operate continuously with high RF power. Above objectives are achieved successfully with the help of this subsystem.

REFERENCES

[1] Ramesh Kumar*, Ashish Tiwari, Rajeev Arora, M. Prasad, N. Bhardwaj, Alok Gupta, Deepak Sharma, Akhilesh Jain, M.K.Badapanda, Nageswar Rao, P. Bagduwal, Nitesh Tiwari, Ashish Bohrey, Mahendra Lad, A. Karnewar, R.M. Pandey, Sanjay Gupta, R. K. Sahu, T. Puntambekar, V. Sathe, D.P. Yadav, B.K. Sindal, R. Sridhar, R.S. Sandha, and Jishnu Dwivedi, **"Installation and Commissioning of Indigenously Developed RF Cavity in Indus-2"**,in Proc. Indian Particle Accelerator Conference (InPAC 2018), Raja Ramanna centre for Advanced Technology (RRCAT), Indore, January 09-12, pp. 56-58

[2] Narendra Bharadwaj#, Nitesh Tiwari, Mahendra Lad, **"Design modifications and up gradations in Indus 2 RF safety interlock system for the safety of recently commissioned insertion devices U1 and U2"**, in Proc. Indian Particle Accelerator Conference (InPAC 2015), Tata Institute of Fundamental Research, Mumbai, December 21-24, pp. 411-414.

[3] N. Bharadwaj, Nitesh Tiwari, M. Lad and P. R. Hannurkar, **"Observation Issues and Remedies during Installation & Operation of RF Interlock System for Indus-2 SRS"**, High Power RF & Microwave (HPRFM 2013), Institute for Plasma Research, Gandhinagar, September 04-06, pp. 272-275.

KALMAN FILTER AS DETUNING ESTIMATOR FOR EXPERIMENTAL RF CAVITY

R. T. Keshwani[1], S. Mukhopadhyay[2], R. D. Gudi[3], Gopal Joshi[2]
[1]Research Scholar HBNI, BARC, Mumbai, [2]Sr. Prof. HBNI, BARC, Mumbai, [3]Prof. IIT Mumbai

Abstract

In an operational accelerator, RF cavity operates in pulsed or CW mode. Value of cavity detuning needs to be known for tuning and tracking of cavity resonance frequency. As direct sensor/s for knowing value of detuning are not available, often model of RF cavity is employed to infer or estimate its value from available measurements. This type of measurement is termed as secondary/inferential measurement. In this paper, RF cavity model based detuning estimation is discussed. Detuning estimator based on Kalman Filter under stochastic state space framework is considered. Such a framework helps to address practical issues like those of measurement noise and model uncertainty. Experimental set up is made using lab prototype RF cavity of 650 MHz and algorithm is evaluated. A comparative assessment with to direct estimator is also carried out.

INTRODUCTION

Different types of particle accelerators have been used worldwide for acceleration of beam particles to specified energy level [1, 2]. Ideally RF cavity must be operated at resonance frequency (f_r) for efficient particle acceleration. However, f_r may shift w.r.t. operational RF frequency (f_{RF}). The difference between f_r and f_{RF} is referred as detuning $\Delta\omega/2\boldsymbol{\pi}$ in Hz or in $\Delta\omega$ rad/sec . Its value forms one of the important operational parameters of RF cavity. However, it is not a directly measurable parameter. Continues time state space (CTSS) model of RF cavity may be used to estimate $\Delta\omega$ from measured inputs and outputs of cavity.

$$\frac{d}{dt}\begin{bmatrix} V_r(t) \\ V_i(t) \end{bmatrix} = \begin{bmatrix} -\omega_{1/2} & -\Delta\omega \\ \Delta\omega & -\omega_{1/2} \end{bmatrix}\begin{bmatrix} V_r(t) \\ V_i(t) \end{bmatrix} +$$

$$\begin{bmatrix} R_L\omega_{1/2} & 0 \\ 0 & R_L\omega_{1/2} \end{bmatrix}\begin{bmatrix} I_r(t) \\ I_i(t) \end{bmatrix} \;\&\; \mathbf{z}(t) = \begin{bmatrix} 1 & 1 \end{bmatrix}\begin{bmatrix} V_r(t) \\ V_i(t) \end{bmatrix}$$

Here, at time instant t, states $V_r(t)$ and $V_i(t)$ are measured from cavity pick up signal while $I_r(t)$ and $I_i(t)$ are cavity input signals. Parameters $\omega_{1/2}$ and R_L are cavity bandwidth (in rad/sec) and loaded resistance respectively. Estimation of $\Delta\omega$ for an operational accelerator has been attempted by various authors using variety of modern techniques like least square estimation [3], observers of various types [4], parameter estimators [5], etc. However, most of these approaches are incapable to account for practical issues like model uncertainty and measurement noise. Model uncertainty basically originates from system properties which are seldom known accurately. Reported literature [6, 7] advocates Kalman filter (KF) based approach, however basic analysis of KF has not been addressed in these papers. In this paper, authors attempt to apply discrete KF (DKF) as $\Delta\omega$ estimator and show that it is better than other estimator like direct estimator.

DKF MODEL AND OPERATION

From CTSS representation, a discrete state space (DSS) model in stochastic formalism may be formed for system model (for assumed measurement noise $\mathbf{v}_k$ & state noise $\mathbf{w}_k$). From it, one directly obtains model of DKF. The DKF model may be further employed for simulation studies in presence of noises $\mathbf{v}_k$ and $\mathbf{w}_k$. Many standard references [8,9,10] describe DKF operation. Figure 1 shows a flow chart of DKF algorithm. From stochastic DSS model of cavity, system matrix **A**, Input matrix **B**, output matrix **H** are formed and they serve as important building blocks of DKF for assumed sampling time and discrete time instant k. The inputs $I_r(k)$ and $I_i(k)$ form matrix $\mathbf{u}_k$ and measurement forms matrix is $\mathbf{z}_k$. $V_r(k)$ and $V_i(k)$ form state vector $\mathbf{x}_k$. In DKF operation, from initially assumed state matrix and their error covariance matrix, assumed tuning parameters like model uncertainty/inaccuracies (in form of state error covariance matrix $\mathbf{Q}_k$, also called process noise) and measurement uncertainty in form $\mathbf{R}_k$, predicated states and corresponding error covariance's are estimated at instant k. The important outcomes of DKF are its predicted and posterior state matrix and its error covariance. The Kalman gain $\mathbf{K}_{k+1}$ of DKF can also be estimated at instant k+1. Once measurement $\mathbf{z}_{k+1}$ is available, state and covariance matrix are updated. The predicted measurements and gain are used to update state matrix and covariance matrix. The difference of predicted measurement from actual one is called innovation or residual sequence ν_{k+1}. If DKF estimates the states of system close to true values, ν_{k+1} approaches a white noise sequence. From states estimated by DKF the $\Delta\omega$ is estimated. Authors have used direct estimator in [11] to estimate $\Delta\omega$ which suffer from serious limitations that one cannot account or compensate for measurement noise and model inaccuracy.

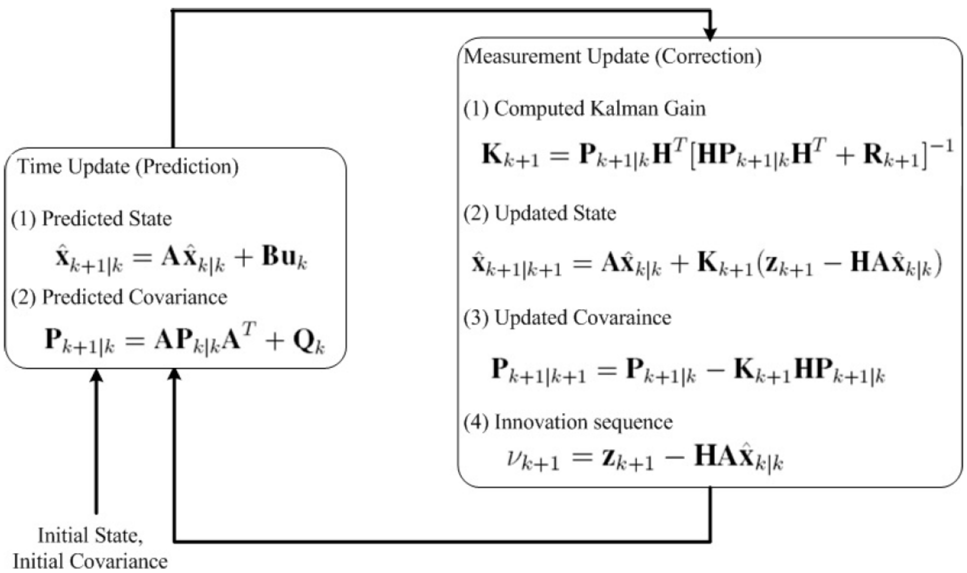

Figure 1: Steps used in DKF operation.

PERFORMANCE EVALUATION OF DKF

Figure 2 shows experimental set up used to evaluate DKF based estimator. A lab prototype RF cavity is excited with Pulsed RF input (RF_{in}) at various f_{RF} from RF signal generator. RF inputs and output are feed to analog demodulators. I_i, Q_i are IQ of input RF demodulator while output RF signal has IQ as I_o and Q_o. These IQ from modulators are acquired using high frequency MSO. The acquired I/O for known $\Delta\omega$ is feed to DKF to estimate its value.

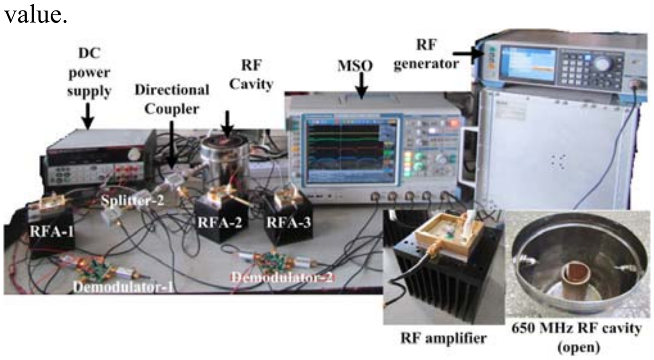

Figure 2: Experimental set up for acquiring readings for $\Delta\omega$ estimation.

Figure 3 shows $\Delta\omega$ estimated directly by solving two equations obtained from DSS model [11] at different f_{RF} for cavity with known f_r app. 650.33 MHz. It is seen that as RF_{in} f_{RF} is changed to values away from f_r, the estimated $\Delta\omega$ becomes noisy leading to poor estimation accuracy. Tuning Tuning of DKF is carried out by adjusting $\mathbf{R}_k$ & $\mathbf{Q}_k$. $\mathbf{R}_k$ can be inferred from sensor noise whereas tuning of

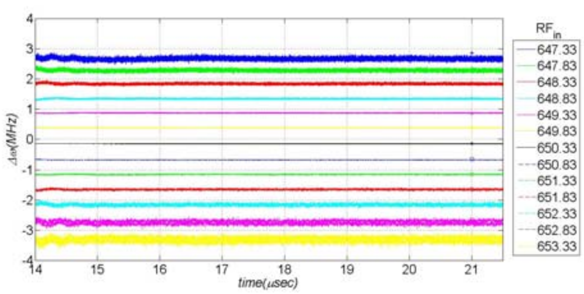

Figure 3: Direct estimated $\Delta\omega$ at various f_{RF}.

$\mathbf{Q}_k$ is tricky part. In our work we have adapted approach from [12]. Variance of innovation sequence v_k is observed as $\mathbf{Q}_k$ is varied. The value of $\mathbf{Q}_k$ matrix where this variance is minimum gives the best state estimates. The same I/O as feed to direct estimator, when feed to DKF leads to lesser noise as seen in figure 4. The noise in estimate is in terms of std. deviation (σ) of estimated $\Delta\omega$. It also shows the noise performance of direct estimator as raw signal. It may be concluded from figure that σ improvement is offered by DKF as compared to direct estimator at various f_{RF}. The ratio of σ of DKF estimates to σ by direct estimator as less than unity implies that DKF estimates have lesser noise as compared to estimates from direct estimator. The reason for this improvement is evident from figure. 5. It is observed that DKF estimates have less noise as compared to direct estimator noise leading to better estimates of $\Delta\omega$.

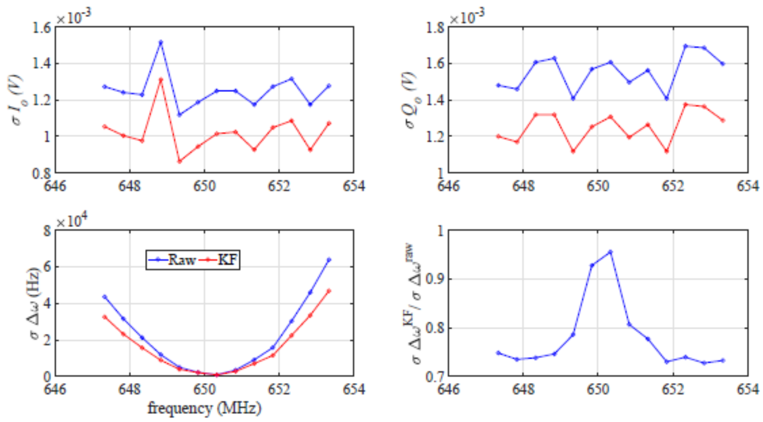

Figure 4: Improvements by DKF.

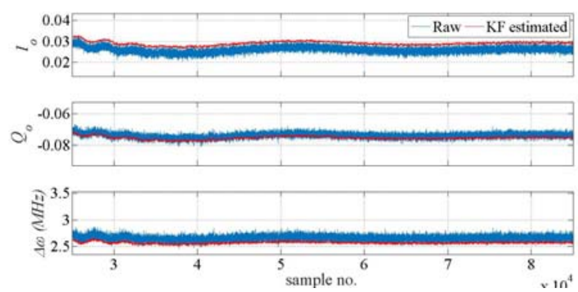

Figure 5: Estimates for KF compared with those for direct estimation case.

CONCLUSION

The main focus of this paper has been to assess performance of DKF as estimator of cavity $\Delta\omega$ w.r.t. to other methods. Amplitude of RF_{in} matters most for estimator accuracy. It is observed that higher amplitude RF_{in} leads to accurate estimation of $\Delta\omega$. In case of direct estimation, there is no mechanism to estimate or reduce noise in estimated parameter. The noise in primary measurements directly affects noise in estimates. One may however resort to better methods like DKF based described in this paper. It works in stochastic state space formalism and offers tuning parameters like measurement noise covariance $\mathbf{R}_k$ to take care of sensor and measurement system noise. It offers tuning state noise covariance $\mathbf{Q}_k$ which accounts for model uncertainty. Mainly KF along with estimated states/parameters also provides variance values of each of them, thus giving value of confidence that may be associated with each estimate. In this work, experimental data acquired from 650 MHz lab RF cavity has seen used to assess KF performance as $\Delta\omega$ estimator. The KF based estimator works well and better than direct estimator.

REFERANCES

[1] T. Wangler, RF Linear accelerators. Wiley series in beam physics and accelerator technology, 1998.

[2] M. Lynch, et. al., "Excess RF power required for RF control of the spallation neutron source(SNS) LINAC, a pulsed high-intensity superconducting proton accelerator," Proceedings of the 2001 Particle Accelerator Conference, Chicago, vol. 1, pp. 503– 505, February 2001.

[3] T. Czarski, et. al., "Cavity control system essential modeling for TESLA linear accelerator," TESLA Report, 2003.

[4] S. Kwon, et. al., "Frequency shift observer for an SNS superconducting RF cavity," IEEE Transactions on Nuclear Science, vol. 50, no. 10, p. 201, 2003.

[5] R. Rybaniec, et. al., "Real Time estimation of superconducting cavities parameters," Ipac 2014: Proceedings of the 5th International Particle Accelerator Conference, pp. 2456–2458, 2014.

[6] Ushakov, A., Echevarria, P., and Neumann, A. (2017). "Detuning compensation in SC cavities using Kalman filters".

[7] Ushakov, A., Echevarria, P., and Neumann, A. (2018). "Developing Kalman filter based detuning control with a digital SRF CW cavity simulator".

[8] R. E. Kalman, "A new approach to linear filtering and prediction problems", Transactions of the ASME–Journal of Basic Engineering 82 (Series D), pp. 35-45, 1960.

[9] R. Faragher, "Understanding the basis of the Kalman Filter via a simple and intuitive derivation", IEEE Signal Processing Magazine, September, 2012, pp. 128-132.

[10] G. Welch and G. Bishop, "An introduction to Kalman filter", UNC-Chapel Hill, USA, July 2006, paper TR 95-041.

[11] Rajesh T. Keshwani, S. Mukhopadhyay, R. D. Gudi, Dr. Gopal Joshi, "Performance Analysis and Evaluation of Estimator for RF cavity detuning measurement", Int. conference on Information and Signal Processing (ICONSIP-II), COEP, 26-27th Aug 2022.

[12] T.U.Bhatt, et. al. , " Estimation of sub-criticality using extended kalman filtering technique", Annals of Nuclear Energy, 60:98–105, Oct 2013.

THERMO-MECHANICAL ANALYSIS OF MEHIPA COUPLERS

***Sonal Sharma, Rajesh Kumar**

Ion Accelerator Development Division, Bhabha Atomic Research Centre, Mumbai - 400085, India

*sonal@barc.gov.in

Abstract

RF coaxial couplers are required to provide high RF power (approximately 40 kW at 325 MHz) to the SSR cavities of MEHIPA. Each SSR cavity requires different power. The coupler design has been optimized so that the same type of coupler can be used to feed all the cavities. CST simulation of this coupler has been done [1]. It has been designed provide good match at input. Along with RF and thermal simulations [1] it is necessary to know the stresses at the alumina window brazing joints [2]. During full power operations these brazing joints may break if the temperature and stresses are too high. So, preliminary level simulations have been carried out in 2D-comsol software to calculate stresses at the inner and outer side of the alumina brazing joints. This paper describes this thermo-mechanical analysis of the coupler.

INTRODUCTION

The power requirement for MEHIPA SSR cavities varies from 6 kW to 40 kW. Same type of coupler will be used to feed all the cavities. This coupler has 6-1/8” input line, inner and outer bellows for flexibility, ceramic window, air cooled inner antenna for capacitive coupling etc. It has a coaxial geometry and consists of single alumina disks of 7mm thickness which acts as RF window. CST simulation of the coupler is done to know the RF and Thermal behaviour [1]. The results from the thermal simulation are imported in Comsol 2D software to know the stresses at the brazing joints. The most weak places of coupler is places of brazing ceramic to copper sleeves and brazing of copper sleeves to flange and to antenna [2]. There are two reasons of stresses during operation: atmospheric pressure to the window and change of size due to heating/cooling. According to literature available in any case the stress has be below 100 MPa at the joint for increased life cycle of ceramic [2]. To reduce the stress it is required to reduce the temperature gradient at the brazing joints. For this generally some design changes are done which includes increasing the size of the alumina disk, improving the cooling etc. To study this behavior first thermal analysis was carried out in CST for different phases with full reflection as well as 20% reflection cases. Temperature profiles were obtained along the radius of the ceramic for these different conditions. These temperature profiles were exported to comsol 2D for mechanical stress analysis. This analysis has been carried and results are presented.

THERMAL ANALYSIS OF THE COUPLER

Thermal simulation has been coupled with RF simulations to obtain the temperature profile and heat flow values of the RF coupler [1]. Configuration used for vacuum part of coupler is given in fig 1.

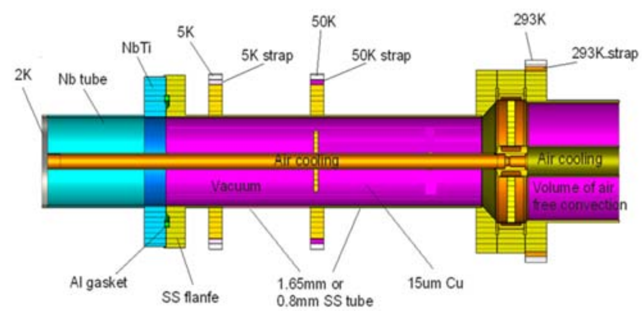

Figure 1. Configuration of vacuum part of coupler for thermal simulations

Two intercepts at 5k and 50k are used to cool the outer conductor of the cold part of coupler. Inner conductor is air cooled. Mesh size has been optimized for convergence. The tetrahedrons used are about 62000 for thermal simulation. Heat flow values for static and dynamic (50kW, 20% reflection worst phase) cases are given in Table 1.

For worst phase, the simulated model in fig 2 shows the heat flow and temperature profile.

Table 1. Heat flow values static and dynamic case

Heat load	Heat flow 2K, W	Heat flow 5K, W	Heat flow 50K, W
static	0.24	2.68	8.58
Dynamic(50 kW, 20% reflection)	0.44	3.1	9.9

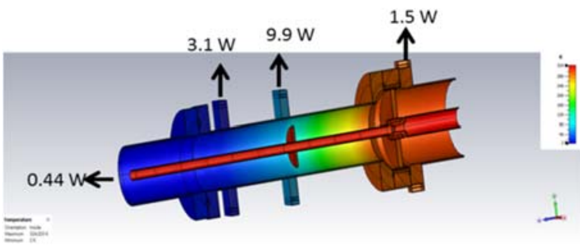

Figure 2: Thermal profile with heat flow for 50 kW, 20%reflection

THERMO-MECHANICAL ANALYSIS

The window configuration for thermo-mechanical analysis is given in fig 3. The most weak places of coupler is places of brazing of ceramic to copper sleeves and brazing of copper sleeves to flange and to antenna[2].

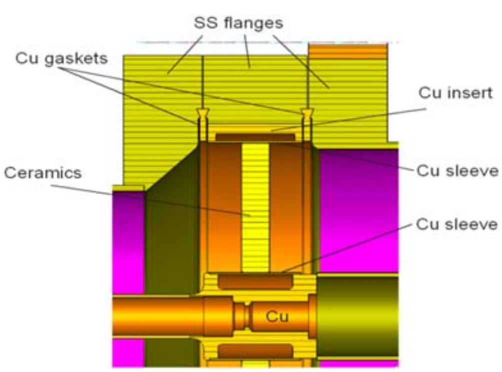

Figure 3: Window configuration for thermo-mechanical analysis

Maximum acceptable stress

Based on the graph given in fig 4 (available from literature) we can consider the stress level < 100 MPa at the joint as safe level. It provides ~ 1e4 cycles (RF on / RF off) before distruction. So, stress < 80 MPa is preferable (1e5 cycles).

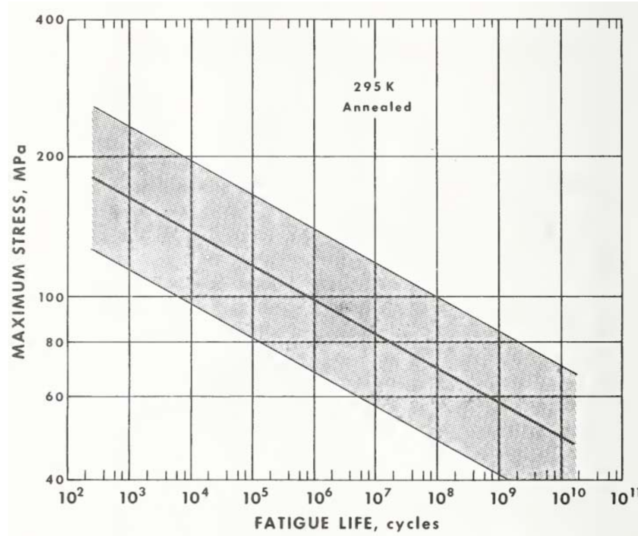

Figure 4.2. Dependence of maximum stress at 295 K upon number of cycles to failure.

Figure 4: max stress vs fatigue life [3]

Stress analysis of the coupler

The temperature profile along the ceramic for 50 kW, 20% reflection is obtained from thermal results. This profile is shown in fig 5. It is imported in Comsol 2D software to obtain stresses and displacements due to atmospheric pressure and temperature at the inner and outer joints of ceramic.

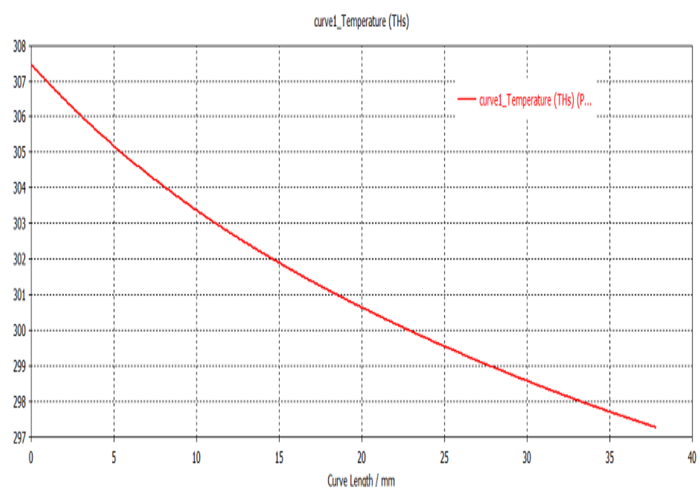

Figure 5: temperature variation along the ceramic

There are two reasons of stresses during operation: atmospheric pressure to the window and change of size due to heating/cooling. These stresses are observed using Comsol. These are Von mises stress. The stresses at different locations of the joints (the inner and outer sleeves with ceramic) with 1 atmospheric pressure and without RF power (or thermal effects) are given in fig 6. The stresses with the full RF power (which leads to heating due to thermal effects) and 1 atmospheric pressure is shown in fig 7.

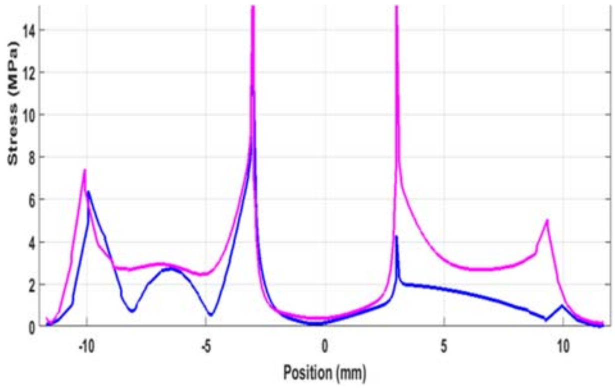

Figure 6: Stresses without RF power at different locations of the joints

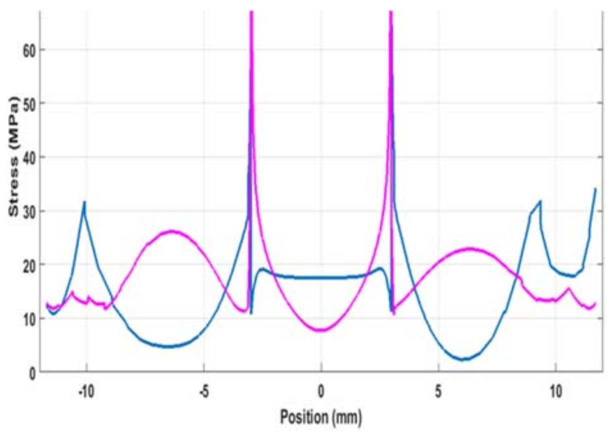

Figure 7: Stresses with 50 kW, 20% reflection (with thermal effects) at different locations of the joints

As seen in fig 7 the maximum stress under the effect of atmospheric pressure and 50 kW, 20% reflection case is less than 70 MPa at outer sleeve alumina joint which is a very safe limit. Typical deformation and stresses (colors) effects on the ceramic with inner and outer sleeve are shown in fig 8.

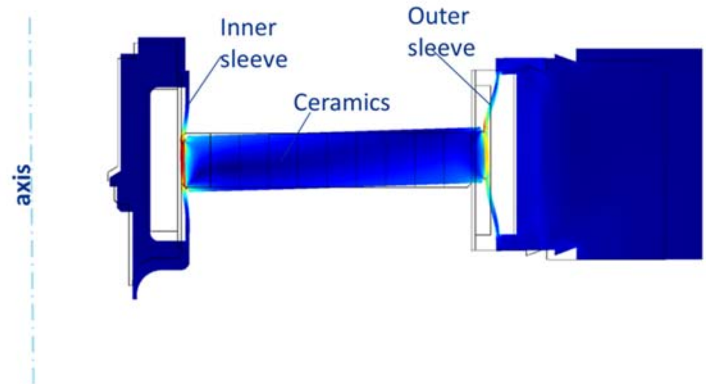

Figure 8: Deformation and stresses (colours) due to atm pressure and thermal expansion

CONCLUSION

Thermal simulations of the coupler have been done to analyse the heat load and maximum temperature values. Temperature profile along the ceramic length is imported in Comsol software to get the thermo-mechanical coupled stress values at different locations of brazing joints. The maximum value of stress is about 70 MPa which is within the acceptable limits.

ACKNOWLEDGEMENT

The author would like to thank Mrs Shreya G Sarkar, APPD, BARC for helping in simulation and stress analysis of the coupler. Also I would like to thank Mr Sergey for useful discussions.

REFERENCES

[1] Sonal Sharma and Rajesh Kumar, “Design of 325 MHz RF couplers for superconducting spoke resonators in MEHIPA-1”, Proceedings of the DAE-BRNS Indian particle accelerator conference (InPAC 2022), VECC, Kolkata, India, March 2022

[2] S. Kazakov, “Thermal properties of 650MHz coupler”, 650 MHz Coupler FDR/PRR, Feb 2020.

[3] N.J. Simon et.al., ”Properties of copper and copper alloys at cryogenic temperatures*”;* page 124 ;NIST publications .

CONTROL AND INSTRUMENTATION SYSTEM OF INDIGENOUS LHP100 HELIUM LIQUEFIER PLANT AT BARC

Sanjay Jain[1], Ankit Jain[2], Mohananand Jadhav[2], Ratna Bhamra[1], Y S Nirgude[1], V Srinivas[1], P K Kavalan[1], Mukesh Goyal[2], Anindya Chakravarty[2]

Abstract

Cryo-Technology Division, BARC is developing a 100 l/hr helium liquefaction system [1] (LHP 100) [2]. The process design of LHP100 is based on modified Claude cycle [3]. In contrast to the LHP50 [4, 5], the LHP100 makes use of liquid and vapour nitrogen precooling to enhance the refrigeration capacity. LHP50 helium liquefier has been manually operated extensively. The operational experience from the LHP50 cryo plant has been utilized in the development of control system for the LHP100 liquefier. The major components of the LHP100 system consist of a process screw compressor with gas management system, cold box with vacuum system, high effectiveness plate-fin type heat exchangers, high speed turboexpanders, charcoal absorbers, bellow sealed control valves and helium Dewar with interconnecting cryogenic pipelines. Present article describes the detailed philosophy of the control system for the LHP100 liquefier along with details of the supervisory control system. The control system consists of independent feedback loops for some of the above component systems and plant automation according to an elaborate flow control diagram implemented through PLC and supervisory control system. The complete automation/control system of the LHP100 plant is being developed by Reactor Control Division and Cryo-technology Division, BARC. The high speed turboexpander brake control system and precision pressure control loops have already been developed using microcontroller and PC based system and have been reported earlier [6]. The present article reports the PLC implementation and simulated testing of these systems. The PLC system has been integrated with EPICS SCADA software using Channel Access (CA) protocol.

INTRODUCTION

The helium liquefier (LHP 50) [4, 5] based on modified Claude cycle [3] at Cryogenic Technology Division (CrTD), BARC was commissioned in 2015. The reported liquefaction rate was 32 litres/ hour and refrigeration capacity at 4.8K was around 193 W. The liquefier was successfully operated continuously for more than a month to establish long term reliability of the system. Most of the components are developed either in-house or with local vendors. So far, operations of the liquefier have been carried out manually. The experience gained in LHP50 and results obtained from subsequently experimentation using Microcontroller based Control System for CP1000/CP2000 Helium Refrigeration Plants [6] has been used in control system designing of LHP100[1,2]. The complete automation of the cryogenic R&Dfacility has been taken up by E&I group of BARC and worked out detailed C&I requirements along with CrTD

LHP 100 PROCESS DESCRIPTION

First stage of the process is helium screw compressor where Helium gets compressed and its discharge is connected to helium liquefier (Coldbox). Fig 1 depicts the LHP100 process. Post compression, there are oil separators in the compressor package, where oil separation occurs by gravity. He gas stream after entering the cold box piping from the HP header forms the inlet stream and flows through Heat exchangers HEX. Stream cools down as it passes through HEX and cool down is aided by the cold return stream in the LP side of the HEXs. Next stage of cooling is through Turbo expander, the flow of gas through first turbine (TEX 4101) is being regulated by Control Valve (BSCV 4107), where stream expands around 5 bar (a) and temperature drop of about 10 K. This stream is further expanded to 1.5 bar (a) and cooled to about 10 K in Second turbine (TEX 4102). Post this expansion, the stream conjoins the return stream.

The other part of the inlet stream, the J-T stream continues its passage along HEX , cooling down along the way. At the upstream of charcoal absorber (ACB 4103), its temperature falls down to around 11 K. This low temperature gas inside the ACB is freed from neon impurities. The purified stream passes through HEX for further cooling and then it expands through BSCV4109. It is further cooled in HEX 4105B before finally undergoing J-T expansion in BSCV 4111 to form the two phase mist.

The two phase mist gets transferred from the exit of BSCV 4111 to the receiver Dewar by flowing through a vacuum jacketed, super insulated transfer line.

IMPLEMENTATION OF VARIOUS OPERATING STATES OF THE PLANT

The control system for the plant has been designed in such a way that it automatically performs its operations as per the below selected state and operator commands.

Idle State is a state when PLC is switched 'ON'. PLC shall read the position feed-back of all the valves and the same signals shall be transmitted to the control valves. All control loops shall remain deactivated by default. Alarms will be activated. In this mode, compressor startup procedure will be followed.

Process State In this state as in Fig 2, room temperature helium gas (at around 300K) is cooled down to liquid helium temperature (at around 5K). The Dewar hookup option is available to the operator. Depending on the Dewar and Second turbine (TEX4102) exit temperatures the Dewar

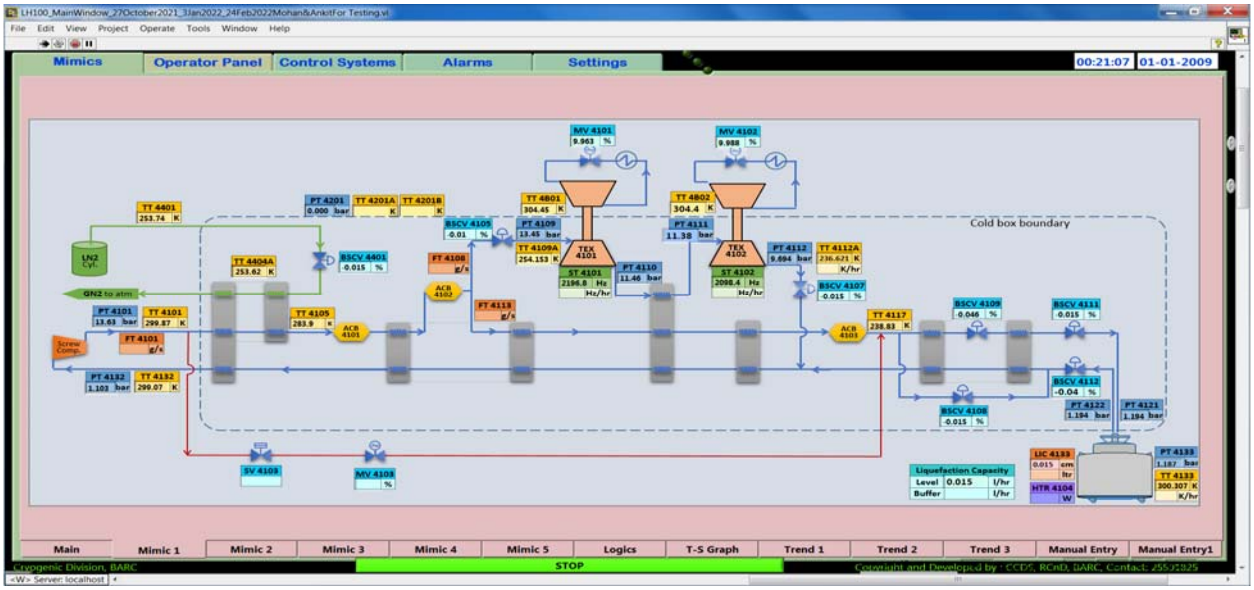

Figure 1: LHP100 Process

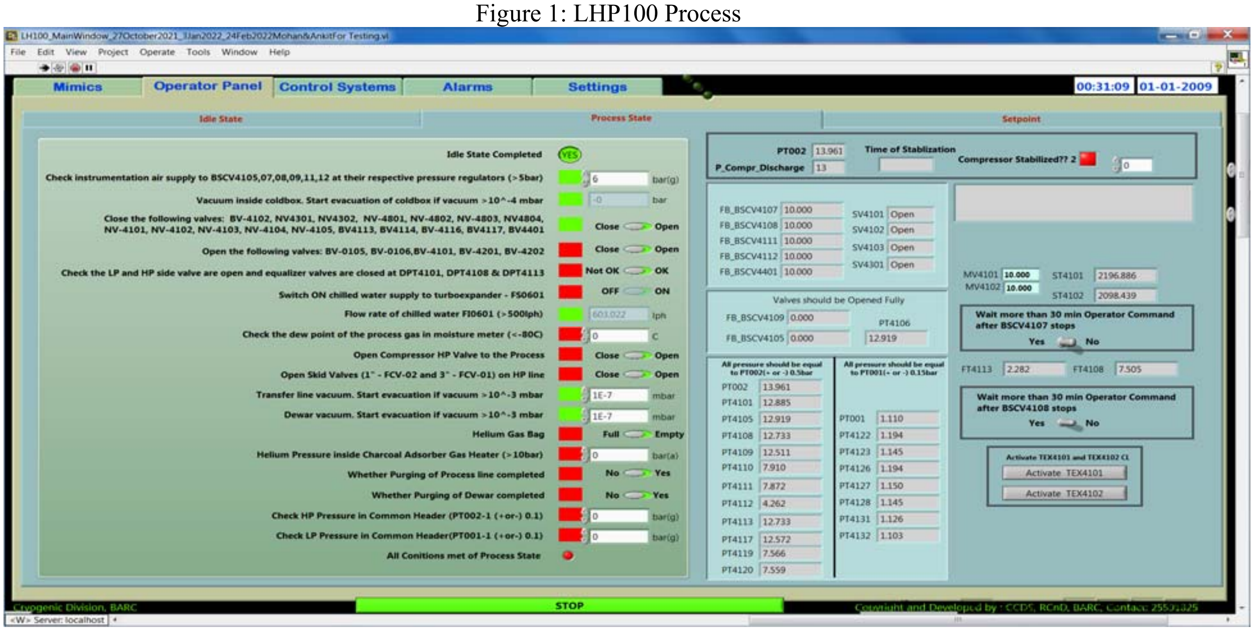

Figure 2: GUI window of LHP100 (Process State)

hook-up logic gets activated. Process startup will be followed by shutdown (as and when required by the user).

Shutdown State This state refers to a planned shutdown when the desired operation or experiments are over. In this mode, the helium liquefier will be systematically brought to shut down state by closing the flow through the turbine circuit

Apart from the core predefined states of the control system, few more independent control states as given in Fig 3 are required whose existence does not depend on the procedure of the core states. These control states can be independently activated/deactivated by the operator through GUI. There are total 14 control loops (11 PID control + 3 ON/OFF control) implemented in the customized MPROGICON PLC based control system.

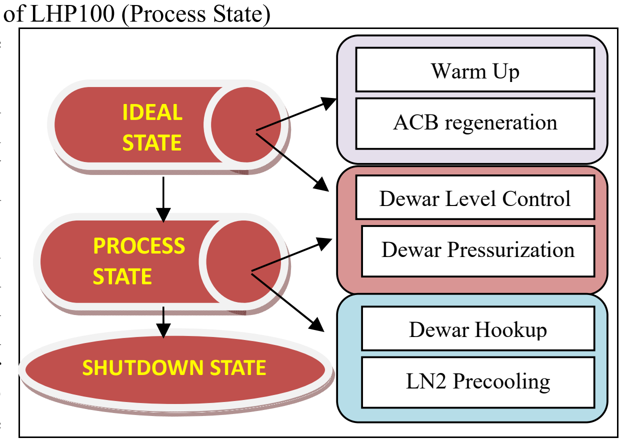

Figure 3: LHP100 Operating States

All control loops implemented have following over rides:

Manual operation of valve/voltage supply: The control loop will be disabled and the valve/voltage supply can be operated physically at the site.

Operation from HMI: The control loop will be disabled and the valve/voltage supply can be operated from the HMI.

Overriding control parameters: In this method, there is facility to change the set point during the operation Fig 4. The control will have a bumpless transfer from old set point to new point in a particular time interval (user defined at the time of setpoint change).

Ramp rate of setpoint change= (New S.P. – Old S.P.)/Time interval

Figure 4: Control Valve Override Window

Table 1 below listed sensors used in LHP100, temperature inputs are conditioned with conditioning modules having accuracy < ± 0.5K at operating temp 25^{0}C and resolution of the order of 0.1K.

Sensor	Type	Range//output	Quantity
Temperature Sensors			
Resistance based	PT-100(60K – 350K-750K)	~ 18-130-290 Ohm	40
Silicon Diode*	Calibrated Si Diode	1.4K-500K 1.64V – 0.09V	40
Pressure Transmitter			
Absolute	GEMS/ SMART/ABB	0-20, 0-6 bar(a)//4-20 mA	30
DPT	GEMS/ SMART/ABB	0-20/0-6 bar (DP)//4-20 mA	5
Speed			
Magnetic Pick-up	LC	Upto 40V peak pulses	2
Optical	Monarch Instruments	TTL/0 to 5V/4 to 20 mA	2

Table 1: List of Sensors in LHP100

TESTING METHOD AND RESULT

For testing of various control loops, process model has been developed. Model takes output of PLC as an input and computes field parameters and send computed parameters to PLC. PC based input and output cards are the interface of model for the reading/writing of the field inputs from PLC. The testing of PID loops were carried out by monitoring the output of PID loops in different scenarios viz Constant Set point, Step jump in set point and Varying Set point. Fig 5 and Fig 6 is the output of turbine ST4101 speed and motorized valve MV 4101 control. Temperature T4110A which is used to compute set point for ST4101, from model T4110A is changed from 250 K to 110 K in 10 minutes at a constant rate. The speed set point range has been decided such that if the set point falls in between 3000 Hz and 3500 Hz, the set point will be fixed at its earlier value. When the set point crosses this range, the set point changes at very fast ramp rate (500 Hz in 60 seconds) to final value.

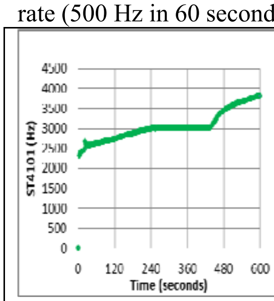

Figure 5: Variation of Turbine Speed ST4101as per process speed set point

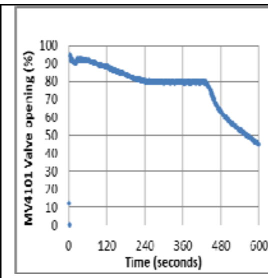

Figure 6: Controlling of valve MV4101

The results of the tests conducted were found to be as per required logic. Since, it is not possible to conduct all tests using online simulator, the no. of tests conducted are limited to few PID loops. More comprehensive tests will be conducted after the integration of PLC with the plant. Integration of PLC system with EPICS SCADA software using Channel Access (CA) protocol is under progress.

REFERENCES

[1] M Goyal, et al., "Recent improvements in the Indigenously Developed Cryogenic Systems at CrTD, BARC", Indian Journal of Cryogenics Vol. 44, pp 17-22 (2019).

[2] M Goyal, et al., "An update on Indigenous Helium liquefaction/ refrigeration systems at BARC" presented at 28th National Symposium on Cryogenics and Superconductivity (2022)

[3] Barron R F 1985 Cryogenic Systems (New York: Oxford University Press)

[4] N. A. Ansari et al., "Development of helium refrigeration/liquefaction system at BARC, India", IOP Conference Series: Material Science and Engineering 171 012007. (2017)

[5] A. Chakravarty, et al., "Operational analysis and Update on Helium Refrigerator/Liquefier Development at BARC", Indian Journal of Cryogenics Vol. 41, pp 18-25. (2016)

[6] S. Jain et al., "Development of Microcontroller based Control System for CP1000/CP2000 Helium Refrigeration Plants at BARC" presented at 28th National Symposium on Cryogenics and Superconductivity (2022).

Development of a versatile low temperature irradiation system for radiation damage studies

S. Chinnathambi, S. Julie, S. Amirthapandian and C. David

Materials Science Group, Indira Gandhi Centre for Atomic Reasearch, Kalpakkam – 603 102

e-mail : small@igcar.gov.in

A versatile, low-temperature ion-irradiation system is developed and it is usable at the end stations of the 1.7 MV tandetron and 150 kV accelerators at MSG, IGCAR. The comprehensive system consisting of (a) beam-defining slits, which ensures beam uniformity while using raster scanned (50 × 50 mm^2) and defocussed beams, (b)an indigenously developed insertable water-cooled Faraday cup and (c) a low-temperature sample holder, has been tested for the conduct of low-temperature irradiations down to 10K. The sample holder is cooled with the help of a closed-cycle refrigerator (CCR) yielding a temperature stability of $\pm$ 0.5K, during irradiations. A tilt table design of the system enables quick change of samples. The design, development and recent results obtained from the irradiation system are discussed..

Key words: Low temperature Ion irradiation system, radiation damage, vacuum

INTRODUCTION

The most profound effects of irradiation in materials occur in the core of nuclear power reactors, where atoms comprising the structural components are displaced numerous times throughout engineering lifetimes. Essential irradiation effects such as low-temperature radiation hardening and embrittlement, irradiation induced precipitation, phase stability, irradiation creep, and void swelling affect the performance of structural materials in nuclear reactors. Hence there is a considerable thrust in understanding the radiation effects of materials. In this context, the concept of “ion simulation of neutron damage” using ion irradiation has grown in popularity [1]. The simulation vests on the similarity in the type of primary damage state, i.e., the collision cascade and average primary recoil energy between neutron and heavy-ion irradiations, are comparable. Low-temperature irradiation is one of the most important experimental methods for fundamental research in radiation damage because the primary damage state at the end of the thermal-spike quench process can be observed without the effects of thermal diffusion. In this paper, the development of a low temperature irradiation system and preliminary experimental results obtained using the system are discussed.

EXPERIMENTAL SET-UP

Low Temperature Irradiation System

The system reported here is the result of numerous evolutionary models that were investigated in order to perform irradiations under conditions that correspond to stage-I of the annealing stages. In our earlier experimental set-up, closed cycle refrigerator (CCR) was mounted vertically and copper braid was used for connecting sample holder and cold finger. Even though the cold finger temperature was 10K the minimum sample temperature that could be achieved was 120K. As a refinement, in the new set-up, the CCR was mounted horizontally and cold finger was oriented perpendicular to beam path (Figure 1). The irradiation system was assembled behind the UHV irradiation chamber.

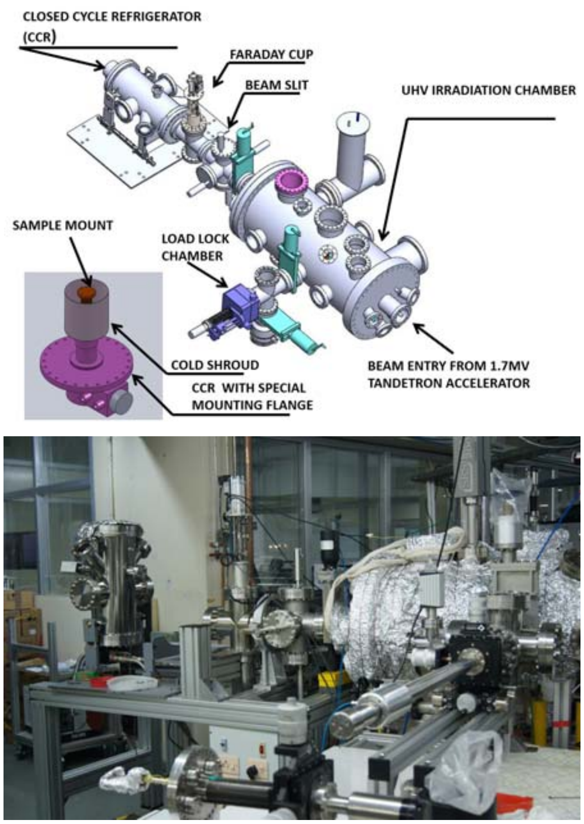

Figure 1. Schematic diagram and photograph (vertical sample-mounting condition) of the low temperature ion irradiation system at the experimental end-station of 1.7MV tandetron accelerator

CCR Mounted Irradiation Chamber

A chamber (SS 304) (length- 510 mm) with the end flange of DIN 200CF was fabricated with ports for beam viewing, light collection and vacuum monitoring. The back and front flat surfaces of the cylindrical chamber was connected to the CCR flange and DIN 200CF to DIN 100CF zero length flange, respectively. The centre of gravity of the combined system (CCR+ cylindrical chamber) is at 220 mm from back end of the chamber. At this point, a versatile hinge joint support (on both sides) was provided with locking pin arrangement at 0° and 90°. The hinge joint support allows the cylindrical chamber assembly to swing from 0° to 90°, between horizontal to vertical orientations. Thus facilitating sample mounting on the cold head of CCR. A quick-change cotter pin in the hinge provides a safety mechanism during sample mounting. After sample fixing the chamber assembly is swung to the horizontal orientation and allowed to rest in the front end supports. The front-end supports are inter connected with resting plate which allow an uniform resting of cylindrical chamber.

The front end supports (2 Nos.) and back end supports (2 Nos.) are made to slide on linear guide way with ball screw arrangement. This arrangement is made to rest on 10mm thick, base plate of dimensions, 650× 800mm. The base plate is made to rest on an Alstrut prefabricated structure of height 800 mm from the ground, having leveling screws for finer adjustments. The beamline height is 1250 mm from the floor level. The front and rear end supports have capability for vertical manipulation which ensures leveling the chamber to the beam line assembly.

The operational steps are enlisted below. After mounting the sample on the CCR cold head with the help of GE low temperature varnish in vertical position, the arrangement is made to swing to horizontal position. Subsequently, the adjustment of linear guide ways facilitates sliding of the assembly to match with the four- way cross chamber housing the Faraday cup. The chamber is locked in the position with the help of locking arrangement in the linear guide ways, ensuring safety. One of the four-way cross's ports serves as a pumping port for achieving vacuum in the system using turbo-molecular pumps. The temperature on the sample holder is measured using a silicon diode temperature sensor, the minimum temperature attained on the sample holder is 7K. A 1.4 MeV Ni^+ beam with a current density of 140 nA/cm^2 was incident on the sample holder for 6 hours; the sample temperature remained invariant at 10K, variation within ±10%.

A 150 kV gaseous ion accelerator with an ionoluminescence spectrometer installed in the beamlines is available at the laboratory. Given its simplicity, the system's transferability across experimental end-stations of other accelerators is straightforward, allowing it to broaden its experimental utility. In a previous report [2], we demonstrated the use of in-situ iono-luminescence studies to establish defect signatures in oxide constituents of ODS alloys under room temperature (RT) irradiations. The irradiation system allows for low temperature iono-luminescence investigations to examine the defect-complex generation during the quench of the thermal spike and evolution during annealing.

Results

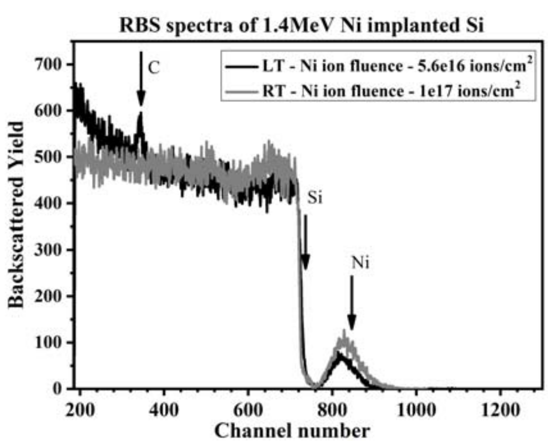

Figure 2. RBS spectra using 3.6 MeV He^{2+} recorded in Si samples implanted with 1.4 MeV Ni ions at room temperature and low temperature

While the system's effectiveness for the conduct of low-temperature irradiation has been evaluated, considering that the sample has been mounted on the cold-finger, it is important to estimate the impurities gettering of onto the sample surface. As reported these are known to influence the void nucleation and void swelling. Si samples were irradiated with 1.4 MeV Ni^{+} ions at RT and 10 K, to fluences of 1×10^{17} ions cm^{-2} and 5.6×10^{17} ions cm^{-2}, respectively. The Rutherford Backscattering Spectrometry (RBS) used to estimate the implanted Ni and impurity concentrations also served as dose-calibration of the system. The RBS spectra carried out using 3.6 MeV He^{2+} ions are shown in Figure 2. As observed, the carbon concentration is higher in the low temperature ion irradiated samples as compared to its counterpart irradiated to a higher Ni dose. Although the vacuum in the chamber prior to low-temperature cooling was ~ 2×10^{-8} mbar, the gettering of impurities on the cooled samples is a potential source of carbon contamination. A secondary liquid nitrogen trap in the chamber is a solution to this problem.

SUMMARY

A versatile low temperature ion irradiation system with ion implantation and in-situ ionoluminescence experiments capabilities has been developed. The system's effectiveness for the conduct of irradiation with enhanced temperature stability has been evaluated. The impurity concentrations measured by RBS show that the carbon buildup during RT implantation is indiscernible. On the contrary LT implantation showed carbon content, despite being carried out at vacuum levels an order or more better. A prospective solution to avoid carbon buildup is installation of a secondary liquid nitrogen trap in the chamber.

ACKNOWLEDGEMENT

The authors acknowledges the members of accelerator lab at IGCAR for their support

REFERENCES

1. S. Taller, G. Van Coevering, B. D. Wirth and G S. Was, Predicting structural material degradation in advanced nuclear reactors with ion irradiation, *Scientific reports*, Vol. 11, pp. 2949 (2021).
2. Sruthi Mohan, Gurpreet Kaur, S K Srivastava, P Magudapathy, C. David, G. Amarendra, Correlation between anion related defects and ion beam induced luminescence in $Y_4Zr_3O_{12}$, Appl. Phys. Lett. Vol. 119, pp. 031901 (2021)

Low Flux Heavy Ion irradiation Set up at BARC-TIFR Pelletron Accelerator

J. P. Nair[1]*, H. Sparrow[1], R. S. Worlikar[2], S. Chakraborthy[3], R. N. Lokare[1], M. L. Yadav[1], J. A. Gore[1], A. K. Gupta[1]

1. Nuclear Physics Division, Bhabha Atomic Research Center, Trombay, Mumbai
2. Pelletron Linac Facility, Tata Institute of Fundamental Research, Colaba, Mumbai
3. Electronic Division, Bhabha Atomic Research Center, Trombay, Mumbai

Abstract

Low flux of heavy ions is required for calibration of various detectors besides other potential irradiation applications. Ease of irradiation of multiple samples necessitates a sample changing mechanism compatible with ultra-high vacuum environment. In order to obtain a fluence of ~10^6 particles/cm^2, the particles need to be counted using detector and associated electronics. An amplifier coupled with pulse shaper and counter are employed for counting particles. A set up has been designed and developed in-house accordingly, to ensure irradiation of multiple samples as per the user requirements. Details of the set-up, sample changer, particle flux and fluence measurements along with its effective utilization shall be presented in this paper.

The samples were mounted in the irradiation chamber and changed remotely using a Rotary Vacuum feedthrough in combination with a video camera & monitor. Heavy ions from Pelletron Accelerator were scattered using gold foil and the scattered beam at +/-45^o ports was used for irradiation and monitoring, respectively. In the present work, scattered Lithium beam at 44 MeV from Pelletron was used for irradiation. Flux and fluence measurements were carried out at 45° mirror symmetry using PIN Diode detector and an Amplifier developed by Electronic Division, BARC. Six no. of samples can be loaded and changed remotely using a rotary vacuum feed-through without breaking vacuum.

Optically Stimulated Luminance Detectors (OSLDs) developed by RP&AD, BARC for dose measurements, to be utilised in space-based applications, were irradiated for various doses using this set up, successfully.

*jpnair@tifr.res.in

Introduction

Higher LET (Linear Energy Transfer) particles are needed to irradiate samples to deposit higher dose. Heavy ions because of their high Z deposit higher energy due to considerable energy loss in the samples. As heavy ion irradiation requires the samples should be in ultra-high vacuum sample changing requires venting air and re-establishing vacuum. A set up to get low flux heavy ions from the high flux pelletron beam are needed for controlled irradiation. Dose accumulated depends on particle energy loss and number of particles deposited in the sample for which particle particle flux (hence fluence) needs to be counted. Energy loss in the OSLD matrix was calculated using SRIM code. To achieve all the above requirements a set up was designed and fabricated in house. This set up was tested and employed as low flux heavy ion irradiation set up at BARC-TIFR Pelletron accelerator. The set up details testing and its u;tilisation is described in this paper.

Methodology

To get low flux of the order of 10^3, Lithium ions from Pelletron (of the order of 10^{10} particles) were scattered using Gold foil of 1.35 mg/cm^2 thickness. Scattered beam at +/-45^o were used for irradiation and measurements respectively.

Calculation

Angle Opening for 10 mm diameter at 28 cms:
TanΘ 1/28= 0.0357. Θ = 2.045^o Angle variation: 43^o-45^o-47^o
dΩ= A/l^2 = 3.14/256= 0.004.
[A= 3.14*1/4= 0.78cm^2 l= 28cms].
Energy variation at 10mm diameter for 44MeV Lithium:
43.215 MeV - 43.145 MeV - 43.073 MeV (for 43^o - 45^o – 47^o respectively)
Flux variation calculated is within 15-20%

Setup

A scattering chamber of 26cms diameter having 40KF ports at +/-45^{o} along with target ladder was fabricated.

Frequent changing of samples necessitates vacuum breaks which limits time available for irradiation. To overcome this, an irradiation chamber of 20 cms diameter to accommodate multiple samples for irradiation having 40KF port to mate with the scattering chamber was made. A gate valve was used between these chambers for isolating vacuum during sample changes.

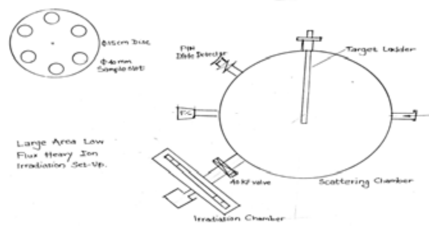

Schematic of the set up

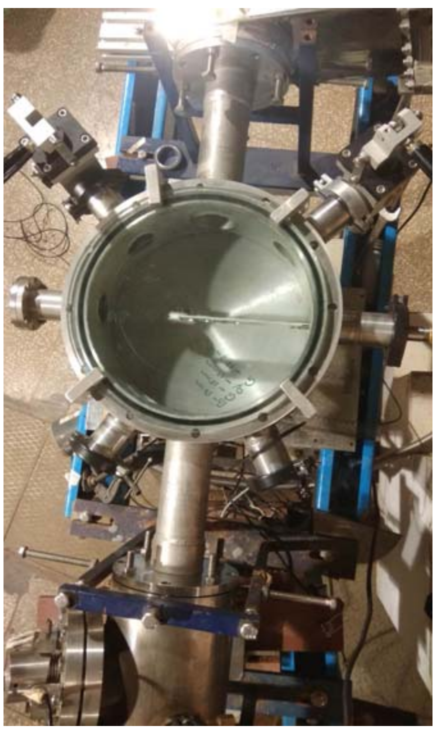

Scattering chamber with+/-45^{o} 40kF ports

The irradiation chamber can accommodate six samples and is provided with pumping port which is connected to a rotary vacuum. The irradiation chamber has a disc of 15 cms diameter having circular slots on which samples are mounted. Four samples of 5mm diameter was mounted in each disc, so that total width of samples will be in 10mm diameter. The samples are aligned to the 40 KF port for irradiation by rotation using a DC geared motor which is coupled to the disc via Vacuum Rotary Feed-through. The vacuum feed-through, couple rotary movement from DC motor in air to the disc in vacuum. The sample position can be viewed through a glass window on the irradiation chamber. A camera mounted on this glass window, with a monitor in the counting room facilitates remote changing of samples mounted inside the irradiation chamber.

Irradiation chamber with Rotary Vacuum Feedthrough and 40KF port

Samples mounted on disc to be fixed in the irradiation chamber

To measure the particle flux PIN diode (10mm X 10 mm) detectors supplied by Electronic Division, BARC was used. A stand-alone electronic module comprising Bias supply, Pre amplifier, Amplifier and Digitiser to facilitate counting of particles was developed by Electronic Division, BARC, exclusively for this purpose.

PIN diode detector and Amplifier module Supplied by Electronic Division, BARC

A block diagram showing the various features of the amplifier module is shown below. PIN diode detector and counter were connected from the module.

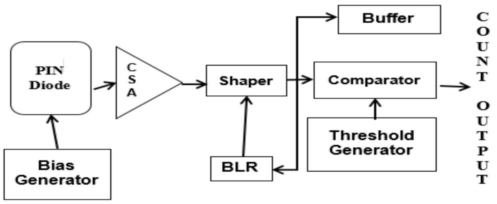

Block diagram of electronic module

This scattering and irradiation chambers were tested for UHV compatibility and mock trials of sample changing were carried out. The electronic module with PIN diode detector was tested for performance. Satisfactory trials of the set up lead to irradiation of OSLDs for Dose calibration by Radiation Physics and Advisory Division, BARC for their space based applications.

Results

The disc with samples were loaded multiple times for irradiation. The vacuum rotary feed-through based sample changing system worked successfully and 52 samples were irradiated using this set up. Particle flux maintained unchanged and estimated fluence was achieved by varying time of irradiation. The doses were calculated based on energy deposited by Lithium ion and the particle fluence accumulated in the samples. Doses estimated from calculations were 20 milliGrays to 200 milliGrays.

Conclusions and future scope

Low flux heavy ion irradiation set up was successfully fabricated in house, tested and was used by Radiation Physics and Advisory Division for testing of Optically Stimulated Luminance Detectors (OSLD). The energy response of detectors were found to be linear. Modifications in the set up to accommodate large number of samples to optimise allotted beam time more for irradiation will be taken up.

Acknowledgements

We sincerely thank valuable and whole hearted support of Pelletron and Linac staff of the facility. We also appreciate support extended by TIFR work shop for all the fabrication.